

Pertanika Journal of
**SCIENCE &
TECHNOLOGY**

JST

VOL. 25 (S) JUL. 2017

A special issue devoted to
Advances in Science & Technology Research

Guest Editors
Aidah Jumahat, Muhammad Fairuz Azmi & Anizah Kalam



PERTANIKA
JOURNALS

A scientific journal published by Universiti Putra Malaysia Press

Journal of Science & Technology

About the Journal

Overview

Pertanika Journal of Science & Technology (JST) is the official journal of Universiti Putra Malaysia published by UPM Press. It is an open-access online scientific journal which is free of charge. It publishes the scientific outputs. It neither accepts nor commissions third party content.

Recognized internationally as the leading peer-reviewed interdisciplinary journal devoted to the publication of original papers, it serves as a forum for practical approaches to improving quality in issues pertaining to science and engineering and its related fields.

JST is a **quarterly** (January, April, July and October) periodical that considers for publication original articles as per its scope. The journal publishes in **English** and it is open to authors around the world regardless of the nationality.

The Journal is available world-wide.

Aims and scope

Pertanika Journal of Science and Technology aims to provide a forum for high quality research related to science and engineering research. Areas relevant to the scope of the journal include: bioinformatics, bioscience, biotechnology and bio-molecular sciences, chemistry, computer science, ecology, engineering, engineering design, environmental control and management, mathematics and statistics, medicine and health sciences, nanotechnology, physics, safety and emergency management, and related fields of study.

History

Pertanika was founded in 1978. A decision was made in 1992 to streamline Pertanika into three journals as Journal of Tropical Agricultural Science, Journal of Science & Technology, and Journal of Social Sciences & Humanities to meet the need for specialised journals in areas of study aligned with the interdisciplinary strengths of the university.

After almost 25 years, as an interdisciplinary Journal of Science & Technology, the revamped journal now focuses on research in science and engineering and its related fields.

Goal of *Pertanika*

Our goal is to bring the highest quality research to the widest possible audience.

Quality

We aim for excellence, sustained by a responsible and professional approach to journal publishing. Submissions are guaranteed to receive a decision within 14 weeks. The elapsed time from submission to publication for the articles averages 5-6 months.

Abstracting and indexing of *Pertanika*

Pertanika is almost **40 years old**; this accumulated knowledge has resulted in Pertanika JST being abstracted and indexed in **SCOPUS** (Elsevier), Clarivate Analytics [*formerly known as Thomson (ISI)*] **Web of Science™ Core Collection** Emerging Sources Citation Index (ESCI). Web of Knowledge [BIOSIS & CAB Abstracts], **EBSCO** and EBSCOhost, **DOAJ**, **ERA**, **Google Scholar**, **TIB**, **MyCite**, Islamic World Science Citation Center (ISC), ASEAN Citation Index (ACI), **Cabell's Directories** & Journal Guide.

Future vision

We are continuously improving access to our journal archives, content, and research services. We have the drive to realise exciting new horizons that will benefit not only the academic community, but society itself.

Citing journal articles

The abbreviation for Pertanika Journal of Science & Technology is *Pertanika J. Sci. Technol.*

Publication policy

Pertanika policy prohibits an author from submitting the same manuscript for concurrent consideration by two or more publications. It prohibits as well publication of any manuscript that has already been published either in whole or substantial part elsewhere. It also does not permit publication of manuscript that has been published in full in Proceedings.

Code of Ethics

The Pertanika Journals and Universiti Putra Malaysia takes seriously the responsibility of all of its journal publications to reflect the highest in publication ethics. Thus all journals and journal editors are expected to abide by the Journal's codes of ethics. Refer to Pertanika's **Code of Ethics** for full details, or visit the Journal's web link at http://www.pertanika.upm.edu.my/code_of_ethics.php

International Standard Serial Number (ISSN)

An ISSN is an 8-digit code used to identify periodicals such as journals of all kinds and on all media—print and electronic. All Pertanika journals have ISSN as well as an e-ISSN.

Journal of Science & Technology: ISSN 0128-7680 (*Print*); ISSN 2231-8526 (*Online*).

Lag time

A decision on acceptance or rejection of a manuscript is reached in 3 to 4 months (average 14 weeks). The elapsed time from submission to publication for the articles averages 5-6 months.

Authorship

Authors are not permitted to add or remove any names from the authorship provided at the time of initial submission without the consent of the Journal's Chief Executive Editor.

Manuscript preparation

Refer to Pertanika's **INSTRUCTIONS TO AUTHORS** at the back of this journal.

Most scientific papers are prepared according to a format called IMRAD. The term represents the first letters of the words **I**ntroduction, **M**aterials and **M**ethods, **R**esults, **A**nd, **D**iscussion. IMRAD is simply a more 'defined' version of the "IBC" [Introduction, Body, Conclusion] format used for all academic writing. IMRAD indicates a pattern or format rather than a complete list of headings or components of research papers; the missing parts of a paper are: *Title*, *Authors*, *Keywords*, *Abstract*, *Conclusions*, and *References*. Additionally, some papers include Acknowledgments and Appendices.

The *Introduction* explains the scope and objective of the study in the light of current knowledge on the subject; the *Materials and Methods* describes how the study was conducted; the *Results* section reports what was found in the study; and the *Discussion* section explains meaning and significance of the results and provides suggestions for future directions of research. The manuscript must be prepared according to the Journal's **INSTRUCTIONS TO AUTHORS**.

Editorial process

Authors are notified with an acknowledgement containing a *Manuscript ID* on receipt of a manuscript, and upon the editorial decision regarding publication.

Pertanika follows a **double-blind peer-review** process. Manuscripts deemed suitable for publication are usually sent to reviewers. Authors are encouraged to suggest names of at least three potential reviewers at the time of submission of their manuscript to Pertanika, but the editors will make the final choice. The editors are not, however, bound by these suggestions.

Notification of the editorial decision is usually provided within ten to fourteen weeks from the receipt of manuscript. Publication of solicited manuscripts is not guaranteed. In most cases, manuscripts are accepted conditionally, pending an author's revision of the material.

As articles are double-blind reviewed, material that might identify authorship of the paper should be placed only on page 2 as described in the first-4 page format in Pertanika's **INSTRUCTIONS TO AUTHORS** given at the back of this journal.

The Journal's peer-review

In the peer-review process, three referees independently evaluate the scientific quality of the submitted manuscripts.

Peer reviewers are experts chosen by journal editors to provide written assessment of the **strengths** and **weaknesses** of written research, with the aim of improving the reporting of research and identifying the most appropriate and highest quality material for the journal.

Operating and review process

What happens to a manuscript once it is submitted to *Pertanika*? Typically, there are seven steps to the editorial review process:

1. The Journal's chief executive editor and the editorial board examine the paper to determine whether it is appropriate for the journal and should be reviewed. If not appropriate, the manuscript is rejected outright and the author is informed.
2. The chief executive editor sends the article-identifying information having been removed, to three reviewers. Typically, one of these is from the Journal's editorial board. Others are specialists in the subject matter represented by the article. The chief executive editor asks them to complete the review in three weeks.

Comments to authors are about the appropriateness and adequacy of the theoretical or conceptual framework, literature review, method, results and discussion, and conclusions. Reviewers often include suggestions for strengthening of the manuscript. Comments to the editor are in the nature of the significance of the work and its potential contribution to the literature.

3. The chief executive editor, in consultation with the editor-in-chief, examines the reviews and decides whether to reject the manuscript, invite the author(s) to revise and resubmit the manuscript, or seek additional reviews. Final acceptance or rejection rests with the Editor-in-Chief, who reserves the right to refuse any material for publication. In rare instances, the manuscript is accepted with almost no revision. Almost without exception, reviewers' comments (to the author) are forwarded to the author. If a revision is indicated, the editor provides guidelines for attending to the reviewers' suggestions and perhaps additional advice about revising the manuscript.

4. The authors decide whether and how to address the reviewers' comments and criticisms and the editor's concerns. The authors return a revised version of the paper to the chief executive editor along with specific information describing how they have answered' the concerns of the reviewers and the editor, usually in a tabular form. The author(s) may also submit a rebuttal if there is a need especially when the author disagrees with certain comments provided by reviewer(s).
5. The chief executive editor sends the revised paper out for re-review. Typically, at least one of the original reviewers will be asked to examine the article.
6. When the reviewers have completed their work, the chief executive editor in consultation with the editorial board and the editor-in-chief examine their comments and decide whether the paper is ready to be published, needs another round of revisions, or should be rejected.
7. If the decision is to accept, an acceptance letter is sent to all the author(s), the paper is sent to the Press. The article should appear in print in approximately three months.

The Publisher ensures that the paper adheres to the correct style (in-text citations, the reference list, and tables are typical areas of concern, clarity, and grammar). The authors are asked to respond to any minor queries by the Publisher. Following these corrections, page proofs are mailed to the corresponding authors for their final approval. At this point, **only essential changes are accepted**. Finally, the article appears in the pages of the Journal and is posted on-line.



Pertanika Journal of

**SCIENCE &
TECHNOLOGY**

A special issue devoted to
Advances in Science & Technology Research

Vol. 25 (S) Jul. 2017
(Special Edition)

Guest Editors
Aidah Jumahat, Muhammad Fairuz Azmi & Anizah Kalam

A scientific journal published by Universiti Putra Malaysia Press



EDITOR-IN-CHIEF**Mohd Adzir Mahdi***Physics, Optical Communications***CHIEF EXECUTIVE EDITOR****Nayan Deep S. Kanwal***Environmental Issues – Landscape Plant Modelling Applications***UNIVERSITY PUBLICATIONS COMMITTEE****Husaini Omar, Chair****EDITORIAL STAFF****Journal Officers:**Kanagamalar Silvarajoo, *ScholarOne*Tee Syin-Ying, *ScholarOne***Editorial Assistants:**

Zulinaardawati Kamarudin

Florence Jiyom

Ummi Fairuz Hanapi

COPY EDITORS

Doreen Dillah

Crescentia Morais

Pooja Terasha Stanslas

PRODUCTION STAFF**Pre-press Officers:**

Kanagamalar Silvarajoo

Nur Farrah Dila Ismail

Layout & Typeset:

Wong Wai Mann

WEBMASTER

Mohd Nazri Othman

PUBLICITY & PRESS RELEASEMagdalene Pokar (*ResearchSEA*)

Florence Jiyom

EDITORIAL OFFICE**JOURNAL DIVISION**

Office of the Deputy Vice Chancellor (R&I)

1st Floor, IDEA Tower II

UPM-MTDC Technology Centre

Universiti Putra Malaysia

43400 Serdang, Selangor Malaysia.

Gen Enq.: +603 8946 1622 | 1616

E-mail: executive_editor.pertanika@upm.myURL: www.journals-jd.upm.edu.my**PUBLISHER**

Kamariah Mohd Saidin

UPM Press

Universiti Putra Malaysia

43400 UPM, Serdang, Selangor, Malaysia.

Tel: +603 8946 8855, 8946 8854

Fax: +603 8941 6172

E-mail: penerbit@putra.upm.edu.myURL: <http://penerbit.upm.edu.my>**EDITORIAL BOARD****2015-2017****Abdul Halim Shaari***Superconductivity and Magnetism, Universiti Putra Malaysia, Malaysia.***Adem Kilicman***Mathematical Sciences, Universiti Putra Malaysia, Malaysia.***Ahmad Makmom Abdullah***Ecophysiology and Air Pollution Modelling, Universiti Putra Malaysia, Malaysia.***Ali A. Moosavi-Movahedi***Biophysical Chemistry, University of Tehran, Tehran, Iran.***Amu Therwath***Oncology, Molecular Biology, Université Paris, France.***Angelina Chin***Mathematics, Group Theory and Generalisations, Ring Theory, University of Malaya, Malaysia.***Bassim H. Hameed***Chemical Engineering: Reaction Engineering, Environmental Catalysis & Adsorption, Universiti Sains Malaysia, Malaysia.***Biswa Mohan Biswal***Medical, Clinical Oncology, Radiotherapy, Universiti Sains Malaysia, Malaysia.***Christopher G. Jesudason***Mathematical Chemistry, Molecular Dynamics Simulations, Thermodynamics and General Physical Theory, University of Malaya, Malaysia.***Hari M. Srivastava***Mathematics and Statistics, University of Victoria, Canada.***Ivan D. Rukhlenko***Nonlinear Optics, Silicon Photonics, Plasmonics and Nanotechnology, Monash University, Australia.***Kaniraj R. Shenbaga***Geotechnical Engineering, Universiti Malaysia Sarawak, Malaysia.***Kanury Rao***Senior Scientist & Head, Immunology Group, International Center for Genetic Engineering and Biotechnology, Immunology, Infectious Disease Biology and System Biology, International Centre for Genetic Engineering & Biotechnology, New Delhi, India.***Karen Ann Crouse***Chemistry, Material Chemistry, Metal Complexes – Synthesis, Reactivity, Bioactivity, Universiti Putra Malaysia, Malaysia.***Ki-Hyung Kim***Computer and Wireless Sensor Networks, AIOU University, Korea.***Kunnawee Kanitpong***Transportation Engineering-Road Traffic Safety, Highway Materials and Construction, Asian Institute of Technology, Thailand.***Megat Mohd Hamdan***Megat Ahmad Mechanical and Manufacturing Engineering, Universiti Pertahanan Nasional Malaysia, Malaysia.***Mirnalini Kandiah***Public Health Nutrition, Nutritional Epidemiology, UCSI University, Malaysia.***Mohamed Othman***Communication Technology and Network, Scientific Computing, Universiti Putra Malaysia, Malaysia.***Mohd. Ali Hassan***Bioprocess Engineering, Environmental Biotechnology, Universiti Putra Malaysia, Malaysia.***Mohd Sapuan Salit***Concurrent Engineering and Composite Materials, Universiti Putra Malaysia, Malaysia.***Narongrit Sombatsompop***Engineering & Technology: Materials and Polymer Research, King Mongkut's University of Technology Thonburi (KMUTT), Thailand.***Prakash C. Sinha***Physical Oceanography, Mathematical Modelling, Fluid Mechanics, Numerical Techniques, Universiti Malaysia Terengganu, Malaysia.***Rajinder Singh***Biotechnology, Biomolecular Sciences, Molecular Markers/ Genetic Mapping, Malaysia Palm Oil Board, Kajang, Malaysia.***Renuganth Varatharajoo***Engineering, Space System, Universiti Putra Malaysia, Malaysia.***Riyanto T. Bambang***Electrical Engineering, Control, Intelligent Systems & Robotics, Bandung Institute of Technology, Indonesia.***Sabira Khatun***Engineering, Computer Systems & Software Engineering, Applied Mathematics, Universiti Malaysia Pahang, Malaysia.***Shiv Dutt Gupta***Director, IHMR, Health Management, Public Health, Epidemiology, Chronic and Non-communicable Diseases, Indian Institute of Health Management Research, India.***Suan-Choo Cheah***Biotechnology, Plant Molecular Biology, Asiatic Centre for Genome Technology (ACGT), Kuala Lumpur, Malaysia.***Wagar Asrar***Engineering, Computational Fluid Dynamics, Experimental Aerodynamics, International Islamic University, Malaysia.***Wing Keong Ng***Aquaculture, Aquatic Animal Nutrition, Aqua Feed Technology, Universiti Sains Malaysia, Malaysia.***Yudi Samyudia***Chemical Engineering, Advanced Process Engineering, Curtin University of Technology, Malaysia.***INTERNATIONAL ADVISORY BOARD****2017-2019****Adarsh Sandhu***Editorial Consultant for Nature Nanotechnology and Contributing Writer for Nature Photonics, Physics, Magnetoresistive Semiconducting Magnetic Field Sensors, Nano-Bio-Magnetism, Magnetic Particle Colloids, Point of Care Diagnostics, Medical Physics, Scanning Hall Probe Microscopy, Synthesis and Application of Graphene, Electronics-Inspired Interdisciplinary Research Institute (EIIRIS), Toyohashi University of Technology, Japan.***Graham Megson***Computer Science, The University of Westminster, U.K.***Kuan-Chong Ting***Agricultural and Biological Engineering, University of Illinois at Urbana-Champaign, USA.***Malin Premaratne***Advanced Computing and Simulation, Monash University, Australia.***Mohammed Ismail Elnaggar***Electrical Engineering, Ohio State University, USA.***Peter G. Alderson***Bioscience, The University of Nottingham, Malaysia Campus.***Peter J. Heggs***Chemical Engineering, University of Leeds, U.K.***Ravi Prakash***Vice Chancellor, JUIT, Mechanical Engineering, Machine Design, Biomedical and Materials Science, Jaypee University of Information Technology, India.***Said S.E.H. Elnashaie***Environmental and Sustainable Engineering, Penn. State University at Harrisburg, USA.***Suhash Chandra Dutta Roy***Electrical Engineering, Indian Institute of Technology (IIT) Delhi, India.***Vijay Arora***Quantum and Nano-Engineering Processes, Wilkes University, USA.***Yi Li***Chemistry, Photochemical Studies, Organic Compounds, Chemical Engineering, Chinese Academy of Sciences, Beijing, China.***ABSTRACTING/INDEXING**

Pertanika is now over 40 years old; this accumulated knowledge has resulted the journals being indexed in abstracted in SCOPUS (Elsevier), Web of Science Core Collection (formerly ISI) [ESCI, BIOSIS & CAB Abstracts], EBSCO & EBSCOhost, ERA, DOAJ, AGRICOLA (National Agric. Library, USA), Cabell's Directories, Google Scholar, MyAIS, Islamic World Science Citation Center (ISC), ASEAN Citation Index (ACI) & Rubriq (Journal Guide).



The publisher of *Pertanika* will not be responsible for the statements made by the authors in any articles published in the journal. Under no circumstances will the publisher of this publication be liable for any loss or damage caused by your reliance on the advice, opinion or information obtained either explicitly or implied through the contents of this publication.

All rights of reproduction are reserved in respect of all papers, articles, illustrations, etc., published in *Pertanika*. *Pertanika* provides free access to the full text of research articles for anyone, web-wide. It does not charge either its authors or author-institution for refereeing/publishing outgoing articles or user-institution for accessing incoming articles.

No material published in *Pertanika* may be reproduced or stored on microfilm or in electronic, optical or magnetic form without the written authorization of the Publisher.

Copyright © 2017 Universiti Putra Malaysia Press. All Rights Reserved.



Preface

We are pleased to present this special issue of Volume 3 *Pertanika Journal of Science and Technology (JST)* which is a compilation of selected papers presented at the 3rd International Conference on Science and Social Research (CSSR2016). The CSSR2016 was held on the 6th – 7th December 2016 in Putrajaya, Malaysia. The theme of the conference was “Waves of Interdisciplinary Research”. It covers multi-disciplinary research areas from science and technology to social science and humanities. The conference track is divided into three major areas: Track 1: Engineering, Science & Technology; Track 2: Clinical & Health sciences; and Track 3: Arts, Humanities & Social sciences. All the papers submitted to CSSR2016 were subjected to rigorous peer reviewing process to ensure quality and consistency before they were accepted for presentation.

A total of 188 papers in Track 1 (Engineering, Science & Technology) and Track 2 (Clinical & Health sciences) were presented during the conference, 29 of which were accepted for publication in this special issue. The theme of the special issue is “Advances in Science and Technology Research” which covers the following topics: Chemical Engineering, Signal processing, Water and Wastewater Treatment Technology, Algae Biotechnology, Clinical Epidemiology, Control System Engineering, Chemical Sciences, Infrastructural Engineering, Air-Conditioning System, Metals and Metal Alloy Materials, Inorganic Chemistry, Organic Waste Treatment, Robotic and Automation, Solar Energy, Tissue Culture, Power Engineering, Agriculture Engineering, Health Systems Management, Electrical Engineering, Chemical Science, Environment Science, Civil, Materials and Mechanical Engineering.

We would like to thank the contributors as well as the reviewers for their commitment and patience which made this publication a success. We hope this would encourage researchers from around the world to be more active in publishing their research output, in particular good quality science and technology papers, that would be useful for academics and practitioners alike. Special thanks to the Chief Executive Editor, UPM Journals, Dr. Nayan Kanwal, and the journal division staff for their guidance and support in making this issue possible.

Guest Editors:

Aidah Jumahat (*Assoc. Prof. Dr.*)

Muhammad Fairuz Azmi (*Dr.*)

Anizah Kalam (*Dr.*)

July 2017



Pertanika Journal of Science & Technology
Vol. 25 (S) Jul. 2017

Contents

Advances in Science & Technology Research

- Analysis of Agarwood Smoke Chemical Compounds using Solvent Trap, GC-FID and GC-MS 1
Nurlaila Ismail, Mastura Ibrahim, Seema Zareen, Mohd Hezri Fazalul Rahiman, Saiful Nizam Tajuddin and Mohd Nasir Taib
- Ammonia Nitrogen Adsorption using Spent Mushroom Substrate Biochar (SMSB) 9
Siti Fatimah Halim Soon Kong Yong and Chia Chay Tay
- Isolation and Adaptation of Diatoms in a New Formulated Enriched MediumS 21
Syafiq Hayati Mohd Ali, Khairul Adzfa Radzun and Norazlina Ahmad
- Low- Glycaemic Index Diet to Improve Dietary Intake among Women with Gestational Diabetes Mellitus 31
Farhanah, A. S., Barakatun Nisak, M. Y., Zalilah, M. S. and Nor Azlin, M. I.
- The Effect of Varying PID Gains on Position Transient Response of a Robotic Hand System 43
Salleh, N. M., Shauri, R. L. A., Nasir, K., Remeli, N. H. and Kamal, M. M.
- Classification of Car Paint Primers Using Pyrolysis-Gas Chromatography-Mass Spectrometry (Py-GC-MS) and Chemometric Techniques 53
Raja Zubaidah Raja Sabaradin, Norashikin Saim, Rozita Osman and Hafizan Juahir
- Experimental Study on Bearing Strength of Concrete Blocks under Concentric Compression Load 67
Mohd Raizamzamani Md Zain and Norrul Azmi Yahya
- Computational Simulation of Indoor Thermal Environment in a Tropical Educational Hall with Displacement Ventilation 77
Qi Jie Kwong, Hon Fai Chen and Azli Abd Razak
- Microstructure and Mechanical Properties of Hybrid Super ElasticNiTi Alloy with Steel Rebar for Reinforced Concrete Beam 89
Nubailah Abd. Hamid, Muhammad Akmal Ahmad Shazalli, Muhammad Hussain Ismail and Azmi Ibrahim

Optimisation of Biomethane Production by Anaerobic Digestion of Food Waste	101
<i>Nurul Shahida Osman, Zainon Mohd Noor, Zatilfarihiah Rasdi, Iwana Izni Zainuddin and Noor Azrimi Umor</i>	
Effects of Varying Impedance Parameters for Position-based Impedance Control of A Three-fingered Robot	111
<i>Nasir, K., Shauri, R. L. A., Salleh, N. M. and Remeli, N. H.</i>	
Concentrated Solar Thermal Thermoelectric Power Generation under Natural and Forced Convection Cooling	123
<i>Dee, S., Singh, B., Remeli, M. F., Tan, L. and Oberoi, A.</i>	
Somatic Embryogenesis in Sugar Palm (<i>Arenga pinnata</i> Wurm Merr.) from Zygotic Embryo Explants	133
<i>Nazatul Asikin Muda and Asmah Awal</i>	
Synchronisation of Output Voltage Waveforms in Phase Synchronous inverter with LCL Filter for Smart Grid Systems	145
<i>Tawfikur Rahman, M. I. Ibrahimy and S. M. A. Motakabber</i>	
Physico-chemical Properties of Residual Oil Extracted from Oil Palm Decanter Cake	157
<i>Suhaini Raeze, Alawi Sulaiman, Azhari Samsu Baharuddin, Mohd Noriznan Mokhtar and Zainuri Busu</i>	
Determinants of Patient's Satisfaction towards Hospital Services in a Specialist Centre	169
<i>Siti Munira Yasin, Nazri Syamil Abdull Latip, Farnaza Ariffin, Hilwati Hashim and Mazlifah Omar</i>	
Design of Perfect Tracking Self-Tuning Fuzzy PID Controller with Reference Model	179
<i>Nur Sakinah Abdul Aziz, Mazidah Tajjudin and Ramli Adnan</i>	
Synthesis and Corrosion Inhibition Studies of N-((4 and 3-chlorophenyl) carbamothioyl) Benzamide in 1M H ₂ SO ₄	189
<i>Norsakina Zurina Zulkifli, Karimah Kassim and Nurul Atikah Nordin</i>	
Effect of Operating Parameters on Decolourisation of Palm Oil Mill Effluent (POME) using Electrocoagulation Process	197
<i>Nur Syuhaidah Mohd Aris, Shariff Che Ibrahim, Borhannuddin Arifin and Yahaya Hawari</i>	
The Impact of Vegetation on the Local Variations of Rainfall	207
<i>Rohayu Haron Narashid, Ruslan Rainis and Zulyadini A. Rahaman</i>	
Evaluation of Cold In-Place Recycling Mix using Polymer Modified Asphalt Emulsion	219
<i>Mohd Izzat Asyraf Mohamad Kamal, Ahmad Kamil Arshad and Juraidah Ahmad</i>	

CFD Analysis on Indoor Temperature and Velocity: Effects of Incident Wind Angle and Outlet Position <i>Ali, N. M., Abd Razak, A., Mohamad, M. F. and Bahsan, R.</i>	227
Investigation of the Injection Moulding Plastic Flows Behaviour of PETCylindrical Containers with Multiple-Cavity Mould <i>Najiy Rizal Suriani Rizal, Muhammad Ameer Rosman, Aidah Jumahat and Noriah Yusoff</i>	239
Equivalent Dose Measurements from Digital Intra- and Extra- Oral Imaging Examinations <i>Norfariha Che Mohamed, Hapizah Nawawi, Mohd Yusmiadil Putera Mohd Yusof and Khoo Kok Siong</i>	251
Impact of Container, Temperature and Microcarriers on Inflammation and Endothelial Activation in Human Endothelial Cells <i>Muid, S., Froemming, G. R. A., Ali, A. M. and Nawawi, H.</i>	263
Low-Density Lipoprotein Concentration is an Independent Predictor for Oxidised LDL in Patients with Familial Hypercholesterolaemia <i>Nur Suhana Hamzan, Radzi Rahmat, Hapizah Mohd Nawawi and Thuhairah Hasrah Abdul Rahman</i>	275
Ceiling Geometry and Daylighting Performance of Side Lit Historical Museum Galleries UnderTropical Overcast Sky Condition <i>Sabarinah Sh Ahmad, Noraini Ahmad and Anuar Talib</i>	287
Tensile and Compressive Properties of Unidirectional <i>Arenga Pinnata</i> Fibre Reinforced Epoxy Composite <i>Aidah Jumahat, Muhamad Faris Syafiq Khalid, Zuraidah Salleh and Mohammad Jawaaid</i>	299
Hole Size Effects on the Open Hole Tensile Properties of Woven Kevlar-Glass Fibre Hybrid Composite Laminates <i>Norazean Shaari and Aidah Jumahat</i>	309





Analysis of Agarwood Smoke Chemical Compounds using Solvent Trap, GC-FID and GC-MS

Nurlaila Ismail^{1*}, Mastura Ibrahim², Seema Zareen²,
Mohd Hezri Fazalul Rahiman¹, Saiful Nizam Tajuddin² and Mohd Nasir Taib¹

¹Faculty of Electrical Engineering, Universiti Teknologi MARA (UiTM), 40450 Shah Alam, Selangor, Malaysia

²Faculty of Industrial Science and Technology, Universiti Malaysia Pahang (UMP), 26300 Gambang, Pahang, Malaysia

ABSTRACT

Agarwood or gaharu, due to its unique scent and quality is considered one of the most expensive wood in the world. This paper uses solvent trap, Gas Chromatography-Flame Ionization Detector (GC-FID) and Gas Chromatography-Mass Spectrometry (GC-MS) to establish agarwood quality, and is part of ongoing research. The result showed that monoterpenes hydrocarbon, sesquiterpenes hydrocarbon and oxygenated sesquiterpene contribute to agarwood smoke. Among many compounds extracted, 2-hydroxy-benzaldehyde, β -selinene and guaia-1(10),11-dien-15,2-olide were found dominant in monoterpenes hydrocarbon, sesquiterpenes hydrocarbon and oxygenated sesquiterpenes respectively. This finding pointed to the utility of solvent trap in extracting chemical compounds of agarwood smoke. This study is also useful for further research on establishing the grade of agarwood.

Keywords: Agarwood, GC-FID, GC-MS, Quality, solvent trap

ARTICLE INFO

Article history:

Received: 05 January 2017

Accepted: 17 January 2017

E-mail addresses:

nurlaila@ieee.org (Nurlaila Ismail),

seema@ump.edu.my (Seema Zareen),

hezrif@salam.uitm.edu.my (Mohd Hezri Fazalul Rahiman),

saifulnizam@ump.edu.my (Saiful Nizam Tajuddin),

dr.nasir@ieee.org (Mohd Nasir Taib)

*Corresponding Author

INTRODUCTION

Agarwood or Gaharu is known as Woods of God due to its unique scent (Hamid, 2011). Agarwood has been widely used as incense, and as an ingredient in perfumes, during religious ceremony and in traditional medical preparation. In the Middle East, agarwood is burnt during weddings and as a symbol of wealth. Due to that, agarwood is in high demand and one of the most expensive woods in the world. Agarwood and its essential oil are considered premium and prices are based

on their quality (Hamid, 2011; Naef, 2011). The price for top grade oil ranges between USD126 and USD633 per tola or 12 cm³ and for high quality wood, it is approximately USD30000 per kg (Jayachandran, Sekar, Parthiban, Amirtham, & Suresh, 2014; Lias, Ali, Jamil, Zainal, & Ab Ghani, 2015).

Traditionally, agarwood is graded based on its physical appearance such as colour and odour (Nor Azah et al., 2008). An agarwood which is dark and black, as well as having strong and lasting odour is considered high quality. This is based on human perception through visual observation and smell; in short, based on human experiences. This method has limitations as highlighted by Hidayat, Shakaff, Ahmad, and Adom (2010) in which the sense of smell weakens when dealing with many samples at the same time, resulting in grades being inconsistent (Hidayat et al., 2010).

The solvent trap is one of the extraction methods where hexane and ethyl acetate solvent are used to dissolve agarwood smoke (Ishihara, Tsuneya, & Uneyama, 1993). A previous study discovered the volatile compounds from smoke using TENAX TA sampling tube with solvent hexane to dissolve smoke (Ishihara, Tsuneya, & Uneyama, 1993). In the study, cluster of sesquiterpene group and aromatic compounds were detected. This technique was applied to determine the active volatile compounds in the smoke and headspace volatiles from *Cryptomeria* species *Japonica* (Yamada & Yatagai, 2007).

Researchers from Japan revealed that agarwood is a mixture of monoterpenes, sesquiterpenes and its chromone derivatives (Ishihara, Tsuneya, & Uneyama, 1993; Espinoza et al., 2014). In their studies, Gas Chromatography – Mass Spectrometry (GC-MS) technique was used to characterise the chemical composition of agarwood high (Kanankoh) and low (Jinkoh) quality. Some of the compounds were guaia-1(10),11-dien-15-al, benzaldehyde, β -agarofuran, and epoxybulnese (Ishihara, Tsuneya, & Uneyama, 1993; Yamada & Yatagai, 2007). Furthermore, methods used to extract the agarwood and its oil also affect the results of extraction. In 2013, Espinoza et al. found 2-(2-phenylethyl) chromones using direct analysis in real time and time of-flight mass spectrometry (DART-TOFMS). On the other hand, dry Gas – Chromatography (GC) and preparative Thin Layer Chromatograph (TLC) were performed by Yoshii et al. and found out that agarospirol, agarol and agarofurans in their agarwood samples (Espinoza et al., 2014). Several researchers agreed that Gas Chromatography – Flame Ionization Detector (GC-FID) and GC-MS are the most common analytical methods to identify the agarwood compounds (Marriott, Shellie, & Cornwell, 2001; Pripdeevech, Khummueng, & Park, 2011; Tajuddin & Yusoff, 2010). The analysis was conducted especially in 12 tabulated guaia-1(10),11-dien-15-ol, karanone, jinkoheremol and isoamyl dodecanoate as major compounds. Generally, it can be said that the compounds are varied accordingly to extraction, identification as well as quality of the agarwood.

MATERIALS AND METHOD

Agarwood chipwood used in this study was obtained from Faculty of Industrial Sciences and Technology, Universiti Malaysia Pahang (UMP), Pahang. Low and high-quality samples were

purchased from an authorised agarwood dealer in Kelantan and commercial samples were purchased from a local supplier, Konsesi Utama Sdn. Bhd. All samples were prepared in dry conditions. They were then ground and baked in an oven at a temperature of 40°C until a constant weight was achieved.

Solvent trap extraction: Each sample was burnt under inverted glass funnel and which allows the smoke to stream through a passage. Later, using an electric pump, the smoke was extracted and eventually dissolved as shown in Figure 1. The duration of the extraction was 30 minutes and hexane was used as solvent.

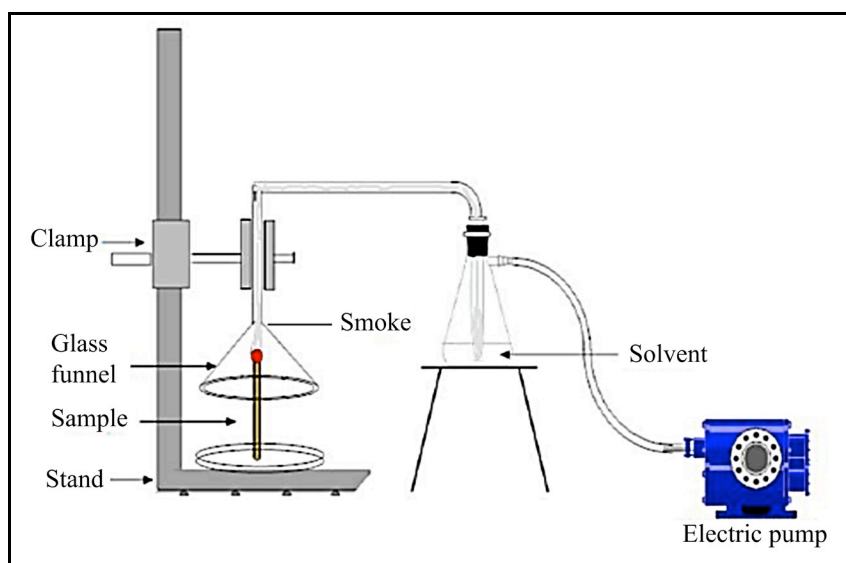


Figure 1. Schematic diagram of solvent trap (Mastura, 2014)

All samples in this study were analysed using the GC-MS and GF-FID. The analysis was completed using the experiment parameters of DM-1MS for column with 30 m length, 0.25 mm diameter and 0.25 μm film thicknesses. After that, 1 μL was injected into sample with the split ratio of 1:5.

The compounds were identified by comparing their retention indices (RI) with published data. Retention Indices or Kovats Index were calculated using a linear hydrocarbon (C8 – C22) as stated in study by Joulain and Konig, 1998.

RESULTS AND DISCUSSION

Table 1 shows the chemical composition of high, low and commercial types of agarwood in hexane solvent trap. The table lists a total of 27 volatile compounds that was identified by GC-FID and GC-MS. It shows that monoterpenes hydrocarbon, sesquiterpenes hydrocarbon and oxygenated sesquiterpenes were major groups in agarwood smoke. This finding is

consistent with those of earlier studies which showed agarwood is a mixture of monoterpene, sesquiterpenes and its chromone derivatives (Ishihara, Tsuneya, & Uneyama, 1993). It is also observed that compounds from the sesquiterpene group were absent in low quality agarwood. In addition, high quality agarwood produced a high percentage of peak area, 29.12%, whereas 17.31% of peak area for low quality agarwood. Meanwhile, commercial agarwood afforded 27.55%. The monoterpene hydrocarbon group produced a high percentage of peak area for all types of samples and less percentage in the oxygenated sesquiterpene group. Eleven compounds (from monoterpenes hydrocarbon and sesquiterpenes hydrocarbon) were detected in high quality and commercial samples. However, no compounds from group sesquiterpenes hydrocarbon were detected in low quality samples. Furthermore, in low quality samples, only two compounds - pentadecanoic acid (0.38%) and guaia-1(10),11-dien-15,2-olide (8.96%) - were detected. This finding revealed that for low quality agarwood, there were not many compounds from sesquiterpenes hydrocarbon and oxygenated sesquiterpenes groups. It is interesting to note the presences of all 27 compounds in commercial samples. It is believed that there were compounds from other substances which were added into agarwood during the manufacturing process.

Table 1
Chemical compound (% relative peak area) of three types of agarwood in hexane solvent trap

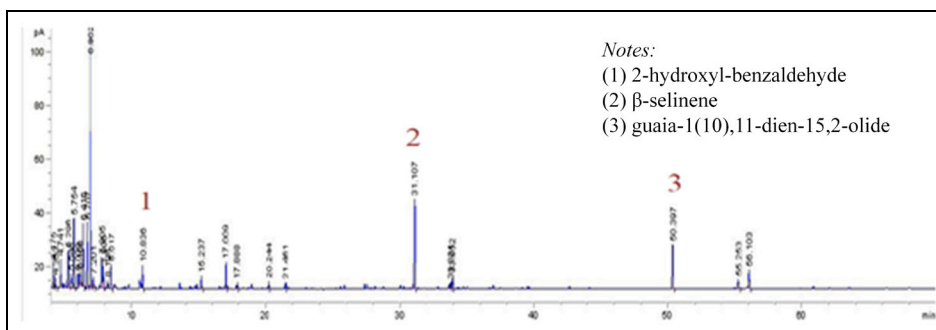
Compound	¹ KI	Types of agarwood			Identification
		High	Low	Commercial	
Monoterpene Hydrocarbon					
furfuryl alcohol	830	3.99	0.29	6.12	³ RI
benzaldehyde	935	3.52	0.43	1.71	RI, ⁴ MS
phenol	956	2.02	2-	1.67	RI
p-methylanisol	1002	1.12	1.04	0.31	RI
2-hydroxy-benzaldehyde	1003	2.01	4.04	3.50	RI, MS
guaiacol	1062	-	-	1.74	RI
acetophenone	1066	0.38	0.41	0.19	RI, MS
p-methoxyphenol	1198	0.50	1.30	0.37	RI
4-phenyl-2-butanone	1210	-	-	0.10	RI, MS
p-vinylguaiacol	1286	-	0.46	0.40	RI
vanillin	1367	-	-	0.11	RI
Sesquiterpenes Hydrocarbon					
β -maaliene	1414	-	-	0.11	RI, MS
aromadendrane	1443	-	-	0.39	RI, MS
β -selinene	1486	8.79	-	1.01	RI, MS
α -murolene	1496	-	-	0.16	RI

Table 1 (continue)

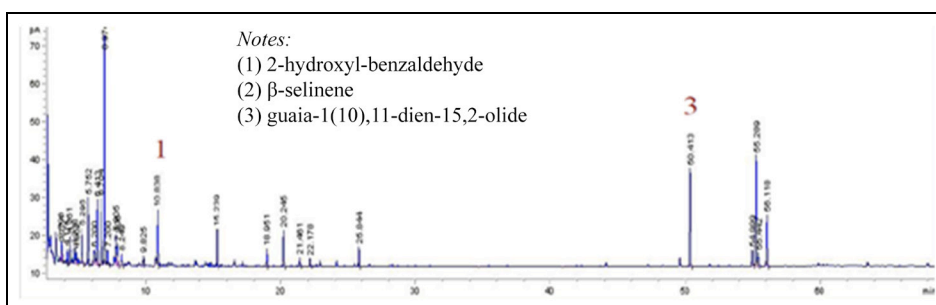
Oxygenated Sesquiterpenes					
α -elemol	1530	-	-	0.25	RI
nor-ketoagarofuran	1555	0.62	-	0.09	RI, MS
tridecanol	1561	1.30	-	0.20	RI
epoxybulnesene	1572	-	-	0.22	RI
caryophyllene oxide	1600	-	-	0.24	RI
epi- α -cadinol	1640	-	-	0.07	
selina-4, 11-dien-14-al	1758	-	-	0.09	RI
oxo-agarospirol	1822	-	-	0.17	RI
pentadecanoic acid	1842	-	0.38	2.02	RI
hexadecanol	1865	-	-	0.65	RI
guaia-1(10),11-dien-15,2-olide	2019	4.87	8.96	5.14	RI
Others					
2-(2-phenylethyl) chromone	2296	-	-	0.52	RI
Sesquiterpene Hydrocarbons		3.28	13.28	2.99	
Oxygenated Sesquiterpenes		70.46	62.02	73.58	
Others		74.34	77.83	78.18	

¹KI: Kovats retention indices on DB-1 column, ²-: not identified ³RI: linear retention indices relative to the retention time on DB-1 column of a homologous series of n-alkanes (C8-C22), ⁴MS: identification by comparison of MS with those of the NIST library

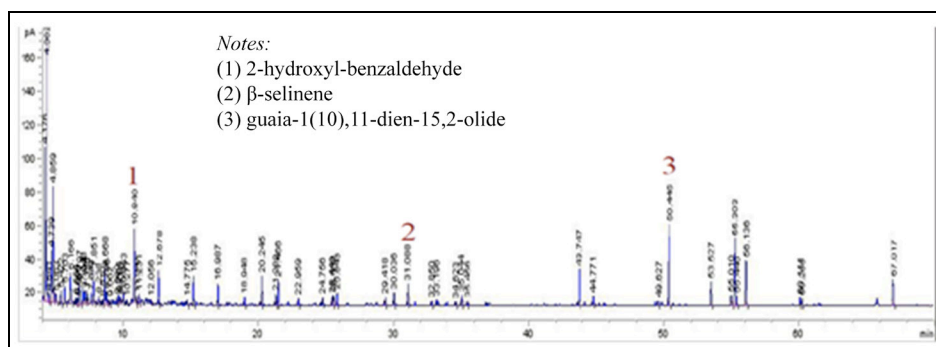
Figure 2 shows the GC-FID chromatogram of those three types of samples. The pattern was slightly different for high quality sample. It appeared that a cluster of monoterpene group at retention time ranges from 4.00 to 12.00 for all types of samples. The compounds of sesquiterpene group was barely noticed in all types of samples. Specifically, 2-hydroxy-benzaldehyde, β -selinene and guaia-1(10),11-dien-15,2-olide exist in high and commercial groups. On the other note, β -selinene was absent in the low-quality sample.



(a)



(b)



(c)

Figure 2. GC-FID chromatogram of: (a) high quality; (b) low quality; and (c) commercial agarwood in hexane solvent trap

CONCLUSION

This study has shown that the proposed solvent trap, GC-FID and GC-MS, was successful in characterising agarwood smoke from high, low and commercial types. Three major groups were found: monoterpenes hydrocarbon, sesquiterpenes hydrocarbon and oxygenated sesquiterpenes. Among all the compounds, three were most significant. They were 2-hydroxy-benzaldehyde, β -selinene and guaia-1(10),11-dien-15,2-olide. This finding confirms that of earlier studies

which pointed to agarwood being a combination of monoterpenes, sesquiterpenes and chromone derivatives (Ishihara, Tsuneya, & Uneyama, 1993). Thus, further study is useful to establish the grade of agarwood.

ACKNOWLEDGEMENTS

The authors thank Institute of Research Management and Innovation (IRMI), Ministry of Education Malaysia and Faculty of Electrical Engineering, Universiti Teknologi MARA Shah Alam for their support. This study was made possible by PRGS Grant Code: PRGS/2/2015/TK06/UITM/02/5.

REFERENCES

- Espinoza, E. O., Lancaster, C. A., Kreitals, N. M., Hata, M., Cody, R. B., & Blanchette, R. A. (2014). Distinguishing wild from cultivated agarwood (*Aquilaria* spp.) using direct analysis in real time and time-of-flight mass spectrometry. *Rapid Commun. Mass Spectrom*, 28, 281–289.
- Hamid, K. H. K. (2011). *Enhancing the world of fragrance through Malaysian bio-gaharu*. UPENA, UiTM, Malaysia.
- Hidayat, W., Shakaff, A. Y. M., Ahmad, M. N., & Adom, A. H. (2010). Classification of agarwood oil using an electronic nose. *Sensors*, 10(5), 4675–4685.
- Ishihara, M., Tsuneya, T., & Uneyama, K. (1993). Components of the volatile concentrate of agarwood. *Journal of Essential Oil Research*, 5(3), 283–289.
- Jayachandran, K., Sekar, I., Parthiban, K. T., Amirtham D., & Suresh, K. K. (2014). Analysis of different grades of agarwood (*Aquilaria Malaccensis* Lamk.) oil through GC-MS. *Indian Journal of Natural Products and Resources*, 5(1), 44–47.
- Joulian, D., & Konig, W. A. (1998). *The atlas of spectral data of sesquiterpene hydrocarbons*. E. B.–Verlag, Germany.
- Lias, S., Ali, N. A. M., Jamil, M., Zainal, M. H., & Ab Ghani, S. H. (2015, May). Classification of pure and mixture Agarwood oils by Electronic Nose and Discriminant Factorial Analysis (DFA). In *International Conference on Smart Sensors and Application (ICSSA)*, (pp. 7–10). IEEE.
- Marriott, P. J., Shellie, R., & Cornwell, C. (2001). Gas chromatographic technologies for the analysis of essential oils. *Journal of Chromatography A*, 936(1), 1–22.
- Mastura, I. (2014). *Chemical analysis of agarwood incense smoke extracted by various technique using Gas Chromatography and Mass Spectrometry (master's thesis)*, Faculty of Industrial Sciences and Technology, Universiti Malaysia Pahang.
- Naef, R. (2011). The volatile and semi-volatile constituents of Agarwood, the infected Heartwood of *Aquilaria* species: A review. *Flavour Fragrance Journal*, 26, 73–89
- Nor Azah, M. A., Chang, Y. S., Mailina, J., Abu Said, A., Abd. Majid, J., Saidatul Husni, S., ... & Nik Yasmin, Y. (2008). Comparison of chemical profiles of selected Gaharu oils from Peninsular Malaysia. *The Malaysian Journal of Analytical Sciences*, 12(2), 338 – 340.

Nurlaila Ismail, Mastura Ibrahim, Seema Zareen, Mohd Hezri Fazalul Rahiman, Saiful Nizam Tajuddin and
Mohd Nasir Taib

- Pripdeevech, P., Khummueng, W., & Park, S. K. (2011). Identification of odor-active components of Agarwood essential oils from Thailand by Solid Phase Microextraction-GC/MS and GC-O. *Journal of Essential Oil Research*, 23(4), 46-53.
- Tajuddin, S. N., & Yusoff, M. (2010). Chemical composition of volatile oils of *Aquilaria Malaccensis* (Thymelaeaceae) from Malaysia. *Natural Product Communication*, 5(12), 1965-1968.
- Wahyu, H., Ali Yeon, M. S., Mohd, N. A., & Abdul, H. A. (2010). Classification of Agarwood oil using an electronic nose. *Sensors*, 10, 4675-4685.
- Yamada, H., & Yatagai, M. (2007). The components of the smoke and headspace volatiles from *Cryptomeria Japonica* D. Don. *Journal of Essential Oil Research*, 19, 231-233.

Ammonia Nitrogen Adsorption using Spent Mushroom Substrate Biochar (SMSB)

Siti Fatimah Halim^{1,2}, Soon Kong Yong^{1*} and Chia Chay Tay¹

¹Faculty of Applied Sciences, Universiti Teknologi MARA (UiTM), 40450 Shah Alam, Selangor, Malaysia

²Lembaga Kenaf dan Tembakau Negara, 16150 Kubang Kerian, Kota Bharu, Kelantan, Malaysia

ABSTRACT

The objective of this study is to elucidate sorption mechanism of ammonia-N by Spent Mushroom Substrate Biochar (SMSB), produced from pyrolysis process of Spent Mushroom Substrate (SMS) at 550°C for two hours. Surface functional group, ash contents, and elemental compositions were analysed using Boehm titration, furnace and Inductively Coupled Plasma-Optical Emission Spectroscopy (ICP-OES) respectively. Sorption parameters (i.e., sorbent dosage, input ammonia-N concentration, and contact time) were optimised, and the sorption data were analysed using kinetic models (i.e., pseudo-first-order and pseudo-second-order), and isotherm models (i.e., Langmuir, Freundlich, and Dubinin-Radushkevich (D-R)). The surface of SMSB consists of carboxylic (0.3 mmol/g), phenolic (0.5 mmol/g), and basic functional groups (0.2 mmol/g). Sorption of ammonia-N was best described by the pseudo-second-order kinetic model and the Dubinin-Radushkevich (D-R) isotherm model. The D-R sorption capacity for SMSB was 12.6 mg/g, and correlates well with the amount of acid functional groups (i.e., carboxylic and phenolic groups) in SMSB (i.e., 14.4 mg/g). The low Freundlich constant ($n = 0.754$), and low D-R mean free energy per mol of the adsorbate ($E = 4.4$ kJ/mol) indicates a physical sorption process, and ammonia-N binds with acid functional groups through weak forces. The result shows great potential of SMSB for removing ammonia-N in wastewater.

Keywords: Activated carbon, ammonia, ammonium, charcoal, nutrient, sewage wastewater

ARTICLE INFO

Article history:

Received: 05 January 2017

Accepted: 17 January 2017

E-mail addresses:

sitifatihahalim91@gmail.com (Siti Fatimah Halim),

yongsk@salam.uitm.edu.my (Soon Kong Yong),

taychiay@gmail.com (Chia Chay Tay)

*Corresponding Author

INTRODUCTION

Sewage wastewater contains ammonia-N due to microbial degradation of nitrogen-rich organic matter such as urine, faeces, and by-products in the industrial effluents. Ammonia-N is a plant nutrient and is the major constituent in fertiliser. Ironically, excessive use of fertiliser has contributed to

high ammonia-N in wastewater, causing eutrophication and harming living organism (Aziz, Adlan, Zahari, & Alias, 2004). An aqueous ammonia concentration of 0.2 mg/L may be hazardous to aquatic organisms (Lin, Chan, Jiang, & Lan, 2007). Moreover, high concentration of ammonia-N decreases the biological treatment performance in a sewage treatment plant from increased algae growth (Bashir, Aziz, Yusoff, & Adlan, 2010). Ammonia-N in sewage wastewater may be recycled by zeolite for fertilising agricultural soils (Saleh, Mahmoud, & Rashad, 2013). However, direct application may cause sedimentation in wastewater treatment plant, incurring additional maintenance cost. Spent Mushroom Substrate (SMS) may be used for adsorbing ammonia-N from wastewater. For every 1 kg production of mushrooms, approximately 5 kg of SMS is produced. Most of the SMS is disposed into landfill or composed as agricultural fertiliser (Finney, Ryu, Sharifi, & Swithenbank, 2009). Studies had examined the potentials of SMS for environmental decontamination, such as treatment for acid mine drainage (Cheong, Das, Roy, & Bhattacharya, 2010), bioremediation, and as a biosorbent (García-Delgado, Yunta, & Eymar, 2015). Spent mushroom compost may be pyrolysed at a low oxygen environment to produce a relatively stable, carbon-rich material called biochar, minimise microbial degradation that releases pollutants from SMS into the environment. Spent mushroom compost is recommended as feedstock for biochar production because it contains carbon-rich sawdust (Liu, Zhang, Li, Feng, & Zhang, 2014).

Partial degradation of cellulosic materials and adding lime in SMS has given it unique chemical and physical properties compared with rubber wood sawdust. In fact, SMS has been converted to biochar and its sorption for ammonia-N from aqueous system has been reported (Liu et al., 2013). However, the sorption capacity for SMSB and its link to the surface functional groups in SMSB has not been reported. Greater understanding of surface interactions between SMSB and ammonia-N may provide more information for possible application of SMSB for recycling ammonia-N from wastewater streams. This study aims to (i) determine the elemental composition and surface functional groups in SMSB; (ii) optimise the sorption parameters (i.e., sorbent dosage, contact time, and input ammonia-N concentration) on sorption capacity of ammonia-N by SMSB; (iii) elucidate the ammonia-N sorption mechanism by SMSB.

MATERIALS AND METHOD

Spent mushroom substrate was autoclaved, oven-dried at 105°C for one week, and sieved to 710 µm using a 25-mesh screen. The dried SMS was pyrolysed at 550°C, 2 hours, and at nitrogen atmosphere to produce SMSB. Inorganic ash component in SMSB was eliminated by agitation with 0.05 M HCl, deionised water, and 0.05 M CaCl₂ solution (Chen, Zhou, & Lin, 2015). Then, SMSB was oven-dried again at 105°C for 24 hours, and sieved using a 25-mesh screen. All sieved SMSB was stored in an air-tight container containing anhydrous calcium chloride.

A proximate analysis was conducted to determine the contents of moisture, ash, and fixed carbon for SMSB through gravimetric approach. The moisture in SMS samples (0.05 g) was removed by drying them in an oven at 105°C for 24 hours. The dried SMS samples were then

combusted in the furnace at 600°C for 6 hours to produce ash. The dried SMS and its ash was cooled in a desiccator for about one hour before being weighed with a calibrated analytical balance. Fixed carbon was determined from the yield of SMSB. The volatile matter for SMSB was determined by the difference of the initial weight for SMS, and with the weights of moisture, ash and fixed carbon. The pH value, compositions of elements and surface functional groups were determined on SMSB. Elemental analyses were conducted using the carbon-hydrogen-nitrogen-oxygen (CHNO) elemental analyser, and inductively coupled plasma-optical emission spectroscopy (ICP-OES). For analysis using ICP-OES, 0.05 g of ash samples from SMS and SMSB were digested in 1 mL of 37% HCl and 7 mL of 65% HNO₃ at 200°C for an hour. The digested mixture was then filtered, diluted and analysed for various metal contents (Ca, Cd, Cr, Cu, K, Mg, Mn, Pb and Zn). The surface functional groups for SMSB was determined using method described elsewhere (Boehm, 2008).

Ammonia-N stock solution (1000 mg/L) was prepared by dissolving 1.908 g ammonium chloride (NH₄Cl) in 500 mL of deionised water. The initial ammonia-N concentration for all sorption experiments (except for sorption isotherm) is 50 mg/L. Initial solution pH for all sorption experiment was 6.2. For optimisation of sorbent dosage, SMSB samples at various weights were added to 50 mL of ammonia-N solution to make 0.5, 1.0, 2.0, 5.0 g/L in sorbent dosage, and agitated for 120 minutes. Sorption kinetics experiment was conducted at 1.0 g/L of SMSB dosage, and sorption data was collected at seven contact times (i.e., 10, 20, 30, 40, 50, 60 and 70 minutes). For sorption isotherm experiment, SMSB samples were agitated with ammonia-N solutions at various ammonia-N concentration (i.e., 2.6, 11, 32, 55, 78 mg/L), 1.0 g/L sorbent dosage, and 60 minutes contact time. The mixtures of SMSB and ammonia-N solutions were sealed in conical flasks and agitated with an orbital shaker at 150 rpm. The mixtures were centrifuged, and the supernatants were filtered with 0.45 µm syringe filters. The pH values for ammonia solution were recorded using a calibrated pH meter before and after contact with SMSB. The residual ammonia-N in the solution was determined via calorimetric method using Nessler's reagent. Ammonia-N removal percentage (%) and sorption capacity, q_t (mg/g) for SMSB were calculated using Eq [1] and Eq [2], respectively. All sorption data was analysed with linearised kinetic models (i.e., pseudo-first-order & pseudo-second-order) and isotherm models (i.e., Langmuir, Freundlich, D-R) (Table 1).

$$\text{Removal}\% = \frac{[NH_3]_i - [NH_3]_f}{[NH_3]_i} \times 100 \quad [1]$$

$$q_t = \frac{[NH_3]_i - [NH_3]_f}{m_{SMSB}} \times V_{NH_3} \quad [2]$$

Table 1
 Linearised kinetic models (pseudo-first-order & pseudo-second-order) and isotherm models (Langmuir, Freundlich and D-R)

Kinetic/isotherm models	Linearized equation
Pseudo-first-order	$\log(q_e - q_t) = \log q_e - \frac{k_1 t}{2.303}$
Pseudo-second-order	$\frac{t}{q_t} = \frac{1}{k_2 q_e^2} + \left(\frac{1}{q_e}\right)t$
Langmuir	$\frac{1}{q_e} = \left(\frac{1}{K_L q_{\max}}\right) \frac{1}{C_e} + \frac{1}{q_{\max}}$
Freundlich	$\ln q_e = \frac{1}{n} (\ln C_e) + \ln K_F$
D-R	$q_e = q_{\max} - K \varepsilon^2$ $\varepsilon = RT \ln \left(1 + \frac{1}{C_e}\right)$ $E = \frac{1}{\sqrt{2K}}$

$[NH_3]_i$ and $[NH_3]_f$ are the initial and final concentrations for ammonia-N (mg/L); m_{SMSB} is the mass for SMSB (g); V_{NH_3} is the volume for ammonia-N solution (L); t is the contact time between SMSB and ammonia solution (minute); q_e is the equilibrium sorption capacity (mg/g), k_1 (min^{-1}) and k_2 (g/mg min) are the rate constant for the pseudo-first-order and pseudo-second-order equation respectively; q_{\max} is the maximum sorption capacity of SMSB in the Langmuir or D-R models (mg/g); n is the empirical constant for Freundlich model (L/mg); K_L , K_F and K are the constants for Langmuir (L/mg), Freundlich (mg/g), and D-R model (mol^2/J^2) respectively; ε is Polanyi potential (J/mol) related to equilibrium concentration C_e ; R is gas constant (8.314 J/mol) and T is the absolute temperature; and E is the mean free energy of adsorption per mol of the adsorbate (kJ/mol).

Sewage wastewater was collected from a sewage treatment plant at Nilai. The water parameters of the effluent (i.e., pH, temperature, salinity, electric conductivity, and dissolved oxygen) were measured immediately using the YSI 556 multiprobe system. One litre of effluent was preserved with 2 mL of concentrated HCl (37% w/w) and stored at $<4^\circ\text{C}$. Sorption experiment was conducted by agitating 0.03 g and 0.06 g SMSB with 30 mL effluent in 50 mL centrifuge tubes for 60 minutes at constant temperature (25°C). The mixtures were filtered with $0.45 \mu\text{m}$ syringe filter, and the concentration of ammonia-N in the supernatant was analysed using Nessler's reagent calorimetric method.

RESULTS AND DISCUSSION

Ash content for SMS (27.8% w/w) is slightly higher than that of rubber wood sawdust (22.7% w/w) (Ghani et al., 2013), due to the fact that SMS was added with 5% lime (CaCO_3). For SMSB, the weight percentage (% w/w) for moisture, fixed carbon, ash, and volatile matter are 5.0%, 37.0%, 6.5%, and 51.5% respectively.

Table 2 shows elemental compositions for SMS, and SMSB. Pyrolysis process has increased percentage of C and H contents, and decreased O and N. The H/C_{org} molar ratio for SMSB (0.4) was lower than that of SMS (1.6), indicating that SMSB is more stable than SMS (Budai et al. 2013). Soluble fraction from the ash in SMSB was removed during the leaching process with HCl solution, involving the loss of Ca (by 10% w/w) and K (by 0.4% w/w). However, presence of heavy metals such as Cr, Pb and Zn remain unchanged.

Table 2
Elemental composition (% w/w dry basis) for SMS and SMSB

Elements	SMS	SMSB
C	44.0	72.8
O	21.4	18.6
H	5.8	2.0
N	1.0	0.1
S	0.1	0
Ca	12.8	2.8
Cr	0.1	0.1
K	0.5	0.1
Mg	0.8	0.8
Pb	0.2	0.2
Zn	0.1	0.1

The acidic functional groups on the surface of SMSB consists of primarily carboxylic (0.3 mmol/g) and phenolic groups (0.5 mmol/g). The amount for basic functional groups for SMSB was 0.2 mmol/g.

Figure 1 shows the percentage removal (%) of ammonia-N from the aqueous solution containing different dosages of SMSB. The percentage removal (%) for ammonia-N increased with increasing SMSB dosage by up to 1.0 g/L. Then, the percentage removal (%) began to concave slightly towards 5.0 g/L sorbent dosage, reaching 23% ammonia removal. Based on this result, sorbent dosage of 1.0 g/L was adopted for all sorption experiments.

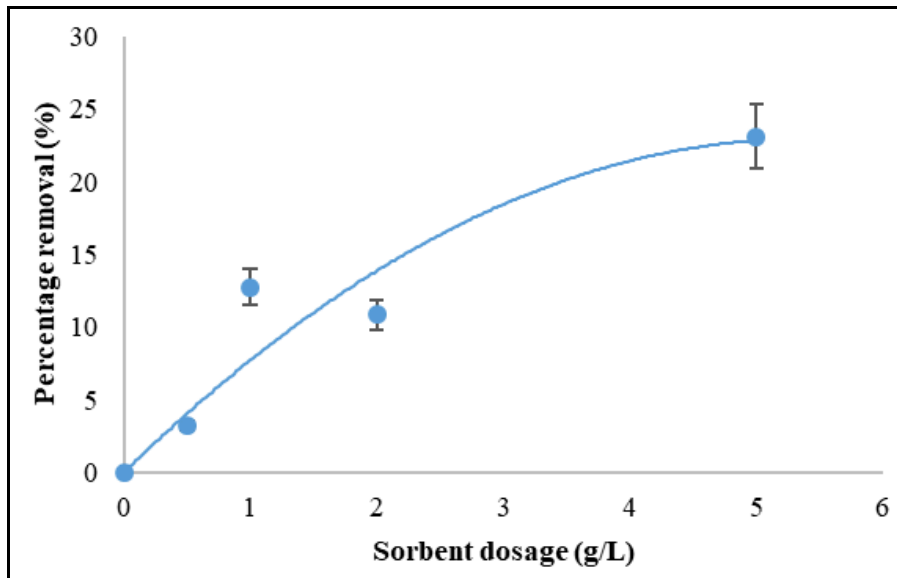


Figure 1. Percentage removal of ammonia-N as a function of SMSB sorbent dosage (g/L) (Initial ammonia-N concentration = 50 mg/L; solution pH = 6.2; agitation speed = 150 rpm; contact time = 120 minutes)

Figure 2 shows SMSB q_e values for sorption of ammonia-N as a function of contact time (minutes). A rapid initial sorption stage occurred till the 10th minute, then proceeded with at a lower sorption rate, and reached equilibrium at the 60th minute with an equilibrium sorption capacity, q_e of 3.0 mg/g. The ammonia-N sorption kinetic data for SMSB was better described by the pseudo-second-order kinetic model ($R^2= 0.942$) compared with the pseudo-first-order model ($R^2 = 0.644$), showing that the rate limiting step may be controlled using chemical process (Yong, Bolan, Lombi, & Skinner, 2013).

Table 3

Kinetic models parameters for adsorption of ammonia-N by SMSB

Kinetic models	R^2	q_e [mg/g]	k
Pseudo-first-order	0.644	2.73×10^{15}	-1.47
Pseudo-second-order	0.942	3.88	0.011

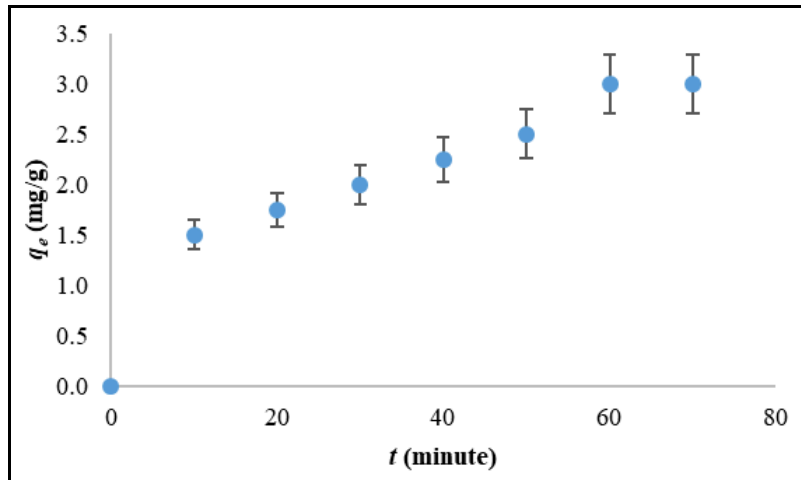


Figure 2. Ammonia-N sorption capacity for SMSB, q_e as a function of contact time, t (minutes) (Sorbent dosage = 1.0g/L; Initial ammonia-N concentration = 50 mg/L; solution pH = 6.2; Agitation speed = 150 rpm)

Figure 3 shows the ammonia-N sorption capacity for SMSB, q_e (mg/g) as a function of equilibrium ammonia-N concentration, C_e (mg/L). The ammonia-N adsorption by SMSB increased with increasing initial ammonia-N concentration, whereby, the q_e value increased from 0.05 to 4.41 mg/g. High initial ammonia-N concentration may overcome mass transfer resistance between aqueous and solid phase. The sorption isotherm parameters for SMSB is shown in Table 4. The ammonia-N sorption data for SMSB was best described by D-R isotherm model ($R^2 = 0.996$). Even though sorption data also fits well with Langmuir model ($R^2 = 0.987$), the q_{\max} value could not be calculated due to the negative intercept value in the $1/q_e$ versus $1/C_e$ plot. In fact, the q_{\max} value for Langmuir and D-R models are similar (Shi, Wang, & Zheng, 2013) and may be used to elucidate SMSB sorption capacity. The q_{\max} value for the D-R model (12.6 mg/g) translates to 0.7 mmol NH_4 per unit gram of SMSB. This correlates well with the result from Boehm titration, whereby, the total acid functional groups was 0.8 mmol/g. Carboxylic and phenolic groups become negative-charge upon deprotonation, and may act as binding sites for retaining the positive-charged-ammonia-N (Shaaban et al., 2014). The E value was 4.4 kJ/mol, indicating physical nature of the adsorption process between ammonia-N and SMSB (Yunnen, Changshi, & Jinxia, 2016). The low n value from the Freundlich model (0.754) suggested less favourable sorption process and corroborates the weak physical interactions between ammonia-N and SMSB surface.

Table 4

Isotherm models parameters for adsorption of ammonia-N by SMSB

Isotherm models	R^2	q_{\max} [mg/g]	K_L [mg/L]	K_f [mg/g]	K	n
Langmuir	0.987	-0.83	-0.0223	-	-	-
Freundlich	0.990	-	-	0.0163	-	0.754
D-R	0.996	12.6	-	-	0.0257	-

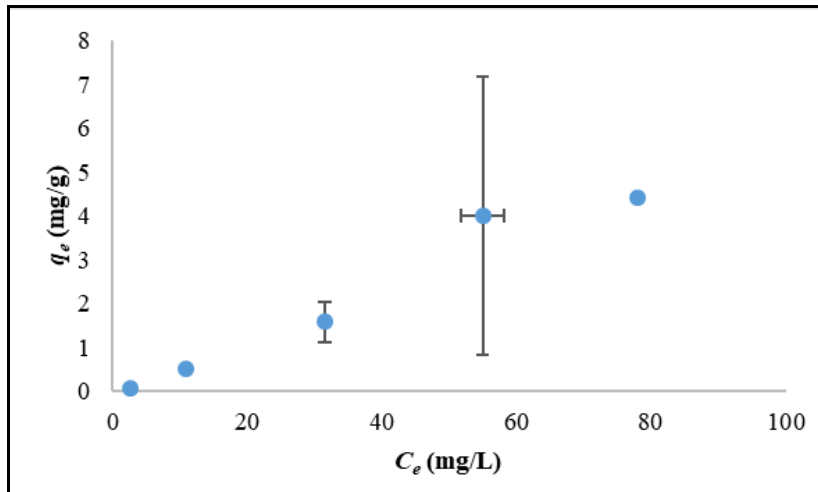


Figure 3. Ammonia-N sorption capacity for SMSB, q_e (mg/g) as a function of equilibrium ammonia-N concentration, C_e (mg/L) (Sorbent dosage = 1.0 g/L; Contact time = 60 minutes; solution pH = 6.2; Agitation speed = 150 rpm)

Table 5 shows the comparison of Langmuir and D-R q_{\max} value for SMSB and various selected clay-based and carbon-based sorbents for sorption of ammonia-N. The q_{\max} value for SMSB is comparable with those of zeolite and corn straw biochar, and is higher than commercial activated carbon (AC), and AC derivatives. This shows the great potential of SMSB as sorbent for ammonia-N from wastewater.

Table 5
Ammonia-N sorption capacity, q_{\max} (mg/g) for various sorbents and SMSB

Sorbent	Isotherm model	q_{\max} [mg/g]	Reference
Zeolite (Z3)	Langmuir	15.2	(Bernal & Lopez-Real, 1993)
Sepiolite	Langmuir	1.5	
Corn straw biochar	Langmuir	14.46	(Gai et al., 2014)
Rice husk biochar	Langmuir	3.2	(Zhu et al., 2012)
	D-R	6.8	
AC	D-R	0.48	(Shi, Wang, & Zheng, 2013)
HNO ₃ -treated AC	D-R	1.39	
HCl-treated AC	D-R	0.45	
SMSB	D-R	12.6	This study

Table 6 shows the parameters for sewage wastewater. The percentage removal of ammonia-N for SMSB at 1.0 g/L and 2.0 g/L were similar (5.3 %), with a sorption capacity of 0.80 mg/g. It indicates that the different dosage of SMSB did not affect the percentage removal of ammonia-N in real sewage wastewater.

Table 6
Parameters for sewage wastewater collected from Nilai, Negeri Sembilan

Water parameter	Average values
Ammonia-N	15.7 ± 2.01
Temperature (°C)	28.21 ± 0.01
DO (mg/L)	6.223 ± 0.161
DO (%)	79.87 ± 2.079
pH	8.037 ± 0.006
Salinity (ppt)	0.16 ± 0
TDS (g/L)	0.219 ± 0
Conductivity (mS/cm)	0.337 ± 0

CONCLUSION

In this study, batch studies were conducted for adsorption of ammonia-N from aqueous solution using SMSB as absorbent. The results from ash content, elemental analyses, and Boehm titration indicate that the dynamic behaviour and adsorption capacities of SMSB can be attributed to its surface properties. The optimum conditions for ammonia-N removal was at a dosage of 1.0 g/L and contact time of 60 minutes. Kinetic data was well described by the pseudo-second-order model. Sorption isotherm was best fitted with D-R model, where the maximum adsorption capacity was 12.6 mg/g. The sorption capacity for SMSB is comparable to establish sorbent such as zeolite, and is also greater than commercial activated carbon. Despite that, interaction between ammonia-N and SMSB surface is physical. This study shows that SMSB can be applied for recycling ammonia-N from sewage wastewater for fertilising agricultural soils.

ACKNOWLEDGEMENT

The authors gratefully acknowledge the help of the Ministry of Higher Education (MOHE) of Malaysia in granting them the Research Acculturation Collaborative Effort [600-RMI RACE 16/6/2 (2/2014)] research grant, and C&C Mushroom Cultivation Farm Sdn. Bhd., Muar, Johor for providing SMS samples.

REFERENCES

- Aziz, H. A., Adlan, M. N., Zahari, M. S. M., & Alias, S. (2004). Removal of ammoniacal nitrogen (N-NH₃) from municipal solid waste leachate by using activated carbon and limestone. *Waste Management and Research*, 22(5), 371-375.
- Bashir, M. J. K., Aziz, H. A., Yusoff, M. S., & Adlan, M. N. (2010). Application of response surface methodology (RSM) for optimization of ammoniacal nitrogen removal from semi-aerobic landfill leachate using ion exchange resin. *Desalination*, 254, 154-161.
- Bernal, M., & Lopez-Real, J. (1993). Natural zeolites and sepiolite as ammonium and ammonia adsorbent materials. *Bioresource Technology*, 43, 27-33.

- Boehm, H. P. (2008). Chapter thirteen - Surface chemical characterization of carbons from adsorption studies. In E. J. Bottani & J. M. D. Tascón (Ed.), *Adsorption by Carbons* (p. 301-327). Amsterdam: Elsevier.
- Budai, A., Zimmerman, A., Cowie, A., Webber, J., Singh, B., Glaser, B., ... & Lehmann, J. (2013). Biochar carbon stability test method: An assessment of methods to determine biochar carbon stability. *Carbon Methodology, IBI document*.
- Chen, C., Zhou, W., & Lin, D. (2015). Sorption characteristics of N-nitrosodimethylamine onto biochar from aqueous solution. *Bioresource Technology, 179*, 359-366.
- Cheong, Y. W., Das, B. K., Roy, A., & Bhattacharya, J. (2010). Performance of a SAPS-based chemo-bioreactor treating acid mine drainage using low-DOC spent mushroom compost, and limestone as substrate. *Mine Water and the Environment, 29*, 217-224.
- Finney, K. N., Ryu, C., Sharifi, V. N., & Swithenbank, J. (2009). The reuse of spent mushroom compost and coal tailings for energy recovery: Comparison of thermal treatment technologies. *Bioresource Technology, 100*, 310-315.
- Gai, X., Wang, H., Liu, J., Zhai, L., Liu, S., Ren, T., & Liu, H. (2014). Effects of feedstock and pyrolysis temperature on biochar adsorption of ammonium and nitrate. *PLoS one 9*, e113888.
- García-Delgado, C., Yunta, F., & Eymar, E. (2015). Bioremediation of multi-polluted soil by spent mushroom (*Agaricus bisporus*) substrate: Polycyclic aromatic hydrocarbons degradation and Pb availability. *Journal of Hazardous Materials, 300*, 281-288.
- Ghani, W. A. W. A. K., Mohd, A., da Silva, G., Bachmann, R. T., Taufiq-Yap, Y. H., Rashid, U., & Al-Muhtaseb, A. a. H. (2013). Biochar production from waste rubber-wood-sawdust and its potential use in C sequestration: Chemical and physical characterization. *Industrial Crops and Products, 44*, 18-24.
- Lin, L., Chan, G. Y. S., Jiang, B. L., & Lan, C. Y. (2007). Use of ammoniacal nitrogen tolerant microalgae in landfill leachate treatment. *Waste Management, 27*, 1376-1382.
- Liu, N., Zhou, C. J., Fu, S. F., Ashraf, M. I., Zhao, E. F., Shi, H., ... & Hong, Z. B. (2013). Study on characteristics of ammonium nitrogen adsorption by biochar prepared in different temperature. *Advanced Materials Research, 724-725*, 452-456.
- Liu, X., Zhang, Y., Li, Z., Feng, R., & Zhang, Y. (2014). Characterization of corncob-derived biochar and pyrolysis kinetics in comparison with corn stalk and sawdust. *Bioresource Technology, 170*, 76-82.
- Saleh, M. E., Mahmoud, A. H., & Rashad, M. (2008). Biochar usage as a cost-effective bio-sorbent for removing NH₄-N from wastewater. *Proceedings of the Global Climate Change Biodiversity and Sustainability: Challenges and Opportunities, 6(7)*, 2170-2176.
- Shaaban, A., S, S. M., Dimin, M. F., Juoi, J. M., Mohd Husin, M. H., & Mitan, N. M. M. (2014). Influence of heating temperature and holding time on biochars derived from rubber wood sawdust via slow pyrolysis. *Journal of Analytical and Applied Pyrolysis, 107*, 31-39.
- Shi, M., Wang, Z., & Zheng, Z. (2013). Effect of Na⁺ impregnated activated carbon on the adsorption of NH₄⁺-N from aqueous solution. *Journal of Environmental Sciences, 25*, 1501-1510.
- Yong, S. K., Bolan, N., Lombi, E., & Skinner, W. (2013). Synthesis and characterization of thiolated chitosan beads for removal of Cu(II) and Cd(II) from wastewater. *Water, Air, and Soil Pollution, 224*, 1-12.

Ammonia Nitrogen Adsorption using Spent Mushroom Substrate

- Yunnen, C., Changshi, X., & Jinxia, N. (2016). Removal of ammonia nitrogen from wastewater using modified activated sludge. *Polish Journal of Environmental Studies*, 25, 419-425.
- Zhu, K., Fu, H., Zhang, J., Lv, X., Tang, J., & Xu, X. (2012). Studies on removal of $\text{NH}_4^+\text{-N}$ from aqueous solution by using the activated carbons derived from rice husk. *Biomass and Bioenergy*, 43, 18-25.





Isolation and Adaptation of Diatoms in a New Formulated Enriched Medium

Syafiqah Hayati Mohd Ali¹, Khairul Adzfa Radzun² and Norazlina Ahmad^{1*}

¹Faculty of Pharmacy, Universiti Teknologi MARA (UiTM), 42300 Puncak Alam, Selangor, Malaysia

²Faculty of Applied Sciences, Universiti Teknologi MARA (UiTM), 40450 Shah Alam, Selangor, Malaysia

ABSTRACT

This study describes the adaptations of diatoms, *Cylindrotheca fusiformis* and other marine diatoms, in a new formulated enriched medium Tris-phosphate seawater (TP-SW). The medium was designed to maintain long-term cultures of wide-range marine diatoms in laboratory that produces high biomass of cultures. The diatoms were adapted and cultivated in the medium for 15 days and the number of cells was recorded daily. It was found that the number of cells declined after two weeks indicating death phase of the cells. This indicates that the TP-SW medium has supported the growth of diatoms during the period and can be used to cultivate diatoms *in vitro*. Studies on the TP-SW medium must be done to obtain optimal medium that can provide not only a conducive environment for the survival of diatoms but also high biomass production.

Keywords: Adaptation, diatoms, enriched medium, growth, nutrient

INTRODUCTION

Diatoms contribute to about one fifth of the world's photosynthesis for 200,000 different species in the sea (Armbrust,

2009). Diatoms are useful in various fields including biofuel production (Chaffin, Mishra, Kuhaneck, Heckathorn, & Bridgeman, 2011) paleoclimate research (Morley, Leng, & Sloane, 2005) forensic investigation (Zimmerman & Wallace, 2008), water quality monitoring (Tan, Sheldon, Bunn, & Zhang, 2012) marine culture (Pahl, Lewis, King, & Chen, 2012) and also biological materials production (Fan, Chow, & Zhang, 2009).

Diatoms can be cultivated in laboratory using artificial and enriched growth media. Artificial media is a defined media where exact composition of every element in it needs

ARTICLE INFO

Article history:

Received: 05 January 2017

Accepted: 17 January 2017

E-mail addresses:

syafiqahayati@gmail.com (Syafiqah Hayati Mohd Ali),

khairuladzfa@salam.uitm.edu.my (Khairul Adzfa Radzun),

linaahmad8@gmail.com (Norazlina Ahmad)

*Corresponding Author

to be controlled. Enriched media are prepared by adding nutrients to natural seawater or lake, thus these types of media are not defined (Andersen, 2005). For growth of marine diatoms, natural seawater is sufficient to provide enough nutrients, with incorporations of micro and macro elements. The *f/2* medium is a widely used enriched medium to cultivate various species of coastal microalgae especially diatoms (Guillard & Ryther, 1962; Guillard, 1975). Though this medium can ensure long term growth of diatoms, it does not produce high biomass of cultures. Thus, the TP-SW medium is developed as a new enriched medium that can increase the biomass and growth rate of the cultures. The TP-SW medium also facilitates the study of Malaysian diatoms *in vitro*.

In this study, diatom samples were collected from Pantai Remis, Kuala Selangor, and another diatom of known specie, *Cylindrotheca fusiformis*, was obtained from University of Texas (UTEX) in which both were used in the adaptation of the new enriched medium. *C. fusiformis* is widely studied for its lipid content and fatty acids. According to a study, *C. fusiformis* is a potential source of acid or also known as EPA Omega-3 fatty acid (Kiran, 2012). In aquaculture, *C. fusiformis* and other species of diatoms can be used to produce therapeutic proteins (Fischer, Robl, Sumper, & Kroger, 1999). Different strains of diatoms can be well adapted to different environments with different nutrient requirements. Therefore, development of a medium that can support the growth of a wide range of diatoms is beneficial economically.

MATERIALS AND METHOD

Preparation and Composition of TP-SW Medium

The composition of the media is shown in Table 1. Master stocks of all nutrients were prepared, and required volumes were dispensed aseptically into 1L working stock, the final solution which was used in the cultivation in this study. Filter sterilised vitamins were added after the final solution was autoclaved.

Diatoms Sample Collection

Water samples were collected by filling approximately half of 50 mL Falcon tube. Early detection of diatoms was made by observing the fresh water samples under light microscope (Leica, DM2500). *C. fusiformis* and the water samples collected from Pantai Remis, Kuala Selangor (N03° 12.145' E101° 18.329') were then centrifuged (NF800) at 4000 rpm for 10 minutes. The supernatant was discarded, and the pellets were transferred into a 50 mL conical flask containing 30 mL of the commercial *f/2* medium which was purchased from UTEX.

Table 1
The nutrient composition of TP-SW and f/2 media

Nutrient Category	Nutrient in TP-SW	Concentration in working solution (mM)	Nutrient in f/2	Concentration in working solution (mM)
Nitrogen	NH ₄ Cl	15.0	NaNO ₃	0.882
Phosphate	KH ₂ PO ₄	0.89	NaH ₂ PO ₄	0.036
Macro elements	CaCl ₂ .2H ₂ O	0.44	-	
	MgSO ₄ .7H ₂ O	0.42	-	
	Na ₂ SiO ₃ .5H ₂ O	0.47	Na ₂ SiO ₃ .9H ₂ O	0.0528
Micro elements	H ₂ BO ₃	0.18	-	
	(NH ₄) ₆ MO ₇ O ₂₄ .4H ₂ O	0.00089	Na ₂ MoO ₄ .2H ₂ O	0.000026
	CoCl ₂ .6H ₂ O	0.012	CoCl ₂ .6H ₂ O	0.000042
	Na ₂ SeO ₃	0.0001	-	
	VOSO ₄ .XH ₂ O	0.000012	-	
	ZnSO ₄ .7H ₂ O	0.079	Zn ₅ O ₄ .7H ₂ O	0.0000765
	MnCl ₂ .4H ₂ O	0.026	MnCl ₂ .4H ₂ O	0.00091
	CuSO ₄ .5H ₂ O	0.011	CuSO ₄ .5H ₂ O	0.0000393
	Fe ₂ (SO ₄) ₃ .7H ₂ O	0.018	FeCl ₃ .6H ₂ O	0.0117
Chelating agent	Na ₂ EDTA, pH 8.0	0.55	Na ₂ EDTA.2H ₂ O	0.0117
Buffer	Tris-HCL, pH 7.4	10.0		
Vitamins	Thiamine, B1	0.23	Thiamine, B1	0.000296
	Cyanocobalamin, B12	0.0005	Cyanocobalamin, B12	0.000000369

Cultivation of Diatoms in TP-SW Medium

Diatoms cells were allowed to replicate and after two weeks of cultivation, they were observed under Scanning Electron Microscope (ESEM Fei Quanta 450 Feg) at the Imaging Centre in Universiti Teknologi MARA to identify the diatoms species. The cultures were centrifuged, and diatoms cells were harvested. These cells were then transferred into a sterile 50 mL conical flask containing fresh 30 mL TP-SW medium for early adaptation in the new formulated medium. The medium was added periodically until a total volume of 400 mL was reached. The experiment was conducted in triplicate. All flasks were left under continuous fluorescence light with intensity of 65 $\mu\text{mol m}^{-2} \text{s}^{-1}$ and were agitated on an orbital shaker at 95 rpm. Cell counts were taken daily using haemocytometer (Neubauer, Marienfeld, Germany) to record the growth of the cells in each medium.

RESULTS AND DISCUSSION

Isolation and identification of Diatoms

Seven diatoms species from four different genera were isolated from Pantai Remis. The diatoms were morphologically identified based on the observation obtained from SEM. Figure 1 shows the SEM images from the isolated diatoms. Morphological identification was performed as described in the following references: (Hilaludin, 2011; Naz, Burhan, & Ahmad Siddiqui, 2012; Shamsudin, 1990)

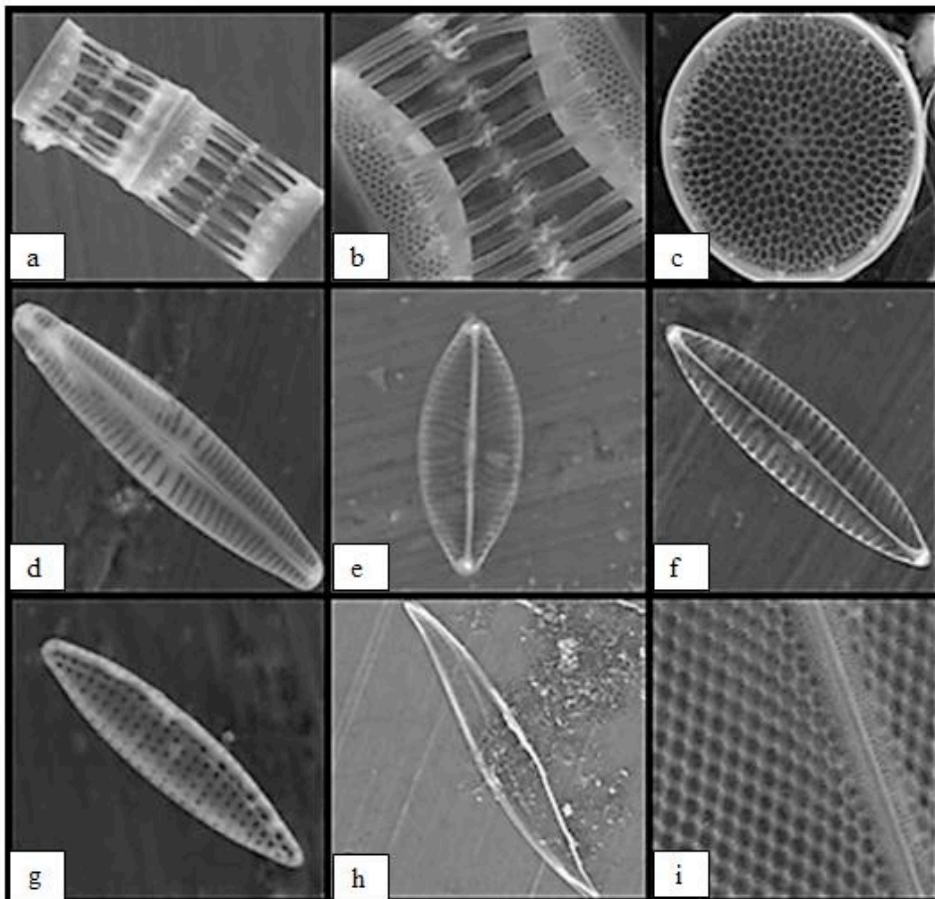


Figure 1. SEM images of isolated diatoms from Pantai Remis: (a-b) *Skeletonema* sp.; (c) *Thalassiosira* sp.; (d-g), *Navicula* sp.; and (h-i) *Pleurosigma* sp.

Adaptation of Diatoms in TP-SW Medium

Table 2 depicts the concentration of few selected nutrients from both media for comparison. Almost all elements in the TP-SW medium are significantly higher in concentration compared with the *f/2* medium. For instance, nitrogen in the TP-SW is nearly 15 times higher than the concentration in the *f/2*. Nitrogen is found in higher concentration in the TP-SW to increase its bioavailability to prevent it from becoming the limiting nutrient. Nitrogen is an indispensable nutrient for all organisms including diatoms as it is needed for the biosynthesis of macromolecules, for example nucleic acid, proteins and chlorophylls (Hockin, Mock, Mulholland, Kopriva, & Malin, 2012)

Table 2
Comparison of selected nutrients in f/2 and TP-SW media

Elements	Concentration in working solution (mM)	
	TP-SW	<i>f/2</i>
Nitrogen	15.005	0.882
Phosphate	0.89	0.0036
Silica	0.47	0.0528
Magnesium	0.42	Undefined
Calcium	0.44	Undefined
Iron	0.036	0.0117

Based on a study on phosphate concentration (Katiyar, Lall, & Singh, 2010), diatoms increased in population with the increase in concentration of phosphate in the cultivation medium. Based on the study, the optimum concentration of phosphate was 0.05 mM. In this study, the concentration of phosphate in the TP-SW medium is above the recommended concentration, which is 0.89 mM. Thus, excess phosphate may exert an effect on depressing the diatoms growth as shown by diatoms from Pantai Remis (see Figure 2).

In TP-SW medium, magnesium and calcium were added at a concentration of 0.42 mM and 0.44 mM respectively. While in the *f/2* medium, these elements were not incorporated but may be readily available in the seawater in lower amounts. Calcium can be found inside the chloroplast while magnesium can be found in chlorophyll. Magnesium also acts as co-factor of enzyme (Radzun et al., 2015).

The TP-SW medium has higher concentration of iron than the *f/2* medium. Since diatoms are photosynthetic algae, the iron acts as one of the growth-limiting element in the media. Iron is an important component of the photosynthetic apparatus and mitochondrial electron transport chain (Kustka, Allen, & Morel, 2007). Iron limitation may cause a reduction in the cells' production of chlorophyll which reduces the efficiency of photosynthesis (Lewandowska & Kosakowska, 2004). Silica is especially important to diatoms as it is needed in the production of their siliceous cell wall called frustules. The formation of frustules depends significantly on the availability of silicic acid, which is the precursor of silica (Hildebrand & Lerch, 2015).

Diatoms from Pantai Remis and *C. fusiformis* were adapted in the TP-SW, and the cell densities of cultures in the media were recorded daily. The results are shown in Figures 2 and 3. Since diatoms cells were only few at the beginning of the experiment, it is best to grow them in small volume of the new enriched medium so that the cells will reach exponential phase at a faster rate. Thus, the cells were first inoculated into 30 mL of the medium in a 50-mL conical flask for early adaptation. Large surface area to volume ratio allows gas diffusion into the medium, thus facilitating cell growth (Andersen, 2005). Having a small volume of cultivation medium for early adaptation of a small number of cells is an advantage. Theoretically, it will provide lesser gap between the cells inside the flask, thus promoting cell communication and sexual/asexual reproduction which in turn increases the number of cells (Bates & Davidovich, 2002).

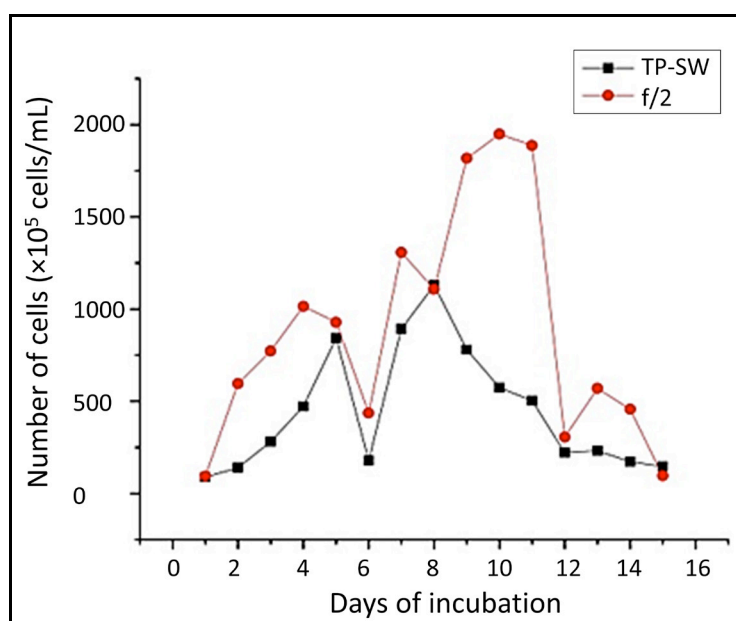


Figure 2. Cell density of diatoms from Pantai Remis against days of incubation

Growth of diatoms cells isolated from Pantai Remis in both media was measured and recorded from day 1 to day 15 as shown in Figure 2. Number of cells in the f/2 medium was found to increase from day 1 to day 4, while in the TP-SW medium, the number of cells increased from day 1 to day 5. On day 6, cell density in both media dipped to a value as diatoms lifespan generally lasted less than a week, usually around six days (Maldonado, Riesgo, Bucci, & Ru, 2010) depending on the species. However, cell density in both media increased in the following day (day 6 to day 8) until the next six days where the number of cells again decreased. Cell density in both media continued to decline from day 14 as the nutrients started to deplete. The cells cultivated in the f/2 medium showed highest cell density at day 10 with 2.0×10^8 cells/mL while in the TP-SW medium, the highest cell density was achieved at day 8 with 1.0×10^8 cells/mL. Figure 2 shows the cell density in the TP-SW medium is lower than that in the f/2 medium.

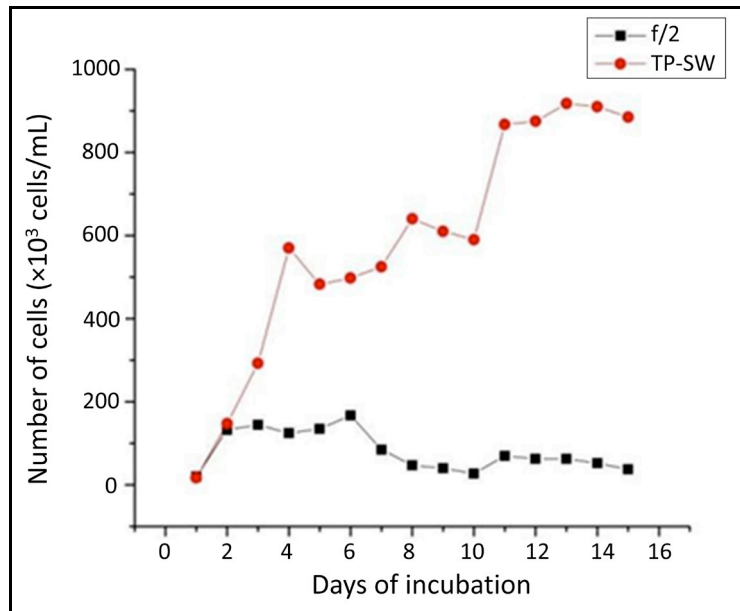


Figure 3. Cell density of *C. fusiformis* against days of incubation

In Figure 3, diatoms *C. fusiformis* showed an excellent adaptation in the TP-SW medium in terms of cells density. The number of cells recorded shot up from day 2 to day 4. After day 4, the cell density started to fluctuate but still showed increasing number of cells until day 14. Meanwhile, the cell growth performance in the f/2 medium was progressing very slowly compared to the cells in the TP-SW medium starting from day one of cultivation. After a week, the number of cells of *C. fusiformis* in the f/2 medium started to decline most probably due to the decrease in nutrients. Nevertheless, diatoms *C. fusiformis* adapted in the TP-SW medium achieved the highest cell density on day 13 of cultivation with 9.0×10^7 cells/mL which was higher than diatoms in the f/2 with 2.0×10^7 cells/mL on day 6.

Besides nutrients, another factor that contributed to the cells' response towards the cultivation media is turbulence or agitation. Diatoms cells in the present study were agitated by continuous mixing on an orbital shaker at 95 rpm. The advantage of allowing algal suspension in continuous movement is to prevent sedimentation of the cells (Stengel, 1970), while stimulating nutrient uptake by maintaining active contact of nutrients with the algal cells surface (Schumacher & Whitford, 1965). This will lead to stimulation of metabolic activities which will help the cells to adapt to a new environment (Müntz, 1965).

This study showed the life span of diatoms varies among species, and it depends greatly on a number of factors such as nutrient availability, other species-specific requirements as well as environmental conditions (e.g., temperature) as these factors affect their survival and cell replication. Diatoms adapted in the TP-SW and f/2 media showed significant difference in growth performance in terms of cell numbers. Nonetheless, the fact that the cells were able to survive in the TP-SW proved that the medium was suitable to cultivate diatoms. Even though the diatoms were first introduced to the f/2 medium in the early adaptation, they have proven

that they can survive in different growth medium. This is because diatoms are able to adapt to continuously changing nutrient conditions. In the ocean, this is displayed by the efficiency of growth-limiting nutrients (e.g., silicon, iron and nitrogen) uptake of diatoms in upwelling environments (Bromke et al., 2013).

CONCLUSION

The adaptation of diatoms in a new cultivation medium varies among species in which from the experiment, the growth performance of diatoms from Pantai Remis in the TP-SW differs greatly compared to the growth performance of diatoms *C. fusiformis* in similar medium. Nevertheless, TP-SW is an enriched medium that is suitable as a growth medium for diatoms for *in vitro* studies. Future nutrient optimisation of the TP-SW is highly recommended in order to improve the cell growth performance in terms of biomass and growth rate to cultivate a wide range of diatom species.

ACKNOWLEDGEMENTS

This research was conducted at the Faculty of Pharmacy, Universiti Teknologi Mara (UiTM, Malaysia) and was funded by Malaysian Ministry of Higher Education under the Fundamental Research Scheme Grants (FRGS). The authors thank his colleagues for their support in undertaking this research.

REFERENCES

- Andersen, R. A. (2005). *Algal Culturing Techniques*. Elsevier/Academic Press.
- Armbrust, E. V. (2009). The life of diatoms in the world's oceans. *Nature*, 459(7244), 185–192.
- Bates, S. S., & Davidovich, N. A. (2002). Factors affecting the sexual reproduction of diatoms, with emphasis on *Pseudo-nitzschia* spp. *Lifehab Life Histories of Microalgal Species Causing Harmful Blooms*, (Bates), 31–36.
- Bromke, M. A., Giavalisco, P., Willmitzer, L., & Hesse, H. (2013). Metabolic analysis of adaptation to short-term changes in culture conditions of the marine diatom *Thalassiosira pseudonana*. *PLoS ONE*, 8(6), 1–9.
- Chaffin, J. D., Mishra, S., Kuhaneck, R. M., Heckathorn, S. A., & Bridgeman, T. B. (2011). Environmental controls on growth and lipid content for the freshwater diatom, *Fragilaria capucina*: A candidate for biofuel production. *Journal of Applied Phycology*, 24(5), 1045–1051.
- Fan, T. X., Chow, S. K., & Zhang, D. (2009). Biomorphic mineralization: From biology to materials. *Progress in Materials Science*, 54(5), 542–659.
- Fischer, H., Robl, I., Sumper, M., & Kröger, N. (1999). Targeting and covalent modification of cell wall and membrane proteins heterologously expressed in the diatom *Cylindrotheca fusiformis* (Bacillariophyceae). *Journal of Phycology*, 35(1), 113–120.
- Guillard, R. R. L. (1975). Culture of phytoplankton for feeding marine invertebrates. (pp 26-60). In Smith W. L. and Chanley M. H. (Eds.) *Culture of Marine Invertebrate Animals*. Plenum Press, New York, USA.

- Guillard, R. R. L. & Ryther, J. H. (1962). Studies of marine planktonic diatoms. I. *Cyclotella nana* Hustedt and *Detonula confervacea* Cleve. *Canadian Journal of Microbiology*, 8(2), 229-239.
- Hilaluddin, F., Leaw, C. P., & Lim, P. T. (2011). Morphological observation of common pennate diatoms (*Bacillariophyceae*) from Sarawak estuarine waters. *Annals of Microscopy*, 11, 12-23.
- Hildebrand, M., & Lerch, S. J. L. (2015). Diatom silica biomineralization: Parallel development of approaches and understanding. *Seminars in Cell and Developmental Biology*, 46, 27-35.
- Hockin, N. L., Mock, T., Mulholland, F., Kopriva, S., & Malin, G. (2012). The response of diatom central carbon metabolism to nitrogen starvation is different from that of green algae and higher plants. *Plant Physiology*, 158(1), 299-312.
- Katiyar, D., Lall, A. M., & Singh, B. (2010). Effect of phosphate on growth of diatoms. *Indian Journal of Scientific Research*, 1(2), 103-106.
- Kocata, A., & Büyükl, B. (2009). Effects of light and temperature on the growth rate of potentially harmful marine diatom: *Thalassiosira allenii* Takano (*Bacillariophyceae*). *African Journal of Biotechnology*, 8(19), 4983-4990.
- Kustka, A. B., Allen, A. E., & Morel, F. M. M. (2007). Sequence analysis and transcriptional regulation of iron acquisition genes in two marine diatoms. *Journal of Phycology*, 43(4), 715-729.
- Lehr, F., & Posten, C. (2009). Closed photo-bioreactors as tools for biofuel production. *Current Opinion in Biotechnology*, 20(3), 280-285.
- Lewandowska, J., & Kosakowska, A. (2004). Effect of iron limitation on cells of the diatom *Cyclotella meneghiniana* Kützing. *Oceanologia*, 46(2).
- Maldonado, M., Riesgo, A., Bucci, A., & Ru, K. (2010). Revisiting silicon budgets at atropical continental shelf: Silica standing stocks in sponges surpass those in diatoms, 55(5), 2001-2010.
- Morley, D. W., Leng, M. J., & Sloane, H. J. (2005). Late glacial and Holocene environmental change in the Lake Baikal region documented by oxygen isotopes from diatom silica. *Global and Planetary Change*, 46(1), 221-233.
- Müntz, K. (1965). Vergleichende Untersuchungen über die Stickstoff-und Glucose-Aufnahme von *Chlorella* aus Nährlösungen in Abhängigkeit von den Durchmischungs-Bedingungen. *Journal of Basic Microbiology*, 5(5), 362-377.
- Naz, T., Burhan, Z., & Ahmad Siddiqui, P. J. (2012). A preliminary guide for the taxonomic identification of diatom (*Bacillariophyta*) species from coast of Pakistan. *New York Science Journal*, 5(3), 70-80.
- Pahl, S. L., Lewis, D. M., King, K. D., & Chen, F. (2012). Heterotrophic growth and nutritional aspects of the diatom *Cyclotella cryptica* (*Bacillariophyceae*): Effect of nitrogen source and concentration. *Journal of Applied Phycology*, 24(2), 301-307.
- Radzun, K. A., Wolf, J., Jakob, G., Zhang, E., Stephens, E., Ross, I., & Hankamer, B. (2015). Automated nutrient screening system enables high-throughput optimisation of microalgae production conditions. *Biotechnology for Biofuels*, 8(1), 65.
- Schumacher, G. J., & Whitford, L. A. (1965). Respiration and P₃₂ uptake in various species of freshwater algae as affected by a current. *Journal of Phycology*, 1(2), 78-80.

- Shamsudin, L. (1990). *Diatom marin di perairan Malaysia*. Dewan Bahasa dan Pustaka, Kementerian Pendidikan Malaysia. Retrieved from <https://books.google.com.my/books>
- Stengel, E. (1970). Anlagentypen und Verfahren der technischen Algenmassenproduktion1. *Berichte Der Deutschen Botanischen Gesellschaft*, 83(11), 589–606.
- Tan, X., Sheldon, F., Bunn, S. E., & Zhang, Q. (2012). Using diatom indices for water quality assessment in a subtropical river, China. *Environmental Science and Pollution Research*, 20(6), 4164–4175.
- Zakaria, M. R. (2009). *Effect of Water Quality and Marine Phytoplankton Community Structure On Shrimp Production In Tropical Ponds*. Universiti Putra Malaysia.
- Zimmerman, K. A., & Wallace, J. R. (2008). The potential to determine a post-mortem submersion interval based on algal/diatom diversity on decomposing mammalian carcasses in brackish ponds in Delaware. *Journal of Forensic Sciences*, 53(4), 935–41.



Low- Glycaemic Index Diet to Improve Dietary Intake among Women with Gestational Diabetes Mellitus

Farhanah, A. S.^{1,3}, Barakatun Nisak, M. Y.^{1*}, Zalilah, M. S.¹ and Nor Azlin, M. I.²

¹Department of Nutrition and Dietetics, Faculty of Medicine and Health Sciences, Universiti Putra Malaysia (UPM), 43400 Serdang, Selangor, Malaysia

²Department of Obstetrics and Gynaecology, Universiti Kebangsaan Malaysia Medical Centre (UKMMC), 56000 Kuala Lumpur, Malaysia

³Department of Nutrition and Dietetics, Faculty of Health Science, Universiti Teknologi Mara (UiTM), 42300 Bandar Puncak Alam, Selangor, Malaysia

ABSTRACT

This study examines the effect of a low glycaemic index (LGI) intervention to improve dietary intake among women with Gestational Diabetes Mellitus (GDM). Women with GDM were randomised to receive either a low GI intervention (LGI; n = 20) or standard nutrition therapy (SNT; n = 20) for a 4-week period. Food Frequency Questionnaire (FFQ) and Three-Day Diet Record assessed the dietary intake and food choices. Dietary intake and food choices of the participants were comparable at baseline. At the end of the study, energy, protein, fat and carbohydrate were reduced in both groups ($p < 0.05$). In the LGI group, fibre and calcium intake was higher compared with SNT group. More participants in the LGI group consumed rice from the low GI varieties, the whole grain breads and the low GI biscuits ($p < 0.05$) compared with participants in the SNT group. The diet GI reduced significantly in the LGI group (50 ± 9 units) compared with the SNT group (57 ± 6) ($p < 0.05$). Findings showed low GI dietary intervention improved the dietary intake of women with GDM.

Keywords: Carbohydrate, dietary intake, Gestational Diabetes Mellitus, low glycaemic index

ARTICLE INFO

Article history:

Received: 05 January 2017

Accepted: 17 January 2017

E-mail addresses:

farhanah9516@puncakalam.uitm.edu.my (Farhanah, A. S.),

bnisak@medic.upm.edu.my (Barakatun Nisak, M. Y.),

zalilahms@upm.edu.my (Zalilah, M. S.),

azlinm@ppukm.ukm.edu.my (NorAzlin, M. I.)

*Corresponding Author

INTRODUCTION

Maternal diet is important to ensure optimum foetal growth, and this includes sufficient energy, protein, calcium, and iron intake. In general, dietary recommendations for women with gestational diabetes mellitus (GDM) is not very different from normal pregnancy. However, due to abnormality of blood glucose excursion in women with GDM, carbohydrate

management has become the interest of dietary therapy. This is because dietary carbohydrate is a major determinant of maternal blood glucose excursion especially at the postprandial stage (American Diabetes Association, 2008).

An increase in maternal blood glucose during pregnancy can lead to greater incidence of adverse maternal and infant outcomes, including increased risk of developing type 2 diabetes after pregnancy and foetal macrosomia (American Diabetes Association, 2003). An intensive blood glucose management for GDM will reduce neonatal complications. Therefore, the primary goal of the medical nutrition therapy in GDM is to ensure adequate pregnancy weight gain and foetal growth while maintaining euglycemia and avoiding ketones (Mareno, Mauricio, & Hernandez, 2016)

Carbohydrates which have a low glycaemic index (LGI) have a strong influence on glycaemic responses (American Diabetes Association, 2008). In an acute study, the serum glucose spiked after the consumption of a high GI meal compared with a low GI meal, although the amount of CHO remained constant (Galgani, Aguirre, & Diaz, 2006). In a long-term trial, low GI dietary intervention showed improvement in 2-hPPG at lunch, pre-prandial and 2hr postprandial glucose at dinner towards the end of pregnancy (Perera et al., 2012).

The impact of LGI diet in women with GDM has been investigated in a few well-designed randomised controlled trial (RCT) (Louie et al., 2011; Moses, Barker, Winter, Petocz, & Brand-Miller, 2009), one each for Iran (Afaghi, Ghanei, & Ziaee, 2013), Canada (Grant, Wolever, O' Connor, Nisenbaum, & Josse, 2011) and Mexico (Parera et al., 2012). All of these studies suggested that LGI diet may become a new alternative strategy in reducing postprandial blood glucose in women with GDM without restriction of the dietary CHO (Louie et al., 2011; Afaghi, Ghanei, & Ziaee, 2013; Moses et al., 2009; Perera et al., 2012; Grant et al., 2011). However, only two studies compared the dietary intakes of participants at baseline and at the end of the study (Louie et al., 2011; Moses et al., 2009).

LGI dietary intervention may be compromised as it may limit food choices and varieties; some LGI foods are high in fat and sugar. A recent study has shown that LGI diet in Asia has its own limitations (Barakatun Nisak et al., 2014) due to the limited availability of LGI foods in the market. Additionally, prices of LGI foods are more expensive than HGI (high glycaemic meals) (Barakatun Nisak, Ruzita, Norimah, Gilbertson, & Kamaruddin, 2010).

Although the beneficial effects of a low GI diet have been noted, the findings may not be generalised to the Asian dietary context because of the cultural and food pattern differences between Western and Asian countries (Barakatun Nisak et al., 2014). For example, in Malaysia, white rice, an HGI food, is usually consumed twice daily. This study is conducted to determine the effect of a low GI diet on dietary intake and food choices among women with GDM. It is hypothesised that participants in LGI group achieves significantly improvement in dietary intake than standard nutrition therapy (SNT) group.

MATERIALS AND METHODS

Study Design and Ethical Approval

This is a randomised controlled study to compare the effects of a low GI diet against SNT on dietary intake and food choices in women with GDM. The duration of the study is four weeks,

and it was conducted at Universiti Kebangsaan Malaysia Medical Centre (UKMMC). Clinical research and Ethics Committee of UKMMC approved the study protocol and all participants provided written consent prior enrolment into the study.

Subjects' Selection and Sample Size

The sample size for this study was 40 women with GDM. They were pregnant women aged 18 - 45 years with confirmed diagnosis of GDM between 18 and 23 weeks of gestation. They had a pre-pregnancy BMI of $> 23 \text{ kg/m}^2$ (World Health Organization, 2000) and a haemoglobin level of $\geq 11 \text{ g/dl}$ (World Health Organization, International Obesity Task Force, & International Association for the Study of Obesity, 2011). Participants excluded from the study were those on insulin therapy and reported having chronic hyperemesis gravidarum, complicated pregnancy, food allergy, having gastrointestinal disease that interfered with bowel function and dietary intake (i.e., gastroparesis, diarrhoea due to chronic inflammatory bowel disease and galactosaemia).

The sample size required for the study was calculated based on the mean differences in glucose control by 0.5 mmol/L and variance of 1 mmol/L between the control and low GI intervention in women with GDM (Perera et al., 2012). This study used 95% confidence level and additional 20% for considering the drop-out rate

Dietary Intervention

The participants subscribed to either low GI or the SNT dietary intervention in which the outcomes were measured after a 4-week period. All participants received individualised counselling. Dietary intervention and recommendations were similarly structured and the only differences was in the type of carbohydrates consumed. Nutritional prescriptions are based on the MNT for GDM (REF- CPG and MNT diabetes). Macronutrient composition was set at 50-55% for carbohydrates, 15-20% for protein and 30% fat based on the previous survey on dietetics practices (Farhanah, Fatin Nasirah, Barakatun Nisak, Nor Azlin, & Zalilah, 2014). Energy requirement was calculated based on pre-pregnancy BMI (REF). Participants with pre-pregnancy BMI between 23 and 24.9 kg/m^2 were provided with 30 to 35 kcal/kg and pre-pregnancy BMI $> 25 \text{ kg/m}^2$ were given 25 to 30 kcal/kg.

To maintain the same amount of carbohydrates, participants were instructed to eat according to carbohydrate exchange systems. In this exchange system, one exchange of carbohydrates is equal to 15 g of carbohydrates and they were allowed to exchange the carbohydrates within the same food groups (American Diabetes Association, 2003). In the LGI group, participants received education to substitute high GI to low GI foods. The list of low GI and high GI foods for one exchange of carbohydrates within the same food groups was provided. Participants needed to incorporate at least one low GI food in each meal and distribute low GI foods for each meal throughout the day in order to achieve the daily diet GI's goal (Barakatun Nisak, Ruzita, Norimah, Gilbertson, & Kamaruddin, 2010). In the SNT group, participants were instructed to eat a high fibre carbohydrate containing foods without referring to the GI concept.

All participants received advice on eating pattern for small frequent meals, distributed evenly throughout the day and portion size controlled by using a plate method (Farhanah et

al., 2014.) They also received a set of meal plan based on their energy requirement and food baskets that contained recommended foods. In an LGI group, the food basket consisted of basmati rice, pasta, whole grain bread, barley, hi-calcium biscuits and low-fat milk. In the SNT, the food baskets consisted of white rice, whole grain bread, instant oats, meehoon, cream crackers and cornflakes.

Dietary Assessment

Participants provided information on their usual dietary intake for the past one month at baseline and during the 4-week study using the food frequency questionnaire (FFQ). The diet GI and GL (glycaemic load) were also calculated from the FFQ. The FFQ is adapted from Norimah and Kather (2003) and consisted of 137 food items which were listed under 14 food groups in order to identify specific sources of carbohydrate that contributed to the GI value of the study participants. These 14 food groups included rice, bread, noodle and pasta, kuih, dough, starchy vegetables, fruits, milk and dairy products, biscuits, beverages, breakfast cereals, miscellaneous, confectionery, legume, and sucrose.

The participants also recorded foods and beverages consumed over the last 24 hours for three days throughout the intervention period. They were asked to record intake for two week-days and one weekend day. The amount of foods consumed was based on the standard household measurement Suzana, Noor, Nik Shanita, Rafidah and Roslina (2009).

Nutrient analysis was done using the Dietary Plus Software developed by Ng (2010) for energy, protein, fat, carbohydrate, calcium, iron and cholesterol. Dietary GI and GL was also analysed using this software. A majority of the foods consumed by the participants were gleaned from the database. However, for certain cases where the food was not available in the database, the methods described previously (Barakatun Nisak et al., 2010) were used to estimate the GI of the foods. In general, the estimation of GI values was based on similar matched factors of the individual ingredients of the foods such as the type of fibre (soluble or insoluble), fat content, acidity, particle size, protein, and cooking and processing methods.

Statistical Analysis

Data was analysed using SPSS version 21 (SPSS Inc. Chicago, USA) and the significant level was set at $p < 0.05$. Results were expressed as mean \pm SD, unless otherwise stated. Descriptive statistics were used to present the baseline socio-demographic, obstetric characteristic and dietary intake. Comparisons between two groups were analysed using the independent T-Test. The effect of dietary intervention on dietary intake was assessed using General Linear Model (GLM) over time, between time and treatment group, and time interaction with repeated measures on time.

RESULTS

We screened 480 participants but almost 92% of them (n = 440) were not eligible mainly because they exceeded 34 weeks of gestations (n = 396). A total of 40 participants signed the informed consent letter. They were randomised to LGI (n = 20) or SNT (n = 20). All participants completed the study (Figure 1).

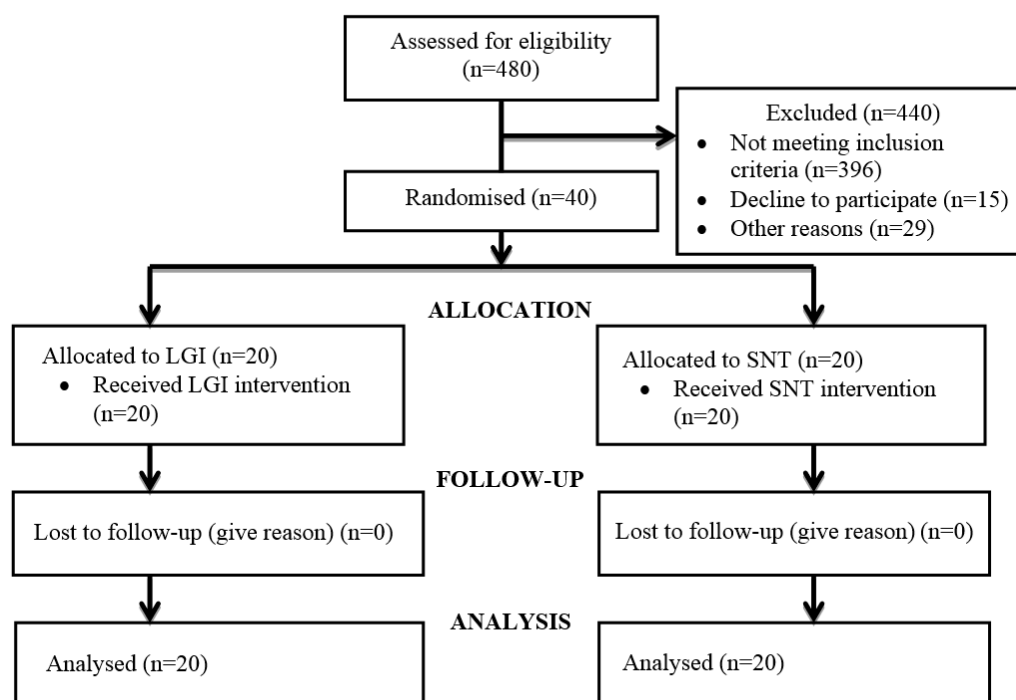


Figure 1. Participants enrolment and follow-up

At baseline, no significant differences were noted in the participant’s characteristics between the LGI and control SNT groups. Participants on average had 32.5 ± 4 gestation weeks with majority of them having a history of GDM (75%) (Table 1).

Table 1
Obstetrical characteristics of participants in the LGI and SNT group at baseline

Characteristics	LGI Group (n=20)	SNT Group (n=20)	p-value
	Means \pm SD	Means \pm SD	
Age [#]	33 \pm 3.1	32 \pm 4.9	0.4
Pre-pregnancy BMI (kg/m ²) [#]	29.7 \pm 6.8	28.5 \pm 6.4	0.5
Body weight (kg) [#]	70.4 \pm 16.1	70.4 \pm 17.6	0.9
Height (cm) [#]	154 \pm 5.9	156 \pm 5.1	0.2
Week of gestation [#]	27 \pm 4.4	24.6 \pm 3.4	0.06
History of GDM (%) [*]	45%	30%	0.3

Statistical Analysis: t-test[#], descriptive^{*}

Table 2 shows energy, protein, fat and carbohydrate over time were significantly reduced in the LGI and SNT group ($p < 0.05$). Furthermore, percentage of fat and carbohydrate significantly reduced within 4 weeks of intervention in both groups over time ($p < 0.05$). Nevertheless, no significant interaction (time*group) and group effect was noted in all nutrients as shown in Table 2.

Table 2

Comparison of daily nutrient intake data (Mean \pm SD) calculated from food frequency questionnaires of the participants in the LGI and SNT over 4 weeks period

Nutrient	Group			P			Time	Time* group Group	Group
	Low Glycaemic Index (n=20)		Δ	Standard Nutrition Therapy (n=20)		Δ			
	Baseline Mean \pm SD	Week 4 Mean \pm SD		Baseline Mean \pm SD	Week 4 Mean \pm SD				
Energy (kcal)	2599 \pm 1476	2234 \pm 1115	-365	2031 \pm 744	1842 \pm 708	-189	<0.05	ns	ns
Protein (g)	109 \pm 70	86 \pm 48	-22	83 \pm 43	76 \pm 44	-6	<0.05	Ns	ns
Protein (g/kg body weight)	1.5	1.2	-0.3	1.2	1.1	-0.1	ns	Ns	ns
Protein (%)	17 \pm 9	15 \pm 2	-1.7	15 \pm 7	16 \pm 4	1.1	<0.05	Ns	ns
Fat (g)	85 \pm 50	75 \pm 38	-10	60 \pm 26	59 \pm 27	-1	<0.05	Ns	ns
Fat (%)	28 \pm 9	31 \pm 4	2.5	27 \pm 5	29 \pm 5	2.4	<0.05	Ns	ns
CHO (g)	363 \pm 201	290 \pm 154	-72	278 \pm 104	243 \pm 85	-35	<0.05	Ns	ns
CHO (%)	55 \pm 6	52 \pm 5	-3.6	56 \pm 7	53 \pm 7	-2.3	<0.05	Ns	ns
Cholesterol (mg)	323 \pm 239	302 \pm 236	-20	284 \pm 177	289 \pm 183	5	ns	Ns	ns

Statistical Analysis: General Linear Model (GLM)

Participants in the LGI group had higher dietary calcium compared with those in the SNT group ($p < 0.05$ Table 3). The fibre intake of the participants in the LGI group seemed to be higher than the SNT group with no statistically significant difference but the differences in the means was moderate (eta squared = 0.08). Dietary GI in the LGI group seemed to be significantly lower than the SNT group with the difference of 7 units of GI ($p < 0.05$) (Table 3).

Table 3

Daily nutrient intake data (Mean± SD) calculated from 3-day food records of the participants in the LGI and SNT over 4 weeks

Nutrient	Low Glycaemic Index (n=20) Mean ± SD	Standard Nutrition Therapy (n=20) Mean ± SD	p-value
Energy (kcal)	1456± 358	1431 ±374	0.8
kcal/ kg body weight	19.85 ±7.6	18.79 ±6.9	0.6
Protein (g)	70 ±16	64 ±13	0.2
g/1000kcal	49 ± 7.5	46 ±6.8	0.1
% Protein	19 ±3	17± 3	0.09
Fat (g)	45 ±21	42 ±14	0.5
g/1000kcal	30.4 8.8	30 7.1	0.8
Dietary fibre (g)	17± 16	11 ±5	0.09
g/1000kcal	12.2 ±10	7.5 ±2.6	0.05
Ca (mg)	702 ±309	500 ±278	<0.05
Fe (mg)	30± 75	16 ±14	0.3
Cholesterol (mg)	255 ±120	253 ±120	0.9
Dietary GI	50± 9	57 ±6	<0.05
Dietary GL	24 ±7	26± 5	0.4

Statistical analysis: t-test

Table 4 compares the carbohydrate sources between LGI and SNT groups based on a 3-day food records throughout the intervention. It has been documented that the main source of carbohydrate between both groups were from rice. However, in the LGI group, it has been reported that 22% of rice consumed were from the low GI rice varieties such as basmati and parboiled ($p<0.05$).

About 40% of the rice that were consumed by the participants in the SNT group came from HGI rice varieties such as white rice, fragrance rice and instant rice which was significantly higher than the LGI group ($p<0.05$). During the intervention, whole grain bread and LGI biscuits were highly preferable in the LGI group as compared with participants in the SNT group ($p<0.05$).

Table 4
Comparison of carbohydrate sources between LGI and SNT groups based on 3-day food records

Cho Sources	Low Glycaemic Index (mean±SD)	Standard Nutrition Therapy (mean±SD)	Total
Total rice (%)	40 ± 12	44 ± 18	ns
Low GI varieties (%)	22 ± 15	3.5 ± 9	<0.05
High GI varieties (%)	18 ± 15	40.5 ± 23	<0.05
Total bread (%)	9.5 ± 5.5	6.6 ± 9.2	ns
Whole grain (%)	6.6 ± 6.3	1.4 ± 4.2	<0.05
Whole meal (%)	0.5 ± 1.4	0.6 ± 2.6	ns
White bread (%)	2.4 ± 5.1	4.4 ± 7.6	ns
Total noodle and pasta (%)	7.4 ± 8.2	11 ± 9.7	ns
Noodle wheat based (%)	0.4 ± 2.2	0.7 ± 3.3	ns
Noodle rise base (%)	5.7 ± 6.5	10 ± 10	ns
Pasta (%)	1.3 ± 5.8	0.3 ± 1.3	ns
Total Kuih (%)	7.2 ± 11	7.7 ± 9	ns
Kuih-wheat based (%)	4.6 ± 8.4	6.5 ± 8.7	ns
Kuih rice based (%)	2.6 ± 8.9	1.2 ± 4.3	ns
Total dough (%)	3.2 ± 4.9	6.7 ± 9.2	ns
Low GI varieties (%)	0.7 ± 2.4	0.6 ± 2.6	ns
Other varieties (%)	2.5 ± 4.7	5.9 ± 8.8	ns
Starch vegetables (%)	0.6 ± 0.9	1.0 ± 3.0	ns
Low GI varieties (%)	0 ± 0	0 ± 0	ns
Other varieties (%)	0.6 ± 0.9	1.0 ± 3.0	ns
Total Fruits (%)	7.6 ± 10	4.8 ± 5.2	ns
Low GI varieties (%)	3.9 ± 6.2	2.3 ± 4.8	ns
Other varieties (%)	3.7 ± 6.9	2.5 ± 3.6	ns
Milk and dairy products (%)	9.8 ± 8.5	4.9 ± 6.8	ns
Biscuits (%)	5.4 ± 6.3	5.2 ± 6.0	ns
Low GI varieties (%)	4.4 ± 5.9	1.0 ± 4.4	<0.05
Other varieties (%)	1.0 ± 2.2	4.2 ± 4.9	ns
Beverages (%)	4.3 ± 6.3	1.5 ± 2.1	ns
Low GI varieties (%)	2.9 ± 5.6	0.4 ± 1.2	ns
Other varieties (%)	1.4 ± 2.4	1.1 ± 2.0	ns
Breakfast cereals (%)	1.0 ± 3.4	0.9 ± 2.3	ns
Low GI varieties (%)	0.6 ± 2.4	0.2 ± 1.1	ns
Other varieties (%)	0.4 ± 1.3	0.7 ± 2.1	ns
Miscellaneous (%)	0 ± 0	0.1 ± 0.2	ns
Confectionery (%)	0 ± 0	1.5 ± 3.6	ns
Legume (%)	2.1 ± 4.8	0.1 ± 0.2	ns
Sucrose added (%)	1.9 ± 2.2	4.0 ± 6.1	ns
Total	100	100	

Statistical Analysis: t-test

DISCUSSION

This study examined the effects of low GI diet on the metabolic response of women with GDM in Malaysia. The energy, protein, fat, CHO and dietary fibre intake of the participants in the LGI and SNT group were similar. Furthermore, there was no significant difference in the dietary of GI and GL between both groups. Nevertheless, it showed that the percentage of CHO was higher among Malaysian women with GDM compared with women with GDM from Western countries (Moses et al., 2009; Perera et al., 2012). This may be due to the fact Asian staple food consist of polished rice and refined wheat with HGI and GL values (Ludwig, 2002).

It is interesting to note that, participants who were in the LGI group has significantly lower dietary GI intake compared with the SNT group ($p < 0.05$). The dietary data of the participants were obtained from the 3-day food records and FFQ.

The incorporation of GI concept in the LGI group has significantly affected the dietary GI of the participants. Dietary assessment based on a 3-day food records from this study showed significant differences in dietary GI between LGI and SNT group which was 7 units ($p < 0.05$). This may be due to an increase in consumption of basmati rice, whole grain bread, pasta, milk, and dairy products, barley biscuits and legumes, which are mostly from the low GI varieties.

The pattern of food intake in this study was similar to that observed in the previous study among participant with T2DM, whereby, the participants in the LGI group were more likely to consume food with low GI value such as parboiled and Basmati rice, whole grain bread, pasta, temperate-climate fruits and biscuits from LGI varieties (Barakatun Nisak, Ruzita, Norimah, Gilbertson, & Kamaruddin, 2010). Meanwhile, in study that involved women with previous history of GDM, fibre intake was significantly higher among participant in LGI group ($p < 0.001$) compared with those who were allocated to the control group (Shyam et al., 2013).

Perera et al. (2012) and Moses et al. (2009) also found that participants in the LGI group have achieved and maintained significantly lower dietary GI than the control group. Dietary GI was reduced as much as 8 units in Moses et al. (2009) while 4 units reduction was reported by Perera et al. (2012) at the end of the study among participants in the LGI group.

Rice is a staple of over half of the world's population and provides 20% of the world's energy supply (Food & Agriculture Organization, 2004). Most of the white rice varieties are a GI food (Sugiyama, Tang, Wakaki, & Koyama, 2003). This was supported by a study done by Barakatun Nisak, Talib and Karim (2005) who studied the GI of eight types of commercial rice in Malaysia, reported that the GI value of Malaysian rice was categorised as medium to high GI food with the range of 60 to 87. Almost 97% of Malaysian consumed white rice twice daily (Norimah & Kather, 2003). This is also in accordance with our earlier observation, which showed that the largest proportion of carbohydrate sources was from rice, with the percentage of 40 and 44 in the LGI and SNT group respectively. However, more than half (22%) of the rice from the LGI group was in from low GI category ($p < 0.05$).

Participants in the GI group were advised to substitute white rice with parboiled and Basmati rice to reduce the dietary GI throughout the study (Barakatun Nisak et al., 2011). The participants in this study were also given a food basket of cereals, pasta, milk and biscuits from the low GI food categories. This may be one of the factors that improved the dietary GI of LGI group in this study. This was in line with Grant et al. (2011) and Louie et al. (2011) who

provided food samples, list of foods and menu planning based on participant's assignment to increase adherence to the diet prescribed.

Brand-Miller, Petocz, Hayne and Colagiuri (2003) found that a reduction of 10 units of dietary GI is considered clinically significant with a positive effect on the glycaemic outcomes. In this study, the dietary GI of LGI group was 7 units lower than SNT group.

Reported intake of energy, protein, fat and carbohydrate reduced significantly throughout time ($p < 0.05$). The participants in both the LGI and SNT group have achieved the carbohydrate recommendation target, with the range of 50% to 55% of total energy intake. It is encouraging to compare the result with the previous study of women with GDM who discovered reduction in carbohydrate percentage in both the GI group as well as control group (Moses et al., 2009; Perera et al., 2012).

Fibre intake, which could be a confounding variable in determining the potential advantages of a LGI diet, was similar with no significant difference between both groups. However, the intakes of dietary fibre in the LGI group were higher (12.2 g/1000 kcal/day) than those women in the SNT group (7.5 g/1000 kcal/day). This is due to fibre-rich foods which are LGI foods (Riccardi, Rivellese, & Giacco, 2008). Furthermore, the higher the viscous or soluble fibre is, the lower its GI (Kirpitch & Maryniuk, 2011). This increases the viscosity of the intestinal content, which slows down the interaction between starch and digestive enzymes resulting in lower and lower glycaemic excursions (Kirpitch & Maryniuk, 2011).

The calcium intake of participants in the LGI group appeared to be higher than the SNT group ($p < 0.05$). This may be due to higher intake of milk and dairy products among participants in LGI groups. Overall, the implementation of the LGI diet has improved dietary quality in women with GDM as well as patients with T2DM in Malaysia (Barakatun Nisak, Ruzita, Norimah, Gilbertson, & Kamaruddin, 2010).

A recent study has stated that subscribing the low GI diet in Asia has its own limitations as the availability of low GI foods in the market is not as high GI foods (Barakatun Nisak et al., 2014). Besides, the prices of low GI foods are higher than high GI meals (Barakatun Nisak et al., 2010). Though the availability of low GI local Malaysian foods is limited, the few GI studies that have been done in Malaysia have proven that incorporation of GI concept dietetic management is feasible and has shown an improvement glycaemic control and dietary quality of patient with type 2 diabetes and women with history of GDM (Barakatun Nisak, Ruzita, Norimah, Azmi, & Fatimah, 2009; Shyam et al., 2013).

CONCLUSION

In conclusion, the incorporation of the LGI dietary strategy in dietetic management of GDM did not lead to poor quality of food consumed by the participants in LGI group. On the contrary, participants in the LGI group had greater intake of fibre and calcium than participants in SNT group. The reduction in dietary GI in LGI group has provided another dietary management option for managing GDM in Malaysia. Future trial is required to add more data on GI of Malaysian food. This would assist the feasibility of women with GDM to maintain low GI dietary intake in a traditional Asian diet.

ACKNOWLEDGEMENTS

The authors would like to thank the MOSTI, Science Fund that enabled them to undertake this study, the medical laboratory technologists of the Endocrine Unit, Universiti Kebangsaan Malaysia Medical Centre for their assistance, and lastly, the patients who participated in the study.

REFERENCES

- Afaghi, A., Ghanei, & Ziaee, A. (2013). Effect of low glycaemic load diet with and without wheat bran on glucose control in Gestational Diabetes Mellitus: A randomized trial. *Indian Journal of Endocrinology and Metabolism*, 17(4), 689-692.
- American Diabetes Association. (2007). Medical nutrition therapy and lifestyle intervention. *Diabetes Care*, 30 (Suppl. 2), s188-s193.
- American Diabetes Association. (2008). Nutrition recommendation and interventions for diabetes: A position statement of the American Diabetes Association. *Diabetes Care*, 31, s61-78.
- American Diabetes Association. (2003). Gestational Diabetes Mellitus. *Diabetes Care*, 26(1), S103-S105.
- Barakatun Nisak, M. Y., Ruzita, A. T., Norimah, K., Gilbertson, H., & Kamaruddin, N. A. (2010). Improvement of dietary quality with the aid of low glycaemic index diet in Asian patients with type 2 diabetes mellitus. *Journal of American College of Nutrition*, 29(3), 161-170.
- Barakatun Nisak, M. Y., Talib, R. A. & Karim, N. A. (2005). Glycemic Index of eight types of commercial rice in Malaysia. *Malaysian Journal Of Nutrition*, 11, 151-163.
- Barakatun Nisak, M. Y., Ruzita, A. T., Norimah, A. K., Azmi, N. K., & Fatimah, A. (2009). Acute effect of low and high glycaemic index meals on post-prandial glycemia and insulin responses in patients with type 2 diabetes mellitus. *Malaysian Journal of Medicine and Health Sciences*, 5(1), 11-20.
- Barakatun Nisak, M. Y., Firouzi, S., Shariff, Z. M., Mustafa, N., Ismail, N. A. M., & Kamaruddin, N. A. (2014). Weighing the evidence of low glycaemic index dietary intervention for the management of gestational diabetes mellitus: An Asian perspective. *International Journal of Food Sciences and Nutrition*, 65(2), 144-150.
- Brand-Miller, J., Petocz, P., Hayne, S., & Colagiuri, S. (2003). Low glycaemic index diets in the management of diabetes, a meta-analysis of randomized control trials. *Diabetes Care*, 26,2261-2267.
- Farhanah, A. S., Fatin Nasirah, M. D., Barakatun Nisak, M. Y., Nor Azlin, M. I., & Zalilah, M. S. (2014). Current dietetic practices in the management of gestational diabetes mellitus: A survey of Malaysian dietitians. *Asian Journal of Clinical Nutrition*, 6(3), 67-74.
- Food & Agriculture Organization. (2004). Rice is life. Retrieved on 1 August 2015 from http://www.fao.org/newsroom/en/focus/2004_6887/
- Galgani, J., Aguirre, C., & Diaz, E. (2006). Acute effect of meal glycaemic index and glycaemic load on blood glucose and insulin responses in humans. *Nutrition Journal*, 5(22), 1-7.
- Grant, S. M., Wolever, T. M. S., O' Connor, D. L., Nisenbaum, R., & Josse, R. G. (2011). Effect of a low glycaemic index diet on blood glucose in women with gestational hyperglycaemia. *Diabetes Research and Clinical Practice*, 91, 15-22.

- Kirpitch, A. R., & Maryniuk, M. D. (2011). The 3R's of glycaemic index: Recommendations, research, and the real world. *Clinical Diabetes*, 29(4), 155-159.
- Louie, J. C., Markovic, T. P., Perera, N., Foote, D., Ross, G. P., & Brand-Miller, J. C. (2011). A randomized controlled trial investigating the effects of a low glycaemic index diet on pregnancy outcomes in gestational diabetes mellitus. *Diabetes Care*, 34(11), 2341-2346.
- Ludwig D. S. (2002). The glycaemic index. Physiological mechanisms relating to obesity, diabetes, and cardiovascular disease. *The Journal of the American Medical Association*, 287, 2414-23.
- Mareno C. C., Mauricio, D., & Hernandez, M. (2016). Role of medical nutrition therapy in the management of gestational diabetes mellitus. *Current Diabetes Report*, 16(4).
- Moses, R. G., Barker, M., Winter, M., Petocz, P., & Brand-Miller, J. C. (2009). Can a low-glycaemic index diet reduce the need for insulin in gestational diabetes mellitus? *Diabetes Care*, 32(6), 996-1000.
- Ng, T. N. K. W. (2010). DietPLUS- a user-friendly '2 in 1' food composition database and calculator of nutrient intakes. *Malaysian Journal of Nutrition*, 16(1), 125-130.
- Norimah, A. K., & Kather, H. M. M. (2003). Nutritional status and food habits of middle- aged adults in selected areas of Selangor. *Malaysian Journal of Nutrition*, 9(2), 125-136.
- Perera, O. P., Nakash, M. B., Rodriguez-Cano, A., Legorreta, J. L., Parra-Covarrubias, A., & Vadillo-Ortega, F. (2012). Low glycaemic index carbohydrates versus all types of carbohydrates for treating diabetes in pregnancy: A randomised clinical trial to evaluate the effect of glycaemic control. *International Journal of Endocrinology*, 1-10.
- Riccardi, G., Rivellese, A., & Giacco, R. (2008). Role of glycaemic index and glycaemic load in the healthy state, in prediabetes, and in diabetes. *American Society for Clinical Nutrition*, 87(1), 269S-274S.
- Shyam, S., Arshad, F., Ghani, R. A., Wahab, N. A., Safii, N. S., Nisak, M. Y. B., ... & Kamaruddin, N. A. (2013). Low glycaemic index diets improve glucose tolerance and body weight in women with previous history of gestational diabetes: A six months randomized trial. *Nutrition Journal*, 12(68), 1-12.
- Sugiyama, M., Tang, A. C., Wakaki, Y., & Koyama, W. (2003). Glycaemic index of single and mixed meal foods among common Japanese foods with white rice as a reference food. *European Journal of Clinical Nutrition*, 57, 743-752.
- Suzana, S., Noor, A. M. Y., Nik Shanita, S., Rafidah, G., & Roslina, A. (2009). *Atlas of food exchanges and portion sizes* (2nd ed). Kuala Lumpur: MDC Publishers.
- World Health Organization. (2011). Hemoglobin concentration for the diagnosis of anemia and assessment of severity. Vitamin and mineral nutrition information system. Retrieved on 16 June 2014 from <http://www.who.int/vmnis/indicators/haemoglobin.pdf>
- World Health Organization, International Obesity Task Force, & International Association for the Study of Obesity. (2000). *The Asia-Pacific perspective: Redefining Obesity and its Treatment*. Hong Kong.



The Effect of Varying PID Gains on Position Transient Response of a Robotic Hand System

Salleh, N. M., Shauri, R. L. A.*, Nasir, K., Remeli, N. H. and Kamal, M. M.

Faculty of Electrical Engineering, Universiti Teknologi MARA (UiTM), 40450 Shah Alam, Selangor, Malaysia

ABSTRACT

In an earlier study, a three-fingered robot hand was developed for assembly work. Proportional Integral Derivative (PID) control was used to control the position of a DC micromotor measured by an encoder. However, PID control alone could not cater the nonlinearities due to friction of gears and varying loads applied to the finger. Therefore, in order to develop an intelligent control algorithm in future, the effects of varying PID gains need to be investigated to distinguish the optimal value that could produce the best transient response performance. This paper discusses the effect of varying PID gains on position transient response of the joint motor of robot hand through real-time experiments. Several ranges of K_p , K_i and K_d were identified based on the required transient response parameters such as percentage overshoot (%OS), settling time (T_s) of within 2%, steady state error (SSE) and rise time (T_r). The gains are tuned across the range by a fixed interval with the tuning order starting from K_p , K_i and K_d . It can be observed that the suitable ranges of PID are 0.3 to 0.5 for K_p , 1.15 to 1.45 for K_i and 0.10 to 0.14 for K_d . Meanwhile, the optimum value of 0.4, 1.45 and 0.10 for K_p , K_i and K_d respectively is found to produce 0 of % OS, 5.09 sec of T_s and 2.48 sec of T_r . Hence, the gains can be applied to the development of an improved position control using intelligent method for the robot hand in future works.

Keywords: : PID control, PID parameter tuning, position control, transient response, real-time experiment

ARTICLE INFO

Article history:

Received: 05 January 2017

Accepted: 17 January 2017

E-mail addresses:

sharizasalleh@gmail.com (Salleh, N. M.),

ruhizan@salam.uitm.edu.my (Shauri, R. L. A.),

khairunnisanasir@yahoo.com (Nasir, K.),

hananiremeli@gmail.com (Remeli, N. H.),

mahani724@salam.uitm.edu.my (Kamal, M. M.)

*Corresponding Author

INTRODUCTION

Current research and development in robotic technologies are aiming at creating robust and autonomous manufacturing system (Brogårdh, 2007; Lovchik & Diftler 1999). Producing robots that could imitate human capabilities is beneficial in many fields such as medical, rehabilitation, industry, and even military. It is not only the operating system that is important but also the robot design.

Lovchik and Diftler (1999) produced a robot hand for teleoperation in outer space. Meanwhile, the presence of robot manipulators in the industry could solve the shortage of skilled labour, thus, reducing production cost.

Programming is important to make the robot fully automated. In the integrated programming, it has one main component which is a control system. The controller is a component which has to generate an appropriate control signal and it is applied in systems and process control and needs to be optimised in order to obtain a good control system stability in an intelligent autonomous system. The most common controller used in industries is Conventional Proportional Integral Derivative (PID) control. This is due to its practicality and simple mathematical equation involved. For example, Li and Yu (2011) applied PID Controller to control 7-DOF exoskeleton. PID controller is tuned using their own novel tuning approach based on common conventional tuning methods. Meanwhile, Sonoda and Godler (2011) developed a robotic finger with twisted string actuation controlled by PI controller.

However, new researches combined PID with embedded intelligent control algorithms such as Fuzzy Control Logic (FLC), Adaptive Neuro Fuzzy Inference System (ANFIS), Artificial Neural Network (ANN) and Genetic Algorithm (GA) to improve the tuning of PID gains. Yu, Li and Carmona (2013) examined the application of robotic hand for patient's rehabilitation. The support device must be a simple structure, light weight, low-cost, easy maintenance, and uses soft actuator. The fuzzy-PID method has been used to accommodate the varying loads of patient hands for control. Some examples of intelligent control system combined with Fuzzy-PID is found in (Erden & Leblebicioglu, 2004). This study is to develop a three-joint robot leg that can be used for any required positions. The fuzzy-PID controller was designed for this three-joint robot leg for accurate position and trajectory tracking control. To create the rules for Fuzzy, it needs optimal investigation to understand transient behaviour by optimum trajectories planned by the user. The result shows selected control method has better outcome than conventional PID Controller. Chopra, Singla and Dewan (2014) studied embedded intelligent system control to improve linearity of PID control compared with intelligent control. The results showed that PID with embedded intelligent control performed better than stand-alone PID control for non-linear systems. However, this study only used simulations and not real time control. Even though the intelligent system is applied into the control systems, the PID control is still required. The results using PID control will be used as references to manipulate any control method in future control design.

In previous study, a robot hand which consists of three fingers and a palm was developed. All the seven joints are actuated by DC micromotors. The finger mechanism was analysed by Shauri, Remeli, Jani and Jaafar (2014) and Azri and Shauri (2014). However, the robot hand requires an intelligent PID control to produce precise motions. It can be observed in a separate experiment that the tuning of PID gains (K_P , K_I and K_D) could not be solved using Ziegler Nichols method. Therefore, this paper investigates the effect of varying PID gains on the transient response of the finger joint position through real-time experiment. Trial and error method was used for this purpose because the dynamic equation of the motor was not available. The range of PID gains that complies the required transient response parameters are first determined. Then, the comparisons between the transient responses of the gains between

the ranges are compared to determine the optimum value of each K_p , K_i and K_d . The analysis is based on transient response parameters which included percentage overshoot (%OS), settling time (T_s) of within 2% of a given step input, steady state error (SSE) and rise time (T_R).

PID Control and Transient Response

PID control is generally used for controlling automation system and processes in industrial plants. Even though PID controller does not involve complex mathematical calculation, it can assure the satisfaction in performances of a wide range of process plants (Visioli, 2001). The PID control is an acceptable controller, easy to be understood and adequate for many practical systems (Wang et al., 1999). However, gain parameters need to be tuned to make sure it could produce good transient parameter performances.

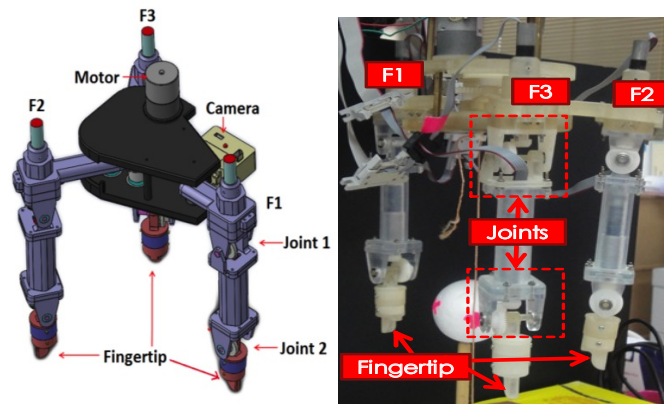
In control systems, transient response can be defined as the behaviour of the system following a sudden change in its input. The transient response parameters that have been used to evaluate the control system performance in order to attain the optimum value for gain parameters are as follows:

- Maximum Overshoot (%OS): The excess value of output response beyond the desired value of angle position at the peak time. It is also calculated as percentage of exceeded value to the input step response.
- Settling Time (T_s): The time required for the transient's damped oscillations to settle and maintain their values within $\pm 2\%$ or $\pm 5\%$ of the steady-state value. In this study, the $\pm 2\%$ of T_s is used.
- Rise Time (T_R): The time required by the response to rise between 10% and 90% of the final value.

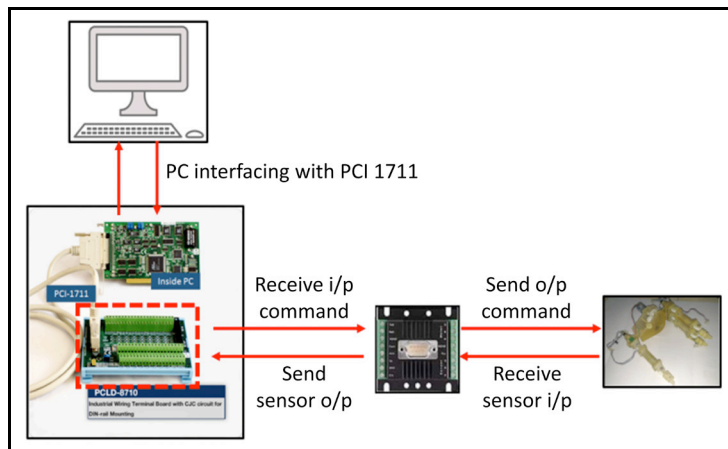
Real-Time Control System and Architecture

Figure 1(a) shows the robot hand which consists of three fingers and a palm. It also consists of the controller, interfacing device, motor driver, actuator and sensor as shown in Figure 1(b). Every two joints of each finger are actuated by DC micromotors. An interfacing contains two devices which are Advantech PCI-1711 interfacing card and PCLD-8710 input output terminal connected using 68-pin SCSI cable. Analog voltage from the terminal is sent to the motor driver to actuate the DC micromotor and a magnetic encoder measures the actual position in terms of signal pulses.

The MATLAB Simulink software with real-time control toolbox is used to control the DC micromotor position in a real time. An advantage of using MATLAB real-time control compared with microcontrollers is that the control parameters can be directly changed by the user without having to rebuild and upload the programming. In this paper, one of the fingertips has been used to investigate the tuned gain parameters to the performance of position control. The results of this investigation can be used as reference for setting the gain parameters of other fingers in future studies.



(a)



(b)

Figure 1. Robot hand system: (a) Three-fingered robot hand (Shauri et al., 2014); and (b) Software and hardware interfacing

Identification of Range for PID Gains

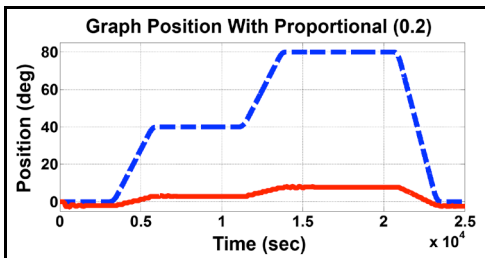
The PID gains for lower and upper limits are determined based on the transient response performance for each varying gain. The required transient response parameters are 0% of OS and short duration of T_s , and T_R . First, the K_p tuning began with a value which is close to zero, then increased by 0.1 interval to find the response with least ripple and steady state error. While K_p gain is tuned, the K_i and K_d are set to zero. Once the optimal value of K_p is determined, K_i is tuned by 0.15 interval. Optimum value of K_i is selected based on the fastest response with the minimum %OS.

Finally, the K_p and K_i , K_d is tuned by increasing the interval by 0.02 until the transient response could arrive at its desired position in the shortest T_s and T_R , 0% of OS and without ripples on the signal. Every transient response from the tuning steps was compared and analysed manually.

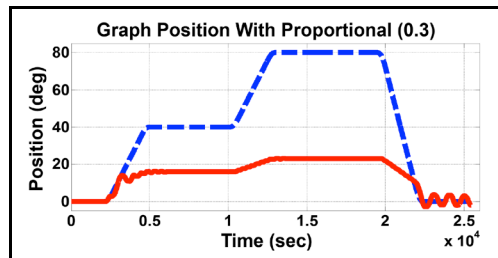
RESULTS AND DISCUSSION

Proportional Gains Parameter Tuning

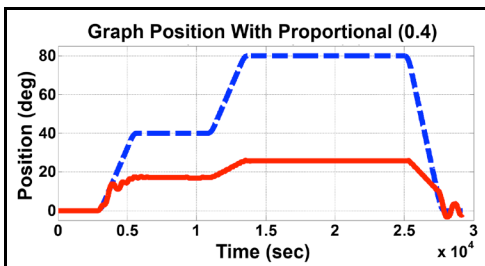
From graphs as shown in Figure 2, it can be observed that the values of K_p between 0.3 and 0.5 are accepted as the best range of K_p . K_p at 0.5 is selected as the best value due to its lowest SSE. Among the tested range of K_p , 0.2 gives the highest SSE while K_p at 0.6 gives the lowest SSE but it starts to produce ripples on the signal. It can be concluded that the ripples will occur after K_p is set above 0.6. The comparison between the SSE values for each varying K_p ranging between 0.2 and 2.2 is shown in Table 1.



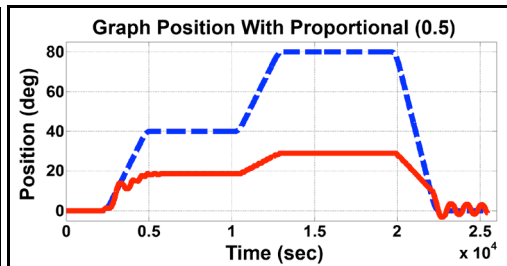
(a)



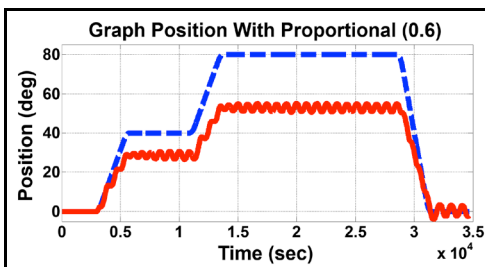
(b)



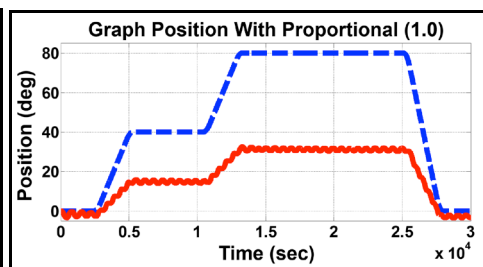
(c)



(d)



(e)



(f)

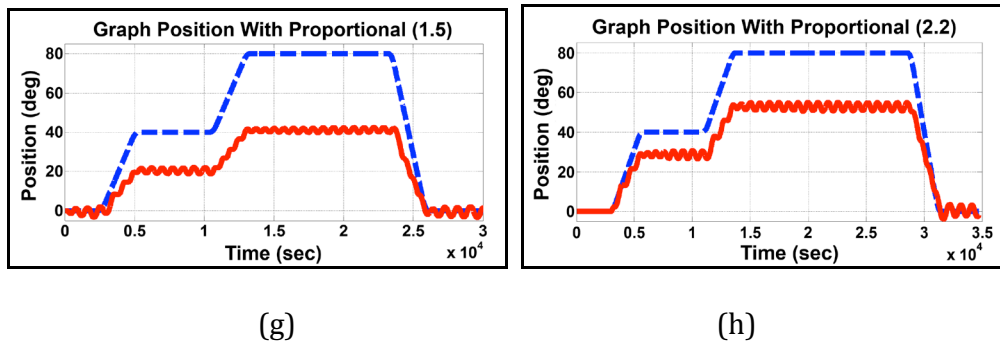


Figure 2. Effect of varying proportional gain K_p ($K_p, 0, 0$): (a) 0.2, 0, 0; (b) 0.3, 0, 0; (c) 0.4, 0, 0; (d) 0.5, 0, 0; (e) 0.6, 0, 0, (f) 1.0, 0, 0; (g) 1.5, 0, 0; and (h) 2.2, 0, 0

Table 1
Proportional gain tuning

Proportional Gain (K_p)	SSE
0.2	72.27
0.3	57.08
0.4	54.12
0.5	51.03
0.6	29.16
1.0	49.48
1.5	40.06
2.2	29.16

Integral Gains Parameter Tuning

The results as shown in Table 2 indicate that K_p at 0.4 gives the lowest T_s and T_R compared with K_p at 0.5. Furthermore, when the position returned from 80 to 0, the % OS for K_p at 0.4 gives lower value than K_p at 0.5. Therefore, the new optimum value of 0.4 for K_p is used for the K_i tuning within the range of 0.85 to 1.60.

From the same table, the value of K_i between 1.15 and 1.45 are accepted as the best range of K_i . To obtain the optimal K_i , this range is compared based on the best value of the transient parameters. K_i at 1.60 gives lowest T_s but also an amount of 4.22% of OS when the position returned from 80 to 0. Meanwhile, K_i at 1.45 gives acceptable T_s with lowest T_R and % OS compared with the other K_i values. Thus, 1.45 is chosen as the optimal value for K_i . The transient response for each varying K_i is shown in Figure 3.

The Effect of Varying PID Gains on Position Transient Response

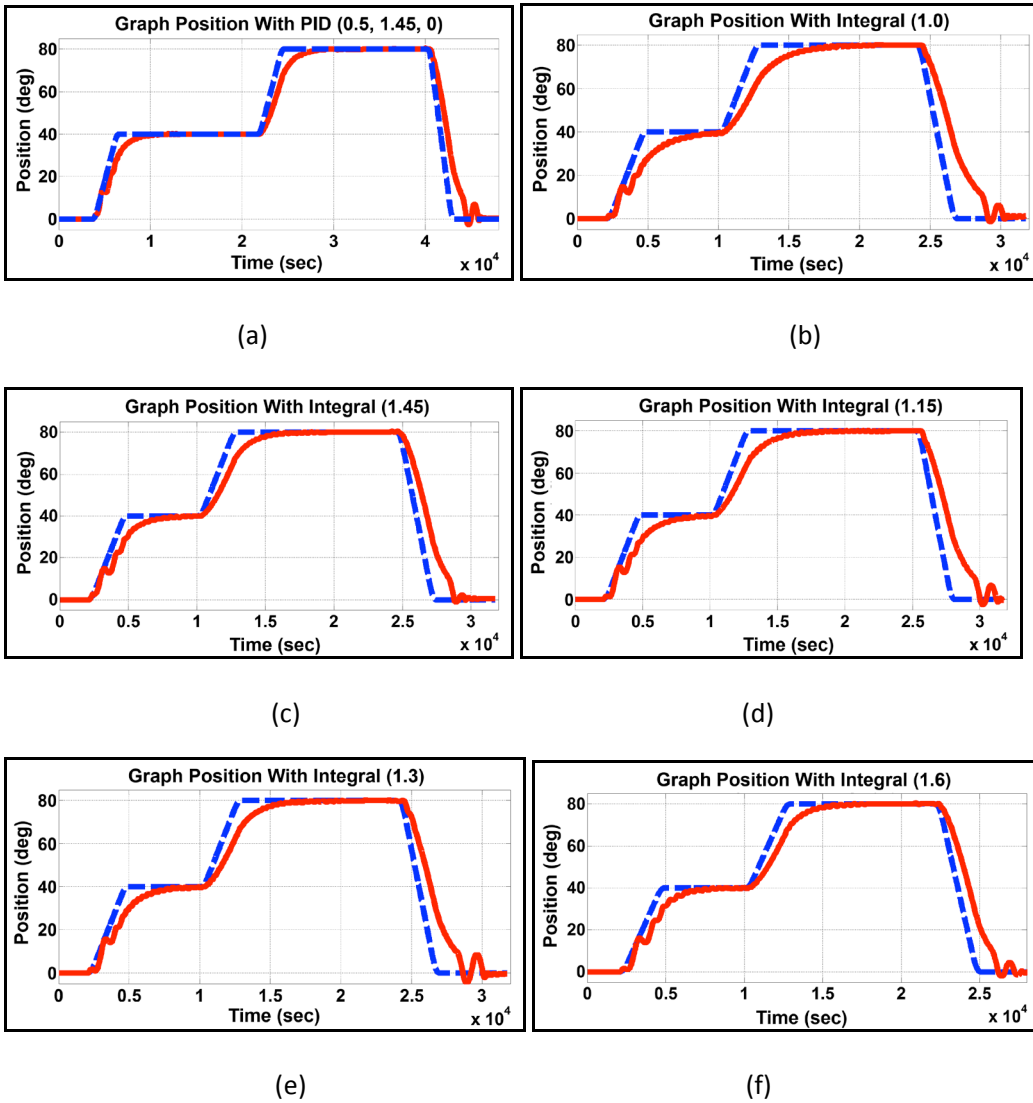


Figure 3. Effect of varying integral gain K_i ($K_p, K_i, 0$): (a) 0.5, 1.45, 0; (b) 0.4, 1.0, 0; (c) 0.4, 1.15, 0; (d) 0.4, 1.45, 0; (e) 0.4, 1.3, 0; and (f) 0.4, 1.6, 0

Table 2
Integral gain tuning

$(K_p, K_i, 0)$	Transient Parameters		
	T_s	T_R	%OS (at 0°)
0.5, 1.45, 0	5.42	2.50	6.89
0.4, 1.00, 0	6.51	3.04	6.05
0.4, 1.15, 0	5.84	2.74	6.54
0.4, 1.30, 0	5.52	2.57	8.37
0.4, 1.45, 0	5.15	2.39	2.18
0.4, 1.60, 0	4.71	2.70	4.22

Derivative Gains Parameter Tuning

After the optimum values for K_p and K_i was determined, K_d varied between 0.08 and 0.16. The results in Table 3 show that the acceptable range of K_d is between 0.10 to 0.12 where the optimal value of 0.10 produces the lowest T_R and T_S . Besides, the same value is able to eliminate the ripples and overshoots that occur with the other K_d values. Several sets of other K_p , K_i and K_d which are closer to the value of the optimum K_p : 0.4, K_i : 1.45 and K_d : 0.10 were tested. The comparison between the transient response performance is shown in Table 4 and in Figure 5. It can be concluded that the optimum value of PID gives lowest T_S , T_R and 0% of OS.

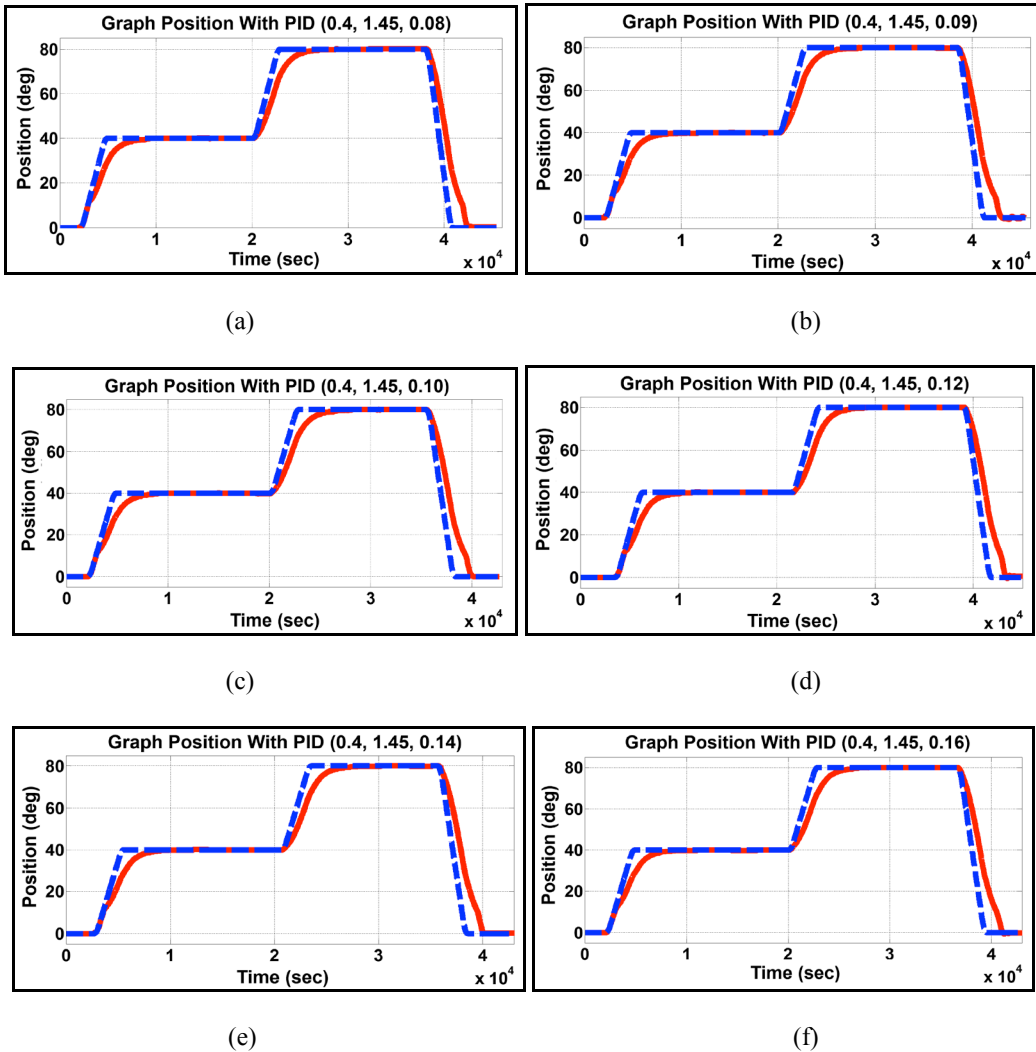


Figure 4. Effect of varying derivative gain K_D (K_p , K_i , K_D): (a) 0.4, 1.5, 0.08; (b) 0.4, 1.45, 0.09; (c) 0.4, 1.45, 0.10; (d) 0.4, 1.45, 0.12; (e) 0.4, 1.45, 0.14; and (f) 0.4, 1.45, 0.16

Table 3
Derivative gain tuning

Derivative Gain (K_D)	Transient Parameters	
	T_s	T_R
0.08	5.26	2.52
0.09	5.17	2.53
0.10	5.09	2.48
0.12	5.23	2.50
0.14	5.10	2.53
0.16	5.27	2.54

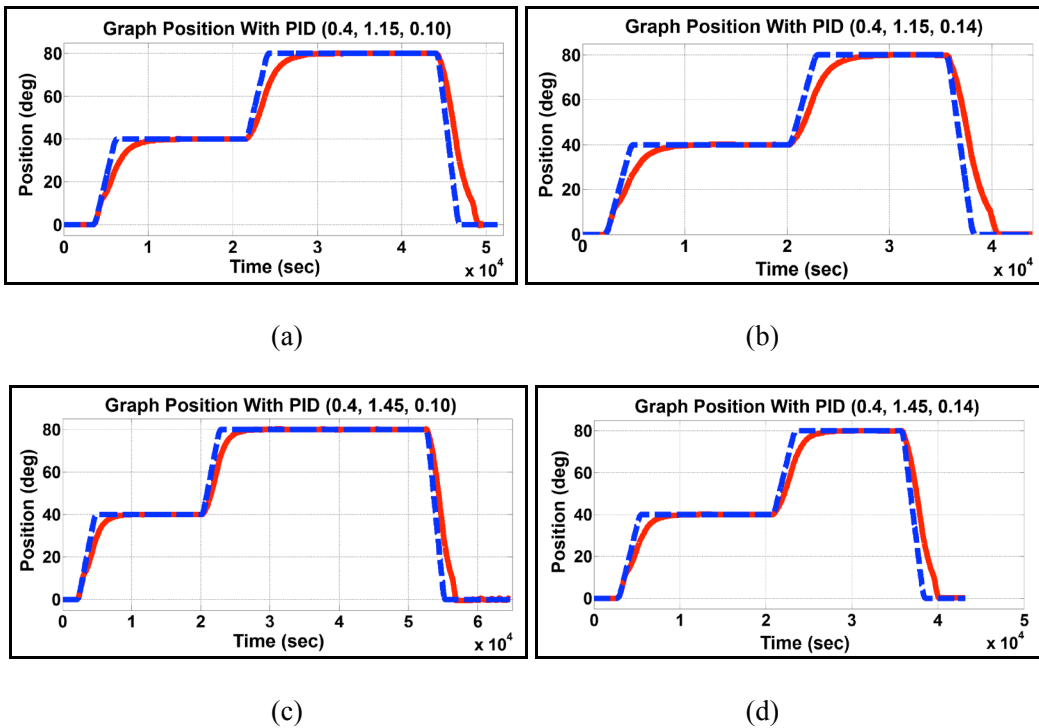


Figure 5. Effect of varying PID gains (K_p , K_i , K_D): (a) 0.4, 1.15, 0.10; (b) 0.4, 1.15, 0.14; (c) 0.4, 1.45

Table 4
Transient parameter of varying PID

PID Gains			Transient Parameters	
K_p	K_i	K_D	T_s (sec)	T_R (sec)
0.4	1.15	0.10	6.14	2.81
0.4	1.45	0.10	5.09	2.48
0.4	1.15	0.14	6.16	2.88
0.4	1.45	0.14	5.10	2.53

CONCLUSION

This study examined the varying PID gains on position transient response of a robotic hand system using a trial and error method. The results showed K_p , K_i and K_d at 0.4, 1.45 and 0.10 respectively are the optimum values to give 5.09 sec T_s , 2.48 sec T_R and 0% of OS. The suitable range of the K_p , K_i and K_d was obtained and will be used to design PID-Fuzzy Control for robot hand in future works.

ACKNOWLEDGEMENTS

This research was supported by Research Management Centre (RMC) and Faculty of Electrical Engineering, Universiti Teknologi MARA, Malaysia through Academic and Research Assimilation Grant (600-RMI/DANA 5/3 ARAS (11/2015)).

REFERENCES

- Azri, M. H. B. M., & Shauri, R. L. A. (2014). Finite element analysis of a three-fingered robot hand design. *Proceedings of the 2014 IEEE 4th International Conference on System Engineering and Technology*, 4, 1-6.
- Brogårdh, T. (2007). Present and future robot control development—An industrial perspective. *Annual Reviews in Control*, 31(1), 69–79.
- Chopra, V., Singla, S. K., & Dewan, L. (2014). Comparative analysis of tuning a PID controller using intelligent methods. *Acta Polytechnica Hungarica*, 11(8), 235–249.
- Erden, M. S., & Leblebicioglu, K. (2004). Fuzzy controller design for a three joint robot leg in protraction phase - An optimal behavior inspired fuzzy controller design. *Proceedings of the First International Conference on Informatics in Control, Automation and Robotics*, 2, 302–306.
- Li, X., & Yu, W. (2011). A systematic tuning method of PID controller for robot manipulators. *IEEE International Conference on Control and Automation, ICCA*, 274–279.
- Lovchik, C. S., & Diftler, M. A. (1999). The robonaut hand: A dexterous robot hand for space. *Robotics and Automation*, 2(May), 907–912.
- Shauri, R. L. A., Remeli, N. H., Jani, S. A. M., & Jaafar, J. (2014). Development of 7-DOF three-fingered robotic hand for industrial work. *Proceedings - 4th IEEE International Conference on Control System, Computing and Engineering, ICCSCE 2014*, (November), 75–79.
- Sonoda, T., & Godler, I. (2011). Position and force control of a robotic finger with twisted strings actuation. *In Advanced Intelligent Mechanics (AIM)* (pp. 611-616).
- Visioli, A. (2001). Optimal tuning of PID controllers for integral and unstable processes. *Control Theory and Applications, IEE Proceedings - JOUR*.
- Wang, Q. G., Lee, T. H., Fung, H. W., Bi, Q., & Zhang, Y. (1999). PID tuning for improved performance. *IEEE Transactions on Control Systems Technology*, 7(4), 457–465.
- Yu, W., Li, X., & Carmona, R. (2013). A novel PID tuning method for robot control. *Industrial Robot: An International Journal*, 40(6), 574–582.



Classification of Car Paint Primers Using Pyrolysis-Gas Chromatography-Mass Spectrometry (Py-GC-MS) and Chemometric Techniques

Raja Zubaidah Raja Sabaradin¹, Norashikin Saim^{1*}, Rozita Osman¹ and Hafizan Juahir²

¹Faculty of Applied Science, Universiti Teknologi MARA (UiTM), 40450 Shah Alam, Selangor, Malaysia

²East Coast Environmental Research Institute, Universiti Sultan Zainal Abidin (UNISZA), 21300 Gong Badak Campus, Kuala Terengganu, Malaysia

ABSTRACT

Pyrolysis-gas chromatography-mass spectrometry (Py-GC-MS) has been recognised as an effective technique to analyse car paint. This study was conducted to assess the combination of Py-GC-MS and chemometric techniques to classify car paint primer, the inner layer of car paint system. Fifty car paint primer samples from various manufacturers were analysed using Py-GC-MS, and data set of identified pyrolysis products was subjected to principal component analysis (PCA) and discriminant analysis (DA). The PCA rendered 16 principal components with 86.33% of the total variance. The DA was useful to classify the car paint primer samples according to their types (1k and 2k primer) with 100% correct classification in the test set for all three modes (standard, stepwise forward and stepwise backward). Three compounds, indolizine, 1,3-benzenedicarbonitrile and p-terphenyl, were the most significant compounds in discriminating the car paint primer samples.

Keywords: Car paint primer, chemometric analysis, Py-GC-MS

ARTICLE INFO

Article history:

Received: 05 January 2017

Accepted: 17 January 2017

E-mail addresses:

rajazubaidah2512@gmail.com (Raja Zubaidah Raja Sabaradin),

noras691@salam.uitm.edu.my (Norashikin Saim),

rozit471@salam.uitm.edu.my (Rozita Osman),

hafizanjuahir@unisza.edu.my (Hafizan Juahir)

*Corresponding Author

INTRODUCTION

Automotive paint analysis is one of the important analyses in the forensic laboratory for accidents or hit-and-run cases. Generally, traces of automotive paint can be recovered either from the victim's car, human body or at the scene of the accident. These automotive paint chips are valuable evidence as they can be linked to the vehicles involved. The paint

finish normally consists of four very thin layers, namely cathodic electro deposition (CED), primer, basecoat and clearcoat.

In examining car paint, the optical and spectrometric methods are commonly used in order to obtain information about its colour, morphology and chemical composition (Trzcińska, Zięba-Palus, & Kościelniak, 2009; Zięba-Palus, Michalska, & Wesełucha-Birczyn, 2008). Fourier transform infrared spectroscopy (FTIR) is the most common spectrometric method used in car paint analysis. This method is sensitive to molecular structure and therefore provides much information about the chemical composition of a paint sample. However, if a small amount of sample is recovered, identification of the organic pigments using FTIR is almost impossible, thus reducing its discriminating power (Zięba-Palus et al., 2011).

Pyrolysis-Gas Chromatography-Mass Spectrometry (Py-GC-MS) has gained interest in forensic investigation as it can be applied for trace analysis. This method has been applied to differentiate types of binders of paint coatings (Zięba-Palus, Zadora, & Milczarek, 2008) and clear coat of car paint (Plage, Berg, & Luhn, 2008). Burns and Doolan (2005) showed that Py-GC-MS was able to discriminate paint samples indistinguishable using FTIR analysis.

The chemometric techniques with spectroscopic data produce efficient, rapid and more robust outcome than a classical visual comparison (Muehlethaler, Massonnet, & Esseiva, 2011). This technique has been widely used to discriminate and classify the samples. This method is efficient in exploring and analysing spectroscopic data sets. It has been applied in the analysis of household paint (Muehlethaler et al., 2011), spray paint (Muehlethaler, Massonnet, & Esseiva, 2014), ballpoint inks (Borba, de Honorato, & de Juan, 2015), and inkjet inks (Gál, Oravec, Gemeiner, & Čeppan, 2015).

In this study, car paint primer samples from various manufacturers were analysed using Py-GC-MS. This study used two types of car paint primer, 1k and 2k types. The 1k car paint primer refers to the “one component” paint which does not require hardener and can be directly applied on the surface, while the 2k car paint primer is a “two-component” paint mixed with hardener at certain ratio before it can be applied on the surface. Otherwise, the car paint primer will not harden on the surface. Chemometric techniques have been used to evaluate the potential of Py-GC-MS data of car paint primers in forensic investigation.

MATERIALS AND METHOD

Car paint primer samples, as listed in Table 1, were obtained from workshops in Selangor, Malaysia. The 1k car paint primer samples were directly applied on the aluminium sheet and baked for 20 minutes at 120°C. The 2k primer samples were prepared by mixing them with the hardener and applied on the aluminium sheet before they were baked in the oven at 60°C for 30 minutes. The car paint primer sheet was polymerised for at least three days. The samples were scrapped off using a utility knife prior to analysis.

Table 1
List of samples

Car primer type	Sample
1k	P001 – P005 (5 samples)
2k	P006 – P050 (45 samples)

The Py-GC-MS analysis was conducted using a PY-2020iD pyrolyzer attached to Agilent Technologies 7890A gas chromatograph coupled with Agilent Technologies 5975C mass spectrometer. All samples were weighed prior to the analysis (0.3 mg). The samples were then placed inside a quartz tube held in the platinum coil of pyroprobe. The pyrolysis was performed at the temperature of 750°C for 6 seconds with interface of 350°C. The product of the pyrolysis was then transferred to the chromatographic capillary column (30 m x 0.25 mm, 0.25 m) for separation. The stationary phase of the gas chromatography (GC) column consisted of 5% diphenylpolysiloxane and 95% dimethylpolysiloxane. The GC parameter was set at 40°C for 30 minutes, ramped at 10°C/min at 280°C for 20 minutes. Elution times for all compounds were obtained within 30 minutes. The analysis was run at least three times for each sample. The compounds were identified using NIST08 MS library search with quality matching more than 80%.

Py-GC-MS data set is large and has complex information. The data set of pyrolysis products was subjected to chemometric techniques (principal component analysis (PCA) and discriminant analysis (DA) to display the most significant patterns and possible groupings and sources of data variation. In this study, XLSTAT2014 software was used for the multivariate statistical calculations.

The PCA is an exploratory, multivariate, statistical technique that can be used to examine data variability. This technique provides information on the most meaningful parameters that describe the whole data set rendering data reduction with minimum loss of the original information (Vega, Pardo, Barrado, & Deban, 1998). The PCA was applied on the data set from the Py-GC-MS to identify and determine the sources of car paint primer compounds.

The DA determines the variables that discriminate between two or more naturally occurring groups/clusters. It constructs a discriminant function (DF) for each group (Singh, Malik, Mohan, Sinha, & Singh, 2004, 2005). The DFs were calculated using equation (1)

$$f(G_i) = k_i + \sum_{j=1}^n w_{ij}P_{ij} \quad (1)$$

Where i is the number of groups (G), k_i the constant inherent to each group, n the number of parameters used to classify a set of data into a given group and w_j is the weight coefficient assigned via DF analysis (DFA) to a given parameter (p_j). In this study, DA was applied to the pyrolysis products using the standard, forward stepwise and backward stepwise modes. In the forward stepwise mode, variables were included step-by-step beginning from the most significant variables until no significant changes were seen. In backward stepwise mode,

variables were removed step-by-step beginning with the less significant variables until no significant changes were noted. The DA may help in identifying the significant compounds for classification of the car primer according to their types.

RESULTS AND DISCUSSION

Figure 1 shows selected pyrograms of two different types of car paint primer, 1k (P003 and P004) and 2k (P021 and P024). The patterns of these pyrograms correspond with the product of degradation of the polymer and its monomer. Similar patterns were observed in the first 15 minutes. However, after 15 minutes of analysis, some differences in the patterns of the pyrograms showed the potential of Py-GC-MS in differentiating the car paint primer samples. Milczarek, Zięba-Palus and Kościelniak (2005) found the relative intensities of some important compounds may be used based on the highest observed peak in the pyrograms. In this study, two compounds, styrene (7.15 minutes) and azulene (12.35 minutes) were selected.

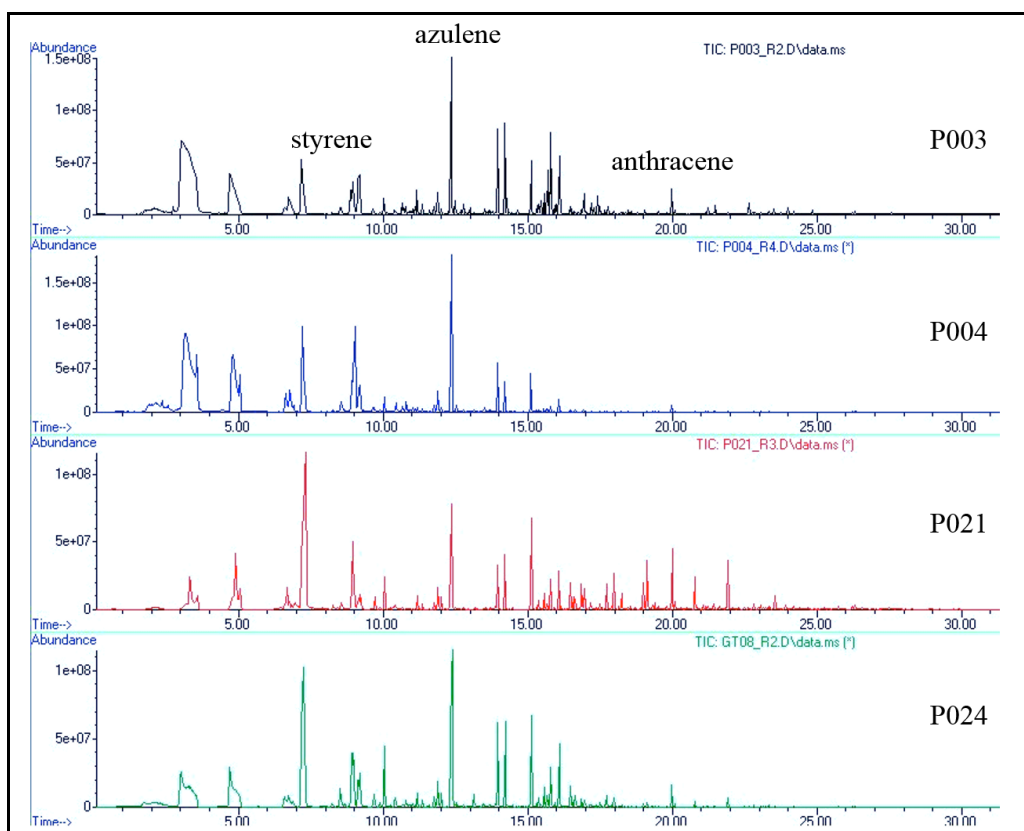


Figure 1. Pyrograms of car paint primer of different types

Evaluating the discriminating ability of pyrograms for car paint primer samples was based on the procedure recommended by Zięba-Palus, Michalska, Weselucha-Birczyn and Kościelniak (2008). The baseline of the pyrogram was shifted to the level of 10% of largest peak height. Visible peaks with relative height larger than 10% were marked with 'A'. Similarly, when the baseline was downshifted to the level of 5% of largest peak height, new peaks that appeared on the pyrogram were marked with 'B'. Consequently, 'C' was given for the compounds with signals of relative height in range from 2 to 5%. Peaks with relative height less than 2% were marked with 'ND' as these peaks were very small and their reproducibility considered as inconsistent. Compounds identified in pyrograms of the selected car paint primer samples are listed in Table 2.

Common compounds in these primer samples include toluene, ethylbenzene, styrene, α -methylstyrene, indene, naphthalene and azulene with retention time of 4.70, 6.60, 7.15, 8.90, 10.00, 11.90 and 12.35 respectively. Toluene, ethylbenzene, α -methylstyrene, and naphthalene are the products of degradation of the polystyrene, a basic component of car paint primer. Azulene was the major compound (marked as 'A') present in all samples except P019 and P025. Thus, differentiating the car paint primer based on the compounds of level 'A' and 'B' was not possible as these compounds were observed in all samples.

Most compounds identified after 20 minutes of the analysis were minor compounds (marked as 'C' or 'ND'). Anthracene (20 minutes) was observed in almost all car paint primer samples. Some minor compounds, such as indolizine, were observed only in sample P005, triphenylmethane in sample P002 and di-*p*-tolylacetylene in sample P003. Sample P041 can be distinguished from other samples due to the presence of 3-methyl-methyl ester benzoic acid, (1-methylenebut-2-enyl) benzene, (*Z*)-7-hexadecene, methyl ester hexadecenoic acid, n-hexadecenoic acid. These compounds are most probably products of degradation of the main components. Thus, these minor compounds may be used in discriminating the car paint primer samples.

The PCA applied to the data set of 65 pyrolysis products resulted in 16 varifactors (VFs) explaining 86.33% of total variance. The PCs generated by PCA are sometimes not readily interpreted. Therefore, it is advisable to rotate the PCs by Varimax rotation. Varimax rotations applied on the PCs with eigenvalues greater than 1 are considered significant (Kim & Mueller, 1987) in obtaining new groups of variables called Varimax factors (VFs). The VF coefficients have a correlation greater than 0.75, between 0.75 and 0.50, and between 0.50 and 0.30 are considered to have "strong", "moderate", and "weak" significant factor loading respectively (Liu, Lin, & Kuo, 2003). Table 3 shows the factor loadings after Varimax rotation.

There were five VFs associated with strong loading in the identification and determination of the sources of car primer compounds. The VF1 explained 18.33% of total variance with strong loading (>0.75) of cis-stilbene, (E)-stilbene, o-terphenyl, m-terphenyl, benzo(c) phenanthrene, benz(a)anthracene and triphenylene. This is the group of isomers with three different types of benzene arrangement. The stilbene and terphenyl isomers have two and three benzene rings respectively. The benzo(c)phenanthrene and benz(a)anthracene are the isomer of triphenylene with 4 benzene rings fused together. VF2 with 11.58% of the total variance has strong loading of (E)-cinnamaldehyde, 1,3-benzenedicarbonitrile, benzophenone, benzo(h) quinoline and phenanthridine. The strong loading in VF3 are 3-methyl-methyl ester benzoic acid, 1-methylenebut-2-enyl benzene, (Z)-7-hexadecene, methyl ester hexadecanoic acid, n-hexadecanoic acid and methyl ester octadecanoic acid. The carboxylic acid is commonly found in car paint primer binder. Phenol, di-p-tolylacetylene and benzo(kl)xanthene are the dominant compounds in VF4. Phenol may be the product of degradation of the other main components in the car paint primer. The VF5 with relatively low variance (6.05%) has strong loading on naphthalene and 1,4-dihydronaphthalene which are the products of polystyrene degradation.

Discriminant analysis was applied to the raw data of pyrolysis products using standard, forward stepwise and backward stepwise modes. The standard, forward stepwise and backward stepwise modes yielded 100% correctly assigned based on 48, 3 and 47 compounds (Table 4 and Table 5) respectively. Forward stepwise DA shows that indolizine, 1,3-benzenedicarbonitrile and benzo[kl]xanthene are the discriminating compounds. Therefore, DA results suggested these were the most significant compounds in discriminating between the types of car paint primer.

Table 3
Loading of car primer compounds on significant principal components for Py-GC-MS dataset

Compound	VF1	VF2	VF3	VF4	VF5	VF6	VF7	VF8	VF9	VF10	VF11	VF12	VF13	VF14	VF15	VF16
Pyridine	0.010	0.038	-0.025	0.067	-0.134	0.050	0.076	0.032	0.024	0.134	0.047	-0.007	0.934	0.013	-0.014	0.007
Toluene	0.239	0.130	0.080	0.167	-0.006	0.009	0.821	-0.019	-0.064	0.115	0.062	0.054	0.058	-0.153	-0.107	-0.031
Phenol	-0.082	-0.070	-0.025	0.915	0.060	0.052	-0.021	-0.009	-0.026	0.147	0.063	0.015	0.100	-0.078	-0.056	0.020
(E)-Cinnamaldehyde	0.045	0.877	-0.005	-0.041	0.050	-0.075	-0.010	0.040	0.050	0.133	0.081	-0.302	-0.122	-0.044	-0.021	0.005
Indolizine	-0.107	-0.017	-0.012	-0.091	-0.436	-0.013	0.179	-0.030	-0.020	0.474	-0.367	-0.026	0.160	-0.151	0.219	-0.174
Naphthalene	-0.139	0.103	0.081	0.076	0.849	0.098	-0.043	-0.148	-0.011	-0.080	-0.023	0.025	-0.010	-0.025	0.051	0.019
1,4-Dihydronaphthalene	0.209	0.140	0.035	-0.014	0.842	-0.036	0.218	-0.021	0.026	0.147	0.059	0.004	-0.095	0.091	-0.001	-0.085
Azulene	-0.031	0.050	0.043	0.028	-0.039	-0.017	-0.078	-0.055	-0.068	0.087	-0.126	0.052	-0.006	0.043	0.093	0.789
Benzof[b]thiophene	-0.005	-0.050	-0.032	-0.021	0.023	-0.122	-0.123	0.014	-0.097	-0.074	0.079	-0.003	-0.017	0.028	0.862	0.035
3-methyl-methyl ester Benzoic acid	-0.006	-0.013	0.997	-0.006	0.017	-0.011	0.028	-0.003	0.001	-0.004	0.003	-0.001	-0.002	0.013	-0.006	-0.004
(1-Methylenebut-2-enyl)benzene	-0.006	-0.013	0.997	-0.006	0.017	-0.011	0.028	-0.003	0.001	-0.004	0.003	-0.001	-0.002	0.013	-0.006	-0.004
Quinoline	0.133	-0.084	-0.091	0.160	0.016	0.872	-0.026	0.082	-0.182	-0.048	0.006	-0.014	0.050	0.043	-0.126	-0.042
1,3-Benzenedicarbonitrile	-0.040	0.779	-0.026	-0.031	0.090	-0.079	0.044	0.001	0.029	-0.011	0.018	0.346	0.457	0.131	-0.020	0.009
cis-Stilbene	0.889	-0.154	-0.107	-0.112	0.122	-0.033	0.026	0.092	-0.100	-0.077	0.047	-0.058	-0.038	-0.066	0.077	0.026
(Z)-7-Hexadecene	-0.006	-0.013	0.997	-0.006	0.017	-0.011	0.028	-0.003	0.001	-0.004	0.003	-0.001	-0.002	0.013	-0.006	-0.004
Benzophenone	-0.012	0.882	-0.025	-0.018	0.040	-0.059	0.026	0.010	0.023	0.037	0.004	0.422	-0.057	0.015	-0.015	0.006
Benzo[h]quinoline	0.017	0.966	-0.018	-0.026	0.027	-0.065	0.010	0.005	0.015	0.092	0.007	-0.008	-0.084	0.029	-0.025	-0.003

Table 3 (continue)

Phenanthridine	-0.047	0.955	-0.029	0.012	0.072	0.026	0.033	-0.020	0.061	-0.021	0.004	0.179	0.159	-0.005	0.010	0.021
(E)-Stilbene	0.796	-0.274	0.019	-0.199	0.139	-0.116	0.062	0.124	-0.094	0.133	0.096	-0.063	-0.167	-0.058	0.085	-0.169
o-Terphenyl	0.903	0.090	0.141	-0.038	-0.072	0.026	0.020	-0.266	-0.036	-0.013	0.026	-0.069	-0.003	0.071	0.072	-0.065
methyl ester hexadecanoic acid	-0.006	-0.013	0.997	-0.006	0.017	-0.011	0.028	-0.003	0.001	-0.004	0.003	-0.001	-0.002	0.013	-0.006	-0.004
n-hexadecanoic acid	-0.006	-0.013	0.997	-0.006	0.017	-0.011	0.028	-0.003	0.001	-0.004	0.003	-0.001	-0.002	0.013	-0.006	-0.004
Triphenylmethane	-0.052	0.334	-0.024	0.003	0.042	-0.020	0.039	0.012	0.024	-0.067	-0.002	0.899	0.013	-0.014	0.008	0.018
di-p-Tolylacetylene	-0.011	-0.013	-0.011	0.853	0.033	-0.143	-0.020	0.063	0.037	-0.064	-0.187	-0.026	-0.103	0.224	0.040	-0.051
methyl ester octadecanoic acid	-0.006	-0.013	0.997	-0.006	0.017	-0.011	0.028	-0.003	0.001	-0.004	0.003	-0.001	-0.002	0.013	-0.006	-0.004
m-Terphenyl	0.878	-0.086	-0.055	-0.020	-0.216	0.151	-0.006	-0.146	-0.036	-0.049	0.061	0.014	0.026	0.038	-0.099	-0.047
Benzo[k]xanthene	-0.067	-0.059	-0.023	0.956	0.057	0.000	-0.022	0.010	-0.010	0.097	-0.003	0.005	0.050	0.001	-0.032	0.001
Benzo[c]phenanthrene	0.862	-0.085	-0.059	-0.018	-0.055	0.040	0.111	-0.057	0.144	-0.102	-0.160	0.001	0.012	-0.151	-0.055	0.216
Benzo[a]anthracene	0.856	0.253	-0.061	-0.044	0.018	0.122	0.105	-0.016	-0.161	-0.026	-0.140	-0.110	-0.036	-0.070	-0.060	0.194
Triphenylene	0.776	0.140	-0.069	0.292	-0.173	0.038	0.072	-0.145	0.157	-0.010	0.143	-0.079	0.268	0.069	-0.094	-0.056
Eigenvalue	11.92	7.53	6.82	4.98	3.93	3.43	2.53	2.43	2.22	1.91	1.74	1.56	1.48	1.37	1.16	1.12
% Total variance	18.33	11.58	10.48	7.66	6.05	5.27	3.89	3.74	3.42	2.93	2.67	2.40	2.28	2.10	1.78	1.72
Cumulative % variance	18.33	29.91	40.40	48.06	54.11	59.38	63.27	67.01	70.43	73.36	76.04	78.44	80.71	82.82	84.60	86.33

Note: Strong loading (>0.75) are shown in bold.

Table 4
Classification matrix for discriminant analysis of the car paint primer

Types of primer	% correct	Types of primer assigned by DA	
		1k primer	2k primer
Standard mode DA			
1k primer	100	5	0
2k primer	100	0	45
Total	100	5	45
Forward mode DA			
1k primer	100	5	0
2k primer	100	0	45
Total	100	5	45
Backward mode DA			
1k primer	100	5	0
2k primer	100	0	45
Total	100	5	45

Table 5
Classification functions for discriminant analysis of car primer samples

Compounds	Standard mode		Forward stepwise mode		Backward stepwise mode	
	1k	2k	1k	2k	1k	2k
Benzene	-1441447.618	-16795.507			-638559.461	2814.644
Pyridine	-40944687.829	-474203.056			-17561028.515	96931.418
Toluene	1995270.795	23494.723			849695.910	-4485.385
Picolinyl 7,13,16-docosatrienoate	-2831065.997	-32019.700			-1239189.704	6861.102
Ethylbenzene	-7350966.436	-85136.028			-3128795.210	17988.445
o-Xylene	259065.704	2828.988			118412.628	-606.394
Phenylacetylene	-4256027.814	-50816.304			-1781073.452	9633.249
Styrene	700536.209	8241.749			299024.941	-1564.968
Benzenemethanimine	6848166.983	72835.565			3110111.278	-18464.623
Benzaldehyde	-5290716.603	-52239.454			-2518795.096	15463.376
. alpha. -Methylstyrene	-12066779.675	-130571.615			-5383066.123	32674.829
Benzonitrile	4880848.495	54905.953			2125812.068	-12384.468
Indene	2737615.042	30625.433			1197173.072	-6999.111
Acetophenone	-12126060.982	-125789.985			-5621381.786	33083.632
Cinnamaldehyde, (E)-	14848496.715	149036.072			7056352.958	-41283.239
Indolizine	110940160.620	1340844.749	441.341	284.523	46245746.413	-239284.765
Benzyl nitrile	3996569.350	37083.529			1940472.641	-13135.630
2-Methylindene	1594699.703	16701.774			724081.629	-4562.647
Naphthalene	1331520.775	16654.586			515835.345	-3268.133
Azulene	-3658782.020	-37985.575			-1679536.189	10356.539
1-Naphthalenol	11266848.097	126993.690			4948654.039	-27325.119
Quinoline	-10286412.580	-114007.066			-4499208.348	27342.574
Isoquinoline	104436143.696	1159032.151			46083094.564	-266212.614

Table 5 (continue)

1,3-Benzenedicarbonitrile	87446451.883	1006893.258	99.335	60.131	37662011.636	-209067.414
Benzocycloheptatriene	2908559.426	34845.358			1179039.548	-7397.322
9-Octadecene, (E)-	-17983104.984	-196454.874			-7973240.130	48031.193
Dibenzofuran	5655282.252	60878.509			2532065.913	-15404.527
cis-Stilbene	-225308.395	-5503.048				
1(2H)-Acenaphthylene	-12029492.475	-127183.904			-5446228.210	33609.115
N-Allylphthalimide	11913340.486	133731.283			5199927.219	-30240.562
1H-Phenylene	923210.568	11302.127			347335.343	-2763.345
4-Ethylbiphenyl	-53908726.413	-605649.768			-23539106.730	136113.381
Fluorene	3765631.345	45194.574			1557260.192	-8743.814
Benzo[h]quinoline	-13123181.704	-147194.181			-5839733.116	30700.499
Phenanthridine	-107741265.688	-1192105.329			-47520773.899	278750.813
(E)-Stilbene	7767507.177	89122.005			3343616.094	-18929.377
9H-Fluoren-9-one	30417273.818	347322.102			13212983.897	-72884.288
Dibenzo [a, e] cyclooctene	-3847294.601	-47488.353			-1555260.302	8493.467
o-Terphenyl	-10109697.258	-113132.272			-4511505.644	23600.828
Triphenylmethane	-40181193.566	-536631.141			-15236399.172	72633.296
Fluoranthene	-3875215.347	-40697.564			-1745779.751	11312.862
Pyrene	-7768013.508	-88552.562			-3367986.622	18915.949
p-Terphenyl	-8176666.898	-96228.533			-3478688.136	18517.307
m-Terphenyl	7489445.660	77952.664			3558965.610	-18047.395
Benzo[kl]xanthene	14486943.084	172203.863	95.114	58.841	6243654.465	-29134.441
Benzo[c]phenanthrene	-142186320.695	-1624557.001			-61124138.845	355347.255
Benz[a]anthracene	133750853.794	1525758.365			57546046.819	-335506.879
Triphenylene	-5714616.456	-58616.908			-2730587.801	14266.536

CONCLUSION

The pyrogram of car paint samples showed that Py-GC-MS is a reliable, very informative analytical technique in the analysis of automotive paint in forensic investigation. Since the pyrograms obtained were quite similar, some minor compounds may be considered in differentiating the samples. As the Py-GC-MS datasets were complex, chemometric techniques were applied to the dataset for uncovering the relationship between variables. The strong loadings from PCA revealed the significant compounds in the car paint primer samples. These compounds may be important in the manufacturing of car paint primer. Using forward stepwise mode of DA, the car paint primer samples can be categorised into two types, 1k and 2k based on three compounds, indolizine, 1,3-benzenedicarbonitrile and p-terphenyl.

ACKNOWLEDGEMENT

The authors acknowledge ERGS funding (600-RMI/ERGS 5/3 (5/2012)) that enable them to carry out this study.

REFERENCES

- Borba, F. D. S. L., Honorato, R. S., & de Juan, A. (2015). Use of Raman spectroscopy and chemometrics to distinguish blue ballpoint pen inks. *Forensic Science International*, 249, 73-82.
- Burns, D. T., & Doolan, K. P. (2005). A comparison of pyrolysis-gas chromatography-mass spectrometry and Fourier transform infrared spectroscopy for the analysis of a series of modified alkyd paint resins. *ChimicaActa*, 539, 157-164.
- Gál, L., Oravec, M., Gemeiner, P., & Čeppan, M. (2015). Principal component analysis for the forensic discrimination of black inkjet inks based on the Vis-NIR fibre optics reflection spectra. *Forensic Science International*, 257, 285-292.
- Kim, J. O., & Mueller, C. W. (1987). *Introduction to factor analysis: What it is and how to do it*. Sage University Press, Newbury Park.
- Liu, C. W., Lin, K. H., & Kuo, Y. M. (2003). Application of factor analysis in the assessment of groundwater quality in a blackfoot disease area in Taiwan. *Science of the Total Environment*, 313, 77-89.
- Milczarek, J. M., Zięba-Palus, J., & Kościelniak, P. (2005). Application of pyrolysis-gas chromatography-mass spectrometry to car paint analysis for forensic purposes. *Problems of Forensic Sciences*, LXI, 7-18.
- Muehlethaler, C., Massonnet, G., & Esseiva, P. (2011). The application of chemometrics on Infrared and Raman spectra as a tool for the forensic analysis of paints. *Forensic Science International*, 209, 173-182.
- Muehlethaler, C., Massonnet, G., & Esseiva, P. (2014). Discrimination and classification of FTIR spectra of red, blue and green spray paints using a multivariate statistical approach. *Forensic Science International*, 244, 170-178.
- Plage B., Berg, A. D., & Luhn, S. (2008). The discrimination of automotive clear coats by pyrolysis-gas chromatography/mass spectrometry and comparison of samples by a chromatogram library software. *Forensic Science International*, 177, 146-152.
- Singh, K. P., Malik, A., Mohan, D., Sinha, S., & Singh, V. K. (2004). Multivariate statistical techniques for the evaluation of spatial and temporal variations in water quality of Gomti River (India) - A case study. *Water Research*, 38(18), 3980-3992.
- Singh, K. P., Malik, A., Mohan, D., Sinha, S., & Singh, V. K. (2005). Chemometric data analysis of pollutant in wastewater case study. *Analytical ChimicaActa*, 532, 15-25.
- Trzcińska, B., Zięba-Palus, J., & Kościelniak, P. (2009). Application of microspectrometry in the visible range to differentiation of car paints for forensic purposes. *Journal of Molecular Structure*, 924-926, 393-399.
- Vega, M., Pardo, R., Barrado, E., & Deban, L. (1998). Assessment of seasonal and polluting effects on the quality of river water by exploratory data analysis. *Water Research*, 32, 3581-3592.
- Zięba-Palus, J., Michalska, A., & Weselucha-Birczyn', A. (2011). Characterisation of paint samples by infrared and Raman spectroscopy for criminalistic purposes. *Journal of Molecular Structure*, 993, 134-141.

- Zięba-Palus, J., Zadora, G., & Milczarek, J. M. (2008). Differentiation and evaluation of evidence value of styrene acrylic urethane topcoat car paints analysed by pyrolysis-gas chromatography. *Journal of Chromatography A*, 1179, 47-58.
- Zięba-Palus, J., Zadora, G., Milczarek, J. M., & Kościelniak, P. (2008). Pyrolysis-gas chromatography/mass spectrometry analysis as a useful tool in forensic examination of automotive paint traces. *Journal of Chromatography A*, 1179, 41-46.



Experimental Study on Bearing Strength of Concrete Blocks under Concentric Compression Load

Mohd Raizamzamani Md Zain^{1,3*} and Norrul Azmi Yahya^{1,2}

¹*Faculty of Civil Engineering, Universiti Teknologi MARA (UiTM), 40450 Shah Alam, Selangor, Malaysia*

²*Queensland University of Technology, Brisbane, QLD 4001, Australia*

³*Kyoto University, Kyoto, Japan*

ABSTRACT

The present study examines the interaction between concrete and steel plate, particularly on the load bearing capacity of concrete blocks under confinement effects. 12 concrete blocks with the dimensions of 200 mm × 200 mm in cross section and 200 mm high were tested up to failure under compression load through 10 mm thickness of steel bearing plate. A series of experimental testing were performed to determine the maximum load bearing capacity in different sizes of steel plate and to identify the possible failure modes. The experimental data obtained from the experimental investigations were compared with pre-existing experimental data obtained from literature and mathematical formulation in various international standards. Experimental results indicate that the use of larger bearing plate gave higher value of load bearing capacity compared with small bearing plate due to larger contact area, thus, resulting in better effect of confinement. It was found that the concrete blocks fail in the shape of inverse pyramid when the steel plate is placed on top of it. Besides, other failures are vertical cracks and splitting cracks which appeared at the outer edge of contact area.

Keywords: Bearing strength, concrete block, confinement effects, steel bearing plate

INTRODUCTION

Bearing capacity characteristic of concrete is a very important parameter in designing structure support for building and other infrastructure such as concrete footing, anchorage for pre-stress member and even for concrete pedestal in bridges. The size of concrete blocks and steel plate can affect the load transfer and failure mechanism of concrete bearing. However, problems may

ARTICLE INFO

Article history:

Received: 05 January 2017

Accepted: 17 January 2017

E-mail addresses:

raizam@salam.uitm.edu.my (Mohd Raizamzamani Md Zain)

azmi_216@yahoo.com (Norrul Azmi Yahya)

*Corresponding Author

arise if there is lack of quantitative understanding of the concrete bearing capacity and its generation mechanism.

According to researchers (Escobar-Sandoval, Andren, & Gary, 2006; Ince & Arici, 2004; Rao & Swamy, 1974), vertical and radial cracking occurred with the use of plain concrete blocks subjected to high compressive loading. In order to provide a much higher compressive load without facing failure, the dimension of the column concrete should be extended. Nevertheless, this solution involves a high cost and not suitable. Another method was by placing steel plate on top of concrete block as can be seen on concrete bridge pedestal and the capacity of that concrete towards the load applied on it is called as load bearing capacity.

The load-bearing capacity was first studied by Bauschinger (1876), Meyerhof (1953), Shelson (1957), and Au and Baird (1960). Researchers noticed a formation of an inverted pyramid under the loading bearing plate and formulated a theory for concrete bearing capacity based on that observation.

Various types of concrete blocks such as rectangular section, square section and circular section were used by researchers to study the behaviour of load bearing strength of concrete. The understanding of bearing capacity of concrete is important for the design purpose of concrete members such foundation structures, end-bearing zone of pre-stressed post-tensioned beam, bridge bearing on concrete columns and many others (Al-Sahawneh, Amjad, Hassan, & Khair, 2013).

The bearing capacity of concrete is somehow always related to the variety of design problems as shown by Rao and Swamy (1974), and Yahya and Dhanasekar (2014). The bearing capacity can be calculated by the steel plate positioned at the touching surface of the concrete cubes. The increase in bearing capacity was related to the increase in the concrete strength, reduction in the height of the concrete blocks and the total to loaded area ratio either for the plain or unreinforced concrete cubes (Ahmed, Burley, & Rigden, 1998; Al-Ta'an, 2005). Ragip, Ince and Arici (2004) found that parameters such as the loaded area, loaded member cross-section, specimen size, specimen height, conditions of loading and concrete compressive strength can hugely affect the bearing resistance of the concrete blocks.

The position of steel plate at the touching surface of concrete blocks either at the centre or the edge of the concrete blocks (centrically and eccentrically loaded bearing strength) also plays an essential role in the bearing strength of the concrete (Ahmed, Burley, & Rigden, 1998). The different position of steel plates shows a different kind of crack failures for the blocks.

Even though previous experimental studies do not specify all the pertinent aspects of the bearing problem if unreinforced concrete been chosen, there was a need to investigate the effect of having difference sizes of steel plate on the touching surface of concrete block. There is lack of knowledge on the behaviour and generation mechanism of the bearing capacity of unreinforced concrete blocks which means there is a need for further investigation especially for the design purposes of concrete members. Therefore, the aim of this study were: a) to investigate the ultimate bearing capacity of normal plain concrete blocks subjected to axial thrust; and b) observe the failure modes of the specimens.

Analytical Consideration

In order to estimate the bearing capacity of concrete, Hawkins (1968) had derived an expression for ratios of A_2/A_1 ranging from 1 to 40 as follows:

$$\frac{f'_{cc}}{f'_c} = 1 + \frac{4.15}{\sqrt{f'_c}} \left(\sqrt{\frac{A_2}{A_1}} - 1 \right) \quad (1)$$

Where,

f'_{cc} represents the concrete bearing strength

A_1 represents the bearing plate area

A_2 represents the area of the lower base of the largest frustum of a pyramid

f'_c represents the concrete compressive strength (MPa)

In addition, Shelson (1957) proposed a formula in order to determine the bearing capacity of concrete as given by Equation 2.

$$f = f'_c \left(\sqrt[3]{\frac{A}{A'}} \right) \quad (2)$$

In which, f denotes the maximum concrete bearing capacity, A as the total area of the concrete, A' as the loaded area on top of the concrete and f'_c represents the compressive (cube) strength of concrete (MPa). In this study, both expressions were used as a comparison with the results on the bearing strength of concrete blocks obtained via experimental measurements.

MATERIALS AND METHOD

Preparation of Specimens

The concrete with the characteristic strength of 50 N/mm² was poured into the moulds with the dimension of 200 mm × 200 mm in cross section and 200 mm in height. All the specimens were cast from a concrete mix as shown in Table 1. After the concrete undergoes the hardening process, the specimen was cured in curing tank. From a batch of concrete, three 150 mm × 150 mm concrete cubes were cast as control specimens. The concrete cubes were tested up to the failure for their compressive strength after being stored in a curing tank for 7 and 28 days to inspect the mechanical properties of the mix and the result is displayed in Figure 1. A total of 12 concrete blocks have been tested up to failure subjected to concentric compressive load. There are three unreinforced concrete blocks tested without the steel plate on top of it and nine unreinforced concrete blocks tested through square steel plates with dimensions of 75 mm × 75 mm, 100 mm × 100 mm, and 150 mm × 150 mm; respectively as shown in Table 2. The 10 mm thickness of square steel plates was concentrically placed at the top surface of the concrete block specimens. In this study, 10 mm plate thickness was selected due to the reason that it is a typical range for the steel plate thickness in most experimental setup performed by previous

studies ranging from 8 mm to 15 mm (Ahmed, Burley, & Rigden, 1998; Escobar-Sandoval, Andren, & Gary, 2006).

Table 1
Proportion of concrete per m²

Cement (kg)	Water (kg/m ³)	Fine Aggregates (kg)	Coarse Aggregates (kg)	
			10 mm	20 mm
71.78	26.4	77.55	73.43	146.85

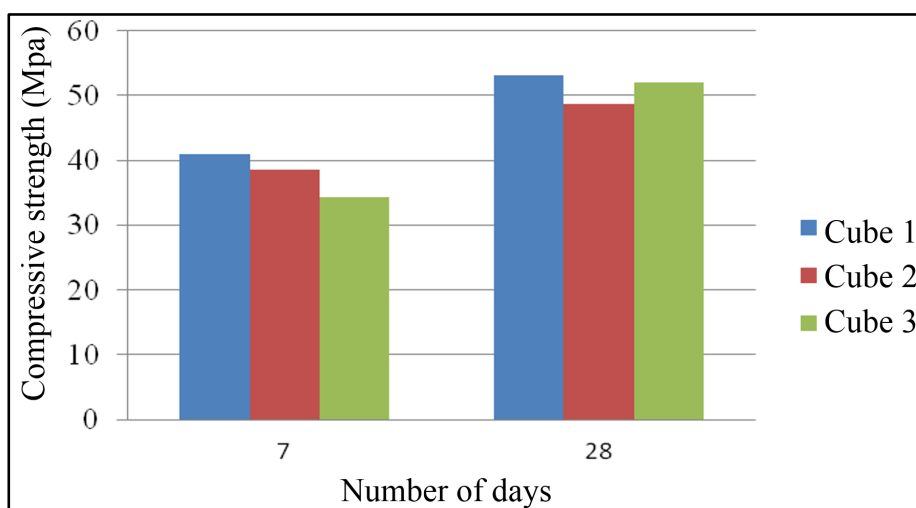


Figure 1. Mechanical properties of the concrete mix

Table 2
Details configuration of concrete specimens

Specimen designation	Length of concrete cube, L	Width of concrete cube, B	Height of concrete cube, H	Length of steel plate, l	Width of steel plate, b	Thickness of steel plate, t
PCS*				-	-	-
C75/75	200 mm	200 mm	200 mm	75 mm	75 mm	
C100/100				100 mm	100 mm	10 mm
C150/150				150 mm	150 mm	

Note that:

PCS denotes the unreinforced (plain) concrete without the steel plate

C75/75 denotes the plain concrete with the steel plate dimension of 75 mm × 75 mm

C100/100 denotes the plain concrete with the steel plate dimension of 100 mm × 100 mm

C150/150 denotes the plain concrete with the steel plate dimension of 150 mm × 150 mm

Experimental Details and Test Setup

All concrete block specimens have been tested up to failure subjected to axially compressive loading using the Universal testing machine (UTM) with the capacity of 1000 kN to determine the increase in bearing strength resulting from different sizes of steel plates. In order to ensure smooth contact between the bearing plate and concrete surface, the bearing surface of the machine and specimen was cleaned either on the top or bottom surface. The upper platen of the testing machine bore directly on the entire area of the bearing plate.

The piston was gently lowered to the top of the concrete block specimen using a lever. The specimens were loaded continuously until failure. The experimental set-up of the concrete block specimens is shown in Figure 2. The ultimate load and any crack deformities on the concrete block specimen were observed and recorded.



Figure 2. Experimental setup

RESULTS AND DISCUSSION

Load Bearing Capacity-Deformation Relationships

Based on the results obtained through the experimental measurements for the 12 concrete block specimens, the ultimate load bearing capacity and displacement relationship are provided. The graph of load bearing capacity versus deformation for different plate sizes used is shown in Figure 3.

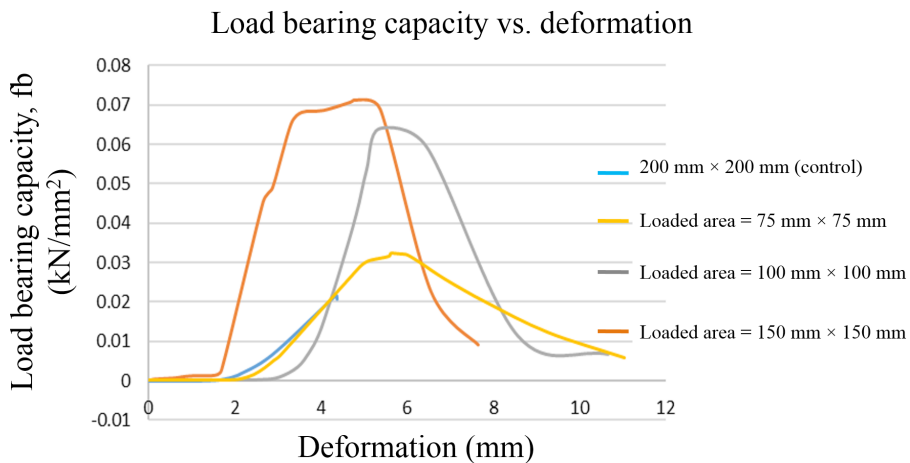


Figure 3. Graph of load bearing capacity (kN/mm²) versus deformation (mm)
 Note: Unloaded area = 200 mm × 200 mm

Figure 3 shows the concrete block specimen tested without the steel plate labelled as PCS, the maximum value of bearing strength was recorded as 0.024 kN/mm² with 5.62 mm deformation. Meanwhile, for concrete specimens with the contact area of 75 mm × 75 mm and 100 mm × 100 mm denotes as C75/75 and C100/100 respectively, the average value of bearing strength recorded was 0.089 kN/mm² with 5.06 mm deformation and 0.072 kN/mm² with 5.74 mm deformation respectively. In addition, for the specimen with the size of loaded area of 150 mm × 150 mm known as C150/150, the average value of bearing strength recorded was 0.043 kN/mm² with 6.50 mm deformation. The result of each type of specimen and its comparison with previous studies are shown in Table 3 and Table 4.

Table 3
 Results of bearing strength test

Specimen Designation	Ultimate Load (kN)	Bearing Strength (N/mm ²)	Deformation (mm)
PCS	939.85	24	5.62
C75/75	499.10	89	5.06
C100/100	721.39	72	5.74
C150/150	971.45	43	6.50

Table 4
 Comparison between experimental test and earlier studies

Specimen Designation	f _b (Exp.) (N/mm ²)	f _{b(H)} (Hawkins, 1968) (N/mm ²)	f _{b(S)} (Shelson, 1957) (N/mm ²)	f _b / f _{b(H)}	f _b / f _{b(S)}
C75/75	89	99	96	0.90	0.93
C100/100	72	79	79	0.91	0.91
C150/150	43	60	61	0.72	0.70

Experimental results demonstrate that the concrete block specimens with the plate dimension of 150 mm × 150 mm gave lower value of bearing strength compared with the plate with the dimension of 75 mm × 75 mm and 100 mm × 100 mm. Test on the bearing capacity of plain concrete have served to fill an essential gap in the experimental data. As can be seen from the deformation of specimen, the larger cross-sectional area of the steel plate used have the tendency to increase the deformation of the concrete block specimen.

This result supports the widely held belief that the maximum bearing strength of concrete can be increased by increasing the ratio of unloaded to loaded area. The load that implies on the concrete specimen was transferred through square steel plate into the concrete block with a larger contact area. This indicates that the increase in the surrounding area corresponds with value in terms of load carrying capacity before the concrete specimen reaches its limiting value (Rao & Swamy, 1974).

Confinement Effects

The relationship between the ratio of unloaded to loaded area and the effects of confinement provided by the surrounding concrete play an important role in estimating if higher confinement effect will provide an increasing or decreasing value of load bearing capacity of concrete blocks. In this case, the effects of confinement were defined as the ratio of unloaded area of concrete block specimen divided by the loaded area of square steel plate as shown in Figure 4.

The use of different square steel plate with the dimensions of 75 mm × 75 mm, 100 mm × 100 mm, and 150 mm × 150 mm gave different value of A_2/A_1 which are 7.11, 4, and 1.78 respectively. Figure 4 shows the increasing value in load bearing capacity correlates with the increasing effects of confinement. The smaller cross-sectional area of steel plate had higher effects of confinement compared with larger cross-sectional area of steel plate.

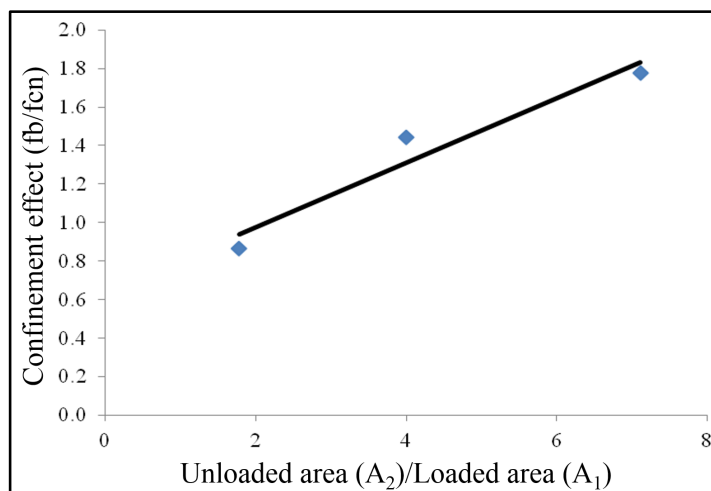


Figure 4. Relationship between confinement effect and load bearing area

Mode of Failures

The failure of concrete blocks occurs when the forces applied on top of it exceeds the strength of concrete. The type of failure modes that have been observed during the experimental testing is in the forms of localised damage, especially at the outer edge of the contact area. It has found that this observation is comparable with previous studies (Al-Sahawneh, Amjad, Hassan, & Khair, 2013; Rao & Swamy, 1974; Zhou, Hu, & Zheng, 2013) where the inverse pyramid failure has been observed at the outer edge of contact area, as shown in Figure 5. Other types of failure that have been observed during the measurements include splitting crack, brittle fracture and splitting wedge. It should be noted that there is no formation of inverted pyramid shape when the loaded area of 150 mm × 150 mm in cross section was used.

Figure 5(a) and 5(b) shows as the applied load gradually increases, the vertical crack occurs inside the concrete block specimen. Then, when the load reaches its limiting value, an inverse pyramid shape can be observed on the specimens. A conical wedge punched out from beneath the steel bearing plate is shown in Figure 5(b).

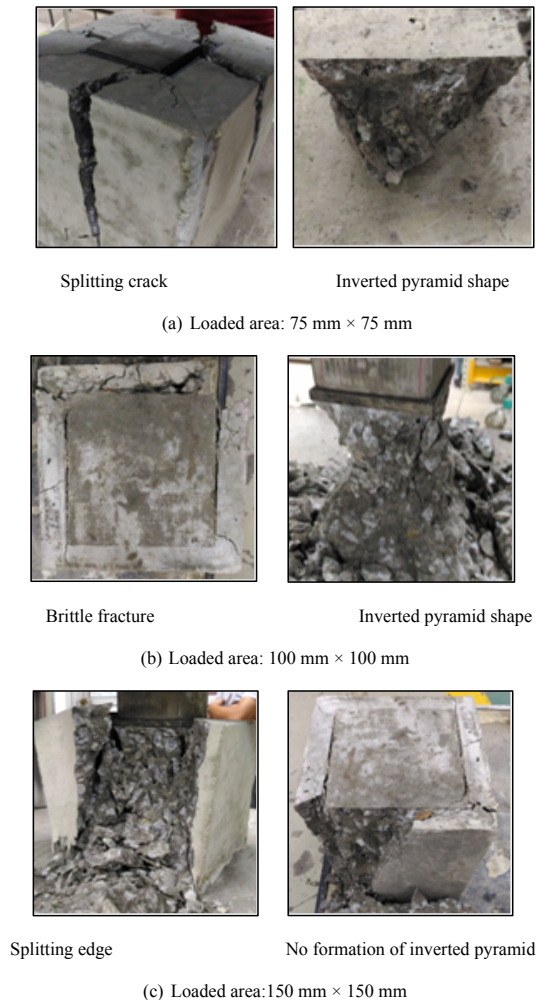


Figure 5. Modes of failure for different steel plate dimensions

CONCLUSION

The following conclusion can be drawn from his study: (1) When the specimen is loaded via a larger steel plate, an increase in deformation was observed due to the lower value of unloaded to loaded area. However, the localised damage prior to ultimate load starts to appear at the outer part of the concrete block specimens; (2) Different types of failure were observed for the different dimension of steel plate that has been used on top of concrete surface. It has been shown that when the load is being loaded through the smaller steel plate, the failure that occurs were in the formation of an inverted pyramid under the loading plate causing horizontal pressure leading to the concrete failure. When the maximum tensile stress at the top of the block exceeds the tensile strength of the concrete, then the failure can occur at the concrete blocks; and (3) The use of steel bearing plate with the dimension of 150 mm × 150 mm in cross section on the top of concrete surface results in no formation of inverted pyramid. However, edge splitting failure mode has been identified on the specimen. The occurrence of splitting was due to the existence of the edge damage at the outer edge of concrete block and it has been confirmed in the real field, especially in concrete bridge pedestal.

ACKNOWLEDGEMENT

The authors gratefully acknowledge the financial supports by Ministry of Higher Education under Research Acculturation Grant Scheme (RAGS) (RAGS/1/2015/TK01/UITM/03/1) and Universiti Teknologi MARA (UiTM) under LESTARI Research Grant (600-IRMI/Dana KCM 5/3/LESTARI (126/2017)). Authors would also like to thank all staff in Concrete, Fabrication and Heavy Structures Laboratories, Faculty of Civil Engineering, Universiti Teknologi MARA (UiTM), Shah Alam for their assistance in completing these experimental works.

REFERENCES

- Ahmed, T., Burley, E., & Rigden, S. (1998). Bearing capacity of plain and reinforced concrete loaded over a limited area. *Structural Journal*, 95(3), 330-342.
- Al-Sahawneh, E. I., Amjad, A. Y., Hassan, R. H., & Khair Al-Deen, B. (2013). A proposed model at failure stage to assess the bearing stress of normal weight concrete. *International Journal of Engineering Research and Application*, 3, 793-802.
- Al-Ta'an, S. A. (2005). *Bearing capacity of steel fibrous concrete*. Civil Engineering Department, Mosul University, Mosul.
- Au, T., & Baird, D. L. (1960). Bearing capacity of concrete blocks. *Journal of the American Concrete Institute*, 56, 869-880.
- Bauschinger, J. (1876). Tests with blocks of natural stone. *Mechanisch and Technischen Laboratorium der Kgl. Technischen Hochschule, Munich*, 6(13).
- Escobar-Sandoval, E. D., Whittaker, A. S., & Dargus, G. F. (2006). Concentrically loaded circular steel plates bearing on plain concrete. *Journal of Structure Engineering*, 132(11), 1784-1792.
- Hawkins, N. M. (1968). The bearing strength of concrete loaded through flexible plates. *Magazine of Concrete Research*, 20(63), 95-102.

- Ince, R., & Arici, E. (2004). Size effect in bearing strength of concrete cubes. *Construction and Building Materials*, 18, 603-609.
- Meyerhof, G. G. (1953). The bearing capacity of concrete and rock. *Magazine of Concrete Research*, 4(12), 107-116.
- Rao, C. K., & Swamy, R. N. (1974). Bearing strength of steel fibre reinforced concrete. *Building Science*, 9(4), 263-268.
- Shelson, W. (1957). Bearing capacity of concrete. *Journal of the American Concrete Institute*, 54(5), 405-414.
- Yahya, N. A., & Dhanasekar, M. (2014). Explicit finite element modelling of bridge girder bearing pedestals. In Smith, Scott T. (Ed.), *23rd Australasian Conference on the Mechanics of Structures and Materials (ACMSM23)* (pp.849-853). Southern Cross University, Byron Bay, Australia.
- Zhou, W., Hu, H., & Zheng, W. (2013). Bearing capacity of reactive powder concrete reinforced by steel fibers. *Construction and Building Materials*, 48, 1179-1186.



Computational Simulation of Indoor Thermal Environment in a Tropical Educational Hall with Displacement Ventilation

Qi Jie Kwong^{1*}, Hon Fai Chen² and Azli Abd Razak³

¹Faculty of Architecture, Planning and Surveying, Universiti Teknologi MARA (UiTM), 40450 Shah Alam, Malaysia

²FOSTEM, Inti International University, Bandar Baru Nilai, 71800 Nilai, Negeri Sembilan, Malaysia

³Faculty of Mechanical Engineering, Universiti Teknologi MARA (UiTM), 40450 Shah Alam, Malaysia

ABSTRACT

Displacement ventilation (DV) has been found to be effective in cooling large indoor spaces, but its effectiveness in providing thermal comfort in tropical buildings requires more detailed analysis to be made. This study examines the thermal environment in a lecture hall cooled via DV using FloEFD, a computational fluid dynamics (CFD) software. A calibrated CFD simulation model was developed to replicate the actual atmospheric conditions of the DV-cooled lecture hall. Results indicate that some parts of the hall received more cooling and air movement than required which would result in local thermal discomfort, especially at the front seating areas. The CFD results were consistent with those of earlier studies which validated the simulation model. The findings can be used to determine the locations which are more prone to steep thermal gradients in addition to reducing thermal discomfort, which include suitable arrangements of occupants in the lecture hall when it is not fully occupied and resetting the diffusers' supply air temperature.

Keywords: Computational fluid dynamics (CFD), Displacement ventilation (DV), lecture hall, thermal comfort, thermal environment

ARTICLE INFO

Article history:

Received: 05 January 2017

Accepted: 17 January 2017

E-mail addresses:

kwong.qjie@mail.com (Qi Jie Kwong),

henry_chf@hotmail.com (Hon Fai Chen),

azlirazak@salam.uitm.edu.my (Azli Abd Razak)

*Corresponding Author

INTRODUCTION

As people are spending most of their time indoors, the need for sustaining indoor thermal comfort becomes important. In typical university settings, lecture halls are generally occupied by students attending lectures or training sessions. Such places also depend solely on air conditioning and mechanical ventilation systems to maintain indoor thermal

comfort as they are usually enclosed with fabric-covered sound absorbing wall and heavy building materials which limit the use of natural ventilation.

Displacement ventilation (DV) has been used in many large buildings, such as the auditoria, conference halls, lecture rooms and other spaces with high ceilings (Liu, Min, & Song, 2015). This type of ventilation system is based on the concept of thermal stratification by supplying cool air from the diffusers, and this dense cool air slowly rises after it absorbs heat generated by various heat sources (occupant, office equipment and artificial lighting). The heat is then discharged from the indoor space as it reaches the ceiling exhaust grilles. This method has been found to be very effective in maintaining occupant thermal comfort and reducing cooling costs compared with mixing air systems (Gilani, Montazeri, & Blocken, 2016). An earlier study also found that DV was effective in maintaining favourable thermal comfort in a passive school's classroom (Wang, Kuckelkorn, Zhao, & Spliethoff, 2013). However, some studies found that this technology runs the risk of creating local thermal discomfort due to cold draughts at the floor level when the supply of air temperature is too low.

Using numerical method or computer software as a research tool to simulate indoor environments is increasingly popular among building experts and researchers worldwide, largely owing to the high accuracy of its results. Among the simulation software, Computational Fluid Dynamics (CFD) technique is one of the most commonly used programmes in the study of indoor thermal environments. This computational technique has the capability to predict the complex flow structure, and with very detailed simulation outcomes at every point of the flow domain. Many indoor environmental studies have employed CFD-based programmes in determining the local temperature and air velocity profiles, and the outcomes were used to estimate the thermal comfort conditions (Abou-deif, Fouad, & Khalil, 2013; Catalina, Virgone, & Kuznik, 2009; Webb, 2013). Previous works have compared the accuracies of CFD simulation with theoretical experiments and actual field measurements, and concluded that this powerful software could serve as an effective tool in estimating the actual thermal conditions of a particular building space (Cheng, Niu, & Gao, 2012; Hajdukiewicz, Geron, & Keane, 2013). Another advantage of applying CFD technique in experiments related to indoor environment is that the simulated outcomes are often used to complement the equipment-generated data (Wang, Zhao, Kuckelkorn, Liu, Liu, & Zhang, 2014; Wong & Mohd Rafique, 2010) as the latter is often restricted to the availability of measuring devices.

This paper reports on the simulation results of thermal environment in a large educational hall located in a tropical country using a commercially available CFD software –FloEFD 12.0, which incorporated Solidworks as the modelling module for the creation of a 3D simulation model. A comparison of the simulated and experimental results based on the recommended comfort ranges for air temperature and velocity is also presented which can provide useful information about the use of DV systems in Malaysian buildings.

MATERIALS AND METHOD

Pilot Survey

A pilot survey was conducted in a lecture hall installed with a DV system. The survey was carried out from November to December 2014. The lecture hall had three sections – middle, left and right seating areas, and an interior environment as shown in Figure 1. There were 215 seats: 12 rows at the centre, and 10 rows at both left and right seating areas. The thermal comfort parameters, such as air temperature, air velocity, relative humidity and room surface temperatures, were measured using calibrated electronic meters as shown in Figure 2 for both comparison and validation purposes. The meters were placed at the centre of the lecture hall and positioned at about 0.6 m above floor level as per the requirement of American Society of Heating, Refrigerating and Air-Conditioning Engineers, Standard 55 (ASHRAE, 2010) for evaluating the thermal environment of seated occupants. Written consent was acquired from the lecturers and the management of the educational institute. Measurements were taken around half an hour after the lecture sessions commenced to ensure that the indoor temperature and air velocity distribution were even.

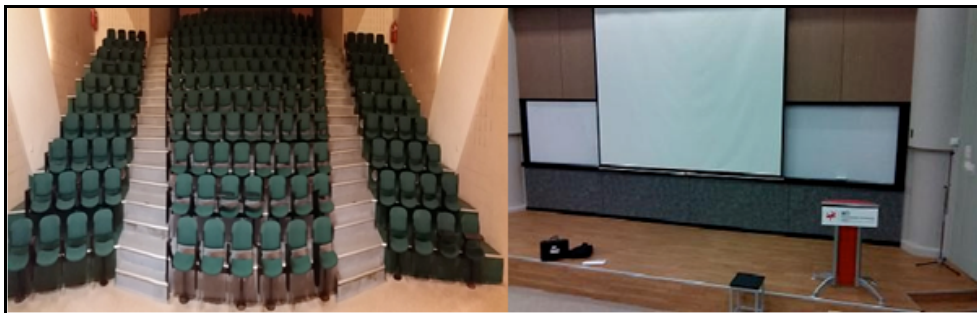


Figure 1. Internal environment of the lecture hall

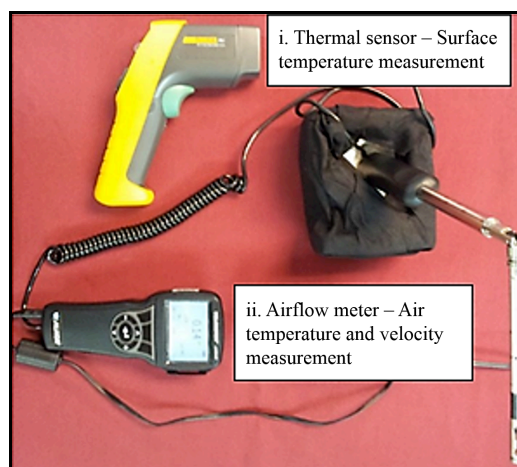


Figure 2. Equipment used for field measurement

Development of the Simulation Model

In order to understand the airflow pattern and temperature distribution in the DV-cooled lecture hall, a simulation model of the latter was developed according to the actual geometrical configuration using the FloEFD software, which is a CAD-integrated CFD tool. The FloEFD is a very effective tool for detailed modelling of indoor air conditions, which includes comfort parameters (Mentor Graphics, 2015). This CFD solver employs a modified $k - \epsilon$ two-equation turbulence model which uses the finite element method. The model was developed based on a partially occupied occupancy level, which is about 50% of the total available seats to replicate the actual situation of the observed lecture sessions. Other occupancy rates, both higher and lower than the prescribed occupancy value, seldom occurred as the lecture hall was normally reserved for combined lecture sessions, which consisted of 100-120 occupants.

The specification of boundary conditions is an integral part of any CFD problem as the results are directly dependent upon the input of boundary conditions. The locations where the simulated “fluid” enter and exit the lecture hall model were the air-conditioning inlet diffusers and exhaust grilles. The hall’s surface temperatures, air velocity, temperature of the supply air diffusers and exhaust grilles were set according to field data obtained from the pilot survey, as presented in Table 1. Figure 3 shows the lecture hall with 107 occupants. Existing heat sources within the hall were modelled as heat fluxes to show the amount of heat generated and the heat dissipating rates were obtained from ASHRAE Standard 55 (2010) and Chartered Institution of Building Services Engineers Concise Handbook (2008). Occupants in the lecture hall were modelled using mannequins with heat flux values of 60W/m² for students (seated) and 70W/m² for the lecturer/trainer (standing), while each of the lighting fittings was represented with a heat dissipation rate of 12W/m². The temperature and velocity values obtained from the simulation were then compared with the results obtained from field measurements for validation purpose. Results of the stipulated threshold values and that of earlier works were compared.

Table 1
Input values for boundary conditions

Air-conditioning Equipment	Temperature (°C)	Velocity (m/s)	Pressure (atm)	Boundary type
Ceiling diffusers	18.4	4.98	1	Flow inlet
Stage wall diffusers	15.4	1.15	1	Flow inlet
Door wall diffusers	15.6	0.95	1	Flow inlet
Under seat diffusers	18.5	3.34	1	Flow inlet
Ceiling exhaust grilles	20.0	0.45	1	Flow outlet

Table 2
Input values for heat sources

Heat Source	Heat Dissipation Rate	Heat type
Seated mannequin	60 W/ m ²	Surface source
Artificial lighting	12 W/ m ²	Surface source
Standing mannequin	70 W/ m ²	Surface source

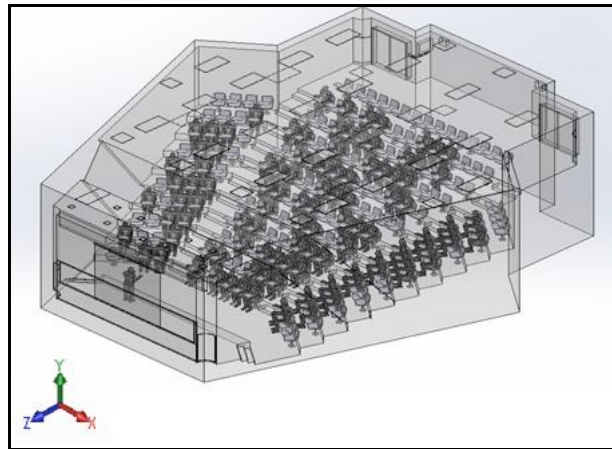


Figure 3. CFD simulation model of the lecture hall

RESULTS AND DISCUSSION

Field Measurements

During the pilot survey, the indoor thermal parameters which included supply air temperature at the diffusers, room surface temperatures (wall, door, floor and ceiling) as well as air velocities at the supply diffusers and exhaust grilles were recorded (as this information was essential for the simulation of indoor environment and for validation purpose). The room surface temperatures, as shown in Table 3, were used to calculate the mean radiant temperature (MRT). The thermal comfort parameters are shown in Table 4. The air temperature ranged from 20.9 to 21.5°C, while the air velocity was found within the range of 0.05 to 0.26 m/s. These measured values are generally not within the recommended comfort ranges stipulated in the Malaysian Standard (MS) 1525 (2014), which is a local energy guideline for non-residential buildings. This suggests that some of the occupants may find the thermal environment unacceptable. An operative temperature of 21.98°C was calculated, and it should be noted that only the thermal environmental parameters at the centre of the lecture hall, which was between the sixth and seventh row along the middle seating area, was measured.

Table 3
Lecture hall's surface temperatures

Location/ Surface Temperature	Min (°C)	Max (°C)	Mean (°C)
Ceiling (Up), T_1	21	22.6	21.97
Floor (Down), T_2	22.1	23.9	23.42
Wall (Left), T_3	22.1	23.7	22.75
Wall (Right), T_4	22.4	23.9	23.46
Whiteboard (Front), T_5	22	23.4	22.47
Door (Back), T_6	22.1	24.2	23.35

Table 4
Thermal environmental parameters

Parameter	Min (°C)	Max (°C)	Mean (°C)
Air Temperature, T_a (°C)	20.9	21.5	21.14
Air Velocity, v (m/s)	0.05	0.26	0.13
Humidity, RH (%)	68.8	72.6	70.78
Mean Radiant Temperature, T_{MRT} (°C)	21.79	23.45	22.81
Operative Temperature, T_{op} (°C)	-	-	21.98

Simulation Model

A model was developed to simulate the airflow pattern and temperature distribution within a partially occupied lecture theatre with about 50% occupancy rate. It was assumed that the left and right seating areas had the same distribution of occupants.

Since the field data collection was conducted at the centre of the lecture theatre, the coordinates of this location in the CFD model were identified at $X = 8.05$, $Y = 4.8$, $Z = 8.8$. Thus, the temperature and velocity profiles of this point were simulated and analysed and presented in Figure 4 to 6. Areas with cooler temperature are depicted by blue and cyan colours, while warmer temperatures are shaded in orange and red. It can be observed that the predicted temperature at the selected point of measurement ranged from 19.59 to 22.04°C, and air velocity varied between 0.05 and 0.22 m/s, which were relatively lower than the findings of Wang et al. (2013) and Liu et al. (2015). This may be due to difference in thermal boundary condition settings as well as the types of simulation selected. Besides, the mean simulated air temperature and velocity were calculated by averaging the point temperature taken along plane $Y = 4.8$ m which corresponded with 0.6 m above the floor level, which is the stipulated measuring location for seated occupants (Table 5).

Table 5
Simulated range of temperature and velocity at measuring point

Min	Temperature (°C)		Min	Velocity (m/s)	
	Max	Mean		Max	Mean
19.59	22.04	20.37	0.055	0.216	0.140

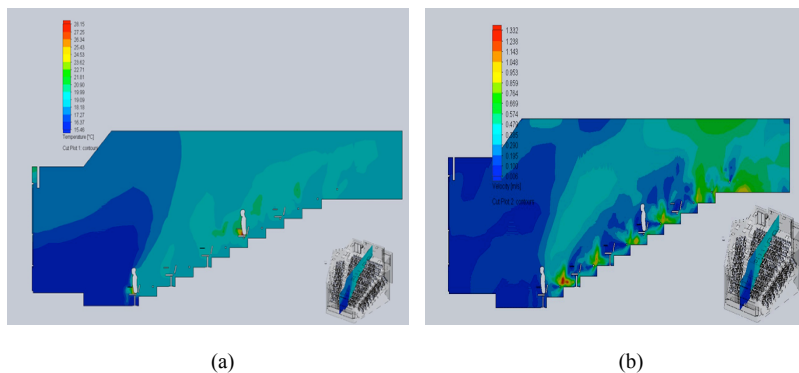


Figure 4. Simulated temperature and air velocity profile at $X = 8.05$ m. (a) Cut plot of temperature contour; and (b) Cut plot of air velocity contour

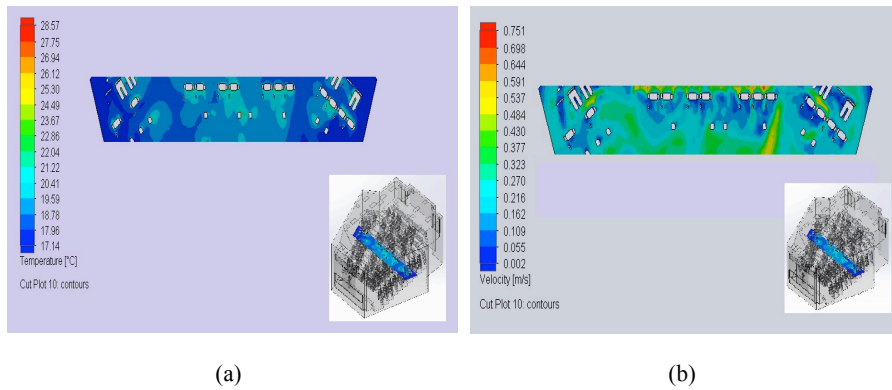


Figure 5. Simulated temperature and air velocity profile at Y = 4.80 m. (a) Cut plot of temperature contour; and (b) Cut plot of air velocity contour

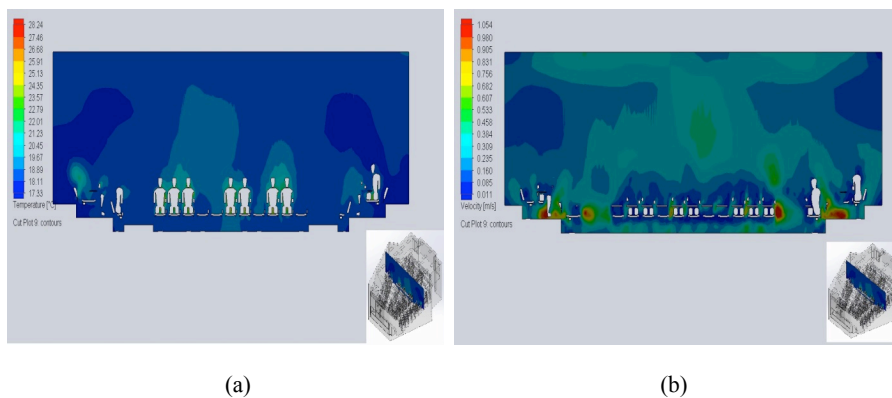


Figure 6. Simulated temperature and air velocity profile at Z= 8.80 m. (a) Cut plot of temperature contour; and (b) Cut plot of air velocity contour

Cool air was supplied into the indoor space through a combination of wall diffusers, ceiling diffusers and under seat diffusers. The supply and return air conditions for each of the diffuser was modelled according to the actual environment in the lecture hall. The contour plots of the air temperature as shown in Figure 4(a) and Figure 7(a) demonstrates that the students seated at the first row would experience cooler air temperatures due to the location being nearer to the wall diffusers on stage, which supplied conditioned air at a temperature of about 15°C. The same condition prevailed at the seating areas near the side doors that had wall diffusers installed beside the doors. Such condition was also reported in an earlier work, where the occupants seated adjacent to the diffusers were more likely to be thermally uncomfortable due to the steep thermal gradients (Wang et al., 2013).

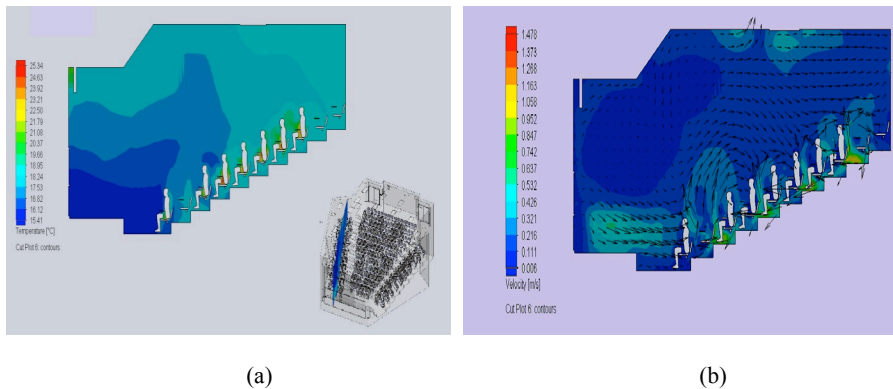


Figure 7. Simulated temperature and air velocity profiles at the left seating area. (a) Cut plot of temperature contour; and (b) Cut plot of air velocity contour

Other than the selected measuring point, the local air temperature and velocity at the area with the highest occupant density, which was at the left area of the lecture hall, were also analysed. Based on the plotted temperature gradients in Figure 7(a), it can be observed that the use of under seat diffusers may cause local thermal discomfort to some of the occupants in this area. The predicted temperature around the human model varied from the head to foot-leg regions. The air temperature rises as the air moves upwards, which is the heat rejection method of the DV system. Lower temperature regions were found at around the foot-leg region of the mannequins with a mean predicted temperature of 19°C, whereas temperature surrounding the body (chest and back regions) of the human model was about 23°C. It was also found that a higher temperature existed between the thigh and knee area of the mannequins. Such differences in temperature surrounding the mannequins suggest that local discomfort will most likely occur, since the vertical temperature difference was more than the permitted 3°C (ASHRAE, 2010). This suggest that the air temperature should be increased by 1 to 2°C to sustain thermal comfort. An interesting finding in the simulation is that the predicted temperature around the lighting is only around 17 to 18°C. This shows that the heat produced by the light fittings does not have any significant effect on the thermal surroundings, as compact fluorescent lamps (CFL) do not generate as much heat as the incandescent lamps.

Figure 7(b) shows the air velocity profile of the left seating area. The contour plot indicates the presence of high air movements (0.30– 0.95 m/s) around the foot-leg region of mannequins, especially those positioned at the odd number rows because of the underfloor diffusers. If only the perceived air velocity at the core of the mannequins was considered, no sign of draught was found in this seating area as the air velocity was only within the range of 0.11 – 0.32 m/s. This outcome demonstrates that the air flow in the lecture hall was carefully controlled to minimise the possible occurrence of draught, which is among the factors that cause thermal discomfort.

Validation of CFD Model with Empirical Results

The simulation outcomes have to be validated to strengthen its reliability. From Figure 4, the predicted air temperatures at the measuring spot during the field survey were within the range of 19 to 22°C with a mean value of 20.37°C. On the other hand, the mean air temperature measured in the lecture hall was 21.14°C, which indicates a difference of 0.7°C between the measured and simulated outcomes. This shows that the predicted temperature was slightly underestimated. As for the air velocity profile, the predicted outcomes at the location of Y = 4.8m were within the range of 0.05 to 0.22 m/s with an average value of 0.14 m/s, while the measured mean air velocity was 0.13 m/s. Hence a slight difference of 0.01 m/s was found between the simulated and empirical values.

Table 6
Percentage difference between empirical and simulated results

Thermal Parameter	Empirical	Simulated	Differences (%)
Air Temperature (°C)	21.14	20.37	3.5
Air Velocity (m/s)	0.13	0.14	7.7

There are several reasons for this slight variation in results. First, the CFD model was simulated under a steady state condition in this work, which did not fully demonstrate the real-life fluid and heat transfer processes that are mostly transient in nature. Additionally, the fluctuations in the air and surface temperatures with time may have affected the thermal conditions, even though efforts were made to collect field data only after the lecture sessions commenced for half an hour to minimise the potential variations of the thermal parameters. Another factor that led to this discrepancy was the inlet flow patterns, where air flows were set to discharge at an angle of 45° from the diffuser surfaces. The surface temperatures of the wall, ceiling and floor of the lecture hall were fixed at a constant value at which only the selected part of the hall's indoor surface was measured to represent the whole section. These assumptions and simplifications may have influenced the accuracy of the predicted results. Nevertheless, it can be concluded that the prediction showed good correlation with the empirical ones, since the percentage differences between the two results were lower than 10%.

CONCLUSION

Simulations of indoor thermal environments using CFD could provide very convincing and reliable results. A calibrated CFD model of a lecture hall cooled via DV was developed in this work, and the indoor thermal parameters were simulated, analysed and compared with the field survey results. Overall, the simulation outcomes showed that the air temperature and velocity profiles were not within the recommended ranges stipulated in the MS 1525(2014), which was in line with the field survey data. The simulated results depicted good distributions of air temperature and velocity within the seated areas of the partially occupied lecture hall. Albeit minor discrepancies, a good correlation between the simulated and empirical results were obtained in this work, which indicates the applicability of this CFD tool in assessing

the thermal environment of DV-cooled spaces. Other than the selected measuring point, the left seating area, which was with the highest occupant density, the simulation results revealed that some occupants seated in that area are expected to experience some level of local thermal discomfort due to the steep temperature gradient between the head and foot-leg regions. Therefore, an adjustment of supply of air temperature and relocating the occupants to other seating areas with lower vertical temperature differences should be considered.

The results showed that the DV system is an effective air conditioning technology to be used in large room areas in the tropics, only if the system is carefully controlled to prevent any form of local thermal discomfort, especially at locations where the air diffusers are installed. Since the occupant thermal adaptation was not evaluated in this work, future studies on evaluating the thermal experience of the occupants, which include psychological adaptation and expectation, are suggested. Other than that, the same model can be used to simulate other occupancy levels, especially the thermal comfort conditions of occupants when the lecture hall is fully occupied.

ACKNOWLEDGEMENTS

This work was funded by the Fundamental Research Grant Scheme (Grant No: 600-RMI/FRGS 5/3(73/2013)). The authors acknowledge the support of the technical staff of the Inti International University, Malaysia in carrying out the CFD simulations and to Mr. Hisham from Universiti Putra Malaysia for providing (at no charge) the indoor air quality meters for field measurements.

REFERENCES

- Abou-deif, T. M., Fouad, M. A., & Khalil, E. E. (2013). Numerical investigation of flow patterns and thermal comfort in air-conditioned lecture rooms. *International Journal of Mechanical, Aerospace, Industrial, Mechatronic and Manufacturing Engineering*, 7(5), 917–922.
- American Society of Heating, Refrigerating and Air-Conditioning Engineers. (2010). Standard 55: Thermal environmental conditions for human occupancy, ANSI/ASHRAE. ISSN 1041 – 2336.
- Catalina, T., Virgone, J., & Kuznik, F.(2009). Evaluation of thermal comfort using combined CFD and experimentation study in a test room equipped with a cooling ceiling. *Building and Environment*, 44(8), 1740–1750. doi:10.1016/j.buildenv.2008.11.015.
- Chartered Institution of Building Services Engineers (CIBSE). (2008). *CIBSE Concise Handbook*. The Chartered Institution of Building Services Engineers London. ISBN 978 – 1 – 903287 – 94 – 1.
- Cheng, Y., Niu, J., & Gao, N. (2012). Stratified air distribution systems in a large lecture theatre : A numerical method to optimize thermal comfort and maximize energy saving. *Energy and Buildings*, 55, 515-525. doi:10.1016/j.enbuild.2012.09.021.
- Gilani, S., Montazeri, H., & Blocken, B.(2016). CFD simulation of stratified indoor environment in displacement ventilation: Validation and sensitivity analysis. *Building and Environment*, 95, 299–313. doi:10.1016/j.buildenv.2015.09.010.
- Hajdukiewicz, M., Geron, M., & Keane, M. M. (2013). Calibrated CFD simulation to evaluate thermal comfort in a highly-glazed naturally ventilated room. *Building and Environment*, 70, 73–89. doi: 10.1016/j.buildenv.2013.08.020

- Liu, B., Min, K., & Song, J. (2015). Effect of thermal plume on personal thermal comfort in displacement ventilation at one side of the room. *Procedia Engineering*, 121, 1058–1066. doi: 10.1016/j.proeng.2015.09.103
- Malaysian Standard (MS) 1525. (2014). Code of practice on energy efficiency and use of renewable energy for non-residential buildings. *Malaysian Standard*.
- Mentor Graphics. (2015). FloEFD Products [Online]. Retrieved from <http://www.mentor.com/products/mechanical/products/floefd/>
- Wang, Y., Kuckelkorn, J., Zhao, F. Y., & Spliethoff, H. (2013). Indoor environment of a classroom in a passive school building with displacement ventilation. *Proceedings of BS2013: 13th Conference of International Building Performance Simulation Association, Chambéry, France, August 26 - 28, 2013, 1902 - 1909*.
- Wang, Y., Zhao, F., Kuckelkorn, J., Liu, D., Liu, J., & Zhang, J.(2014). Classroom energy efficiency and air environment with displacement natural ventilation in a passive public school building. *Energy and Buildings*, 70, 258–270. doi:10.1016/j.enbuild.2013.11.071.
- Webb, M. (2013). Building energy and CFD simulation to verify thermal comfort in under floor air distribution (UFAD) design, *Proceedings of BS2013: 13th Conference of International Building Performance Simulation Association, Chambéry, France, August 26 - 28, 2013*. 1886– 1893.
- Wong, S. J., & Mohd Rafique, S. M. S. (2010). Thermal modelling in product design using FloEFDTMPro: From concept to reality. *WCE 2010 - World Congress on Engineering 2010, 2*, 1263– 1267.



Microstructure and Mechanical Properties of Hybrid Super Elastic NiTi Alloy with Steel Rebar for Reinforced Concrete Beam

Nubailah Abd. Hamid^{1*}, Muhammad Akmal Ahmad Shazalli²,
Muhammad Hussain Ismail² and Azmi Ibrahim²

¹Faculty of Civil Engineering, Universiti Teknologi MARA (UiTM), 40450 Shah Alam, Selangor, Malaysia

²Faculty of Mechanical Engineering, Universiti Teknologi MARA (UiTM), 40450 Shah Alam, Selangor, Malaysia

ABSTRACT

NiTi is well known for its shape memory effect and super elasticity (SE), and is widely used in medical, dentistry and aerospace applications. For shape memory, NiTi has the ability to undergo deformation at certain temperature then recover to its original shape while SE occurs at narrow temperature range just above its transformation temperature. It shows that this material remembers its original shape and is elastic under stress. The application of nitinol as partial replacement in reinforced concrete beam for seismic resistant structures is popular due to its re-centring capability and distinctive properties. Using Shape Memory Alloy (SMA) in structures has its downsides. Hence, hybrid reinforced concrete beam with SMA was introduced to improve the structure's ductility and energy dissipation. Hence, this research is aimed at distinguishing microstructure and mechanical properties of SMA and steel rebar. Not much is known about how SMA behaves when subjected to compression. Therefore, X-Ray Diffraction (XRD) was used to analyse if any secondary phase exists and Differential Scanning Calorimetry (DSC) test was used to analyse the phase transformation. The results showed hybrid NiTi-steel rebar can address some deficiencies of NiTi and in terms of costs. On the other hand, combining them will result in super elastic recovery, displacement ductility and strength capacity for seismic resistant design.

Keywords: Hybrid NiTi, shape memory alloy, shape memory effect (SME), superelasticity (SE)

ARTICLE INFO

Article history:

Received: 05 January 2017

Accepted: 17 January 2017

E-mail addresses:

*nubailah_hamid@yahoo.com (Nubailah Abd. Hamid),
park_jan11@yahoo.com (Muhammad Akmal Ahmad Shazalli),
muhammadhussain_ismail@yahoo.co.uk
(Muhammad Hussain Ismail),
azmii716@yahoo.com (Azmi Ibrahim)

*Corresponding Author

INTRODUCTION

Shape memory alloys (SMAs) are metals that remember their original shapes. They are useful as actuators, which are materials that “change shape, stiffness, position, natural

frequency, and other mechanical characteristics in response to temperature or electromagnetic fields” (Rogers, 1995). The potential use of SMAs, especially as smart rebar, as partial replacement in reinforced concrete beam can provide insights into the development of this material for seismic resistant design and broadened the spectrum of this research into many scientific fields. The diverse applications for these metals have made them increasingly important and visible to the world. This study focused on NiTi since the alloys have been found to be the most useful of all SMAs. The objectives of this study are to determine the mechanical properties of as well as compare super elastic nickel titanium and steel rebar under compressive loading. The properties of NiTi in terms of its hardness and microstructure will be discussed.

There have been many studies on the equilibrium phase diagram of the Ni–Ti system. The phase diagram of Ni-Ti alloy system is important for heat treatments of the alloys and improvement of its shape memory characteristics (Zanaboni, 2008). The author focused on the central region of the phase diagram situated around the equiatomic NiTi composition. The reason is that solid solution B2 austenite phase of a near-equiatomic Ni-Ti alloy exhibits a unique behaviour based on the reversible martensitic. In Figure 1, the right boundary of B2 phase is almost vertical. On the other hand, there is pronounced solubility of Ni atoms in NiTi intermetallic on the Ni-rich side in the temperature range between 830°C and 1310°C. At temperatures below 650°C, there is a very narrow NiTi-phase region, and it is generally accepted that this region accommodates composition only between 50.0 and 50.5% Ni (Rogers, 1995). The NiTi phase retains the B2 order until a low temperature when the martensitic transformation occurs.

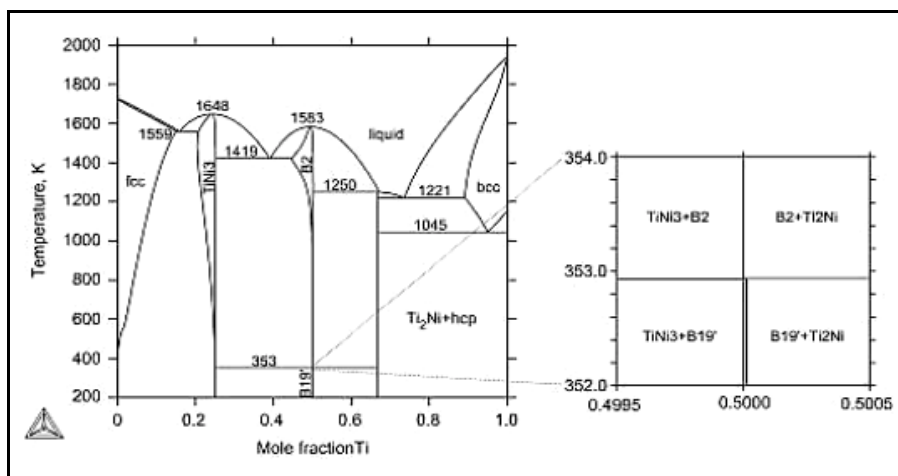


Figure 1. Calculated phase diagram of NiTi binary system, in which the phase equilibrium between B2 and B19S phases is added together with stable phase NiTi₂ and NiTi (Kubanova, 2014)

MATERIALS AND METHOD

Materials

NiTi samples used for the experiment was manufactured in China and the material carefully selected and heat treated to ensure it exhibits super elastic response at room temperature. NiTi used was A_r-6.3, with circular cross section of 8mm in diameter and the nominal composition were 56.02% Ni and 43.89% Ti with grain size 8. In addition, 10 mm diameter bars of mild steel rebar with f_{yk} (characteristic strength of 500 MPa) was also prepared for comparison. The standard specimens of Ni-Ti alloy and mild structural steel were fabricated according to ASTM E8/E8M-09 (2009a), and their length was 10 mm.

Cutting of the Specimen

The machinability of NiTi significantly depends on the cutting speed and feed rate, which are typically very high. According to Elahinia, Andani and Haberland (2014), the machining process of the NiTi alloys is quite difficult and challenging despite their properties and resistance to deformation that can cause severe tool wear. In addition, machining NiTi components with high cutting feed and speed will help to extend their tool life and improve product quality, although these elevated speeds result in hardening of the subsurface zones of the part (Weinert & Petzoldt, 2004). Hence, by taking into account these factors, non-conventional machining was employed, where abrasive methods such as grinding and saws were selected. Thus, an abrasive cutter machine was used to cut the NiTi and mild steel rebar into 10 mm for each sample.

Surface Cleaning Process

In order to get a flat smooth surface, samples of NiTi from China and mild steel rebar were subjected to a grinding process. The grinding process of each sample required five grades of abrasive sandpaper in order to obtain the smooth surface and to remove the scar resulting from the cutting process. The grade of the sand paper starts from coarse to fine which are 240, 320, 400, 600 and 1200. The smooth and near mirror image will be helpful in order to get a clear image of the microstructure of samples. After finishing the process of grinding the specimen, the latter was polished using a polishing machine. The cleaning alumina powder was used. The alumina powder consists of four grades starting from 10 μm , 5 μm , 3 μm . For the final finish, the 1 μm alumina powder was used. This cleaning agent helped in order to get the mirror look for the sample. Then, the samples were dried using an air compressor to prevent any rust from occurring on the surfaces.

Mechanical Behaviour Test - Monotonic Compression Test and Hardness Test

The behaviour of the SE of material was analysed through monotonic compression test in order to compare the mechanical properties of SMA and steel. All the tests were performed at room temperature using a 250 kN Servo Hydraulic Fatigue Testing System Instron 8802 equipped

with a data acquisition system as shown in Figure 2. Some equipment incorporated in this test were universal testing machines driven by mechanical screw to apply the load with hydraulic systems testing machine, and the Vernier Caliper was used to measure the compressive sample.

Compression tests on SMA are important. Furthermore, little is known about super elastic SMA when subjected to compression. Therefore, a minimum of two samples for each different condition was prepared to observe the behaviour of the samples upon the exertion of maximum stress. This compression test was conducted according to the standard of ASTM E9, and the above-mentioned loading protocol was input using Blue Hill 2 software. The dimension of the samples before and after the compression was measured, and the compression speed was 0.2505 mm/m.

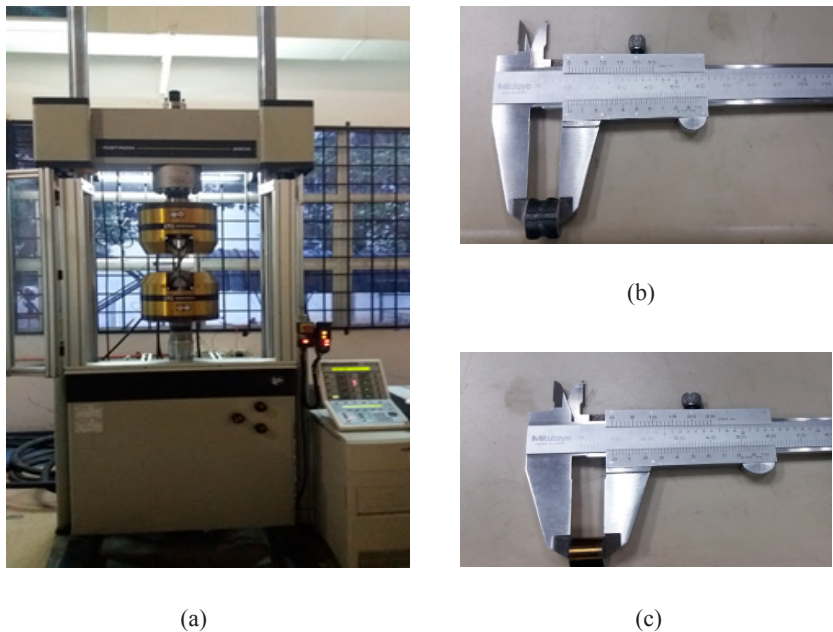


Figure 2. (a) Servo hydraulic fatigue testing system Instron 8802 and standard compression sample for (b) steel rebar (c) NiTi

In order to measure the micro hardness of the samples, Vickers micro hardness test were conducted with 4.9 N of load applied within 15 seconds according to Mortagy and Farag (2007). In addition, nano-indentation was recommended to be used instead of micro-indentation in spite of the fact micro hardness readings were influenced by elastic recovery and yield true hardness values (Cheng, 2004).

Phase Analysis - Scanning Electron Microscopy (SEM), Differential Scanning Calorimetry (DSC) and X-Ray Diffraction (XRD)

The phase analysis of both specimens was obtained through the XRD, SEM and DSC analysis. In order to observe the effect of the microstructure on the sample, SEM analysis was used. In this test, backscattered image whereas the SEM that uses mainly secondary electrons to image the specimen, rather than secondary electrons was used. The purpose of conducting this test was to identify the type of microstructure. The samples again were polished using silicon powder and ground using 240, 320, 600 and 1200 abrasive grit paper as mentioned in the XRD section. Polishing can produce a mirror-like image for the microstructure of the samples which was carefully analysed using the 80× and 500× magnifications.

The samples were analysed using DSC to analyse its transformation temperature. The machine used in this research was the DSC-1 Mettler Toledo, a different scanning calorimetry machine. The samples were crushed to obtain mass between 7 mg to 10 mg to be placed in the DSC capsules (Bansiddhi & Dunand, 2009). The samples heated and later cooled at a rate of 10oC/min under nitrogen cover gas. Two DSC cycles ranging from -50 to 200°C were performed consecutively for each sample and the second cycle was used to determine the transformation enthalpy and the phase transformation temperatures.

The purpose of conducting the XRD is to identify its phase and its composition present in all the samples using the RigakuUltima IV. Before the XRD process began, the specimen was ground using the 240, 320, 600 and 1200 abrasive grit papers and was polished using the polishing powder to obtain reflective surface. A wavelength of 1.540562Å with a diffraction angle from 30 to 90 at scanning speed of 0.5/min was used to perform the analysis. The peak observed in the XRD result was compared with the phase of NiTi alloy to identify the phase composition of the samples.

RESULTS AND DISCUSSION

Mechanical Behaviour Test - Compression Test and Hardness Test

Figure 3 shows the failure of NiTi samples with differences sizes of diameters. For this test, samples diameter of 8 mm and 12 mm were used. The maximum load for the 8 mm diameter sample was 138.346 kN and the maximum compressive stress obtained is 2752.307 MPa at 31.58%. The result obtained for NiTi 12 mm samples is 239.954 kN with lower compressive stress reading obtained as compared to 8 mm diameter samples at 29.29%, was 2121.656 MPa as expected as stated by Desroches (2004), that the small diameter of shape memory alloys show higher strength and damping properties as compared with the higher diameter of bars.

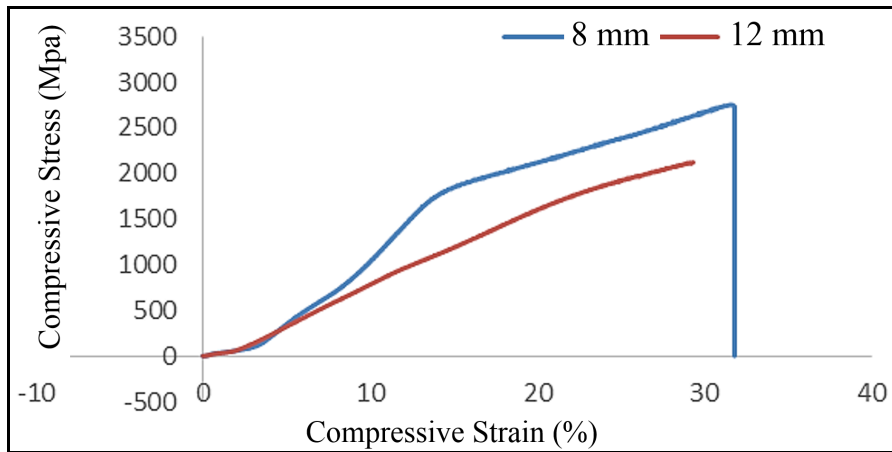


Figure 3. Compressive Stress-Strain curve for 8 mm and 12 mm of NiTi

Table 1
Hardness value for NiTi alloy and mild steel rebar

Point	NiTi alloy (HV)			Mild Steel rebar (HV)		
	D1	D2	Hardness	D1	D2	Hardness
1	76.2	78.9	308.3	84.1	85.4	253.2
2	79	80.4	292.2	92.9	100.3	198.8
3	76.7	78	310.1	82.8	85.1	258.3
4	83.1	79.7	280.1	90.7	92.3	225.4
5	74.6	7.9	327.7	89.5	90.7	2228.4

Table 1 shows the value of hardness for a sample of NiTi and Mild Steel rebar at different points determined by using Vickers hardness test. By referring to the study made by Kaya (2014), he stated that the hardness of a material refers to the strength of the material and the change in the strength is related to the formation of precipitates. For a mild steel rebar sample, at the different point of the test, it gave a different value of hardness. Thus, an average value of hardness for mild steel repair was 232.82. Meanwhile, for NiTi, the value of hardness was also similar with mild steel where each point gives a different reading. Therefore, an average value of hardness calculated was 303.68 HV. Based on data collected, there were similarities of two samples which recorded the highest value of hardness located at the centre of the sample. Bain (1997-1908) reported a slight difference of hardness value obtained from same sample each time during an experiment. There are few factors that affect the differences between each point such as grains, defects, grain boundaries and impurities of the specimen itself. The microhardness was measured by the residual area after load was removed. In the case of the super elastic materials, the elastic part was recovered upon load removal causing a decrease in the size of the residual area resulting in the hardness value appearing larger.

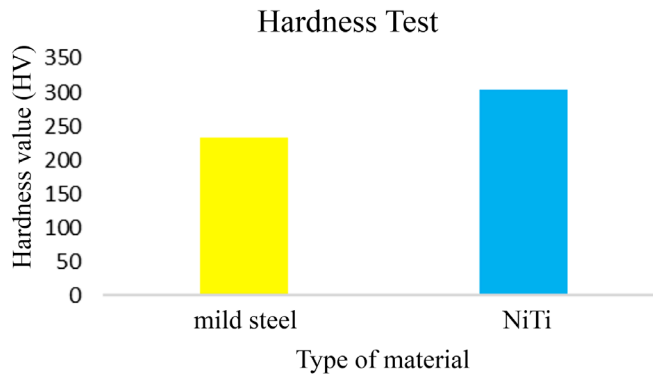


Figure 4. Average of hardness value

Figure 4 shows the data of average hardness value of mild steel rebar and NiTi alloy. It shows a slightly difference in hardness value for mild steel rebar and NiTi where the latter shows higher hardness value compared with mild steel. The differences between both samples were about 13.2%. From the test, it showed that the NiTi alloy has greater resistance to deformation compared with mild steel rebar due to greater hardness. From the SE aspects, the higher the hardness, the higher the SE. This is because SE depends on the strength of the matrix which is affected by the existence of dislocations, precipitates or both. The hardness of the material is also affected by the microstructure and composition of element in material. This is discussed in detail in the XRD and SEM analysis.

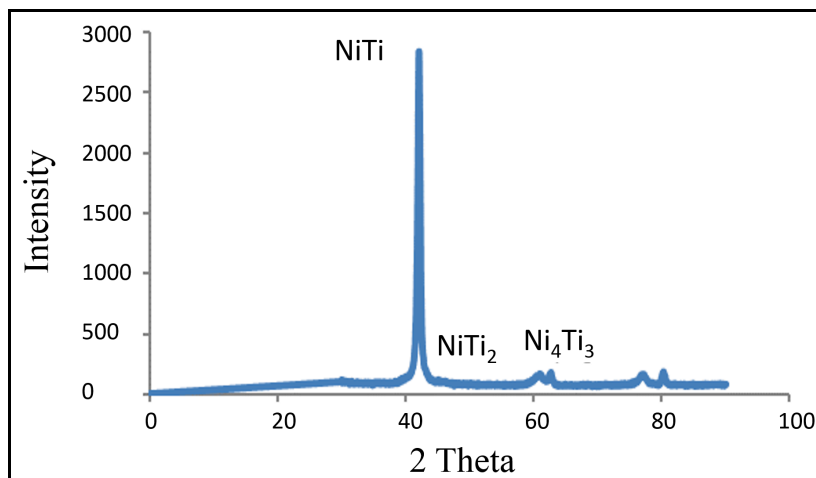


Figure 5. XRD analysis of NiTi

Figure 5 shows the result of received samples of NiTi which is nickel rich, revealing the existence of phase, namely NiTi at the maximum wave peak. The value of the intensity of the maximum peak was 2 thetas, 42.1°. The graph also shows the presence of the secondary phase of NiTi₂ and Ni₄Ti₃. Each phase has a different condition where for NiTi it is in a stable phase. Mortagy and Farag (2007) stated that presence of Ni₄Ti₃ is important in order for an improvement in SE behaviour. It gives effect in terms of size, density, and coherency of Ni₄Ti₃ itself. For the NiTi₂ phase, Mortagy and Farag (2007) concluded that the presence of NiTi₂ does not give effect in terms of mechanical behaviour and SE. Therefore, their existence was negligible in this study.

Meanwhile, Figure 6 shows the phase exists in the mild steel rebar where at maximum wave peak, constructive interference are Fe₃C. By referring to the phase diagram of the Iron-Iron Carbide, the Fe₃C shows that the phase is iron carbide or its other name cementite. The carbon content was about 6.67% C. This intermetallic compound is metastable; it remains as a compound indefinitely at room temperature. It is the hardest structure that appears on the diagram and the crystal structure was orthorhombic. The phase has a low tensile strength, but high in compressive strength.

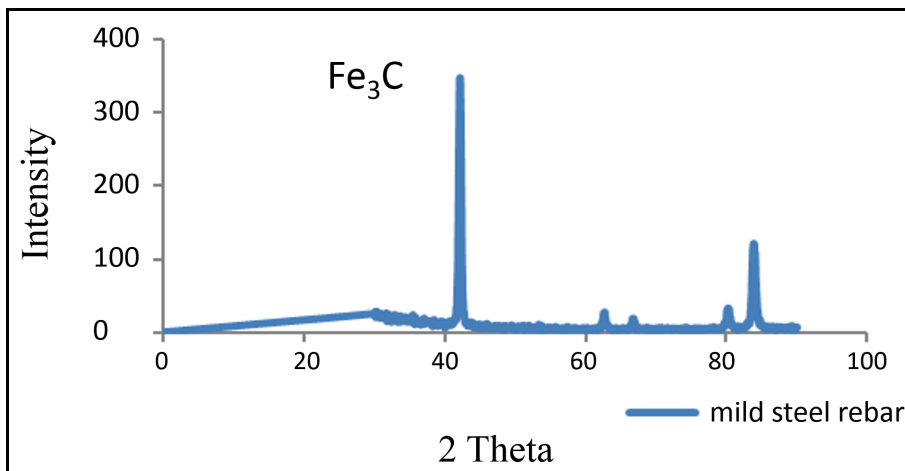


Figure 6. XRD analysis of mild steel rebar

Scanning Electron Microscopy (SEM)

Azimi et al. (2011) pointed to two categories of fracture, ductile and brittle. Ductile fractures are defined as slow tearing of the material with the expenditure of considerable energy, displaying a dimpled surface created by growth of internal voids of the metal and an appreciable gross plastic deformation. Brittle fracture on the other hand is characterised by a rapid rate of crack propagation (due to fluctuating stress cycles), with no gross deformation.

From the study, the main difference in the microstructure of the samples is the topography of surface where it classified both material as either brittle or ductile. Figure 7 and 8 show the fracture image of both material which reveal their characteristics. For the NiTi, the topography

image at the surface of the samples shows that the material undergoes brittle behaviour. This image may explain the graph produced in compression test where the graph declines sharply after the material fails.

Energy-dispersive X-ray spectroscopy (EDX) was conducted to obtain the chemical characterisation of each sample. By doing EDX, it reveals the presence of element in material and its composition. For NiTi samples, the composition of nickel elements at that particular area was about 56.99% while for titanium, it was 43.01%. Some points that were observed through EDX for NiTi sample also showed the same result, whereby the composition of nickel was higher than titanium. This proved the received sample of NiTi is Ni rich.

Figure 8 shows the fracture image of mild steel rebar that also underwent EDX. The topography surface shows that the material underwent ductile behaviour. Azimi et al. (2011) revealed that ductile fracture decreases the diameter of the sample, called necking. It begins after the ultimate stress reaches its maximum level. So, a neck is formed as the sample of mild steel is elongated. The EDX result shows two main element exists in mild steel rebar, carbon and iron. The carbon percentage was about 22.21% while the iron about 70.80%. So, the composition of iron is higher compared with carbon.

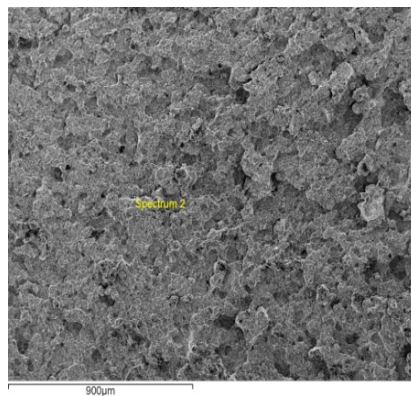


Figure 9. Fracture of NiTi

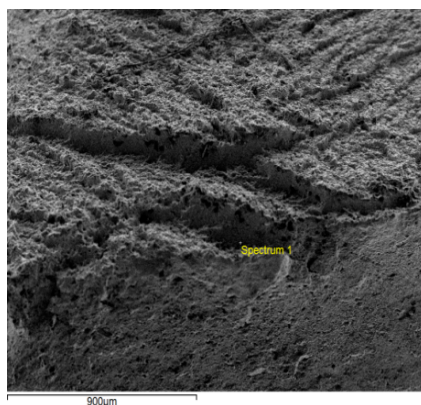


Figure 8. Fracture of mild steel rebar

The formation of a neck introduces a triaxial state of stress in the region. A hydrostatic component of tension acts along the axis of the specimen at the centre of the neck region. Many fine inclusions form in this region which grow and coalesce into a central crack. This crack grows in a direction perpendicular to the axis of the instrument until it approaches the surface of the instrument. The central crack which forms early tends to concentrate the deformation at its tip in narrow bands of high shear strain.

Differential Scanning Calorimetry

For the Ni-rich NiTi, the austenite transformation during heating starts at a temperature of -24.42°C . The austenite finishes at -19.47°C as shown in Figure 9. The size of the peak will determine the SE characteristic of NiTi. Therefore, the wider the peak, the greater the SE behaviour of NiTi. Meanwhile, for the cooling curve, it represents the transformation of martensitic. The onset of the peak represents the martensite start temperature (M_s). The end set of the peak represents the martensite finish temperature (M_f). The transformation of martensitic during cooling starts at -3.06°C and ends at a temperature of -49.46°C .

Figure 10 shows the DSC curve for measuring phase transformation temperature for mild steel rebar. Same with the DSC curve of NiTi, mild steel rebar also contains two curves which represent heating and cooling conditions of the samples. For heating, there is a small peak.

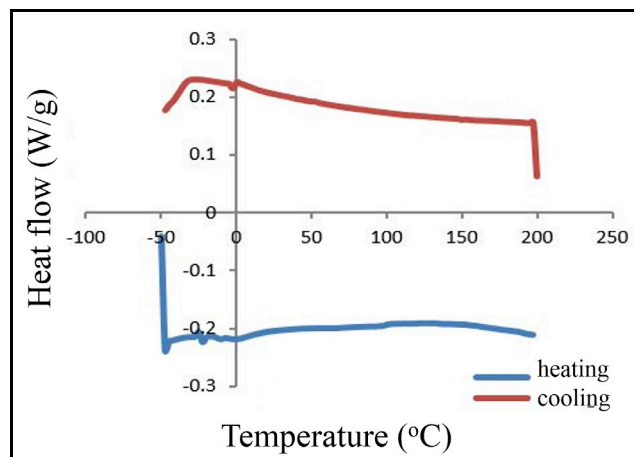


Figure 9. DSC curve for NiTi

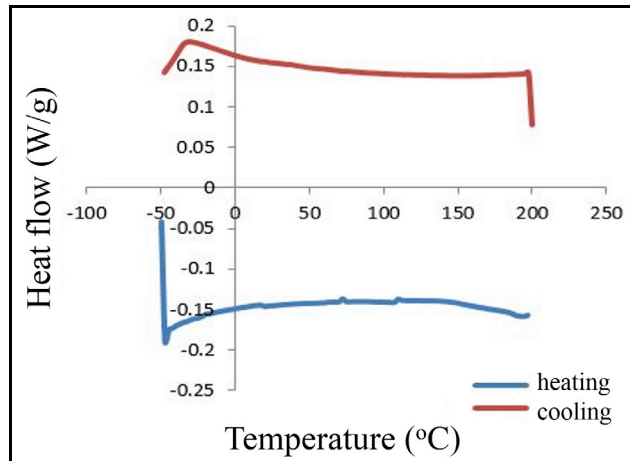


Figure 10. DSC curve for mild steel rebar

CONCLUSION

In this study, the mechanical properties of both materials were identified. The comparison between phase constituent of super elastic nickel titanium and mild steel rebar was conducted. The correlation between both materials in order to see the potential of the materials to be hybrid was found. A few conclusions can be drawn. First, can be clearly seen from the graph of stress vs. strain, the elastic modulus of NiTi is lower compared with mild steel rebar. So, NiTi has a lower stiffness. Second, the hardness for NiTi is higher compared with mild steel rebar. The microstructure of the samples has influences result of hardness test. It can be proven through DSC and SEM test the effect of the structure on the materials, Last but not least, the phase transformation for NiTi was relatively wide, particularly during cooling, which contributed to Ni-rich composition. The Ni content influences the transformation temperature.

The results obtained from this research hopefully will help the researchers in identifying the mechanical characteristic of the materials.

ACKNOWLEDGMENTS

The authors acknowledge the research grants provided by Ministry of Education, 600-RMI/FRGS 5/3 (22/2013), and UiTM internal grant 600-RMI/DANA 5/3/PSI (141/2013), 600-RMI/DANA 5/3/CIFI (29/2013) to undertake this research.

REFERENCES

- Azimi, S., Delvari, P., Hajarian, H. C., Saghiri, M. A., Karamifar, K., & Lotfi, M. (2011). Cyclic fatigue resistance and fractographic analysis of RaCe and ProTaper rotary NiTi instruments. *Iranian Endodontic Journal*, 6(2), 80-85.
- Bain, R. (1996-1997). *Detailed Report on Hardness Test*, Rine Engineering Pvt Limited: Baddi, India.

- Bansiddhi, A., & Dunand, D. C. (2009). Shape-memory NiTi–Nb foams. *Journal of Materials Research*, 24(06), 2107-2117.
- Cheng, F. T. (2004). On the indeterminacy in hardness of shape memory alloys. *Journal of Materials Science and Technology*, 700-702.
- Elahinia, M., Andani, M. T., & Haberland, C. (2014). Shape memory and super elastic alloys. *High Temperature Materials and Mechanisms*, 355.
- Kaya, I. (2014). Shape memory behaviour of single and polycrystalline nickel rich nickel titanium alloys.
- Kuběnová, M. (2014). Příprava a martenzitické transformaceslitinnabáziNiTi.
- Mortagy, O., & Farag, M. (2007). Effect of heat treatment on the superelasticity and hardness of NiTi. *In International Conference on Modeling and Optimization of Structures, Processes and Systems (ICMOSPTS'07)*, Durban.
- Rogers, C. (1995). Intelligent materials. *Scientific American*, 273(3), 122-5.
- Weinert, K., & Petzoldt, V. (2004). Machining of NiTi based shape memory alloys. *Materials Science and Engineering: A*, 378(1), 180-184.
- Zanaboni, E. (2008). One way and two way-shape memory effect: Thermo-mechanical characterization of Ni-Ti wires. *UniversitadegliStudi di Pavia, Pavia, Italy*.

Optimisation of Biomethane Production by Anaerobic Digestion of Food Waste

Nurul Shahida Osman¹, Zainon Mohd Noor^{1*}, Zatilfarihiah Rasdi²,
Iwana Izni Zainuddin³ and Noor Azrimi Umor³

^{1,2}*School of Biology, Faculty of Applied Sciences, Universiti Teknologi MARA (UiTM), 40450 Shah Alam, Selangor, Malaysia*

²*Preclinical Sciences Studies, Faculty of Dentistry Universiti Teknologi MARA (UiTM) Sungai Buloh Campus, 47000 Sungai Buloh, Selangor, Malaysia*

³*Faculty of Applied Sciences, Universiti Teknologi MARA (UiTM) Negeri Sembilan, 72000 Kuala Pilah Campus, Negeri Sembilan, Malaysia*

ABSTRACT

Food waste is a mixture of organic residues that affect fermentation process. Thus, appropriate parameters should be optimised to ensure high biomethane production. In this research, response surface methodology (RSM) was utilised for building models, evaluating the significance of several independent factors (pH, temperature, substrate concentration and inocula size) and determining optimum conditions for desirable responses (biomethane yield). The RSM and contour plots set the optimum working factors in order to accomplish the desired biomethane yield. Results suggest that biomethane yield can be increased when pH and temperature are increased. Thus, the main effects of parameters are pH and temperature.

Keywords: Anaerobic digestion, biomethane yield, response surface methodology

ARTICLE INFO

Article history:

Received: 05 January 2017

Accepted: 17 January 2017

E-mail addresses:

nurul_shahida90@yahoo.com (Nurul Shahida Osman),

dzainonmn@salam.uitm.edu.my (Zainon Mohd Noor),

zatilfarihiah@salam.uitm.edu.my (Zatilfarihiah Rasdi),

iwana@ns.uitm.edu.my (Iwana Izni Zainuddin),

noorazrimi@ns.uitm.edu.my (Noor Azrimi Umor)

*Corresponding Author

INTRODUCTION

Anaerobic digestion (AD) is an organic process that happens when microscopic organisms separate natural matter in the environment with or without oxygen (Zhang et al., 2007). Generally, AD processes are applied to waste water and sewage sludge treatments. However, recently the focus of AD has switched from treatments of waste such as Biology Oxygen Demand (BOD) removal to bioenergy production. An organised anaerobic digestion of biological leftover

in a surrounded landfill will create bioenergy in the form of methane. Bioenergy production using AD technique contains around 60% of methane (CH₄) and 40% of carbon dioxide (CO₂) (Molino, Nanna, Ding, Bikson, & Braccio, 2013). Therefore, AD has enormous potential for recuperating bioenergy by using organic waste such as food waste.

Microorganisms are a promising energy source. Good techniques to produce ecologically sound bioenergy synthesis can provide mankind with cheap raw material or substrate, for an environmentally friendly source of energy. It is estimated that approximately 50% of all nourishment produced is gone, changed over or squandered (Joint Declaration against Food Waste, 2010). In Malaysia, 8000 tons of foods are squandered every day (Solid Waste and Public Cleansing Management Corporation, 2008). Thus, food waste is considered as a potential source of bioenergy using the AD technique. Since food waste is a mixture of organic residues that may be affect the fermentation process, suitable parameters need to be optimised to ensure high biomethane production throughout the process.

The RSM is a mathematical and statistical instrument that uses measurable data from different experimental designs to define and concurrently explain multivariate equations (Keshani, Luqman Chuah, Nourouzi, Russly, & Jamilah, 2010). It investigates the connections between several descriptive factors and one or more response factors (Carley, Kamneva, & Reminga, 2004). The aim of this paper is to examine parameters that affect biomethane production using RSM.

MATERIALS AND METHODOLOGY

Inocula and Substrate

An anaerobic sludge was taken from a clarifier tank in Universiti Teknologi MARA (UiTM), Shah Alam, Selangor, and utilised as an inoculum. It (anaerobic sludge was used within a week, and fresh inocula were gathered again from the similar location to ensure consistency in their characteristics.

Food wastes were obtained from the Cafeteria, UiTM. They consisted in equal parts wastes from the kitchen, namely fruit peel and vegetable parts. As the waste contained impurities, they were sieved to remove the coarse contaminants before the granulating process. A weekly sampling was done.

Analytical Methods and Data Analysis

The parameters analysed for the classification were: Total Solid (TS), Volatile Solid (VS), Total Suspended Solid (TSS), Volatile Suspended Solid (VSS) and Chemical Oxygen Demand (COD) contents referring to the Standard Methods of American Public Health Association (APHA, 1998). Composition of carbon (C), hydrogen (H), nitrogen (N), sulphur (S) and C/N ratio were analysed using Thermo Scientific Flash 2000 CHNS-O. Protein and carbohydrate contents were also analysed using Bradford Assay and High Performance Liquid Chromatography (HPLC) at mobile phase of 100% distilled water, temperature 85°C, flow rate of mL/min with glucose used as standard. The formula in (1) was used to model the kinetics of the biomethane production and to determine specific biomethane production potential (Methane yield). Areas

of methane sample and standard methane were measured using gas chromatography for each digester. The methane yield was measured in the unit of ppm.

$$\frac{\text{Area of methane sample}}{\text{Area of standard methane}} \times 57.6 \quad (1)$$

Biomethane Fermentation

The experiment was aimed at estimating the anaerobic digestion of four dissimilar parameters: temperature, pH, substrate concentration (in volume of 68.6 VS/l) and inocula concentration (in volume of COD ranging 75 – 99 mg/l). The tests were carried out in 160 mL serum flasks comprising 100mL media. All serum bottles were loaded with a specific volume of substrate and inoculated with a specific volume of inocula which was then adjusted to a specific pH before incubation for 24 hours in serum bottles to produce methane gas for 15 days of Hydraulic Retention Time (HRT). All bottles were flushed with nitrogen gas to ensure anaerobic conditions throughout the experiments and tightly capped with rubber septum (butyl rubber) before incubation at 35°C. The total gas is measured at 24-hour interval by releasing the pressure in the bottles using 10 mL syringe. The biomethane production was analysed using a gas chromatography equipped with a thermal conductivity detector, and the column was packed with Porapak Q (80/100 mesh). The temperature of injector and column were kept at 0°C and 50°C. Nitrogen was used as the transporter gas at a flow rate of 30 ml/min, and 8% methane gas was used as standard.

Experimental Design

The RSM was used to define the optimum conditions of the biomethane production during anaerobic fermentation of food waste and anaerobic sludge by using Statsoft Statistica 6.0. The optimisation procedure was divided into two designs - Two-level Factorial Design and Central Composite Design (CCD).

In the factorial design, the influence of all experimental variables, factors and interaction effects on the response are studied. Four variables, which are expected to affect biomethane production, were selected based on an earlier study by the present authors. The factors in the two-level factorial design are listed in Table 1.

Table 1
Variables in actual values, for screening by the two-level factorial design

	Variable	Unit	Low Level (-1)	High Level (+1)
A	pH	pH	6.5	8.2
B	Temperature	°C	3.5	37
C	Inoculum Size	%	105	20
D	Substrate Concentration	g/L	40	80

A CCD was established after identifying significant factors by the two-level factorial design. It was utilised to make models between the variables, to optimise the biomethane yield and to decide the main effects of parameters. Therefore, 13 tests were created based on the second-order CCD with two independent variables. The variables in CCD are listed in Table 2. The tests were randomised in order to minimise the effects of unsolved variables in the actual responses due to unimportant factors.

Table 2
Coded and actual values of variables selected for CCD

Variables	Unit	-2	-1	0	+1	+2
pH	pH	6.15	6.5	7.35	8.2	8.55
Temperature	°C	34.59	35.00	36.00	37.00	37.41

RESULTS AND DISCUSSION

Two-Level Factorial Design

In the two-level factorial design of four factors concept, a total matrix would have been based on $2^4 = 16$ runs and 6 were centre point runs for statistical reasons. Thus, a factorial design matrix of 22 runs was used. Each variable was examined at high (+1) and low (-1) levels. The runs of the centre point were included in the matrix, and statistical study was used to recognise the effects of each factor on biomethane production. The runs were randomised for statistical purposes. The significance of factors was identified at confidence level above 95 % ($P > 0.05$). Table 3 shows the maximum and minimum methane yields are 2.97 ppm and

Table 3
Analysis of variance for the regression model and the respective model terms

Variables	F-Ratio	P-Value
A	42.01	0.0001
B	10.30	0.0051
C	7.420	0.0144
D	7.09	0.0164
AB	23.79	0.0001
AC	3.29	0.0872
AD	0.72	0.4088
BC	8.40	0.0100
BD	3.70	0.0714
CD	0.045	0.8349
ABC	09.60	0.0065
ABD	13.82	0.0018
ACD	36.54	0.0001
BCD	47.06	0.0001
Lack of Fit	0.6470	
R ²	0.9263	

1.13 ppm respectively. Here, A, B, C, D, AB, AC, AD, BC, BD, CD, ABC, ABD, ACD, BCD are significant model terms. According to the analysis of variance, the model for methane production was highly significant ($P < 0.0001$), while the lack of fit was not significant ($P > 0.05$). The coefficient of determination (R^2) was 0.9263.

Central Composite Design

Based on the identification of factors by the two-level factorial design, a central composite design was created for factors that significantly affected methane production. All the non-significant variables were kept at central points ('0' coded level) of the levels used in the two-level factorial design. Table 2 above shows the coded and real values of the levels of factors selected in CCD. The design matrix of the variables together with the experimental results are shown in Table 4.

Table 4
Central composite design of variables for methane yield

Runs	pH	Temperature (°C)	Methane Yield (ppm)
1	7.35	34.59	0.6197
2	8.20	37.00	0.9702
3	8.55	36.00	1.0573
4	6.15	36.00	0.5085
5	7.35	36.00	0.6236
6	6.50	35.00	0.5139
7	8.20	35.00	0.7695
8	6.50	37.00	0.5975
9	7.35	36.00	0.6374
10	7.35	36.00	0.6937
11	7.35	37.41	0.7080
12	7.35	36.00	0.6990
13	7.35	36.00	0.7018

In Tables 5 and 6, the response surface study permitted the development the experimental connection where each response variable (Y_i) was assessed as a function of pH (X_1) and temperature (X_2) and expected as the sum of constant (β_0), two first order effects (linear terms in X_1 and X_2 ; one interaction term in X_1X_2) and two second order effects (quadratic terms in X_1^2 and X_2^2). The obtained results were analysed using ANOVA to get the significant model terms. Only those found significant ($P < 0.05$) were included in the reduced model. As shown in Table 6 and Equation 2, the obtained model for expecting the response variables explained the main, quadratic and interaction effects of factors affecting the response variables. The predictable regression coefficients of the polynomial response surface model along with the corresponding R^2 values are shown in Table 5. It was found that the values of "Prob > F" less than 0.05 indicate the model terms are significant.

In this case, X_1 , X_2 and X_1^2 are significant model terms. Values greater than 1.1 indicated the model terms are not significant. Analysis of variance also confirmed that the model is highly significant ($P > 0.05$) for all response variables. The probability (P) values of all regression model were less than 0.05 which had no indication of lack of fit. The R^2 values for these response variables were higher than 0.80 (0.9613), thus ensuring an acceptable qualification of the regression models to experimental data. The following response surface models Equation (2) were plotted to the response variable (Y_1), two independent variables (X_1 and X_2):

$$Y_1 = 0.67 + 0.18X_1 + 0.051X_2 + 0.053X_1^2 - 6.269E - 0.03X_2^2 + 0.29X_1X_2 \quad (2)$$

Table 5
Regression coefficients, R^2 , adjusted R^2 probability values and lack of fit for each variable

Regression coefficient	Methane Yield (ppm)
β_0	+0.67
β_1	+0.18
β_2	+0.051
β_3	+0.053
β_4	- 6.269E-003
β_5	+0.29
Regression (p-value)	0.9613
Lack of fit	0.3525

Table 6
ANOVA and regression coefficients of the first and second order polynomial regression models

	Variables	Main effects	Quadratic effects	Interaction effects
Y_1	X_1	X_2	X_1^2	X_2^2
p-value	0.0001	0.0096	0.0110	0.6987
F-ratio	146.69	12.46	11.74	0.16
				$X_1 X_2$
				0.1966
				2.04

Optimisation of Biomethane Production

The predicted versus actual plots for concentration (Y_1) is shown in Figure 1. The observed points on these plots indicate that the actual values are dispersed relatively close to the straight line and in this case, $R^2 = 0.9613$. The 3D response surface was plotted to well imagine interface effects of independent variables on the biomethane yield. The plots are shown as a function of two factors at one time. These plots are useful in understanding both the main and the interaction effects of these factors.

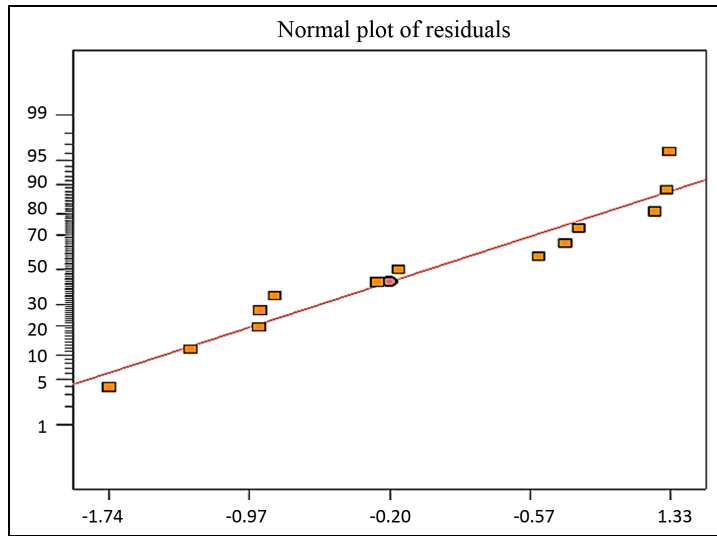


Figure 1. Predicted versus actual data for biomethane yield

As shown in Figures 2 and 3, the existence of curvatures in the biomethane yield curve set that the variation of methane yield (Y_i) was clarified as a nonlinear function. It is clear from the figures that the biomethane yield increased corresponding with the pH and temperature. Referring to Table 6, the main parameter effects are in the following order: Main effect pH > temperature. P values of parameters are 0.0001 and 0.0096 respectively. It can be seen from Figures 2 and 3, when pH was 7.35, the methane yield is 0.6711 ppm at temperature 36°C. This was supported by Foster, Perez & Romero (2008) where a higher temperature implies greater biomethane production in a shorter time.

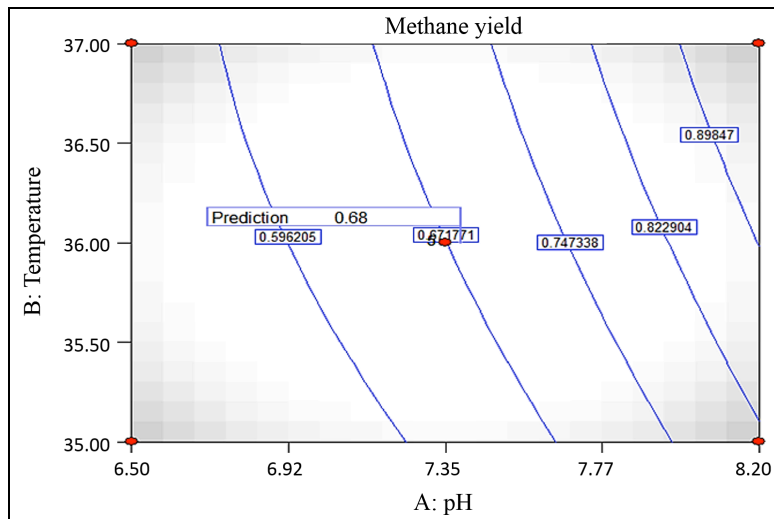


Figure 2. Contour plots graph for biomethane yield as a function of pH (A) and temperature (B)

A sharp increase in temperature should be avoided because they can bring a reduction in biomethane production due to the death of particular bacterial strains that are sensitive to temperature changes. Moreover, each group of microorganisms has a dissimilar optimum pH range. Methanogenic bacteria are extremely sensitive. The optimum pH is between 6.5 and 7.2 (Turovskiy & Mathai, 2006). Lower pH condition was due to accumulation of volatile fatty acids (VFAs) and increment of alkalinity (Appels, Baeyens, Degrève, & Dewil, 2008). The pH values beneath the optimum temperature can restrain methane bacteria activity (Appels et al., 2008; Nurul Shahida, Zainon, & Zatilfarihiah, 2015).

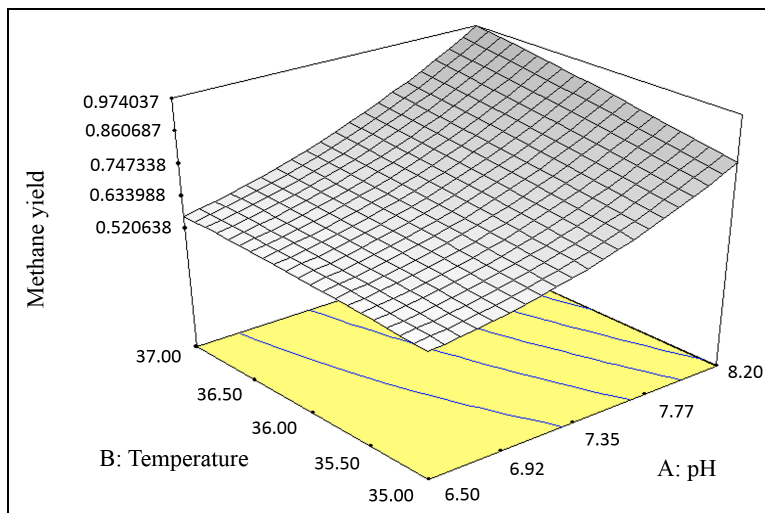


Figure 3. Three-Dimensional plots graph for biomethane yield as a function of pH (A) and temperature (B)

CONCLUSION

The RSM is a convenient technique for building models, evaluating the significance of several independent variables (pH, temperature, substrate concentration and Inocula size) and determining optimum conditions for desirable responses (biomethane yield). The RSM and contour plots set the optimum functioning factors that can be obtained graphically in order to achieve the desired biomethane yield. Therefore, it is suggested that the biomethane yield can be increased corresponding with the pH and temperature. The main effects of parameters are in the following order: Main effect of pH > Temperature.

ACKNOWLEDGEMENTS

The authors acknowledge with gratitude the editorial support from their main supervisor Assoc. Prof. Dr. Zainon Mohd Noor and co-supervisor Zatilfarihiah Rasdi, Iwana Izni Zainuddin and Noor Azrimi Umor. The authors also gratefully acknowledge Universiti Teknologi MARA (UiTM) Malaysia in providing the Exploratory Research Grant Scheme (ERGS) Fund: 600-RMI/ERGS 5/3 (11/2013).

REFERENCES

- Appels, L., Baeyens, J., Degreève, J., & Dewil, R. (2008). Principles and potential of the anaerobic digestion of waste-activated sludge. *Bioresour Technol*, 34, 755- 781.
- American Public Health Association (APHA). (1998). Standard methods for the examination of water and wastewater. 18th ed. American Public Health Association, Washington, DC, USA.
- Carley, K. M., Kamneva, N. Y., & Reminga, J. (2004). Technical report of response surfaces methodology CASOS. USA: School of Computer Science, Carnegie Mellon University, ISRI-CASOS.CMU-ISRI-04136.
- Foster, T., Perez, M., & Romero, L. I. (2008). Thermophilic anaerobic digestion of source- sorted organic. Fraction of municipal waste. *Bioresour Technol*, 99, 6763-6770.
- Joint Declaration against Food Waste. (2010). EU- and UN- Declaration. Retrieved from www.greencook.n/images/stories/joint_declaration_against_food_waste.pdf.
- Keshani, S., Luqman Chuah, A., Nourouzi, M. M., Russly A. R., & Jamilah, B. (2010). Optimization of concentration process on pomelo fruit juice using Response Surface Methodology (RSM). *International Food Research Journal*, 17, 733- 742.
- Molino, A., Nanna, F. Ding, Y, Bikson, B., & Braccio, G. (2013). Biomethane production by anaerobic digestion of organic waste. *Fuel*, 103, 1003-1009.
- Nurul Shahida, O., Zainon, M. N., & Zatifarihiah, R. (2015). The preliminary anaerobic fermentation of food wastes using anaerobic sludge. *Advances in Environmental Biology*, 9, 11-15.
- Solid Waste and Public Cleansing Management Corporation, (2008). Retrieved from <http://www.ppsppa.gov.my>.
- Turovskiy, I. S., & Mathai, P. K. (2006). *Wastewater Sludge Processing*. Wiley, New York, USA.
- Zhang, R., El-Mashad, H. M., Hartman, K., Wang, F., Liu, G., Choate, C., & Gamble, P. (2007). Characterization of food waste as feedstock for anaerobic digestion. *Bioresour Technol*, 98, 929-935.



Effects of Varying Impedance Parameters for Position-based Impedance Control of A Three-fingered Robot

Nasir, K., Shauri, R. L. A.*, Salleh, N. M. and Remeli, N. H.

Faculty of Electrical Engineering, Universiti Teknologi MARA (UiTM), 40450 Shah Alam, Selangor, Malaysia

ABSTRACT

A prototype of three-fingered robot hand was very rigid in its motion, and prone to damages when dealing with hard surfaces or when subjected to external environmental forces. The robot hand could damage fragile objects during grasping tasks if a position control alone is used. Therefore, this study proposes application of force control to the robot hand to improve its current grasping capabilities. Impedance control that considers the dynamic of the robot to produce the softness like human hand was implemented in this study. The dynamical behaviour of the robot hand strongly depends on the impedance parameters known as virtual mass, damping and stiffness. Therefore, the optimal values of impedance parameters need to be investigated to develop a position-based impedance control for the robot finger. Hence, the objective of this study is to determine the optimal value of impedance parameters to impose desired dynamics to the robot system. A constant force weighing 100 g was used by implementing varying impedance parameters to the tip-end's position. Three experiments were conducted: first to decide the order of parameters to be adjusted, then to determine the optimal value of impedance parameters, and finally to test the optimal values with random force applied to the robot finger. The determined optimal values are: *stiffness*=1000, *damping*=10 and *mass*=1. Thus, the combined parameters have proven that the modified position is capable of responding according to the exerted contact force.

Keywords: Dynamic behaviour, impedance control, impedance parameters, robot finger

ARTICLE INFO

Article history:

Received: 05 January 2017

Accepted: 17 January 2017

E-mail addresses:

khairunnisanasir@yahoo.com (Nasir, K.),
ruhizan@salam.uitm.edu.my (Shauri, R. L. A.),
sharizasalleh@gmail.com (Salleh, N. M.),
hananirameli@gmail.com (Remeli, N. H.)

*Corresponding Author

INTRODUCTION

In recent years, various robot arms which mimic the capabilities of human hand have been developed with various types of end effectors depending on the needs and objectives of the manipulation. According to Gabriel, Jorge and Fernando (2009), in order to build a robotic hand that possess the human sense of touch, the robot needs to be equipped

with force or tactile sensors. Force control can be developed to control the robot hand based on the information received by the sensor.

Studies have examined various approaches to satisfy the desired manipulation task. It can be concluded that there are two main control schemes in controlling force, hybrid control and impedance control (Anderson & Spong, 1988; Chern & Danwei, 1998; Doulgeri & Arimoto, 1999; Fernando & Paulo, 1999; Heinrichs & Sepehri, 1999; Liu & Goldenberg, 1991; Yoshikawa, 2000). Hybrid control enables the position tracking and force references in which the direction of task space of this control system is separated into two subspaces known as position-controlled and force-controlled direction. Meanwhile, impedance control is an approach that applies the virtual mass, damper and spring to control the dynamic relation of the robot with the environment, thus producing a mass-spring-dashpot system.

According to Liu and Goldenberg, (1991), hybrid control scheme could distinguish the position controlled and the force controlled subspaces. However, Yoshikawa (2000) has claimed that hybrid control scheme does not consider the dynamics of the manipulator strictly. This was also raised by Anderson and Spong (1988), that hybrid control scheme fails to recognise the importance of manipulator impedance. Failure to take note of dynamics of manipulator could reduce manipulation capability. According to Hogan (1984), impedance control can address this issue by taking into account the manipulator's dynamic behaviour. Impedance control scheme has been the focus of many related studies. For example, study by Saiki (2012) has applied on impedance control for manipulation of bolt and nut in real-time experiment, while in Saiki (2011), impedance control was implemented through the estimation of force instead of physically using force sensor. Furthermore, Maekawa, Tanie and Komoriya (1996) examined the application of tactile sensor to provide dynamic adjustment for the grasping control of a multi-fingered hand. The study revealed that the system successfully implemented the method in real time experiments on a two-fingered hand.

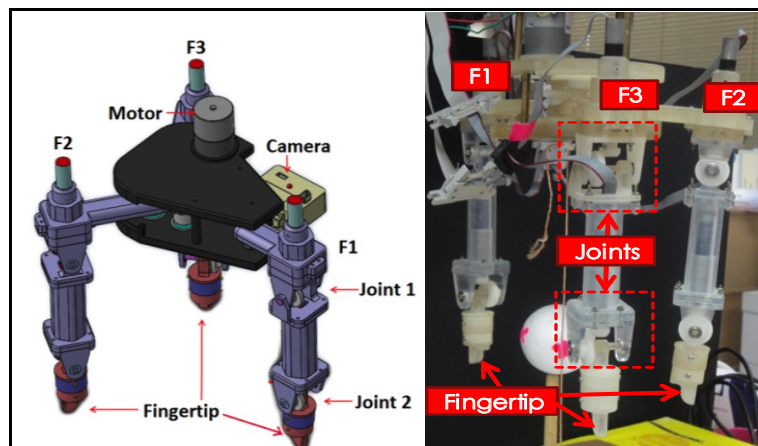
In this paper, impedance control is proposed for a three-fingered robot hand that was developed earlier. The robot hand had performed grasping of different shapes of object successfully using PID position control. However, using position control alone can damage the manipulated object during grasping when provided with inaccurate object position. This is due to the absence of touch sensor capability of the finger to accommodate the excessive force from the object. In order to mimic the human hand for gentler grasping, a position-based impedance control is proposed to modify the current trajectory position of robot finger according to the force during grasping. Thus, the optimal value of impedance parameters for designing a position-based impedance control is examined. The algorithms were developed in MATLAB Simulink and tested through real time experiments. Finally, the experimental results are analysed and the discussions on the output system performance are presented.

MATERIALS AND METHOD

Robot Hand Configurations

The robot hand consists of a palm and three fingers. One finger is fixed to the palm while the other two fingers are movable. Each finger has two joints which makes up the total of seven

degree-of-freedom (DOF) including one DOF at the palm. The joint is actuated by a DC-Micro motor equipped with an increment encoder while the palm is actuated by a DC-motor without encoder. Figure 1(a) shows the fabricated robot finger which was designed using Solid Works software and undergone FEA analysis to verify the feasibility of the design to withstand external force at a specified value (Azri & Shauri, 2014) and for the robot hand (Jaafar & Shauri, 2015) for the modified fingertip as shown in Figure 1(b) where two force sensors are installed for force control implementation. Futek LLB130 sub-miniature load cells were installed to measure the force in two directions, namely x -axis and z -axis. The specification of the load cell is shown in Table 1 and further explanation on the selection of the force sensors are discussed in (Nasir, Shauri, & Jaafar, 2016).



(a)



(b)

Figure 1. Three-fingered robot hand: (a) fabricated robot hand; and (b) fabricated tip-end of robot finger

Table 1
Sensor specification (Nasir, Shauri, & Jaafar, 2016)

Item	Specification
Model	Futek LLB130
Outer diameter	9.53mm
Load button diameter	2.29mm
Overall height	3.30mm
Capacity	22.2N (5lb)
Rated output	2mV/V
Sensitivity	0.1% (0.022N)

Position-Based Impedance Control Implementation

An appropriate compliant behaviour of robot’s fingertip is required when it interacts with the environment in order to provide sense of touch and prevent damage to the robot hand. Impedance control is a well-established concept consisting of virtual stiffness, damping and inertia of the dynamic system which can be created from a virtual spring, damper and mass applied to the end-effector respectively. The purpose of the control is to regulate the motion of the motor joints by treating the end-effector as an impedance when an external force is exerted onto the tip-end led by the dynamic relation of a single motor expressed as follows:

$$F = M_d(\Delta\ddot{P}) + D_d(\Delta\dot{P}) + K_d(\Delta P) \quad [1]$$

F is the contact force exerted to the tip-end with the environment while M_d , D_d , K_d are the impedance parameters known as mass, damping and stiffness coefficients respectively. Meanwhile, $\Delta\ddot{P}$, $\Delta\dot{P}$ and ΔP represent acceleration, velocity and position of the robot fingertip respectively. Focusing on ΔP , it presents the trajectory perturbation that shows the difference between modified and targeted positions. The dynamic relation in equation [1] demonstrates the relationship between effort and motion of the tip-end trajectory that makes the end-effector behave as a mass-spring-dashpot system.

In this work, the position-based approach is used to modify the targeted position, P_d of robot work based on the amount of contact force. The contact force occurs when there is interaction between the robot fingertip and the object. Therefore, the contact force for the robot fingertip is given by the difference between the measured external force, F_{ext} and a fixed force reference, F_{ref} . F_{ref} is used as a threshold to activate the impedance control where the targeted position, P_d will be extended when F_{ext} exceeds F_{ref} . The above equation [1] can be rewritten as below.

$$F_{ext} - F_{ref} = M_d (\Delta\ddot{P}) + D_d (\Delta\dot{P}) + K_d (\Delta P) \quad [2]$$

Thus, the modified position of robot’s tip-end, $P_{d(new)}$ produced by the impedance control can be calculated by summing the P_d with the ΔP .

$$P_{d(new)} = P_d + \Delta P \quad [3]$$

Impedance control is developed separately for x -axis and z -axis directions of the robot finger. The external forces were measured using embedded force sensors in the fingertip in both directions. The basic concept of the applied impedance control is described in Figure 2 and block diagram of the control system is shown in Figure 3. Referring to Figure 3, the red dotted line represents the design phase of the impedance control described in this study while the kinematics and position control were developed in a separate study.

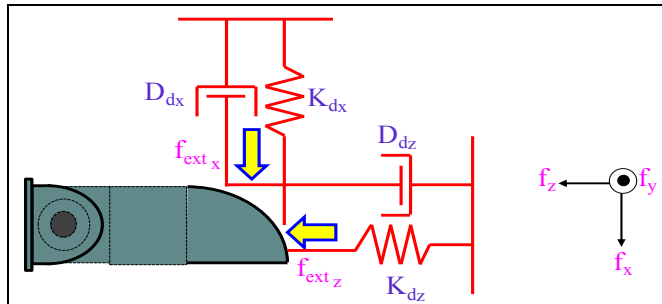


Figure 2. Basic concept of impedance control

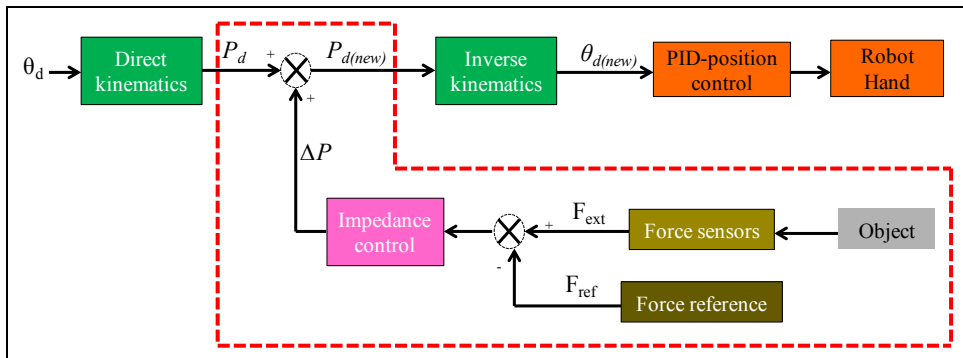


Figure 3. Block diagram of robot fingertip

Determination of Optimal Impedance Parameters

In this section, the position-based impedance control approach is implemented on the modified robot fingertip design. Three real-time experiments were conducted to investigate the effect of varying each parameter to the position of the robot’s tip-end involving the motion of two joints of the finger. Both axes will apply the same concept of impedance control, thus for simplicity, the experiments were organised only in z -axis direction. In these experiments, F_{ref} is set at 0.2N. The impedance control will only be activated when the F_{ext} exceeds F_{ref} which could affect the robot’s tip-end position as shown in equation [3]. Otherwise, $P_{d(new)}$ is equal to the initial P_d which was set at 0.08905 m in z -axis direction. The experimental setup is described in Figure 4.

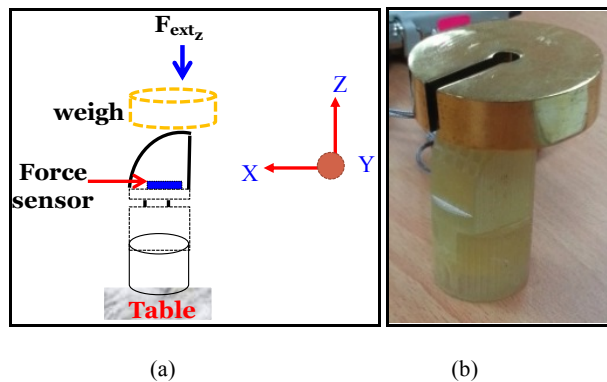


Figure 4. Experimental setup: (a) illustration; and (b) actual

First experiment is carried out to observe the effect of each impedance parameter to $P_{d(new)}$ when impedance control is activated. The values of M_d , D_d and K_d are each tested at multiple of 10 which are 0, 1, 10, 100 and 1000. Only one impedance parameter is set at one time while the others are set to 0. 100 g weight is applied to the fingertip for each variation to provide a constant external force at about 2 N. Here, each response of $P_{d(new)}$ is compared to the F_{ext} where $P_{d(new)}$ is required to generate a compliant behaviour when F_{ext} exceeds F_{ref} . Justification is made in which impedance parameter provides the most compliant behaviour on the $P_{d(new)}$ to decide the adjusting order for the next experiment.

In the next experiment, using the previous adjusting order, the optimal value of each M_d , D_d and K_d were determined based on the appropriate stiffness required for the robot finger. The parameter values were also adjusted at multiple of 10 - 1, 10, 100 and 1000. Similarly, a 100 g weight is applied for each variation. The response of $P_{d(new)}$ is also compared to F_{ext} that exceeds the threshold. Each adjusted parameter will be fixed at its optimal value for adjusting the other parameter until all the impedance parameters achieved the control requirement.

Finally, all impedance parameters obtained in the second experiment were used to execute the complete impedance control algorithm in z-axis direction. The control is tested by applying several random forces to the robot's tip-end. The response behaviour of $P_{d(new)}$ is recorded and analysed to check the performance of the proposed position-based impedance control.

RESULTS AND DISCUSSION

The results are shown in two graphs which represent the measured force in Newton (N) and the modified position in meter (m) based on the varied impedance parameters within the sampling time of 1 millisecond (ms). The experimental results of $P_{d(new)}$ and measured F_{ext} when varying M_d , D_d and K_d are shown in Figures 5(a), 5(b) and 5(c), respectively. Compared with M_d and D_d , it can be observed that varying K_d provides the most compliant behavioural response on the $P_{d(new)}$. Thus, it shows that K_d is the most influential parameter for impedance control. Hence, the adjustment order of impedance parameter will be in the sequence of K_d , D_d and M_d .

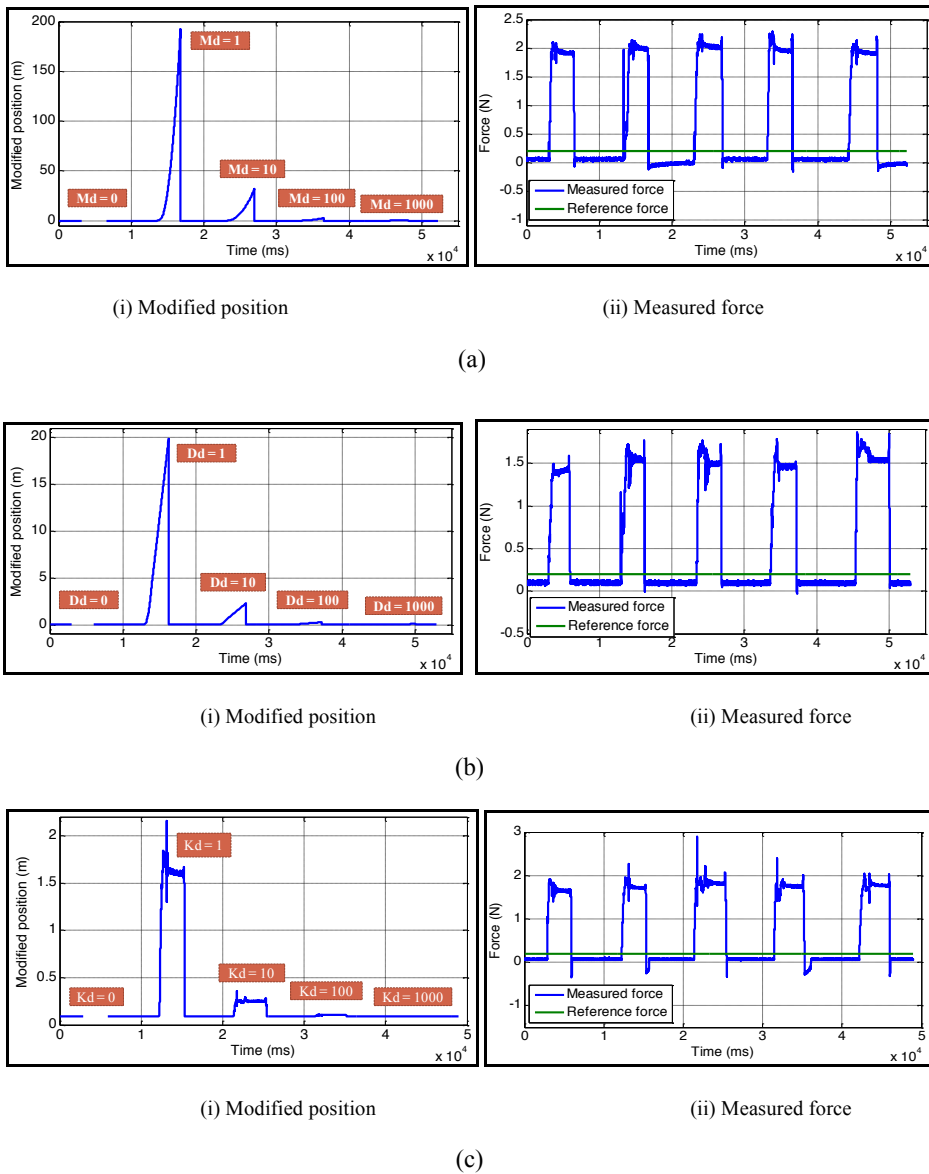


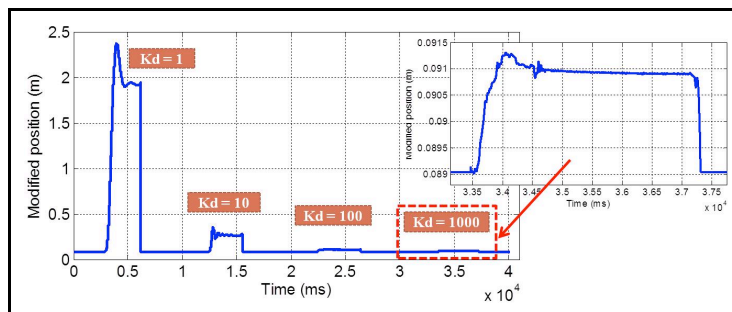
Figure 5. Impedance control response for each varying impedance parameter: (a) varying mass, M_d ; (b) varying damping, D_d ; and (c) varying stiffness, K_d

By following the adjustment order of impedance parameters that had been decided in first experiment, the results of varying the impedance parameters are presented in Figure 6, Figure 7 and Figure 8 for K_d , D_d and M_d respectively. According to Figure 6, for 100 g in weight, the K_d adjusted at 1, 10, 100 and 1000 produced ΔP about 180 cm, 23 cm, 5 cm and 2 cm respectively. As the K_d increased the distance of the modified position, ΔP shortened which indicated the increase in stiffness. It shows that K_d at 1000 produced the most rigid behaviour among all adjusted values with ΔP of 2 cm while K_d at 1 produced the least stiffness with ΔP of

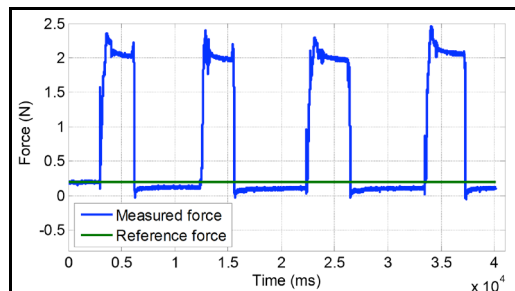
180 cm. Referring to equation [3], ΔP affected $P_{d(new)}$ or in other words, the reachability of the robot's tip-end which depended on the dimension of the robot finger. Hence, considering the current finger dimensions, the stiffness, K_d at 1000 is sufficient for the robot finger to operate in the desired working range.

Subsequently, the value D_d is determined when K_d is set at 1000. Referring to the Figure 7(a), it can be observed that the larger the D_d value, the less sensitive $P_{d(new)}$. Meanwhile, the lesser value of D_d shows a more sensitive behaviour; however, it could lead to instability of control. D_d set between 10 to 100 was observed to provide sufficient sensitivity of control for $P_{d(new)}$. Taking the smaller optimal value, D_d is at 10.

Finally, the value M_d is determined when K_d and D_d are set at 1000 and 10 respectively. Based on the result in Figure 8(a), the increment of M_d resulted in more oscillations on the $P_{d(new)}$ response while the less value of M_d helps in smoothing the $P_{d(new)}$ response. Among all the adjusted values, M_d is observed to be the best at 1 with the least oscillations occurring on $P_{d(new)}$.



(a)



(b)

Figure 6. Determined value of K_d : (a) modified position; and (b) measured force

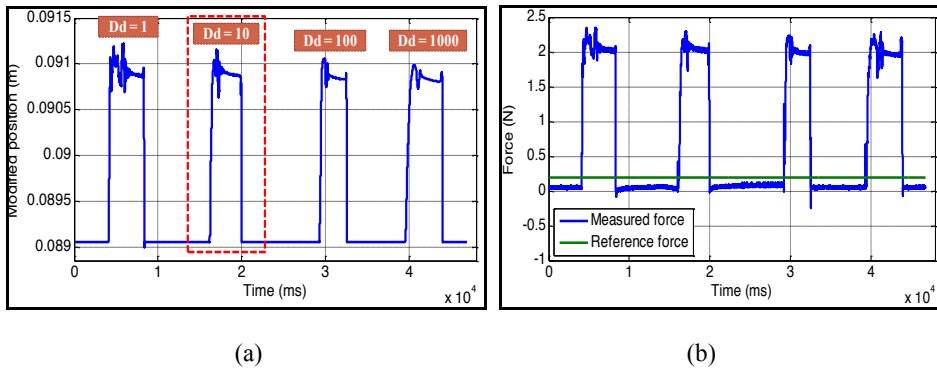


Figure 7. Determined value of D_d : (a) modified position; and (b) measured force

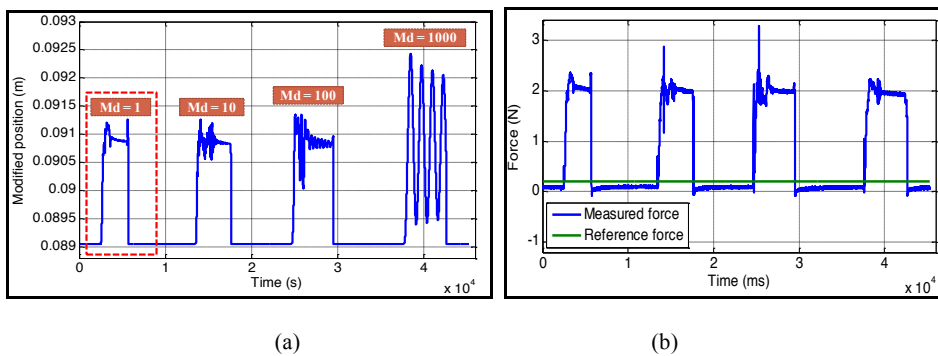


Figure 8. Determined value of M_d : (a) modified position; and (b) measured force

The determined impedance parameters, $M_d = 1$, $D_d = 10$ and $K_d = 1000$ were used in the impedance control algorithm in the third experiment. Figure 9 shows the resulted $P_{d(new)}$ for three random forces applied on the robot's tip-end at different times. It can be observed that $P_{d(new)}$ increased the distance in z -axis compared with P_d when F_{ext} is measured above the F_{ref} . This proved that the developed position-based impedance control had successfully performed the compliant behaviour when the contact force occurred at between 1800 ms and 6000 ms. In future, the proposed optimal values can be used as a reference to modify the dynamic behaviour of the robot finger according to the user and the assigned tasks.

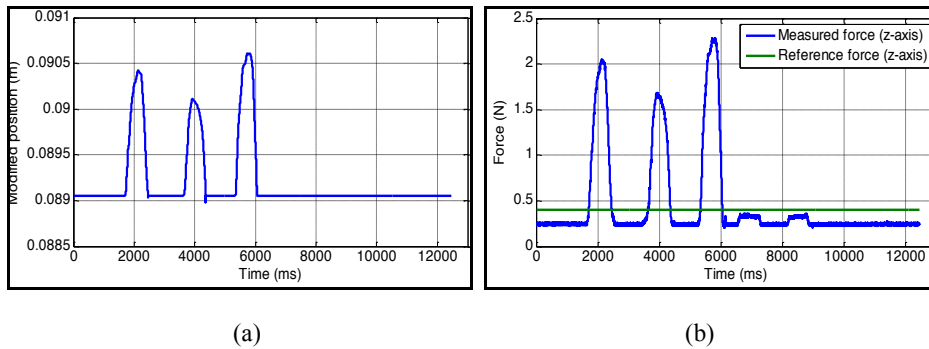


Figure 9. Testing the complete developed impedance control

CONCLUSION

A position-based impedance control was successfully applied to a robot finger and verified in real-time experiments. The algorithm was executed through MATLAB Simulink. Three experiments were conducted to investigate the effect of varying impedance parameters on the tip-end's position when external forces were applied. Results of the first experiment revealed that K_d had the most influence on the dynamic of the finger compared with D_d and M_d . Therefore, the adjustment order of impedance parameter was decided to be in the sequence of K_d , D_d and M_d . Meanwhile, from the second experiment, the optimal value for K_d , D_d and M_d were determined at 1000, 10 and 1 respectively. Finally, from the third experiment, the test result proved that the developed position-based impedance control performed compliant behaviour when different random external forces were applied.

ACKNOWLEDGEMENTS

The authors thank the Ministry of Higher Education for providing funds to undertake this study (600-RMI/FRGS 5/3 (86/2013)). The authors express their gratitude to Research Management Institute (RMI) and Faculty of Electrical Engineering, Universiti Teknologi MARA for providing financial support and equipment to conduct this research.

REFERENCES

- Anderson, R., & Spong, M. W. (1998). Hybrid impedance control of robotic manipulators. *IEEE Journal of Robotics and Automation*, 4, 549-556.
- Azri, M. H., & Shauri, R. L. A. (2014). Finite element analysis of a three-fingered robot hand design. *IEEE 4th International Conference in System Engineering and Technology*, 1-6.
- Chien, C., & Danwei, W. (1998). Learning impedance control for robotic manipulators. *IEEE Transactions on Robotics and Automation*, 14, 452-465.
- Doulgeri, Z., & Arimoto, S. (1999). A force commanded impedance control for a robot finger with uncertain kinematics. *The International Journal of Robotics Research*, 18, 1013-1029.

- Fernando, A., & Paulo, A. (1999). Force-Impedance Control: A new control strategy of robotic manipulators. *Recent advances in Mechatronics*, 126-137.
- Gabriel, J. G., Jorge, P., & Fernando, T. (2009). Survey of Visual and Force/Tactile Control of robots for physical interaction in Spain. *Sensors*, 9689-9733.
- Heinrichs, B., & Sepehri, N., (1999). Relationship of position-based impedance control to explicit force control: Theory and experiments. *Proceedings of the American Control Conference*, 2072-2076.
- Hogan, N. (1984). Impedance Control: An approach to manipulation. *Proceedings of the American Control Conference*, 304-313.
- Jaafar, J., & Shauri, R. L. A. (2015). Fingertip structural analysis—A simulated design evaluation. *Jurnal Teknologi*, 76.
- Liu, G. J., & Goldenberg, A. A. (1991). Robust hybrid impedance control of robot manipulators. *IEEE International Conference Proceedings in Robotics and Automation*, 1, 287-292.
- Maekawa, H., Tanie, K., & Komoriya, K. (1996). Dynamic grasping force control using tactile feedback for grasp of multifingered hand. *IEEE International Conference Proceedings in Robotics and Automation*, 3, 2462-2469.
- Nasir, K., Shauri, R. L. A., & Jaafar, J. (2016). Calibration of embedded force sensor for robotic hand manipulation. *IEEE 12th International Colloquium on Signal Processing and Its Applications*, 351-355.
- Saiki, K. (2012). *Autonomous assembly work by using arm robot with impedance control* (Master's thesis), *School of Engineering, Chiba University Graduate School of Engineering*.
- Saiki, K., Shauri, R. L. A., & Nonami, K. (2011). Force Sensorless Impedance Control of Dual-Arm Manipulator-Hand System. *Journal of System Design and Dynamics*, 5, 13.
- Yoshikawa, T. (2000). Force control of robot manipulators. *IEEE International Conference Proceedings on Robotics and Automation*, 1, 220-226.



Concentrated Solar Thermal Thermoelectric Power Generation under Natural and Forced Convection Cooling

Dee, S.¹, Singh, B.^{1*}, Remeli, M. F.¹, Tan, L.² and Oberoi, A.³

¹Faculty of Mechanical Engineering, Universiti Teknologi MARA (UiTM), 40450 Shah Alam, Malaysia

²School of Engineering, RMIT University, Bundoora, Victoria, 3083, Australia

³Chitkara University, Chandigarh-Patiala National Highway (NH-64), Patiala, Punjab - 140401, India

ABSTRACT

This paper looks at electrical power generation from solar concentrator using thermoelectric generator. An experiment was conducted on a concentrator thermoelectric generator (CTEG) utilising solar thermal energy. The CTEG used a parabolic dish as concentrator with thermoelectric device installed at the focal point to convert thermal energy to generate electricity. The investigation covered the cooling effect of the cold side of the thermoelectric generator using natural and forced convection cooling for optimum output. Forced convection cooling with a fan provided 69% more power output from the CTEG system as the temperature difference across the TEG was greater than the system cooled by natural convection. The outcome of this project showed maximum power output was obtained for the CTEG system cooled by forced convection cooling.

Keywords: Concentrated solar energy, forced convection, thermoelectric generator, thermal energy

INTRODUCTION

Population growth and technological advancement impose heavy demands for

energy (Fan, Singh, & Akbarzadeh, 2010) namely fossil fuels, such as natural gas, oil and coal (Xie, Dai, Wang, & Sumathy, 2011). However, there is also an environmental cost. Biomass, solar, wind and other renewable energy are able to sustain our demand and overcome environmental problems caused by rapid industrialisation (Zhu, Matsuura, Suzuki, & Tsuchiya, 2014) while fossil fuels are non-renewable energy that takes billions of years to replenish and their depletion rate is faster than their replacement (Eswaramoorthy, Shanmugam, & Veerappan, 2013).

ARTICLE INFO

Article history:

Received: 05 January 2017

Accepted: 17 January 2017

E-mail addresses:

deetefanny@gmail.com (Dee, S.),

baljit@salam.uitm.edu.my (Singh, B.),

fairuzremeli@gmail.com (Remeli, M. F.),

lippong.tan@rmit.edu.au (Tan, L.),

amandeep_oberoi@hotmail.com (Oberoi, A.)

*Corresponding Author

As the world's supply of the fossil fuels shrinks, there is a great need for renewable energy, which is clean and affordable, to meet global energy demand (Barlev, Vidu, & Stroeve, 2011). Currently, renewable energy resources have become important due to their demand and capacity to supply sustainable electricity generation system (Khan & Arsalan, 2016). This is coupled with interest in sustainable power production and the need to reduce CO₂ emissions (Benoit, Sprea, Gauthier, & Flamant, 2016).

The solar energy is the most reliable and sustainable energy resource for production of electric and thermal energy (Kossyvakis, Vossou, Provatidis, & Hristoforou, 2015). It is considered as the largest and widely distributed renewable energy resource on the planet and can be utilised in many applications either in passive or active solar architecture such as solar water heating, photovoltaic electricity generation and solar thermal generation (Zhang et al., 2013). The solar energy application can be categorised under solar thermal or solar photovoltaic (Ong, 2015). Two technologies can be used to convert solar energy to electricity. The photovoltaic converts sunlight into electricity directly, without resorting to any heat engine, using solar cells. Solar thermal technologies on the other hand convert solar energy into thermal energy, which can be used to run heat engines to produce electricity.

Photovoltaic systems are largely and widely used in domestic applications. The solar thermal system is generally used to generate electricity by utilising heat energy to produce steam to run turbines. This system is very bulky and requires very high maintenance. Alternatively, the solar thermal system can be used for power generation using thermoelectric generator (TEG) to generate electricity. The solar thermal conversion system technology can be implemented using the TEG without the use of the photovoltaic (Trinh, Gonz, Lesage, Wa, & Ha, 2014). The TEG provides an alternative to power generation using concentrated solar energy as compared to steam engines. It is more reliable, robust and acts as a solid-state heat engine for thermal energy to electrical energy conversion. The solar thermal collector can be classified into two categories based on the concentrate ratio: concentrating and non-concentrating (Tian & Zhao, 2013). The concentrator that utilises lens are not able to focus scattered light. The solar concentrating solar thermal thermoelectric consists of thermal collector and a device generator.

The thermoelectric generator (TEG) is based on the concept of Seebeck effect, converting thermal energy to electricity. The thermoelectric device is most commonly used as heat pumps for cooling (Singh et al., 2015). The TEG can also act as a heat engine to produce electricity from heat sources. The TEG is unlike the heat engine which has many parts. It is in the form of solid state, economical, extremely reliable, compact and safe device. The thermo elements in a TEG consist of n-type and p-type semiconductors, and connected electrically in series and thermally in parallel. The output power and the performance of the TEG not only depends on the material properties but also the geometric structure (Singh, Tan, Date, & Akbarzadeh, 2012). With recent developments in the TEG technologies, integration of TEG for power generation promises a sustainable way of generating electricity from solar energy.

MATERIALS AND METHOD

In this work, an experiment was conducted on a concentrator thermoelectric generator (CTEG) using solar thermal energy. The CTEG system consists of parabolic dish collector with an

aperture diameter of 0.545 m used to concentrate sunlight to thermoelectric device installed at the focal point to convert thermal energy into electricity. A heat sink was used to simulate the heat transfer from the TEG under natural convection cooling and forced convection cooling. A micro channel heat sink and water flow channel was used to remove heat from the TEG cold side.

CTEG with Passive and Active Cooling

Parameters that affect the performance of CTEG are solar radiation, wind and ambient temperature. In this work, one side of the TEG was heated, and the other side was maintained at low temperature using passive or active cooling modes. Figure 1 shows the passive cooling mode. The active cooling mode using fan was also tested. Figure 2 shows the actual setup used for experimental analysis.

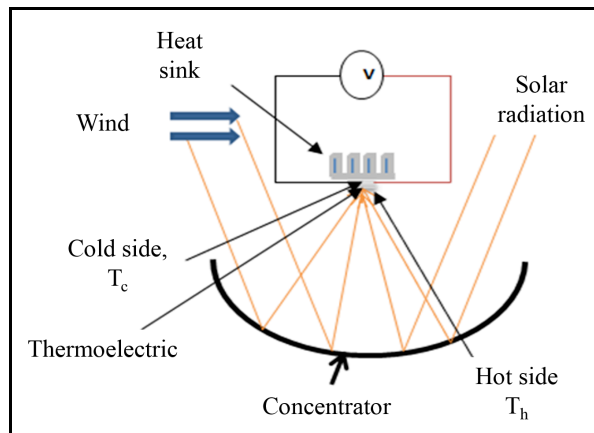


Figure 1. The CTEG using passive cooling modes

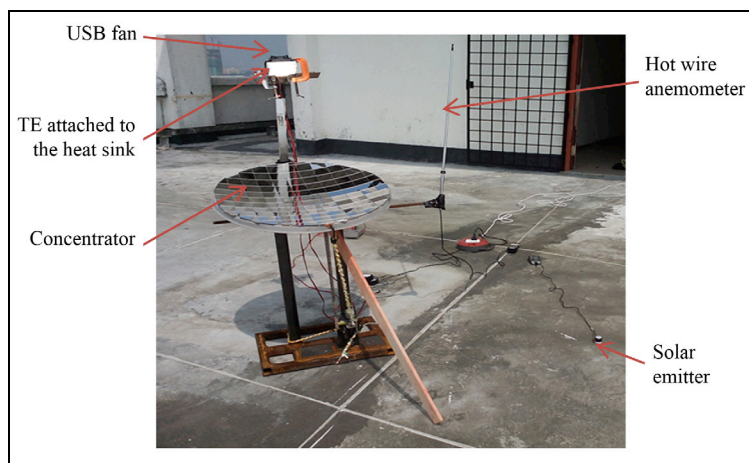


Figure 2. The CTEG setup

Experimental Setup

Concept. The main goal of this experiment was to convert concentrated solar thermal energy directly into electrical energy. The CTEG system consists of a parabolic dish collector plate and BiTe-based thermoelectric attached to the heat sink. The heat sink was used to remove waste heat from the TEG cold side and the concentrator focused the thermal energy with the help of single tracking axis system to track the sun continuously.

Test Apparatus. In order to verify power produced by the CTEG system, a series of experiments were conducted including the measurement of temperature and electrical output. The parameter measured to test the performance of the CTEG was temperature, voltage, solar radiation, and air speed. The temperature reading was obtained using the four-channel wire thermo sensor. The voltage reading was recorded using a digital multimeter. The solar emitter was used to take the reading for solar radiation, and hot wire anemometer was used to take the reading of the air movement and ambient temperature. The experiment was conducted at top floor level 21, Tower1, Kompleks Kejuruteraan Mekanikal, UiTM Shah Alam. The location is at 3.164° N and 101° E. The axis of the reflector needed to be parallel to the incoming radiation in order to focus to the solar ray's incidents to the concentrated area. That means the concentrator should continuously track the sun. This was done by adjusting it using the angle adjuster to have the bright spot of the solar radiation and reflected to the TEG. The reading of hot temperature, T_h and cold temperature, T_c was taken every 20 minutes including voltmeter reading, solar radiation, ambient temperature and air movement. The duration of the experiment was four hours, from 11 am until 3 pm.

Component Specification. A parabolic dish was used as a concentrator, and the focal length of this parabolic was 30 cm. In order to enhance the reflectivity, the whole surface was covered with 26.08 cm² mirrors. The depth, major axis and minor axis of the parabolic dish was 3.6 cm, 62.0 cm and 54.5 cm respectively. The mirror was cleaned to achieve best reflection.

One TEG cell was attached to the focal point of the CTEG. The TEG used in this experiment was made up of bismuth and telluride (BiTe) type of semiconductor. Bismuth telluride cells are widely used as thermoelectric coolers (Peltier effect) and can be used for power generation at temperatures lower than 200°C. It has relatively high Seebeck coefficient ($\sim 190 \mu\text{V/K}$) and high figure of merit ($\sim 2 \times 10^{-3} \text{ K}^{-1}$), with individual dimensions of 40 mm (length) by 40 mm (width) by 3.9 mm (height) and 127 thermo elements per cell. The maximum open circuit voltage is 15 V, and maximum operating temperature is 200°C. The cooling system operated under two conditions: natural convection and forced convection using 12 V DC cooling fan. The natural convection was induced by natural wind. A variable electric resistance load was used to measure maximum output power.

RESULTS AND DISCUSSION

Solar Radiation, Air Movement and Ambient Temperature

The sun radiation, air movement and ambient temperature were measured from 11 am until 3.00 pm. The reading was taken every 20 minutes. The experiment was conducted when the weather

was sunny throughout. From Figure 3, it is clearly seen that the sun radiation reading was not constant due to the formation of clouds. Air movement was also intermittent as shown in Figure 4. The ambient temperature was almost constant. All of these conditions were important for the CTEG performance under natural convection. When the sun radiation was at the lowest, the temperature at the hot side of the TEG was also low.

The air movement was important for the CTEG operating under natural wind. The highest air movement was recoded at 1.2 m/s. The air movement influenced the result of the cold side of the TEG.

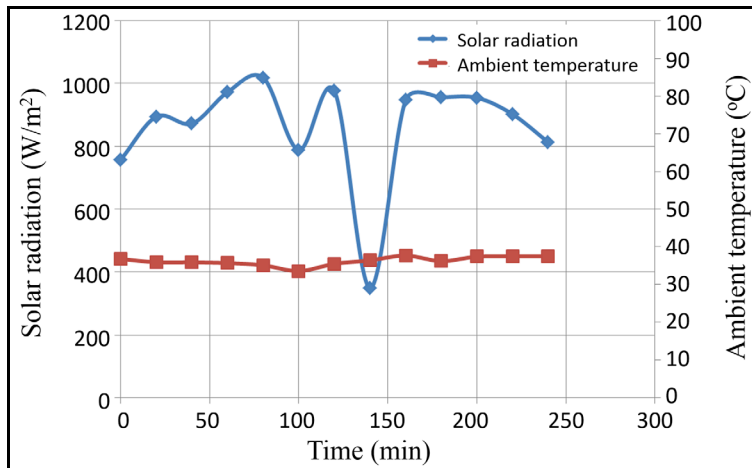


Figure 3. Solar radiation versus time for the CTEG operating under forced convection cooling

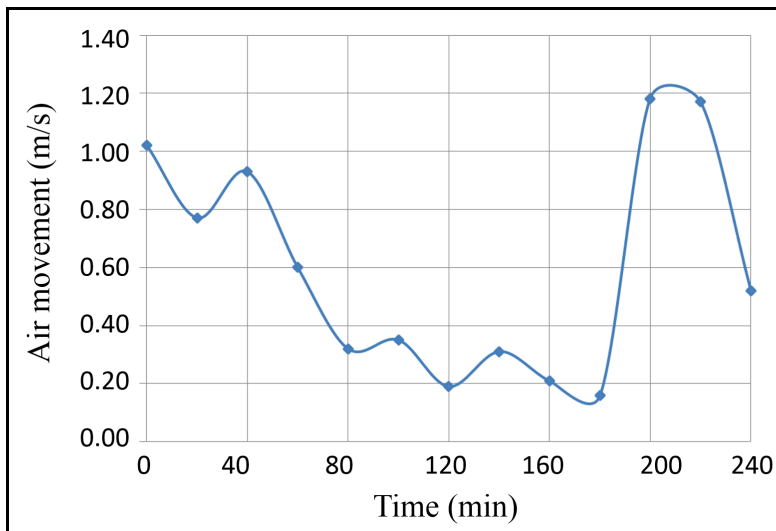


Figure 4. Air movement versus time for the CTEG operating under natural convection cooling modes

Thermoelectric Differential and Electrical Potential

The CTEG reading was measured and recorded. Electrical potential was generated based on temperature differential across the TEG. Figure 5 shows the result of the CTEG operating under the DC fan forced convection cooling, while Figure 6 shows results of the CTEG operating under natural convection cooling. From Figures 5 and 6, it can be concluded that as the thermal differential across the TEG increases, the voltage also increases linearly. Forced convection cooling provided by the fan resulted in higher potential difference generated from the TEG.

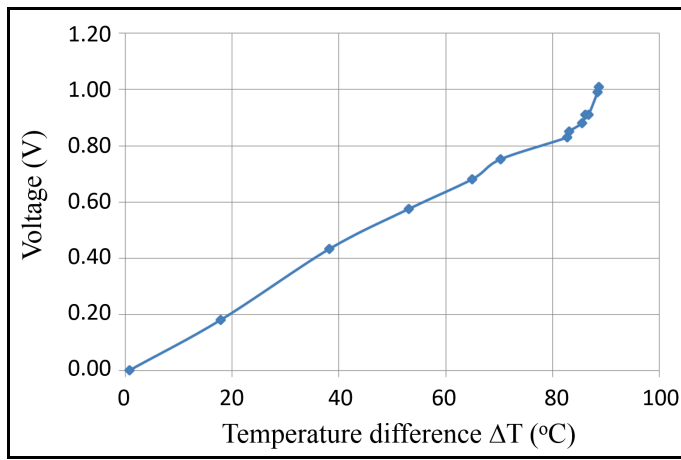


Figure 5. Electrical potential versus temperature difference operating under DC fan forced convection cooling modes

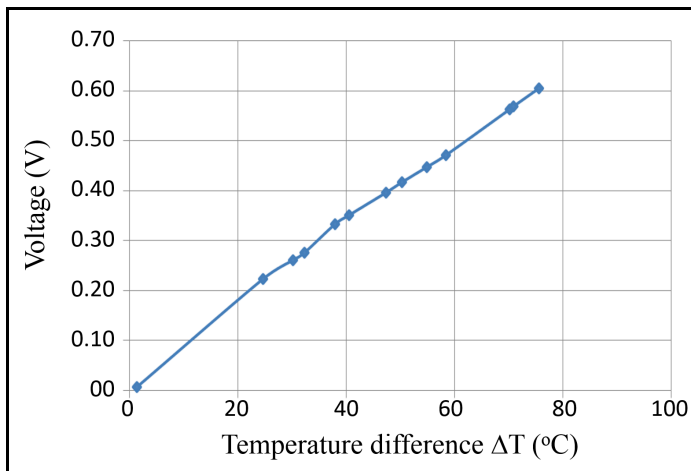


Figure 6. Electrical potential versus temperature difference operating under natural convection (natural wind) cooling modes

Figures 7 and 8 show results for the CTEG operating under natural and forced convection cooling modes. The temperature difference between cold and hot sides is shown in both figures. In Figure 7, there is a dip in the hot side at 120th minute. This is due to the absence of solar radiation during cloudy weather, which was only momentary. Figure 8 shows the hot and cold side temperature of the TEG depends on the solar radiation. The inconsistency shown for the hot and cold side temperature is due to the availability of the solar radiation and the tracking system of the CTEG. It can be concluded the hot side temperature is dependent on solar radiation, and the cold side remains almost constant with time. The higher temperature difference between the surfaces of the TEG is because of the higher solar radiation and temperature differences fluctuate with the solar radiation. By using the cooling fan, the temperature of the cold side was much lower than the same setup operating under natural convection. This results in higher potential differences generated by the TEG.

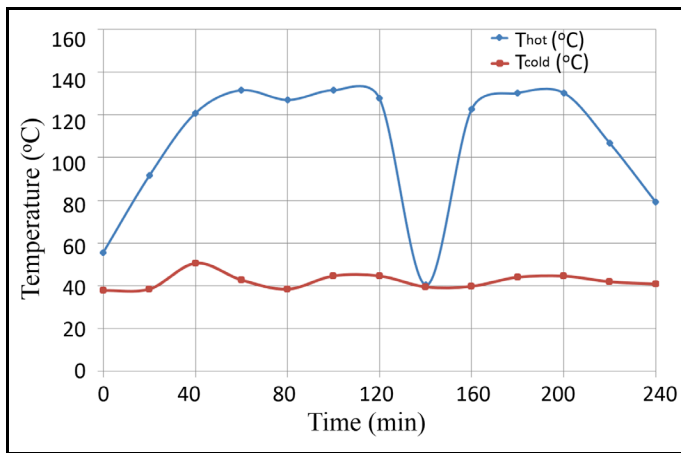


Figure 7. The TEG hot side and cold side temperature versus time for DC fan forced convection cooling

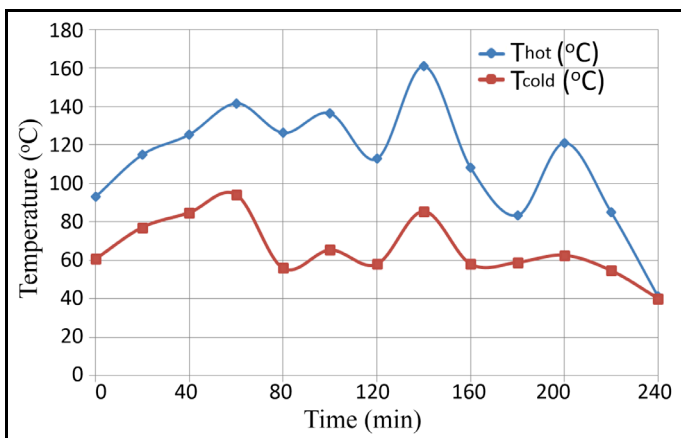


Figure 8. The TEG hot side and cold side temperature versus time for natural convection cooling

Figure 9 shows the power output of the CTEG system for natural and forced convection cooling. The results show that the maximum power output was at 22 mW for forced convection cooling and 13 mW for natural convection. This results in 69% increase in the output power when the cooling for the TEG was performed using a heat sink with a fan. However, the increase in the output power for forced convection cooling was to compensate the power required to run the fan. This will then reduce the net maximum power output for the forced convection cooling output. Forced convection cooling will still be a preferred choice to obtain higher power output from the CTEG, even after compensating the power needed for the running of the cooling fan.

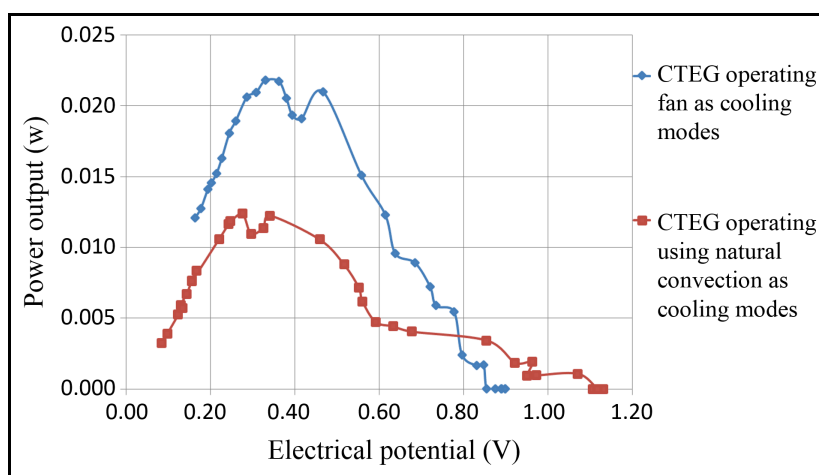


Figure 9. Power Output versus electrical potential for the CTEG operating at forced convection and natural convection cooling modes

CONCLUSION

In conclusion, the maximum power output obtained for the CTEG system was achieved by forced convection cooling. The CTEG system cooled by forced convection cooling produced higher temperature differential than natural convection cooling, thus resulting in higher electrical potential. Forced convection cooling with a fan provided 69% more power output from the CTEG system as the temperature difference across the TEG was higher than the system cooled by natural convection. Forced convection cooling provides higher heat transfer coefficient for heat transfer, thus resulting in higher power generation from the system.

REFERENCES

- Barlev, D., Vidu, R., & Stroeve, P. (2011). Solar energy materials and solar cells innovation in concentrated solar power. *Solar Energy Materials and Solar Cells*, 95(10), 2703–2725.
- Benoit, H., Sprea, L., Gauthier, D., & Flamant, G. (2016). Review of heat transfer fluids in tube-receivers used in concentrating solar thermal systems: Properties and heat transfer coefficients. *Renewable and Sustainable Energy Reviews*, 55, 298–315.

- Eswaramoorthy, M., Shanmugam, S., & Veerappan, A. R. (2013). Experimental study on solar parabolic dish thermoelectric generator. *International Journal of Energy Engineering (IJEE)* Jun. 2013, 3(3), 62-66.
- Fan, H., Singh, R., & Akbarzadeh, A. (2010). Power generation from thermoelectric cells by using high concentrated solar dish. *Proceedings of the Solar10, the 48th ANZSES Annual Conference*.
- Khan, J., & Arsalan, M. H. (2016). Solar power technologies for sustainable electricity generation – A review. *Renewable and Sustainable Energy Reviews*, 55, 414–425.
- Kossyvakis, D. N., Vossou, C. G., Provatidis, C. G., & Hristoforou, E. V. (2015). Computational analysis and performance optimization of a solar thermoelectric generator. *Renewable Energy*, 81, 150–161.
- Ong, K. S. (2015). Review of solar, heat pipe and thermoelectric hybrid systems for power generation and heating. *International Journal of Low-Carbon Technologies*, 1–6.
- Singh, B., Saoud, A., Remeli, M. F., Ding, L. C., Date, A., & Akbarzadeh, A. (2015). Design and construction of a simple thermoelectric generator heat exchanger for power generation from salinity gradient solar pond. *Jurnal Teknologi*, 76(5), 21-24.
- Singh, B., Tan, L. P., Date, A., & Akbarzadeh, A. (2012). Power generation from salinity gradient solar pond using thermoelectric generators for renewable energy application. *2012 IEEE International Conference on Power and Energy (PECon)*, 89-92.
- Tian Y., & Zhao, C. Y. (2013). A review of solar collectors and thermal energy storage in solar thermal application. *Applied Energy*, 104, 538–553.
- Trinh, J. C. S. V. A., Gonz, I., Lesage, J., Wa, S. S., & Ha, M. (2014). Solar thermal energy conversion to electrical power. *Applied Thermal Engineering*, 70, 675–686.
- Xie, W. T., Dai, Y. J., Wang, R. Z., & Sumathy, K. (2011). Concentrated solar energy applications using Fresnel lenses: A review. *Renewable and Sustainable Energy Reviews*, 15(6), 2588–2606.
- Zhang, M., Miao, L., Pu, Y., Tanemura, S., Fisher, C. A. J., Xu, G., Xin, C., & Zhu, G. (2013). Efficient , low-cost solar thermoelectric cogenerators comprising evacuated tubular solar collectors and thermoelectric modules. *Applied Energy*, 109, 51–59.
- Zhu, N., Matsuura, T., Suzuki, R., & Tsuchiya, T. (2014). Development of a small solar power generation system based on TEG. *Energy Procedia*, 52, 651–658.





Somatic Embryogenesis in Sugar Palm (*Arenga pinnata* Wurmb Merr.) from Zygotic Embryo Explants

Nazatul Asikin Muda^{1*} and Asmah Awal²

¹Faculty of Plantation and Agrotechnology, Universiti Teknologi MARA (UiTM), 40450 Shah Alam, Selangor, Malaysia

²Agricultural Biotechnology Research Group, Faculty of Plantation and Agrotechnology, Universiti Teknologi MARA (UiTM), 40450 Shah Alam, Selangor, Malaysia

ABSTRACT

In this paper, a micropropagation protocol of sugar palm (*Arenga pinnata* Wurmb Merr) through callogenesis and somatic embryogenesis was examined. Callus induction frequency and somatic embryogenesis response were dependent on plant growth regulators (PGRs) and genotype. Semi-compact and compact embryogenic calluses were induced from excised immature zygotic embryo (IZE) cultured on semi-solid MS (Murashige & Skoog, 1962) medium supplemented with various concentration and combination of 2,4-dichlorophenoxyacetic acid (2,4-D) and 6-benzyl aminopurine acid (BAP). MS medium supplemented with 0.4 mg/L 2,4-D and 0.5 mg/L BAP was found optimum to induce 100% rate of embryogenic calluses and maximum degree of callus formation after 8 and 12 weeks of culture. The incorporation of increased sucrose concentration (60.0 g/L) and 2.0 g/L casein hydrolysate (CH) to the culture medium with similar PGRs composition enhanced the induction of globular somatic embryos (SEs), while addition of silver nitrate (AgNO₃) produced SEs of different stages. SEs matured in MS medium containing 1.0 mg/L BAP and 1.0 mg/L naphthalene-acetic acid (NAA) formed cotyledon-stage embryos. Clonal roots regeneration was obtained on half-strength MS devoid of PGRs after 4 months of culture. Frequent subcultures increased embryogenesis rate favourably.

Keywords: Embryogenic callus induction, immature zygotic embryo (IZE), plant growth regulators (PGRs), somatic embryogenesis, sugar palm

ARTICLE INFO

Article history:

Received: 05 January 2017

Accepted: 17 January 2017

E-mail addresses:

naza_asyiq87@yahoo.com (Nazatul Asikin Muda),

asmah138@salam.uitm.edu.my (Asmah Awal)

*Corresponding Author

INTRODUCTION

Sugar palm (*Arenga pinnata* Wurmb Merr) is a multipurpose crop that belongs to the palm species (*Arecaeae*). The communities that live within the rainforests and along their borders have depended on this crop for their livelihood. In the Asian regions, sugar palm

trees have economic importance, being an alternative source of sugar, starch, alcohol and fibres. They are also used in many industrial sectors such as food, beverages, construction, pharmaceutical and crafts (Moore, 2013).

Sugar palm is normally pollinated through seeds and offshoots. However, both seed and vegetative propagation has several limitations including slow fruit development, slow seed germination, non-uniform seedlings, and prolonged dormancy period (Janick & Paull, 2005). Rapid propagation of sugar palm using seeds is not suitable due to heterozygosity and dioecious nature of sugar palm that may result in producing off-type plant. Offshoot propagation is a slow method and not suited for mass propagation due to limited production naturally and the fact that offshoot production of most palm trees is limited to a certain period of their life cycle (Zaid & De Wet, 2013). Therefore, to overcome these propagation problems and to maintain the germplasm, it is beneficial to use the plant tissue culture techniques for multiplication of sugar palm.

Plant tissue culture techniques are used to maintain or grow plant cells, tissues or organs under sterile conditions on a nutrient culture medium of known composition. The capacity of plant parts or cell to grow into a full plant is termed as "totipotency". Tissue culture techniques are often used for commercial production of plants as well as plant research. Plant tissue culture involves the use of explants, small pieces of plant tissues which are cultured in a nutrient medium under sterile conditions (Smith, 2013). Since the nutrient medium is the only source of nutrition, it should supply all the basic requirements such as carbohydrates, amino acids, minerals, hormones, salts and etc. to cater for plant growth.

Plant growth regulators (PGRs) or plant hormones are organic molecules, critical component in plant tissue culture media that profoundly affect different plant processes such as growth and morphogenesis (Jha, 2005). The five major groups of PGRs i.e. auxins, cytokinins, gibberellins, abscisic acid and ethylene are generally active at very low concentrations and usually work together in coordinating the growth and development of cells, although auxins and cytokinins are by far the most important for plant tissue culturist in determining shoots (high cytokinin-to-auxin ratio), roots (low cytokinin-to-auxin ratio) or callus (relatively high levels of both). The PGRs are also essential to stimulate the development of non-zygotic embryos, growth and development of callus, proliferation of auxiliary roots and development of adventitious roots as well as the establishment of somatic embryogenesis (Beyl, 2011).

Somatic embryogenesis is an efficient approach of plant micropropagation, where embryos are developed from adult somatic cells, known as somatic embryos (SEs). These SEs are bipolar and not connected to explant or callus cells by vascular tissue. While auxins such as NAA and indole-3-butyric acid (IBA) are usually used to induce rhizogenesis on microcuttings, 2,4-D and dicamba (DIC), are commonly used to induce somatic embryogenesis. The ABA is often used to enhance embryo maturation. Somatic embryogenesis has been reported in a number of plant systems which includes palm species (El Bar & El Dawayati, 2014; Kanchanapoom & Phongdara, 2010). Since the SEs are formed without undergoing any fertilisation, they are genetically identical to the parent tissues and are consequently clones. In plant biotechnology, somatic embryogenesis offers numerous benefits mainly at commercial-scale as this system offers an alternative approach to conventional propagation through the unlimited production

of clones with elite traits. Both callogenesis and somatic embryogenesis systems are crucial for plant clonal propagation and are usually an integral part of genetic transformation studies.

SEs induction has been previously reported in sugar palm (Devi, Purwito, & Husni, 2014; Putih, Satria, & Thaib, 2003; Nazatul-Asikin, Awal, Mohd Yusoff, & Shamsiah, 2016). It has been reported that there are some major obstacles in practical application of *in vitro* regeneration method, which may limit the use of this method such as low, irregular multiplication rate of SEs, limited regeneration capacity and loss of totipotency. The present research was designed to evaluate the ideal plant growth regulators (auxin/cytokinin) levels for optimum embryogenic callus induction and somatic embryogenesis of sugar palm for mass propagation throughout peninsular Malaysia.

MATERIALS AND METHODS

Preparation of Plant Materials

Fresh fruits of sugar palm were used as a source of immature zygotic embryo (IZE) explants. Open pollinated bunches were harvested 7-15 weeks after anthesis. Fruitlets were detached from the stalk and soaked in soap water and washed under running tap water. Surface sterilisation was carried out by soaking the fresh fruits in 70% ethanol for 30 minutes, rinsing three times with sterile distilled water and followed by soaking in 50% sodium hypochlorite added with a few drops of Tween 20 for another 30 minutes. After another three sequential rinses with sterile distilled water, plant materials were air dried in laminar air flow chamber (Brand BioBase, BBS-V18000) and cultured on MS medium supplemented with different concentration of PGRs at any possible combinations.

The pH of all media was adjusted to 5.8 prior to autoclaving at 121°C for 20 minutes. The most effective treatment for the induction of callus and embryogenic callus was evaluated. Cultures were then incubated under complete darkness at the temperature of 25±2°C. Periodic subcultures were applied at an interval of four weeks throughout the culture process. Each treatment was replicated 10 times and the experiment was conducted twice. The percentage of callus induction frequency of explant (CIF), average callus fresh weight (ACF), average callus diameter (ACD), its response for degree of callus formation (DCF) and callus morphology were monitored as growth parameters. Results were recorded after 8 weeks of culture.

Somatic Embryogenesis Establishment

Embryogenic calluses at semi globular/globular stage were transferred to SEs maturation medium composed of MS basal medium supplemented with 3%, 4%, 5% and 6% sucrose and casein hydrolysate (CH) at 1.0 – 2.0 g/L. AgNO₃ added medium proliferated SEs. Proliferated SEs were maintained in the same culture media until they reach cotyledonary-developmental stage. Maturation of cotyledonary-stage SEs was established in MS medium complemented with 1.0 mg/L BAP and 1.0 mg/L NAA. Cultures were incubated under cool-white fluorescent light (50-60 μmol m⁻² s⁻¹) at the temperature of 25±2°C and 16-hour's photoperiod. The average number of SEs per explant, ACD (cm), DCF and SEs developmental stages were recorded after 8 weeks of culture.

Somatic Embryogenesis Germination

Culturing 50 SEs determined the germination of SEs and subsequent clonal roots/shoots regeneration at cotyledonary-developmental stage on MS medium supplemented with various compositions of PGRs. Data was recorded based on the parameters of the frequency of clonal shoot regeneration (%) and the frequency of clonal root regeneration (%) for each treatment. MS medium in absence of PGRs (control) served as a control treatment.

Statistical Analysis

The completely randomised design (CRD) was used with 10 replicates for each treatment. Each replicate consisted of one explant. Statistical analysis was done using Statistical Package for the Social Sciences (SPSS) software and the values were expressed as mean \pm standard error (SE). The statistical significant difference between means was analysed using analysis of variance (ANOVA) followed by Tukey post-hoc test for comparison between different treatments. Statistical significance was set up at $P < 0.05$.

RESULTS AND DISCUSSION

Embryogenic Callus Initiation and Maintenance

Callus culture was established from IZE explants of sugar palm after being cultured in the dark for four weeks at 25°C. The frequency of primary callus induction (CIF) was calculated accordingly as: $CIF = (\text{explants forming callus out} / \text{total number of embryos being cultured}) \times 100$. Meanwhile, the degree of callus formation (DCF) was classified according to a range of mean size/diameter of the callus formed. Figure 3(a) and Figure 3(b) indicate the growth formation of calluses on IZE explants. In most palm species, high concentrations of auxins particularly 2, 4-D is usually used to initiate callus from zygotic embryo explants (Marbun, Toruan-Mathius, Utomo, & Liwang, 2015). By contrast, in sugar palm, in the presence of high auxin, explants tend to become necrotic and callus tissues growth was hindered.

In general, the primary callus growth was quite slow during the first month of culture. The calluses sizes were very small and the embryogenic callus structures were hardly distinguishable. However, the calluses growth accelerated favourably after 8 weeks of culture and continued to grow in the months after they were accompanied with frequent subcultures. The primary CIF was ranged from 50 to 100% (Figure 1) while ACF (g) and ACD (cm) ranged from 0.28 – 0.68 g and 0.30 - 0.85 cm respectively after 8 weeks of culture. As the callus tissues developed, the colour changed from translucent white to beige or yellowish green. The most optimum CIF (100%) was obtained on the MS medium supplemented with 0.4 mg/L 2, 4-D and 0.5 mg/L NAA with the ACD of 0.850 ± 0.06 cm (DCF: ++) and the AFC of 0.675 ± 0.02 g. Globular-shaped SEs were also detected. While the least CIF was observed on MS + 0.5 mg/L 2,4-D + 1.0 mg/L at 50%, the lowest AFC (0.275 ± 0.02 g) and ACD (0.300 ± 0.09 cm)

were found on MS + 0.2 mg/L 2,4-D + 0.5 mg/L BAP (DCF: +) and MS + 0.3 mg/L 2,4-D + 0.5 mg/L BAP (DCF: +) respectively. The MS devoid of PGRs showed no response for callus development. Statistical analysis using ANOVA and Tukey test showed a significant difference among different treatments ($P < 0.05$) (Table 1). The growth response of callus was dependent on the genotype, type and concentrations of PGRs used.

Browning of calluses was also observed on some treatments. Browning of culture is frequently reported in palm species tissue culture system as a result of accumulation of phenolic substances in culture media. In date palm, the lethal browning of explant was prevented by adding activated charcoal to the culture media, followed by frequent subcultures (Al-Khalifah & Shanavaskhan, 2012). Similar corrective measures were also used in oil palm embryogenic callus culture, where it effectively minimized the oxidation and adsorbed toxic phenolic compounds in culture. At the same time, embryogenic callus induction and somatic embryogenesis were also enhanced (Thuzar, Vanavichit, Tragoonrung, & Jantasuriyarat, 2012). In our study, on 2,4-D + BAP added medium, browning was hardly a problem for callus induction, even without the addition of activated charcoal. Frequent subcultures measure also reduced the browning of cultures favourably.

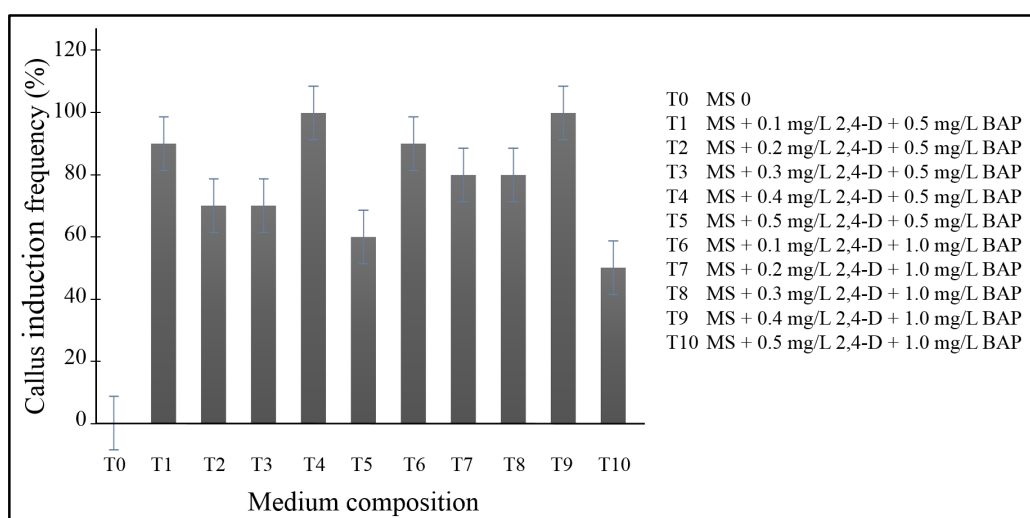


Figure 1. Primary callus induction frequency (%) of IZE explants cultured on MS media supplemented with various concentrations of 2,4-D and BAP after 8 Weeks of Culture. Primary callus induction frequency = (Number of explants inducing callus / Total number of explants cultured) \times 100. Error bars indicate the standard error of the mean of ten replicates

Table 1
Statistical analysis on callus development of IZE explants of sugar palm on induction media after 8 weeks of culture

Medium Composition	Average callus fresh weight (g)	Average callus diameter (cm)	Degree of callus formation	Morphology
MS 0	0.000±0.00 ^a	0.000±0.00 ^a	-	No callus
MS + 0.1 mg/L 2,4-D + 0.5 mg/L BAP	0.475±0.05 ^{bcd}	0.650±0.02 ^{cd}	++	Compact, translucent, beige callus
MS + 0.2 mg/L 2,4-D + 0.5 mg/L BAP	0.275±0.02 ^b	0.425±0.07 ^{bc}	+	Compact, translucent, beige callus
MS + 0.3 mg/L 2,4-D + 0.5 mg/L BAP	0.350±0.03 ^{bc}	0.300±0.09 ^{ab}	+	Semi-friable, translucent, beige callus
MS + 0.4 mg/L 2,4-D + 0.5 mg/L BAP	0.675±0.02 ^d	0.850±0.06 ^d	++	Semi-friable, translucent, beige callus
MS + 0.5 mg/L 2,4-D + 0.5 mg/L BAP	0.450±0.06 ^{bc}	0.350±0.08 ^{bc}	+	Compact, translucent white, beige callus
MS + 0.1 mg/L 2,4-D + 1.0 mg/L BAP	0.288±0.04 ^b	0.425±0.05 ^{bc}	+	Compact, translucent white, beige callus.
MS + 0.2 mg/L 2,4-D + 1.0 mg/L BAP	0.325±0.05 ^{bc}	0.350±0.08 ^{bc}	+	Semi-friable, translucent, beige callus
MS + 0.3 mg/L 2,4-D + 1.0 mg/L BAP	0.375±0.05 ^{bc}	0.575±0.02 ^{bcd}	++	Compact, translucent white, beige callus
MS + 0.4 mg/L 2,4-D + 1.0 mg/L BAP	0.525±0.02 ^{cd}	0.500±0.04 ^{bc}	++	Semi-friable, translucent, beige callus
MS + 0.5 mg/L 2,4-D + 1.0 mg/L BAP	0.300±0.06 ^b	0.325±0.08 ^b	+	Compact, translucent white, beige callus

¹Each value within a column is the average of four replications ± standard error (SE). Values followed by the same letter(s) are not significantly different by Tukey-test at $P < 0.05$. ²Standard error of mean (SEM) was calculated by dividing SD by the square root of sample size (n) [$SE = \sigma/\sqrt{n}$]. ³Degree of callus formation: i.e. ‘-’, ‘+’, ‘++’, ‘+++’, ‘++++’, ‘+++++’: ‘No response’, ‘< 0.50 cm’, ‘0.51 – 1.00 cm’, ‘1.01 – 1.50 cm’, ‘1.51 – 2.00 cm’ and ‘> 2.01 cm’ respectively. Data were presented as mean ± SE

Somatic Embryogenesis Establishment

Plant regeneration through somatic embryogenesis occurs in five consecutive steps viz., embryogenic cultures, proliferation of embryogenic cultures, pre-maturation of somatic embryos, maturation of somatic embryos and plant development on medium lacking PGRs (Von Arnold, Sabala, Bozhkov, Dyachok, & Filonova, 2002). Somatic embryogenesis may be direct or indirect in which in the former, somatic embryos are formed directly from explant without the formation of intermediate callus phase. Whereas in indirect somatic embryogenesis, callus is produced first from the explant followed by the regeneration of embryoids from the callus (Slater, Scott, & Fowler, 2003). The initiation of somatic embryos in sugar palm was rather complicated as different steps of induction required addition of various PGRs to the culture medium.

In the present study, somatic embryogenesis proceeded through indirect route as indicated by the induction of intervening callus phase. The SEs were proliferated by transferring the embryogenic calluses to fresh culture medium containing different levels of sucrose (3-6%) and casein hydrolysate (CH) at either 1.0 or 2.0 g/L. Within 4-6 weeks of transfer and frequent subcultures, calluses grew rapidly with matured SEs at semi-globular/globular and heart-shaped stages were detected. The SEs were shiny, beige coloured and grew in clumps (Figure 3(c)). Awal, Taha and Hasbullah (2010) reported optimum direct somatic embryogenesis of *Begonia x hiemalis* Fotsch var. Schwabenland Red on similar culture medium composition.

The average number of maturing SEs per explant, ACD (cm), its formation degree (DCF) and SEs developmental stages after four weeks of transfer are shown in Table 2. Significant difference between all treatments was proved with Tukey test at $P < 0.05$ (Table 3). Apparently, pseudoroots development was also observed in MS culture medium with 5% sucrose and 1.0 g/L CH. Similar case of pseudoroots growth was also reported in previous research of sugar palm. It was explained that the formation of pseudoroots in cultures was caused by unstable hormonal balance and its formation was claimed to hinder the formation of clonal sprouts (Devi, Purwito, & Husni, 2014).

The matured clumps of globular SEs were then transferred to elongation medium consisted of similar composition of PGRs for optimum callus induction and 1.0 mg/L AgNO₃. After 4-6 weeks of transfer, the somatic embryos elongated and completed the three stages development of somatic embryogenesis (globular, heart-shape, torpedo) [Figure 3d]. Upon transfer to maturation medium containing 1.0 mg/L BAP and 1.0 mg/L NAA, the SEs further developed into clear structures of cotyledonary stage (Figure 3e). The different stages of somatic embryos were observed under light microscope (Olympus, Model CH2oi) and images were captured with a digital camera (Fujifilm FinePix F550EXR).

The developed somatic embryos were then transferred to triiodobenzoic acid (TIBA) added medium for three weeks. The TIBA is an auxin polar transport inhibitor, which inhibits the simulation of *in vitro* lateral root formation (Chen & Chang, 2004) and instead stimulated bud formation (Murashige, 1965). Previous research in sugar palm described the induction and maturation of globular-stage SEs from zygotic embryo explants in the culture media supplemented with high auxin/cytokinin concentration. The authors did not report on further development of the globular SEs after maturation due to high contamination rate, death of explants and limited observation time frame (Devi, Purwito, & Husni, 2014). Nazatul-Asikin (2016) reported optimum induction of embryogenic callus and SEs in sugar palm using basal stem explants after 3 months of culture on MS medium supplemented with low auxin/cytokinin concentration. The report was similar to Wang, Chen, Wu, Lin and Chang, (2013) whom also obtained SEs from the callus of betel nut (*Areca catechu*) cultured on reduced-auxin media.

Table 2
Statistical analysis on the embryogenic callus and somatic SEs of IZE explants of sugar palm responses after 12 weeks of culture

MS Medium Composition (g/L)		Average number of globular somatic embryos per explant	Average callus diameter (ACD) (cm)	Degree of callus formation (DCF)	Somatic embryogenesis developmental stage(s)
Sucrose	Casein hydrolysate (CH)				
30	1.0	17.00±1.99 ^a	2.250±0.17 ^a	+++++	Semi-globular, globular
40	1.0	26.33±2.33 ^a	2.825 ± 0.18 ^{ab}	+++++	Globular, heart-shape
50	1.0	36.33±2.33 ^a	3.100±0.16 ^c	+++++	Globular, heart-shape, pseudoroots
60	1.0	29.67±3.93 ^a	2.600±0.10 ^{ab}	+++++	Globular
30	2.0	29.00±0.58 ^a	2.975±0.23 ^{ab}	+++++	Globular
40	2.0	17.67±1.20 ^a	2.525±0.20 ^{ab}	+++++	Globular, heart-shape, semi-globular
50	2.0	65.33±7.69 ^b	3.275±0.15 ^{ab}	+++++	Semi-globular, globular
60	2.0	91.33±10.69 ^c	3.100 ± 0.35 ^{ab}	+++++	Semi-globular, globular, heart shape

¹Value of average number of somatic embryos per explant is the average of three replications ± standard error (SE). ²Value of average callus diameter is the average of four replications ± standard error (SE). ³Values followed by the same letter(s) are not significantly different by Tukey-test at P<0.05. ⁴Standard error of mean (SEM) was calculated by dividing SD by the square root of sample size (n) [SE = σ/\sqrt{n}]. ⁵Degree of callus formation: i.e. '-', '+', '++', '+++', '++++', '+++++': 'No response', '<0.50 cm', '0.51 – 1.00 cm', '1.01 – 1.50 cm', '1.51 – 2.00 cm' and '>2.01 cm' respectively. Data were presented as mean ± SE

Somatic Embryos Germination

The optimum germination frequency of SEs of sugar palm was determined on half strength MS medium (½ MS) at 30% (Figure 2). Yellowish green clonal roots with approximate size of 0.5-0.7 cm were visible after four months of culture (Figure 3(f)). No regeneration of clonal shoots/roots of SEs was observed on MS0 and any MS media in the presence of PGRs. Instead, all SEs turned brown and gradually deteriorated. This is contradictory to the result obtained by Abohaterm and Baaziz (2011), where they reported a 32% germination rate of date palm SEs on MS medium deprived of PGRs.

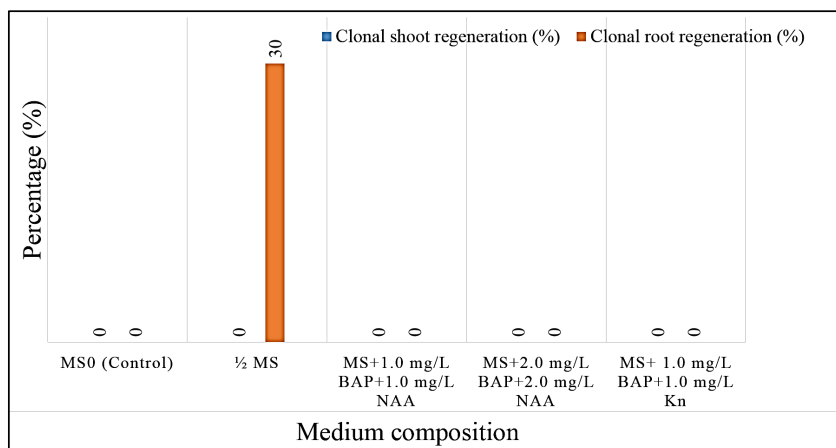


Figure 2. Clonal shoots regeneration and clonal root regeneration frequencies (%) of SEs of sugar palm cultured on different germination media after 4 months of culture. The frequency of clonal shoot regeneration (CSR) and clonal root regeneration (CRR) = Number of explants inducing clonal shoots or roots / Total number of explants cultured) × 100

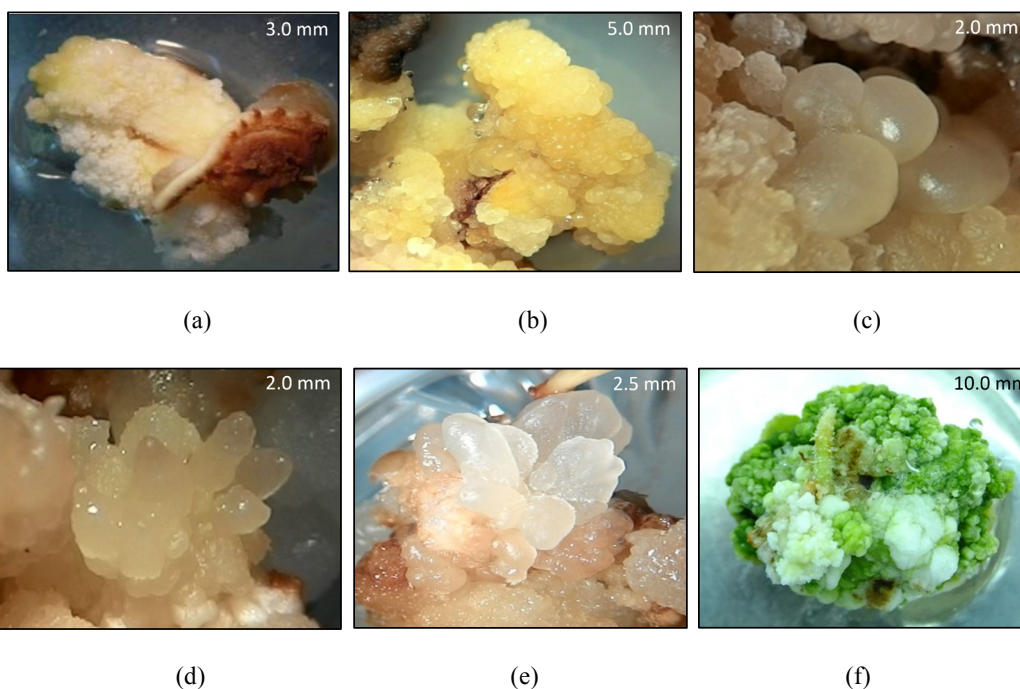


Figure 3. Somatic embryogenesis system from IZE explants of sugar palm (*Arenga pinnata* Wurmb Merr): (a) primary callus induction of IZE explants after 6-8 weeks of culture in culture medium consisted of 0.4 mg/L 2,4-Dichloropenoxyacetic acid (2, 4-D) + 0.5 mg/L benzyl aminopurine acid (BAP); (b, c) progression of globular somatic embryos on primary callus in optimum proliferation culture medium containing 6% sucrose and 2.0 g/L casein hydrolysate (CH); (d) torpedo – stage somatic embryos in clumps on MS + 3% sucrose + 0.4 mg/L 2,4-D + 0.5 mg/L BAP + 1.0 mg/L AgNO₃; (e) progression of somatic embryogenesis from cotyledonary stage on MS + 1.0 mg/L BAP and 1.0 mg/L NAA; and (f) clonal root regeneration (arrow) in half-strength MS medium for germination under light condition

CONCLUSION

The present investigation suggested that the embryogenic callus culture from IZE explants is efficient for clonal propagation of sugar palm. Somatic embryogenesis pathway of sugar palm from IZE explants as well as regeneration of clonal roots from matured somatic embryos (SEs) were successfully determined. However, supplementary investigations to revise this protocol are needed to achieve conversion of cotyledon-stage SEs into complete plantlets for mass propagation and genetic transformation of this species.

ACKNOWLEDGEMENTS

The authors acknowledge the financial support of Universiti Teknologi MARA (UiTM) Shah Alam, Selangor and Mybrain15 scholarship, Ministry of Higher Education (MOHE), Malaysia via research grant 600-RMI/DANA5/3/REI (1/2013),

REFERENCES

- Abohatem, M., & Baaziz, M. (2011). Multiplication and germination of somatic embryos obtained from cell suspensions of date palm (*Phoenix dactylifera*). *Proceedings of the Fifth International Date Palm Conference*, Abu Dhabi, UAE March 16 – 18, 2014. ISBN978-9948-22-868-4 (pp. 231-238).
- Awal, A., Taha, R. M., & Hasbullah, N. A. (2010). Induction of somatic embryogenesis and SEM in *Begonia x hiemalis* Fotsch in vitro. *VII International Symposium on In Vitro Culture and Horticultural Breeding: IVCHB Proceeding*, (pp 39-44).
- Al-Khalifah, N. S., & Shanavaskhan, A. E. (2012). Micropropagation of date palms. Asia-Pacific Consortium on Agricultural Biotechnology (APCoAB) and Association of Agricultural Research Institutions in the Near East and North Africa (AARINENA), (pp. 54)
- Beyl, A. C. (2011). PGRs and their use in micropropagation. In R. N. Trigiano & D. J. Gray (Eds.), *Plant tissue culture, Development and Biotechnology* (pp. 33-57). CRC Press: USA.
- Chen, J., & Chang, W. (2004). TIBA effects the induction of direct somatic embryogenesis from leaf explants of *Oncidium*. *Plant Cell Tissue Organ Culture*, 79, 315-320.
- Devi, M. G., Purwito, A., & Husni, A. (2014). Globular embryo induction of sugar palm (*Arengapinnata* (Wurmb) Merr.). *International Journal of Bioscience, Biochemistry and Bioinformatics*, 4(1), 60.
- El Bar, O. H. A., & El Dawayati, M. M. (2014). Histological changes on regeneration in vitro culture of date palm (*Phoenix dactylifera*) leaf explants. *Australian Journal of Crop Science*, 8(6), 848.
- Janick, J., & Paull, R. E. (2005). *The encyclopedia of fruit and nuts*. Cambridge, United Kingdom. Cambridge University Press (pp. 87-88).
- Jha, T. B. (2005). *Plant tissue culture: basic and applied*. Universities Press, Hyderabad, India (pp. 34).
- Kanchanapoom, K., & Phongdara, A. (2010). The effect of chitosan on organogenesis of oil palm embryo-derived callus. *NotulaeBotanicaeHortiAgrobotanici Cluj-Napoca*, 38(1), 213.
- Marbun, C. L. M., Toruan-Mathius, N., Utomo, C., & Liwang, T. (2015). Micropropagation of embryogenic callus of oil palm (*Elaeis Guineensis Jacq.*) using temporary immersion system. *Procedia Chemistry*, 14, 122-129.

- Moore, H. E. (2013). Palm. Retrieved from <http://global.britannica.com/plant/palm-tree>
- Murashige, T. (1965). Effects of stem elongation retardants and gibberellin on callus growth and organ formation in tobacco tissue culture. *Physiol. Plant*, 18, 665–673.
- Murashige, T., & Skoog, F. (1962). A revised medium for rapid growth and bioassays with tobacco tissue cultures. *Physiologia Plantarum*, 15, 473-497.
- Nazatul-Asikin, M., Awal, A., Mohd Yusoff, A., & Shamsiah, A. (2016). Embryogenic callus induction of *Arengapinnata* Wurm. Merr (sugar palm) from basal stem explant. *International Journal of Advances in Agricultural and Environmental Engineering (IJAAEE)*, 3(1), 106-109.
- Putih, R., Satria, B., & Thaib, R. (2003). Vegetative propagation effort of enau (*Arengapinnata* (Wurm. Merr.) by shoot regeneration *in vitro*. *Stigma*, 11(3), 208-212.
- Slater, A., Scott, N. W., & Fowler, M. R. (2003). *Plant Biotechnology*. Oxford, England: Oxford University Press.
- Smith, R. H. (2013). *Plant tissue culture: Techniques and experiments*. Elsevier, Academic Press, U.S.A.
- Thuzar, M., Vanavichit, A., Tragoonrung, S., & Jantasuriyarat, C. (2012). Recloning of regenerated plantlets from elite oil palm (*Elaiesguinensis* Jacq.) cv. Tenera. *African Journal of Biotechnology*, 11(82), 14761-14770.
- Von Arnold, S., Sabala, I., Bozhkov, P., Dyachok, J., & Filonova, L. (2002). Review developmental pathways of somatic embryogenesis. *Plant Cell, Tissue and Organ Culture*, 69, 233–249.
- Wang, H. C., Chen, J. T., Wu, S. P., Lin, M. C., & Chang, W. C. (2003). Plant regeneration through somatic embryogenesis from zygotic embryo-derived callus of *Areca catechu* L. (*Areaceae*). *In Vitro Cellular and Developmental Biology-Plant*, 39(1), 34-36.
- Zaid, A., & De Wet, P. F. (2013). *Date production support: Namibia*. Retrieved from <http://www.fao.org.htm>.



Synchronisation of Output Voltage Waveforms in Phase Synchronous inverter with LCL Filter for Smart Grid Systems

Tawfikur Rahman*, M. I. Ibrahimy and S. M. A. Motakabber

Department of Electrical and Computer Engineering, International Islamic University Malaysia (IIUM), 53100 Kuala Lumpur, Malaysia

ABSTRACT

A new smart grid system is widely used for energy supply system because it is simple, available, low cost, high efficiency and environmentally friendly. Conventionally, inverter techniques are utilised to convert input DC into output AC with the same frequency and phase. This process suffers the same problem which is a higher harmonic distortion, phase synchronisation, lower quality of waveform and long distance, among others. In this paper, three phase synchronous inverters (PSI) were used to direct synchronous PWM control, LCL filter, three phase RLC load, three phase Yg-Delta transformer, 5 km feeder with 2 MW load. PWM was used to generate the pulse signal for synchronisation. However, LCL filters were used to remove the noise in inverter output and transformer output side of the design. A balanced three phase load (10 kVAR) and also the input DC voltage 500 V were considered in this design. Three phase transformer (100kVA/260V/25kV) was used to increase the inverter output voltage and current with the fundamental frequency (50 Hz). The system conversion efficiency was 99.96% and phase synchronous error for each phase was approximately 4.5 degrees.

Keywords: Choke coil, controller, LCL filter, PSI, transformer

ARTICLE INFO

Article history:

Received: 05 January 2017

Accepted: 17 January 2017

E-mail addresses:

tawfikurr@gmail.com (Tawfikur Rahman),

amotakabber@iium.edu.my (S. M. A. Motakabber),

ibrahimy@iium.edu.my (M. I. Ibrahimy)

*Corresponding Author

INTRODUCTION

A new smart grid system is an open system that connects distribution network systems for solar, wind power and so on (Zidar, Georgilakis, Hatziargyriou, Capuder, & Škrlec, 2016). The distribution network systems consist of local area network, power storage and distributed generators that can be operated on the main grid-connected modes. This system consists of two types of feeders such as sensitive and non-sensitive

load feeder. Generally, it is used in the distribution network for domestic and small cottage industries in a rural area and the island. The sensitive-load feeders are used to continuously supply the power in grid network; therefore, every feeder connected with the system should have a minimum number of micro sources to fulfil the inner feeder load. The non-sensitive-load feeder is utilised to shut down if there is a power quality problem on the grid, utility or a disturbance (Rahman, Ibrahimy, Motakabber, & Mostafa, 2014; Zidaret al., 2016).

Grid energy systems such as solar and wind connect with the new smart grid system. Grid source, replaces itself and is usually available throughout an unremitting source (Zhang, Armstrong, & Elgandy, 2016). Sunlight is directly converted into DC by using solar panels and then convert it to AC (Hassaine, Olias, Quintero, & Barrado, 2014). In the case of wind systems, generally wind passes through directly through a big propeller blades to move the generator to produce the AC/DC electrical power. Likewise, energy sources are converted into electrical power to supply the grid systems with suitable techniques.

Inversion is a process that changes the input DC to output AC by means of a desired output current, voltage and frequency. An electrical power inverter circuit can perform this type of alteration. The terms voltage-sustained and current-sustained are used as a part of reference to power electrical inverter circuits. A voltage-sustained power electrical inverter is one within that the DC input voltage or current is fundamentally consistent and free of the load current strained. However, the phase synchronous inverter (PSI) brings up the load voltage through the strained current structure and is fixed. The grid system inverters can create three various types of output waveforms such as square wave, modified square wave or close to a sine wave and pure sine wave. The square wave inverter is a simple type of electrical inverter whose output is a rectangle wave shape. Due to sharply rising and falling edges, there are many higher order harmonic frequencies involved in this wave. Though this type of inverter is simple in construction, low cost and efficient, quality of its power is poor. However, this type of inverter is still in demand (Rahman et al., 2014). The modified square wave has better power quality and its output is composed of many square waves with different amplitude. Due to its sharp rising and falling edges, it contains a higher harmonic frequencies and close to a sine wave, which results in improved power quality and efficiency. Its circuit is more complex and expensive, but better quality of power compared with the square wave inverter. This type of inverter is suitable for small and medium systems (Rahman, Ibrahimy, Motakabber, & Mostafa, 2016). The pure sine wave inverter output voltage waveform looks like a sine wave, this wave shape is desirable for sensitive system and it provides a good power quality. There is some harmonic distortion to enable supply of clean energy and which makes it perfect for running electronic systems for household and industrial application with less noise. This type of inverter circuits is very complex and expensive as well as inefficient. However, it provides clean and good quality of power (Wen, Boroyevich, Burgos, Shen, & Mattavelli, 2016).

The three phases inverter is exceptionally appealing for commercial enterprise application systems because of its high current rating, high voltage rating, and high efficiency. In this inverter, the overall performance is impressive because the system produces less harmonic, switching loss and it also costs less. The increase in quantitative measure corresponds with the output voltage waveform. The SPWM control method is used to control the semiconductor switches and synchronise phases between inverter and the utility grid (Ahuja & Kumar,

2014). In the inversion system, filters are utilised in the inverter interface circuit to reduce harmonic. The LC is one kind of traditional filter that decreases the % THD. Indeed, several types of PWM control systems are utilised to reduce harmonic distortion and ensure proper phase synchronisation. Multilevel inverter is used in switching device because it reduces switching losses and improves system efficiency. Therefore, it is generally utilised as part of renewable energy application (Tayebi & Batarseh, 2016). As a result of the improved utilisation of the nonlinear loads, the limitation of harmonics becomes more difficult. The state-space comparisons are produced by analysing the single stage full bridge inverter. The fuzzy logic and PI controllers are utilised for the experimental simulation. The fuzzy logic controller is able to reduce the overall system's harmonic distortion whereas the general PI controller is not that efficient (Rahman et al., 2014).

MATERIALS AND METHOD

The PSI circuit has been designed by using MATLAB 2014a/SIMULINK/SIMPOWER. The logic circuit of the PSI was designed and simulated.

Phase Synchronous Inverter

The phase synchronous inverter is an electronic device that can be synchronised between invert phase and grid phase with appropriate transformer and filter. Figure 1 shows a three phase PSI circuit diagram that consists of two input terminals, three output terminals and six gate pulses.

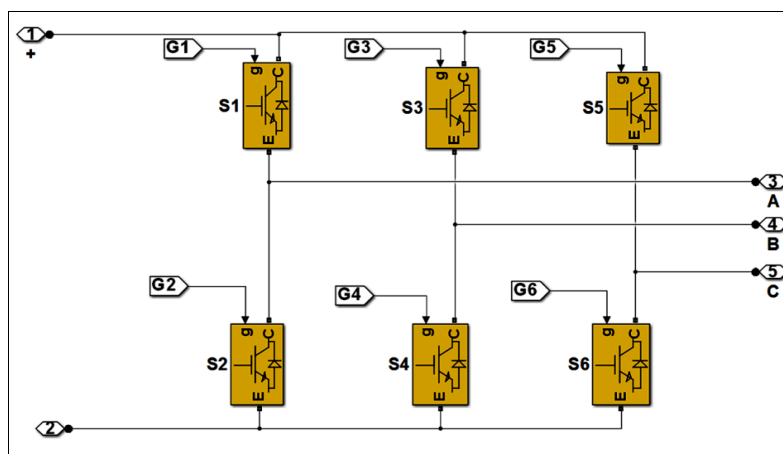


Figure 1. Three phase PSI circuit diagram

The driving input DC voltage $\pm 250\text{V}$ is chosen for the PSI circuit. The IGBT (internal resistance $1\text{e}^{-03}\Omega$ and snubber resistance $1\text{e}^{05}\Omega$) is used as the logic control switch for the PSI. The advantage of the IGBT as switch is that it can safely operate with high voltage and high frequency. In addition, the solid-state switch like IGBT works as an ideal switch. Therefore, during the operation, at ON condition the voltage across the device is zero volt and the OFF

condition in the device is zero Amp. In this design, the IGBT is controlled by pulse width modulation (PWM) signal and therefore, IGBT switches remain either on or off state during its operation. As a result, there is no power loss in the IGBT switch and the efficiency of the circuit will be improved.

Design of A Synchronous Switching Topology

There are eight switching condition modes of process in a cycle to make a three-phase output voltage from the inverter; a group of switches are triggered at 120° phase apart, 0°, 120° and 240° respectively. A carrier based PWM method was used to control the three phase circuit switches. The PWM controller generates pulses for carrier based pulse width modulation converts using two level switching circuit as shown in Figure 2.

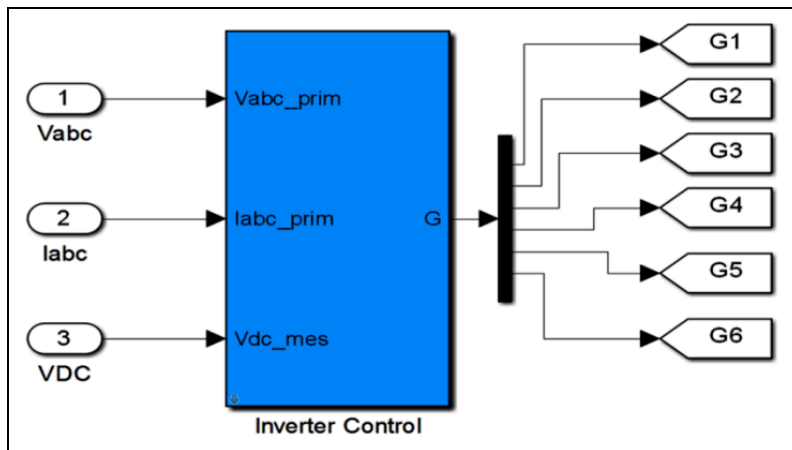


Figure 2. The inverters controller MATLAB block diagram

The PWM controller can control switching IGBT of the three-phase circuit. The input reference/sample signal from the new smart grid is used for phase synchronisation. When the input sample signal amplitude is greater than the carrier voltage amplitude, the switches show $S1=S3=S5=1$ or ON condition, consequently the other switches are $S2=S4=S6=0$ or OFF state shows in Table 1.

Table 1
Inverter switching condition

S1	S3	S5	V_{oa}	V_{ob}	V_{oc}
S2'	S4'	S5'			
0	0	0	$-\frac{V_{dc}}{2}$	$-\frac{V_{dc}}{2}$	$-\frac{V_{dc}}{2}$
0	0	1	$-\frac{V_{dc}}{2}$	$-\frac{V_{dc}}{2}$	$+\frac{V_{dc}}{2}$
0	1	1	$-\frac{V_{dc}}{2}$	$+\frac{V_{dc}}{2}$	$+\frac{V_{dc}}{2}$
1	0	0	$+\frac{V_{dc}}{2}$	$-\frac{V_{dc}}{2}$	$-\frac{V_{dc}}{2}$
1	0	1	$+\frac{V_{dc}}{2}$	$-\frac{V_{dc}}{2}$	$+\frac{V_{dc}}{2}$
1	1	0	$+\frac{V_{dc}}{2}$	$+\frac{V_{dc}}{2}$	$-\frac{V_{dc}}{2}$
1	1	1		$+\frac{V_{dc}}{2}$	$+\frac{V_{dc}}{2}$

Output LCL Filter Design

Different parameters must be considered in a LCL filter designing which are filter size, switching ripple current and current ripple etc. The capacitor resonance frequency may cause a resonance with the grid requirements of to the reactive power. So, active damping is a resistor in series added by the capacitor. On the other hand, the passive damping has been implemented, then active is also be useful. The subsequent parameters are required for the LCL filter design. Figure 3 shows the single phase LCL filter circuit.

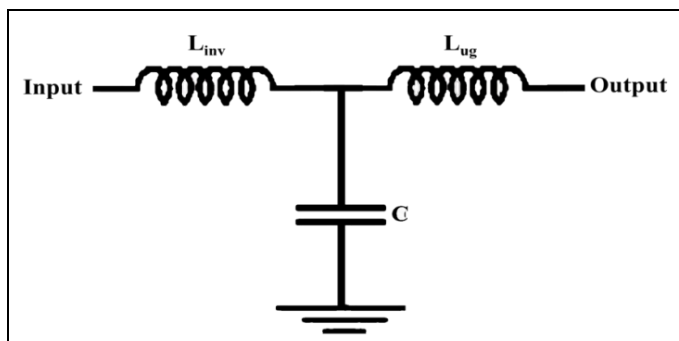


Figure 3. The single phase LCL filter circuit

The LCL filter value depends on a percentage of the base value (Rahman et al., 2016):

$$Z = \frac{V_n^2}{S_n} \quad (1)$$

$$Z = \frac{1}{Z \times \omega} \quad (2)$$

The inverter side inductance L_{inv} can limit the current ripple of the output side which is 10% of normal amplitude.

$$L_{inv} = \frac{V_{DC}}{16 f_s \times \Delta I_L} \quad (3)$$

The grid side inductance L_{ug} can be calculated as:

$$L_{ug} = r \times L_{inv} \quad (4)$$

The control of the resonant frequency depends on the distance and one half of the switching frequency due to attenuation in the switching frequency of the inverter. The design of the LCL filter, resonant frequency can be calculated as:

$$f_{Res} = \frac{1}{2\pi} \sqrt{\frac{L_{inv} \times L_{ug}}{L_{inv} \times L_{ug} \times C_f}} \quad (5)$$

Where,

V_n is the phase to phase RMS voltage

V_{DC} is the input DC voltage

f_s is the fundamental frequency Harz

f_{sw} is the switching frequency Harz

f_{Res} is the resonance frequency Harz

Design of A Synchronous PSI System

Synchronous inverter was designed and simulated by using MATLAB2014a/Simulink/simpower block. The three-inverter design is completed based on six IGBT based inverter respectively. The two IGBT is called a half phase inverter circuit. Final design of the three-phase inverter circuit is constructed by combining three half phase inverter. Generally, a diode is used in reverse biased condition with each IGBT to protect the device (IGBT) from high voltage surge. If the switches are turned OFF the flywheel diodes provide an alternate path for the load current.

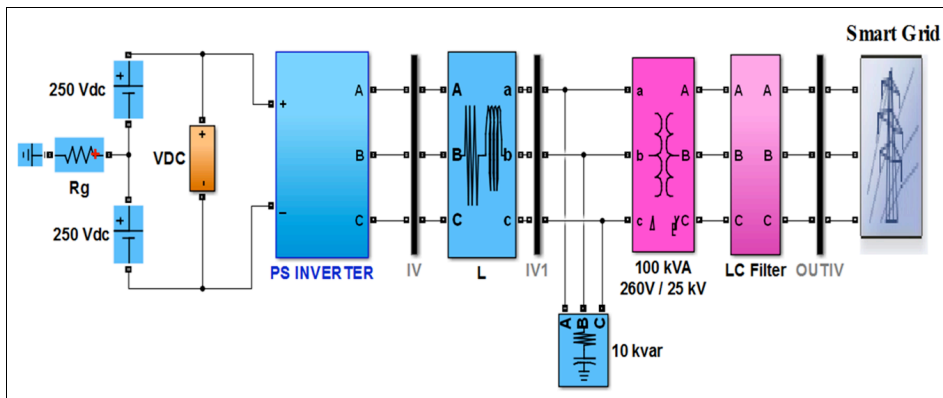
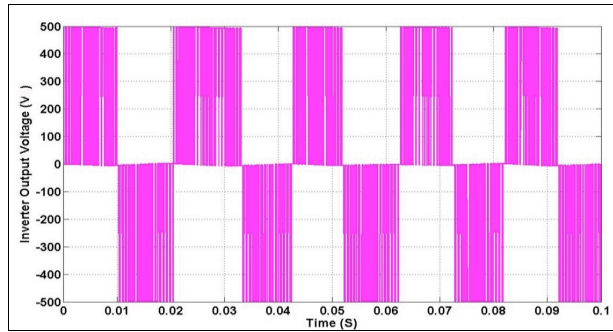


Figure 4. Block diagram of the phase synchronous system

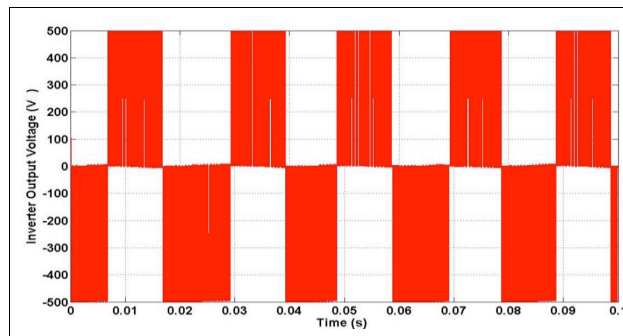
Figure 4 shows a synchronous inverter block diagram for the PSI system which includes DC voltage source, electronic switches, synchronous controller, one output LCL filter with 10 kVAR three phase load, transformer and feeder. In this system, inverter input sources generally use DC voltage which is converted into AC voltage. The PSI controllers are controlled inverter switch for synchronising the inverter and micro-grid phase. The LCL filter reduces DC ripple current and decreases high frequency distortion resulting in lower switching loss. Three phase load depends on the load flow of the system. The step-up transformer two winding are coupled with inverter and new smart grid. The first winding (Δ) indicates a high voltage wye connection and second winding (Y) indicates low voltage wye connection. However, feeder is used to the lossless distributed LC line because it cannot represent correctly the frequency dependence of RLC parameter of the line.

RESULTS AND DISCUSSION

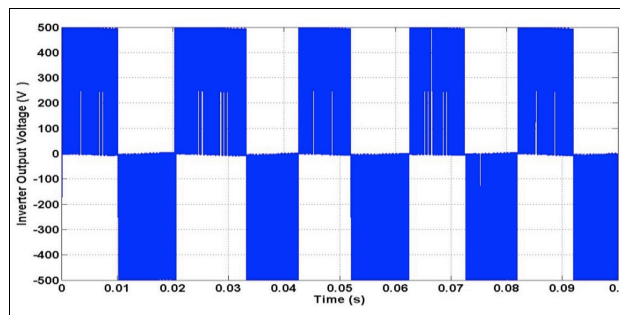
The phase synchronous inverter was simulated using MATLAB2014a. Figure 5 shows the phase synchronous inverter output voltage waveform without filtering. In this system, the controller used in the inverter gate sends signal to generate the pulse signal. A sampled pulse signal was used to synchronise the inverter output phase with the new smart grid phase. A 1.665 kHz carrier frequency with modulation index of 1 was utilised in a pulse controller to generate 50 Hz voltage wave. The magenta, red and blue colours represent the three-phase voltage V_a , V_b , V_c and V_{abc} respectively. From Figure 5, it is observed that the output voltage waveform of the inverter is a control signal and its output voltage is approximately ± 500 V.



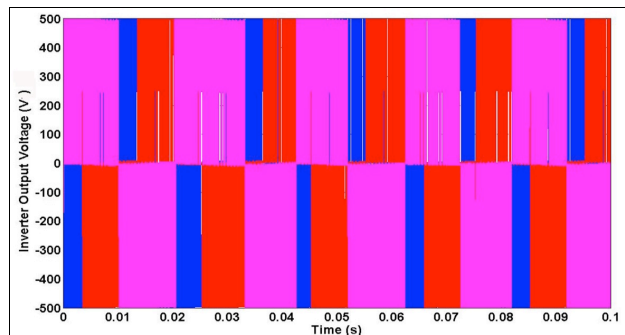
(a)



(b)



(c)



(d)

Figure 5. Inverter output voltage waveform for: (a) V_a ; (b) V_b ; (c) V_c ; and (d) V_{abc} without filtering

Figure 6 shows the inverter output phase-to-phase current is around ± 2 A, for the three phase RLC load of 10 kVAR, active power 100W, capacitive reactive power 10e3var, inductive reactive power 0var, normal phase to phase voltage 240 V and fundamental frequency 50 Hz.

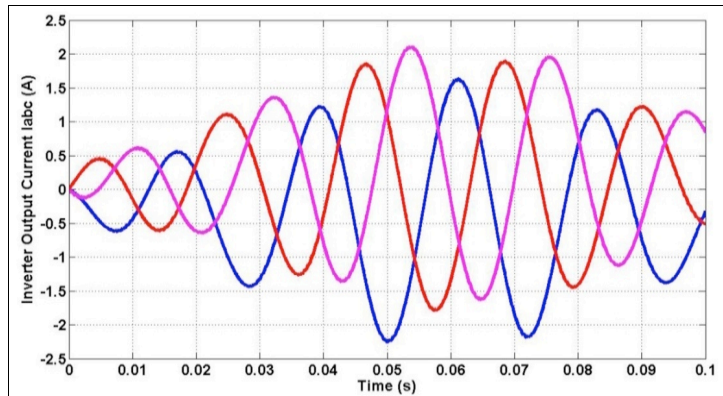


Figure 6. Inverter output current waveform without filter

Figure 7 and figure 8 show the inductor output phase-to-phase voltage and current output waveform which is around $\pm 300V_{p-p}$ and ± 2 A, for the three phase RLC branch resistance $R=500e^{-6} \times 377/50/2 \Omega$ and inductance $L=500e^{-6}/2$ H.

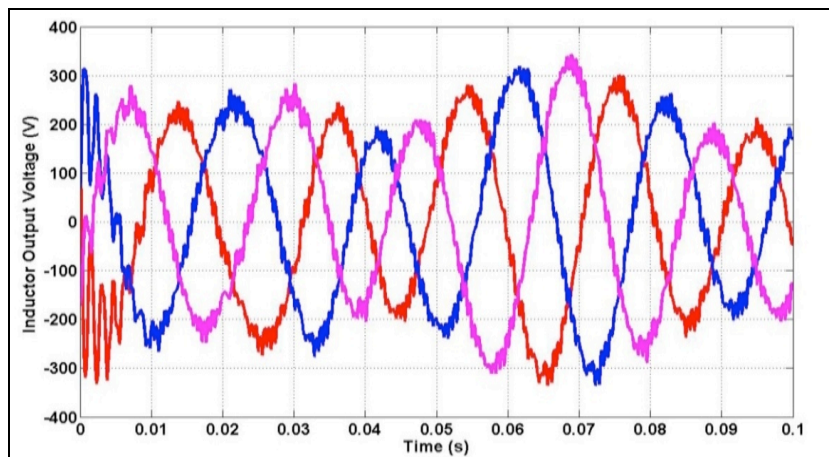


Figure 7. Inductor output voltage waveform without filter

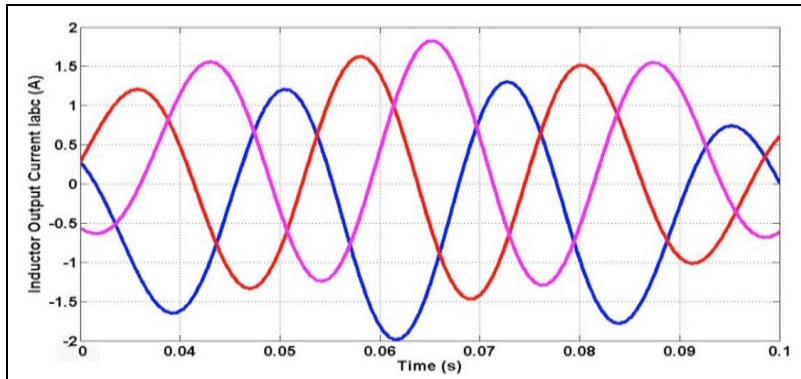


Figure 8. Inductor output current waveform without filter

The inverter output voltage pulses pass through a transformer primary winding. The secondary winding is connected to the LCL filter which produces higher harmonic frequencies and generates the pure sinusoidal wave as shown in Figure 9 and Figure 10. In this paper, the simulated results of the inverter with transformer are: normal power $P_n=100e^3$ VA, frequency $f_n=50$ Hz, p-p output voltage $V_{abc}=\pm 2e^4$ kV and the load current $=\pm 91.42$ A. From the simulation results, the phase difference between the inverter voltage and grid voltage is 50 with THD of 0.04%.

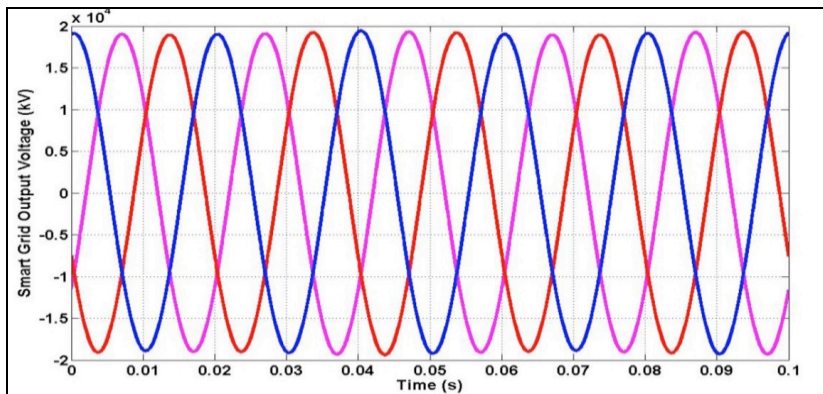


Figure 9. Smart grid output voltage waveform with filter

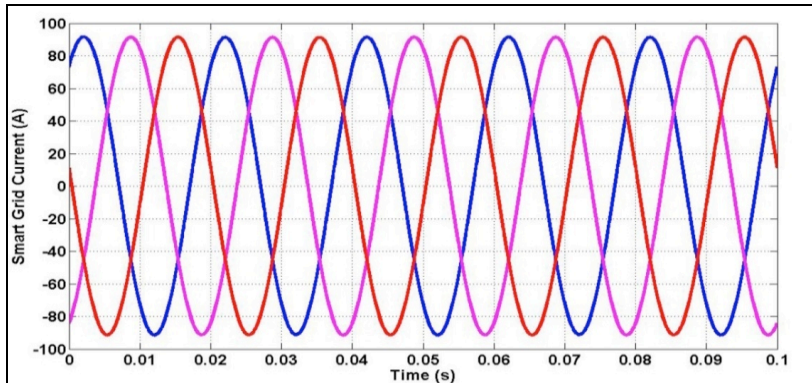


Figure 10. Smart grid output current waveform with filter

Figure 11 shows the result of the phase synchronisation inverter waveform. The signals V_{ab} , V_{bc} and V_{ca} represent the new smart grid sampling signal while the signals V_{ab}' , V_{bc}' and V_{ca}' represent the phase synchronous inverter controller signal. Also, it can be seen that PSI phase and smart grid phase are almost synchronised. It can also be seen the phase angles among the phase voltages $V_{ab}-V_{bc}$, $V_{bc}-V_{ca}$, $V_{ca}-V_{ab}$, are 91.8° , 211.1° and 27.3° without filtering condition. On the other hand, the THD of each output voltage is 0.04% and the phase angles are 124.08° , 244.6° and 4.5° with filtering condition.

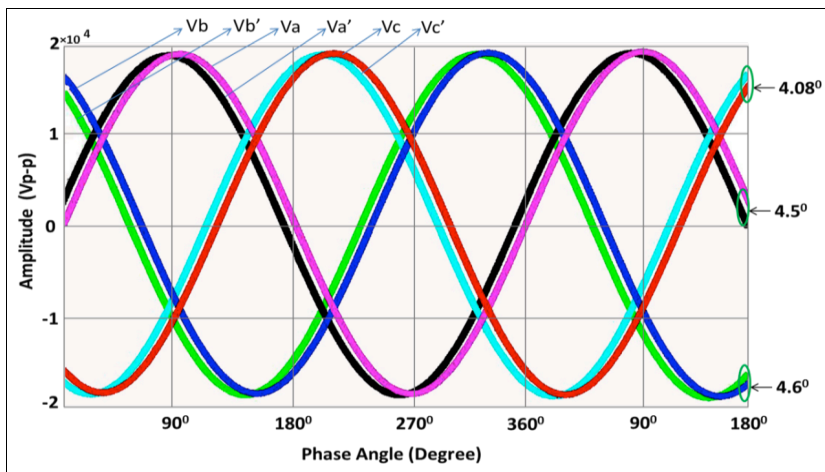


Figure 11. Phase Synchronisation inverter and smart grid phase synchronous waveform

CONCLUSION

In PSI based new smart grid inverter in interface circuit, impulse generator and output LCL filter are the main problems in this design. Due to the power loss of the circuit switching frequency, the reduction of the overall system efficiency occurred. Nevertheless, the design was unable to avoid the reduction of the switching loss, similar to smart grid phase by introducing a pulse

controller based switching phenomenon which increases the overall system efficiency which is 99.96%. In this paper of the PSI system was aimed at synchronising the inverter with smart grid phase. The simulation result shows that the value of inverter phase angle is at an acceptable level of IEEE standard. Particularly, the phase angle ratio is closely synchronised at 4.5° , 4.08° and 4.6° which is lower than the maximum allowable angle as per requirements of IEEE standard (Phase angle $<5^\circ$). The PSI system was proposed and researched both theoretically and numerically. As indicated by our prediction, the PSI is appropriate for applications where the AC voltage as an output needs to be higher than DC as an input and economically feasible.

ACKNOWLEDGEMENT

This research was supported by the Malaysian Ministry of Education through the Fundamental Research Grant Scheme under the project ID: FRGS15-190-0431.

REFERENCES

- Ahuja, R. K., & Kumar, A. (2014). Analysis and control of three phase multilevel inverters with sinusoidal pwm feeding balanced loads using MATLAB. *International Journal of Engineering Research and General Science*, 2(4).
- Hassaine, L., Olias, E., Quintero, J., & Barrado, A. (2014). Power control for grid connected applications based on the phase shifting of the inverter output voltage with respect to the grid voltage. *International Journal of Electrical Power & Energy Systems*, 57, 250-260.
- Rahman, T., Ibrahimy, M. I., Motakabber, S. M., & Mostafa, M. G. (2014). Three phase three layer phase synchronous inverter for microgrid system. *International Conference on Computer and Communication Engineering (ICCCCE)* (pp. 44-47)
- Rahman, T., Ibrahimy, M. I., Motakabber, S. M., & Mostafa, M. G. (2016). Simulation and evaluation of a phase synchronous inverter for micro-grid system. *International Postgraduate Conference on Engineering Research* (pp. 27-28).
- Tayebi, S. M., Mu, X., & Batarseh, I. (2016, March). Improved three-phase micro-inverter using dynamic dead time optimization and phase-skipping control techniques. *2016 IEEE Applied Power Electronics Conference and Exposition (APEC)* (pp. 1381-1386). IEEE.
- Wen, B., Boroyevich, D., Burgos, R., Shen, Z., & Mattavelli, P. (2016). Impedance-based analysis of active frequency drift islanding detection for grid-tied inverter system. *IEEE Transactions on Industry Applications*, 52(1), 332-341.
- Zhang, W., Armstrong, M., & Elgendy, M. (2016). DC component detection in grid connected inverter systems, using a mid-ground low pass filter approach. *8th IET International Conference on Power Electronics, Machines and Drives* (pp. 1-6)
- Zidar, M., Georgilakis, P. S., Hatziargyriou, N. D., Capuder, T., & Škrlec, D. (2016). Review of energy storage allocation in power distribution networks: applications, methods and future research. *IET Generation, Transmission & Distribution*, 10(3), 645-652.

Physico-chemical Properties of Residual Oil Extracted from Oil Palm Decanter Cake

Suhaini Raeze^{1*}, Alawi Sulaiman¹, Azhari Samsu Baharuddin²,
Mohd Noriznan Mokhtar² and Zainuri Busu³

¹Faculty of Plantation and Agrotechnology, Universiti Teknologi MARA (UiTM), 40450 Shah Alam, Selangor, Malaysia

²Department of Process and Food Engineering, Faculty of Engineering, Universiti Putra Malaysia (UPM), 43400 Serdang, Selangor, Malaysia

³FTJ Bio Power Sdn. Bhd., Jalan Liku, 59100 Kuala Lumpur, Malaysia

ABSTRACT

In this study, residual oil from oil palm decanter cake (OPDC) was recovered using n-hexane through Soxhlet extraction process. The residual oil recovered was analysed for its physical and chemical properties. The oil content, moisture, Free Fatty Acid (FFA), Peroxide Value (PV), Iodine Value (IV), Deterioration of Bleachability Index (DOBI) and carotene were measured as 15.43±0.45% (dry), 70.96±0.14%, 6.42±0.11%, 4.37±0.04 meq/kg, 53.28±0.02 g/100 g, 1.93±0.03 and 833.20±39 ppm respectively. The results showed that its fatty acid composition, carotene and IV were comparable with the Malaysian Palm Oil Board (MPOB) standard for crude palm oil (CPO), whilst the properties of the other value had slightly exceeded due to oxidation during the extraction process.

Keywords: Carotene, crude palm oil (CPO), oil palm decanter cake (OPDC), physico-chemical properties, Soxhlet extraction

ARTICLE INFO

Article history:

Received: 05 January 2017

Accepted: 17 January 2017

E-mail addresses:

suhaini.raeze@gmail.com (Suhaini Raeze),
dr_alawi@salam.uitm.edu.my (Alawi Sulaiman),
azharis@upm.edu.my (Azhari Samsu Baharuddin),
noriznan@upm.edu.my (Mohd Noriznan Mokhtar),
zainuri.b@feldaglobal.com (Zainuri Busu)

*Corresponding Author

INTRODUCTION

Oil palm was first introduced to South East Asia in the 19th century. Since then, Indonesia and Malaysia have become the world largest palm oil producers accounting for 85% of the world palm oil production (Koushki, Nahidi, & Cheraghali, 2015). In a study by Mohd Fauzi and Sarmidi (2010), about 80% of the palm oil production is for human consumption whilst the rest was used in animal feed preparation and other industries. Due to

rapid expansion of palm oil production to meet growing demand, large quantities of biomass wastes such as empty fruit bunch (EFB), mesocarp fibre (MF), palm kernel shell (PKS), palm kernel cake (PKC), oil palm decanter cake (OPDC) and palm oil mill effluent (POME) were unfortunately also generated in the mill (Abdullah & Sulaiman, 2013; Embrandiri, Rupani, Quaik, Ibrahim, & Singh, 2012).

The abundance of waste generated has become a major concern due to their environmental effects with attendant impact on sustainability of the palm oil industry. According to Maniam et al. (2013), in Malaysia alone, over 83 million tonnes of dry solid biomass was produced annually by the palm oil industry and the figure is expected to increase up to 85-110 million tonnes by 2020. The POME is the most significant pollutant making up 50% of the waste generated at the mill while OPDC is neglected and left for natural degradation in certain mills (Abdul Razak, Ibrahim, Phang, & Hassan, 2012). Generally, the OPDC consumes a large space at the mill. However, problems will arise when the OPDC becomes dry and could potentially become a fire hazard at the mill (Dewayanto, Isha, & Nordin, 2014). Hence, any strategy in overcoming the environmental problems due to oil palm biomass waste and ways to fully utilise the potential of these biomass wastes into high-value product is welcomed by the government and the palm oil industry.

Currently, CPO is produced in the mills by mechanically extracting it from the digested mesocarp of the palm fruits and using screw presses for the oil extraction process. However, the setback of this mechanical method is that some oil still remains in the mesocarp (Subramaniam, Menon, Sin, & Choo, 2013). It was also reported in other studies presence of residual oils in other oil palm biomass besides mesocarp such as in EFB, POME, OPDC and others. Due to the oil losses in these biomass wastes, it has also brought negative impact to the total oil extraction rate (OER) in palm oil industry (Sahad, Md. Som, Baharuddin, Mokhtar, Busu, & Sulaiman, 2014). Additionally, the presence of residual oil in the biomass waste has indirectly hindered further development in utilising biomass waste. Norul Izani, Paridah, Astimar, Mohd Nor and Anwar (2012), found that the residual oil in EFB need to be removed first before further treatment can be made to EFB in making fibre board and it was reaffirmed by Adam et al. (2014) where the oil in OPDC was removed first before the OPDC-natural polymer composite (NPC) can be produced. In addition, POME alone is made up of 95-96% water, 4-5% total solids, 2-4% of suspended solids and 0.6-0.7% of oil (Wan Sharifudin et al., 2015).

Adam et al. (2014) explained that OPDC was produced from a decanter machine installed after the clarification process of CPO in order to improve the separation of oil and solid. The physical characteristic of the OPDC obtained was a brown-blackish paste made up of oil palm fibre debris. Other than that, OPDC contains mainly water (76% wet basis), residual oil (12% dry basis), nutrients, cellulose, lignin and ash (Maniam et al., 2013). According to Dewayanto, Isha and Nordin (2014), the production rate of OPDC is approximately 4-5 wt% of fresh fruit bunch (FFB) processed which is equivalent to 3.6 million tonnes in 2012. Previously, OPDC is commonly used as fertiliser and animal feed due to the presence of carbon (C), nitrogen (N), phosphorus (P), potassium (K) and magnesium (Mg) (Dewayanto, Husin, Liew, & Nordin, 2010). To date, OPDC has been utilised as feedstock for the production of cellulose and polyose

(Abdul Razak et al., 2012), bio-surfactant (Noparat, Maneerat, & Saimmai, 2014), bio-diesel (Maniamet al., 2013), bio-butanol (Loyarkat, Cheirsilp, & Umsakul, 2013), bio-oil (Dewayanto, Isha, & Nordin, 2014) and as a main component in producing OPDC-NPC (Adam et al., 2014). Previously, Sahad et al. (2014) examined the characteristics and physico-chemical properties of OPDC for better understanding in residual oil recovery. A further study on the residual oil extracted from OPDC should be carry out to understand its material, physical and chemical properties. Thus, this study was carried out to investigate and confirm the physico-chemical properties of residual oil extracted from OPDC.

MATERIALS AND METHOD

Sample Preparation

The OPDC sample was obtained from a three-phase decanter located at FELDA Trolak Palm Oil Mill, Perak. Based on MPOB Test Method (2004), the OPDC sample was stored at -20°C to maintain its freshness and inhibit degradation. Prior to analysis, the sample was defrosted, oven dried at 103°C (UNB-400 Memmert, USA) and ground to fine powder of <250 µm. The percentage of moisture content was determined using the formula below (1).

$$\text{Moisture content (\%)} = \frac{(\text{Initial weight of sample} - \text{Weight after drying}) \text{ (g)}}{\text{Initial weight of sample (g)}} \times 100\% \quad (1)$$

Extraction of Oil from OPDC using Soxhlet Extraction

Ten grams of dried and ground OPDC was extracted using 300 ml of n-hexane (Merck, Germany) for eight hours in a Soxhlet extractor. The extracted oil was concentrated by removing n-hexane using vacuum rotary evaporator and left in an oven for a while to ensure complete removal of n-hexane. The percentage of oil content was calculated using equation (2).

$$\text{Oil content (\% dry basis)} = \frac{\text{Weight of extracted oil (g)}}{\text{Initial weight of dry sample (g)}} \times 100\% \quad (2)$$

Chemical Properties Analysis of Residual Oil Extracted from OPDC

The residual oil extracted was analysed for FFA, DOBI, PV, IV and carotene content using MPOB Test Method (2004). Each sample was obtained in triplicate. Fatty acid composition was obtained using method AOAC 996.06, 17th Edition.

Fourier Transform Infrared Spectrometer (FTIR) Analysis

The Perkin Elmer Spectrometer, USA was used in this study. A thin film of OPDC was placed between KBr plates and four scans of spectrum in 500-4000 cm⁻¹ range were accumulated. A blank KBr plate was used as background for measurement. By using FTIR, the presence of functional groups in OPDC was determined.

Microscopic Observations on OPDC

A Dino-Lite Digital Microscope PREMIER AM/AD7013 Series (Taiwan), at a magnification 200x was used to observe the attachment of oil onto OPDC. Fresh OPDC was mixed with 2 mL of distilled water and placed on a microscope slide. A few drops of Sudan (III) dye solution (Merck, Germany) were added to increase contrast of the preparation.

RESULTS AND DISCUSSION

FTIR Analysis and Microscopic View

Based on standard method outline by MPOB, Soxhlet extraction in palm oil was carried out for eight hours. Extraction can be terminated when the yellowish colour of the sample has faded in the extraction chamber of the extractor. In this study, it was observed that after 8 hours of extraction, the yellowish colour of the sample faded indicating that the residual oil in OPDC was successfully recovered. Thus, in order to support this observation, FTIR analysis was carried out to prove that the oil was indeed recovered.

Figure 1(a) showed the FTIR spectra of OPDC before and after extraction. Based on the FTIR result before extraction, several functional groups could be identified. For lignocellulosic material, the O-H group usually corresponds to band at 3600-3200 cm^{-1} and in this study, the peak appeared at 3351.64 cm^{-1} (Sim, Mohamed, Mohd Irwan, Sarman, & Samsudin, 2012; Zakaria, Roslan, Amran, Chia, & Bakaruddin, 2014). Absorption bands at (2928.57 cm^{-1} , 2851.64 cm^{-1}) and (1744.86 cm^{-1} , 1626.90 cm^{-1}) corresponds to the stretching region of CH_2 and CH_3 , C=O stretching vibration of carboxyl group (Sahad et al., 2014). According to Laurens and Wolfrum (2011), the hydroxyl and phosphate group are represented at band 1200-500 cm^{-1} and showed the characteristics for lipids and fingerprints for phospholipids. In this study, the peak appeared at 1032.49 cm^{-1} and thus, indicating the presence of residual oil in OPDC.

In addition, the presence of oil in OPDC was further supported by the microscopic view of OPDC in Figure 1(b). From Figure 1(b), several free oils and some oil attached to OPDC fibres can be observed. Based on the result, most of the oil droplets was less than 50 μm in size. According to Abbas, Jameel, Muyubi, Karim and Alam (2011), oil droplets in oil-water mixture, with sizes ranging from 20 to 150 μm , are classified as a dispersed oil mixture. According to Chow and Ho (2002), the small oil droplets may have originated from two sources; from the ripe or unripe oil cells which may be covered by phospholipids membrane and another is from the turbulent pumping at various stages of milling process. The surfactants of the cellular fragments tend to be adsorbed at the interface of these oil droplets and thus stabilise them.

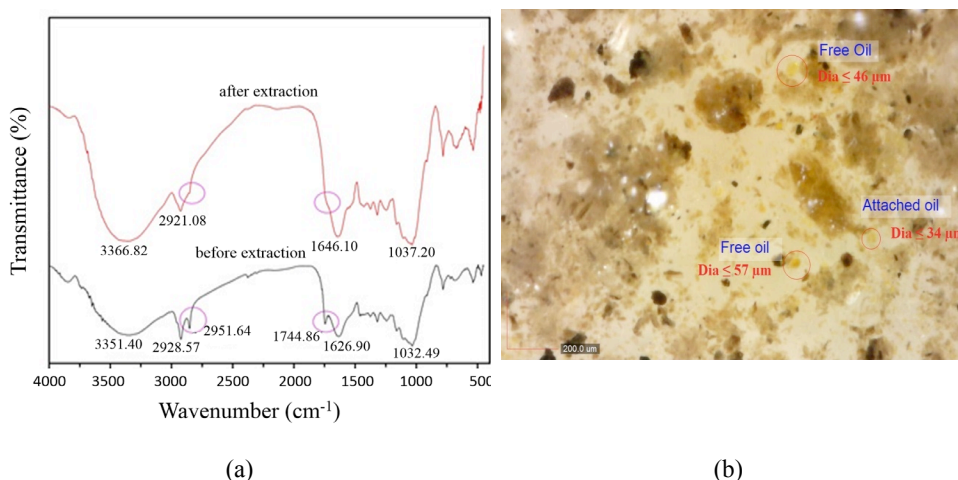


Figure 1. (a) FTIR spectra of OPDC before and after extraction; and (b) Microscopic view of oil attachment in fresh OPDC

Nonetheless, after the extraction of oil, several disappearances of the peaks in the FTIR spectra were observed. The prominent peaks that disappeared were at band 2951.64 cm⁻¹ and 1744.86 cm⁻¹. The evident peak of 2951.64 cm⁻¹ represent the C-H asymmetric and symmetric stretching vibration of long alkyl chain whereas the peak at 1744.86 cm⁻¹ represents carbonyl of carboxyl group (Laurens & Wolfrum, 2011). These peaks were responsible in indicating the characteristics of lipids. Thus, this proves that the residual oil in OPDC was fully recovered using n-hexane in Soxhlet extraction process.

Physico-Chemical Properties of Residual Oil Extracted from OPDC

Physical analysis of residual oil extracted from OPDC. The extracted oil from OPDC is semi-solid at room temperature and is yellowish to brownish in colour. Table 1 shows the physico-chemical properties of OPDC compared with previous studies, and the MPOB standard for CPO. From this study, the oil recovered from OPDC was 15.43±0.45% (dry basis) whilst the moisture content was about 70.96±0.14%. A substantial amount of residual oil recovered from this study is consistent with a previous study by Sahad (2015). Although the oil content was quite low considering the annual FFB processed in the mill, the abundance of OPDC at the mill will gradually ensure the residual oil recovered become significant. The moisture content as shown in this study is similar with that reported by Dewayanto, Husin, Liew and Nordin (2010), Maniam et al. (2013) and Sahad (2015).

Table 1

Physico-chemical properties analysis of residual oil extracted from OPDC and comparison with previous study and MPOB standard for CPO

Properties	This study	Previous study (Sahad, 2015)	MPOB standard for CPO (Source: MS 814:2007)
Physical analysis			
Oil yield (%) (dry)	15.43±0.45	12.55±3.15	-
Moisture content (%)	70.96±0.14	78.2±1.27	<0.25
Chemical analysis			
FFA (%)	6.42±0.11	6-15%	<5.0
DOBI	1.93±0.03	1-2	>2.3
PV (meq/kg)	4.37±0.04	-	<2.0
IV (g/100g)	53.28±0.02	-	50.4 to 53.7
Carotene content (ppm)	833.20±39.00	614.67±64.21	474-689
Mean ± standard deviation			

Chemical analysis of residual oil extracted from OPDC. The FFA value is an important parameter in determining the CPO quality during production, storage and marketing because it indicates the level of deterioration in oil (Li et al., 2012; Tan, Ghazali, Kuntom, Tan, & Ariffin, 2009). In this study, the FFA value was 6.42±0.11% which has slightly exceeded the standard limit for CPO (<5%) based on MPOB. Nonetheless, the FFA value obtained in this study is consistent with that of Sahad (2015). FFA value will be affected when there is any delay in processing starting from FFB harvesting, storage tank and bruised fruits that will release lipase enzyme which triggered FFA formation and become hydrolysed during the sterilisation process (Sahad, 2015; Vincent, Shamsudin, & Baharuddin, 2014). According to Sahad (2015), the deterioration in FFA value in the residual oil extracted may be due to degradation of OPDC, improper sampling and prolonged thermal treatment during the extraction process.

The DOBI analysis is a good indicator for oxidative status and to determine the oil quality. In this study, DOBI value obtained was 1.93±0.04, which meant the quality of the oil was poor. The DOBI of commercial CPO in palm oil mill is graded as: poor (1.78-2.30), fair (2.31-2.92), good (2.93-3.24) and excellent (above 3.24) (Abdul Hadi, Ng, Choo, & Ma, 2012). Similar to factors that can affect FFA value, the same also applies to DOBI. Mat Jusoh, Abd Rashid and Omar (2013) found the DOBI value decreased significantly due to lengthened thermal treatment as sterilisation process takes some time. The other reasons for low DOBI are high percentage of unripe fruit bunches, contamination of CPO with condensation and oxidation of oils (Abdul Hadi et al., 2012). Thus, in this study, since the OPDC was also exposed to prolonged thermal treatment during oven drying and oil extraction process, it had indirectly caused lipid oxidation in the residual oil extracted.

The PV is an indicator that shows the degree of oxidation in oils (Ekwenye, 2006). There are several factors affecting PV such as temperature, storage time, light and contact with air (Kaleem et al., 2015; Mobin Siddique, Ahmad, Ibrahim, Hena, Rafatullah, & Mohd Omar, 2010). The oxidation process are also explained by Nwabueze and Okocha (2008), whereby when the double bonds in the unsaturated fatty acids are attacked, peroxides will be released

leading to decomposition; thus, secondary products are produced which caused rancidity. Rancidity is also referred to as the spoilage of fats and oils during storage, and usually accompanied with foul odour (Ekwenye, 2006). The PV limit for CPO set by MPOB is below 2.0 meq/kg whereas the PV in this study has exceeded the standard limit with 4.37 ± 0.04 meq/kg. This meant that lipid oxidation has occurred and similar to studies conducted on CPO, the PV of residual oil extracted from OPDC was also affected with prolonged exposure to heat, light, air and long storage time. An earlier study by Sahad (2015) did not examine the PV of residual oil recovered. Information on PV is important because it can measure the extent of primary oxidation of oils (rancidification) that has occurred and this is pivotal because potentially toxic compounds can be produced (Kaleem et al., 2015).

The IV is an indicator to measure the degree of unsaturation or double bonds of fats and oils and the ease of oxidation (Ahmad Tarmizi, Siew, & Kuntom, 2008). Besides that, it can also be used to define the quality and functionality of the fractions (Kumar & Krishna, 2014). In a study by Mobin Siddique et al. (2010), the position of the double bonds or the amount of olefinic carbon are not indicated by IV, however, it is still able to provide overall status of unsaturation in oils so that the position of double bonds prone to oxidation can be identified. Based on Malaysian Standard MS814:2007, the IV range for CPO is about 50.4 to 53.7. Palm oil is unique as it has an almost equal amount of saturated and unsaturated fatty acids. The IV of the residual oil extracted in this study is 53.28 ± 0.02 g/100 g which is in accordance with the IV for CPO. Nonetheless, similar with PV, IV is also prone to oxidation if exposed to air and light (Mobin Siddique et al., 2010). Nonetheless, similar to PV, IV has not been tackled by Sahad (2015). Thus, this study provides information on residual oil recovered from OPDC.

The distinctive orange-red colour of crude palm oil is due to its high content of carotene (700-800 ppm) with 90% of the total carotenoids made of α - and β -carotene and they also act as precursors of vitamin A with β -carotene having the highest provitamin A activity (Mohd Fauzi & Sarmidi, 2010; Sundram, Sambanthamurthi, & Tan, 2003). Additionally, carotenoids also act as biological antioxidant by having themselves oxidised first before the oxidative attack on triacylglycerols (TAG) and thus, maintaining the stability and quality of palm oil (Mba, Dumont, & Ngadi, 2015). According to Sundram, Sambanthamurthi and Tan (2003), carotenes are sensitive to oxygen and light and the oxidation of carotenes is accelerated by hydroperoxides generated from lipid oxidation. In this study, a significant amount of carotene, 833.20 ± 39.00 ppm was obtained in the extracted oil. Although several parameters, FFA, DOBI and PV showed lipid oxidation, fortunately the carotene content in the residual oil extracted from OPDC was not greatly affected.

Fatty Acid Composition

Similar to all oils, the major constituents of palm oil are triacylglycerols (TAG) with over 95% of palm oil consisting of mixtures of TAGs, which is glycerol molecules, each esterified with three fatty acids (Sundram et al., 2003). The fatty acids are any class of aliphatic acids such as palmitic acid (C16:0), stearic acid (C18:0) and oleic acid (C18:1) in animal and vegetable fats and oil (Sundram et al., 2003). According to Koushki, Nahidi and Cheraghali (2015), the

major fatty acids in palm oil are palmitic acid (C16:0), stearic acid (C18:0), oleic acid (C18:1), linoleic acid (C18:2) and myristic acid (C14:0).

The fatty acid composition of the residual oil extracted from OPDC was compared with that of an earlier study by Sahad (2015) and typical fatty acid composition in CPO (Sundram, Sambanthamurthi, & Tan, 2003) in order to confirm whether the compositions were the same (see Figure 2). In this study, the major components of fatty acids extracted are (C16:0) with 45.04%, (C18:1) with 37.49%, (C18:0) with 4.46%, (C18:2n6c) with 9.03% and (C14:0) with 1.09% respectively. Based on the result, more than 50% of the fatty acid composition is made up of saturated fatty acids (palmitic acid, stearic acid and myristic acid). Similar trend was also observed in both previous studies and thus confirming that the composition is the same although the (C16:0) in Sahad, (2015) was slightly higher than this study and CPO whereas its (C18:2n6c) was slightly lower. Palm oil is known for its uniqueness for having an almost equal composition of saturated fatty acids and unsaturated fatty acids making it naturally semi-solid at room temperature (Mba, Dumont, & Ngadi, 2015).

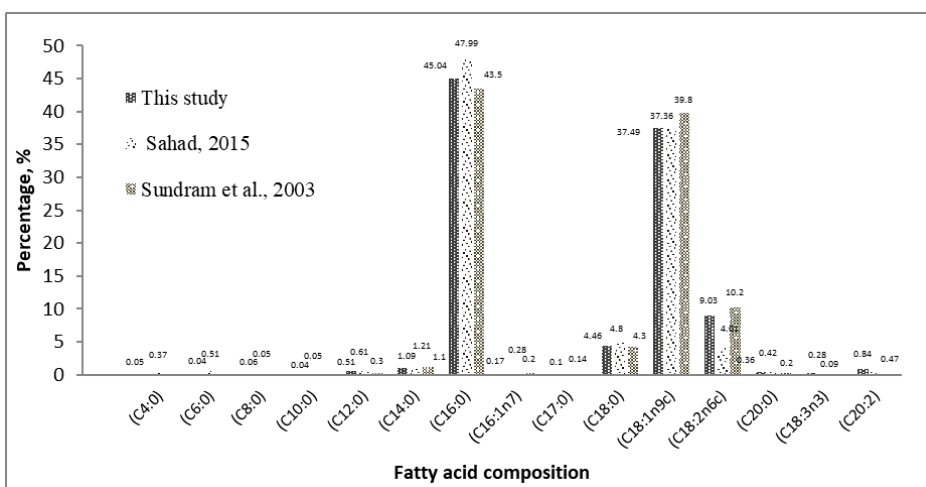


Figure 2. Fatty acid composition (%) of residual oil extracted from OPDC and comparison with previous studies

CONCLUSION

In this study, residual oil from OPDC was successfully recovered and its physico-chemical properties were determined. The residual oil extracted showed satisfactory oil content of $15.43 \pm 0.45\%$ (dry basis) with IV of 53.28 ± 0.02 (g/100 g) and a significant amount of carotene at 833.20 ± 39.00 ppm. Since its IV and carotene content is comparable to standard CPO, this also means that there are possibilities for further study in improvising the properties of the residual oil so that it can be utilised in other areas or turned into value-added products.

ACKNOWLEDGEMENTS

The authors express their gratitude the Ministry of Higher Education (MOHE) LRGS Research Grant (600/RMI/LRGS 5/3 1/2012) for financially supporting this study. Thanks also to Universiti Teknologi MARA for providing us the opportunity to undertake this study.

REFERENCES

- Adam, M. A., Sulaiman, A., Said, C. M. S., Md Som, A., Baharuddin, A. S., & Mokhtar, M. N. (2014). Preliminary study of oil palm decanter cake natural polymer composite (OPDC-NPC). *Advanced Materials Research*, 911, 40-44.
- Abbas, O. A., Jameel, A. T., Muyubi, A. S., Karim, M. I., & Alam, M. Z. (2011). Removal of oil and grease as emerging pollutants of concern (EPC) in wastewater stream. *IIUM Engineering Journal* 12(4), *Special Issue on Biotechnology*, 161-169.
- Abdullah, N., & Sulaiman, F. (2013). The oil palm wastes in Malaysia, Chapter 3. In Matovic, M. D. (Ed.), *Biomass Now - Sustainable Growth and Use* (pp. 75-100). In Tech Publishing, Rijeka, Croatia.
- Abdul Hadi, N., Ng, M. H., Choo, Y. M., & Ma, A. N. (2012). Dry heating of palm fruits: Effect on selected parameters. *American Journal of Engineering and Applied Sciences*, 5(2), 128-131.
- Abdul Razak, M. N., Ibrahim, M. F., Phang, L. Y., & Hassan, M. A. (2012). Utilization of oil palm decanter cake for cellulase and polyoses production. *Biotechnology and Bioprocess Engineering*, 17, 547-555.
- Ahmad Tarmizi, A. H., Siew, W. L., & Kuntom, A. (2008). Palm-based standard reference materials for iodine value and slip melting point. *Analytical Chemistry Insights*, 3, 127-133.
- Association of Official Agricultural Chemists (AOAC). (1997). *Official Methods of Analysis 17th Ed.* Washington, DC: Association of Official Agricultural Chemists.
- Chow, M. C., & Ho, C. C. (2002). Chemical composition of oil droplets from palm oil mill sludge. *Journal of Oil Palm Research*, 14(1), 25-34.
- Dewayanto, N., Husin, M. H., Liew, K. Y., & Nordin, M. R. (2010). Waste to valuable by-product: Kinetic and thermodynamic studies of Cd, Cu and Pb ion removal by decanter cake. *Journal of Engineering and Technology* 1(1), 85-98.
- Dewayanto, N., Isha, R., & Nordin, M. R. (2014). Use of palm oil decanter cake as a new substrate for the production of bio-oil by vacuum pyrolysis. *Energy Conversion and Management*, 86, 226-232.
- Embrandiri, A., Rupani, P. F., Quaik, S., Ibrahim, M. H., & Singh, R. P. (2012). Environmental sustainability in the palm oil industry; Palm waste as nutrient supplement and effects on plant growth characteristics. *International Conference on Environmental, Biomedical and Biotechnology*. Singapore.
- Ekwenye, U. N. (2006). Chemical characteristics of palm oil biodeterioration. *Biokemistri*, 18(2), 141-149.
- Kaleem, A., Aziz, S., Iqtedar, M., Abdullah, R., Aftab, M., Rashid, F., ... & Naz, S. (2015). Investigating changes and effect of peroxide values in cooking oils subject to light and heat. *FUUAST Journal of Biology*, 5(2), 191-196.
- Koushki, M., Nahidi, M., & Cheraghali, F. (2015). Physico-chemical properties, fatty acid profile and nutrition in palm oil. *Journal of Paramedical Sciences*, 6(3).

- Kumar, P. K. P., & Krishna, A. G. G. (2014). Physico-chemical characteristics and nutraceutical distribution of crude palm oil and its fraction. *Grasas Aceites*, 65(e018), 1–12.
- Laurens, L. M. L., & Wolfrum, E. J. (2011). Feasibility of spectroscopic characterization of algal lipids: Chemometric correlation of NIR and FTIR spectra with exogeneous lipids in algal biomass. *BioEnergy Research*, 4(1), 22-35.
- Li, R., Xia, Q., Tang, M., Zhao, S., Chen, W., Lei, X., & Bai, X., (2012). Chemical composition of Chinese palm fruit and chemical properties of the oil extracts. *African Journal of Biotechnology*, 11(39), 9377-9382.
- Loyarkat, S., Cheirsilp, B., & Umsakul, K. (2013). Decanter cake waste as a renewable substrate for biobutanol production by *Clostridium beijerinckii*. *Process Biochemistry*, 48, 1933-1941.
- Malaysian Standard, MS 814:2007. Palm Oil – Specification (Second Revision). Standards and Industrial Research Institute of Malaysia (SIRIM), Kuala Lumpur, 2008.
- Maniam, G. P., Hindryawati, N., Nurfitri, I., Jose, R., Ab. Rahim, M. H., Dahalan, F. A., & Yusoff, M. M. (2013). Decanter cake as a feedstock for biodiesel production: A first report. *Energy Conversion and Management*, 76, 527-532.
- Mat Jusoh, J., Abd Rashid, N., & Omar, Z. (2013). Effect of sterilization process on deterioration of bleachability index (DOBI) of crude palm oil (CPO) extracted from different degree of oil palm ripeness. *International Journal of Bioscience, Biochemistry and Bioinformatics*, 3(4).
- Mba, O. I., Dumont, M. J., & Ngadi, M. (2015). Palm oil: Processing, characterization and utilization in the food industry – A review. *Food Bioscience*, 10, 26-41.
- Mobin Siddique, B., Ahmad, A., Ibrahim, M. H., Hena, S., Rafatullah, M., & Mohd Omar, A. K. (2010). Physico-chemical properties of blends of palm olein with other vegetable oils samples. *Grasas y aceites*, 61(4), 423-429.
- Mohd Fauzi, N. A., & Sarmidi, M. R. (2010). Extraction of heat treated palm oil and their stability on β -carotene during storage. *Journal of Science and Technology*, 45-54.
- MPOB Test Method. (2004). A compendium of test on palm oil products, palm kernel products, fatty acids, food related products and others. Malaysian Palm Oil Board (MPOB).
- Noparat, P., Maneerat, S., & Saimmai, A. (2014). Utilization of palm oil decanter cake as a novel substrate for biosurfactant production from a new and promising strain of *Ochrobactrum anthropi* 2/3. *World Journal of Microbiology and Biotechnology*, 30(3), 865–877.
- Norul Izani, M. A., Paridah, M. T., Astimar, A. A., Mohd Nor, M. Y., & Anwar, U. M. K. (2012). Mechanical and dimensional stability properties of medium-density fibreboard produced from treated oil palm empty fruit bunch. *Journal of Applied Sciences*, 12(6), 561-567.
- Nwabueze, T. U., & Okocha, K. S. (2008). Extraction performances of polar and non-polar solvents on the physical and chemical indices of African breadfruit (*Treculia Africana*) seed oil. *African Journal of Food Science*, (2), 119-125.
- Sahad, N., Md. Som, A., Baharuddin, A. S., Mokhtar, N., Busu, Z., & Sulaiman, A. (2014). Physicochemical characterization of oil palm decanter cake (OPDC) for residual oil recovery. *BioResources*, 9(4), 6361-6372.

- Sahad, N. (2015). *Characterization of oil palm decanter cake (OPDC) and comparison of residual crude palm oil recovery from OPDC using d-limonene and n-hexane* (Unpublished Masters thesis), Universiti Teknologi MARA.
- Sim, S. F., Mohamed, M., Mohd Irwan, L. N. A. L., Sarman, P. N. S., & Samsudin, S. N. S. (2012). Computer-assisted analysis of Fourier transform infrared (FTIR) spectra for characterization of various treated and untreated agriculture biomass, *BioResearch*, 7(4), 5367-5380.
- Subramaniam, V., Menon, N. R., Sin, H., & Choo, Y. M. (2013). The development of a residual oil recovery system to increase the revenue of a palm oil mill. *Journal of Oil Palm Research*, 23(1), 116-122.
- Sundram, K., Sambanthamurthi, R., & Tan, Y. A., (2003). Palm fruit chemistry and nutrition. *Asia Pacific Journal of Clinical Nutrition*, 12(3), 355-362.
- Tan, C. H., M. Ghazali, H., Kuntom, A., Tan, C. P., & Ariffin, A. A. (2009). Extraction and physicochemical properties of low free fatty acid crude palm oil. *Food Chemistry*, 113, 645-650.
- Vincent, C. J., Shamsudin, R., & Baharuddin, A. S. (2014). Pre-treatment of oil palm fruits: A review. *Journal of Food Engineering*, 143, 123-131.
- Wan Sharifudin, W. S. S. A., Sulaiman, A., Mokhtar, N., Baharuddin, A. S., Tabatabaei, M., Busu, Z., & Subbian, K. (2015). Presence of residual oil in relation to solid particle distribution in palm oil mill effluent. *BioResources*, 10(4), 7591-7603.
- Zakaria, S., Roslan, R., Amran, U. A., Chia, C. H., & Bakaruddin, S. B. (2014). Characterization of residue from EFB and kenaf core fibres in the liquefaction process. *Sains Malaysiana*, 43(3), 429-435.



Determinants of Patient's Satisfaction towards Hospital Services in a Specialist Centre

Siti Munira Yasin^{1*}, Nazri Syamil Abdull Latip², Farnaza Ariffin³,
Hilwati Hashim⁴ and Mazlifah Omar⁵

¹Population Health and Preventive Medicine Discipline, Faculty of Medicine,
Universiti Teknologi MARA (UiTM), 47000 Sungai Buloh, Malaysia

²Faculty of Medicine, Universiti Teknologi MARA (UiTM), 47000 Sungai Buloh, Malaysia

³Primary Care Medicine Discipline, Faculty of Medicine, Universiti Teknologi MARA (UiTM),
47000 Sungai Buloh, Malaysia

⁴Radiology Discipline, Faculty of Medicine, Universiti Teknologi MARA (UiTM), 47000 Sungai Buloh, Malaysia

⁵Rehabilitation Discipline, Faculty of Medicine, Universiti Teknologi MARA (UiTM), 47000 Sungai Buloh,
Malaysia

ABSTRACT

Patient satisfaction plays a crucial role in assessing the quality of services provided by healthcare services. The purpose of the present study was to determine the factors influencing patient satisfaction towards services of a specialist medical centre. A cross sectional study was conducted among 300 patients attending a semi-private multidisciplinary specialist centre in Malaysia. They were provided with a set of self-administered questionnaires on patient satisfaction with the services received at the facility. Patient satisfaction was divided into three main components: patient characteristics, delivery of services and hospital characteristics. Additional qualitative comments were also obtained. The mainstay of the analysis was multivariate logistic regression. Altogether, 273 (91.2%) of the patients rated their overall satisfaction as "good" or "very good". Hospital characteristics (i.e., cleanliness; OR: 30.58 (95% CI: 3.52 – 265.79), hospital appearance; OR: 12.69 (95% CI: 1.51 – 106.53) had the strongest influence on the patient's overall satisfaction. The findings revealed that the reason a majority of patients liked the

hospital was related to good quality of services (18.7%), comfort (21.9%) and the friendly staff (8.8%). Hence, hospital characteristics are the most important determinants of overall patient satisfaction. In addition, the quality of delivery services and a friendly staff should also be considered when improving hospital services in a multidisciplinary specialist centre.

Keywords: Hospital characteristics, patient satisfaction, quality of services, specialist centre

ARTICLE INFO

Article history:

Received: 05 January 2017

Accepted: 17 January 2017

E-mail addresses:

smunira@salam.uitm.edu.my (Siti Munira Yasin),
nazrisyamil@gmail.com (Nazri Syamil Abdull Latip),
farnaza@salam.uitm.edu.my (Farnaza Ariffin),
hilwa167@salam.uitm.edu.my (Hilwati Hashim),
mazlifahomar@salam.uitm.edu.my (Mazlifah Omar)

*Corresponding Author

INTRODUCTION

In the service industry, customer satisfaction is achieved when expectations of the customer match performance (Aagja & Garg, 2010). In the healthcare setting, patients are regarded as customers, and their satisfaction is achieved if their technical services and interpersonal care are met (Campbell, Roland, & Buetow, 2000).

Patient satisfaction is a multidimensional concept, which is currently not fully understood. Part of that concept includes patient perceptions of health service quality and aspects outside the control of health-care professionals such as various hospital characteristics, e.g., teaching status, physical appearance and size (Finkelstein, Singh, Silvers, Neuhauser, & Rosenthal, 1998; MacAllister, Zimring, & Ryherd, 2016) and patient demographics (Young, Meterko, & Desai, 2000). The concept also includes various factors that may influence patient satisfaction, associated with the quality of service provided. For example, Chahal and Kumari (2010) suggested that patient perception of the quality of the hospital service are based on the following : physical environment (comprising ambient condition, social factor and tangibles), interaction quality (comprising attitude and behaviour, expertise and process quality), and outcome quality (comprising waiting time, patient satisfaction and loyalty). A study in Malaysia suggested five dimensions, including admission, medical service, overall service, discharge and social responsibility, as a distinct construct for hospital service quality (Amin & Nasharuddin, 2013). In addition, the patients' evaluation of the quality of services also indicated an interaction between patients and doctors, which then boosts the confidence of the patients regarding the quality of services provided by the hospital (Mohd Suki, Chiam Chwee Lian, & Mohd Suki, 2011). Nonetheless, factors associated with satisfaction also vary according to the setting (Thi, Briancon, Empereur, & Guillemin, 2002), suggesting that the results cannot easily be generalized to the setting of a specialist centre with various specialties.

Hence, in an increasingly competitive market environment with many choices for patients, it is vital for healthcare professionals to understand the most influential determinants of customer satisfaction, whether they are most affected by the quality of services provided by the healthcare professionals or by the alterable allocated physical environmental resources. This information can be used to adjust for such factors when comparing the performance of individual physicians or hospitals, based on satisfaction data.

Therefore, the objective of the present study was to assess satisfaction ratings in relation to hospital characteristics, delivery of services and patient characteristics. The study was also aimed at understanding factors that may be associated with overall patient satisfaction.

MATERIALS AND METHODS

This is a cross-sectional study conducted in a semi-private multidisciplinary specialist centre in Malaysia. This clinical specialist centre comprised various specialties and sub-specialties, including inpatient and outpatient facilities. The centre has approximately 100 beds, three outpatient clinics, an Emergency department, an Operation Theatre and other related facilities. Data collection was conducted within 2 weeks, and participants were selected from each department via simple random sampling. Inclusion criteria were patients or visitors who came to the clinic or were admitted to the hospital and were able to read and understand Bahasa

Malaysia. Informed consent was obtained from the patients, and the present study was approved by the ethical review board of the university.

Measures

Patient satisfaction, socio-demographic characteristics, and waiting time were adapted from a previously validated survey comprising 37 items (Schoenfelder, Klewer, & Kugler, 2011). The survey was translated into Bahasa Malaysia, pretested and subjected to validity testing among 30 patients. Patient satisfaction regarding service and medical aspects of care was assessed through 15 items using a five-point ordinal rating (very poor, poor, acceptable, good and excellent). One item collected information concerning overall satisfaction using the same five response categories.

Other information was divided into three main components: patient characteristics, delivery of services and hospital characteristics. Data regarding patient characteristics included age, gender, number of prior hospitalisations and source of admission (e.g., specialist, self-admission and emergency). Hospital characteristics included clinical facilities, whereas delivery of services included service efficiency, courtesy and treatment provided.

A comment section at the end of the questionnaire was aimed at eliciting some suggestions to improve the clinic.

Statistical Analysis

All the data was analysed using SPSS version 22. A P value of less than 0.05 was considered significant. The data was categorized into five groups in which the highest rating was 5 (very good), and the lowest rating was 1 (very poor). Since the data were skewed towards higher satisfaction, a non-parametric test, such as the Mann-Whitney U test, was conducted for two variables, and the Kruskal-Wallis test was conducted for more than two variables. The dependent variables (overall satisfaction) were dichotomised into dissatisfied (fair/poor/very poor) versus satisfied (good/very good). All associations were considered significant at $P \leq 0.05$.

All variables were analysed by simple logistic regression to identify the association between the factors under study and customer satisfaction. Next, multiple logistic regression was performed, controlling for all sociodemographic characteristics using the Forward Method.

The handwritten comment section was manually analysed by the identification of codes and common themes. The research team resolved any discrepancies through discussions. The themes from the matrices and coding were identified and agreed upon by all researchers.

RESULTS

A total of 300 patients participated in the present study. The ages of the patients ranged from 9-75 years, with a mean age of 41.2 years. The majority of the patients were Malay and married, accounting for the most of the patients, 86.7% ($n = 26$) and 81.0% ($n = 243$), respectively. Cardiology had the highest number of patients, which was 119 (42.3%), followed by surgery and primary care departments. For waiting time, the pharmacy had the highest number, which was 85 (28.3%), followed by the clinic, 42 (14%), the registration counter, 16 (5.3%) and

the laboratory, 1 (0.3%). Some of the patients provided suggestions on how to improve the clinic; a total of 25 (8.3%) patients suggested having more car parks, while 15 (5.0%) patients suggested the addition of more chairs in the waiting area (Table 1).

Table 1
Relationship between patient and hospital characteristics and overall patient satisfaction

Variables	Patient nos (%)	Satisfaction Ratings	P Value
Age (years)			
< 10	1 (0.3)	5.00	0.42a
11-20	8 (2.7)	4.42	
21-30	45 (15.3)	4.17	
31-40	41 (13.9)	4.26	
41-50	46 (15.6)	4.27	
51-60	73 (24.8)	4.12	
61-70	60 (20.4)	4.16	
> 70	20 (6.8)	4.35	
Quantity of hospitalisation			
None	73 (25.1)	4.06	<0.01a
1-2 times	91 (31.3)	4.36	
3-4 times	34 (11.7)	4.15	
> 5 times	93 (31.9)	4.16	
Patient			
Inpatient	54 (18.1)	4.54	<0.01b
Outpatient	244 (81.9)	4.13	
Working status			
Employed	153 (51.3)	4.27	0.16a
Unemployed	86 (28.9)	4.12	
Pensioner	59 (19.8)	4.20	
Race			
Malay	260 (86.7)	4.19	0.02a
Chinese	18 (6.0)	4.59	
Indian	19 (6.3)	4.11	
Others	3 (1.0)	4.00	
Marital Status			
Married	243 (81.0)	4.19	0.28a
Widowed	1 (0.3)	5.00	
Divorced	13 (4.3)	4.31	
Single	43 (14.4)	4.28	

Table 1 (continue)

Highest Education Level		---	0.03a
Primary School	42 (14.1)	4.43	
Secondary School	111 (37.2)	4.12	
Diploma or Degree	115 (38.6)	4.18	
Master's or Higher	30 (10.1)	4.28	
Department		---	0.01a
Surgery	31 (11.0)	4.52	
Internal Medicine	19 (6.7)	4.31	
Primary Care	29 (10.3)	4.36	
Paediatrics	4 (1.4)	4.25	
Obs and Gyn	15 (5.3)	3.87	
Cardiology	119 (42.3)	4.16	
Respiratory	7 (2.5)	4.20	
Nephrology	1 (0.3)	5.00	
Urology	0 (0.0)	---	
Endocrinology	19 (6.7)	4.00	
Radiology	0 (0.0)	---	
Rehab	3 (1.1)	4.33	
Others	34 (12.1)	4.19	

Notes: a Kruskal-Wallis test; and b Mann-Whitney U test

Table 2

Bivariate analysis of satisfaction ratings

Satisfaction Measure	All Patients ^a	Satisfied Patients ^b	Dissatisfied Patients ^c
Clinic Facilities ^d			
State of Repair/maintenance***	4.14	4.25 (155)	3.78 (102)
Outside appearance*	4.30	4.22(152)	3.71(103)
Cleanliness*	4.34	4.23(153)	3.73(104)
Ventilation**	4.30	4.18(147)	4.56(189)
Services and efficiency			
Front counter staff*	3.94	4.24(121)	4.00(154)
Nursing staff***	3.93	4.26(157)	3.84(108)
Lab staff***	3.94	4.26(158)	3.91(117)
Pharmacy staff*	3.84	4.25(155)	4.02(128)
Maintenance staff**	3.83	4.26(157)	4.02(129)
Admission			
Admission procedure***	3.75	4.29(161)	3.99(125)
Information about the*** admission and costs	3.88	4.28(160)	4.03(129)
Satisfaction with nursing care***	3.66	4.28(160)	3.95(121)
Satisfaction with clinic*** brochure and information	4.18	4.31(163)	4.01(126)

Table 2 (continue)

Care and Treatment Provided			
Information provided on your care and treatment options by your doctor & staff*	4.06	4.24(154)	4.03(129)
Pre-hospital discharge			
Preparation for discharge from hospital***	3.44	4.30(162)	4.06(133)
Instructions regarding medications*	3.48	4.26(157)	4.11(138)
Information provided on how to access relevant community services***	3.46	4.27(158)	4.13(140)
Satisfaction with clinic brochures & information*	3.81	4.27(158)	4.12(140)

^aOverall group median

^bOverall satisfaction of excellent and good; Grouped Median (Mean Rank)

^cOverall satisfaction of fair, acceptable, poor and very poor; Grouped Median (Mean Rank)

^dDifferences between satisfied and dissatisfied patients using the Mann-Whitney U test

* $<.05$; ** $<.01$; *** $<.001$

Overall, 273 (91.2%) of the patients rated the overall satisfaction as “good” or “very good”. Table 2 shows that the highest group median was ‘cleanliness’ (4.34), followed by ‘ventilation’ and ‘outside appearance’, which had the same group median of 4.30. The lowest mean score was obtained for ‘preparation for discharge from hospital’ (3.44), followed by ‘information provided on how to access relevant community services’ (3.46). Overall, the patients were significantly satisfied with the overall services in all sections ($P<0.05$).

Table 3

Multivariate analysis of overall satisfaction based on different categories

Variables	Odds Ratio (95% CI)	P Value
Cleanliness	30.58 (3.52 – 265.79)	<0.01
Outside Appearance	12.69 (1.51 – 106.53)	0.02
Admission procedure	8.80 (2.59 – 29.88)	<0.01
State of repair/maintenance	8.74 (2.24 – 34.01)	<0.01
Nursing staff services	6.96 (1.98 – 24.63)	<0.01
Lab staff services	5.29 (1.62 – 17.28)	<0.01
Satisfaction with nursing care	4.13 (1.18 – 14.48)	0.03
Maintenance staff services	3.99 (1.35 – 11.79)	0.01
Information about admission cost	3.59 (1.14 – 11.35)	0.03
Pharmacy staff services	3.10 (0.87 – 11.05)	0.08
Preparation for discharge from hospital	3.03 (1.03 – 8.92)	0.04

Note: CI, Confidence Interval

Table 3 displays the multivariate logistic regression of the patient satisfaction based on the various categories, after controlling for sociodemographic characteristics. Eleven variables were identified as positively associated with overall satisfaction. Cleanliness had the highest association, with an odds ratio of 30.58 times satisfied customers compared with non-satisfied, followed by the outside appearance of the hospital. The lowest was preparation for discharge from the hospital.

Ninety-one participants answered the comments section. The findings revealed that the results were divided into these three different themes: good infrastructure of the hospital and environment, friendly services from healthcare professionals, and quality healthcare. Among the subthemes that emerged, the majority reported that the reason they liked the hospital is its good quality services (18.7%), comfort (21.9%) and friendly staff (8.8%).

DISCUSSION

The study identified 11 predictors of overall satisfaction after attending a multidisciplinary specialist medical centre. The findings indicated that the variables related to hospital characteristics have a greater impact on satisfaction rather than delivery services and patient characteristics.

Factors Influencing Patient Characteristics

With regards to sociodemographic characteristics and satisfaction rating, the number of previous hospitalizations was significantly associated with satisfaction. Individuals who were admitted at least once were more satisfied compared with no previous admission. Nonetheless, with an increasing number of admissions, the satisfaction level was reduced. This finding is supported by other studies (Quintana et al., 2006). Additionally, the overall satisfaction is dependent on the level of education. The results of the present study showed lower educated individuals were more satisfied. This is in contrast with another study, which revealed no such differences in education level (Ramsey et al., 2012). There is no direct explanation for this difference, it is postulated that less-educated individuals were more attracted to the hospital appearance compared to the private sector.

Factors Influencing Hospital Characteristics

The present study revealed that the most important determinant of a good customer satisfaction is the physical appearance of the health facilities. This finding is supported by prior studies which found that patients were more concerned about comfort and cleanliness after subsequent admission (Quintana et al., 2006). Similarly, Soleimanpour et al. (2011) highlighted that cleanliness is an important contributor to patient satisfaction, particularly in the emergency department. Thus, maintaining the comfort and cleanliness is important to promote good patient perception and impressions towards the hospital services. Patients also emphasized other physical characteristics, such as good lighting, ample car park and large waiting areas, to improve their satisfaction. However, this was in contrast to the findings of Schoenfelder, Schaal, Klewer and Kugler (2014) who suggested that patient assessment of the delivery of services had

a greater impact on the overall satisfaction compared with the hospital characteristics. Thus, the quality of services provided by the clinical centre in the present study was comparable to that of other private hospitals, hence it was not a prominent factor in the present study.

Factors Influencing the Delivery of Care

With regard to delivery of care and communications, the present study revealed that this factor was the second important contributor to patient satisfaction after hospital characteristics. An organized procedure has a positive effect on satisfaction as it helped to ensure a good stay at the hospital (Pini et al., 2014). In the present study, the highest contributors to the delivery of care include the admission procedure staff, such that a smoothly running admission enables the patients to feel guided, particularly involving the initial stage of hospital admission or clinic appointments. This factor apparently has positive effects on satisfaction. The waiting time and procedures throughout the visit are also important. Previous findings suggested that a long waiting time can induce a negative effect on the quality of the hospital (Kumari, Amberkar, & Nandit, 2012). Hence, increasing the number of workers and opening more counters were part of the measures suggested by the respondents. Furthermore, good communication with patients is essential to good patient satisfaction, consistent with many previous prior studies (Mira, Tomás, Virtudes-Pérez, Nebot, & Rodríguez-Marín, 2009; Schoenfelder, Klewer, & Kugler, 2011). Lastly, the results of the present study also highlight the need for providing comprehensible information prior to and after discharge. Yet, the intensity of this relation was weak compared with the other variables in the multivariate regression model as also observed in other studies.

The study has some limitations. Firstly, the majority of the patients at the specialist centre were Malays, hence it may be difficult to generalize these results to other ethnic groups. Secondly, most of the data was obtained from the cardiology department, as this department has the most number of patients, and this may lead to bias in the overall results, particularly in terms of the services provided. The present study would benefit better from an equal distribution of the number of patients from each category. Lastly, the duration of the present study was too diverse. It would be better in the future to strictly focus on certain units, to ensure more targeted interventions or improvements in the quality of services provided. Nonetheless, the strength of the present study includes a good participation rate among respondents, and this study is the first on customer satisfaction in a specialist centre in Malaysia. Future studies can focus on other hospital settings or clinic-based primary care settings, as the expectations of customers might differ.

CONCLUSION

Overall, high levels of satisfaction were recorded as well as comments. The study concludes that the most important determining factor of patient satisfaction is the physical environment of the hospital. In addition, the delivery of care and friendly staff should also be emphasised to further enhance satisfaction.

ACKNOWLEDGEMENTS

This research is part of a 3-Year Undergraduate Medical Student Elective Research Project. This work was partially funded by a grant from the Fundamental Research Grant (FRGS/1/2015/SKK05/UITM/03/1). The authors would like to thank the respondents who participated in this project.

REFERENCES

- Aagja, J. P., & Garg, R. (2010). Measuring perceived service quality for public hospitals (PubHosQual) in the Indian context. *International Journal of Pharmaceutical and Healthcare Marketing*, 4(1), 60-83. doi:10.1108/17506121011036033
- Amin, M., & Nasharuddin, S. Z. (2013). Hospital service quality and its effects on patient satisfaction and behavioural intention. *Clinical Governance: An International Journal*, 18(3), 238-254. doi:10.1108/CGIJ-05-2012-0016
- Campbell, S. M., Roland, M. O., & Buetow, S. A. (2000). Defining quality of care. *Social Science and Medicine*, 51(11), 1611-1625.
- Chahal, H., & Kumari, N. (2010). Development of multidimensional scale for healthcare service quality (HCSQ) in Indian context. *Journal of Indian Business Research*, 2(4), 230-255 doi:10.1108/17554191011084157
- Finkelstein, B. S., Singh, J., Silvers, J., Neuhauser, D., & Rosenthal, G. E. (1998). Patient and hospital characteristics associated with patient assessments of hospital obstetrical care. *Medical Care*, 36(8), AS68-AS78.
- Kumari, K. M., Amberkar, M., & Nandit, P. B. (2012). Patients' response to waiting time in an out-patient pharmacy at a tertiary care hospital.
- MacAllister, L., Zimring, C., & Ryherd, E. (2016). Environmental variables that influence patient satisfaction: A review of the literature. *Herd*. doi: 10.1177/1937586716660825
- Mira, J. J., Tomás, O., Virtudes-Pérez, M., Nebot, C., & Rodríguez-Marín, J. (2009). Predictors of patient satisfaction in surgery. *Surgery*, 145(5), 536-541.
- Mohd Suki, N., Chiam Chwee Lian, J., & Mohd Suki, N. (2011). Do patients' perceptions exceed their expectations in private healthcare settings? *International Journal of Health Care Quality Assurance*, 24(1), 42-56.
- Pini, A., Sarafis, P., Malliarou, M., Tsounis, A., Igoumenidis, M., Bamidis, P., & Niakas, D. (2014). Assessment of patient satisfaction of the quality of health care provided by outpatient services of an oncology hospital. *Global Journal of Health Science*, 6(5), 196-203. doi: 10.5539/gjhs.v6n5p196
- Quintana, J. M., Gonzalez, N., Bilbao, A., Aizpuru, F., Escobar, A., Esteban, C., & Thompson, A. (2006). Predictors of patient satisfaction with hospital health care. *BMC Health Services Research*, 6, 102. doi: 10.1186/1472-6963-6-102
- Quintana, J. M., González, N., Bilbao, A., Aizpuru, F., Escobar, A., Esteban, C., & Thompson, A. (2006). Predictors of patient satisfaction with hospital health care. *BMC Health Services Research*, 6, 102.

- Ramsey, S. D., Zeliadt, S. B., Blough, D. K., Fedorenko, C. R., Fairweather, M. E., McDermott, C. L., & Arora, N. K. (2012). Complementary and alternative medicine use, patient-reported outcomes, and treatment satisfaction among men with localized prostate cancer. *Journal of Urology*, *79*(5), 1034-1041.
- Schoenfelder, T., Klewer, J., & Kugler, J. (2011). Determinants of patient satisfaction: A study among 39 hospitals in an in-patient setting in Germany. *International Journal for Quality in Health Care*, *23*(5), 503-509.
- Schoenfelder, T., Klewer, J., & Kugler, J. (2011). Determinants of patient satisfaction: A study among 39 hospitals in an in-patient setting in Germany. *International Journal for Quality in Health Care*, *23*(5), 503-509. doi: 10.1093/intqhc/mzr038
- Schoenfelder, T., Schaal, T., Klewer, J., & Kugler, J. (2014). Patient satisfaction in urology: Effects of hospital characteristics, demographic data and patients' perceptions of received care. *Journal of Urology*, *11*(4), 1834-1840.
- Soleimanpour, H., Gholipouri, C., Salarilak, S., Raoufi, P., Vahidi, R. G., Rouhi, A. J., & Soleimanpour, M. (2011). Emergency department patient satisfaction survey in Imam Reza Hospital, Tabriz, Iran. *International Journal of Emergency Medicine*, *4*(1), 1-7. doi: 10.1186/1865-1380-4-2
- Thi, P. L. N., Briancon, S., Empereur, F., & Guillemin, F. (2002). Factors determining inpatient satisfaction with care. *Social Science and Medicine*, *54*(4), 493-504.
- Young, G. J., Meterko, M., & Desai, K. R. (2000). Patient satisfaction with hospital care: Effects of demographic and institutional characteristics. *Medical Care*, *38*(3), 325-334.

Design of Perfect Tracking Self-Tuning Fuzzy PID Controller with Reference Model

Nur Sakinah Abdul Aziz, Mazidah Tajjudin* and Ramli Adnan

Faculty of Electrical Engineering, Universiti Teknologi MARA (UiTM), 40450 Shah Alam, Selangor, Malaysia

ABSTRACT

Fuzzy Logic is a popular method to tune a PID controller. By using Fuzzy Logic, the PID is tuned automatically based on information of output error, which is better than other tuning rule methods. Fuzzy Logic Control will tune gains of PID controller by using a set of fuzzy rules designed specifically for that. However, specific transient requirements of the process output cannot be assigned to the controller. This research proposes a new method to overcome this problem by using a reference model. Step input from the reference model that contains the desired response information will be compared against the actual output. The reference model can be pre-selected by the user as desired. This study was simulated on a steam temperature process model while few sets of first-order model were used as reference. The results showed that the proposed Fuzzy PID controller with reference model provides better performance with perfect tracking during transient and steady-state.

Keywords: Component, PID controller, Reference model, Self-tuning fuzzy control, Steam temperature control

INTRODUCTION

The proportional integral derivative (PID) controller, a combination of Proportional (P), Integral (I), and Derivative (D) operations is

commonly used in the process industry due to its simplicity and efficiency in a simple process control application. This combination is sufficient to produce satisfactory output, but somehow, a better alternative is always required as the process becomes more complex (Tang, Cui, Hua, Li, & Yang, 2012). For instance, PID controller has stability, reliability, and controllability as its combinations are based on mathematical models (Vindhya & Reddy, 2013).

The performance of PID control depends on the tuning of its parameters to obtain a

ARTICLE INFO

Article history:

Received: 05 January 2017

Accepted: 17 January 2017

E-mail addresses:

sakinah1918@gmail.com (Nur Sakinah Abdul Aziz),

mazidah@salam.uitm.edu.my (Mazidah Tajjudin),

ramli324@salam.uitm.edu.my (Ramli Adnan)

*Corresponding Author

perfect combination. It is hard to achieve desired responses despite many tuning rules discussed in the literature. Sometimes, a compromise between overshoot and the speed of response has to be made. In addition, PID controller is not suitable for complex processes and non-linear, as it is hard to modify the controller parameters and may need to be repeated on line tuning (Li, 1998; Korkmas, Aydogdu, & Dogan, 2012). Therefore, self-tuning fuzzy PID was introduced, and the Fuzzy Logic Controller (FLC) had been successfully applied to various control applications, including non-linear dynamic systems (Tajjudin, Hezri, Rahiman, Ishak, & Arshad, 2013; Vindhya & Reddy, 2013).

According to Precup and Hellendoorn, fuzzy logic is a better alternative to PID with rule-based tuning because it does not require a precise process model (Precup & Hellendoorn, 2011). Therefore, fuzzy PID is superior in handling the change in process dynamics (Das, Pan, Majumder, Das, & Gupta, 2011), and it accommodates real-time control applications. By combining the fuzzy method and PID controller, the problems faced by the latter can be solved (Yi, Wang, Zhao, Li, & Shi, 2013). Studies have shown that when the FLC is combined with PID controller, it will improve the transient response of the system such as shorter output response and a reduction of overshoot (Arulmozhiyal & Kandiban, 2012; Chen, Petráš, & Xue, 2009; Sinthipsomboon et al., 2011; Tsai, Chen, & Hwang, 2004). The FLC is an automatic tuning because the system can be adjusted to get the desired output. Therefore, the system depends only on feedback loop to make the output response becomes the desired output. This is a problem that must be faced by control engineers, and the difficulty lies in creating a membership function and fuzzy rules for the system (Hajiloo & Xie, 2013). However, the performance of fuzzy PID depends on the how much experience the human operator has. In designing a self-tuning fuzzy PID, fuzzy rules were set based on the error and rate of output error to determine the value of optimal PID that minimises the output error. Unfortunately, a desired transient performance of each application cannot be set beforehand.

This study proposed a solution to overcome this problem by introducing a reference model to the set point so that the output response will be aligned with the desired response. The fuzzy PID controller without reference model still has steady state error and overshoot (Habib, 2001). Therefore, by adding the reference model, it will get a better output response. This controller acts as a self-tuning device to improve the traditional PID controller (Adnan et al., 2011; Lou, Kuo, & Sheu, 1996). It is a step to evaluate the controller performance in terms of transient such as settling time, rise time and overshoot (Han, Kim, Kim, & Lee, 2003; Lou, Kuo, & Sheu, 1996). This paper presents simulation results of the proposed controller on a steam distillation process using four first-order reference models. The output will be compared with a fuzzy PID controller, where it is shown that the proposed method is more flexible and efficient for a perfect tracking control.

MATERIALS AND METHOD

The plant that is used in this study was obtained from an empirical model of steam temperature for a steam distillation process. Only linear region is considered in the study. The details are

described in (Tajjudin et al., 2013) for further information. The steam temperature is described by a second-order model as given below:

$$G(s) = \frac{0.000366}{(s + 0.011)(s + 0.0074)} ; 70^{\circ}\text{C} < T < 100^{\circ}\text{C} \quad (1)$$

Fuzzy PID Controller

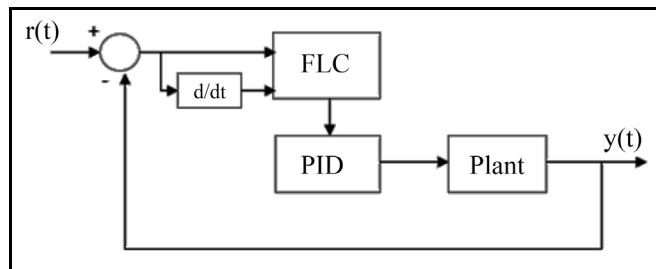


Figure 1. Fuzzy PID controller

Figure 1 shows the structure of Fuzzy PID controller. The FLC obtained input signals from output error, and rate of the error relative to the set point is normally a constant value. Using these inputs, FLC will identify an optimal value of gain for the PID by analysing the relationship of input-output set in the fuzzy rules. Prior to designing the rules, input and output variables were divided accordingly by membership functions that were then assigned literally with Linguistic Variable (LV). In this study, the LV is listed in Table 1.

Table 1
Linguistic variable

Linguistic Variable	Definition
NB	Negative Big
NM	Negative Medium
NS	Negative Small
Z	Zero
PS	Positive Small
PM	Positive Medium
PB	Positive Big

Membership function (MF) of error is shown in Figure 2 with a defined full range of $\pm 60^{\circ}\text{C}$ to represent the steam temperature. The MF divided the range equally using triangular function and was assigned to the rate of error but the range was selected as $\pm 20^{\circ}\text{C}$ that was found suitable during the study. The MF is shown in Figure 3. Figure 4 shows the MF of the output that will determine the value of PID gain. In this case, the same design of MF was used for each P, I and D. So, the range is normalised between -1 and 1, and it will be multiplied with a constant to get the actual gain of P, I and D, accordingly.

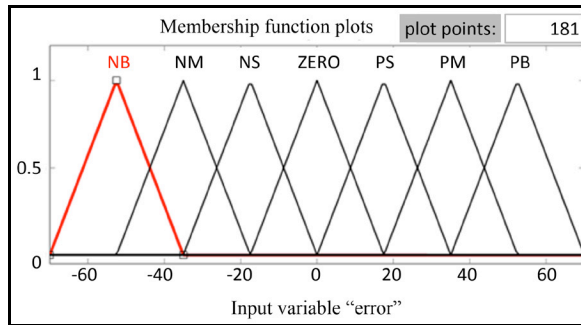


Figure 2. Membership function of error

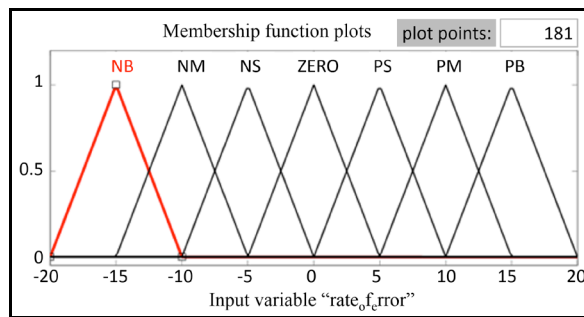


Figure 3. Membership function of rate of error

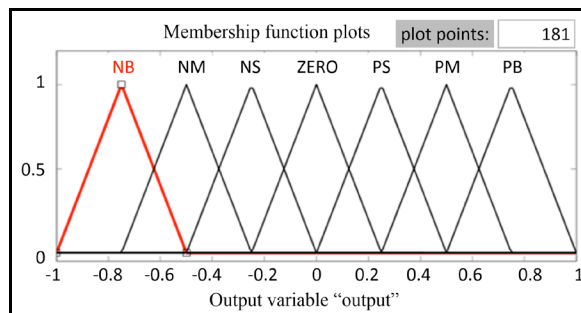


Figure 4. Membership function of output

Fuzzy Rules mapped the relationship between input and output using *if – then* rules for all the membership functions defined earlier. These rules operate based on by human logic and decision-making capability (Table 2). The interconnected membership function between input and output will hence produce 49 fuzzy rules.

Table 2
The proposed fuzzy rule

Rate of Error	Error						
	NB	NM	NS	Z	PS	PM	PB
NB	NB	NB	NB	NM	NS	NS	Z
NM	NB	NM	NM	NM	NS	Z	PS
NS	NB	NM	NS	NS	Z	PS	PM
Z	NM	NM	NS	Z	PS	PM	PB
PS	NS	NS	Z	PS	PS	PM	PB
PM	NS	Z	PS	PM	PM	PM	PB
PB	Z	PS	PM	PB	PB	PB	PB

Fuzzy PID with Reference Model

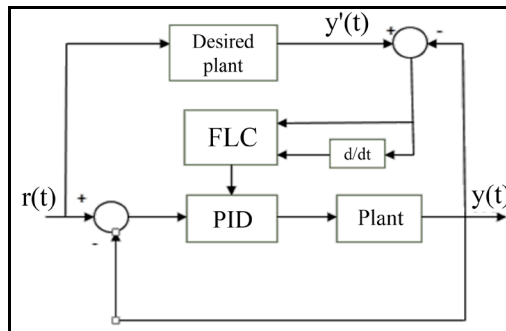


Figure 5. Fuzzy PID with reference model

Figure 5 shows the structure of the proposed Fuzzy PID with reference model. The new feature introduced in this paper is the desired plant that acts as a reference model to define the desired output to the system. By referring to Figure 5, the constant set point input is supplied to the desired plant before it is compared with the actual output. In the new structure, FLC will obtain the error between desired plant and actual output to synthesise the optimal PID gain. Hence, hypothetically, the output can be shaped during its transient as desired. In this paper, first-order transfer function has been evaluated as a reference model to the steam distillation plant control.

The first-order transfer function is given by:

$$G(s) = a / (s + a) \tag{2}$$

Where a is constant. The value of a is related to the time constant, τ as described by the following equation:

$$\tau = 1 / a \tag{3}$$

Thus, by adjusting a , the time constant of a response is adjusted which is related to the speed during transient. In this paper, only four models were evaluated based on different values of a as shown in Table 3. Obviously, a larger value of a produces a smaller time constant for a faster response.

Table 3
First-order reference model

τ	a
200	0.005
100	0.01
50	0.02
20	0.05

RESULTS AND DISCUSSION

In this section, simulation results of the proposed controller will be presented and compared with a standard fuzzy PID controller. All membership functions and fuzzy rules governing the FLC were maintained for both controllers. Comparison will be done based on transient performance criteria such as settling time and overshoot.

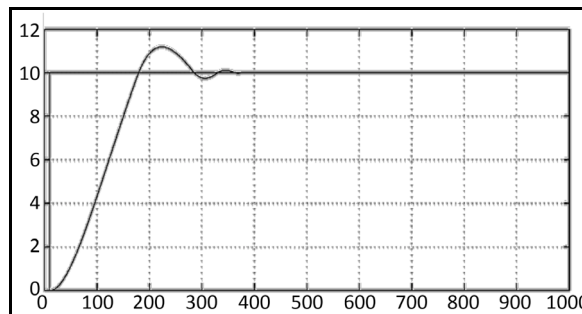


Figure 6. Output response from Fuzzy PID controller

Figure 6 shows the output response of a fuzzy PID. The magnitude of set point was set to 10°C which corresponds to 70°C to 80°C . The steam temperature overshoot over 10% from its set point.

Figure 7 shows the output of a fuzzy PID with reference model when $a = 0.005$ which corresponds with 200 seconds of time constant. It can be observed that the output response is very slow but it followed the response of the model perfectly towards the set point.

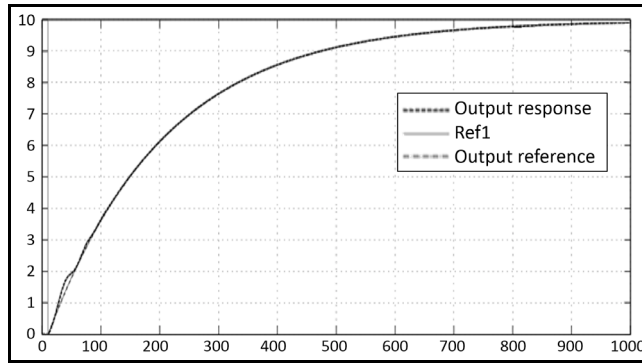


Figure 7. Output response for $a = 0.005$

In Figure 8, the speed of the response was improved when a was set to 0.01. Again, the output response could track the output of a model perfectly towards set point.

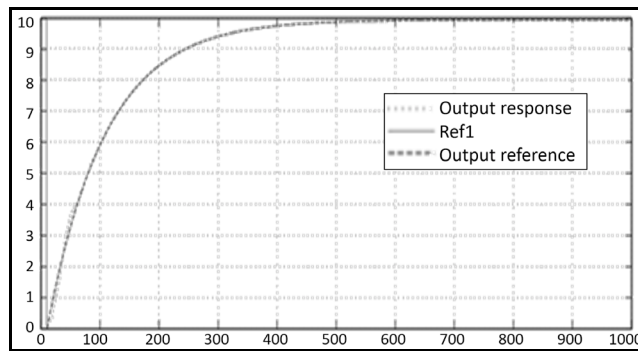


Figure 8. Output response for $a = 0.01$

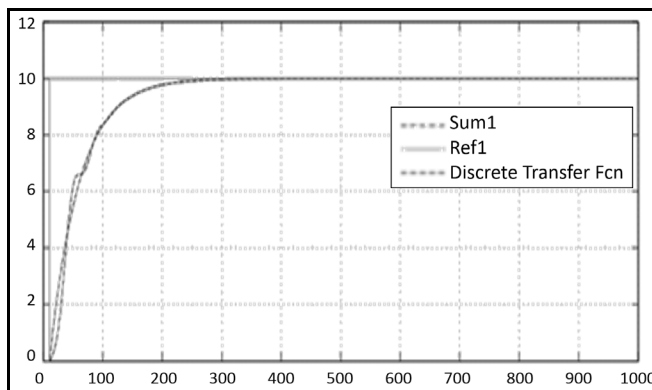


Figure 9. Output response for $a = 0.02$

Figure 9 shows a response of a fuzzy PID when a was set to 0.01. The output response was fast and approached set point within 200 seconds without overshoot.

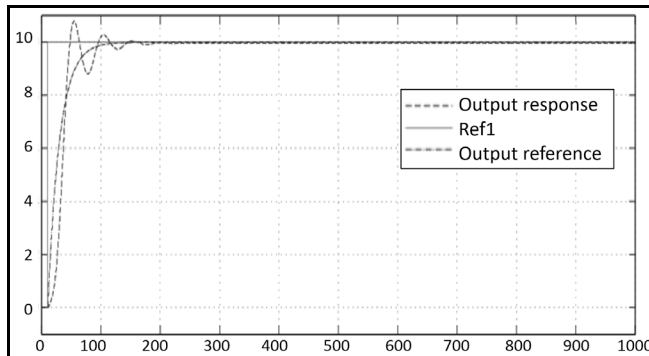


Figure 10. Output response for $a=0.05$

Figure 10 also shows the output response when $a = 0.05$. The output was trying to track the model output, but the desired transient is too fast, causing high control output command. As a result, the output overshoot by 9% but returned to the set point within 150 seconds.

Table 4 is a summary of data for ease of comparison. In general, it can be observed that the proposed fuzzy PID with model reference had significantly improved the output response during its transience. Furthermore, the proposed method provides control flexibility in adjusting the desired transient performance by providing a valid model reference at the set point. From the results, the validity of the proposed method had been proven but somehow, the desired speed was limited to 20 seconds of time constant which is equivalent to $1/0.05$. Beyond this value, the output response will have significant overshoot which is undesirable in this kind of process.

Table 4
Output response of the controller

Type of controller	Transient	
	T_s (s)	OS%
Fuzzy PID	400	10
Fuzzy PID with Reference Model		
0.005	800	0
0.01	400	0
0.02	200	0
0.05	150	9

CONCLUSION

This paper proposed a new structure of fuzzy PID with model reference, which showed better flexibility to the existing fuzzy PID control because desired transient performances can be assigned easily using a standard first-order transfer function. The results from simulation on a steam distillation process had shown significant improvement over the same fuzzy PID controller where the proposed system could track the desired model output perfectly until $a = 0.05$. The performance might be improved if a second-order model is used as a reference model instead.

ACKNOWLEDGMENTS

This research was funded by LESTARI (39/2015). The authors would like to thank the Faculty of Electrical Engineering, UiTM Malaysia for the facilities provided during this research. We would also like to express our gratitude to Institute of Research Management & Innovation (IRMI) UiTM and members of PICon Research Interest Group for their feedback and support.

REFERENCES

- Adnan, R., Tajjudin, M., Ishak, N., Ismail, H., Hezri, M., & Rahiman, F. (2011). Self-tuning Fuzzy PID Controller for electro-hydraulic cylinder. *Proceedings of the 2011 IEEE 7th International Colloquium on Signal Processing and its Applications, 4-6 Mar 2011*, (pp. 395-398) Malaysia.
- Arulmozhiyal R., & Kandiban, R. (2012). Design of Fuzzy PID Controller for Brushless DC Motor, *I(5)*, 3092–3096.
- Chen, Y. Q., Petráš, I., & Xue, D. (2009). Fractional order control - A tutorial, *Proceedings of the 2009 American Control Conference, 10-12 June 2009*, (pp. 1397-1411) USA.
- Das, S., Pan, I., Majumder, B., Das, S., & Gupta, A. (2011). Control of nuclear reactor power with thermal-hydraulic effects via fuzzy PI λ D μ controllers. *Proceedings of the 2011 International Conference on Communication and Industrial Application, 2-6, ICCIA 2011*. doi: 10.1109/ICCIndA.2011.6146648.
- Habib, M. K. (2001). Designing Fuzzy Logic Controllers for DC Servomotors supported by Fuzzy Logic Control Development Environment. *Industrial Electronics Society, 2001. IECON '01. The 27th Annual Conference of the IEEE*, ISBN: 0-7803-7108-9, 29 Nov.-2 Dec. 2001, (pp. 2093-2098) USA: IEEE.
- Hajiloo A., & Xie, W. F. (2013). Fuzzy fractional-order PID controller design using multi-objective optimization. *Proceedings of the IEEE 2013 Joint IFSA World Congress and NAFIPS Annual Meeting (IFSA/NAFIPS), 24-28 June 2013*, (pp. 1445-1450) Edmonton, Ab, Canada.
- Han, W., Kim, S., Kim, S., & Lee, C. (2003). Sensorless vector control of induction motor using improved Self-Tuning Fuzzy PID Controller. *Proceedings of the Society of Instrument and Control Engineers; SICE 2003 annual conference*, (pp. 3112-3117) Fukui, Japan.
- Korkmas D. H., Aydogdu Ö, M., & Dogan, H. (2012). Design and performance comparison of variable parameter nonlinear PID controller and genetic algorithm based PID controller. *Proceedings of the 2012 International Symposium on Innovations in Intelligent Systems and Applications, 2-4 July 2012*, (pp. 1-5) Trabzon, Turkey. doi: 10.1109/INISTA.2012.6246935.

- Li, W. (1998). Design of a hybrid fuzzy logic proportional plus conventional integral-derivative controller, *IEEE Transactions on Fuzzy Systems*, 6(4), 449-463.
- Lou, K., Kuo, C., & Sheu, L. (1996). A novel method for fuzzy self-tuning PID controllers, *Proceedings of the 1996 Asian Fuzzy Systems Symposium Soft Computing in Intelligent Systems and Information Processing, 11-14 Dec. 1996*, (pp. 0-5) Kenting, Taiwan. doi: 10.1109/AFSS.1996.583590.
- Precup R. E., & Hellendoorn, H. (2011). A survey on industrial applications of fuzzy control. *Computers and Industrial*, 62(3), 213–226.
- Sinthipsomboon, K., Hunsacharoonroj, I., Khedari, J., Pongaen, W., & Pratumswan, P. (2011, June). A hybrid of fuzzy and fuzzy self-tuning PID controller for servo electro-hydraulic system. In *Industrial Electronics and Applications (ICIEA), 2011* (pp. 220-225).
- Tang, Y., Cui, M., Hua, C., Li, L., & Yang, Y. (2012). Optimum design of fractional order $PI\lambda D\mu$ controller for AVR system using chaotic ant swarm. *Expert Systems With Applications*, 39(8), 6887–6896.
- Tajjudin, M., Hezri, M., Rahiman, F., Ishak, N., & Arshad, N. M. (2013). Design and Experimental Study of Fuzzy $PI\lambda D\mu$ with Error Filter. *Proceedings of the 2013 3rd International Conference on Instrumentation Control and Automation (ICA), 28-30 Aug. 2013* (pp. 245-250) Ungasan, Indonesia. doi: 10.1109/ICA.2013.6734080.
- Tsai, P., Chen, Y., & Hwang, R. (2004). The model reference control by Auto-Tuning PID-Like Fuzzy Controller. *Proceedings of the 2004 IEEE International Conference on Control Applications, 2-4 Sept. 2004*, (pp. 406-411) Taipei, Taiwan. doi: 10.1109/CCA.2004.1387245.
- Vindhya V., & Reddy, V. (2013). PID-Fuzzy Logic hybrid Controller for a Digitally Controlled DC-DC converter. *Proceedings of the 2013 International Conference on Green Computing, Communication and Conservation of Energy (ICGCE), 12-14 Dec. 2013*, (pp. 362-366) Chennai, India. doi: 10.1109/ICGCE.2013.6823461.
- Yi, T., Wang, C., Zhao, X., Li, J., & Shi, Y. (2013). The design and simulation of controllers for high order system, *Proceedings of the 2013 25th Chinese Control and Decision Conference (CCDC), May 2013*, (pp. 25-27) Guiyang, China. doi: 10.1109/CCDC.2013.6560953.



Synthesis and Corrosion Inhibition Studies of *N*-((4 and 3-chlorophenyl) carbamothioyl) Benzamide in 1M H₂SO₄

Norsakina Zurina Zulkifli², Karimah Kassim^{1,2*} and Nurul Atikah Nordin³

^{1,2}Institute of Science, Universiti Teknologi MARA (UiTM), 40450 Shah Alam, Selangor, Malaysia

²Faculty of Applied Sciences, Universiti Teknologi MARA (UiTM), 34500 Tapah, Perak, Malaysia.

³Faculty of Applied Sciences, Universiti Teknologi MARA (UiTM), 40450 Shah Alam, Selangor, Malaysia

ABSTRACT

In this study, the new compound of thiourea derivatives were successfully synthesized, namely *N*-((3-chlorophenyl) carbamothioyl) benzamide (T1) and *N*-((4-chlorophenyl) carbamothioyl) benzamide (T2). These series of thiourea compounds were prepared from the reaction of benzoyl chloride with ammonium thiocyanate to produce benzoyl isothiocyanate, then direct reaction with amines by using condensation method. Their structures were characterized on the basis elemental analysis and spectroscopic techniques namely infrared and nuclear magnetic resonance. The Infrared spectra showed the significant results of stretching vibrations of the compounds are $\nu(\text{C}=\text{O})$, $\nu(\text{C}=\text{S})$ and $\nu(\text{C}-\text{N})$ at 1533.39-1671.00 cm⁻¹, 1256.64-1261.73 cm⁻¹ and 1144.22-1144.81 cm⁻¹, respectively. These compounds were investigated as corrosion inhibitors on mild steel in 1M H₂SO₄ using linear polarization techniques. Results show the highest inhibition efficiency of T1 is 55% while for T2 is 73%. The percentage inhibition efficiency of T2 is higher than T1 due to the difference position of substituent at *meta* and *para*.

Keywords: Corrosion inhibition, linear polarization, mild steel, thiourea

INTRODUCTION

Corrosion is an event that occurs naturally in our environment. From previous studies, some of inhibitors can be added to the acid media to reduce the rate of corrosion to safe level (Shetty & Shetty, 2008). The inhibitor molecules get bonded to the surface of mild steel by chemisorption, physisorption, or complexation with the polar groups acting as the reactive centres in the molecules (Sundaram & Sundaravadivelu, 2016). The

ARTICLE INFO

Article history:

Received: 05 January 2017

Accepted: 17 January 2017

E-mail addresses:

norsakina@perak.uitm.edu.my (Norsakina Zurina Zulkifli),

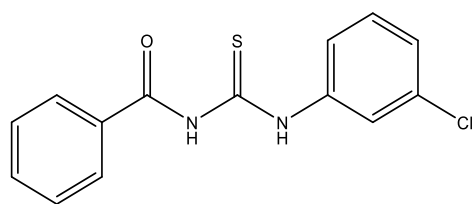
karimah@salam.uitm.edu.my (Karimah Kassim),

[nurulatikhannordin@yahoo.com](mailto:nurulatikahnordin@yahoo.com) (Nurul Atikah Nordin)

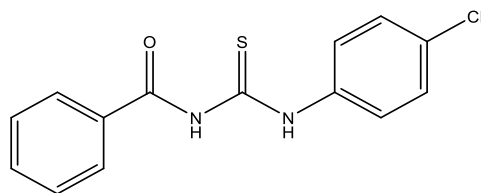
*Corresponding Author

good acid inhibitors used in the industry are compounds having multiple bonds in their molecules, mainly contain nitrogen and sulphur atoms through which are capable of retarding metallic corrosion and easily adsorbed on the metal surface (Shetty, Shetty, & Nayak, 2008). Thiourea is an organosulphur compound which has a group of nitrogen, carbon, hydrogen and sulphur. It is generally identical as urea except the position of oxygen replaced with sulphur atom. Thiourea and its derivatives appear as white, lustrous crystal or flaky solids and very useful in pharmaceuticals (Miftah & Tjahjono, 2015). The chemical structure of thiourea is $(\text{NH}_2)_2\text{CS}$ while urea is $(\text{NH}_2)_2\text{CO}$. Some substituted thiourea derivatives have been studied in considerable detail as effective corrosion inhibitors for mild steel in acidic media (Yadav, Al-Majidi, & Al-Saadie, 2014). The presence of both hard and soft donor atoms in the ligand increases the coordination ability towards a metal centre (Yusoh, Jusoh, Khairul, & Yamin, 2010).

In a continuation of our research, we reported the synthesis of thiourea compounds, namely, *N*-((3-chlorophenyl) carbamothioyl) benzamide [T1] and *N*-((4-chlorophenyl) carbamothioyl) benzamide [T2] as shown in Figure 1. For all the compounds, the only difference was the position of chloride group at *meta* and *para* position. The structures of the ligands have been characterized by elemental analysis (CHNS), IR spectroscopy, ^1H and ^{13}C Nuclear Magnetic Resonance (NMR) and melting point. The compounds were undergoing corrosion inhibition using linear polarization techniques.



(a)



(b)

Figure 1. The chemical structure of the investigated compounds: (a) *N*-((3-chlorophenyl) carbamothioyl) benzamide (T1); and (b) *N*-((4-chlorophenyl) carbamothioyl) benzamide (T2)

MATERIALS AND METHOD

Synthesis of Thiourea Derivatives

The benzoylthiourea ligands were prepared according to the previous study with a slight modification (Al-jeilawi, Al-Majidi, & Al-Saadie, 2013). The purity of ligands was tested by using Nuclear Magnetic Resonance (NMR), Infrared Spectroscopy (IR) and Elemental Analysis (CHNS). The melting point, percentage yield, CHNS, IR and NMR data of the synthesized compounds were shown in Figure 2.

Specimen Preparation

The steel coupons were even and smooth. After polishing, the specimens were washed with distilled water and acetone before being dried and stored in desiccator (Edrah & Hasan, 2010).

Preparation of N-((3-chlorophenyl) carbamothioyl) benzamide [T1]

The ammonium thiocyanate (0.01 mol, 0.761 g) was diluted into 20 ml of acetone to form a solution. Then, (0.01 mol, 1.162 ml) of benzoyl chloride was added into the mixture and stirred for 20 minutes. The 3-chloroaniline (0.01 mol, 1.058 ml) was mixed with 5 ml of acetone to form a solution. The two mixtures were added together into a volumetric flask and refluxed for 3 hours. Then, it was cooled at room temperature and immersed in ice bath. A mixture was filtered and washed using cold ethanol. The preparation of N-((4-chlorophenyl) carbamothioyl) benzamide [T2] was synthesized with a similar procedure.

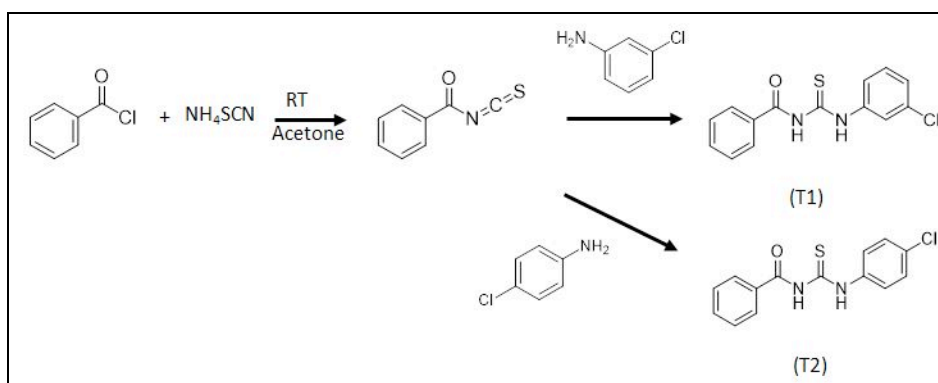


Figure 2. The preparation of (T1) and (T2)

Electrochemical Measurements

A conventional three-electrode system consisting of mild steel as working electrode, platinum as an auxiliary electrode and silver-silver chloride (Ag-AgCl) as reference electrode was used for the measurements. The working electrode of mild steel was allowed to corrode freely in 1M of H₂SO₄ without inhibitor before starting electrochemical measurements and it is open circuit potential (OCP) within 30 minutes (Sundaram & Sundaravadivelu, 2016). The adsorption of

inhibitor molecules on the surface of corroding metal using chronoamperometry technique and corrosion study of coated inhibitor on metal using linear polarization resistance technique.

RESULTS AND DISCUSSION

Chemical Analysis

The elemental analysis data of the product shows the relevant frequencies with the expected thiourea as shown in Table 1. The melting point of the ligands was found to be between 138°C – 160°C.

Table 1
Analytical and physical data of the thiourea ligands

Compound	Colour	M.P (°C)	Percentage yield (%)	Elemental analysis data found (calculated) (%)			
				C	H	N	S
T1	White	138-160	83.37	48.65 (57.83)	4.87 (3.81)	12.46 (9.63)	6.34 (11.03)
T2	White	140-155	95.00	55.06 (57.83)	4.42 (3.81)	10.45 (9.63)	7.74 (11.03)

Spectroscopic Studies

Table 2
FTIR spectral data of compounds

Compounds	Major FTIR Absorptions (cm ⁻¹)			
	C-H	C=O	C=S	C-N
T1	2991.08	1671.00	1256.64	1144.22
T2	3012.79	1533.39	1261.73	1144.81

FTIR Spectroscopy. The T1 and T2 compounds show the important stretching in the FTIR spectra such as $\nu(\text{C}=\text{S})$, $\nu(\text{C}=\text{O})$, $\nu(\text{C}-\text{N})$ and $\nu(\text{N}-\text{H})$ which can be observed around 1261 cm⁻¹, 1550 cm⁻¹, 1144 cm⁻¹, 1600 cm⁻¹ and 3000 cm⁻¹. Based on the previous studies, it is quite similar among the values reported (Al-Jeilawi, Al-Majidi, & Al-Saadie, 2013). With regards to the carbonyl band, $\nu(\text{C}=\text{O})$, T1 were observed at 1671.00 cm⁻¹ while for T2 at 1533.39 cm⁻¹. This is due to the presence of aromatic group and the existence of intramolecular hydrogen bonding. For C-N, the absorption band was clearly observed lower than 1200 cm⁻¹ whereas in the range 1144 cm⁻¹. While, the C=S absorption band was observed at a range between 1261 cm⁻¹ to 1256 cm⁻¹. This band agreed with the results of an earlier study where the type of band

was observed at 1271 cm⁻¹ (Al-Jeilawi, Al-Majidi, & Al-Saadie, 2013). Furthermore, the reading of the C=S band spectra is a slightly high due to the presence of aromatic group acts as large double bond and lower nucleophilic character of the sulphur atom compared to alkylthioureas.

¹H NMR spectroscopy. As shown in Table 3, for both compounds, the resonance for the aromatic group can be observed at 7.0-8.0 ppm. It was found to be a distinctive multiplet resonance because of the unresolved aromatic protons. Meanwhile, the chemical shifts of the amide and thiomide protons for both isomers (T1 and T2) are quite similar. They appeared as a singlet at 9.20 ppm for amide protons and 12.6-12.8 ppm for thiomide respectively. Theoretically, the resonance for this type of group is in the range 12.0 ppm. The downfield of amide protons is mainly due to the formation of the intramolecular hydrogen bonding between the amino proton N-H and the oxygen atom of the carbonyl group which is C=O. Furthermore, all the tested hybrid functional showed relatively good correlation coefficients between the experimental and predicted ¹H chemical shifts.

¹³C NMR spectroscopy. The resonance of aromatic rings, the carbon resonance appeared in the range of 125-132 ppm for both compounds T1 and T2. Meanwhile, for C-Cl carbon resonance was observed in the range of 133-135 ppm. Similarly, the carbon chemical shifts of C=O and C=S are found at 178 ppm and 167 ppm respectively for the both isomers. There is slightly difference in the carbon resonance because they are slightly deshielded due to the formation of intramolecular hydrogen bonding, which increases the electronegativity of oxygen and sulphur atoms. Likewise, to ¹H NMR spectra, the isomerization has a slight influence on the position of chemical shift, with chemical shift variations less than 5 ppm.

Corrosion Studies

Linear polarization resistance. In the linear polarization resistance (LPR) technique, the values of change in potential applied as a result of applied potential obtained from electrochemical measurements are used. The data was obtained from the slopes from the initial linear region of the polarization curves of the potential versus current plots. After measuring the currents and potentials, a plot of the parameters measured for mild steel as the working electrode immersed in 1M H₂SO₄ containing same concentrations of thiourea (0.01M) as inhibitor is presented in Figure 3. The percentage of inhibition efficiency (%) was calculated following the formula;

$$\% \text{ IE} = \frac{i_{corr}^0 - i_{corr}}{i_{corr}^0}$$

where i_{corr}^0 and i_{corr} are the corrosion current densities of presence and absence of inhibitor in solution respectively.

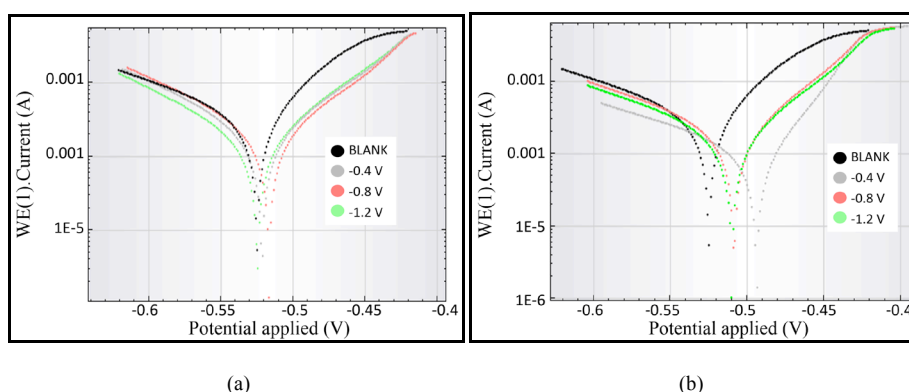


Figure 3. The variation of different potential applied and current change for mild steel corrosion in 1M H₂SO₄ in the presence and absence of inhibitor: (a) *N*-((3-chlorophenyl) carbamothioyl) benzamide (T1); and (b) *N*-((4-chlorophenyl) carbamothioyl) benzamide (T2)

Table 3

Electrochemical parameters for mild steel obtained from polarisation curves in 1M H₂SO₄ in the presence of (a) *N*-((3-chlorophenyl) carbamothioyl) benzamide (T1)

Potential applied (V)	E _{corr} (MV)	β _a (mV/dec)	β _c (mV/dec)	i _{corr} μA/cm ²	% IE
0	-525.040	185.570	69.154	408.340	0
-0.4	-521.520	117.950	96.691	241.600	41
-0.8	-516.770	116.690	94.016	243.960	40
-1.2	-524.790	111.640	80.764	183.620	55

Table 4

Electrochemical parameters for mild steel obtained from polarisation curves in 1M H₂SO₄ in the presence of *N*-((4-chlorophenyl) carbamothioyl) benzamide (T2)

Potential applied (V)	E _{corr} (MV)	β _a (mV/dec)	β _c (mV/dec)	i _{corr} μA/cm ²	% IE
0	-525.040	185.570	69.154	408.340	0
-0.4	-493.840	140.750	53.532	110.200	73
-0.8	-508.560	145.050	77.717	235.250	42
-1.2	-509.990	156.810	84.548	226.930	44

Based on Tables 3 and 4, throughout the linear polarization technique with differences of potential applied, the highest percentage of inhibition efficiency of T2 is 73% and T1 is 55%. Throughout the data, the i_{corr} which is the current density of mild steel with the presence of difference inhibitors are lower than without it. This indicates that there is an adsorption of inhibitor on mild steel (Fouda & Hussein, 2012) and the presence of aromatic group that have electron density which suppressed the reaction (Wang et al., 1995). It can be observed from the Figure 3 and Table 3, the presence of T1 and T2 drastically reduces the corrosion currents and the corrosion potential shifts to the positive direction. The changes in corrosion potential (E_{corr}) to the positive path direction assumes the presence of inhibitors mostly acting as an

anodic inhibitor for mild steel. It is indicated that the inhibition efficiency of both compounds has a positive correlation with same concentration 0.01M of T1 accepted at -1.2 V and 0.01M of T2 accepted at -0.4 V.

Thiourea molecules having a sulphur and two nitrogen atoms which act as donor atoms towards mild steel. The lone pair from these donor atoms are able to transfer electron from the inhibitor onto the metal ((Loto, Loto, & Popoola, 2012). When it forms a covalent bond, the corrosion inhibitor acts as a protective film on the metal. According to this result, the adsorption of inhibitor molecules of T2 is higher than T1 due to differences position of chloride group at *para* and *meta*. The relative yield of T2 is higher than T1, so the chloride group in benzene at monosubstituted benzene is called *ortho*, *para* directing group. Thus *ortho*, *para* directing group is electron-donating group, the process of reduction occurred and electron was released for the adsorption metal. The best potential applied for T2 is -0.4 V because it had the highest inhibition efficiency (73%) while for T1, the best potential applied is -1.2 V because of its highest inhibition efficiency (55%).

CONCLUSION

In conclusion, N-((3-chlorophenyl) carbamothioyl) benzamide (T1) and N-((4-chlorophenyl) carbamothioyl) benzamide (T2) was successfully synthesized and fully characterized by spectroscopic methods. The inhibition efficiency of T2 is greater than T1. The greater the inhibition efficiency, the higher the adsorption of inhibitor molecules on mild steel and corrosion process reduces. All the obtained compounds are anodic type of inhibitors.

ACKNOWLEDGEMENTS

The authors are grateful to the Ministry of Higher Education of Malaysia for the research grant no. 600-RMI/RAGS 5/3 (53/2015) and the Faculty of Applied Sciences, Institute of Science and Universiti Teknologi MARA of Shah Alam and Tapah Campus for providing research facilities.

REFERENCES

- Al-Jeilawi, U. H. R, Al-Majidi, S. M. H., & Al-Saadie, K. A. S. (2013). Corrosion inhibition effects of some new synthesized n-aryl-n'-aryl thiourea derivatives for carbon steel in sulfuric acid media. *Journal of Al-Nahrain University*, 16(4), 80-93.
- Edrah, S., & Hasan S. K. (2010). Studies on thiourea derivatives as corrosion inhibitor for aluminium in sodium hydroxide solution. *Journal of Applied Sciences Research*, 6(8), 1045-1049.
- Fouda, A. E. E., & Hussein, A. (2012). Role of some phenylthiourea derivatives as corrosion inhibitors for carbon steel in HCl solution. *Journal of the Korean Chemical Society*, 56(2), 264 –273.
- Loto, R. T., Loto, C. A., & Popoola, A. P. I. (2012). Corrosion inhibition of thiourea and thiadiazole derivatives: A review. *Journal of Materials and Environmental Science*, 3(5), 885-894.
- Miftah, A. M., & Tjahjono, D. H. (2015). Synthesis and in vitro cytotoxicity of 1-Benzoyl-3-methyl thiourea derivatives. *Procedia Chemistry*, 17, 157-161.

- Shetty, S. D., & Shetty, P. (2008). Inhibition of mild steel corrosion in acid media by N-benzyl-N'-phenyl thiourea. *Indian Journal of Chemical Technology*, 15, 216-220.
- Shetty, S. D., Shetty, P., & Nayak, V. S. (2008). The inhibition action of N-furfuryl-N'-phenyl thiourea on the corrosion of mild steel in acid media. *J. Serb. Chem. Soc.*, 71, 1073–1082.
- Sundaram, R. G., & Sundaravadivelu, M. (2016). Anticorrosion activity of 8-quinoline sulphonyl chloride on mild steel in 1M HCl solution. *Journal of Metallurgy*, 2016, 1-9. Retrieved from <http://dx.doi.org/10.1155/2016/8095206>.
- Wang, J., Cao, C., Chen, J., Zhang, M., Ye, G., & Lin, H. (1995). Anodic desorption of inhibitors. *Journal Chinese Society Corrosion Protection*, 15, 241-248.
- Yadav, M., Kumar, S., Bahadur, I., & Ramjugernath, D. (2014). Corrosion inhibitive effect of synthesized thiourea derivatives on mild steel in a 15% HCl solution. *International Journal of Electrochemical Science*, 6529-6550.
- Yusoh S., Jusoh, R. H., Khairul, W. & Yamin, B. (2010). Synthesis and characterisation a series of N-(3,4-dichlorophenyl)-N0-(2,3 and 4-methylbenzoyl) thiourea derivatives. *Journal of Molecular Structure*, 975, 280-284.

Effect of Operating Parameters on Decolourisation of Palm Oil Mill Effluent (POME) using Electrocoagulation Process

Nur Syuhaidah Mohd Aris¹, Shariff Ibrahim^{1*}, Borhannuddin Arifin¹ and Yahaya Hawari²

¹Faculty of Applied Sciences, Universiti Teknologi MARA (UiTM), 40450 Shah Alam, Selangor, Malaysia

²Milling and Processing Unit, Engineering and Processing Division, Malaysian Palm Oil Board (MPOB), Bandar Baru Bangi, 43000 Kajang, Selangor, Malaysia

ABSTRACT

Electrocoagulation has proven to be an effective method in the treatment of wastewater. This study evaluated the decolourisation of Palm Oil Mill Effluent (POME) using electrocoagulation (EC) batch reactor by utilising aluminium as sacrificial electrode. POME sample source from a final discharged pond at a palm oil mill was characterised for its colour, chemical oxygen demand (COD), pH, conductivity and turbidity; were found to be 2707 PtCo, 3909 mg/L, 7.63, 12.82 mS/cm and 755 NTU respectively. The respective effects of operating parameters such as pH (3 to 11), applied voltage (5 V to 20 V), plate gap (7.5 to 11.5 cm) and operating time (1 to 8 hours) were investigated. The decolourisation of POME was observed to increase with increasing voltage and operating time. Highest removal efficiency was observed at pH 5, 20 V applied voltage, 9.5 cm plate gap and at 8-hour operating time with colour removal efficiency of 89, 79, 78 and 64% respectively. From the findings, it can be concluded that electrocoagulation process using aluminium electrodes is a reliable technique for the removal of colour from POME.

Keywords: Aluminium electrode, effluent, electrocoagulation, POME

ARTICLE INFO

Article history:

Received: 05 January 2017

Accepted: 17 January 2017

E-mail addresses:

nousyuaris@gmail.com (Nur Syuhaidah Mohd Aris),
sha88@salam.uitm.edu.my (Shariff Ibrahim),
borhan545@salam.uitm.edu.my (Borhannuddin Arifin),
yayahawari@mpob.gov.my (Yahaya Hawari)

*Corresponding Author

INTRODUCTION

Malaysia is one of the world's largest palm oil producing country (Kanakaraju, Awangku Metosen, & Nori, 2016). The process of oil extraction results in the generation of liquid waste commonly known as palm oil mill effluent (POME), making crude palm oil production a water intensive activity. It is estimated that from 1 tonne of fresh fruit

bunch (FFB) processed, about 0.67 tonnes of POME are produced. Consequently, in 2014, from 100.42 million tonnes of FFB, about 67.28 million tonnes of POME were generated in Malaysia (Bukhari, Nasrin, & Loh, 2016). POME distinct characteristics are its dark colour, high biochemical oxygen demand (BOD), chemical oxygen demand (COD), and substantial amount of suspended solids (Kanu & Achi, 2011). POME composed of 4–5% solids (mainly organic), 0.5–1% residual oil and about 95% water, and high concentration of organic nitrogen. In extraction of oil in plant-based wastewater, dark brown colour was ascribed to polymerisation of tannins and low molecular weight phenolic compounds as in olive mills wastewater (Adhoum & Monser, 2004).

Besides other traditional methods of remediation such as aerobic and anaerobic ponds, the feasibility of coagulation also was studied by numerous researchers. Electrocoagulation, is a variation of the coagulation process, other than the widely practiced chemical coagulation. Although both electrocoagulation (EC) and chemical coagulation (CC) are used for particle removal in water treatment, they differ in their dosing method. The coagulant is added by electrolytic oxidation in EC, whereas in CC the coagulant is added by the dissolution of a chemical (Harif, Khai, & Adin, 2012). Despite the limited research on EC, it actually has managed to explore an extensive range of applications for both colloidal as well as organic matter removal in sewage and effluent treatment (Kuokkanen, Kuokkanen, Rämö, & Lassi, 2013). Other than that, notable research on the utilization of EC for vegetable oil processing wastewater in the treatment of olive oil mills wastewater has been widely pursued by many researchers (Yazdanbakhsh, Massoudinejad, Arman, & Aghayani, 2013). Agustin, Sengpracha and Phutdhawong (2008) observed that, EC was capable of effectively removing the colour of POME, from intense dark brown to pale yellow.

In this study, POME was treated using electrocoagulation reactor via batch mode. It was characterised for its colour, COD, pH, conductivity and turbidity. Four significant EC operating parameters, namely pH, applied voltage, plate gap and operating time were investigated to assess the effectiveness of POME colour removal.

MATERIALS AND METHOD

Sample Collection

In order to carry out this work, samples of Palm Oil Mill Effluent (POME) from a Palm Oil Mill in the South of Malaysia, producing 20 tonnes per hour were used throughout this study. It was taken from final discharge pond placed after anaerobic pond. The POME was dark brown in colour and contained a large amount of suspended solids. The samples were kept in plastic bottles and refrigerated at 4°C before use.

Experimental Set Up: EC Batch Reactor

A 3-litre EC batch reactor was set up in Figure 1. A GW Laboratory DC power supply (Model: GPS-3030D) with a working range of 0 – 30 V was used. A pair of aluminium or iron plates were used of size 14 cm (L) x 14.5 cm (W) x 0.15 cm (H), immersed in the sample to a depth

of 8 cm. An electrode gap of 9.5 cm was fixed throughout the experiment. The sample was treated at room temperature with constant magnetic stirring. To eliminate electrode passivation at the anode due to the formation of an oxide film, it was rinsed with 1M dilute nitric acid solution after each experiment followed with deionized water.

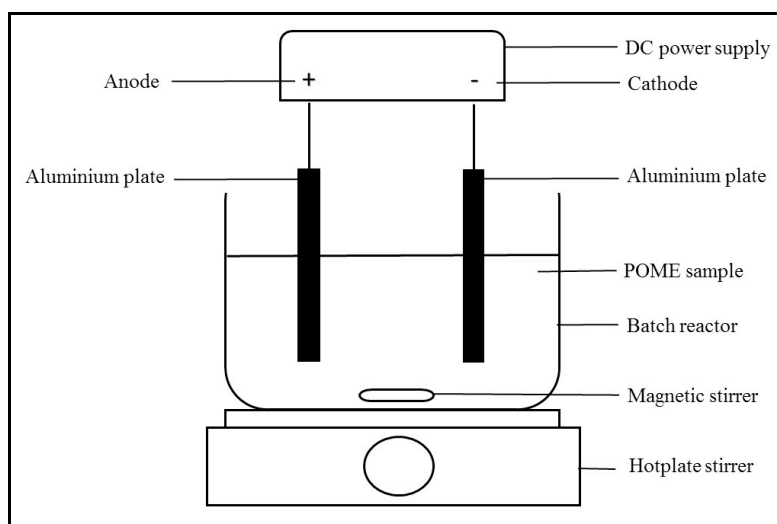


Figure 1. Schematic of EC batch reactor

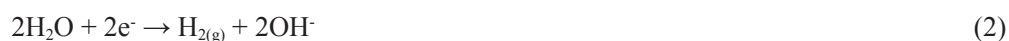
Mechanism of EC Process

Electrocoagulation involves three main stages; the dissolution of metal ions of anode to form coagulant through dispersed double layer compression, the destabilization of pollutants through ion neutralization and the aggregation of unstable phases forming flocs and sludge (Bouhezila, Hariti, Lounici, & Mameri, 2011). The electrocoagulation mechanism can be evaluated from the following equations (Tchamango, Nanseu-Njiki, Ngameni, Hadjiev, & Darchen, 2010).

At anode, the oxidation of aluminium produces Al^{3+} species and the electrode reactions are:

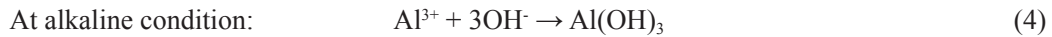
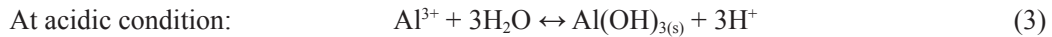


At cathode, the reduction of water takes place to form hydrogen bubbles and the reactions are:



In the EC reactor, the hydrogen bubbles undergo floatation. The Al^{3+} ions undergo further reaction to form precipitates of $\text{Al}(\text{OH})_3$ which produces flocs that combine water contaminants

as a range of coagulant species. The reaction of the metal hydroxides formed are represented by the equations below:



The pollutants and other dissolved contaminants were destabilized by the coagulants, $\text{Al}(\text{OH})_3$. Other than that, an oxygen evolution takes place and the reaction as below:



Characterisation of POME Wastewater

The POME was characterised for its colour, chemical oxygen demand (COD), pH, conductivity and turbidity according to standard methods. POME colour was analysed using HACH spectrophotometer at wavelength maximum of 455 nm. The COD was measured using COD reactor and direct reading from HACH spectrophotometer (Model: DR2800 – Method 8025). The pH was measured using HANNA instrument microprocessor pH meter (Model: pH 211). The conductivity was measured using EUTECH handheld conductivity meter. HACH turbidimeter (Model: 2100P) was used to measure the turbidity of the sample.

Effect of EC Operating Parameters

This investigation explored the behaviour of EC treatment of different operating variables. The effects of pH, applied voltage, plate gap and operating time were evaluated to study the decolourisation efficiency. At the beginning of each run, aluminium plates were placed into the reactor. The 6-hour operating time was started when the DC power supply was switched on. For the effect of pH, the pH was adjusted to pH 3 to 11 by adding drops of 0.5M sodium hydroxide (NaOH) or 0.5M hydrochloric acid (HCl). The voltage varied from 5 to 20 V to study the effects of applied voltage. The plate gap was studied from 7.5 to 11.5 cm. For the effect of operating time, EC process was conducted for 8 hours. During the treatment, POME samples were periodically collected at each hour from the reactor. The samples were filtered to analyse for colour intensity.

RESULTS AND DISCUSSION

Characterisation of POME Wastewater

The data for Characterisation of POME before EC treatment were presented in Table 1. The POME was dark brown in colour with high suspended solids and turbidity which was indicated by the high colour reading (2707 PtCo), COD (3009 mg/L) and turbidity (755 NTU). The pH of POME was at neutral (7.63). The conductivity of POME at 12.82 mS was adequate for an electrolyte during EC treatment as what being mentioned by Esfandyari et al. (2014).

Table 1
Characterisation of POME wastewater

Characterisation	Value
Colour	2707 PtCo
Chemical Oxygen Demand (COD)	3009 mg/L
pH	7.63
Conductivity	12.82 mS
Turbidity	755 NTU

Effect of pH

The amount of Al^{3+} ions generated depends strongly on pH. Thus, pH was studied in the range of 3 to 9. Based on the Figure 2, it was observed at pH 5, the highest colour removal was 89%, followed by pH 11, pH 9 and pH 3 with colour removal efficiency of 63%, 52% and 51% respectively. It was noted that the colour removal efficiency decreased when pH was lower and greater than 5. At lower pH (i.e. below 5), $Al(OH)_3$ tends to dissolve due to its amphoteric behaviour, whereas at higher pH (above 5), monomeric anions $Al(OH)_4^-$ was formed. Both of these situations were not favourable for POME colour removal. These observations were consistent with research done by Kobyas and Delipinar (2008).

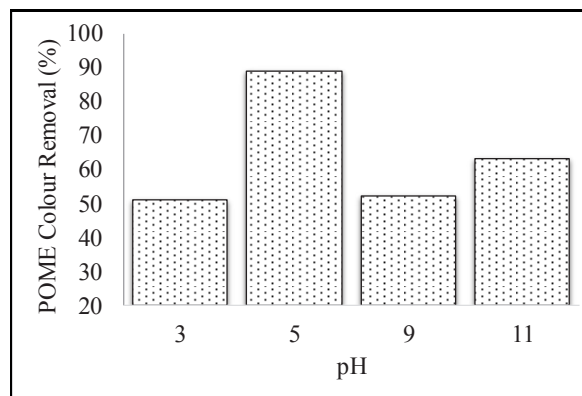


Figure 2. Effect of pH on POME colour removal

Effect of Applied Voltage

The supply of voltage to the electrocoagulation system indicates the amount of Al^{3+} released from the respective plates. The applied voltage was studied in the range of 5 to 20 V. The colour removal efficiency increased from 56 to 79% as the applied voltage was increased from 5 to 20 V (Sengil & Ozacar, 2006). Based on Faraday's law, as the voltage supply increased, the amount of aluminium ion (Al^{3+}) released from the plate and the quantity of resulting coagulant also increased and thus improved colour removal efficiency. The increased applied voltage causes the contact time between hydroxide flocs and colour pollutants to increase, thus floatation process

is improved and colour pollutants are rapidly removed (Bazrafshan, Moein, Mostafapour, & Nakhaie, 2013). This behaviour is in accordance to work done by Adhoum and Monser (2004).

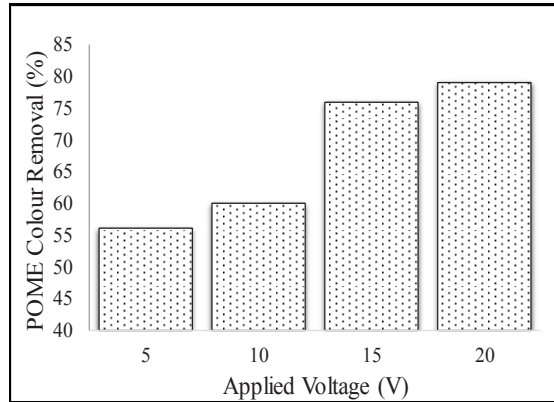


Figure 3. Effect of Applied Voltage on POME colour removal

Effect of Plate Gap

The plate gap plays a crucial factor due the electrostatic field depends on the distance between the anode and the cathode (Khandegar & Saroha, 2012). The electrostatic field strength is substantial as it attracts the ions generated from the plates during the EC process (Bouhezila, Hariti, Lounici, & Mameri, 2011). The plate gap was varied from 7.5 to 11.5 cm. The colour removal efficiency reduces with increasing of plate gap. Maximum colour removal was observed at plate gap of 9.5 cm with 78% removal efficiency. Further the gap, it increases the travel time of the ions, thus leads to a decrease in electrostatic attraction as suggested by Khandegar and Saroha (2012), which subsequently reduces the formation of flocs.

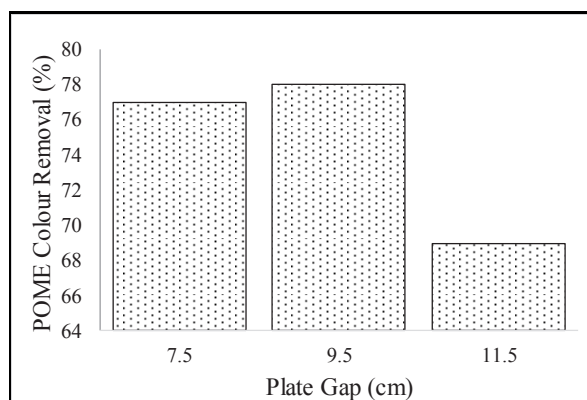


Figure 4. Effect of Plate Gap on POME colour removal

Effect of Operating Time

Operating time is another EC parameter that affects colour removal efficiency. As shown in Figure 5, it was observed that for longer operating times (from 1 to 6 hours), there is an increase in the colour removal efficiency. Theoretically, based on Faraday's law, operation time affects the amount of aluminium ions released from the electrode (Bazrafshan, Moein, Mostafapour, & Nakhaie, 2012). In this process, EC involves two stages which are destabilization and accumulation. The first stage is usually short, whereas the second stage is relatively long (Ni'am, Othman, Sohaili, & Fauzia, 2007). There was a steep increase in the removal efficiency of 37% during the first hour (first stage). From second to eight hours, the removal efficiency increases slowly to 64% (second stage). This is due to the increased quantity of coagulant dissolving from the aluminium electrode, thus destabilize the double layer of the suspended metallic hydroxides (Zhao, Huang, Cheng, Wang, & Fu, 2014).

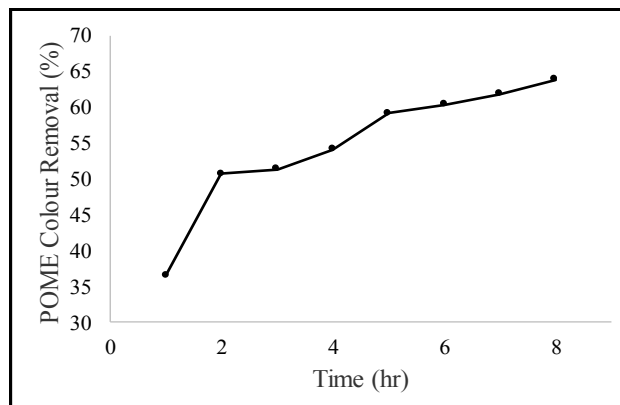


Figure 5. Effect of Operating Time on POME colour removal

CONCLUSION

Batch electrocoagulation studies were conducted to assess the influence of various experimental parameters on the removal of colour pollutants from POME. pH 5 was observed to contribute the highest decolourisation yield of 89%. The treatment rate was shown to increase upon increasing of the applied voltage until 20V with the highest colour removal efficiency of 79%. Besides that, plate gap of 9.5 cm showed the highest decolourisation efficiency of 78%. With an increase in the operating time until 8 hours, there is an increase in colour removal efficiency of 68%. However, at 6 hours-operating time, the EC process reached equilibrium and became stable. Based on these findings, EC process was proven to be a feasible method to decolourize POME.

ACKNOWLEDGEMENTS

The authors gratefully acknowledge the research grant funded by Ministry of Higher Education (MOHE) via Research Management Centre, Universiti Teknologi MARA (FRGS: 600-RMI/FRGS 5/3 (2/2014)) and the research facilities provided by the Postgraduate school, Faculty of Applied Sciences, Universiti Teknologi MARA (UiTM). Special thanks to Malaysian Palm Oil Board (MPOB) and Palm Oil Mill factory (POMTEC) Labu, Negeri Sembilan specifically Mr Shahril for coordinating the research activities.

REFERENCES

- Adhoum, N., & Monser, L. (2004). Decolourisation and removal of phenolic compounds from olive mill wastewater by electrocoagulation. *Chemical Engineering and Processing: Process Intensification*, 43(10), 1281-1287.
- Agustin, M. B., Sengpracha, W. P., & Phutdhawong, W. (2008). Electrocoagulation of palm oil mill effluent. *International Journal of Environmental Research and Public Health*, 5(3), 177-180.
- Bazrafshan, E., Moein, H., Mostafapour, F. K., & Nakhaie, S. (2012). Application of electrocoagulation process for dairy wastewater treatment. *Journal of Chemistry*, 2013, 1-8.
- Bouhezila, F., Hariti, M., Lounici, H., & Mameri, N. (2011). Treatment of the OUED SMAR town landfill leachate by an electrochemical reactor. *Desalination*, 280(1-3), 347-353.
- Bukhari, N. A., Nasrin, A. B., & Loh, S. K., (2016). Palm oil mill effluent as a low-cost substrate for bioflocculant production by *Bacillus marisflavi* NA8. *Bioresources and Bioprocessing*, 3(20), 1-8.
- Esfandiyari, Y., Mahdavi, Y., Seyedsalehi, M., Hoseini, M., Safari, G. H., Ghozikali, M. G., & Jaafari, J. (2014). Degradation and biodegradability improvement of the olive mill wastewater by peroxi-electrocoagulation/electrooxidation-electroflotation process with bipolar aluminium electrodes. *Environmental Science and Pollution Research International*, 22(4), 6288-6297.
- Harif, T., Khai, M., & Adin, A. (2012). Electrocoagulation versus chemical coagulation: Coagulation/flocculation mechanisms and resulting floc characteristics. *Water Research*, 46, 3177-3188.
- Kanakaraju, D., Awangku Metosen, A. N. S., & Nori, H. (2016). Uptake of heavy metals from palm oil mill effluent sludge amended soils in water spinach. *Journal of Sustainability Science and Management*, 11(1), 113-120.
- Kanu, I., & Achi, O. (2011). Industrial effluents and their impact on water quality of receiving rivers in Nigeria. *Journal of Applied Technology in Environmental Sanitation* 1(1), 75-86.
- Khandegar, V., & Saroha, A. K. (2012). Electrochemical treatment of distillery spent wash using aluminium and iron electrodes. *Chinese Journal of Chemical Engineering*, 20(3), 439-443.
- Kobyas, M., & Delipinar, S. (2008). Treatment of the baker's yeast wastewater by electrocoagulation. *Journal of Hazardous Materials*, 154, 1133-40.
- Kuokkanen, V., Kuokkanen, T., Rämö, J., & Lassi, U. (2013). Recent applications of electrocoagulation in treatment of water and wastewater—A review. *Green and Sustainable Chemistry*, 3, 89-121.
- Ni'am, M. F., Othman, F., Sohaili, J., & Fauzia, Z. (2007). Electrocoagulation technique in enhancing COD and suspended solids removal to improve wastewater quality. *Water Science and Technology: A Journal of the International Association on Water Pollution Research*, 56(7), 47-53.

- Sengil, I. A., & Ozacar, M. (2006). Treatment of dairy wastewaters by electrocoagulation using mild steel electrodes. *Journal of Hazardous Materials*, 137, 1197–205.
- Tchamango, S., Nanseu-Njiki, C. P., Ngameni, E., Hadjiev, D., & Darchen, A. (2010). Treatment of dairy effluents by electrocoagulation using aluminium electrodes. *Science of the Total Environment*, 408(4), 947–952.
- Yazdanbakhsh, A. R., Massoudinejad, M. R., Arman, K., & Aghayani, E. (2013). Investigating the potential of electro-coagulation-flotation (ECF) process for pollutants removal from olive oil mill wastewater. *Journal of Application of Environmental Biological Sciences*, 3(3), 22–28.
- Zhao, S., Huang, G., Cheng, G., Wang, Y., & Fu, H. (2014). Hardness, COD and turbidity removals from produced water by electrocoagulation pretreatment prior to reverse osmosis membranes. *Desalination*, 344, 454–462.



The Impact of Vegetation on the Local Variations of Rainfall

Rohayu Haron Narashid^{1*}, Ruslan Rainis² and Zulyadini A. Rahaman³

¹Center of Studies for Surveying Science & Geomatics, Faculty of Architecture, Planning and Surveying, Universiti Teknologi MARA (UiTM) Perlis, 02600 Arau, Perlis, Malaysia

²Section of Geography, School of Humanities, Universiti Sains Malaysia (USM), 11800 Gelugor, Pulau Pinang, Malaysia

³Department of Geography and Environment, Faculty of Human Sciences, Universiti Pendidikan Sultan Idris (UPSI), 35900 Tanjung Malim, Perak, Malaysia

ABSTRACT

Rainfall is one of the microclimatic variables that vary with space. The changes in vegetation characteristics may influence the microclimate elements. To demonstrate rainfall variation due to vegetation, the relationship between rainfall and vegetation should be spatially investigated over a local scale. This paper aims to explore the impact of vegetation on local variations of rainfall based on Geographically Weighted Regression (GWR) approach. The global and local relationship between rainfall and the extracted Normalized Difference Vegetation Index (NDVI) of Landsat 7 ETM+ are quantitatively estimated in 2000 and 2011 within the northern and east coast regions of the Peninsular Malaysia. Based on 277 rainfall stations, the Moran's Index (Moran's I) spatial autocorrelation and Ordinary Least Square (OLS) - GWR methods were applied to analyse the rainfall spatial patterns and to determine rainfall spatial variation, respectively. It was found that, the rainfall spatial patterns exhibit small clustering patterns which leads to non-stationarity. This indicator supports the use of local regression approach in exploring the variation of rainfall due to vegetation. The R-Squared (R^2) from GWR (0.51 and 0.75) significantly improved the R^2 from OLS (0.01 and 0.04) for both years. The approach of GWR in the relationship between rainfall and vegetation provides findings on rainfall spatial variation on a local scale.

Keywords: GWR, Moran's I spatial autocorrelation, NDVI, OLS, rainfall spatial variation

ARTICLE INFO

Article history:

Received: 05 January 2017

Accepted: 17 January 2017

E-mail addresses:

rohayu@perlis.uitm.edu.my (Rohayu Haron Narashid),

rruslan@usm.my (Ruslan Rainis),

zully@fsk.upsi.edu.my (Zulyadini A. Rahaman)

*Corresponding Author

INTRODUCTION

In hydrological cycle, precipitation is the most important component that provides water to the surface of the earth. The variation of precipitation over land area is always related to the changes in global climate. Climate change induces the amount, intensity,

frequency and types of precipitation (Ackerman & Knox, 2011; Arnel, 2002; Ward & Trimble, 2004). At the micro-scale level, spatial variations of the earth's surface characteristics also has a significant impact on the spatial pattern and variations in rainfall.

Vegetation degradation is the result of human activities which led to Land Use Land Cover (LULC) and climate changes. In most cases, the amount of precipitation affects the vegetation patterns of the particular area. However, the effects of latent heat occurring due to deforestation also changes the precipitation pattern and distribution as reported by Avissar and Werth (2005). Thus, the spatial distribution of rainfall can also be influenced by vegetation loss due to land degradation e.g., deforestation and urbanization. As a result of deforestation, the biomass reduction and deterioration in forest area is the main factor for increasing heat. As mentioned by Morie (2007), vegetation degradation increases the frequency of flood since the spatial and temporal rainfall patterns are influenced by urbanization. It can also be seen as the impact of urbanization on the local precipitation for urban areas of developed countries as shown by Shepherd and Mote (2009), and Kishtawal, Niyogi, Tewari, Pielke and Shepherd (2010). Another study carried out by Nicholson (2000) also supported the impact of vegetation degradation on rainfall variation at a larger scale; since land surface features such as vegetation cover are an element that can be correlated with fluctuations in rainfall intensity. Thus, the impact of the rainfall local variability due to vegetation degradation should be investigated.

The earth observation monitoring system has been implemented to support the evidence of critical issues such as vegetation degradation. Remote sensing imagery is the most practical and applicable approach to describe the behaviour of vegetation covers over a wider range of spatial scale. Spectral vegetation indices are one useful approach used to assess the vegetation characteristics such as biomass, plant stress, plant health and crop productions as revealed by Jackson and Huete (1991). The most common vegetation index utilized to measure the amount of vegetation is Normalized Difference Vegetation Index (NDVI), which has been implemented by Tucker (1979) to monitor vegetation healthiness. Lillesand and Kiefer (2004) also mentioned that the health of green vegetation can be characterized based on the interaction of the energy in the spectral visible red (0.58-0.68 micrometres) and near-infrared (0.75-1.1 micrometres). Thus, NDVI algorithm of satellite images can be obtained from the ratio of the visible and near infrared band/channel (see equation 1).

$$NDVI = (NIR - RED) / (NIR + RED) \quad (1)$$

Usually, global spatial statistics are used to determine the spatial relationship between variables. Occurrences of variation, which can be determined by the non-stationary variables such as rainfall, are not completely interpreted and represented. The global spatial statistics in OLS only provides a general indicator to define the relationship between variables. Foody (2003), and Propastin, Kappas and Erasmi, (2008) found the OLS approach is only suitable to quantify the relationship at global and regional scales. However, significant hidden phenomena over location-based occurrences in the non-stationary variables are seldom proven (such as the relationship between rainfall and vegetation) since local variation is hardly measurable.

To show existence of spatial variation, local statistical approach such as the Geographically Weighted Regression (GWR) is more applicable. GWR provides an appropriate basis to

investigate the relationship between variables (Fotheringham, Brunson, & Charlton, 2002). A study carried out by Foody (2003) revealed that OLS regression model demonstrates poor descriptions in the relationship between NDVI of NOAA AVHRR imagery and rainfall depth when the results are found with minimum R^2 of 0.67 as compared to GWR regression model with the increased R^2 to 0.97. Yuan and Roy (2007) also revealed the improvement of GWR results compared to OLS in the relationship between NDVI of NOAA AVHRR imagery and rainfall with the increase R^2 value from 0.24 to 0.67. Research carried out by Usman, Yelwa, Gulumbe, Danbaba, and Nir (2013) proved that GWR a reliable approach in the prediction of the climatic variable such as rainfall and NDVI at local circumstances. Studies such as Zhao, Gao and Wang (2014), and Georganos (2016) are based on the influence of rainfall in the variations of NDVI where rainfall is selected as the exploratory variable.

Local varying relationship between microclimate elements and rainfall as founded in the vegetation-rainfall relationship can be used to define the impact of vegetation towards rainfall spatial variation. In this study, the impact of vegetation to rainfall spatial variation is analysed. The objectives are: (I) to examine the rainfall non-stationarity based on the rainfall spatial patterns; and (II) to determine the local variation in the relationship between rainfall and vegetation.

MATERIALS AND METHOD

Overall Methodology

The methodology of this study is illustrated in Figure 1, and begins with data acquisition, data processing, spatial patterns analysis, spatial variation analysis and maps to show the variation of rainfall. The main data are rainfall depths and Landsat 7 satellite images. As the first objective is to examine the spatial non-stationarity of rainfall, the spatial autocorrelation test has been carried out using Moran's I methods. This is followed by two (2) regression methods i.e. OLS and GWR to determine the rainfall spatial variation based on the relationship between rainfall and vegetation. The final results of this study are the parameter estimated maps represented by the distribution of rainfall spatial variation and their significant identifiable locations.

Study Areas and Datasets

The study area covers states in the (i) northern and (ii) east coast regions of Peninsular Malaysia, i.e. Perlis, Kedah, Pulau Pinang, Perak, Kelantan and Terengganu; an area of 60450 sq. km. The rainfall depths are obtained from 174 and 103 rainfall stations which contributed to 277 data. Figure 2 shows the location of the study areas and rainfall stations.

The main data used are rainfall depths acquired from the Malaysian Department of Irrigation and Drainage (DID). The rainfall descriptive statistics of the study area for 1996-2011 are shown in Table 1 and Figure 3, respectively. Most of the annual rainfall depths are above of the Malaysian Annual Average except in 1998, 2002, 2005 and 2006. Meanwhile, there are seven sets of annual rainfall in 1999, 2000, 2003, 2007, 2008, 2009 and 2011 are above of the long-term rainfall average. The highest and lowest annual rainfall depths are identified in 2009 (3149 mm) and 1998 (2413 mm), respectively.

Satellite images of Landsat 7 ETM+ are used to extract NDVI value of the sampling stations. All satellite images are downloaded from United States Geological Survey (USGS) website. Based on the selected study areas, seven scenes of satellite images have been acquired. The NDVI datasets have been produced in Erdas Imagine 2014 software. Figure 4 shows the selected scenes of Landsat 7 ETM+ used in study area.

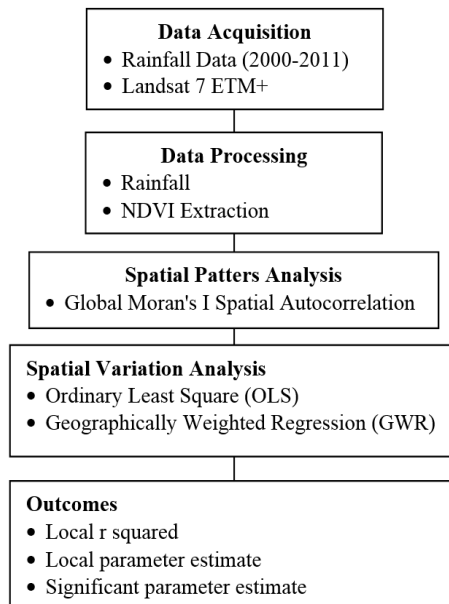


Figure 1. Overall methodology

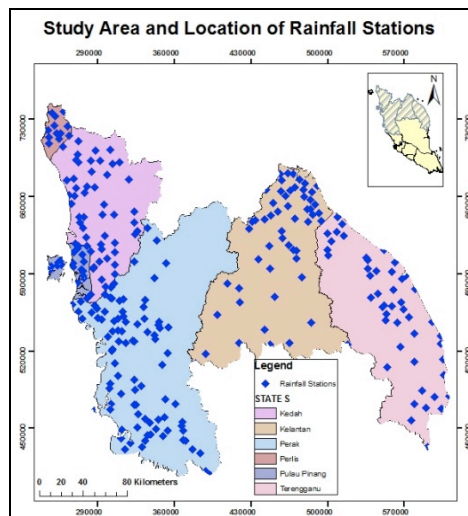


Figure 2. Map of study areas

Table 1
Summary of rainfall descriptive statistics 2000-2011

Year	Annual Average (mm)	Maximum (mm)	Minimum (mm)	Standard Deviation
2000	2591	5486	316	692
2001	2530	5992	702	871
2002	2413	5853	900	621
2003	2995	5726	926	753
2004	2818	5288	185	880
2005	2626	5222	984	894
2006	2347	4043	222	661
2007	2814	8712	1151	926
2008	2543	6464	172	760
2009	2435	4396	894	833
2010	2495	4719	831	636
2011	2734	5726	1083	701

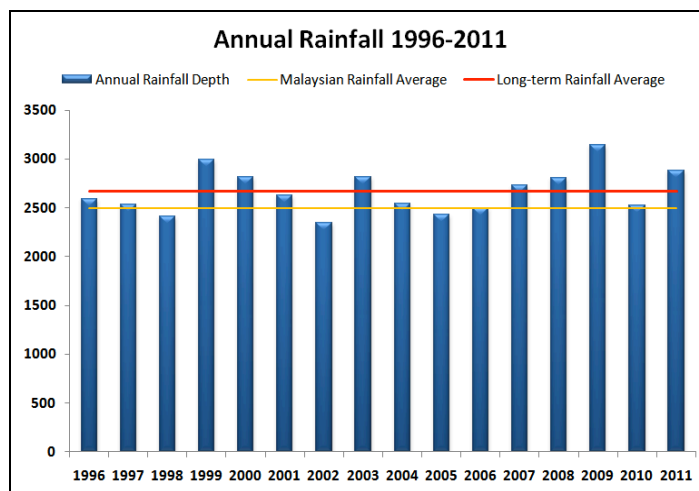


Figure 3. Average of rainfalls for 1996-2011

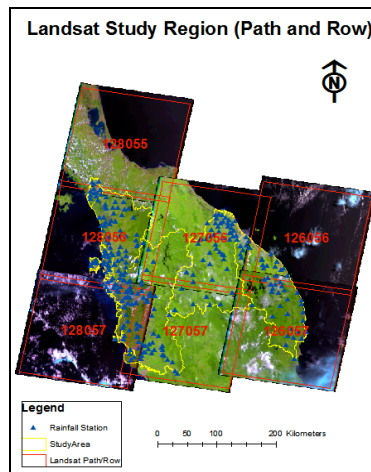


Figure 4. Landsat scenes of study area

Spatial Autocorrelation Tests

The homogenous or heterogeneity behaviour of the investigated variables can be defined via spatial autocorrelation test. In other words, spatial dependency between variable can be identified including the rainfall spatial dependency of that particular area. It can be related to the Tobler’s Law of geography in Tobler (1970) where it was stated as, ‘*everything is related to everything else, but near things are more related than distant things*’. According to Lloyd, 2011, spatial autocorrelation can be measured globally and locally with the concept of geographical versions of univariate statistics approaches. Spatial autocorrelation test based on Moran’s statistics was introduced by Moran (1950) to study the vegetation impact on rainfall spatial variation. In this study, the test was used to examine the significant spatial patterns of rainfall and help in the selection of the appropriate regression method for rainfall-NDVI relationship. The equation of Global Moran’s spatial autocorrelation coefficient, I is shown by Equation 2:

$$I = \frac{\sum_{i=1}^J n(R_i - \bar{R})(R_j - \bar{R})}{\sum_{i=1}^J J(R_i - \bar{R})^2} \quad (2)$$

Where n is the total number of areas, J is the total number of joints, R_i and R_j are the values of rainfall density for two contiguous areas, and \bar{R} is the overall mean of rainfall. Results of Global Moran’s I vary from -1 to +1. The interpretation of Moran’s I results is based on the computed P-Value and Z-Score.

Global and Local Regression Approach

The relationship between variables can be determined using regression analysis. The common technique used in regression analysis is simple linear regression such as Ordinary Least Square (OLS) method. This method can be used to demonstrate the relationship among variables at

global scale. In this study, the relationship between rainfall (R) and its influencing factors such as vegetation (y) can be estimated using Equation 3:

$$y = \beta_0 + \beta_1 R_1 + \dots + \beta_n R_n + \varepsilon \quad (3)$$

Where $\beta_0 - \beta_n$ are the estimated parameter that indicates the relationship between the y and R, and $R_1 - R_n$ values of rainfall density and ε is an error term.

Based on the global approach of OLS, the relationship between variables can locally be explored depending on the behaviour of the variables. A local regression technique called Geographically Weighted Regression (GWR) such as found in Brunsdon, Fotheringham and (1998), and Fotheringham, Brunsdon and Charlton (2002) has been widely used to locally explore the spatial non-stationarity of variables. The local variation in the relationship between rainfall (R) and other variables such as vegetation (y) can be investigated at individual location (μ, v) using GWR model such as shown in Equation 4:

$$y = \beta_0(\mu, v) + \beta_1(\mu, v)R_1 + \dots + \beta_n(\mu, v)R_n + \varepsilon \quad (4)$$

In this study, NDVI which represents the vegetation areas is assigned as the independent variable and rainfall density as the dependent variable. Both regression method i.e. OLS and GWR were used to demonstrate the relationship between rainfall and NDVI at global and local scales. All regression processes were carried out using GWR 4.0 application software developed by Nakaya, Fotheringham, Charlton and Brunsdon, (2009).

RESULTS AND DISCUSSION

Rainfall Spatial Patterns of Study Area

Rainfall spatial patterns have been demonstrated based on Moran's I spatial autocorrelation available in ArcGIS 10.1 software. The graph of rainfall spatial autocorrelation of 2000 and 2011 is shown in Table 2 and found to be clustered in the significant level of 0 (P-Value) with the critical value (Z-Score) of >2.58 . The Moran's Index has low values of 0.305 and 0.534, and Z values at 13.75 and 23.71 respectively. Indicating spatial patterns of rainfall in 2000 and 2011 have a small clustering pattern. This indicator supports the nature of rainfall non-stationarity such as mentioned by Brunsdon et al. (1998) that rainfall varies with location and are not homogeneous throughout the dataset. Thus, the exploration of rainfall-NDVI relationship at the local level can be performed based on the local regression technique, i.e. GWR.

Relationship between Rainfall and Vegetation

Based on two datasets of the study area, the global and local regression between rainfall and NDVI derived from Landsat 7 ETM+ are carried out. The results for both datasets (see Table 3) shows improvement of R^2 from OLS to GWR with the value of R^2 from OLS (0.01 and 0.51) to GWR (0.04 and 0.75) in 2000 and 2011, respectively. The indicator from Akaike Information Criterion (AIC) is used to assess the quality of the relationship established from

OLS and GWR. The results of AIC were found reliable where the AIC values from GWR are found to be lower than AIC of OLS. The map of local R^2 from GWR in 2000 and 2011 are shown in Figures 5(a) and 6(a), respectively.

The results of local parameter estimates of GWR are tabulated in Table 3. To visualize the relationship between rainfall-NDVI at a local scale, the results of GWR should be spatially distributed on the map based on two conditions as demonstrated by Matthews and Yang (2012). i.e., estimation of local coefficient (II) local t-value to identify the significance level.

Table 2
Summary of Global Moran's I annual rainfall between 2000 and 2011

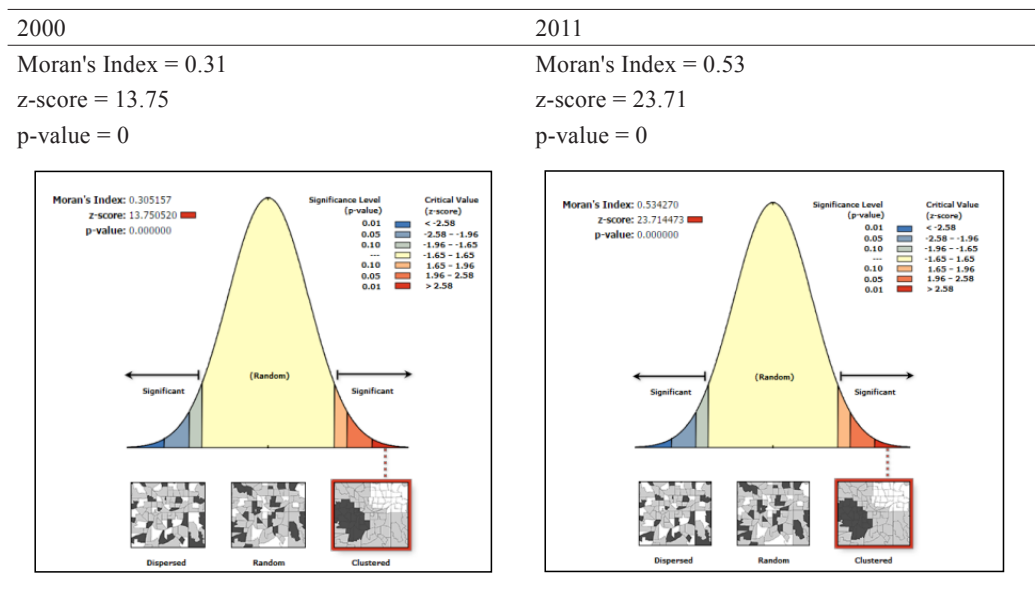


Table 3
 R^2 Parameter estimate (Global and Local)

Regression Methods	R^2		AIC	
	2000	2011	2000	2011
Global (OLS)	0.01	0.04	4544.05	4261.91
Local (GWR)	0.51	0.75	4459.72	3954.63
Local Parameter (Gwr)	Variables			
	Intercept		NDVI	
	2000	2011	2000	2011
Minimum	1784.24	187520	-2046.69	-1703.16
Lower Quartiles	2421.41	2336.19	-396.82	45.72
Median	2919.39	2779.63	167.45	207.15
Upper Quartiles	3170.79	3376.29	632.45	644.45
Maximum	3996.13	4620.92	3128.16	1702.03

The GWR maps of Rainfall-NDVI R^2 for 2000 and 2011 are shown in Figures 5(a) and 5(b), respectively. The NDVI estimated coefficient in the relationship between rainfall-NDVI are shown in Figures 5(c) and (d). With 95% level of confidence, the significant locations indicate 1-NDVI correlation in 2000 and 2011 as shown in Figures 6(a) and (b). In 2000, a total of 228 locations were found at 95% level of confidence. However, the locations with 95% confidence level in 2011 increased to 248 stations. It was found that most of the significant locations in 2000 are within the northern region with increases in the east coast region in 2011. Based on the associated local t values for NDVI of 2000 and 2011, the identified significant locations for both parameters are mapped as in Figure 7.

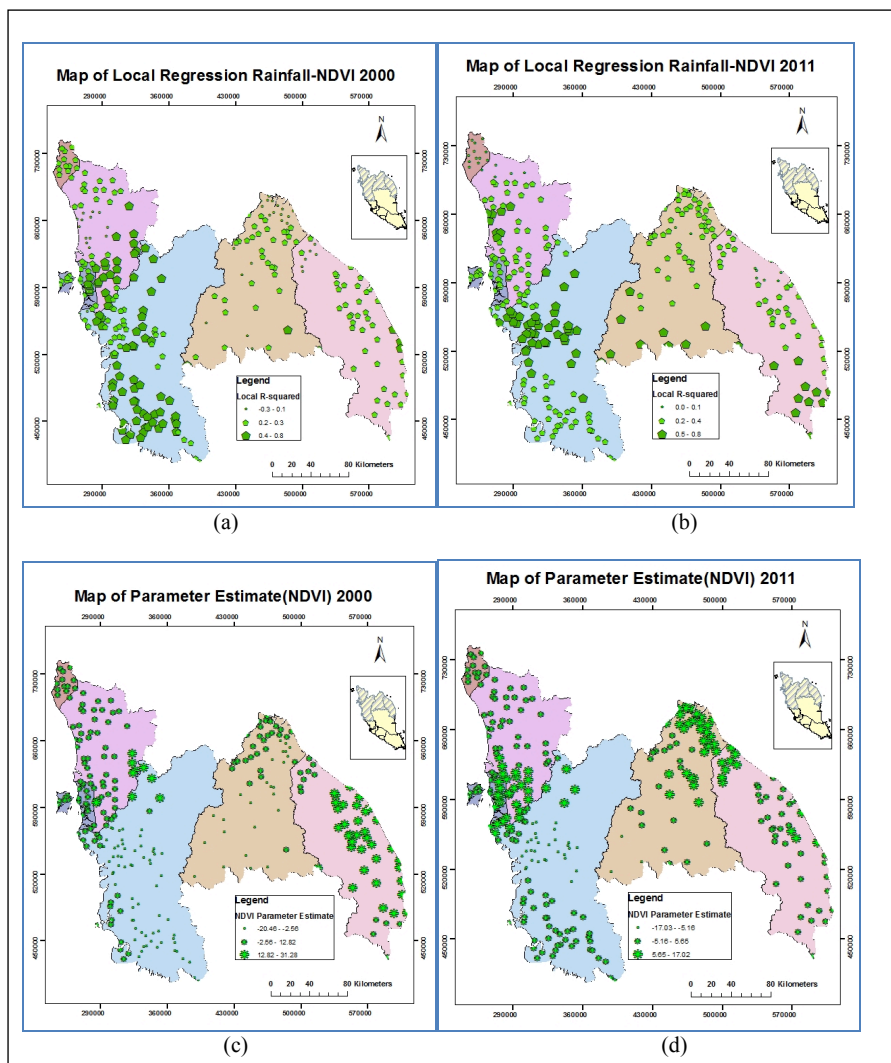


Figure 5. Maps of rainfall spatial variation in 2000 and 2001: (a) Rainfall-NDVI local regression in 2000; (b) Rainfall-NDVI local regression 2011; (c) NDVI estimated coefficient in 2000; and (d) NDVI estimated coefficient in 2011

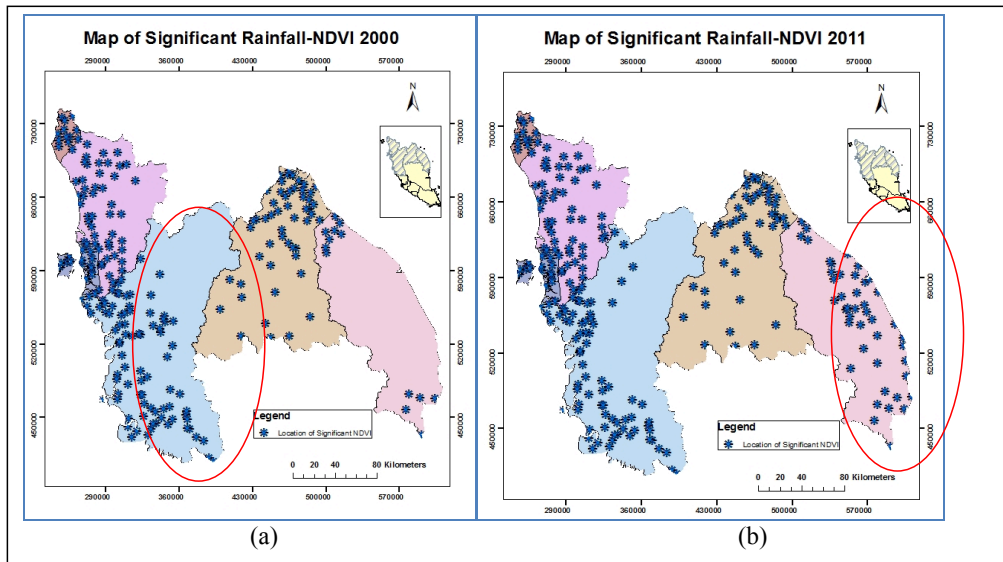


Figure 6. Significant maps based on t-value: (a) Significant rainfall-NDVI in 2000; and (b) Significant rainfall-NDVI in 2011

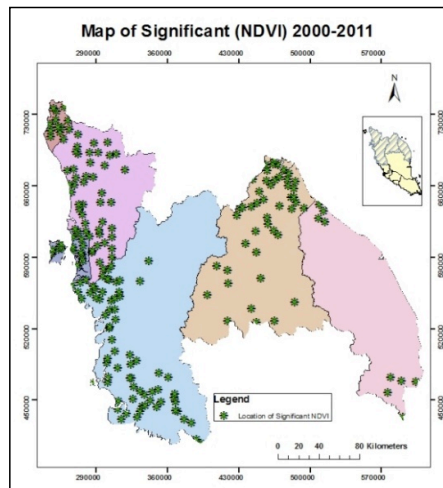


Figure 7. Map of significant locations of rainfall-NDVI for 2000 to 2011

CONCLUSION

Overall, this study has shown that rainfall spatial variation can be affected by surface characteristics such as vegetation. The findings support the evidence of heterogeneity of rainfall spatial variation, and the potential use of GWR to determine the spatial relationship between rainfall and vegetation. The use of remote sensing data from NDVI plays an important role in representing vegetation. The small clustering patterns of rainfall reveal the spatial non-stationarity and the existence of variation in rainfall. Thus, a spatial autocorrelation test

of the variable such as applied by using Moran's I spatial autocorrelation is necessary to be implemented to prove the non-stationarity of the phenomenon and to support the findings of local regression. In the relationship between rainfall and vegetation, the exploration of the significant variation is possible to be carried out using the local approach of GWR. At global, the spatial variation of rainfall may not be identified since the R^2 of OLS was found to be extremely low. However, there is a variation of rainfall at a location when there is strong and significant GWR R^2 . A realistic view of rainfall spatial variation can be depicted by local parameter estimation. The increase of the significant location in the rainfall-vegetation from 2000 to 2011 could be due to vegetation changes that affect rainfall variation in the study area while others indicated consistency in the rainfall-NDVI relationship. Thus, exploring the relationship between rainfall and vegetation at local scale reveals the impact of vegetation on rainfall spatial variation. Future work to investigate local relationship in rainfall spatial variation with combination of vegetation from NDVI and other earth surface characteristics needs to be done.

ACKNOWLEDGEMENTS

The authors are thankful to Universiti Teknologi MARA (UiTM) and Ministry of Higher Education (MOHE), Malaysia who funded the study. The Cooperation of Malaysian Drainage and Irrigation Department (DID) for providing rainfall data used in this study is also gratefully acknowledged.

REFERENCES

- Ackerman, S. A., & Knox, J. A. (2011). *Meteorology: Understanding the atmosphere* (3rd ed.). Sudbury: Mass: Jones & Bartlett Learning.
- Arnel, N. (2002). *Hydrology and global environmental change*. UK: Prentice Hall.
- Avisar, D. R., & Werth. (2005). Global hydroclimatological teleconnections resulting from tropical deforestation. *Journal of Hydrometeorol*, 6, 134–145.
- Brunsdon, C., Fotheringham, S., & Charlton, M. (1998). Geographically weighted regression. *Journal of the Royal Statistical Society: Series D (The Statistician)*, 47(3), 431-443.
- Dirmeyer, P. A., & Shukla, J. (1994) Albedo as a modulator of climate response to tropical deforestation, *Journal of Geophysical Research*, 99(10), 20–877.
- Foody, G. M. (2003). Geographical weighting as a further refinement to regression modelling: An example focused on the NDVI-rainfall relationship. *Remote Sensing Environment*, 88, 283–293.
- Fotheringham, A. S., Brunsdon, C., & Charlton, M. (2002). *Geographically Weighted Regression: The analysis of spatial varying relationships*. Chichester: Wiley.
- Georganos, S. (2016). *Exploring the spatial relationship between NDVI and rainfall in the semi-arid Sahel using geographically weighted regression* (Master Thesis), Lund University, Sweden.
- Jackson, R. D., & Huete, A. R. (1991). Interpreting vegetation indices. *Preventive Veterinary Medicine*, 11, 185 - 200.

- Kishtawal C. M., Niyogi, D., Tewari, M., Pielke, R. A., & Shepherd, J. M. (2010). Urbanization signature in the observed heavy rainfall climatology over India. *International Journal of Climatology*, 30(13), 1908–1916.
- Lloyd, C. D. (2011). *Local Models for Spatial Analysis* (2nd ed.) CRC Press.
- Lillesand, T., & Kiefer, R. W. (2004). *Remote Sensing and Image Interpretation*, (5th ed.). John Wiley, UK.
- Matthews S. A., & Yang, T. C. (2012). Mapping the results of local statistics. *Demographic Research*, 26, 151–166.
- Moran, P. A. P. (1950). Notes on continuous stochastic phenomena. *Biometrika*, 37(1), 17–23.
- Morie, N. D. (2007). *Land use and land cover changes in Harenna Forest, Bale Mountains National Park, Oromia National Regional State, Ethiopia* (Master Thesis), Addis Ababa University.
- Nakaya, T., Fotheringham, A. S., Charlton, M., & Brundson, C. (2009). Semiparametric geographically weighted generalised linear modelling in GWR 4.0. *Proceedings of the 10th International Conference on GeoComputation*, Sydney. Retrieved from http://www.geocomputation.org/2009/PDF/Nakaya_et_al.pdf
- Nicholson, S. E. (2000). The nature of rainfall variability over Africa on times scales of decades to millennia. *Global and Planetary Change*, 26, 137–158.
- Propastin, P., Kappas, M., & Erasmi, S. (2008). Application of geographically weighted regression to investigate the impact of scale on prediction uncertainty by modelling relationship between vegetation and climate. *International Journal of Spatial Data Infrastructures*, 3, 73–94.
- Shepherd J. M., & Mote T. L., (2009) Urban effects on rainfall variability: Potential implications for Georgia's water supply. *Proceedings of the 2009 Georgia Water Resources Conference* (pp. 253-258). The University of Georgia, Athens.
- Tobler, A. W. R. (1970). A computer movie simulating urban growth in the detroit region. *Economic Geography*, 46, 234–240. doi:10.1126/science.11.277.620
- Tucker, C. J. (1979). Red and photographic infrared linear combinations for monitoring vegetation. *Remote Sensing Environment*, 8(2), 127–150.
- Usman, U., Yelwa, S. A., Gulumbe, S. U., Danbaba, A., & Nir, R. (2013). Modelling relationship between NDVI and climatic variables using Geographically Weighted Regression. *Journal of Mathematical Sciences and Applications*, 1(2), 24–28. doi:10.12691/jmsa-1-2-2
- Ward, A. D., & Trimble, S. W. (2004). *Environmental Hydrology*, (2nd ed.). Boca Raton: CRC Press.
- Yuan, F., & Roy, S. S. (2007). Analysis of the relationship between NDVI and climate variables in Minnesota using Geographical Weighted Regression and spatial interpolation. *American Society for Photogrammetry and Remote Sensing - ASPRS Annual Conference 2007: Identifying Geospatial Solutions*, 2, 784-789.
- Zhao, Z., Gao, J., & Wang, Y. (2014). Exploring spatially variable relationships between NDVI and climatic factors in a transition zone using geographically weighted regression. *Theoretical and Applied Climatology*, 120(3-4), 507-519. doi:10.1007/s00704-014-1188-x

Evaluation of Cold In-Place Recycling Mix using Polymer Modified Asphalt Emulsion

Mohd Izzat Asyraf Mohamad Kamal^{1*}, Ahmad Kamil Arshad^{1,2} and Juraidah Ahmad¹

¹Faculty of Civil Engineering, Universiti Teknologi MARA (UiTM), 40450 Shah Alam, Selangor, Malaysia

²Institute for Infrastructure Engineering and Sustainability Management, Universiti Teknologi MARA (UiTM), 40200 Shah Alam, Selangor, Malaysia

ABSTRACT

This paper details a study conducted to evaluate the performance of cold in-place recycling (CIPR) using polymer modified asphalt emulsion (PMAE). The asphalt emulsion was modified using natural rubber latex (NRL). Four proportions of reclaimed asphalt pavement (RAP) which are 0%, 25%, 50% and 75% were mixed with natural aggregates and modified asphalt emulsion using natural rubber latex (NRL). The results showed that the optimum modified asphalt emulsion for each proportion of RAP decreased due to the increase in RAP content. Results obtained from Indirect Tensile Strength (ITS) and Uniaxial Compressive Strength (UCS) test for the mixes complied with the requirements of the Road Engineering Association of Malaysia (REAM) specifications. The unsoaked and soaked ITS values obtained were 0.2 MPa and 0.15 MPa respectively, and the minimum compressive strength of CIPR mix obtained was 0.7 MPa. Based on the evaluation of performance for the four RAP proportions, it was determined that 50% of RAP gave the best combination of the CIPR mixture.

Keywords: Cold-in-place recycling, natural rubber latex, polymer modified asphalt emulsion, reclaimed asphalt pavement

ARTICLE INFO

Article history:

Received: 05 January 2017

Accepted: 17 January 2017

E-mail addresses:

asyrafmohamadkamal@gmail.com

(Mohd Izzat Asyraf Mohamad Kamal),

ahmadkamil@salam.uitm.edu.my (Ahmad Kamil Arshad),

juraidah@salam.uitm.edu.my (Juraidah Ahmad)

*Corresponding Author

INTRODUCTION

CIPR is one of the most preferred structural rehabilitation techniques to be used by highway authorities. Among the advantages of CIPR are low cost, low energy consumption and eco-friendly. CIPR is a rehabilitation technique that reuses existing pavement materials in-situ without involving heat.

The stabilizing agent frequently used for CIPR mixture are cement, asphalt emulsion, and foamed asphalt, which binds the individual aggregate particles together. Previous studies conducted on polymer modified asphalt were carried out on hot mix asphalt (HMA). At present, there is a lack of research performed on CIPR using PMAE. PMAE is not only safe to apply and environmentally friendly, but it can also improve the properties of the CIPR mixture. The use of PMAE appears to result in a more evenly distributed polymer network compared to the use of hot polymer modified binders, and they therefore have greater potential to improve the pavement performance (Forbes, Haverkamp, Robertson, Bryant, & Bearsley, 2001). A mixture of cold recycled mixes with asphalt emulsion has a lower modulus compared to cold recycled mixes with foamed asphalt due to fewer voids and drop asphalt cohesion method in foamed mixes (Yan, Ni, Tao, & Jia, 2009). In China, the results of laboratory testing and field inspection showed that the CIPR with asphalt emulsion used as a stabilizing agent is a suitable technique for rehabilitation of deteriorated asphalt pavement (Yan, Ni, Yang, & Li, 2010).

The main competitive edge of Malaysia's integrated rubber industry compared to other producing countries is the comprehensive R&D which has largely enhanced Malaysia's productivity in terms of output per unit of land, labour and capital (Lembaga Getah Malaysia (LGM), 2016). In 2004, Ruggles mentioned that the first application of natural rubber latex in road construction took place in 1929 in Singapore, then the use of NRL in asphalt had been studied extensively in the 1950's and 1960's. He also stated that, at low temperatures the natural rubber reduces thermal cracking associated with bitumen. As a result of this, road surfaces are resistant to defects and durability of a road surface is increased markedly. Malithong and Thongpin (2010) revealed that by using PR vulcanized NRL to modified asphalt emulsion could serve as a standard asphalt emulsion and are applicable for highway construction.

RAP is widely used throughout the United States to preserve investment by reutilizing valuable aggregate assets. Federal Highway Administration (FHWA) and American Association of State Highway and Transportation Officials (AASHTO) support and promote the appropriate use of recycled materials in highway construction in public policy statements and the resolution of the AASHTO Standing Committee on Highways on "Use of Recycle Materials" (Caltrans, 2005). The use of RAP for highway construction offers many benefits including reduction in the use of virgin materials, reduce land use for disposal of RAP, and saving of energy used to transport RAP waste. Researcher found that incorporating RAP improves some engineering properties like tensile strength, rutting performance, fatigue and stiffness (Huang, Zhang, & Kinger, 2004). Based on a study conducted by Kim and Lee (2006), fine RAP gradation was found to produce higher Marshall Stability and indirect tensile strength values compared to coarser RAP gradation.

MATERIALS AND METHOD

The study focuses on the performance of recycled pavement with different combinations of RAP proportions and new aggregate. Asphalt emulsion was modified by adding NRL as the modifier. Asphalt emulsion used in this study meets the requirements of REAM specification for cold in-place recycling (Road Engineering Association of Malaysia, 2005).

The gradation used for this study was designed to fit in Superpave control points and also to meet REAM grading limit specification. Ordinary Portland Cement (OPC) was used as mineral filler in this mixture and the total amount used is 2% by weight of the combined aggregates as stated by REAM. The combination of aggregate and RAP used are 0:100 for 0% RAP, 25:75 for 25% RAP, 50:50 for 50% RAP, and 75:25 for 75% RAP.

The mix was prepared manually and materials were weighed by proportion consisting of natural aggregate, RAP, and cement and mixed with asphalt emulsion for 15 minutes or until all the aggregates are well coated. Then, the mix was compacted in a 100-mm diameter mould using the Superpave Gyratory Compactor (SGC) by applying 100 gyrations at 1.25° Gyratory angle. The compacted samples were cured at 40°C for 72 hours and allowed to cool to ambient temperature. Prior to testing for UCS and ITS test, the sample is conditioned in water at 25°C for 24 hours. ITS test and bulk density were conducted on the specimens at various PMAE content to obtain the optimum PMAE. The optimum value of ITS and bulk density was used to determine optimum PMAE for each percentage of RAP by averaging both optimum values. The specimens for the compacted recycled mix were then prepared at optimum emulsion content for every RAP proportion. The specimen was tested soaked and unsoaked for the ITS to obtain the Tensile Strength Retained (TSR) value for moisture susceptibility evaluation and UCS to identify its performance at different RAP contents. The TSR is calculated as follows:

$$\text{TSR} = \frac{S_{t \text{ soaked}}}{S_{t \text{ unsoaked}}} \times 100\% \quad (1)$$

where;

T_{SR} = Tensile Strength Retained

$S_{t \text{ soaked}}$ = tensile strength of soaked sample, kPa

$S_{t \text{ unsoaked}}$ = tensile strength of unsoaked sample, kPa

RESULTS AND DISCUSSION

Mix Design

This section focuses on the design of gradation and determination of optimum polymer modified asphalt emulsion. The process for this study was initiated by obtaining RAP and new aggregate. RAP materials were taken from the milled section of the old pavement under restoration (Klang Valley area) while the new aggregate was taken from the quarry (Kajang Rock Quarry). Natural rubber latex and asphalt emulsion were supplied by ACP-DMT Port Klang.

Gradation. Figure 1 shows the gradation that was designed to fit in Superpave control points and also to meet REAM grading limit specification. Ordinary Portland Cement was used as mineral filler in this mixture and the total amount used was 2% by weight of the combined aggregates as stated by the specification.

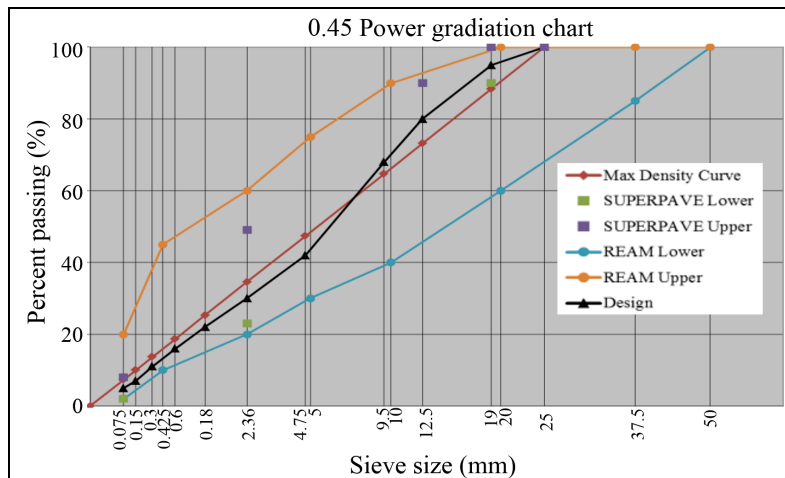


Figure 1. Design aggregate gradation

Optimum Polymer Modified Asphalt Emulsion. ITS test and bulk density at various polymer modified asphalt emulsion content was conducted on the specimens to obtain the optimum polymer modified asphalt emulsion. The optimum value of ITS and bulk density was used to determine the optimum PMAE for each percentage of RAP by averaging both optimum values. The variation of ITS with PMAE content is presented in Figure 2. It can be seen that the higher use of RAP in the mixture will give the least optimum PMAE; this may be due to the existence of bitumen in the RAP. Figure 3 shows the bulk density with total PMAE content. It was observed that, the optimum value of bulk density for each percentage of RAPs is nearly the same within the range of 5.0 to 5.2. This might be due to the same amount of cement used (2%) in all proportion of RAPs which did not affect the overall mixture.

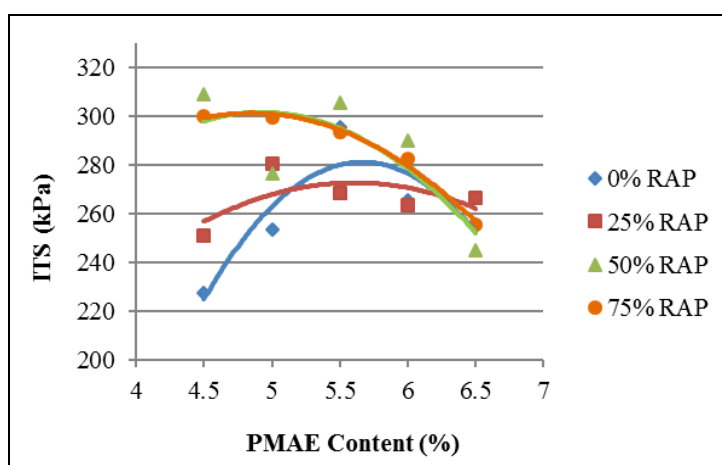


Figure 2. Variation of ITS value with total PMAE content

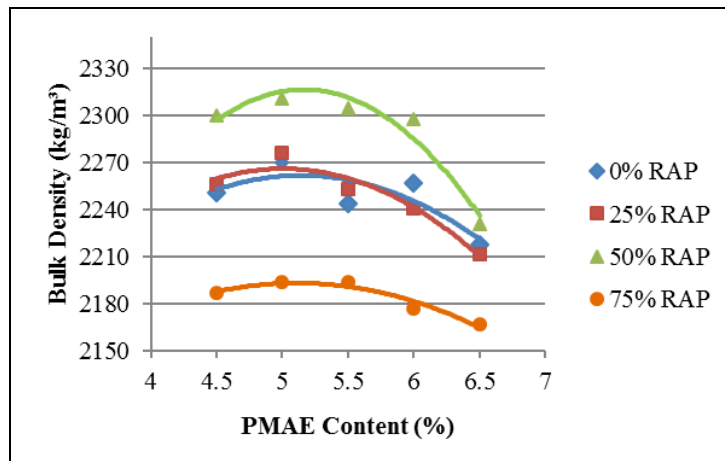


Figure 3. Variation of bulk density with total PMAE content

Table 1 presents the summary of the mix design test results for each percentage of RAPs conducted to obtain optimum PMAE. These optimum PMAE contents were used for the preparation of specimens for performance evaluation.

Table 1
Optimum PMAE for each percentage of RAP

Percentage of RAP	ITS	Bulk Density	Optimum PMAE
0%	5.7	5.1	5.4
25%	5.4	5.0	5.2
50%	4.9	5.2	5.1
75%	4.8	5.1	5.0

Performance Test

Effects of the Indirect Tensile Strength (ITS). Figure 4 shows the indirect tensile strength of unsoaked and soaked conditioned for each percentage of RAP. It can be seen that both unsoaked and soaked at different percentages of RAP complied with the minimum strength specified by the specification. ITS values for the unsoaked specimen at 75% RAP gave the highest ITS values of 0.275 MPa and for soaked specimen, the highest value is 0.236 MPa at 50% RAP. Mixes with 0%, 25%, and 75% RAP have relatively low tensile strength retained (TSR) values. Figure 5 shows the TSR for different percentages of RAP indicates that TSR increases to the optimum value as the RAP content is increased. The highest TSR value was observed for samples with 50% RAP. This is likely due to the amount of water absorbed into the natural aggregate particles that caused a decrease in the resistance to moisture susceptibility. A lower percentage of RAP has a greater capacity to absorb water, while for the mixture containing the higher percentage of RAP the existing bitumen in RAP coat the aggregate particles that prevents water to be absorbed. All samples exceeded the minimum TSR requirement of 75%.

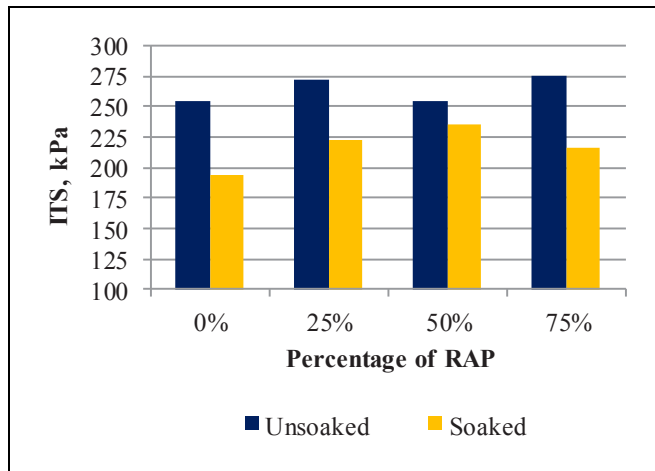


Figure 4. Indirect tensile strength for unsoaked and soaked conditioned for each percentage of RAP

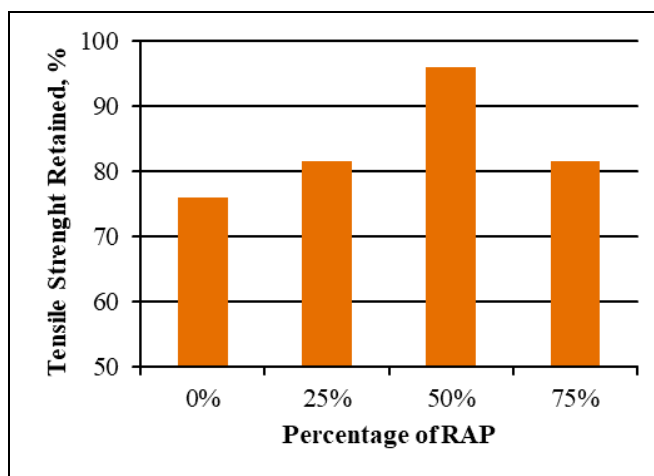


Figure 5. Indirect tensile strength retained (TSR) for each percentage of RAP

Effects of Unconfined Compression Strength (UCS). Figure 6 shows the results of UCS test prepared with different percentages of RAP. They show that the compression strength increases to the optimum value as the percentage of RAP increase, however a further increase in RAP percentage results in a decrease in compression strength. The highest compressive strength value is 2.963 MPa at 50% RAP and lowest at 75% RAP with UCS values of 2.436 MPa; this may be due to the lower fines aggregate content that can be mixed with the asphalt emulsion and therefore, the excess asphalt emulsion acts as a lubricant and reduces the strength. However, the UCS value for all samples exceeded the specification minimum UCS requirement of 0.7 MPa.

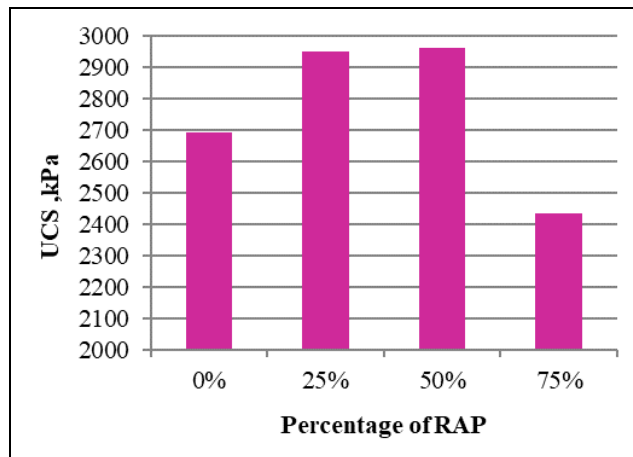


Figure 6. Unconfined compression strength for each percentage of RAP

CONCLUSION

The conclusion of the study are: (1) The value of optimum PMAE content is indirectly proportional to the percentage of RAP used in the mix due to the quantity of bitumen in the RAP providing enough strength to the mix; (2) Mix design procedures for CIPR with PMAE using Super pave gradation system and SGC is acceptable because they fulfilled the REAM specification requirements; and (3) The optimum RAP proportion is 50% because the results presented in ITS and UCS, 50% RAP proportion was the highest compared to other RAP proportions.

ACKNOWLEDGEMENTS

The authors would like to thank the Ministry of Science, Technology and Innovation (MOSTI) for funded this research, Geran Inisiatif Penyelidikan (GIP), Research Management Institute (RMI) UiTM Selangor, Faculty of Civil Engineering UiTM Selangor, Institute for Infrastructure Engineering and Sustainability Management (IIESM) UiTM Selangor and ACP-DMT Sdn. Bhd.

REFERENCES

- Caltrans, 2005. Feasibility of recycling rubber-modified paving materials. State of California Department of Transportation.
- Forbes, A., Haverkamp, R. G., Robertson, T., Bryant, J., & Bearsley, S. (2001). Studies of the microstructure of polymer-modified bitumen emulsions using confocal laser scanning microscopy. *Journal of Microscopy*, 204(3), 252-257.
- Huang, B., Zhang, Z., & Kinger, W. (2004). Fatigue crack characteristic of HMA mixtures containing RAP. In *Proceeding 5th Int. Conf. on Cracking in Pavements, RILEM* (pp. 631-638)
- Kim, Y., & Lee, H. D. (2006). Development of mix design procedure for cold in-place recycling with foamed asphalt. *Journal of Materials in Civil Engineering*, 18(1), 116-124.

- Lembaga Getah Malaysia (LGM). (2016). *The Malaysian Natural Rubber Industry*.
- Malithong, S., & Thongpin, C. (2010). The modification of asphalt emulsion using pre-vulcanized natural rubber latex for highway application. *Advanced Materials Research*, 2010(93-94), 639-642.
- Ruggles, C. S. (2004). The efficient use of environmentally-friendly natural rubber latex in road construction - past, present and the future. *Seminar "Rubber in Transport"*, Breda, The Netherlands, 9-12-2004.
- Road Engineering Association of Malaysia (REAM). (2005). *Specification for Cold in Place Recycling*.
- Yan, J., Ni, F., Tao, Z., & Jia, J. (2009). Development of asphalt emulsion cold in-place recycling specifications. *Asphalt Material Characterization, Accelerated Testing, and Highway Management*, 49-55. doi:10.1061/41042(349)7.
- Yan, J., Ni, F., Yang, M., & Li, J. (2010). An experimental study on fatigue properties of emulsion and foam cold recycled mixes. *Construction and Building Material*, 2151-2156. doi: 10.1016/j.conbuildmat.2010.04.044.

CFD Analysis on Indoor Temperature and Velocity: Effects of Incident Wind Angle and Outlet Position

Ali, N. M., Abd Razak, A.*, Mohamad, M. F. and Bahsan, R.

Faculty of Mechanical Engineering, Universiti Teknologi MARA (UiTM), 40450 Shah Alam, Selangor, Malaysia

ABSTRACT

Ventilation is the process of exchanging air in a closed space to provide good indoor air quality. Computational Fluid Dynamics (CFD) has become one of the most important and reliable tools to assess natural ventilation. This paper presents the effect of wind direction on temperature and velocity inside a building with outlet windows at leeward wall and side wall. The CFD simulation was performed using Reynolds-Average Navier-Stoke (RANS) approach with $k-\epsilon$ model. The selection of standard $k-\epsilon$ model is due to suitability of this model to perform the wind speed profile and temperature profile inside the building. Validation of cross-ventilation is performed based on earlier Particular Image Velocimetry (PIV) measurements and shows very minimal discrepancy between CFD and PIV result. The result of velocity and temperature shows that the wind speed and temperature inside a building strongly depends on the incident winds angle and outlet opening of the building.

Keywords: CFD, outflow position, temperature, velocity, wind direction

INTRODUCTION

Cross-ventilation and natural ventilation research has gained popularity in 1973 due to oil crisis (Kotani, Goto, Ohba, & Kurabuchi,

2009). Natural ventilation provides an opportunity to enhance comfort and health and as well as produce a sustainable built environment. Many researches have worked on how to improve the indoor natural ventilation performance by analysing different parameters and building characteristics. For example, Ohba et al. (2001) conducted a wind tunnel experiment to study the characteristic of air flow inside a simplified model with cross-opening. Furthermore, Seifert, Li, Axley and Rösler (2006), and Derakhshan and Shaker (2016) performed CFD analysis on an isolated building and investigated the

ARTICLE INFO

Article history:

Received: 05 January 2017

Accepted: 17 January 2017

E-mail addresses:

merlisa@salam.uitm.edu.my (Ali, N. M.),

azlirazak@salam.uitm.edu.my (Abd Razak, A.),

faizal3744@salam.uitm.edu.my (Mohamad M. F.),

rosnadiyah@salam.uitm.edu.my (Bahsan, R.)

*Corresponding Author

effect of building configuration (opening location, wall porosities, wall thickness and height to width ratio of opening) and wind direction on ventilation performance. Despite many studies using isolated building, Mohammad Kasim, Zaki, Mat Ali, Ikegaya and Abd Razak (2016) investigated the effect of surrounding building and various opening on ventilation performance. Additionally, there are few study on naturally ventilated building in more complex geometry such as terrace house (Liyana, Abd Razak, Wan Jabarudin, & Harith, 2015; Mohamad, Hagishima, Tanimoto, Ikegaya, & Omar, 2013), high rise apartment (Hyun, Park, & Augenbroe, 2008) and shopping mall (da Graça, Martins, & Horta, 2012).

Computational Fluid Dynamics (CFD) has been used extensively in the research of cross-ventilation of building as confirmed from many CFD studies published in the last 25 years (Jiang & Chen, 2002; Karava, Stathopoulos, & Athienitis, 2011; Kato, Murakami, Mochida, Akabayashi, & Tominaga, 1992; Perén, van Hooff, Leite, & Blocken, 2016; Ramponi & Blocken, 2012a; Seifert, Li, Axley, & Rösler, 2006; Tan & Glicksman, 2005). In CFD analysis, the accuracy and reliability of the turbulence model are the main concern. Large Eddy Simulation (LES) is basically more accurate than Reynolds-Averaged Navier-Stoke (RANS). However, 32 out of 39 studies on natural ventilation used RANS (Ramponi & Blocken, 2012b), proving that it is still the most popular approach. Due to this fact the present study uses RANS models for cross-ventilation flow in a simple isolated building.

In spite of the presence of numerous studies, the effect of various ventilation strategies, such as single-sided ventilation, cross-ventilation, effect of aspect ratio and outlet opening location on isolated building from a viewpoint temperature has not been fully explained. The present study aims to investigate the effect of incident wind angle and outlet position on temperature and velocity by means of CFD simulation. The paper is organized as follows: the numerical setup and validation is described in section 2 and results are presented in section 3. Finally, in section 4 is the conclusion.

MATERIALS AND METHOD

Model Geometry and Parameters

Table 1 shows the geometry of the model used in this simulation. A simulation model was sized at 7.0 m × 5.0 m × 4.0 m (length × width × height) as shown in Figure 1 and Figure 2. Two small openings with dimension 1 m × 1 m (width × height) were installed at the middle of windward, leeward wall (Figure 1) and adjacent wall (Figure 2). The wall porosities (the ratio of the area of opening to the area of the façade wall, *hereafter* w.p) is 5% except for side-wall outlet. For side-wall outlet the w.p is 3.6% due to the larger façade wall compared to the opening area. In this study, the effect of outlet location is more important than the effect of w.p, therefore the w.p change when the location changed. For both configurations the building consists of two florescent lamp which produced the heat emission of about 22 W/m² (standard heat emission as refer to Al-Shemmeri (2011)). Figure 3 shows the wind direction of both configurations. In this study, four incident wind angles are considered, $\theta = 0^\circ, 15^\circ, 30^\circ$ and 45° from the centre line of the horizontal plane (x-y plane).

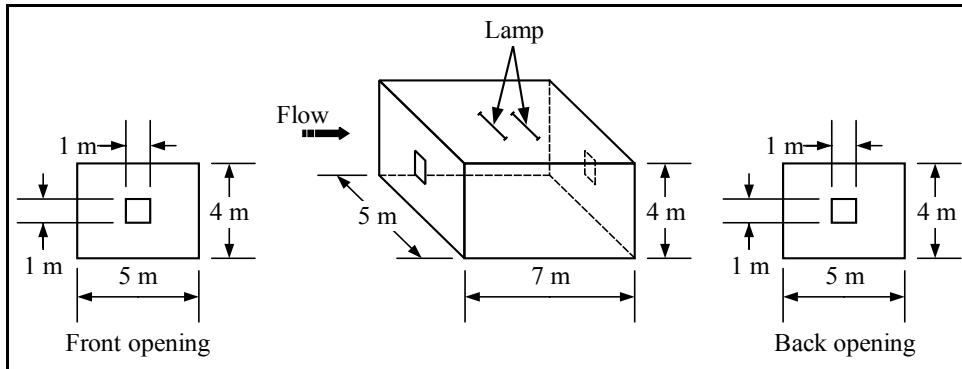


Figure 1. Schematic drawing of leeward outlet building

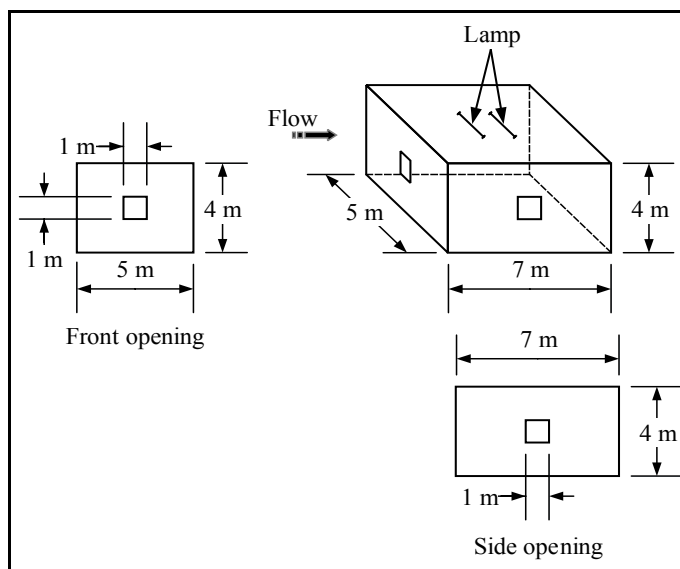


Figure 2. Schematic drawing of side-wall outlet building

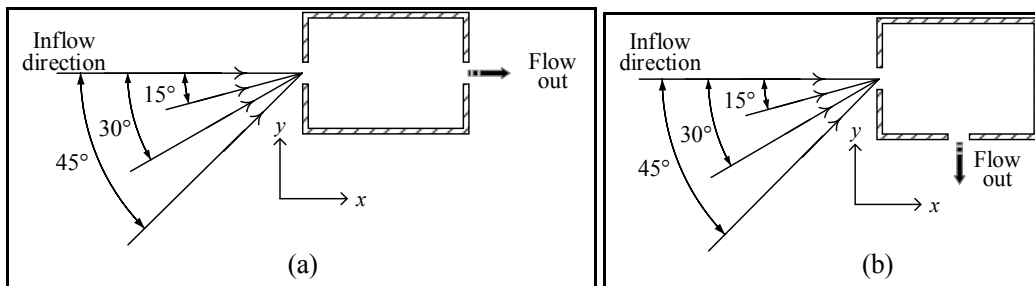


Figure 3. The angle of inflow direction and out flow direction: (a) leeward outlet; and (b) side-wall outlet

Table 1
Geometrical setup for simulation

Configuration	Case	Wind direction	Outlet opening size	Inlet wall porosity (A_{open}/A_{wall})	Outlet wall porosity (A_{open}/A_{wall})	Room dimension $D \times W \times H$
Leeward outlet	LW0	0°				7m × 5m × 4m
	LW15	15°	1m × 1m	5%	5%	
	LW30	30°				
	LW45	45°				
Side-wall outlet	SW0	0°				7m × 5m × 4m
	SW15	15°	1m × 1m	5%	3.6%	
	SW30	30°				
	SW45	45°				

Numerical Setup and Model Validation

Considering the computational cost and the requirement mentioned by Ramponi and Blocken (2012b), RANS approach of standard two-equation $k-\epsilon$ model was chosen for this study. The simulation were performed by commercial CFD software ANSYS Fluent (Fluent, 2015). All simulation was conducted in an isothermal condition where the effect of heat transfer from outside was negligible. The detail of mathematical model of governing equation can be found in (Cheung & Liu, 2011). The upstream mean wind speed (u_{ref}) is 3 m/s, which is to reflect the weak wind condition of Class 1 in Malaysia. The inlet temperature from the ambient air was measured as 306 K and applied at the inlet opening of the flow.

Figure 4 shows the horizontal profiles of the normalised stream wise mean wind speed, measured along the centreline of the building derived from the current analysis and PIV measurement (Karava, Stathopoulos, & Athienitis, 2011). The values were normalised using the upstream mean wind speed, u_{ref} . The profiles obtained by present simulation analysis show excellent agreement with the measurement data (Karava, Stathopoulos, & Athienitis, 2011) with small discrepancies near the inlet and outlet. This is due to the reduced reliability of PIV closed to the wall (Ramponi & Blocken, 2012a). The validation result indicated that the boundary condition and standard $k-\epsilon$ model selected in this study was sufficient to capture the flow profile inside the building with isolated condition. Further analysis was applied by adding the effect of heat load from the florescent lamp to investigate the temperature profile for thermal comfort study.

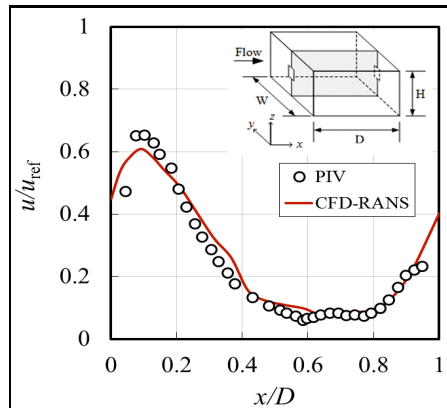


Figure 4. Validation result of streamwise wind speed ratio along the centreline: Comparison between PIV data from Karava, Stathopoulos and Athienitis (2011) and CFD result of current simulation setting

RESULTS AND DISCUSSION

Indoor Air Flow Characteristics

Figure 5 and Figure 6 show the normalised mean wind speed for four different incident wind angles which are 0° , 15° , 30° and 45° with leeward opening. The profile of normalised mean wind speed (u/u_{ref} , v/u_{ref} and w/u_{ref}) was measured along the centreline of stream wise (Figure 5(a) and Figure 6(a)), span wise (Figure 5(b) and Figure 6(b)) and vertical (Figure 5(c) and Figure 6(c)). The mean wind speed of the x -component for leeward wall outlet indicated that the variation was very small for all incident wind angles. This condition is similar to that of Meroney (2009). In the case of side-wall outlet, the variation was very large especially for 0° incident angle compared to other incident angles. The incident angle of 30° shows the lowest wind speed among other incident angles. Inconsistencies of x -component mean wind speed characteristic between these two configurations indicate that the mean wind speed is less dependent on incident angle for stream wise flow.

Normalised mean wind speed in y -component (v/u_{ref}) shows similar trend for $y/W > 0.3$ in both configurations. Huge discrepancies between these two configurations were observed closer to point B. This was due to the effect of the opening for side-wall configuration. The velocity close to point B was influenced by the flow that discharged from the building. In addition, we can conclude that the velocity of y -component is not only influenced by incident wind angle but by the position of opening as well. In y -component peak value of mean wind speed ratio of 45° incident angle is higher than other angle. However, for the z -component the 0° incident angle is more dominant. The same situation occurs in both configurations. Higher incident angle increases the velocity inside the building because the velocity which enters the building is tangent to the streamline along the y -axis. Therefore, it does not affect the vertical profile significantly as shown in Figure 5(c) and Figure 6(c).

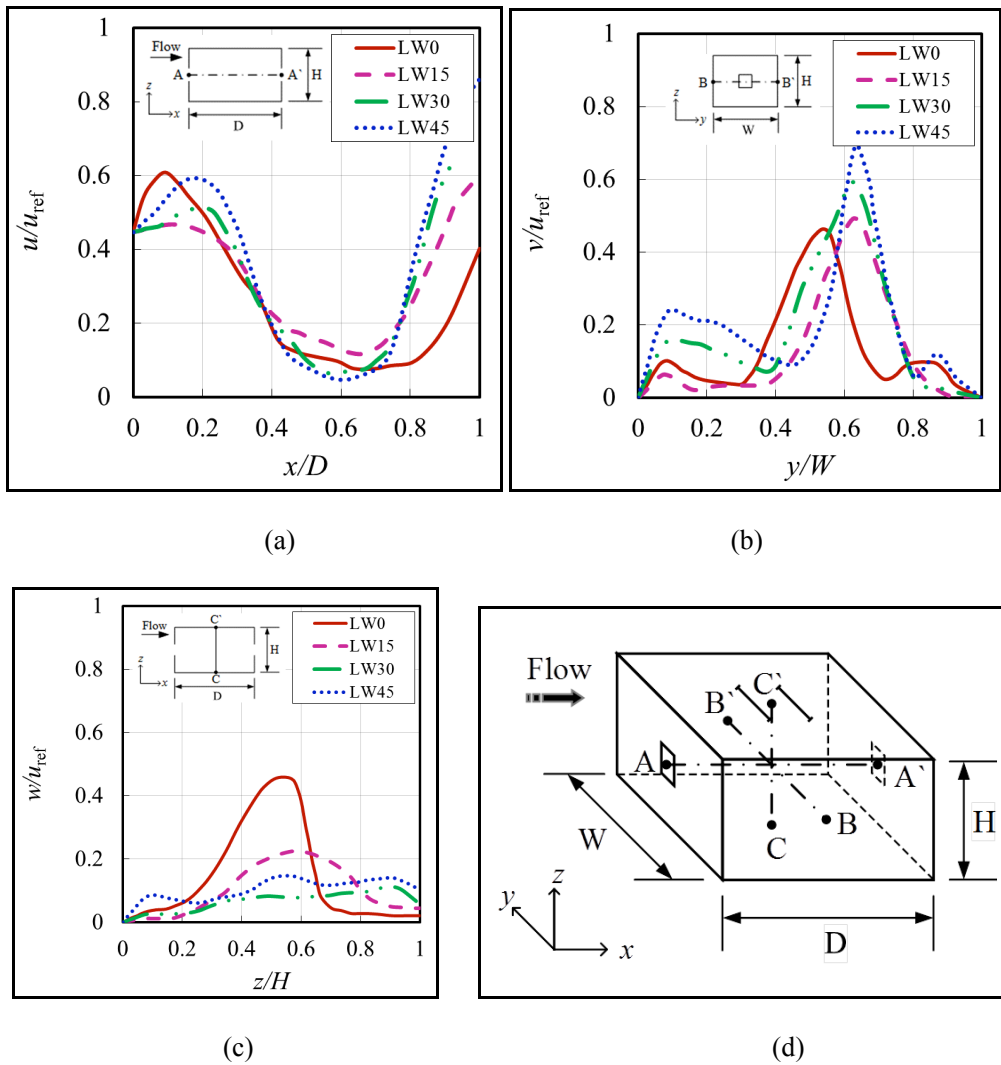


Figure 5. Analysis of normalised mean wind speed profile by variation of incident wind angle for leeward outlet configuration along: (a) stream wise centreline (A – A); (b) span wise centreline (B – B’); (c) vertical centreline (C – C’); and (d) is schematic diagram of measurement line

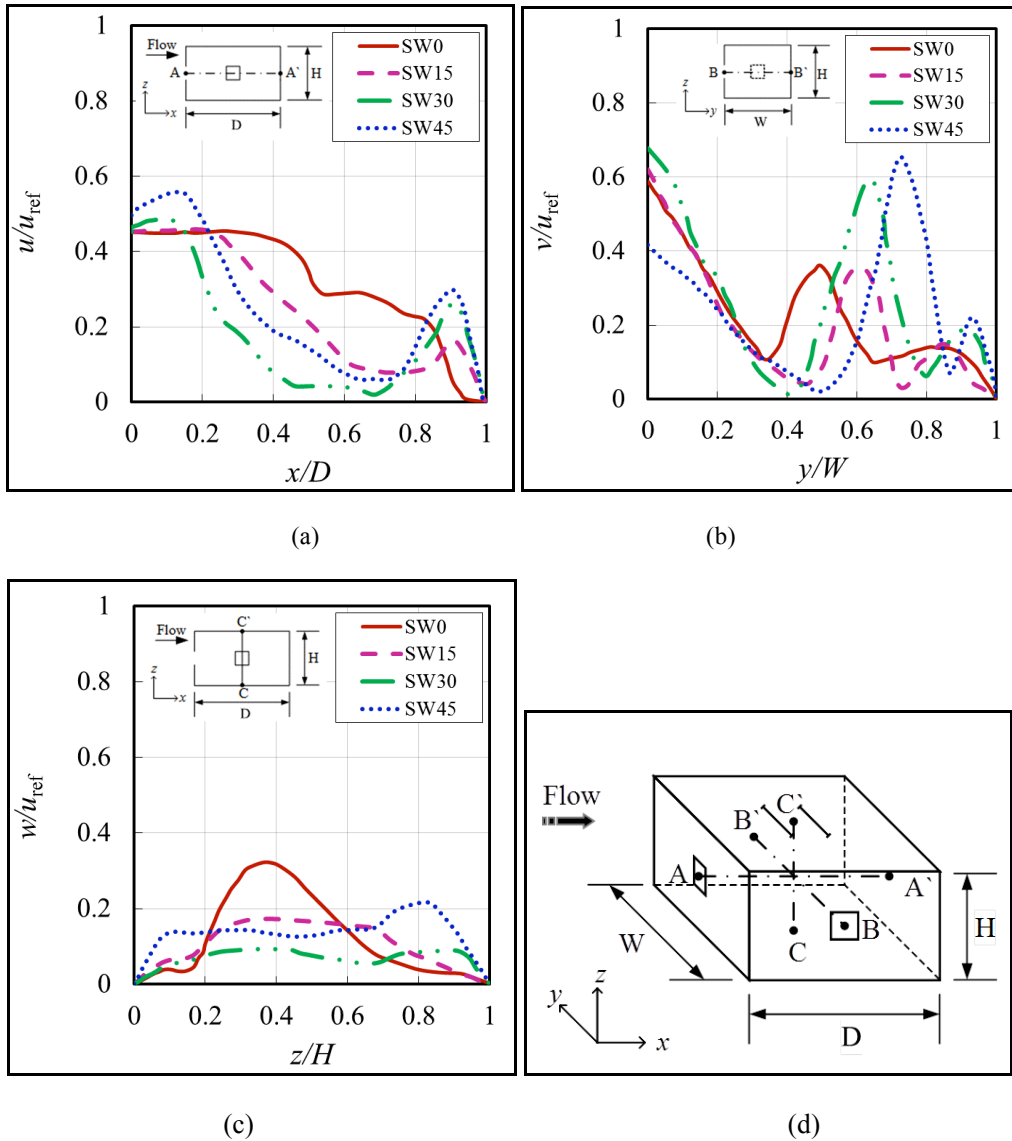


Figure 6. Analysis of wind speed ratio profile by variation of incident wind angle for side-wall outlet configuration along: (a) stream wise centreline (A – A’); (b) span wise centreline (B – B’); (c) vertical centreline (C – C’); and (d) is schematic diagram of measurement line

Normalised Temperature Profile

Effect of incident wind angle on temperature variation for leeward configuration. The qualitative analysis of normalised temperature profile inside the building with leeward outlet is presented in Figure 7. The normalised temperature profiles measured at the centreline of stream wise, span wise and vertical. The sensitivity test was conducted for incident wind angle $\theta = 0^\circ, 15^\circ, 30^\circ$ and 45° . The effect of incident wind angle differs accordingly to the x -, y - and

z -direction. Along the centreline of x -, y - and z -direction the lowest temperature recorded at $\theta = 0^\circ$. However, the highest temperature was captured at $\theta = 15^\circ$ for x -direction and $\theta = 0^\circ$ for y - and z -direction. The effect of heat gain from fluorescent lamp was the main contribution for these inconsistencies. In addition, the contribution of heat gain from fluorescent lamp significantly affects the temperature profile. Figure 5 (a – c) and Figure 7 (a – c) shows that the higher the wind speed the lower the temperature. This can be explain by the fact the wind speed is important tool in transferring heat and providing thermal comfort especially outdoors (Abd Razak, Hagishima, Awang Sa, & Zaki, 2016).

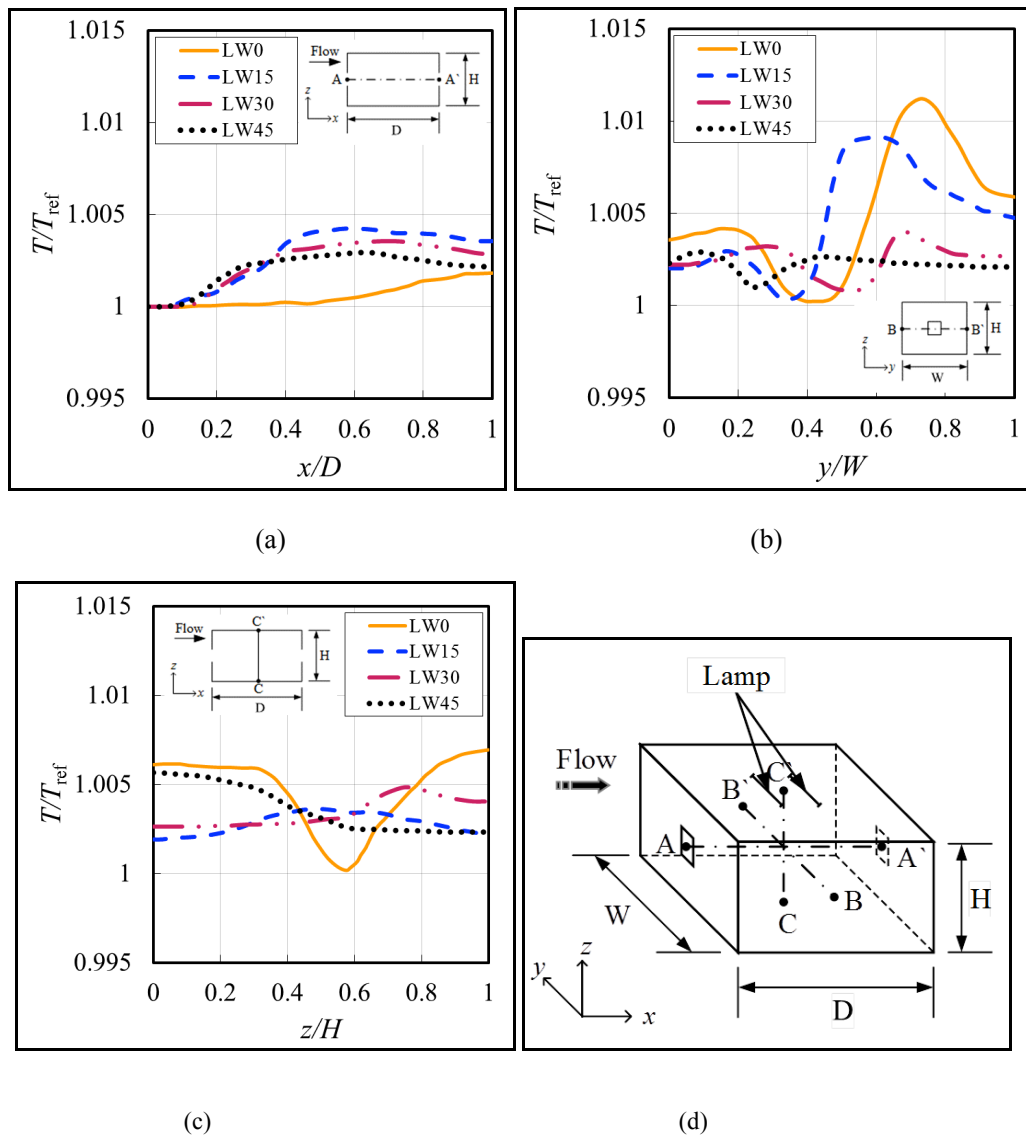


Figure 7. Analysis of temperature ratio profile by variation of incident wind angle for leeward outlet configuration along: (a) streamwise centreline (A – A); (b) spanwise centreline (B – B’); (c) vertical centreline (C – C’); and (d) is schematic diagram of measurement line

Effect of incident wind angle on temperature variation for side-wall configuration. This subsection investigated the effect of incident wind angle. Figure 8 shows the normalised temperature profile inside the building with side-wall outlet. In general effect of incident wind angle on temperature profile significant for vertical air temperature. Closer to the bottom (Figure 8(c)), the highest temperature occurs at $\theta = 15^\circ$ and the lowest temperature occurs at $\theta = 0^\circ$. When the air temperature reaches the top at $z/H = 1$, the highest temperature occurs when the $\theta = 30^\circ$ and the lowest temperature observed at $\theta = 45^\circ$. Figure 8a shows the temperature

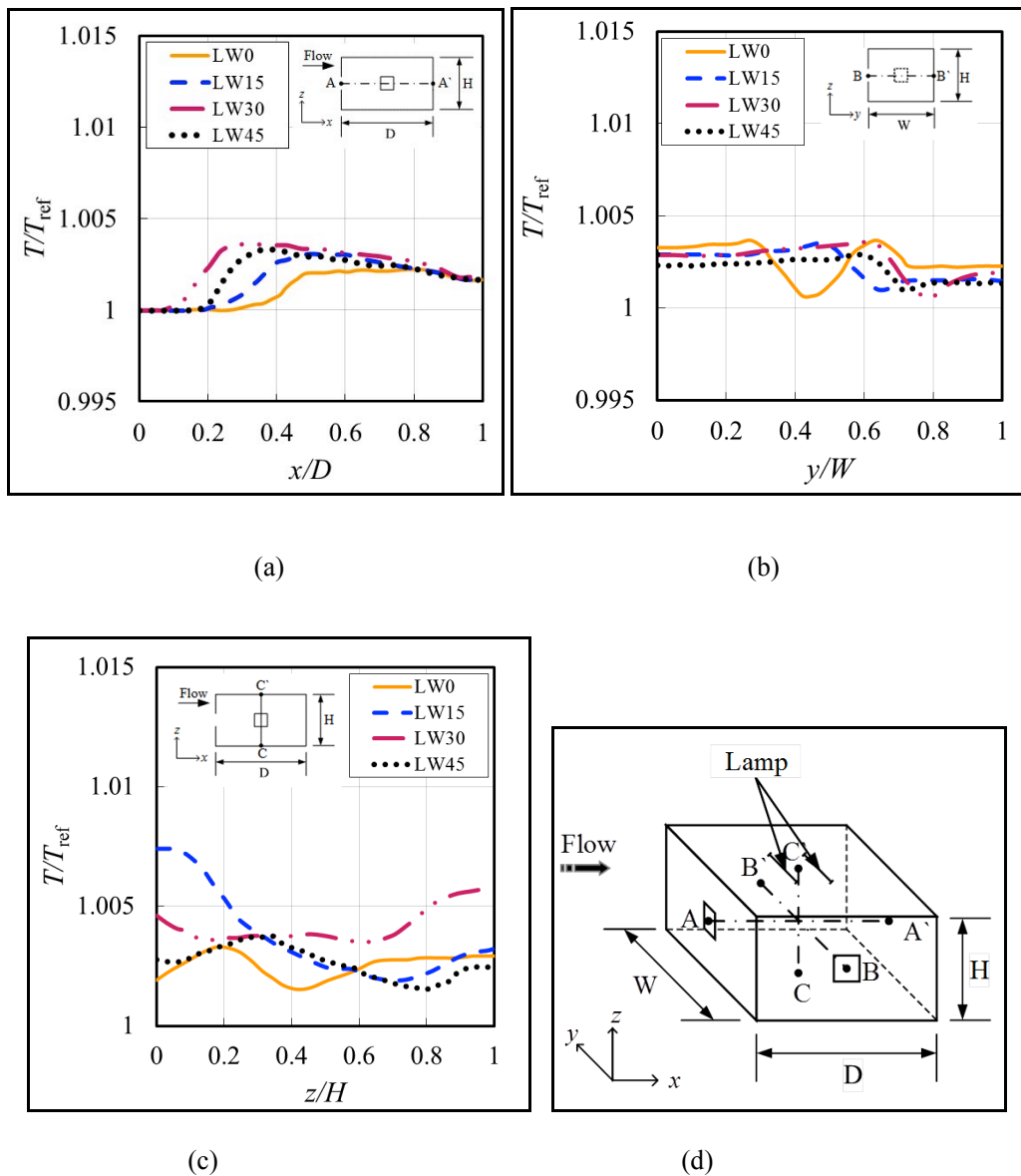


Figure 8. Analysis of temperature ratio profile by variation of incident wind angle for side-wall outlet configuration along: (a) streamwise centreline (A – A); (b) spanwise centreline (B – B’); (c) vertical centreline (C – C’); and (d) is schematic diagram of measurement line

variation on incident wind angle at $0.2 < x/D < 0.5$. Furthermore, along the span wise (Figure 8(b)) the $\theta = 0^\circ$ the temperature drops when it faces incoming flow and rises before it declines to constant temperature until reaches the wall. Similarly, for the leeward outlet configuration, the temperature was strongly influenced by wind speed. As example, the temperature along the ventilation flow path was found to be lower compared to surrounding.

Comparison between opening configurations on temperature variation. Figures 7 and Figure 8 show the temperature variation for two different opening configurations (Table 1) namely leeward outlet and side-wall outlet respectively. Generally, the side-wall outlet has better ventilation performance compared to leeward outlet. Quantitative analysis on the temperature values indicated that side-wall outlet has lower temperature along x -, y - and z -direction compared to leeward outlet. Even though the opening-to-wall ratio for side-wall outlet lower than leeward wall, this parameter was not significant.

CONCLUSION

The effects of incident wind angle and outlet position were examined in this study by solving the cross-ventilation using RANS approach with standard k - ϵ model. This study leads to the following conclusions: (1) The leeward outlet is more suitable for the purpose of pollutant removal but for thermal comfort the side-wall is more suitable; (2) The incident wind angle with $\theta = 45^\circ$ provided a better solution for thermal comfort compared to other incident angle. In addition, $\theta = 0^\circ$ can be considered as alternative for the case of inlet and outlet opening parallel as shown in Figure 2; (3) The temperature profile inside the building has strong correlation with mean wind speed that entering and leaving the building (ventilation rate); and (4) Current finding can be used as preliminary evaluation in building design of the inlet and outlet of cross-ventilation in a naturally ventilated building.

ACKNOWLEDGEMENTS

The authors of this work would like to express their sincere gratitude to Faculty of Mechanical Engineering, Universiti Teknologi MARA (UiTM) for facilitating this research. This research was financially supported by grant-in aid for scientific research (600-RMI/FRGS 5/3 (87/2015)) from the Ministry of Education, Malaysia.

REFERENCES

- Abd Razak, A., Hagishima, A., Awang Sa, Z. A., & Zaki, S. A. (2016). Progress in wind environment and outdoor air ventilation at pedestrian level in urban area. *Applied Mechanics and Materials*, 819, 236-240.
- Al-Shemmeri, T. (2011). *Energy Audits: A Workbook for Energy Management in Buildings*. Wiley.
- Cheung, J. O., & Liu, C.-H. (2011). CFD simulations of natural ventilation behaviour in high-rise buildings in regular and staggered arrangements at various spacings. *Energy and Buildings*, 43(5), 1149-1158.

- da Graça, G. C., Martins, N. R., & Horta, C. S. (2012). Thermal and airflow simulation of a naturally ventilated shopping mall. *Energy and Buildings*, 50, 177-188.
- Derakhshan, S., & Shaker, A. (2016). Numerical study of the cross-ventilation of an isolated building with different opening aspect ratios and locations for various wind directions. *International Journal of Ventilation*, 1-19. doi: 10.1080/14733315.2016.1252146
- Fluent. (2015). Ansys – Fluent User’s Guide. Retrieved on 30 October, 2015, from http://www.arc.vt.edu/ansys_help/flu_ug/flu_ug.html
- Hyun, S., Park, C., & Augenbroe, G. (2008). Analysis of uncertainty in natural ventilation predictions of high-rise apartment buildings. *Building Services Engineering Research and Technology*, 29(4), 311-326.
- Jiang, Y., & Chen, Q. (2002). Effect of fluctuating wind direction on cross natural ventilation in buildings from large eddy simulation. *Building and Environment*, 37(4), 379-386.
- Karava, P., Stathopoulos, T., & Athienitis, A. (2011). Airflow assessment in cross-ventilated buildings with operable façade elements. *Building and Environment*, 46(1), 266-279.
- Kato, S., Murakami, S., Mochida, A., Akabayashi, S. I., & Tominaga, Y. (1992). Velocity-pressure field of cross ventilation with open windows analyzed by wind tunnel and numerical simulation. *Journal of Wind Engineering and Industrial Aerodynamics*, 44(1), 2575-2586.
- Kotani, H., Goto, T., Ohba, M., & Kurabuchi, T. (2009). Review of Cross-ventilation research papers-from the working group for natural ventilation and cross-ventilation of the architectural institute of japan. *International Journal of Ventilation*, 8(3), 233-241.
- Liyana, T., Abd Razak, A., Wan Jabarudin, W. T., & Harith, Z. Y. H. (2015). Cross ventilation analysis on the effect of setback distance of a terraced house using PIV. *Jurnal Teknologi*, 76(5).
- Meroney, R. N. (2009). CFD prediction of airflow in buildings for natural ventilation. *Proceedings of the Eleventh Americas Conference on Wind Engineering, Puerto Rico*.
- Mohamad, M. F., Hagishima, A., Tanimoto, J., Ikegaya, N., & Omar, A. R. (2013). Wind-induced natural ventilation in typical single storey terraced houses in Malaysia. *13th Conference of International Building Performance Simulation Association*.
- Mohammad Kasim, N. F., Zaki, S. A., Mat Ali, M. S., Ikegaya, N., & Abd Razak, A. (2016). Computational study on the influence of different opening position on wind-induced natural ventilation in urban building of cubical array. *4th International Conference on Countermeasures to Urban Heat Island*.
- Ohba, M., Irie, K., & Kurabuchi, T. (2001). Study on airflow characteristics inside and outside a cross-ventilation model, and ventilation flow rates using wind tunnel experiments. *Journal of Wind Engineering and Industrial Aerodynamics*, 89(14), 1513-1524.
- Perén, J. I., van Hooff, T., Leite, B., & Blocken, B. (2016). CFD simulation of wind-driven upward cross ventilation and its enhancement in long buildings: Impact of single-span versus double-span leeward sawtooth roof and opening ratio. *Building and Environment*, 96, 142-156.
- Ramponi, R., & Blocken, B. (2012a). CFD simulation of cross-ventilation flow for different isolated building configurations: Validation with wind tunnel measurements and analysis of physical and numerical diffusion effects. *Journal of Wind Engineering and Industrial Aerodynamics*, 104, 408-418.

- Ramponi, R., & Blocken, B. (2012b). CFD simulation of cross-ventilation for a generic isolated building: Impact of computational parameters. *Building and Environment*, 53, 34-48.
- Seifert, J., Li, Y., Axley, J., & Rösler, M. (2006). Calculation of wind-driven cross ventilation in buildings with large openings. *Journal of Wind Engineering and Industrial Aerodynamics*, 94(12), 925-947.
- Tan, G., & Glicksman, L. R. (2005). Application of integrating multi-zone model with CFD simulation to natural ventilation prediction. *Energy and Buildings*, 37(10), 1049-1057.

Investigation of the Injection Moulding Plastic Flows Behaviour of PET Cylindrical Containers with Multiple-Cavity Mould

Najiy Rizal Suriani Rizal, Muhammad Ameer Rosman, Aidah Jumahat* and Noriah Yusoff

Faculty of Mechanical Engineering, Universiti Teknologi MARA (UiTM), 40450 Shah Alam, Selangor, Malaysia

ABSTRACT

The study aims to investigate the effect of injection moulding parameters on plastic flows behaviour of the multiple-cavity polyethylene terephthalate (PET) cylindrical containers via injection moulding process. The motivation of this study is to present an alternative manufacturing solution to make cylindrical type containers that are commonly used in packaging beverages, such as the 330 ml standard size for packaging carbonated soft drink. The PET cylindrical container was modelled using CATIA drawing software and the injection moulding simulation process was done via Moldflow software. The investigation was done by varying two significant moulding parameters; the material melt temperature and the mould temperature. The effects of these two parameters on the PET plastic flow behaviour were studied. In particular, the simulations of the model were analysed and focused on the mould filling time as well as the moulded PET cylindrical container's shrinkage occurrence. Three types of mould cavities structure were understudied; single-cavity, four-cavity and eight-cavity. Results show that the eight-cavity mould yielded higher production rate. The simulation results indicated that the production rate of 4-cavity and 8-cavity mould increased by 258.5% and 578.8% respectively. It was observed by increasing the melting temperature, the mould filling time is shorter and as a result, the production rate has increased by 7.75% per °C. But with this Moldflow setting, the volumetric shrinkage and the maximum deflection have been significantly affected; increased by 23.15% and 29.26% respectively. The mould filling time and maximum deflection did not show a steady trend line however, the volumetric shrinkage increased by 7.28% per °C.

Keywords: Injection moulding, mould filling time, moulding parameters, polyethylene terephthalate, shrinkage

ARTICLE INFO

Article history:

Received: 05 January 2017

Accepted: 17 January 2017

E-mail addresses:

najiyrizal@gmail.com (Najiy Rizal Suriani Rizal),
m.ameerrosman@gmail.com (Muhammad Ameer Rosman),
aidahjumahat@salam.uitm.edu.my (Aidah Jumahat),
noriahhyusoff@salam.uitm.edu.my (Noriah Yusoff)

*Corresponding Author

INTRODUCTION

The World Packaging Organisation (WPO) found that plastic packaging is replacing glass

and metals. It was highlighted by Demirel, Yaraş and Elçiçek (2011) that plastic industries are currently trying to improve their capabilities of packaging in order to take over the packaging of alcoholic drinks which is a challenge for plastic materials. The main challenge is to be able to contain the product for the required shelf life.

PET consists of multiple long fibre strands of polymers that are produced from continuous melt-phase polymerisation process between terephthalic acid (TA) and ethylene glycol (EG) as explained by Byrne, Ward, Hughes and Cullen (2011). The crystallinity of PET ranges from amorphous to very crystalline depending on the PET processing method. Different levels of crystallinity and morphology of PET affects the product properties. The level of crystallisation is induced thermally when the polymer is heated above the T_g and rapidly quenched (Demirel, Yaraş, & Elçiçek, 2011). A study was conducted using Differential Scanning Calorimetry (DSC) to determine the PET glass transition temperature T_g and melting temperature T_m . The obtained results were 77°C T_g and 252°C T_m , respectively with the degradation temperature of 435°C (Byrne, Ward, Hughes, & Cullen, 2011).

Safety concerns regarding the use of PET in food and beverage packaging have been clarified by various agencies around the world including European Union's (EU) European Food Safety Authority, Health Canada and the U.S. Food & Drug Administration. Bach et al. (2013) showed that under worst case scenario, when the water in PET bottles was exposed to a temperature of 60°C for 10 days, it did contain formaldehyde, acetaldehyde and antimony but the concentrations are far below the specific migration limit (SML). Another research also showed that the quality of the water was not affected by the photochemical ageing of the bottles and if any aldehyde or other organic photoproduct were detected at all, they would be far below the limits of safe drinking (Wegelin et al., 2001).

The development of injection moulding has enabled not only for plastics but also for other materials, such as metals, glass and ceramics, to be melted and injected into moulds. Injection moulding is one of the most important manufacturing processes for polymers because of its processing versatility in producing polymer products with complex and nearly limitless designs, low production energy, low production cost, light weight moulded parts, high production rate, minimal waste, high dimensional steadiness, and good mechanical properties (Chen, Chuang, Hsiao, & Tsai, 2009; Oktem, Erzurumlu, & Uzman, 2007; Song, Liu, Wang, Yu, & Zhao, 2007).

The material requires sufficient amount of heat in order to completely melt in the heating barrel. The melting temperature greatly affects the material flow ability, flow rate, and curing time (Huang & Tai, 2001). Dimensional shrinkage is one of the most critical dimensional flaws resulting from various factors of injection moulding process (Lal & Vasudevan, 2013; Oktem, Erzurumlu, & Uzman, 2007). According to Jansen, Dijkand and Husselman (1998), Nagahanumaiah (2009), and Mehat, Kamaruddin and Othman (2013), one of the main factors contributing to shrinkage is the melting temperature of the polymer. The result of higher packing pressure forces the material to completely fill in the mould during injection process, thus compensating for the shrinkage effect (Zhil'tsova, Oliveira, & Ferreira, 2009). Warpage is defined as the distortion or deflection of a moulded part after it is being ejected off the mould; due to the shrinkage variations within (Reddy & Kumar, 2009). Although the melting temperature and the pressure were mentioned to be the most significant in causing

warpage, many studies have taken mould temperature into account to determine warpage (Chen, Chuang, Hsiao, & Tsai, 2009; Huang & Tai, 2001; Kong, Kim, Member, & Yuen, 2003; Koszkuł & Nabialek, 2007; Kurataran, Ozcelik, & Erzurumlu, 2005; Oktem, Erzurumlu, & Uzman, 2007; Ozcelik & Sonat, 2009). Chen, Chuang, Hsiao and Tsai (2009) conducted a study using Moldflow simulation software in evaluating the characteristics of plastic flow in modern injection moulding process and concluded that by using computer simulation analysis a satisfactory representation of the real procedure can lead to better manufacturing design process.

The range of materials' melting temperature used during the injection moulding process mainly depends on their property. Theoretically, higher melting temperature increases the fluidity of the melted material but, all material will degrade at certain temperature (Sha, Dimov, Griffiths, & Packianther, 2007). From different sources of PET manufacturers, the bottle grade PET pellets will be heated at 5°C to 20°C above the minimum required temperature to remove the moisture content in the compound. This step will ensure all the pellets filled into the heating barrel are completely and evenly melted. The mould temperature also plays an important role in maintaining the fluidity of the melt once it passes through the nozzle from the heating cylinders or barrels. Taking into considerations of different types of PET and part thickness, industries had recommended a range of 90°C to 120°C of mould temperatures for injection moulding process (Sha, Dimov, Griffiths, & Packianther, 2007). This study aims to investigate the potential of producing and utilizing the PET 330 ml size cylindrical container in packaging beverages commonly contained in aluminium cans by investigating the effects of the moulding parameters on the plastic flow behaviour.

MATERIALS AND METHOD

The main idea of this design is to propose an alternative packaging method for the 330-ml size carbonated soft drinks using PET material. The concept design or dimensional specifications were benchmarked against the cans suppliers and manufactures. The common 330 ml size was chosen, thus the relevant specifications for the mould design process was gathered and analysed. Also, the ability of the PET cylindrical container to withstand the carbonated soft drink is critical. The PET must be able to endure the physical stress after being filled with pressurised carbonated soft drink content. The studied design should not be very different from the existing can design, and comply with customers' preferences in terms of size, shape and ergonomics. CATIA V5R21 software was used to draw 3D PET cylindrical container model. The design analysis indicated that cylindrical containers with 100 mm height and 70 mm diameter would be able to hold the required volume of beverage. The container must also have a thickness wall of 1mm with 50.44 mm circumference to enable the can to withstand the pressure build up when it is filled with carbonated soft drink. Comprehensive design processes and modifications were done using CATIA before the data being extracted into Moldflow platform. The 3D model was then validated and saved in the Certificate Trust List (.stl) extension format. In this format the information it is accessible or readable by the Moldflow program. The model was then imported into the Moldflow software for simulation and analysis.

Moldflow Simulation

Once the material properties were made available in the Moldflow, the PET cylindrical container model was then imported from the CATIA database in . stl format. The steps for the simulation process are as follows:

1. The model was verified and modified of any mould defects during the data importing process. Once the can model was successfully checked, the data importing step into Moldflow was completed.
2. The next step was to set the Injection Location(s). This step is required for the melt flow routing logic into the mould cavity during the simulation process.
3. Subsequently, specified the material used for the cylindrical container model; PET,
 Manufacturer: UltrPET
 Trade Name: Bottle Grade Reprocessed
4. In the Analysis Wizard, the Sequence of the simulation was chosen. Here, the Fill+Pack command was selected to analyse the required plastic flow behaviour.
5. The Process Setting is where the process parameters of the simulation were applied and varied. The mould and melt temperatures were set according to Tables 1, 2, and 3.
6. Once the simulation was completed, the simulation results based on the set moulding parameters were tabulated. The results were analysed and recorded. Effects of varying melt temperature and mould temperature were conducted based on 8-cavity PET cylindrical container model.

Table 1
 Process parameters for (i) single-cavity, (ii) 4-cavity, (ii) 8-cavity mould comparison

Melt Temperature	Mould Temperature
285°C	110°C

Table 2
 Process parameters for varying melt temperatures

Melt Temperature	Mould Temperature (constant)
270°C	110°C
280°C	110°C
290°C	110°C
300°C	110°C

Table 3
 Process parameters for varying mould temperatures

Melt Temperature (constant)	Mould Temperature
285°C	90°C
285°C	100°C
285°C	110°C
285°C	120°C

RESULTS AND DISCUSSION

Single, Multiple Cavity Fill Time Comparison

Generally, manufacturers would opt for multiple cavities injection moulding for better production yield. However, the number of cavities was not the only consideration in achieving good mould design and performance. The moulds designed must be able to operate at its optimum with less rejection. The goal is to achieve high production yield. A very straight forward approach in achieving high production rate is by producing more parts in one injection cycle. Thus, multiple cavities are the most optimal option. In order to see how much the production rate can be improved, the PET cylindrical container model was duplicated into four cavities and eight cavities moulds. From here the moulding fill time of the multiple cavities was compared with the single cavity mould. Figure 1 shows the multi-cavity system which was modelled using MouldFlow.

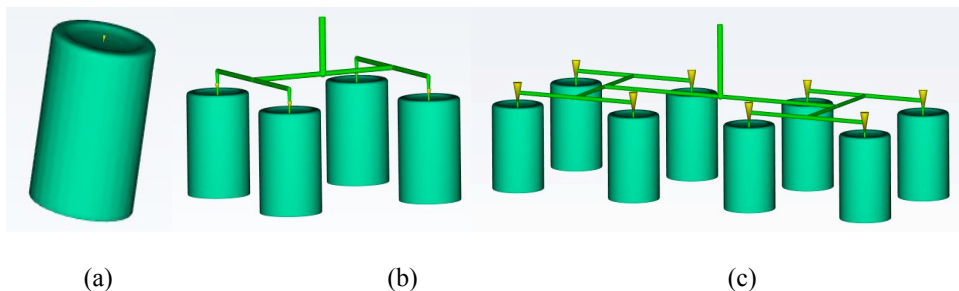


Figure 1. (a) Single-cavity; (b) 4-cavity; and (c) 8-cavity moulds structure

All the three simulation models; single-cavity; 4-cavity; and 8-cavity moulds structure showed a complete and successful filling of the mould cavities but with different filling times (Figure 2). It was observed that more cavities mould reduces the rate of melt fill. This is because of the larger volume of total cavities needed to be filled from a single sprue. A single-cavity mould achieved complete melt fill at 0.25 s. But for a 4-cavity and 8-cavity mould, at the same melt fill time, the melt had only filled a small percentage of the cavity base and hardly reached the base of mould respectively. The time lag for the melt to reach the mould cavity of the 4-cavity and 8-cavity is most likely due to the existence of the runner structure that was compulsory in any mould design. The 8-cavity mould has a longer total length of runner, thus slowing down the melt to reach into the mould cavity.

The pattern of melt flow is similar for all three types mould cavity, with the single-cavity mould achieving the highest percentage of cavity filled, followed by 4-cavity mould and 8-cavity; comparison was made against the same filling time. The mould was completely filled with the melt at 1.27 s for the single-cavity mould, 1.417 s for the 4-cavity mould and 1.497 s for the 8-cavity mould. The minor difference of fill time between single and multiple cavities may be due to the difference in actual injection pressure set during the simulation. The results showed that for the single-cavity mould, it took 95.727 MPa of actual injection pressure, compared to 139.701 MPa for 4-cavity mould and 160.516 MPa for the 8-cavity

mould, respectively. The increase in actual injection pressure showed in the Moldflow can be adopted as the requirement to compensate the increase of cavity volume needed for the injection moulding machine to fill. Therefore, higher actual injection pressure decreases the total fill time for the multiple cavities mould.

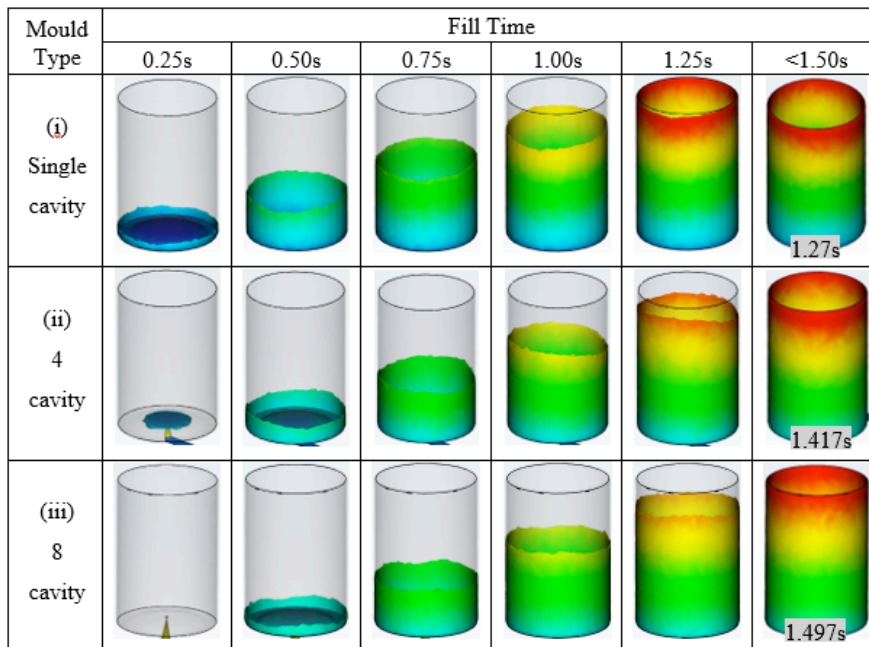


Figure 2. Fill time comparison of single-cavity, 4-cavity, and 8-cavity moulds

By comparing the fill time against the single-cavity mould, the 4-cavity structure mould took 0.147 s longer to fill in the moulds completely but produces four moulded products per shot. Thus, the 4-cavity mould yielded an increment in the production rate by 258.5%. Similarly, for the 8-cavity mould, the mould filling time was 0.227 s longer, but producing eight moulded products per shot compared to the single-cavity mould. Thus, the production rate is 578.7% as compared against the single-cavity mould and it is obviously higher than the 4-cavity mould too. Thus showing that the mould cavity numbers have a direct impact on the increment in the production rate.

Varying Melt Temperature

Based on the plotted results in Figure 3, the filling time was clearly affected by the melting temperature - higher melt temperature led to shorter filling time. This is because the higher melt temperatures increase the fluidity of the melt thus the filling capabilities inside the mould cavities increases accordingly. Fast melt flows were observed from the heating cylinder, through the nozzle and into the mould cavities. The result shows the time taken for the melt to reach different parts of the mould cavities, starting from the centre bottom of the cylindrical container and ending at its top.

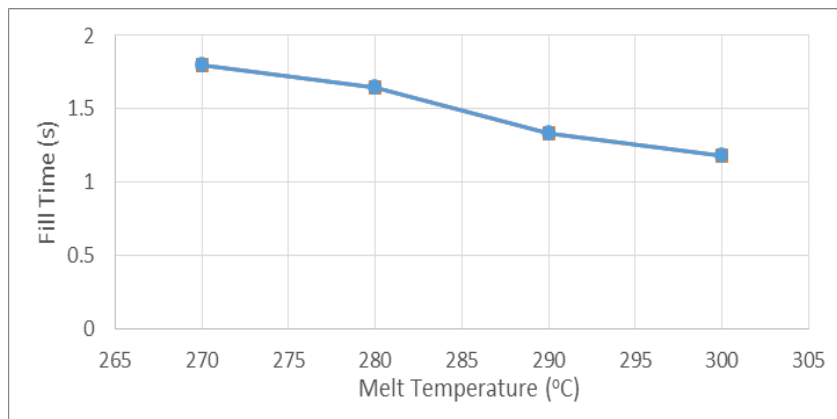


Figure 3. Graph of fill time with varying melt temperature

Contrasting the fill time effect, it was found the volumetric shrinkage (shown as a percentage of the original volume) increased as the melt temperature increased (Figure 4). Volumetric shrinkage is referring to the moulded part shrunk as it is being exposed or cured at the room temperature. For all the simulated melt temperatures, all the parts showed uniform values of shrinkage on the moulded part's wall and base. Thus, the warping effect can be reduced or totally avoided. Also, there were no sink mark signs observed on the moulded parts.

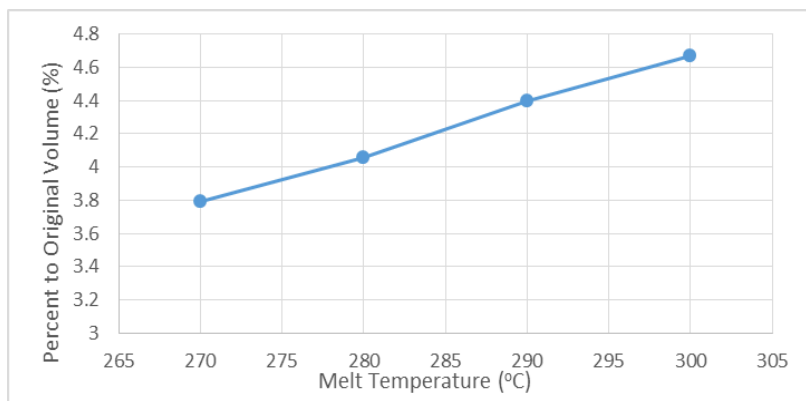


Figure 4. Graph of maximum volumetric shrinkage with varying melt temperature

Similarly, the maximum deflection increased as the melt temperature increased as exhibited in Figure 5. The simulation result indicates the maximum deflection effect at each node of the part. All the moulded parts experienced positive deflection with concave effect; the moulded parts contracted inwards from the expected cylindrical size. The maximum deflections were detected at the rim of the moulded parts, where the melt flow reached latest. The results below are based on the deflected part compared against the expected cylindrical size of the mould cavity.

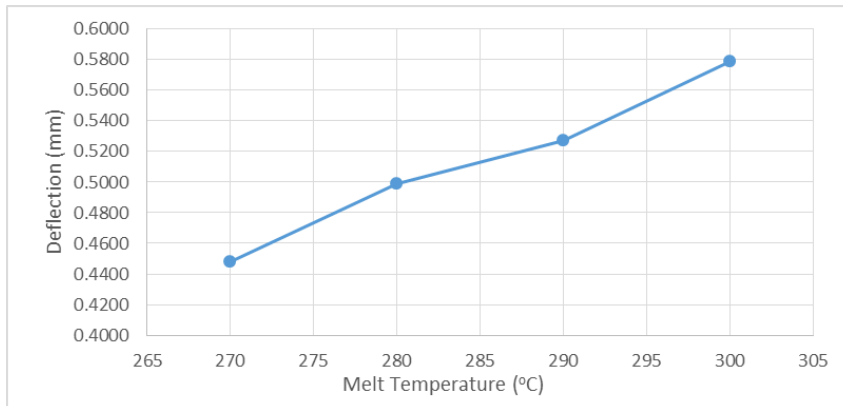


Figure 5. Graph of maximum deflection of part with varying melt temperature

Table 4 presents the overall simulation results obtained by varying the melt temperatures of PET the modelled cylindrical containers. Fill time improved when the melt temperature increased. However, the volumetric shrinkage and the maximum deflections increased with higher melt temperature. The shorter fill time would be most favourable for manufacturers as it would result in higher production rate. But, the volumetric shrinkage and maximum deflection would be increased and led to moulded parts quality issues.

Table 4
Results of PET can simulation varying melt temperatures from 270°C to 300°C

Melt Temperature (°C)	Fill Time (s)	Maximum Volumetric Shrinkage (%)	Maximum Deflection (mm)
270	1.796	3.793	0.4480
280	1.643	4.053	0.4990
290	1.332	4.397	0.5274
300	1.180	4.671	0.5791

Varying Mould Temperature

Figure 6 highlights the results of mould temperature versus the fill time. The fill time gradually increased at the initial stage; between mould temperatures of 90°C to 100°C and significantly shoot up at the mould temperature range between 100°C to 110°C. The fill time becomes steady after it reaches 110°C. It is observed that, further increased in the mould temperature setting above 110°C, does not seem to affect the mould fill time. Similar results were obtained by Sha, Dimov, Griffiths and Packianther (2007), suggested that this behaviour could be due to the expanding air residual which might have hindered the polymer melt flow.

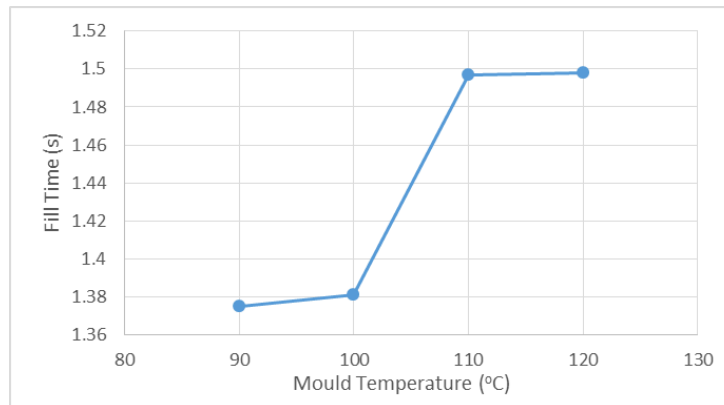


Figure 6. Graph of fill time with varying mould temperature

Figure 7 presents the volumetric shrinkage percentage of moulded parts with the original volume as simulated using MouldFlow. The results show an almost linear trend between the volumetric shrinkage percentage and the mould temperature. This further confirms that mould temperature setting does not directly affect the quality of PET cylindrical container. But the increment in the volumetric shrinkage will have a direct impact on the quality of the moulded parts. A uniform volumetric shrinkage throughout the body and base of the mould cavities and will not encourage warp formation.

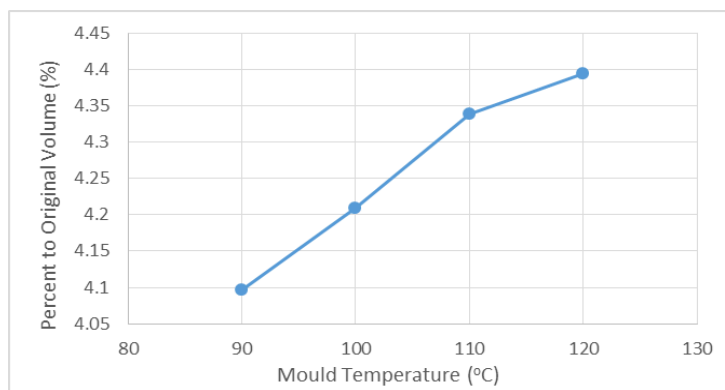


Figure 7. Graph of maximum volumetric shrinkage with varying mould temperature

A notable increment on the maximum deflection is observed for the temperature range between 90°C to 110°C (Figure 8). But the trend drastically decreased after the temperature reaches 110°C. A similar pattern of the maximum deflection effect against the mould temperature was also observed for all the three PET mould cavity design structures.

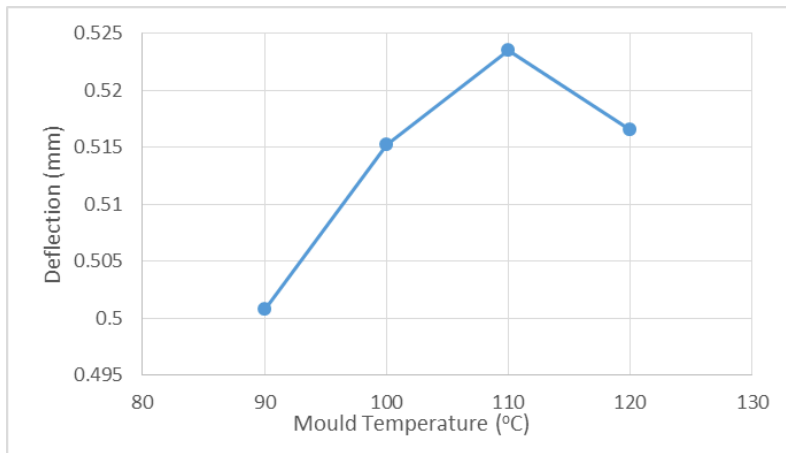


Figure 8. Graph of maximum deflection of part with varying mould temperature

Table 5 showcases the results of the mould temperature effect on the volumetric shrinkage and maximum deflection. The mould temperature was not directly affecting the moulding process of the PET cylindrical containers. It was observed that, the fill time, volumetric shrinkage and deflection were not directly impact the part’s moulding quality as long as the moulding parameters were set at the optimal setting. The mould fill time is a trade-off between the moulding productivity and rejection rate; moulding quality. The challenge is to identify the optimal setting to achieve the most optimum production yield. Simulation results suggests that a lower moulding temperature setting for the PET cylindrical containers reduces the injection moulding time and results in better product quality and higher production rate is.

Table 4

Results of PET can simulation by varying mould temperatures from 90°C to 120°C

Melt Temperature (°C)	Fill Time (s)	Maximum Volumetric Shrinkage (%)	Maximum Deflection (mm)
90	1.375	4.096	0.5008
100	1.381	4.209	0.5152
110	1.497	4.338	0.5235
120	1.498	4.394	0.5165

CONCLUSION

The potential of producing 330 ml size PET cylindrical containers as an alternative packaging solution carbonated soft drinks instead of aluminium cans was thoroughly studied. The mould flow effect of the multiple mould cavities (single cavity, four cavities and eight cavities) concerning the plastic flow and fill time were investigated. The calculated increment of production rate (number of parts produced per second) was 258.5% for 4-cavity mould. With 8-cavity mould, the production rate increased by 578.7%, despite of the fill time increases; as the number of cavities increased. Meanwhile, with a constant mould temperature, it is

observed that higher melt temperature would reduce the time taken to fill the mould cavities. This is because higher melt temperature would result in better fluidity of the melt material thus reducing mould fill time. From the investigation using MouldFlow simulation software, it can be concluded that the moulding parameter setting must be benchmarked according to the material manufacturers' recommendation as well as the mould size condition. Production trials for any new mould design in obtaining the optimal setting parameters is recommended.

ACKNOWLEDGEMENTS

The authors would like to thank Institute of Research Management and Innovation (IRMI), Ministry of Education Malaysia and Institute of Graduate Studies (IPSIS) UiTM for the financial supports. This research works is performed at the Faculty of Mechanical Engineering, UiTM Malaysia under the support of GIP research grant no. 600-IRMI/GIP 5/3 (0018/2016).

REFERENCES

- Bach, C., Dauchy, X., Severin, I., Munoz, J., Etienne, S., & Chagnon, M. (2013). Effect of temperature on the release of intentionally and non-intentionally added substances from polyethylene terephthalate (PET) bottles into water: Chemical analysis and potential toxicity. *Food Chemistry*, 139(1-4), 672-680.
- Byrne, F., Ward, P. G., Hughes, D., & Cullen, J. (2011). Comparative study of the processing conditions required for PLA and PET polymers. *Solutions*, 4-6.
- Chen, C. P., Chuang, M. T., Hsiao, Y. H., & Tsai, C. H. (2009). Simulation and experimental study in determining injection molding process parameters for thin-shell plastic parts via design of experiments analysis. *Expert Systems With Applications*, 36(7), 10752-10759.
- Demirel, B., Yaraş, A., & Elçiçek, H. (2016). Crystallization behaviour of PET materials. *Balıkesir Üniversitesi Fen Bilimleri Enstitüsü Dergisi*, 13(1), 26-35.
- Huang, M. C., & Tai, C. C. (2001). Effective factors in the warpage problem of an injection-molded part with a thin shell feature. *Journal of Materials Processing Technology*, 110(1), 1-9.
- Jansen, K. M. B., Dijk, D. J. V. A. N., & Husselman M. H. (1998). Effect of processing conditions on shrinkage in injection molding. *Polymer Engineering and Science.*, 38(5), 838-846.
- Kong, J. W. Y., Kim, J., Member, S., & Yuen, M. M. F. (2003). Warpage in Plastic Packages: Effects of process conditions, geometry and materials. *IEEE Transactions on Electronics Packaging Manufacturing*, 26(3), 245-252.
- Koszkul, J., & Nabialek, J. (2007). Selected methods of modelling of polymer during the injection moulding process. *Journal of Achievements in Materials and Manufacturing Engineering*, 24(1), 253-259.
- Kurataran, H., Ozcelik, B., & Erzurumlu, T. (2005). Warpage optimization of a bus ceiling lamp base using neural network model and genetic algorithm. *Journal of Materials Processing Technology*, 169(2), 314-319.
- Lal, S. K., & Vasudevan, H. (2013). Optimization of injection moulding process parameters in the moulding of low density polyethylene (LDPE). *International Journal of Engineering Research and Development*, 7(5), 35-39.

- Mehat, N. M., Kamaruddin, S., & Othman, A. R. (2013). Modeling and analysis of injection moulding process parameters for plastic gear industry application. *ISRN Industrial Engineering*, 2013, 1-10.
- Nagahanumaiah, B. R. (2009). Effects of injection molding parameters on shrinkage and weight of plastic part produced by DMLS mold. *Rapid Prototyping Journal*, 15(3), 179-186.
- Oktem, H., Erzurumlu, T., & Uzman, I. (2007). Application of Taguchi optimization technique in determining plastic injection molding process parameters for a thin-shell part. *Materials and Design*, 28(4), 1271-1278.
- Ozcelik, B., & Sonat, I. (2009). Warpage and structural analysis of thin shell plastic in the plastic injection molding. *Materials and Design*, 30(2), 367-375.
- Reddy, B., & Kumar, J. (2009). Application of soft computing for the prediction of warpage of plastic injection molded parts. *Journal of Engineering Science and Technology*, 2(1), 56-62.
- Sha, B., Dimov, S., Griffiths, C., & Packianther, M. S. (2007). Investigation of micro-injection moulding: Factors affecting the replication quality. *Journal of Materials Processing Technology*, 183(2-3), 284-296.
- Song, M. C., Liu, Z., Wang, M. J., Yu, T. M., & Zhao, D. Y. (2007). Research on effects of injection process parameters on the molding process for ultra-thin wall plastic parts. *Journal of Materials Processing Technology*, 187-188, 668-671.
- Wegelin, M., Canonica, S., Alder, C., Marazuela, D., Suter, M. J. F., Bucheli, T., ... & Larroque, M. (2001). Does sunlight change the material and content of polyethylene terephthalate (PET) bottles. *Journal of Water Supply: Research and Technology. – AQUA*, 50(3), 125-133.
- Zhil'tsova, T. V., Oliveira, M. S. A., & Ferreira, J. A. F. (2009). Relative influence of injection molding processing conditions on HDPE acetabular cups dimensional stability. *Journal of Materials Processing Technology*, 209, 3894-3904.

Equivalent Dose Measurements from Digital Intra- and Extra-Oral Imaging Examinations

Norfariha Che Mohamed¹, Hapizah Nawawi³,
Mohd Yusmiaidil Putera Mohd Yusof^{2,3*} and Khoo Kok Siang¹

¹*School of Applied Physics, Faculty of Science and Technology, Universiti Kebangsaan Malaysia (UKM), 43600 Bangi, Selangor, Malaysia*

²*Centre of Oral & Maxillofacial Diagnostics and Medicine Studies, Faculty of Dentistry, Universiti Teknologi MARA (UiTM), Sungai Buloh Campus, 47000 Sungai Buloh, Selangor, Malaysia*

³*Institute of Pathology, Medical Laboratory & Forensics (I-PPerForm), Faculty of Medicine, Universiti Teknologi MARA (UiTM), Sungai Buloh Campus, 47000 Sungai Buloh, Selangor, Malaysia*

ABSTRACT

The aims of this study are to estimate the equivalent dose to the skin, eyes and thyroid in intra- and extra-oral imaging examination and to compare the dose-area product (DAP) derived from the calculation method with Diagnostic Reference Levels (DRL) that has been provided by the Malaysian Ministry of Health (MOH). Dose equivalent is measured by placing Thermoluminescence Dosimeter (TLD-100H) in the anthropomorphic RANDO phantom. Exposure is performed using intra-oral X-ray machine *ActeonSatelec X-Mind*[®] and extra-oral X-ray machine *InstrumentariumOP300*[®], and the value is compared to the equivalent dose of the International Commission on Radiological Protection (ICRP) dose limit. DAP value for both examinations was obtained by using formula and comparing them with the DRL from MOH. The average dose equivalent of intra- and extra-oral radiographic examination is lower than the ICRP dose limit. The doses derived from both examinations did not exceed the prescribed levels when compared with DRL. The doses calculated for intra-oral examination of molar maxillary, molar mandibular and interproximal (bitewing) was 0.880 mGy while periapical examination of the anterior maxillary and mandibular was 0.688 mGy and occlusal examination was 1.100 mGy. For the panoramic examination the dose was 0.011 mGy.m² while lateral cephalometric examination was 0.0054 mGy.m². The doses obtained from this study were within the dose limit and predetermined level. This shows that a patient receives the minimum dose for both dental radiographic examinations with the optimum level of safety which meets the ALARA concept.

ARTICLE INFO

Article history:

Received: 05 January 2017

Accepted: 17 January 2017

E-mail addresses:

fareehafary@gmail.com (Norfariha Che Mohamed),

hapizah@salam.uitm.edu.my (Hapizah Nawawi),

yusmiaidil@salam.uitm.edu.my

(Mohd Yusmiaidil Putera Mohd Yusof),

khoo@ukm.edu.my (Khoo Kok Siang)

*Corresponding Author

Keywords: Dental imaging, diagnostic reference levels, dose-area product, equivalent dose

INTRODUCTION

Dental imaging is used as a diagnostic tool for detecting oral diseases. Its advantages in providing diagnostic information are dependent on the type of examination, whether intra-oral or extra-oral dental imaging. Unlike other radiographic examinations, dental imaging uses low exposure factors. However, some X-ray effects cannot be entirely avoided. As these effects are cumulative over time, frequent use of dental radiography on the same individual may not be absolutely risk free. In addition, the proximity of the patient to the X-ray tube means that the risks associated with dental imaging should not be underestimated.

Sensitive organs close to the X-ray tube, such as the skin, eyes, salivary glands, meninges and thyroid, can be subjected to scattered radiation. Two types of cellular damage, deterministic and stochastic effects are produced by radiation in the absence of adequate repair. Deterministic effects occur above a threshold dose and are characterized by a dose-related increasing risk and associated severity of outcome. A long-recognized adverse deterministic effect is radiation-induced dermatitis. (Hymes, Strom, & Fife, 2006). Stochastic effects, including cancer and hereditary effects are caused by a mutation or other permanent change in which the cell remains viable. The probability of a stochastic effect increases with dose (probably with no threshold, an assumption based on molecular knowledge of carcinogenesis: a very small X-ray dose can cause a base change in DNA), but the severity of the outcome is not related to the dose (Linnet et al., 2012). Epidemiologic literature on low-dose and low-dose rate effects is hindered by limited statistical power at cumulative lifetime radiation levels of less than 100 millisieverts (mSv), even for very large studies. Despite wide confidence limits, the results of individual large and pooled studies of radiation workers reveal modest exposure-related increases in risk of solid tumours at low-dose levels (Cardis et al., 2007; Muirhead et al., 2009). The highest risks from dental radiography are leukaemia and thyroid cancer and incidents of these have been recorded at doses as low as 500 mSv (Sheikh, Bhoweer, Arya, & Arora, 2010). One study states that every one million full-mouth examinations may produce about 100 fatal cancers (Mortazavi et al., 2004). Dentists should take this, and the patient's age, into consideration before requesting repeated imaging examinations.

In any imaging examination, the principle of as low as reasonably achievable (ALARA) is an important concept to be practiced after considering the justification for radiographic examination when the benefits outweigh any risks that may be present (Alcaraz et al., 2011). In dental imaging examination, ALARA should be used to reduce the radiation dose on patients without compromising the image and resulting diagnostic information. The exposure time has been reported to be significantly reduced in digital sensor as compared to the conventional D-speed film and therefore reducing the radiation exposure (Anissi & Geibel, 2014). However, the use of radiation in an examination must always be justified and optimized as proposed by the International Commission on Radiological Protection (ICRP).

The aim of this study is threefold: (i) to evaluate and measure the equivalent dose to the skin, eyes and thyroid in digital intra- and extra-oral dental imaging; (ii) to assess the dose-area product (DAP) derived from the intra- and extra-oral dental imaging; and (iii) to compare the values of derived DAP with the diagnostic reference levels (DRL) as prescribed by the Malaysian Ministry of Health (MOH).

MATERIALS AND METHOD

Prior to the start of the study, the calibration factor (CF) for each TLD-100H chip was obtained by running a calibration process. A total of 40 TLD-100H chips were first irradiated freely in air with gamma rays from a radionuclide Cs-137 source at a distance of 1 m from the source. Gamma ray irradiation time was over 1.30 minutes with a dose of 1 mGy. Next, for the data of response reading per chip, TLD Harshaw reader with WinREMS software (version PL-26732.8.0.0.0, BICRON/Harshaw, 6801 Cochran Road, Solon, OH 44139, USA) was used. The CF value of each TLD-100H chip was obtained using formula as follows (Ali, 2016):

$$\text{Calibration Factor (CF)} = \frac{1 \text{ (mGy)}}{\text{TLD response reading (nC)}}$$

where 1 mGy is the total of gamma ray irradiation dose imposed on the TLD-100H chips and is divided by the response reading of each TLD-100H chip that is recorded in electrical charge, nanoCoulomb (nC).

Two TLD-100H chips were placed at each location of the skin, eyes and thyroid (Figure 1). For radiation dose collection on the thyroid, the chips were inserted into the holes on the anthropomorphic phantom segments (thyroid), while for the skin and eyes, the chips were pasted onto the surface of the phantom. Before being pasted, each chip was wrapped in a sealed plastic container and labelled with the location to avoid doubt and data inaccuracies. After a certain chip was placed neatly and correctly onto the phantom, the phantom was positioned onto the intra-oral X-ray machine *ActeonSatelec X-Mind*[®] and extra-oral X-ray machine *InstrumentariumOP300*[®].

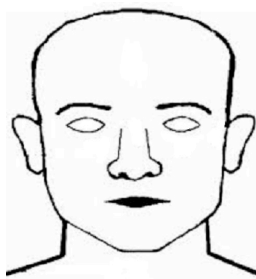


Figure 1. TLD-100H chips location on phantom

After the phantom and TLD-100H chips were placed in a position appropriate for each examination, the exposure was performed using parameters that have been set for each examination. The scanning parameters shown in Table 1 are routinely applied in intra- and extra-oral radiographic examinations at the Faculty of Dentistry, Universiti Teknologi MARA Sungai Buloh Campus, Malaysia. Exposure was performed in the total of three times to get an accurate reading of the values from each examination and the chips were then read. Radiation dose values were recorded in the electricity charging unit, nC. Table 1 shows the scanning parameters for each examination involved in this study. The flow chart in Figure 2 shows briefly the method of data collection for this study.

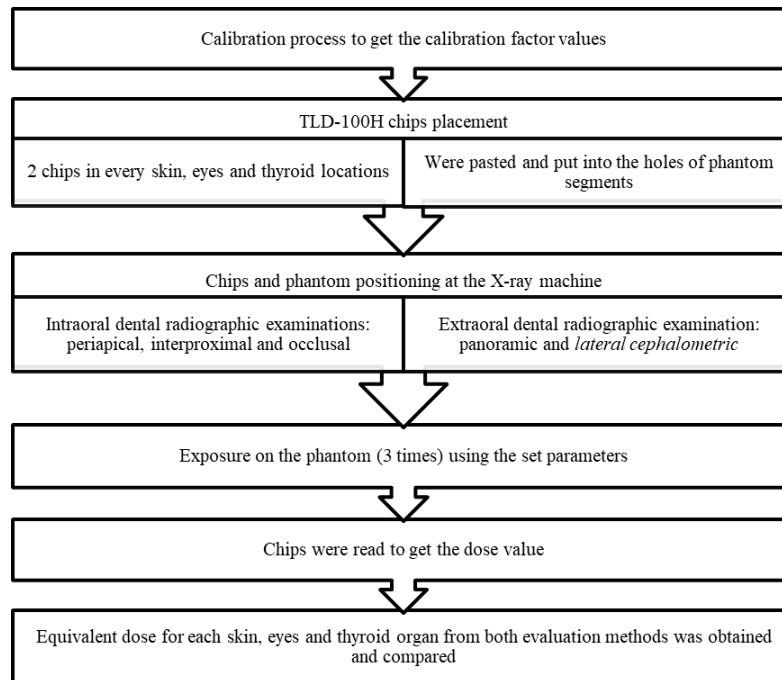


Figure 2. Flow chart of data collection method

The selection of kV and mA for intra-oral examination is based on the standard mode set by the machine manufacturer with a selection voltage of 60 kV and 70 kV and a current value of 4 mA and 8 mA with changeable exposure time. Extra-oral panoramic examination automatically determines parameter values contingent on the anatomy of the patient’s head, with a voltage range of 57–90 kV and a maximum current of 16 mA. In extra-oral lateral cephalometric examination, the parameters are set at 90 kV, 13 mA and 16 s.

Table 1
Scanning parameters and DAP of involved examinations

Examinations	Voltage (kV)	Current (mA)	Exposure time (s)	Dose in air (mGy)	DAP (mGy.cm ²)
Intra-oral					
Periapical Anterior Maxillary	70	8	0.125	0.688	0.688
Periapical Anterior Mandibular	70	8	0.125	0.688	0.688
Periapical Molar Maxillary	70	8	0.160	0.880	0.880
Periapical Molar Mandibular	70	8	0.160	0.880	0.880
Interproximal (Bitewing)	70	8	0.160	0.880	0.880
Occlusal (Maxillary and Mandibular)	70	8	0.200	1.100	1.100
Extra-oral					
Panoramic	66	11.667	16.4	0.417	109.237
Lateral Cephalometric	90	13	16	0.131	54.000

Data Analysis

The radiation dose was obtained by using two methods, one with experimental method using the phantom and the other one is the method of formula calculation. In determining the radiation dose to the skin, eyes and thyroid, the reading of the dose value from the reader was used to be then calculated by using the following formula (Ali, 2016):

$$\text{Equivalent dose, } H_T \text{ (mSv)} = q \text{ (nC)} \cdot CF \text{ (mGy/nC)} \cdot Q \text{ (Sv/Gy)}$$

Where q is the response reading in nC

CF is the calibration factor in mGy/nC, and

Q is the quality factor or radiation weighting factor in Sv/Gy.

In the second method of determining the dose, scanning parameters for each examination such as mAs, kVp, focus to skin distance, focus to sensor distance, size of the collimator and the X-ray machine output was recorded and were used in the following formula (Akinlade, Farai, & Okunade, 2012):

$$DAP \text{ (mGy.cm}^2\text{)} = L \text{ (mAs)} D_o \text{ (mGy/mAs)} A \text{ (cm}^2\text{)}_{(FSD)}$$

Where L is the tube loading, expressed in mAs

D_o is the normalized beam output in mGy / mAs at 1 meter

FSD is the focus to skin distance, and

$A_{(FSD)}$ is the cross-sectional area of the beam on the skin of the patient.

Because DAP is a determinant of the absorbed dose to the area receiving radiation, equivalent dose can also be obtained by performing a conversion unit to mSv. The results of the two calculation methods were further evaluated and compared with the limits and levels that have been recommended by the ICRP and DRL from MOH to determine the level of radiation dose received by the skin, eyes and thyroid organs.

RESULTS

Figure 3 shows the distribution of the CF values for each TLD-100H chip used in this study. Most TLD-100H chips have uniform CF values ranging from 3.681 for number 12 to 0.486 for number 5.

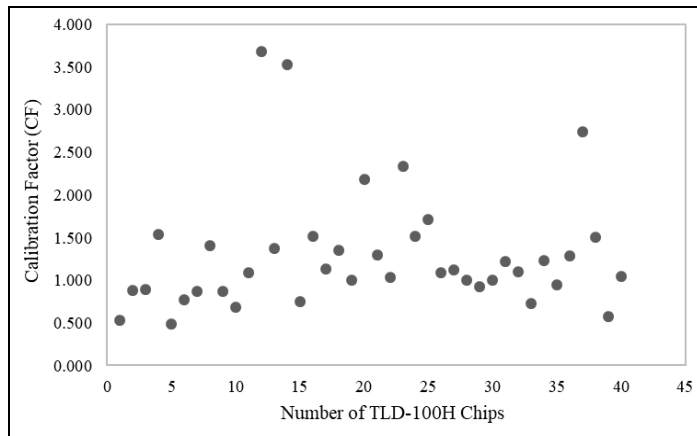


Figure 3. Distribution of calibration factor values for each TLD-100H Chips

Intra-Oral Imaging

Anterior maxillary and mandibular examinations gave the highest dose value to the left skin compared to other organs of study. The mean value of equivalent dose to the skin is 2.770 ± 2.459 mSv for anterior maxillary examination and 2.085 ± 1.624 mSv for anterior mandibular examination (Table 2). In the left molar maxillary periapical examination, the mean value of equivalent dose to the left skin is 1.227 ± 0.958 mSv. For the right molar maxillary periapical examination, the mean value of equivalent dose is 2.943 ± 2.434 mSv, also to the left skin. This is a higher dose than in the left molar maxillary examination. On the left mandibular molar examination, the left eye received a higher mean equivalent dose than any other organ (4.335 ± 3.960 mSv). Meanwhile, examination of the right mandibular molar exhibited the highest means in equivalent dose in the right thyroid (0.952 ± 0.361 mSv).

In the interproximal (bitewing) examination, the mean values of equivalent dose to the skin, eyes and thyroid differed in left and right cases. The left bitewing examination showed the highest mean value of equivalent dose to the left skin (2.890 ± 2.999 mSv), while the right bitewing examination showed the highest mean value of equivalent dose to the right thyroid (2.038 ± 0.327 mSv).

Occlusal examination unveiled a slightly higher exposure time as compared to other intra-oral examination. The mean values of equivalent dose from the maxillary occlusal and mandibular occlusal examinations revealed the highest amount of doses in the left thyroid organ (3.189 ± 2.014 mSv) and the organ of left eye (2.612 ± 0.336 mSv), respectively.

Table 2
Mean values of equivalent dose and standard deviation

	Equivalent dose for posterior maxillary periapical imaging (Mean ± SD)					
	Right organ (mSv)			Left organ (mSv)		
	Skin	Eyes	Thyroid	Skin	Eyes	Thyroid
Left maxillary molar	0.651±0.441	0.635±0.402	0.460±0.175	1.227±0.958	0.819±0.515	0.382±0.176
Right maxillary molar	1.734±1.138	1.573±0.746	1.199±0.473	2.943±2.434	1.181±0.483	2.516±1.634
	Equivalent dose for posterior mandibular periapical radiograph (Mean±SD)					
Left mandibular molar	2.599±0.867	2.363±1.726	4.023±0.106	3.657±1.674	4.335±3.960	1.901±0.445
Right mandibular molar	0.579±0.078	0.483±0.145	0.952±0.361	0.837±0.268	0.664±0.297	0.618±0.427
	Equivalent dose for anterior maxillary and mandibular periapical radiograph (Mean ± SD)					
Anterior maxillary	1.280±0.382	1.777±1.418	0.875±0.406	2.770±2.459	1.329±0.379	2.056±0.439
Anterior mandibular	1.531±0.590	0.769±0.523	1.677±0.505	2.085±1.624	1.710±0.648	1.554±0.456
	Equivalent dose for interproximal bitewing radiograph (Mean ± SD)					
Left bitewing	1.180±0.564	1.464±0.708	1.266±0.764	2.890±2.999	1.076±0.151	1.855±1.511
Right bitewing	1.428±0.525	0.873±0.135	2.038±0.327	1.744±0.828	1.219±0.171	1.201±0.318
	Equivalent dose for occlusal radiograph (Mean ± SD)					
Maxillary occlusal	1.289±0.534	1.582±0.636	1.405±0.745	2.384±2.341	1.290±0.632	3.189±2.014
Mandibular occlusal	1.690±0.734	1.240±0.305	2.255±0.404	2.362±1.745	2.612±0.336	1.546±1.200
	Equivalent dose for extra-oral radiograph (Mean ± SD)					
Panoramic	0.435±0.165	0.404±0.215	0.570±0.184	0.794±0.731	0.425±0.213	1.125±0.999
Lateral cephalometric	0.636±0.348	1.041±0.953	0.670±0.182	1.273±1.041	0.784±0.320	2.361±1.789

Extra-Oral Imaging

Table 2 shows the mean values of equivalent dose and standard deviation (in mSv) obtained in the skin, eyes and thyroid in the panoramic and lateral cephalometric examinations. Based on this finding, the organ which received the highest dose is the left thyroid with mean equivalent dose of 1.125 ± 0.999 mSv for panoramic examination and 2.361 ± 1.789 mSv for lateral cephalometric examination. Due to the higher exposure factor used in lateral cephalometric examination, equivalent doses to each organ under study were slightly higher in lateral cephalometric examination than in panoramic examination.

Dose-Area Product from Formula Calculation

The scanning parameters for intra-oral radiographic examination were set at 70 kV and 8 mA, with different exposure time depending on the type of examination according to the recommendation by the manufacturer. In periapical examination of maxillary and mandibular molar, the exposure time was set at 0.160 s, similar to the interproximal (bitewing) examination. Periapical examination of the anterior maxillary and anterior mandibular used a shorter exposure time of 0.125 s, while occlusal examination used an exposure time of 0.200 s for both maxillary and mandibular examination. The area in which the dose is received is estimated at 1 cm².

DAP for occlusal examination was higher (1.100 mGy.cm²) than the other examinations due to the longer exposure time (0.200 s) (Table 1). By estimating the radiation dose received in the 1 cm² area, the DAP value is equivalent to the entrance surface dose (mGy) for the intra-oral examination. The exposure factors in panoramic examination are determined automatically depending on the anatomy of the patient’s head. This study uses 66 kV and 16.4 s exposure time with a mean current of 11.667 mA. Area exposed to the radiation was 261.96 cm². For lateral cephalometric examination the parameters were set at 90 kV, 13 mA and 16 s, with an exposure area of 412.16 cm². Table 1 shows the DAP for both extra-oral examinations.

According to Table 1, the DAP value is higher for panoramic examination (109.237 ± 24.440 mGy.cm²) even though the mA used is lower than lateral cephalometric examination. This is because the exposure time for panoramic examination is slightly higher (16.4 s) than that for lateral cephalometric examination, which will affect the absorbed dose value in the area exposed. DAP value for lateral cephalometric examination was 54.000 ± 0.872 mGy.cm².

DISCUSSION

From the overall examination of intra- and extra-oral imaging, it was found that the mean values of the equivalent dose to the skin and thyroid are higher than for the eyes and this can be attributed to the sensitivity level of tissues to the radiation. The mean values of equivalent dose obtained from this study are in line with the results of another that has proven that the equivalent dose values to the eyes are lower when compared with the thyroid (Morant et al., 2013). Besides that, other factors may also affect the values of radiation dose received by each organ in this study, such as X-ray tube positioning, placement of TLD chips and the accuracy of the dosimetric system. The values of equivalent dose derived from this in vivo method are subsequently compared with the limit set by ICRP (Table 3).

Table 3
Comparison of equivalent dose values

Equivalent dose	Values from ICRP (mSv)	Mean values of equivalent dose from in-vivo method (mSv)
Eyes	15	Intra-oral examination: 1.450±0.873 Extra-oral examination: 0.664±0.306
Skin	50	Intra-oral examination: 1.843±0.841 Extra-oral examination: 0.784±0.357
Thyroid	50	Intra-oral examination: 1.648±0.899 Extra-oral examination: 1.182±0.823

According to the annual dose limit prescribed by ICRP, the dosimetric data of TLD-100H as a whole is still within the allowed limit. Equivalent dose in a year prescribed by ICRP is 15 mSv for eyes and 50 mSv for skin and thyroid. For the intra-oral examination that has been conducted, the equivalent dose is lower than the limit prescribed, with mean values of 1.450 ± 0.873 mSv for the eyes, 1.843 ± 0.841 mSv for the skin and 1.648 ± 0.899 mSv for the thyroid.

For the extra-oral examination, the equivalent dose on average is also low (0.664 ± 0.306 mSv for eyes, 0.784 ± 0.357 mSv for skin, 1.182 ± 0.823 mSv for thyroid).

The DRL set by MOH was referred to when assessing the DAP data obtained from this study to ensure that the radiation exposure was not excessive. Proposed DRL for intra-oral radiographic examination based on entrance surface dose is 3.18 mGy, and for extra-oral radiographic examination based on kerma-area was 0.016 mGy.m². Based on the findings of the current study, the overall dose values obtained from formula calculation meet the benchmarks prescribed by MOH.

According to Table 1, the values of dose obtained for intra-oral examination of molar maxillary, molar mandibular and interproximal (bitewing) is 0.880 mGy, while for periapical examination of the anterior maxillary and anterior mandibular it is 0.688 mGy. The dose for occlusal examination is slightly higher than for other intra-oral examinations (1.100 mGy), but still within the levels prescribed. The values of dose obtained were compared with the values given by MOH (Figure 4).

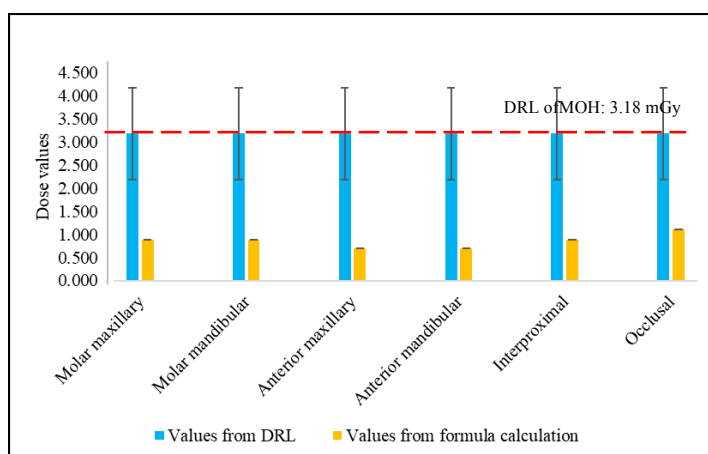


Figure 4. Comparison of dose values from formula calculation with DRL that has been prescribed by MOH for intra-oral examinations

There are significant differences between the DRL of MOH and the values obtained from the formula calculation. For intra-oral examination of molar maxillary, molar mandibular and interproximal (bitewing), the difference is 72%, while the values of periapical examination of the anterior maxillary and anterior mandibular vary by 78% and occlusal examination vary as much as 65% from the DRL. This shows that the dose applied to patients is as low as is reasonable to achieve a high-quality image.

When compared with the DRLs from various international organizations such as the National Radiological Protection Board (NRPB), the American Association of Physicists in Medicine (AAPM) and the Conference of Radiation Control Program Directors (CRCPD), the values of dose derived from this study for intra-oral examination are still low and within the prescribed limits (NRPB 1.80 mGy, AAPM 3.50 mGy, CRCPD 2.10–3.10 mGy).

The values of dose from extra-oral examinations also comply with the levels set by the MOH. Based on Table 1, the values obtained from the formula calculation are 109.237 mGy.cm² and 54.000 mGy.cm² for panoramic and lateral cephalometric examinations, respectively. Since the DRL from MOH is given in mGy.m², unit conversion is made to ease the comparison. Therefore, the value obtained for panoramic examination is 0.011 mGy.m² and for lateral cephalometric examination is 0.0054 mGy.m² (Figure 5).

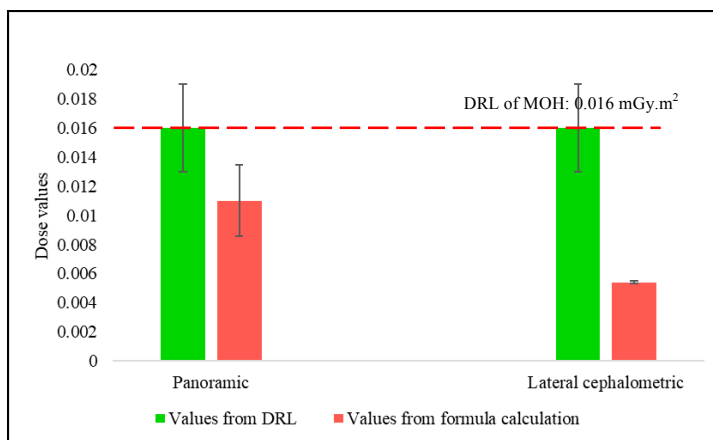


Figure 5. Comparison of dose values from formula calculation with DRL that has been prescribed by MOH for extra-oral examinations

The difference between the values prescribed by the DRL of MOH and the derived values from the formula calculation is 31% for panoramic examination and 66% for lateral cephalometric examination. Lateral cephalometric examination shows that the radiation dose applied to patients to get an image of the head, teeth and jaws is lower than that for the panoramic examination, where higher doses of radiation were applied even if only to get an image of the teeth and jaws.

No DRLs have been set by relevant international organizations for extra-oral dental radiographic examination, thus comparison of DRL is done based on studies that have been conducted and published by the related authors. These studies have proposed DRLs for DAP of 0.0071 mGy.m² (Chu, Lam, & Liang, 2007), 0.0073 mGy.m² (Helmrot & Alm Carlsson, 2005) and 0.0113 mGy.m² (Williams & Montgomery, 2000). These values are comparable with the DRLs prescribed by the MOH.

CONCLUSION

Dental imaging examination is the most common diagnostic tool used in dentistry. However, the principle of justification should be very closely followed due to the fact that the best way to protect patients is to avoid examination that is deemed unnecessary. If all criteria are used preferably, cumulative dose to the patient can be reduced. Each level of radiation dose should be considered potentially dangerous to humans, even at low doses, it may cause tissue damage.

REFERENCES

- Akinlade, B. I., Farai, I. P., & Okunade, A. A. (2012). Survey of dose area product received by patients undergoing common radiological examinations in four centers in Nigeria. *Journal of Applied Clinical Medical Physics*, 13(4), 3712. doi: 10.1120/jacmp.v13i4.3712
- Alcaraz, M., Armero, D., Martínez-Beneyto, Y., Castillo, J., Benavente-García, O., Fernandez, H., & Canteras, M. (2011). Chemical genoprotection: Reducing biological damage to as low as reasonably achievable levels. *Dentomaxillofacial Radiology*, 40(5), 310-314. doi: 10.1259/dmfr/95408354
- Ali, N. M. (2016). *Malaysian Nuclear Agency. Secondary Standard Dosimetry Laboratory (SSDL)*.
- Anissi, H. D., & Geibel, M. A. (2014). Intraoral radiology in general dental practices - A comparison of digital and film-based X-ray systems with regard to radiation protection and dose reduction. *Rofo*, 186(8), 762-767. doi: 10.1055/s-0034-1366256
- Cardis, E., Vrijheid, M., Blettner, M., Gilbert, E., Hakama, M., Hill, C., & Veress, K. (2007). The 15-Country Collaborative Study of Cancer Risk among Radiation Workers in the Nuclear Industry: Estimates of radiation-related cancer risks. *Radiation Research*, 167(4), 396-416. doi: 10.1667/RR0553.1
- Chu, R. Y., Lam, T., & Liang, Y. (2007). GafChromic XR-QA film in testing panoramic dental radiography. *Journal of Applied Clinical Medical Physics*, 8(2), 110-113.
- Helmrot, E., & Alm Carlsson, G. (2005). Measurement of radiation dose in dental radiology. *Radiation Protection Dosimetry*, 114(1-3), 168-171. doi: 10.1093/rpd/nch502
- Hymes, S. R., Strom, E. A., & Fife, C. (2006). Radiation dermatitis: Clinical presentation, pathophysiology, and treatment 2006. *Journal of the American Academy of Dermatology*, 54(1), 28-46. doi: 10.1016/j.jaad.2005.08.054
- Linnet, M. S., Slovis, T. L., Miller, D. L., Kleinerman, R., Lee, C., Rajaraman, P., & de Gonzalez, A. B. (2012). Cancer risks associated with external radiation from diagnostic imaging procedures. *CA: A Cancer Journal for Clinicians*, 62(2), 75-100. doi: 10.3322/caac.21132
- Morant, J. J., Salvadó, M., Hernández-Girón, I., Casanovas, R., Ortega, R., & Calzado, A. (2013). Dosimetry of a cone beam CT device for oral and maxillofacial radiology using Monte Carlo techniques and ICRP adult reference computational phantoms. *Dentomaxillofacial Radiology*, 42(3), 92555893. doi: 10.1259/dmfr/92555893
- Mortazavi, S. M. J., Ghiassi-Nejad, M., Bakhshi, M., Jafari-Zadeh, M., Kavousi, A., Ahmadi, J., & Shareghi, A. (2004). Entrance surface dose measurement on the thyroid gland in orthopantomography: The need for optimization. *International Journal of Radiation Research*, 2(1), 21-26.
- Muirhead, C. R., O'Hagan, J. A., Haylock, R. G., Phillipson, M. A., Willcock, T., Berridge, G. L., & Zhang, W. (2009). Mortality and cancer incidence following occupational radiation exposure: Third analysis of the National Registry for Radiation Workers. *British Journal of Cancer*, 100(1), 206-212. doi: 10.1038/sj.bjc.6604825
- Sheikh, S., Bhoweer, A. K., Arya, S., & Arora, G. (2010). Evaluation of surface radiation dose to the thyroid gland and the gonads during routine full-mouth intraoral periapical and maxillary occlusal radiography. *Contemporary Clinical Dentistry*, 1(2), 83-87. doi: 10.4103/0976-237X.68597
- Williams, J. R., & Montgomery, A. (2000). Measurement of dose in panoramic dental radiology. *British Journal of Radiology*, 73(873), 1002-1006. doi: 10.1259/bjr.73.873.11064656



Impact of Container, Temperature and Microcarriers on Inflammation and Endothelial Activation in Human Endothelial Cells

Muid, S.^{1,2,4}, Froemming, G. R. A.^{1,2,4}, Ali, A. M.³ and Nawawi, H.^{1, 2,4*}

¹Institute of Pathology, Laboratory and Forensic Medicine (I-PPerForM), Universiti Teknologi MARA (UiTM), 68100 Batu Caves, Selangor, Malaysia

²Faculty of Medicine Universiti Teknologi MARA (UiTM), 47000 Sungai Buloh, Selangor, Malaysia

³Faculty of Agriculture and Biotechnology, Universiti Sultan Zainal Abidin (UNISZA),

21300 Kuala Terengganu, Terengganu, Malaysia,

⁴Health & Wellbeing Community of Research, University Technology MARA (UiTM), 40450 Shah Alam, Selangor, Malaysia

ABSTRACT

Human umbilical vein endothelial cells (HUVECs) were cultured on microcarrier beads to accommodate different experiment apparatus such as rotating wall vessel. In this study, fluid operating apparatus (FPA) was used. However, the effect of inflammation and endothelial activation biomarkers in HUVECs cultured on different culture surface and containers are not well established. The effects of temperature changes on these biomarkers in HUVECs grown in FPA, a spaceflight hardware, are still unclear. The objective of this study was to compare the protein and gene expression of inflammation and endothelial activation biomarkers in (i) HUVECs cultured on microcarrier beads in conventional culture flask (CCFMC) vs. conventional culture flask (CCF) (ii) HUVECs cultured on microcarrier in FPA (FPAMC) vs. CCFMC and (iii) HUVEC cultured in FPAMC with ideal temperature (37°C) (FPAMC) vs. simulated space travel temperature (25-37°C), (FPAMC-ST). sICAM-1 and sVCAM-1 protein expression in HUVECs grown in CCFMC were higher than CCF. FPAMC had higher IL-6, TNF- α , ICAM-1, VCAM-1, e-selectin, NF κ B and eNOS gene expression than in CCFMC. FPAMC-ST had higher ICAM-1 and e-selectin protein expression than FPAMC- in ideal temperature. HUVECs are cultured onto microcarrier in simulated space flight temperature compared with ideal temperature had higher protein expression of sICAM-1 and

e-selectin but the protein and gene expression of other biomarkers of inflammation and endothelial activation are comparable. This suggests that differences in culture surface and container are have an impact on the expression of inflammation and adhesion molecule by HUVECs.

ARTICLE INFO

Article history:

Received: 05 January 2017

Accepted: 17 January 2017

E-mail addresses:

suhaila777@gmail.com (Muid, S.),

gabianisahf@gmail.com (Froemming, G. R. A.),

manaf@unisza.edu.my (Ali, A. M.),

hapizah@salam.uitm.edu.my (Nawawi, H.)

*Corresponding Author

Keywords: Adhesion molecules, endothelial cells, fluid processing apparatus (FPA), inflammation, microcarrier beads

INTRODUCTION

Vascular endothelium is an active metabolic component of tissues that has a number of important physiological functions, such as regulation of microvascular fluid and solute exchange, maintenance of anti-thrombogenic vessel surface, regulation of vascular tone and blood flow and control of leukocyte trafficking via surface expression of adhesion molecules (Kvietys & Granger, 1997). It has been postulated that endothelial cells can adapt rapidly to changes in their environment and local conditions (Infanger et al., 2006). The endothelial cells are in close contact and form a smooth layer that prevents blood cell interaction with the vessel wall. Ultra structurally, each cell can be seen to be anchored to an underlying basal lamina. Individual cells are anchored together by adhesion junctions, including prominent tight junctions, which prevent diffusion between cells (Infanger et al., 2006).

Microcarriers were specifically developed for high yield culture from a wide range of animal cells. The surface of the dextran and collagen-based beads has been optimised for efficient attachment and spreading of cells (Chen, Htay, Santos, Gillies, & Helen, 2009). The microcarriers are transparent and allow easy microscopic examination of the attached cells. Some studies have already shown that the microcarrier cell culture system produce cells that closely resemble the *in vivo* features of both morphological phenotype and gene-expression profile (Abbott, 2003; Chen et al., 2009). Previously, human endothelial cells were cultured on microcarriers and flown to International Space Station (ISS) in Fluid Processing Apparatus (FPA), a spaceflight hardware (Muid et al., 2010). This cell culture method has been optimised to accommodate the usage of FPA in the spaceflight experiment since FPA was initially designed for suspensions of microorganisms and not for adherence cells like HUVECs (Nawawi, Muid, Froemming, & Manaf, 2010). However, studies on inflammatory status in microcarrier cultured endothelial cells in FPA compared with conventional culture flask is scarce. Studies focusing on this would contribute to the development of FPA as a suitable culture container for growing endothelial cells in spaceflight experiment.

There is extensive evidence to indicate that heterogeneity develops in part, as a result of variation in exposure of endothelial cells (EC) to environmental stimuli and temperature changes (Cines, Pollak, Buck, & Loscalzo, 1998). During a spaceflight experiment, the cells have to undergo temperature fluctuation, especially during launch and orbiting before reaching the ISS. Upon reaching ISS, endothelial cells are transferred into a 37°C incubator, optimal temperature for the growth of cell culture. It is postulated that temperature fluctuations which occur during spaceflight travel may alter the protein and gene expression of inflammation and endothelial activation. Inflammation and endothelial activation have been involved in the pathogenesis of cardiovascular disease through atherosclerosis (Grenon, Jeanne, Aguado-Zuniga, Conte, & Hughes-Fulford, 2013). Inflammation is associated with increased cytokines such as interleukin 6 (IL-6) and tumour necrosis factor-alpha (TNF- α) leading to endothelial activation by enhanced expression of adhesion molecules [intercellular cell adhesion molecule-1 (ICAM-1), vascular cell adhesion molecule-1 (VCAM-1) and e-selectin], which are critical for monocyte recruitment into the vessel wall across intact endothelium (Rajashekhar et al., 2006). Moderate hypothermia has been shown to suppress inflammatory gene transcription in human

cerebral endothelial cells (Sutcliffe, Smith, Stanimirovic, & Hutchison, 2001). However, there are limited data or studies on the effects of space travel associated temperature fluctuations on these biomarkers in endothelial cells.

Therefore, this study was designed to investigate the expression of inflammatory and endothelial activation biomarkers by: (i) endothelial cells cultured onto conventional cell culture flask with microcarrier beads (CCFMC) and conventional cell culture (CCF); (ii) endothelial cells cultured onto microcarrier beads in different culture containers (conventional culture flask vs. Fluid Processing Apparatus (FPA)- FPAMC; and (iii) endothelial cells cultured on microcarrier beads in FPA at ideal temperature (FPAMC) versus space travel temperature fluctuations (FPAMC-ST).

MATERIALS AND METHOD

Materials

Medium 200 and Low Serum Growth Supplements (LSGS) were obtained from Cascade Biologics, USA. Accutase was purchased from ICN Biomedical, USA. ELISA test kits for e-selectin, sICAM-1, sVCAM-1, IL6 and TNF- α were purchased from Bender MedSystems, Austria. Cytodex 3 microcarrier beads were purchased from GE Healthcare Biosciences AB, Uppsala, Sweden. Phosphate-buffered saline (PBS) was obtained from MP Biomedicals, France while fluid processing apparatus (FPA) was obtained from Bioserve, USA. 4-(2-hydroxyethyl)-1-piperazineethanesulfonic acid (HEPES)-buffered saline was obtained from Gibco, USA and accutase was purchased from ICN Biomedical, USA. QuantigenePlex 2 assay kit was purchased from Panomics, USA.

Cell Culture

Human umbilical vein endothelial cells (HUVECs) were obtained from Cascade Biologics, USA and cultured in medium 200 (M200) supplemented with LSGS in a humidified incubator set at 37°C and 5% carbon dioxide (CO₂) until 80% confluency. Sub-cultivation ratios of HUVECs were 1:3 (culture: medium).

Preparations of Microcarrier Beads

Twenty-five mg of microcarrier beads (cytodex-3) were added into 25 ml Schott Duran bottle. Micropipette was used to transfer 5 ml of PBS (without Magnesium and Calcium) into the bottle to wash the microcarrier beads. The PBS was left to settle down at the bottom of bottle and then decanted. This washing step was repeated 3 times. This microcarrier beads were then sterilised by autoclaving at 121°C, 15 psi in 10 ml of PBS. The microcarrier beads were stored in room temperature before. Before the addition of HUVECs, the sterilised microcarrier beads were washed once with PBS. Subsequently, they were washed again twice with M200 culture medium. Finally, the microcarrier beads were soaked in M200 culture medium for 30 minutes prior to addition of HUVECs.

HUVECs Cultured in Culture Flask

HUVECs was added into T-75cm² cell culture flask with 100,000 cells seeding density/ml. Ten ml M200 culture medium was added into the flask and incubated at 37°C incubator for 12 days. Culture medium M200 (5 ml) was added into the flask periodically every three days.

HUVECs Cultured on Microcarrier Beads in Culture Flask (CCFMC)

M200 culture medium from the T-25 cm² flask was aspirated and discarded. Monolayer of HUVECs in the culture flask was washed with PBS without magnesium (Mg) and calcium (Ca). Two millilitre of PBS was added into culture flask. Culture flask was agitated for 5 seconds. PBS was then discarded from the culture flask. Three millilitre of accutase was added onto the HUVECs monolayer in the culture flask and incubated in the humidified environment at 37°C in CO₂ incubator for 3 minutes. Detachment of HUVECs was observed under phase-contrast microscope. The HUVECs' suspension was transferred into 15 ml centrifuge and spun at 1000 RPM for severely minutes. Supernatant was carefully discarded. The HUVECs pellet was dissolved with 1 ml of M200 medium and suspended for several times to break the cell clumps and produced a uniformly dispersed cell suspension. The number of cells was determined by haemocytometer. A volume of suspension cells containing 100,000 cells was transferred into a sterile siliconized petri dish (60 mm × 20 mm) containing microcarrier beads. Petri dish was positioned in the 45-degree angle. The HUVECs were allowed to attach on the microcarrier beads surface for one hour with gentle agitation for 10 second for every 15 minutes. The HUVECs on the microcarrier beads were then transferred into a T-75 cm² cell culture flask. Then 10 ml of M200 culture medium was added into the cell culture flask and incubated at 37°C humidified in CO₂ incubator for 12 days. Culture medium M200 (5 ml) was added periodically to the flask every three days.

HUVECs in FPA Grown in Ideal (37oc) and Changes of Temperature (FPAMC and FPAMC-ST)

The FPA bio container is a syringe-like device with a cylindrical glass container housed within a Lexan™ sheath. A plunger is provided at the open end of tube (Figure 1). Three rubber septa are provided so as to divide the glass barrel into three chambers, namely culture chamber, stasis chamber and fixative chamber. When the plunger is depressed, a fluid bypass allows fluid from the stasis chamber to be injected into the culture chamber for activation of the culture. Similarly, a termination reagent can be injected from the fixative chamber into the growing culture for growth cessation at the predetermined termination point. Method of culturing HUVECs in FPA were previously described (Nawawi, Muid, Froemming, & Manaf, 2010). Briefly, 25 mg of HUVEC-coated microcarrier beads (with 5×10^5 cells) were prepared according to the above-mentioned method and added into the culture chamber of the FPA. Three millilitre of the M200 culture medium having 20 mM HEPES-buffered saline was also added into the culture chamber. A rubber septum was inserted. An amount of 1.5 ml of M200 culture medium having 20 mM HEPES-buffered saline was added into the stasis chamber. A rubber septum was then inserted. Next, 1.5 ml of M200 culture medium having 20 mM HEPES buffered saline was

added into the fixative chamber. One group of FPAMC was incubated in ideal temperature at 37°C in incubator for 12 days (FPAMC). Other sets of FPAMC were grown according to a simulated temperature changes associated with space travel (FPAMC-ST) as stated in Table 1. Three sets (triplicates) of FPAs having the above configuration were prepared.

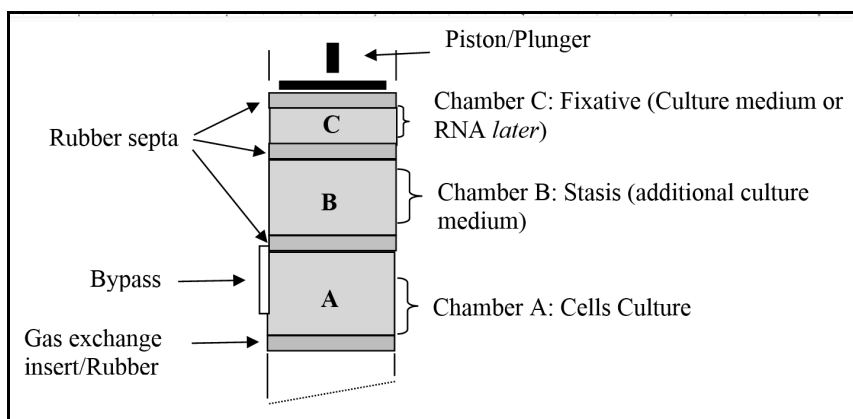


Figure 1. FPA diagram showing the three chambers separated by septa. The fluid bypass enables fluid from the stasis chamber to be injected into the culture chamber during activation and enables the termination reagent to be injected into the growing culture for growth cessation during termination

Table 1
Temperature profile from day 1-12

Time (days)	Temperature (°C)
Day 1	25
Day 2	25
Day 3	37
Day 4-9	37
Day 10	25
Day 11	25
Day 12	37

Soluble Expressions of Cytokine and Adhesion Molecules Measurement in the Supernatant

Soluble inflammatory markers of IL-6, TNF- α , ICAM-1, VCAM-1 and e-selectin in supernatant of HUVECs were measured by ELISA standard kits (Bender Med System, Vienna, Austria). Each test was performed in triplicates according to the instructions provided by the manufacturer. At the end of ELISA testing, absorbance was obtained by spectrophotometer (Micro Quant, Biotek Instruments) at 405 nm wavelength.

DNA Hybridisation Method

The RNA of HUVECs from all samples was extracted using an RNA extraction kit (Qiagen, USA). Cells lysate was obtained from HUVEC cultured in FPAMC-IT and FPAMC-ST. Samples were collected and preceded with QuantigenePlex assay according to manufacturer's protocols. The plate was immediately read using the Bio-Plex system (Bio-Rad Laboratories, Hercules, CA). Results were normalised against glyceraldehyde-3-phosphate dehydrogenase (GAPDH) and hypoxanthine guanine phosphoribosyl transferase-1 (HPRT-1) to obtain standard norm of the ratio. Primer sequence and annealing temperature for each measured gene are shown in Table 2 (Muid et al., 2010).

Table 2
Primer sequence for mrna expression

i) IL-6
Forward primer: GCC TTC GGT CCA GTT GCC TT
reverse primer : GCA GAA TGA GAT GAG TTG TC
ii) ICAM-1 (CD54)
Forward Primer AGAGGTCTCAGAAGGGACCG
Reverse Primer GGGCCATACAGGACACGAAG
III) VCAM-1 (CD106)
Forward primer: GGTGGGACACAAATAAGGGTTTTGG
Reverse primer: CTTGCAATTCTTTTACAGCCTGCC
IV) E-selectin
Forward primer: TGAAGCTCCCACTGAGTCCAA
Reverse primer: GGTGCTAATGTCAGGAGGGAGA
V) TNF- α
Forward primer: CCGGGCGTGGTGGTGAG
Reverse primer: TCTGCCTTTTGGGTCTTGTGAATA
VI) eNOS
Forward primer: ATGGGCAACTTGAAGAGCGTGG
Reverse primer: TAGTACTGGTTGATGAAGTCCC
Reference gene:
i) GAPDH
Forward primer: CCACCCATGGCAAATTCCATGGCA
Reverse primer: TCTAGACGGCAGGTCAGGTCCACC
iii) HPRT-1:
Forward primer: GGCAAACAATGCAAACCTT
Reverse primer: CAAGGGCATATCCTACGACAA

Statistical Analysis

Data was analysed using Statistical Package for the Social Sciences version 22.0. Significant value was set at $p < 0.05$. Results were expressed as mean + standard error means. Independent T- Test was performed to compare the differences between two different groups.

RESULTS

Soluble Protein Expressions of Cytokine and Adhesion Molecules Measurement in the Supernatant

The CCFMC had higher sICAM-1 ($p < 0.0001$) and sVCAM-1 ($p < 0.0001$) level compared with CCF. There was no significance difference in IL-6, TNF- α and e-selectin level was found between CCFMC and CCF. FPAMC had lower IL-6 ($p < 0.05$) and VCAM-1 ($p < 0.05$) levels compared with CCFMC. FPAMC-ST had higher protein expression of sICAM-1 and e-selectin compared with FPAMC-. Both FPAMC-ST and FPAMC- in ideal temperature had similar protein expression of IL-6, TNF- α and VCAM-1. Data is shown in Table 3.

Table 3
Protein expression of inflammation and endothelial activation biomarkers

Biomarkers/ Samples	CCF	CCFMC	FPAMC	FPAMC-ST
IL-6 (pg./ml)	37.8 + 8.0	47.4 + 7.7	14.0 + 2.0 #	13.1 + 2.0
TNF- α (pg/ml)	78.5 + 4.1	59.4 + 1.6	58.2 + 2.7	65.4 + 1.5
sICAM-1 (pg/ml)	1055.4 + 62.1	2778.4 + 61.9 ****	2601.8 + 47.1	7738.7 + 318.2 \$
sVCAM-1 (pg/ml)	450.8 + 55.9	12747.7 + 336.0 ****	5322.6 + 1590.1 #	7013.0 + 1895.4
e-selectin (pg/ml)	1506.5 + 82.5	1953.3 + 126.0	1609.2 + 41.2	2059.5 + 137.9 \$

**** $p < 0.0001$ compared to CCF, # $p < 0.05$ compared to CCFMC, \$ $p < 0.05$ compared to FPAMC
CCF: Conventional culture flask; CCFMC: HUVECs cultured on microcarrier beads in conventional culture flask; FPAMC: HUVECs cultured on microcarrier in FPA; FPAMC-ST: HUVECs cultured in FPAMC with simulated space travel temperature (25-37°C). Data is expressed as Mean + SEM (n=3)

mRNA expression of IL-6, TNF- α , ICAM-1, VCAM-1 and e-selectin

There were no significant differences in the gene expression of IL-6, TNF- α , ICAM-1, VCAM-1, e-selectin, NF κ B and eNOS between CCFMC and CCF. The IL-6 ($p < 0.0001$) and TNF- α ($p < 0.0001$) gene expression in FPAMC were higher than in CCFMC. Similarly, ICAM-1 ($p < 0.0001$), VCAM-1 ($p < 0.0001$), e-selectin ($p < 0.0001$) levels in FPAMC were higher than in CCFMC. The involvement of NF κ B pathway on the increment of cytokines and adhesion molecule was investigated and it was found that NF κ B gene expression in endothelial cells

cultured in FPAMC was higher than in CCFMC ($p < 0.01$). eNOS gene expression in endothelial cells cultured in FPAMC was higher than CCFMC ($p < 0.05$). Both FPAMC and FPA MC-IT expressed similar gene expression of IL-6, TNF- α , ICAM-1, VCAM-1, e-selectin, NF κ B and eNOS. Data is displayed in Table 4.

Table 4
Gene expression of inflammation and endothelial activation biomarkers

Biomarkers/ Samples	CCF	CCFMC	FPAMC	FPAMC-ST
IL-6	0.05+ 0.00	0.02+ 0.005	0.58+ 0.03	1.65+ 0.03
Norm ratio			####	
TNF- α	0.001+ 0.00	0.001+ 0.00	0.13+ 0.04	0.18+ 0.02
Norm ratio			####	
ICAM-1	0.22+ 0.02	0.23+ 0.03	2.81+ 0.12	9.68+ 2.14
Norm ratio			####	
VCAM-1	0.001+ 0.00	0.003+ 0.00	0.77+ 0.28	0.63+0.2
Norm ratio			####	
e-selectin	0.006+ 0.00	0.004+ 0.00	0.39+ 0.08	0.59+ 0.08
Norm ratio			####	
NF κ B	0.17 + 0.01	0.006 + 0.00	0.29 + 0.00	1.10 + 0.1
Norm ratio			##	
eNOS	0.10 + 0.005	0.02 + 0.005	2.89 + 0.10	2.15 + 0.05
Norm ratio			#	

$p < 0.0001$, ## $p < 0.01$, # $p < 0.05$ compared to CCFMC

CCF: Conventional culture flask; CCFMC: HUVECs cultured on microcarrier beads in conventional culture flask; FPAMC: HUVECs cultured on microcarrier in FPA; FPAMC-ST: HUVECs cultured in FPAMC with simulated space travel temperature (25-37°C). Data is expressed as Mean + SEM (n=3)

DISCUSSION

Microcarriers are commonly used to grow anchorage dependent cell lines in suspension culture (Hamid, McCluskey, McClenaghan, & Flatt, 2000). They are inert materials with surface characteristics suitable for promoting cell culture including charge, polarity, chemical structure and hydrophobicity (Levin, Ting-Beall, & Hochmuth, 2001). In this study, Cytodex 3 microcarriers with a surface layer of denatured collagen covalently bound to a matrix of cross linked dextran was used. It has been suggested that in comparison with conventional monolayer culture methods on stacking flat surface, microcarriers provide better surface for cell attachment and a large surface area can be contained in a given reactor volume or other culture system such as fluid operating apparatus (FPA) with a relatively uniform environment (Wong, Peshwa, & Hu, 2004). Even so, there are limited studies on the expression of inflammatory and endothelial activation biomarkers by the endothelial cells grown on microcarrier compared with those grown on flat surface of conventional (polystyrene) culture flask.

This present study has shown that endothelial cells grown on microcarrier (CCFMC) expressed 2.6 and 28.3-fold higher soluble ICAM-1 and VCAM-1 protein expression respectively, than those cells grown on flat surface of cell culture flask (CCF). It has been suggested that the process of cell attachment to any foreign surface can be viewed as a combination of two separate processes which are the initial absorption of cells to microcarrier surface followed by adhesion molecule mediated attachment and cell spreading. The cell adhesion molecule-mediated interactions are important to develop a firm grip of cells so that the cells are remained attached on the microcarrier beads (Wong, Peshwa, & Hu, 2004). The expression of adhesion molecules, either covalently bound to microcarriers or in soluble form in medium promotes subsequent development of firm grip of cells on microcarriers and facilitate cell spreading (Kan, Minamoto, Sunami, Yamam, & Umeda, 1982; Varani, Fligiel, Inman, Beals, & Hillegas, 1995). In most cases, the cell synthesises adhesion molecules on their own (Wong, Peshwa, & Hu, 2004). It can be explained the increased ICAM-1 and VCAM-1 protein expression by endothelial cells grown on microcarrier beads in this present study. However, it is interesting to note that there were no differences in the protein expression of e-selectin and other biomarkers of inflammation between the two groups. In addition, the gene expression of all the studied biomarkers was comparable between both groups. It appears that ICAM-1 and VCAM-1 are most important in providing firm endothelial cell adherence onto the microcarrier beads in facilitating cell spreading and growth in CCF.

Fluid operating apparatus (FPA) is a flight hardware that is widely used by space scientists. FPA comprises three chambers namely, a culture chamber, a stasis chamber and a fixative chamber. It is generally known that FPAs are more suitable as a culture container for non-anchorage dependent cells. To the best of our knowledge, FPA has not been previously utilised for growing anchorage cells including human endothelial cells. Hence, in the present study, the use of FPA in growing HUVECs, one example of anchorage cells was optimised for spaceflight experiment. In addition, microcarrier beads were added to culture HUVECs in FPA. Endothelial cells cultured onto microcarrier beads in FPA had lower ICAM-1 and sVCAM-1 protein expression compared with microcarrier beads in culture flask. However, the result of protein expression was in contrast with gene expression where endothelial cells cultured onto microcarrier in the FPA had higher IL-6, TNF- α , ICAM-1, VCAM-1, e-selectin, NF κ B and eNOS gene expression compared with those cultured in cell culture flask. The reason for the different expression of cytokines and adhesion molecules in the protein and gene levels may be due to the post-translational modification of the protein which can stabilise or enhance degradation (Aiken, Kaake, Wang, & Huang, 2011). Therefore, the protein expression is not always parallel to mRNA abundance, and enhanced gene expression does not guarantee that this gene will result in protein synthesis (Vogel et al., 2010). Another possible reason is protein translation and increased cell surface expression in response to increase gene expression. However, there is a possibility that this cell surface protein is not being secreted into supernatant to become soluble protein expression of adhesion molecule. Therefore, it is suggested that future studies should address and investigate this finding. In this present study, gene expression analysis showed that culturing endothelial cells in the FPA may enhance the expression of cytokines and adhesion molecules. Therefore, it can be postulated that growing endothelial cells in different culture container/apparatus may give a different expression of cytokines and

adhesion molecules, at least in this study. Therefore, in the spaceflight experiments, it is of great importance to have controlled culture cells that have similar environment to avoid any confounding factors.

Since temperature changes occur during spaceflight travel, it is important to investigate whether this actual temperature profile due to space travel temperature fluctuations can give an impact on the expression of inflammation and endothelial activation by endothelial cells cultured in FPA. In this present study, we have found that ICAM-1 and e-selectin protein expression are affected in terms of being temperature sensitive. It has been shown that ICAM-1 and e-selectin expression by HUVECs cultured in FPA with space travel temperature fluctuations is higher than those in ideal temperature (37°C). In our experiment, the temperature changes range is between 25-37°C. This temperature profile was based on the temperature reading recorded by HOBO temperature recorder in the International Space Station (ISS) during a spaceflight mission. Johnson, Haddix, Pohlman and Verrier (1995) reported the down regulation of e-selectin expression in HUVECs incubated at 25°C. In contrast, our study shown e-selectin and ICAM-1 protein expression was higher in space travel temperature profile compared with that at ideal temperature of 37°C. Therefore, it can be suggested that temperature changes can lead to increment of adhesion molecules protein expression in endothelial cells. It also suggested that ICAM-1 and e-selectin are a sensitive towards temperature fluctuations in endothelial cells.

It can be concluded that HUVECs in culture flask with microcarrier beads expressed higher soluble protein expression of ICAM-1 and VCAM-1 but the protein expression of other biomarkers of inflammation and endothelial activation and gene expression of these biomarkers are comparable. Interestingly, endothelial cells cultured onto microcarrier beads in FPA compared with culture flask have increased gene expression of biomarkers of inflammation and endothelial activation. In contrast, the expression of soluble IL-6 and VCAM-1 protein expression is higher in culture flask compared with FPA while there was no difference in other protein biomarkers. This suggests that differences in culture surfaces and containers have impact on the expression of inflammation and adhesion molecule by HUVECs. The HUVECs cultured onto microcarrier beads in simulated space flight temperature compared with ideal temperature had higher protein expression of sICAM-1 and e-selectin but the protein and gene expression of other biomarkers of inflammation and endothelial activation are comparable.

REFERENCES

- Abbott, A. (2003). Cell culture: Biology's new dimension. *Nature*, 424(6951), 870-872.
- Aiken, T., Kaake, R. M., Wang, X., & Huang, L. (2011). Oxidative stress-mediated regulation of proteasome complexes. *Molecular and Cellular Proteomics*, 10(5), R110. 006924.
- Chen, Z., Htay, A., Santos, W. D., Gillies, G. T., & Helen, L. (2009). In vitro angiogenesis by human umbilical vein endothelial cells (HUVEC) induced by three-dimensional co-culture with glioblastoma cells. *Journal of Neuro-oncology*, 92(2), 121-128.
- Cines, D. B., Pollak, E. S., Buck, C. A., & Loscalzo, J. (1998). Endothelial cells in physiology and in the pathophysiology of vascular disorders. *Blood*, 91(10), 3527-3561.

- Grenon, S. M., Jeanne, M., Aguado-Zuniga, J., Conte, M. S., & Hughes-Fulford, M. (2013). Effects of gravitational mechanical unloading in endothelial cells: Association between caveolins, inflammation and adhesion molecules. *Scientific Reports*, 3.
- Hamid, M., McCluskey, J. T., McClenaghan, N. H., & Flatt, P. R. (2000). Culture and function of electrofusion-derived clonal insulin-secreting cells immobilized on solid and macroporous microcarrier beads. *Bioscience Reports*, 20(3), 167-176.
- Infanger, M., Kossmehl, P., Shakibaei, S., Baatout, S., Witzing, A., Grosse, J., & Derradji, H. (2006). Induction of three-dimensional assembly and increase in apoptosis of human endothelial cells by simulated microgravity: Impact of vascular endothelial growth factor. *Apoptosis*, 11(5), 749-764.
- Johnson, M., Haddix, T., Pohlman, T., & Verrier, E. D. (1995). Hypothermia reversibly inhibits endothelial cell expression of e-selectin and tissue factor. *Journal of Cardiac Surgery*, 10(s4), 428-435.
- Kan, N., Minamoto, Y., Sunami, S., Yamam, I., & Umeda, M. (1982). The effects on cell adhesion of fibronectin and gelatin in a serum-free, bovine serum albumin medium. *Cell Structure and Function*, 7(3), 245-252.
- Kvietys, P. R., & Granger, D. N. (1997). Endothelial cell monolayers as a tool for studying microvascular pathophysiology. *American Journal of Physiology-Gastrointestinal and Liver Physiology*, 273(6), G1189-G1199.
- Levin, J. D., Ting-Beall, P., & Hochmuth, R. M. (2001). Correlating the kinetics of cytokine-induced e-selectin adhesion and expression on endothelial cells. *Biophysical Journal*, 80(2), 656-667.
- Muid, S., Froemming, G. R. A., Manaf, A. Muszaphar, S., Yusoff, K., & Nawawi, H. (2010). Changes in protein and gene expression of adhesion molecules and cytokines of endothelial cells immediately following short-term spaceflight travel. *Gravitational and Space Research*, 23(2).
- Nawawi, H., Muid, S., Froemming, G. R. A., & Manaf, A. (2010). Malaysia Patent No. PI 2010002329. Intellectual Property Corporation of Malaysia.
- Rajashekhar, G., Willuweit, A., Patterson, C. E., Sun, P., Hilbig, A., Breier, G., Helisch, A., & Clauss, M. (2006). Continuous endothelial cell activation increases angiogenesis: Evidence for the direct role of endothelium linking angiogenesis and inflammation. *Journal of Vascular Research*, 43(2), 193-204.
- Sutcliffe, I. T., Smith, A. H., Stanimirovic, D., & Hutchison, J. S. (2001). Effects of moderate hypothermia on IL-1 and BGR – induced leukocyte rolling and adhesion in pial microcirculation of mice and on proinflammatory gene expression in human cerebral endothelial cells. *Journal of Cerebral Blood Flow and Metabolism*, 21(11), 1310-1319.
- Varani, J., Fligiel, S. E. G., Inman, D. R., Beals, T. F., & Hillegas, W. J. (1995). Modulation of adhesive properties of DEAE-dextran with laminin. *Journal of Biomedical Materials Research*, 29(8), 993-997.
- Vogel, C., Abreu, R. D. S., Ko, D., Le, S.Y., Shapiro, B. A., Burns, S. C., ... Penalva, L. O. (2010). Sequence signatures and mRNA concentration can explain two-thirds of protein abundance variation in a human cell line. *Molecular Systems Biology*, 6(1), 400.
- Wong, K., Peshwa, M., & Hu, W. S. (2004). Overview of Microcarrier Culture. *Cellular Bioprocess Technology*, 1-8.





Low-Density Lipoprotein Concentration is an Independent Predictor for Oxidised LDL in Patients with Familial Hypercholesterolaemia

Nur Suhana Hamzan, Radzi Rahmat, Hapizah Mohd Nawawi* and Thuhairah Hasrah Abdul Rahman

Institute of Pathology, Laboratory and Forensic Medicine (I-PPerForM), Universiti Teknologi MARA (UiTM), 47000 Sungai Buloh, Selangor, Malaysia

ABSTRACT

Familial hypercholesterolaemia (FH) is an autosomal dominant genetic disorder characterised by severe hypercholesterolaemia leading to premature coronary artery disease (CAD). Oxidised low-density lipoprotein (ox-LDL), F2-isoprostanes (ISP) and malondialdehyde (MDA) are established oxidative stress biomarker, but the status of oxidative stress in FH is not well studied. The aim of this study is to investigate oxidative stress status among FH patients and normocholesterolaemic control (NC) subjects. Ninety-eight FH patients and 100 (age, gender and BMI matched) NC subjects were recruited in series of health screening programmes across the country. Fasting blood samples were analysed for serum ox-LDL, ISP and MDA. Ox-LDL, ISP and MDA concentrations were higher in FH groups compared to NC (mean \pm SEM: 63.0 \pm 6.5 vs 25.5 \pm 1.2 (U/l), $p<0.001$); 749.7 \pm 74.0 vs 354.2 \pm 18.1 pg/ml, $p<0.0001$; 342.4 \pm 46.0 vs 162.7 \pm 13.5 nmol/g, $p<0.0001$). Ox-LDL showed correlation with glucose ($p<0.05$), TC ($p<0.001$), LDL-c ($p<0.001$) and HDL-c ($p<0.01$) in all subjects. LDL-c was associated positively with ox-LDL concentration ($p<0.001$). LDL-c was an independent predictor for ox-LDL concentration ($p<0.001$) after adjustment for the various confounding factors. In conclusion, FH patients have higher

oxidative stress status which contributes to the greater risk of developing atherosclerosis and its related complications. LDL concentration is an independent determinant of ox-LDL, suggesting that both the proatherogenic quantity and quality of LDL coexist in FH which enhance the risk of premature CAD.

ARTICLE INFO

Article history:

Received: 05 January 2017

Accepted: 17 January 2017

E-mail addresses:

nur.suhana.hamzan@gmail.com (Nur Suhana Hamzan),

radzirahmat87@gmail.com (Radzi Rahmat),

hapizah@salam.uitm.edu.my (Hapizah Mohd Nawawi),

tootie_74@yahoo.com (Thuhairah Hasrah Abdul Rahman)

*Corresponding Author

Keywords: Familial hypercholesterolaemia, atherosclerosis, F2-isoprostanes, malondialdehyde, oxidised low-density lipoprotein

INTRODUCTION

Familial hypercholesterolaemia (FH) is a group of genetic disorders involving several genes including low-density lipoprotein receptor (*LDLR*), apolipoprotein B (*APOB*), proprotein convert asecubtilisin/kexin type 9 (*PCSK9*) and other possible genes yet to be described, resulting in severe elevations of blood cholesterol levels (Goldberg et al., 2011). The prevalence of homozygous FH is generally about 1:1 million (Soutar & Naoumova, 2007). However, heterozygous FH is a common genetic disorder occurring in one in every 300 to 500 people in most areas of the world (Hopkins, Toth, Ballantyne, & Rader, 2011). With an approximate population of 30 million in Malaysia, it is estimated that 60,000 individuals are affected and a majority of whom are under diagnosed (Alicezah et al., 2014).

FH is characterised by acute increase of low density lipoprotein (LDL) cholesterol and total cholesterol in the circulation, deposition of cholesterol in peripheral tissues, the presence of tendon xanthomata and accelerated atherosclerosis which leads to the increased risk of premature coronary artery disease (CAD) (Lye et al., 2013). The range of total cholesterol concentrations in heterozygous FH patients are typically in the range of 9.1 to 12.9 mmol/L and in a homozygous range from 16.8 to 25.9 mmol/L (Goldberg et al., 2011). There is evidence that other diseases with increased risk for developing atherosclerosis have also increased status of oxidative stress (Martinez-Hervas et al., 2008; Stephens et al., 2006)

As a result of elevated LDL cholesterol concentrations and its prolonged plasma half- life, it is possible that it will lead to increased susceptibility to free radical attack and oxidation. Hypercholesterolaemia is reported to be associated with enhanced oxidative stress, related to increased lipid peroxidation (Palombo, Lubrano, & Sampietro, 1999). Endothelial cells, smooth muscle cells, neutrophils and monocytes all have the potential to oxidatively modify the LDL, leading to the generation of lipid peroxidation products such as oxidised LDL (ox-LDL) and reactive oxygen species (Nourooz-Zadeh, Smith, & Betteridge, 2001).

Biomarkers of oxidative stress, are used to measure and evaluate products of lipid peroxidation such as Ox-LDL (Hulthe, Bokemark & Fagerberg, 2001; Stocker & Keaney, 2004), F2-Isoprostane (ISP) (de Faria et al., 2014; Vassalle, Petrozzi, Botto, Andreassi, & Zucchelli, 2004) and malondialdehyde (MDA) (Pirinccioglu, Gökalp, Pirinccioglu, Kizil, & Kizil, 2010). These biomarkers of oxidative stress have been used as indicators of normal biological or pathological process. Therefore, the objectives of this study were to compare the oxidative stress status between Familial Hypercholesterolaemia (FH) patients & normocholesterolaemic control (NC) subjects in a Malaysian cohort and to assess the independent predictors, association and correlation of these oxidative stress biomarkers in all subjects.

MATERIALS AND METHODS

This is a case control, observational study involving 98 FH patients and 100 normal control (NC) subjects conducted in a Specialist Lipid Clinic of teaching hospital. The FH subjects and NC in this Malaysian cohort were recruited from the specialist clinics and from various regions in Malaysia, which include the northern, southern and central region of West Malaysia as well as East Malaysia. All patients gave their written informed consent for participation in the study

and the Institutional Ethical Committee approval was obtained prior to the commencement of the study.

For each subject, a set of questionnaires were completed and relevant clinical data was obtained. All patients and control subjects were screened through a protocol consisting of medical history, physical examination, and laboratory tests including fasting glucose, serum lipids, renal profile, and liver function test. Anthropometry measurement including, body mass index (BMI), waist circumference (WC), smoking habits and history of personal CAD were measured and documented. BP was measured by an automated BP reader (Omron HEM-712C, Japan) with the subject in a seated position and after 5-10-minute rest. The systolic (SBP) and diastolic blood pressure (DBP) was measured to the nearest 1 mmHg. BMI was calculated using the formula: $BMI = \text{weight (kg)}/\text{height}^2 (\text{m}^2)$. Waist circumference (WC) was measured to the nearest 0.5 cm using a measuring tape at midway between the inferior margin of the last rib and the iliac crest in a horizontal plane. Hip circumference measurement was taken from the pelvis at the point of maximal protrusion of the buttock (World Health Organization (WHO), 1995). The presence of CAD was assessed based on the subject family history of CAD, the personal clinical history, and previous medical records. Lipid stigmata such as corneal arcus, xanthelasma, achilles tendon xanthomata and tendon xanthomas were examined and documented.

Diagnosis of FH was made based on the Simon Broome's criteria (Goldberg et al., 2011). Patients with diabetes mellitus, renal, liver, thyroid diseases or any other causes of secondary hypercholesterolaemia (Stone, 1994), those with recent febrile illness, concomitant neoplasm, inflammatory disease or immunosuppressive therapy including steroid usage and those taking vitamin supplements were excluded from this study. Inclusion criteria for NC were TC level of < 6.5 and/or LDL-c < 4.0 mmol/L and those who did not fulfil Simon Broome's criteria for definite or possible FH, as well as clinically well with no chronic diseases or on any medications.

Twenty millilitres (ml) overnight (10-12 hours) fasting venous blood samples were collected into plain tubes of serum for routine biochemical analyses, which are fasting serum lipid (FSL), liver function tests (LFT), renal profile (RP) and Ox-LDL and ISP biomarkers. For the MDA TBARS assay, plasma EDTA tubes were used and for fasting blood glucose (FBG), fluoride tubes were used. Routine biochemical analyses that were performed on all subjects consisting of FSL, FPG, LFT and RP. Fasting serum lipids, FPG, LFT and RP were performed on an automated analyser (Cobas Integra 400, Germany) to identify all the health screening programmes participants that presented with exclusion criteria. All the blood samples were collected by non-traumatic venepuncture in the morning between 0800 and 1000 am. Serum was separated within 1 hour of collection, the biochemical analysis was performed within 24 hours and remaining samples were stored at -20°C until biomarkers analysis were performed within 3 months.

Sample size estimation was calculated using Open Epi software, within the power of study 80% and α -level was set at 0.05 of the difference in mean between two groups to have clinical importance and the standard deviation of lipid profile which were 0.8 and 1.3 mmol/L, respectively in study done by Khoo et al. (2000). At 95% confidence interval, a proposed minimal sample size was 84 for the lipid profile using the formula for case control studies (Charan & Biswas, 2013).

Ox-LDL concentrations in each subject were determined using oxidised LDL ELISA kit (Merckodia, Sweden). In the ELISA plate, 25 μL of calibrators, controls and serum samples were added, followed by 100 μL Assay Buffer. The plate then was incubated for 2 hours on a shaker at room temperature. Next, the plate was washed by 6 times and 100 μL enzyme conjugate solution were added. The plate then was incubated for 1 hour on a shaker at room temperature. Next, the plate was washed 6 times before 200 μL Substrate TMB were added. The plate then was again incubated 15 minutes at room temperature. Fifty microlitres of Stop Solution were added, and the plate was shaken for approximately 5 seconds on shaker before absorbance reading using a spectrophotometer. The detection limit of the kit was <1 mU/l with absorbance reading of optimal density at 450 nm.

Plasma ISP levels were analysed by Liquid chromatography-tandem mass spectrometry (LCMSMS) which was performed using a Shimadzu LC system consisting of a binary pump (LC-20AD), an autosampler SIL-20AC (set at 4°C), a column oven (set at 40°C) and a system controller (CBM-20A) which were interfaced with 4000 QTRAPTM (Applied Biosystems, Canada). The procedure of LCMSMS and calibration curve and pre-treatment of samples were optimised by a technical representative from the manufacturer. The analyte was detected by Multiple Reaction Monitoring (MRM) mode and each analyte was monitored for two MRM transitions. Mass spectral data were analysed using Analyst 1.4.2 software. A six-point calibration curve was included with each assay using calibrator concentrations from 100, 250, 400, 500, 1000 and 10000 pg/mL which made up from 3 solutions; solution A = $1\ \mu\text{g/mL}$ ($1\ \mu\text{L}$ reference standard + 999 μL water), solution B = 10 ng/mL (10 μL sol A + 990 μL water), and solution C = 1 ng/mL (100 μL sol B + 990 μL water). Limits of detection were between 116.40–10051.00 ng/mL . Accuracy, range were within 85.5–126%. Separation was performed on reversed phase C-18 Zorbax Zorbax Eclipse 0.5 $\mu\text{L} \times 150\ \text{mm} \times 4.6\ \text{mm}$ I.D column from Agilent coupled to a triple quadrupole mass spectrometer running in negative electrospray ionisation mode with a constant flow rate of 0.5 mL/min was used to separate the analytes. The mobile phase consisted of two eluents, solvent A (water/acetonitrile at 98:2 by volume) and solvent B (100% methanol), both containing 0.01% ammonium hydroxide at pH of 9.5. The pre-treatment consists of liquid extraction of 450 μL serum with diethyl ether with subsequent evaporation with Nitrogen gas steam, followed by reconstitution in 1000 μL of water. Sample injection volume and total run time were 50 μL and 9 min respectively.

Malondialdehyde (MDA) was measured by the TBARS assay method adapted from (Ledwozyw, Michalak, Stepien, & Kadziolka, 1986). This assay was based on the reaction of a chromogenic reagent, 2-thiobarbituric acid, with MDA at 25°C . One molecule of MDA reacts with 2 molecules of 2-thiobarbituric acid via a Knoevenagel-type condensation to yield a pink chromophore the last product of fatty acid peroxidation in absorbance maximum at 532 nm. Sodium hydroxide, 1, 1, 3, 3-tetraethoxypropane (TEP), n-butanol and acid trichloroacetic (TCA) were obtained from Sigma-Aldrich, USA. Hydrochloric acid (HCl), 2-thiobarbituric acid (TBA), Sodium chloride, Potassium dihydrogen phosphate and dipotassium hydrogen phosphate were purchased from Merck, Germany. For MDA standards preparation, 40.5 nmol/ml of MDA stock solution was prepared by the addition of 0.01 ml origin standard stock with 1 litre of distilled water. Then, a series of 9 different concentrations (0.2, 0.4, 0.8, 1.0, 5.0,

10.0, 15.0 and 20.0 nmol/ml) of MDA standards were prepared. An amount of 0.5 ml from each MDA standard was added to 2.5 ml 1.22M TCA in 0.06 M HCl in the test tubes which were then incubated at a room temperature for 15 minutes for protein precipitation. 1.5 ml 0.67% TBA was added into each test tube. The mixture was further heated in a boiling (100°C) water bath for 30 minutes. After cooling to room temperature, 4 ml of n-butanol was added. The mixture was then shaken for 2 minutes with vortex and centrifuged at 3000 rpm for 10 minutes. The top layer of butanol was pipette in a cuvette and the absorbance was measured at 532 nm. A standard curve graph was plotted after all MDA absorbance were obtained. For MDA measurement of plasma samples, a volume of 0.1 ml plasma samples was diluted with 0.4 ml distilled water. The same procedure as standard curve preparation was used on all diluted plasma samples. Protein concentrations in each plasma samples were measured by Cobas Integra 400, Roche Diagnostics, Germany). The result was obtained using MDA standard curve graph which has been plotted before.

Demographic variables are presented as the mean \pm standard deviation (SD) for continuous normally distributed variables, as mean + standard error mean (SEM) for continuous non-normally distributed data, and as percentages for categorical data. Analysis of normality was performed with the Kolmogorov–Smirnov test. Categorical data and proportions were analysed using Chi-square test. Pearson's or Spearman's correlation coefficient was used for analysing the correlation between two variables with normal distribution or non-normal distribution, respectively. A P-value <0.05 was considered statistically significant. The statistical analysis was performed with the Statistical Package for Social Sciences (SPSS version 16.0) software licensed by UiTM.

RESULTS

A total of 99 FH patients from 67 different families (age mean \pm SD: 43.9 \pm 12.2 years, gender: 38 males and 61 females) and 99 control subjects (age mean \pm SD: 44.7 \pm 12.2 years, 40 males and 59 females), were recruited into this study. The FH patients (0.84 \pm 0.07) had higher waist-to-hip ratio (WHR) as compared to NC (0.84 \pm 0.07) vs (0.82 \pm 0.06) ($P < 0.05$).

The levels of TC, TG and LDL-c were significantly elevated in FH patients in comparison with control subjects (8.6 \pm 1.7 mmol/L vs 5.4 \pm 1.0 mmol/L, 2.0 \pm 1.7 mmol/L vs 1.3 \pm 0.6 mmol/L, 6.4 \pm 1.6 mmol/L vs 3.4 \pm 0.9 mmol/L, respectively, $P < 0.0001$). The baseline characteristics of FH patients and control subjects are presented in Table 1.

There were significantly higher ox-LDL, ISP and MDA concentrations in FH compared to controls (63.0 + 6.5 vs 25.5 \pm 1.2; $p < 0.001$; 749.7 \pm 74.0 vs 354.2 \pm 18.1; $p < 0.001$; 342.4 \pm 46.7 vs 162.7 + 13.5 nmol/g, respectively, $p < 0.0001$) (Figure. 1).

Chi square analysis showed significant association between Ox-LDL with WC ($p < 0.03$), WHR ($p < 0.05$), BMI ($p < 0.01$), Systolic BP ($p < 0.01$), TC ($p < 0.0001$), TG ($p < 0.05$), LDL-c ($p < 0.0001$) and smoking status ($p < 0.05$). F2-Isoprostane was positively associated with WC ($p < 0.01$), TC ($p < 0.0001$), TG ($p < 0.05$), LDL-c ($p < 0.0001$) and smoking status ($p < 0.01$) while MDA was significantly associated with glucose ($p < 0.01$), TC ($p < 0.0001$), TG ($p < 0.05$) and LDL-c ($p < 0.0001$) (Table 2).

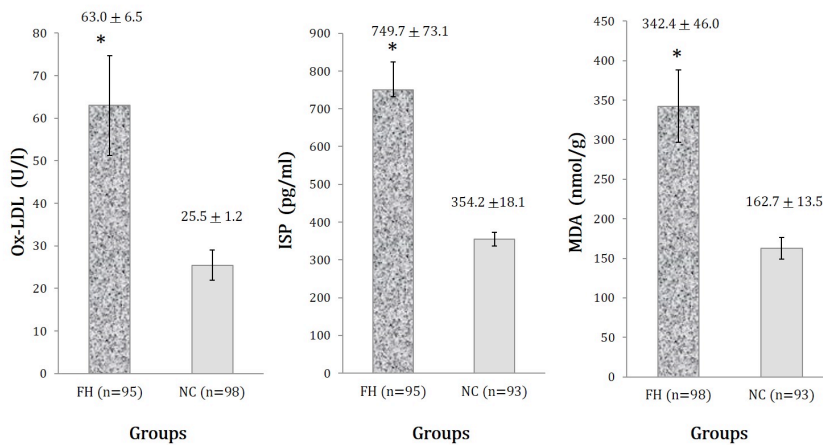


Figure 1. Comparison of Oxidative stress biomarkers concentrations in FH patients and NC subjects. Data were expressed in mean ± SEM. *P<0.001 compared to controls. Ox-LDL: oxidized LDL, ISP: F2-Isoprostane, MDA: Malonaldehyde

Table 1
Clinical and biochemical characteristics of FH patients and controls

Baseline Characteristics	FH (n=98)	Normal controls (NC) (n=100)	P value
¹ Age (years)	44.2 + 12.2	44.7 + 12.2	NS
² Gender (%)			
Males	38 (38.3)	40 (40.4)	NS
Females	61 (61.6)	59 (59.5)	
² Ethnicity (%)			
Malays	71 (72.4)	91 (91.0)	<0.005
Chinese	26 (26.5)	7 (7.0)	
Indians	1 (1.0)	2 (2.0)	
² Current smoker (%)	13(13.1)	17 (17.0)	NS
¹ SBP (mmHg)	133.9 + 21.6	121.2 + 15.6	NS
¹ DBP (mmHg)	76.7 + 10.9	73.0 + 10.3	NS
² Hypertension (%)	20 (20.4)	1 (1.0)	<0.05
² CAD (%)	20 (20.4)	0 (0)	<0.001
¹ BMI (kg/m ²)	24.5+ 4.7	23.5+ 4.8	NS
¹ WHR (cm ²)	0.84+ 0.07	0.82 + 0.06	<0.05
¹ WC (cm)	84.2 + 11.2	77.6 + 11.1	<0.001
² Central Obesity (%)	45 (45.9)	27(27.0)	<0.005
¹ TC (mmol/L)	8.6 + 1.7*	5.4 + 1.0	<0.001
¹ TG (mmol/L)	2.0+ 1.7*	1.3 + 0.6	<0.001
¹ LDL-c (mmol. L)	6.4 + 1.6*	3.4 + 0.9	<0.001
² HDL-c (mmol/L)	1.1 + 0.3	1.4 + 0.3	NS
¹ Glucose (mmol/L)	6.2 + 9.0	4.8 + 1.1	<0.01

¹Data expressed as mean + SD; ²Data expressed as a proportion (%); NS: Not Significant. SBP: Systolic Blood pressure; DBP: Diastolic Blood Pressure; BMI: Body mass index; WHR: Waist-hip ratio; WC: waist circumference; CAD: Personal History of Coronary Artery Disease

Table 2
 Summary of the association between oxidative stress biomarkers and various parameters

Parameters	¹ Ox-LDL (U/L)	¹ F ₂ -Isoprostane (pg/ml)	¹ MDA (nmol/g)
WC (cm)	p<0.03	p<0.01	NS
WHR (cm ²)	p<0.05	NS	NS
BMI (kg/m ²)	p<0.01	NS	NS
SBP (mmHg)	p<0.01	NS	NS
DBP (mmHg)	NS	NS	NS
Glucose (mmol/L)	NS	NS	p<0.01
TC (mmol/L)	p<0.0001	p<0.0001	p<0.0001
TG (mmol/L)	p<0.05	p<0.05	p<0.05
LDL-c (mmol.L)	p<0.0001	p<0.0001	p<0.0001
HDL-c (mmol/L)	NS	NS	NS
Smoking (yes/no)	p<0.05	p<0.01	NS
CAD (yes/no)	NS	NS	NS

¹Data are expressed as a p-value of the chi-square test. NS: Not Significant. WC: waist circumference; WHR: Waist-hip ratio; BMI: Body mass index; SBP: Systolic Blood pressure; DBP: Diastolic Blood Pressure; CHD: Personal History of Coronary Artery Disease; ox-LDL: oxidised LDL; MDA: malondialdehyde

Pearson's correlation analysis showed a positive correlation of glucose (p<0.05), TC (p<0.001) and LDL-c (p<0.001) and HDL-c (p<0.01) with ox-LDL. F₂-Isoprostane showed significant correlation with TC (p<0.001) and LDL-c (p<0.001) while MDA was significantly correlated with diastolic BP (p<0.05) and LDL-c (p<0.05) (Table 3).

Table 3
 Correlation between oxidative stress biomarkers with parameters in all subjects

Parameters	Ox-LDL (U/L)	F ₂ -Isoprostane (pg/ml)*	MDA (nmol/g)
WC (cm)	0.123	0.151	0.036
WHR (cm ²)	0.135	0.054	0.87
BMI (kg/m ²)	0.994	0.126	0.098
SBP (mmHg)	0.085	0.105	0.027
DBP (mmHg)	0.124	0.049	0.167*
Glucose (mmol/L)	0.219*	0.128	0.081
TC (mmol/L)	0.552***	0.459***	0.133
TG (mmol/L)	0.130	0.100	0.051
LDL-c (mmol.L)	0.598***	0.492***	0.150*
HDL-c (mmol/L)	-0.208**	-0.164	-0.133

Data are expressed in Pearson's correlation coefficient (r); *p<0.05, **p<0.01, ***p<0.001. WC: waist circumference; WHR: Waist-hip ratio; BMI: Body mass index; SBP: Systolic Blood pressure; DBP: Diastolic Blood Pressure; ox-LDL: oxidised LDL; MDA: malondialdehyde

Multiple linear regression analysis was performed in all subjects to further explore the independent effect of parameters with the biomarkers as dependent variables. LDL-c was shown to be an independent predictor for ox-LDL concentration ($p < 0.0001$) after correction for various confounding factors i.e. age, gender, ethnicity, smoking status, BMI, WC, WHR, SBP, DBP, glucose, TC, TG, HDL and LDL (Table 4).

Table 4
Independent predictor of oxidative stress biomarkers in all subjects

Dependent variable	Independent variable	Constant	B	SE	Adjusted OR	95% CI	p-value
Ox-LDL (U/l)	LDL-c	-5.059	0.598	0.991	9.861	7.815, 11.726	0.0001*

Ox-LDL: oxidised LDL; LDL-c: Low Density Lipoprotein cholesterol

DISCUSSION

The purpose of this study was to compare the oxidative stress status between FH and NC subjects in the Malaysian cohort and assess the association and predictability of the oxidative stress biomarkers to ox-LDL level. It was hypothesised that FH patients have higher oxidative stress level as compared to NC subjects due to hypercholesterolaemia. Our case-control observational study demonstrated higher concentration of these oxidative stress biomarkers in FH patients than NC. A similar finding was observed in a case-control study among Greeks on oxidative stress biomarkers which showed greater ox-LDL compared to normolipidemic healthy control (Tsouli et al., 2006). Nourooz-Zadeh et al also illustrated that ISP concentration was greater in FH patients than in healthy controls amongst the British (Nourooz-Zadeh et al., 2001). Subsequently, the finding and consistent with the study of FH and MDA amongst the Turks where MDA was found to be significantly higher in patients with homozygous FH than in heterozygotes group and control (Pirinccioglu et al., 2010). However, these studies only recruited a small number of subjects ranging from 11 to 80 persons per group. Our study included a great number of FH subjects and NC clearly showed significant elevation of all three oxidative stress biomarkers, indicating that FH patients have enhanced oxidative stress status which is one of the key features in the pathogenesis of atherogenesis.

This present study clearly showed highly significant associations between the oxidative stress biomarkers with total cholesterol (TC) and low-density lipoprotein cholesterol (LDL-c), while LDL-c were significantly correlated with all the oxidative stress biomarkers. These findings are parallel with previous reports, which revealed a strong correlation and association between ox-LDL and coronary artery disease (CAD) and concluded that circulating ox-LDL is a sensitive biomarker of CAD (Holvoet et al., 2001). Although the finding was consistent with the previous study where the correlation was seen between ISP and LDL-c and the association between ISP and serum cholesterol level were observed in FH patients, no correlation and association were previously observed in the healthy control group, possibly due to the limited numbers of their subject examined ($n=25$). For MDA, our finding was similar to Pirinccioglu et al, where MDA was positively correlated with LDL-c and TC suggesting enhanced oxidative

stress status which is important in the understanding of enhanced atherosclerogenesis in FH and related to their increased risk of developing atherosclerosis-related complications (Pirinccioglu et al., 2010).

Furthermore, in this present study, LDL-c was strongly shown to be an independent predictor for ox-LDL concentration ($p < 0.0001$) after correcting for the various confounding factors. The current finding appears to support the previous literature, where ox-LDL was an independent predictor of developing cardiac events (CE) in patients with CAD suggesting measurement of circulating oxLDL may be helpful in the assessment of future CE in patients with CAD (Shimada et al., 2004). In addition, the concentration of LDL is an independent predictor factor of ox-LDL even after correcting for the various confounding factors suggests that both the proatherogenic quantity and quality coexist in FH which is pivotal in the pathogenesis of premature atherosclerosis-related conditions, especially CAD.

It has been well-established that patients with hypercholesterolaemia have an increased risk for atherosclerosis. Ox-LDL is the most used biomarkers in assessing status of oxidative stress in atherosclerotic patients (Garrido-Urbani, Meguenani, Montecucco, & Imhof, 2014) and elevated ox-LDL also was associated with hypercholesterolaemia in general (Garrido-Urbani et al., 2014) as well as many populations (Li, Yang, & Mehta, 1998; Najafi & Alipoor, 2013; Rodenburg et al., 2006; Tsouli et al., 2006; Tsutsui et al., 2002). Morrow (2005) mentioned that ISP represents a biomarker that has the potential to be a great importance in the assessment of human atherosclerotic cardiovascular disease (Morrow, 2005). Isoprostane and also MDA were the two of the most well-studied markers of lipid peroxidation in CAD and CVD (Ho, Karimi Galoughi, Liu, Bhindi, & Figtree, 2013). Since oxidative stress was associated with hypercholesterolaemia, and FH patients have severely elevated cholesterol in their blood, it is quite surprising that studies on these oxidative stress biomarkers in FH have been scarce.

It is important to note that all subjects included in this present study were not subjected to therapeutic intervention with lipid-lowering, antihypertensive and/or antidiabetic medications which are potential confounding factors in oxidative stress.

Although there have been several reports on FH and oxidative stress biomarkers from various countries, the data has been limited and most studies were mostly among the European cohort (Cracowski et al., 2001; Davì, Falco, & Patrono, 2004; Nourooz-Zadeh et al., 2001; Pirinccioglu et al., 2010). Therefore, this present study may fill in the gap and to the best of our knowledge, this is the first report on the association of oxidative stress biomarkers in clinically diagnosed FH patients of Asian origin. There have been different population studies on hypercholesterolemic subjects but very scarce, specifically in subjects with clinically diagnosed FH.

Among the scarce studies relating oxidative stress and FH subjects, most have reported an enhanced oxidative stress status in FH compared to normal controls. The samples used were small between 30 to 80 samples and only covering American and European cohorts (Nourooz-Zadeh et al., 2001; Pirinccioglu et al., 2010; Real et al., 2010; Reilly et al., 1998; Rodenburg et al., 2006). The only previously reported study for an Asian population was reported by Nawawi et al. (2003). This present study may enhance our understanding of oxidative stress in FH patients within the Asian populations which has a different pattern of confounding factors and genetic make-up.

CONCLUSION

In conclusion, FH patients have enhanced oxidative stress status, which in part, may contribute to increased risk of atherosclerosis and its related complications, especially CAD. The concentration of LDL is an independent predictor of ox-LDL even after the confounding factors are removed, suggesting that both quantity and quality of proatherogenic LDL coexist in FH and possibly synergize each other in the pathogenesis of atherosclerosis. There is a potential role for these oxidative stress biomarkers to be used in risk assessment and monitoring of disease progression among individuals with FH. Hence, future studies are required to assess the role of these oxidative stress biomarkers in predicting the risk of coronary events in FH.

ACKNOWLEDGMENTS

The authors would like to express particular gratitude to the Government of Malaysia for financially supporting this research through Fundamental Research Grant Scheme (grant code: 211501070002) and Long-Term Research Grant Scheme [grant code: 600-RMI/LRGS 3/5(2/2011)].

REFERENCES

- Alicezah, M. K., Razali, R., Rahman, T., Hoh, B. P., Suhana, N. H., Muid, S. & Koshy, M. N. H. M. (2014). Case Report: Homozygous familial hypercholesterolemia. *Malaysian Journal of Pathology*, 36(2), 131–137.
- Charan, J., & Biswas, T. (2013). How to calculate sample size for different study designs in medical research?. *Indian Journal of Psychological Medicine*, 35(2), 121.
- Cracowski, J. L., Ploin, D., Bessard, J., Bagnuet, J. P., Stanke-Labesque, F., Mallion, J. M. & Bessard, G. (2001). Formation of isoprostanes in children with type IIa hypercholesterolemia. *Journal of Cardiovascular Pharmacology*, 38(2), 228–31.
- Davi, G., Falco, A., & Patrono, C. (2004). Determinants of F2-isoprostane biosynthesis and inhibition in man. *Chemistry and Physics of Lipids*.
- de Faria, A. P. C., Fontana, V., Modolo, R., Barbaro, N. R., Sabbatini, A. R., Pansani, I. F., & Moreno, H. (2014). Plasma 8-isoprostane levels are associated with endothelial dysfunction in resistant hypertension. *Clinica Chimica Acta; International Journal of Clinical Chemistry*.
- Garrido-Urbani, S., Meguenani, M., Montecucco, F., & Imhof, B. A. (2014). Immunological aspects of atherosclerosis. *Seminars in Immunopathology*.
- Goldberg, A. C., Hopkins, P. N., Toth, P. P., Ballantyne, C. M., Rader, D. J., Robinson, J. G., ... & McGowan, M. P. (2011). Familial hypercholesterolemia: Screening, diagnosis and management of pediatric and adult patients: Clinical guidance from the National Lipid Association Expert Panel on Familial Hypercholesterolemia. *Journal of Clinical Lipidology*, 5(3), S1-S8.
- Goldberg, A. C., Hopkins, P. N., Toth, P. P., Ballantyne, C. M., Rader, D. J., Robinson, J. G., Ziajka, P. E. (2011). Familial hypercholesterolemia: Screening, diagnosis and management of pediatric and adult patients: Clinical guidance from the National Lipid Association Expert Panel on Familial Hypercholesterolemia. *Journal of Clinical Lipidology*, 5, 133–140)

- Ho, E., Karimi Galougahi, K., Liu, C.-C., Bhindi, R., & Figtree, G. A. (2013). Biological markers of oxidative stress: Applications to cardiovascular research and practice. *Redox Biology*, *1*(1), 483–91.
- Holvoet, P., Macy, E., Landeloos, M., Jones, D., Nancy, J. S., Van De Werf, F., & Tracy, R. P. (2006). Analytical performance and diagnostic accuracy of immunometric assays for the measurement of circulating oxidized LDL. *Clinical Chemistry*, *52*(4), 760–764.
- Hopkins, P. N., Toth, P. P., Ballantyne, C. M., & Rader, D. J. (2011). Familial hypercholesterolemias: prevalence, genetics, diagnosis and screening recommendations from the National Lipid Association Expert Panel on Familial Hypercholesterolemia. *Journal of Clinical Lipidology*, *5*(3 Suppl), S9–17.
- Hulthe, J., Bokemark, L., & Fagerberg, B. (2001). Antibodies to oxidized LDL in relation to intima-media thickness in carotid and femoral arteries in 58-year-old subjectively clinically healthy men. *Arteriosclerosis, Thrombosis, and Vascular Biology*, *21*(1), 101–107.
- Khoo, K. L., van Acker, P., Defesche, J. C., Tan, H., van de Kerkhof, L., Heijnen-van Eijk, S. J., & Deslypere, J. P. (2000). Low-density lipoprotein receptor gene mutations in a Southeast Asian population with familial hypercholesterolemia. *Clinical Genetics*, *58*(2), 98–105.
- Ledwozyw, A., Michalak, J., Stepien, A., & Kadziolka, A. (1986). The relationship between plasma triglycerides, cholesterol, total lipids and lipid peroxidation products during human atherosclerosis. *Clinica Chimica Acta; International Journal of Clinical Chemistry*, *155*(3), 275–283.
- Li, D., Yang, B., & Mehta, J. L. (1998). Ox-LDL induces apoptosis in human coronary artery endothelial cells: role of PKC, PTK, bcl-2, and Fas. *The American Journal of Physiology*, *275*, H568–H576.
- Lye, S.-H., Chahil, J. K., Bagali, P., Alex, L., Vadivelu, J., Ahmad, W. A. W., & Mohamed, R. (2013). Genetic polymorphisms in LDLR, APOB, PCSK9 and other lipid related genes associated with familial hypercholesterolemia in Malaysia. *PloS One*, *8*(4), e60729.
- Martinez-Hervas, S., Fandos, M., Real, J. T., Espinosa, O., Chaves, F. J., Saez, G. T., & Ascaso, J. F. (2008). Insulin resistance and oxidative stress in familial combined hyperlipidemia. *Atherosclerosis*, *199*, 384–389.
- Morrow, J. D. (2005). Quantification of isoprostanes as indices of oxidant stress and the risk of atherosclerosis in humans. *Arteriosclerosis, Thrombosis, and Vascular Biology*.
- Najafi, M., & Alipoor, B. (2013). Serum ox-LDL level is reduced with the extent of stenosis in coronary arteries. *Acta Medica Iranica*, *51*(September 2010), 314–319.
- Nawawi, H., Muid, S., Osman, N. S., Annuar, R., Khalid, B. A. K., & Yusoff, K. (2003). 4P-0981 Enhanced oxidative stress and endothelial dysfunction in patients with familial hypercholesterolaemia. *Atherosclerosis Supplements*, *4*(2), 289–290.
- Nourooz-Zadeh, J., Smith, C. C., & Betteridge, D. J. (2001). Measures of oxidative stress in heterozygous familial hypercholesterolaemia. *Atherosclerosis*, *156*(2), 435–441.
- Palombo, C., Lubrano, V., & Sampietro, T. (1999). Oxidative stress, F2-isoprostanes and endothelial dysfunction in hypercholesterolemia. *Cardiovascular Research*, *44*(3), 474–6.
- Pirinccioglu, A. G., Gokalp, D., Pirinccioglu, M., Kizil, G., & Kizil, M. (2010). Malondialdehyde (MDA) and protein carbonyl (PCO) levels as biomarkers of oxidative stress in subjects with familial hypercholesterolemia. *Clinical Biochemistry*, *43*(15), 1220–1224.

- Real, J. T., Martinez-Hervas, S., Tormos, M. C., Domenech, E., Pallardo, F. V, Saez-Tormo, G., & Garcia-Garcia, a B. (2010). Increased oxidative stress levels and normal antioxidant enzyme activity in circulating mononuclear cells from patients of familial hypercholesterolemia. *Metabolism*, *59*, 293–298.
- Reilly, M. P., Praticò, D., Delanty, N., DiMinno, G., Tremoli, E., Rader, D., & FitzGerald, G. A. (1998). Increased formation of distinct F2 isoprostanes in hypercholesterolemia. *Circulation*, *98*(25), 2822–8.
- Rodenburg, J., Vissers, M. N., Wiegman, A., Miller, E. R., Ridker, P. M., Witztum, J. L., & Tsimikas, S. (2006). Oxidized low-density lipoprotein in children with familial hypercholesterolemia and unaffected siblings: effect of pravastatin. *Journal of the American College of Cardiology*, *47*(9), 1803–1810.
- Shimada, K., Mokuno, H., Matsunaga, E., Miyazaki, T., Sumiyoshi, K., Miyauchi, K., & Daida, H. (2004). Circulating oxidized low-density lipoprotein is an independent predictor for cardiac event in patients with coronary artery disease. *Atherosclerosis*, *174*(2), 343–347.
- Soutar, A. K., & Naoumova, R. P. (2007). Mechanisms of disease: Genetic causes of familial hypercholesterolemia. *Nature Clinical Practice. Cardiovascular Medicine*, *4*(4), 214–225.
- Stemme, S., Faber, B., Holm, J., Wiklund, O., Witztum, J. L., & Hansson, G. K. (1995). T lymphocytes from human atherosclerotic plaques recognize oxidized low density lipoprotein. *Proceedings of the National Academy of Sciences of the United States of America*, *92*, 3893–3897.
- Stephens, J. W., Gable, D. R., Hurel, S. J., Miller, G. J., Cooper, J. A., & Humphries, S. E. (2006). Increased plasma markers of oxidative stress are associated with coronary heart disease in males with diabetes mellitus and with 10-year risk in a prospective sample of males. *Clinical Chemistry*, *52*(3), 446–452.
- Stocker, R., & Keaney, J. F. (2004). Role of oxidative modifications in atherosclerosis. *Physiological Reviews*, *84*(4), 1381–1478.
- Stone, N. J. (1994). Secondary causes of hyperlipidemia. *Med.Clin.North Am.*, *78*, 117–141.
- Tsouli, S. G., Kiortsis, D. N., Lourida, E. S., Xydis, V., Tsironis, L. D., Argyropoulou, M. I., & Tselepis, A. D. (2006). Autoantibody titers against OxLDL are correlated with Achilles tendon thickness in patients with familial hypercholesterolemia. *Journal of Lipid Research*, *47*(10), 2208–14.
- Tsutsui, T., Tsutamoto, T., Wada, A., Maeda, K., Mabuchi, N., Hayashi, M., & Kinoshita, M. (2002). Plasma oxidized low-density lipoprotein as a prognostic predictor in patients with chronic congestive heart failure. *Journal of the American College of Cardiology*, *39*, 957–962.
- Vassalle, C., Petrozzi, L., Botto, N., Andreassi, M. G., & Zucchelli, G. C. (2004). Oxidative stress and its association with coronary artery disease and different atherogenic risk factors. *Journal of Internal Medicine*, *256*(4), 308–315.
- World Health Organization, WHO. (1995). Physical status: the use and interpretation of anthropometry. *Report of a WHO Expert Committee. Technical Report Series, No. 854* (Geneva: World Health Organization.).

Ceiling Geometry and Daylighting Performance of Side Lit Historical Museum Galleries Under Tropical Overcast Sky Condition

Sabarinah Sh Ahmad^{1*}, Noraini Ahmad² and Anuar Talib¹

¹Faculty of Architecture, Planning & Surveying, Universiti Teknologi MARA (UiTM), 40450 Shah Alam, Selangor, Malaysia

²Kulliyah of Architecture & Environmental Design (KAED), International Islamic University (IIUM), Jalan Gombak, 53100 Kuala Lumpur, Malaysia

ABSTRACT

Safe level of daylighting for artefact conservation in historic buildings is a difficult task to achieve. Previous studies indicated that lighting problems in historic museum galleries were mainly due to unshaded walls that allowed direct sun penetration over the display areas. Ceiling geometry can also affect the daylighting performance significantly, particularly on the interior distribution of light. Malaysia, with hot and humid climate, and tropical sky conditions receives plenty of natural light all year around. The fluxes in natural lighting exposures confirm the need for strategic daylight control programme in the exhibition gallery. The study aims to assess the ceiling geometry contribution for four orientations; North, East, South and West through computer simulations. The research approach was based on comparisons between pitched and flat ceiling simulation output data. Further comparisons were performed with the recommended lighting limits for conservation of artefacts. The comparisons allowed better understanding of light damage issues and highlight the control of daylighting distributions through realistic predictive images and ceiling geometry designs. The results showed that the types of exhibits materials and its placement are affected by the ceiling geometry and constant changes in natural lighting exposure. The study confirms that ceiling geometry can act as a control mechanism with the environment

physical features as part of preventive conservation criteria in the exhibition gallery. Thus, a systematic light-monitoring programme in the exhibition gallery is necessary to control illuminance level and cumulative exposure limits, for artefact preservation.

Keywords: Ceiling geometry, daylighting performance, historic building, tropical sky

ARTICLE INFO

Article history:

Received: 05 January 2017

Accepted: 17 January 2017

E-mail addresses:

sabar643@salam.uitm.edu.my (Sabarinah Sh Ahmad),

nurrin@iium.edu.my (Noraini Ahmad),

anuarfaqir@gmail.com (Anuar Talib)

*Corresponding Author

INTRODUCTION

Adaptive reuse of a historic building for a museum or heritage facility can present certain challenges (Ahmad, Ahmad, & Talib, 2013). Corridors and balconies that are partially enclosed or fully opened with natural light penetration are among the main features of historic buildings that serve as exhibition spaces. Nevertheless, these favourable natural lighting conditions either accounted for energy conservation or enhancing the visual quality promoted severe threat on the artefacts. Studies have proven that many of the lighting issues in museum galleries were mainly due to direct sun penetration over the display areas (Ahmad, Ahmad, & Talib, 2012; Del Hoyo-Meléndez, Mecklenburg, & Doménech-Carbó, 2011; De Graaf, Dessouky, & Müller, 2014; Wilson, 2006). The introduction of daylight exhibition spaces in historic museum buildings creates a much more complicated preservation problem due to the untested quantity of light development and variability in illuminance level (Ahmad, Ahmad, & Talib, 2011). Therefore, the design of daylight exhibition spaces, either in a museum or as an integral part of a historic building, need to take consideration not only functional requirements but also preventive conservation planning to preserve every single artefact. Today, there is an urgent worldwide demand for energy saving and sustainability, where passive design with climatic responsiveness should be pursued in all building types (Alrubaih et al., 2013; Toledo, 2007). Toledo (2007), and Maekawa and Beltra (2004) highlighted that climate control can be achieved for both visitors' comfort and material conservation by enhancing their original architectural features.

Lighting Limits for Conservation of Artefacts

Based on the literature review on the recommended lighting limits for artefact conservation by the museums community for safe lighting levels (Thomson, 1990), the following classification is used for daylighting assessment and formed the basis to understand light damage issues in relation to the recommended lighting limits for artefact conservation:

- i) For Category I- Highly responsive/Sensitive materials, ≤ 50 lux
Example: Textiles, costumes, tapestries, paper, parchment, dyed leather, painted or dyed wood, natural history exhibits i.e., botanical specimens, fur and feathers.
- ii) For Category II-Moderately responsive/ sensitive materials, ≤ 200 lux.
Example: Oil and tempera painting, fresco, undyed leather, horn, bone, unpainted wood and lacquer, and some plastics.
- iii) For Category III-Non-responsive/Non-sensitive materials, ≤ 300 lux
Example: Metal, stone, glass, ceramics, enamel, and most minerals.

Ceiling Geometry

Previous research and reviews stated that ceiling geometry is an important part of the lighting scheme, which also effect daylight level and determine whether a space is well lit (Freewan, Shao, & Riffat, 2009; Freewan, 2010; Kim & Chung, 2011; Rakha & Nassar, 2011). Freewan (2010) investigated the accuracy of physical models and RADIANCE simulation in measuring daylight performance using the interactions of louvers and ceiling geometries. The simulation revealed that curved ceiling added to the daylighting uniformity and quality compared to a flat ceiling. Freewan (2010) also found that the curved, chamfered, arched, and sloped-down ceilings (except sloped-up ceiling geometry) improved the daylighting performance in June and December, as well as in March. The study also demonstrated that louvers performed better with curved and chamfered ceiling throughout the year. Furthermore, in other studies by Freewan, Shao and Riffat (2009), they found that curved ceiling improved the performance of a light shelf. The study found that both combinations improved uniformity where the illuminance level increased in the rear part and decreased in the front part of a room. Rakha and Nassar (2011) studied on performance optimization of ceiling form and found that curvilinear ceiling form achieved better daylighting uniformity compared to mesh ceiling form.

The purpose of this research is to explore the effects of ceiling geometries on a historic building's exhibition space with either pitched or flat ceiling on days with maximum and minimum daylight, which are 21 March and 21 December respectively as proposed by Shahriar and Mohit (2007) for peninsular Malaysia. A simulation output data using the reference case at West (existing) orientation and the interior reflectance values were further compared with the recommended lighting limits for artefacts conservation by the museums community for safe light levels. This study is to ascertain whether ceiling geometry can act as passive control mechanism with the environment physical features as part of preventive conservation criteria in the exhibition gallery. By assessing all the findings, the best possible conditions of room orientation and ceiling geometry for long-term preservation of museum artefacts under given sky condition are recommended.

MATERIALS AND METHOD

The study used validated RADIANCE software which is integrated in the IES<VE> programme to analyse the impacts of ceiling geometry provided with different room orientations on daylight level at work plane/exhibit height. The aim was to find the best ceiling geometry and room orientation conditions for daylight control. Radiance is a back-ward ray-tracing comprehensive programme that accurately predicts light levels and rendering that produces synthetic images that are realistic for all sky conditions (Ibrahim & Zain-Ahmed, 2007; Joarder, Ahmed, Price, & Mourshed, 2009).

The simulation parameters are as follows:

- Location: Latitude and Longitude of Melaka is 2° 11' N and, 102° 14' E at elevation 13 m
- Date and Time: 21 March and 21 December (10.00h, 13.00h and 16.00h)
- Sky condition: CIE Overcast sky
- Orientations: North, East, South and West
- Floor area: 43.4 m² (1st floor)
- Pitched ceiling (H): 2.6 m min, 4 m (under pitch), Flat ceiling (H): 3 m
- Window-wall ratio (WWR): 20%
- Opened window: 100% transmittance
- Window sill (H): 900 mm
- Analysis grid: 4 measuring points (at horizontal point of 1 m (H) in all showcases)
- Against the Window Wall (AWW) reflectance: 90%
- Opposite the Window Wall (OWW) reflectance: 60%
- Ceiling Reflectance: 20%
- Floor Reflectance: 30%
- Showcase with wood framing - 6mm clear glass: 80% transmittance
- Showcase back panel reflectance: 30% (Velvety red fabric)

For simulation analysis, a flat ceiling will be examined and compared to the reference case gallery with pitched ceiling as shown in Figure 1; which is considered as the base case in all the cases. All internal surface reflectance values were kept constant. All models had the same floor area, length and width but the ceiling heights values were of different heights. Average daylight measurements were calculated on work plane height (exhibit height) at horizontal point of 1 m (*H*) in all showcases along against and opposite window walls provided with varying room orientations. The source of daylight is side lit from the windows.

Figure 1 shows the positions and configurations of the four showcases, they are labelled as showcases A, B, C and D. The wall along showcases A and B is called the AWW (against window wall), while the wall along showcases C and D is the OWW (opposite window wall). For simulation assessment, the ground floor space underneath the study gallery was hidden as it will not affect the simulation output and will only lengthen the simulation process unnecessarily (Joarder et al., 2009).

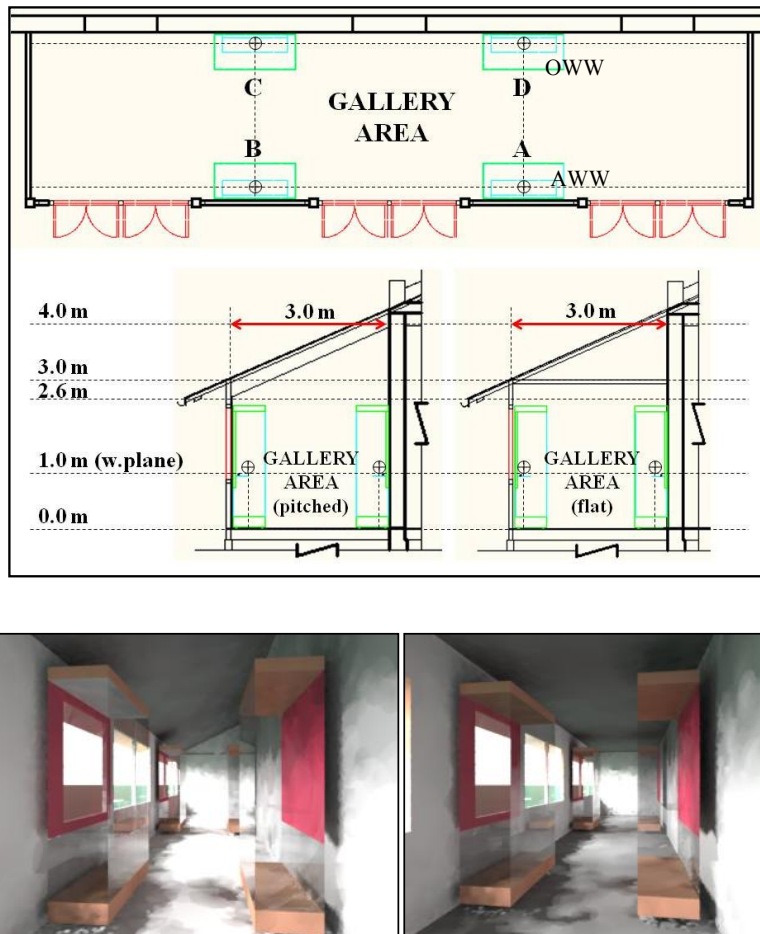


Figure 1. Simulated gallery area dimensions and measuring points for pitched and flat ceiling

RESULTS AND DISCUSSION

Average Illuminance Level (Lux) on Work Plane (Exhibit Height) at Horizontal Points of 1 m (H)

Table 1 shows how the illuminance levels changed at 10.00h, 13.00h and 16.00h in the showcases at four types of room orientations served with different ceiling geometries on 21 March and 21 December for both AWW and OWW at 1 m planar surfaces.

Table 1

Results of simulated average daylight distribution at showcases (AWW & OWW) of four room orientations West (existing), East, South and North at 10.00h, 13.00h and 16.00h on 21 March and 21 December under overcast sky condition

Ceiling Type	Against Window Wall (AWW) at 1m H-horizontal						Opposite Window Wall (OWW) at 1m H-horizontal					
	21 March			21 December			21 March			21 December		
	Pitch Lux	Flat Lux	% change	Pitch Lux	Flat Lux	% change	Pitch Lux	Flat Lux	% change	Pitch Lux	Flat Lux	% change
10.00h												
WEST	12	12	0	12	9	-25	81	76	-6	92	77	-16
EAST	12	11	-8	12	9	-25	81	71	-12	92	76	-17
SOUTH	21	16	-24	12	10	-17	105	66	-37	76	86	13
NORTH	19	10	-47	15	15	0	82	79	-4	90	86	-4
Max	21	16		15	15		105	79		92	86	
Min	12	10		12	9		81	66		76	76	
13.00h												
WEST	23	15	-35	20	15	-25	117	86	-26	123	95	-23
EAST	23	14	-39	20	12	-40	117	91	-22	123	93	-24
SOUTH	23	20	-13	23	17	-26	132	123	-7	146	114	-22
NORTH	20	31	55	21	16	-24	131	96	-27	146	112	-23
Max	23	31		23	17		132	123		146	114	
Min	20	14		20	12		117	86		123	93	
16.00h												
WEST	18	12	-33	12	8	-33	112	94	-16	105	62	-41
EAST	18	12	-33	12	9	-25	112	97	-13	105	73	-30
SOUTH	18	12	-33	20	15	-25	121	65	-46	98	58	-41
NORTH	22	15	-32	15	10	-33	90	96	7	84	96	14
Max	22	15		20	15		121	97		105	96	
Min	18	12		12	8		90	65		84	58	

Figures 2 and 3 illustrate the readings captured in Table 1 by showing the comparisons between pitched and flat ceilings with isolux analysis at South facing orientation on 21 March and 21 December respectively. It can be seen that the AWW records lower illumination readings than the OWW for all conditions. The pitched ceiling also captures higher illumination distribution in the interior space than the flat ceiling. This means more light is distributed on the planar surfaces at 1 m above the floor, which represents the horizontal exhibit surfaces.

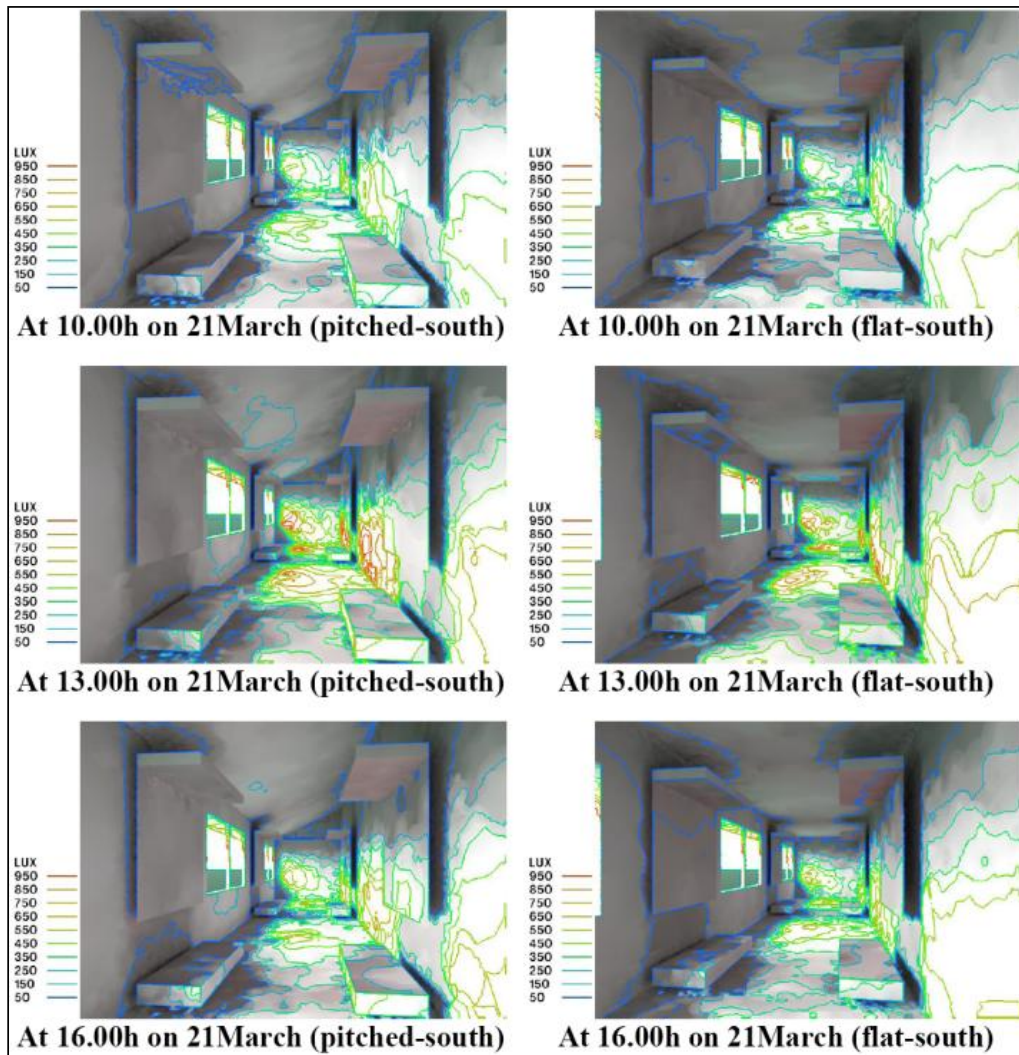


Figure 2. Comparison between pitched and a flat ceiling with isolux analysis on 21 March at 10.00h, 13.00h and 16.00h under overcast sky condition

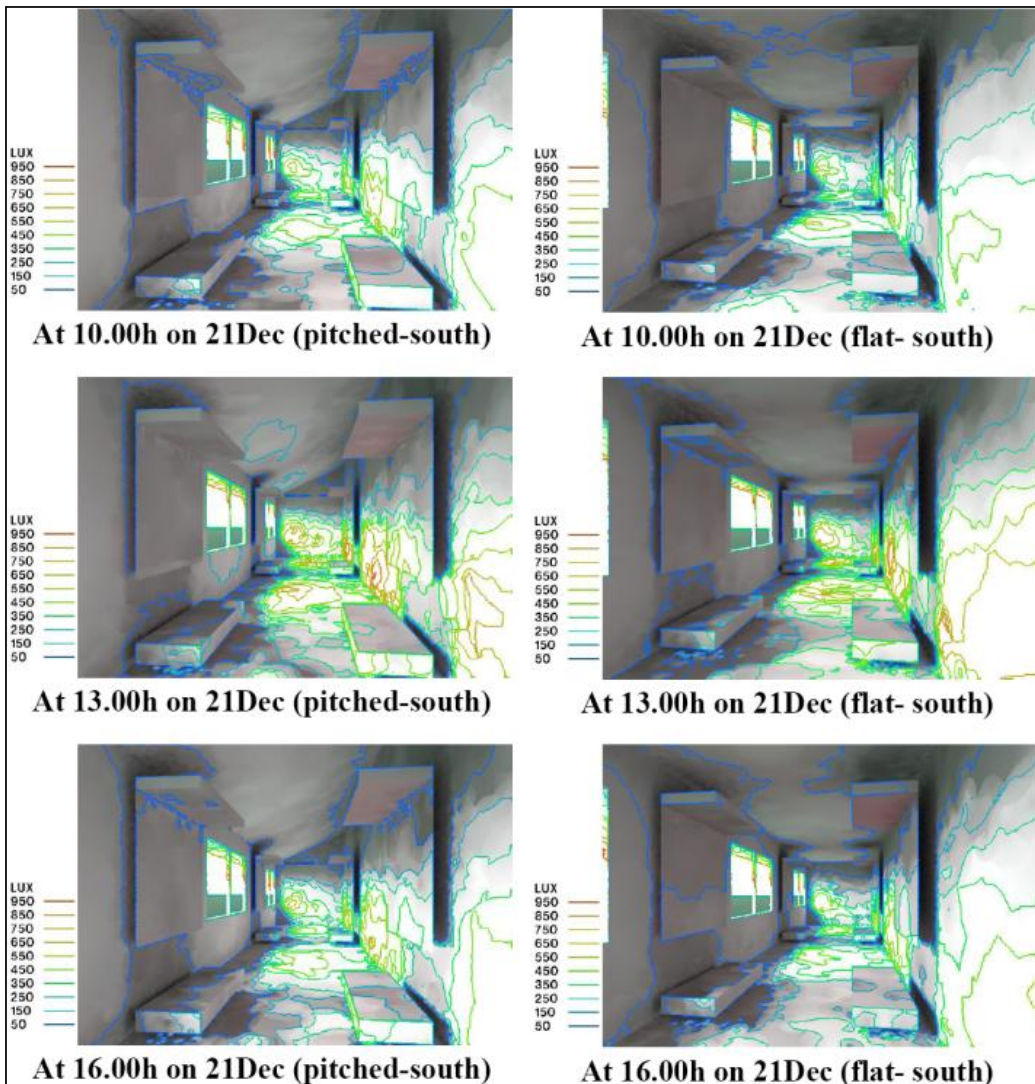


Figure 3. Comparison between pitched and a flat ceiling with isolux analysis on 21 December at 10.00h, 13.00h and 16.00h under overcast sky condition

Against Window Wall (*AWW*) for Showcases A and B

Table 1 shows that for the flat ceiling at *AWW* showcases A and B at East, South and North orientations, there are decreased illuminance level between -8 and -47% (10 to 16lux) in the morning at 10.00h on 21 March compared with the pitched ceiling gallery. Meanwhile, the reduction of illumination between -17 and -25% (9 to 10lux) is observed on 21 December for East, West and South orientations. During this hour, both pitched and flat ceiling at South orientation registered the highest illuminance level of 21lux and 16lux on 21 March respectively. However, the North orientation registered similar and highest illuminance level of 15lux on 21 December for both types of ceiling.

At 13.00h, Table 1 shows that the flat ceiling gallery registers reduced illuminance level between -13 and -39% (14 - 20lux) at the *AWW* showcases A and B at East, South and West orientations on 21 March than the pitched ceiling gallery. Meanwhile, the results for 21 December show decreased illuminance level between -24 and -40% (12 - 17lux) at all orientations.

Table 1 also shows that on 21 March, the pitched ceiling gallery records the highest illuminance level of 23lux at East, West and South orientations respectively. Meanwhile, the highest illuminance level of 31lux is registered at North orientation on the same solstice when using the flat ceiling. On 21 December, both pitched and a flat ceilings register the highest illuminance level of 23lux and 17lux respectively at South orientation.

According to Table 1, at late afternoon (16.00h), the flat ceiling gallery registers decreased illuminance level between -32 and -33% (12 to 15lux) and between -25 and -33% (8 to 15lux) at the *AWW* showcases at all orientations on 21 March and 21 December respectively. Both pitched and a flat ceilings register the highest illuminance level of 22lux and 15lux respectively at North orientation on 21 March, whereas, the highest illuminance level of 20lux and 15lux are observed for pitched and a flat ceilings respectively at South orientation on 21 December.

The overall results show that the pitched ceiling interior has higher illumination than the flat ceiling on the *AWW* side as shown in Table 1 and Figures 2 and 3. Generally, the simulation analysis indicated that at the three indicated hours (10.00h, 13.00h and 16.00h), for both pitched and flat ceiling conditions, enabled exposure limit of below 50lux, 200lux and 300lux for categories I, II and III respectively to be sustained at *AWW* showcases throughout most orientations on both 21 March and 21 December.

Opposite Window Wall (*OWW*) for Showcases C and D

Table 1 shows that at 10.00h, on 21 March, the flat ceiling gallery records decreased illuminance level between -4 and -37% (66 to 79lux) at the opposite window wall (*OWW*) showcases C and D at all orientations compared to the pitched ceiling gallery. Meanwhile, decreased illuminance level between -4 and -17% (76-86lux) are observed at East, West and North orientations on 21 December.

At *OWW*, on 21 March, both pitched and flat ceilings register the highest illuminance level of 105lux and 79lux at South and North orientations respectively as shown in Table 1. It is observed that on 21 December, pitched ceiling registers the highest illuminance level of 92lux at both East and West orientations. Meanwhile, the highest illuminance levels of 86lux at both South and North orientations are observed when using the flat ceiling on the same solstice as shown in Table 1.

At 13.00h, on 21 March and 21 December, the flat ceiling gallery records decreased illuminance level between -7 and -27% (86 to 123lux) and between -22 and -24% (93 to 114lux) respectively at the *OWW* showcases C and D at all orientations in comparison with the pitched ceiling gallery (Table 1). Table 1 also shows that at 13.00h, the *OWW* showcases served by both pitched and a flat ceiling register the highest illuminance level of 132lux and 123lux respectively at South orientation on 21 March. Pitched ceiling indicates the highest

illuminance level of 146lux at both South and North orientations on 21 December, whereas, the flat ceiling gallery with South orientation shows the highest illuminance level of 114lux.

At 16.00h, the *OWW* showcases C and Din a flat ceiling gallery at East, South and West orientations register reduction of illuminance level between -13 and -46% (65-97lux) and between -30 to -41% (58 to 96lux) when compared with the pitched ceiling gallery on March and December solstices respectively (Table 1). The gallery with pitched ceiling indicated highest illuminance level of 112lux at both East and West orientations on 21 March, whereas, highest illuminance level of 97lux were observed at East orientation when using a flat ceiling during the same solstice. On 21 December, both East and West orientations registered highest illuminance level of 105lux for gallery with pitched ceiling and 96lux for flat ceiling at North orientation.

The results show that the pitched ceiling gallery interior has higher illumination than the flat ceiling on the *OWW* side as shown in Table 1 and Figures 2 and 3. However higher illumination levels are a concern when the exhibit are light sensitive and can be damaged when continuously exposed to too much illumination. The simulation analysis indicated that at 10.00h, 13.00h and 16.00h, both pitched and flat ceilings used for all orientations at the *OWW* showcases on both 21 March and December had exceeded the allowable exposure limit of 50lux for Category I-Highly responsive/Sensitive materials. However, the illumination levels are within the recommended lighting limits for artefact conservation for categories II and III of below 200lux and 300lux for category II and III respectively.

CONCLUSION

This study presented a simulation analysis for flat and pitched ceiling geometry performance on daylight level under overcast sky conditions in Melaka, Malaysia. The chosen date and time were 21 March and 21 December to represent the month of maximum and minimum daylight respectively in Malaysia (Shahriar & Mohit, 2007).

Generally, the simulation analysis indicated that the illumination levels are within the recommended lighting limits for artefact conservation for category I, II and III respectively to be sustained at *AWW* showcases throughout most orientations on both 21 March and December. However, the simulation analysis also indicated the illumination levels had exceeded the allowable exposure limit of 50lux for Category I-Highly responsive/Sensitive materials at the *OWW* showcases on both 21 March and December. Nevertheless, at these hours, both ceilings enabled exposure limit of below 200lux and 300lux for category II and III respectively to be sustained at *OWW* showcases for most orientations.

The acquired results from the reference case of pitched ceiling at West orientation served higher illuminance level compared to a flat ceiling type. Generally, the flat ceiling gallery recorded reduced illuminance level in both *AWW* and *OWW* showcases throughout both 21 March and December at most hours and orientations when compared with the pitched ceiling. Therefore, a gallery designed with a flat ceiling allows a significant degree of control towards the illuminance level compared to a pitched ceiling gallery. In design and preventive conservation applications, it is advisable to select a flat ceiling for Category II and III (moderately responsive material and non-responsive material).

Based on the above results, it can be concluded that most showcases at all orientations interacted with the ceiling geometry and responded to the sky vision angle and behaved more expressive in the reflected light direction and distribution. The results revealed that more care should be taken in the preliminary stage of design to avoid placement of light-sensitive materials and moderately sensitive materials in daylight areas, unless proper control and monitoring system are in place. The ceiling geometries assessment addressed major issues on the daylight behaviour and preservation of exhibits, which leave the architects and museum community with choices for design and monitoring strategies for long-term preservations of the exhibits.

The simulation assessment is presented as generic indications of light damage issues in relation to the recommended lighting limits for artefact conservation for specific interior geometry and reflectance values. Spaces with different configurations of form, ceiling geometry and reflectance values can be further researched to arrive at a more comprehensive result.

ACKNOWLEDGEMENTS

The authors would like to express their gratitude to IRMI, Universiti Teknologi MARA (UiTM) for funding the research under the Excellence Fund Research Scheme and International Islamic University Malaysia (IIUM) and participating museums for their kind support. Additional funding was provided by the Malaysian Ministry of Higher Education (MOHE) under the Fundamental Grant Scheme from the Ministry of Higher Education (FRGS 5/3 113/2015) for the publication fees.

REFERENCES

- Ahmad, N., Ahmad, S. S., & Talib, A. (2013). Surface reflectance for illuminance level control in daylight historical museum gallery under tropical sky conditions. *Advanced Materials Research, Trans Tech Publications*, 610, 2854-2858.
- Ahmad, N., Ahmad, S. S., & Talib, A. (2012). Luminous exposures and light-fastness survey in daylight historical museum galleries under tropical sky conditions. *Advanced Materials Research Trans Tech Publications*, 488, 1547-1552.
- Ahmad, N., Ahmad, S. S., & Talib, A. (2011). Illuminance distributions, visual response and limits for conservation of exhibits in Admiral Cheng Ho Gallery, Malaysia. In *IEEE Symposium on Computers and Informatics (ISCI), 2011* (pp. 407-412). IEEE.
- Alrubaih, M. S., Zain, M. F. M., Alghoul, M. A., Ibrahim, N. L. N., Shameri, M. A., & Elayeb, O. (2013). Research and development on aspects of daylighting fundamentals. *Renewable and Sustainable Energy Reviews*, 21, 494-505.
- De Graaf, T., Dessouky, M., & Müller, H. F. (2014). Sustainable lighting of museum buildings. *Renewable Energy*, 67, 30-34.
- Del Hoyo-Meléndez, J. M., Mecklenburg, M. F., & Doménech-Carbó, M. T. (2011). An evaluation of daylight distribution as an initial preventive conservation measure at two Smithsonian Institution Museums, Washington DC, USA. *Journal of Cultural Heritage*, 12(1), 54-64
- Freewan, A. A. (2010). Maximizing the light shelf performance by interaction between light shelf geometries and a curved ceiling. *Energy Conversion and Management*, 51(8), 1600-1604.

- Freewan, A. A., Shao, L., & Riffat, S. (2009). Interactions between louvers and ceiling geometry for maximum daylighting performance. *Renewable Energy*, 34(1), 223-232.
- Ibrahim, N., & Zain-Ahmed, A. (2007). Daylight availability in an office interior due to various fenestration options. In *2nd PALENC Conference and 28th AIVC Conference on Building Low Energy Cooling and Advanced Ventilation Technologies in the 21st Century, Crete island, Greece*, (Vo. 1, pp. 436-440).
- Joarder, M. A. R., Ahmed, Z. N., Price, A. D., & Mourshed, M. (2009). A simulation assessment of the height of light shelves to enhance daylighting quality in tropical office buildings under overcast sky conditions in Dhaka, Bangladesh. In *Proceedings of the Eleventh International IBPSA Conference*, (pp.920-927), Glasgow, Scotland.
- Kim, C. S., & Chung, S. J. (2011). Daylighting simulation as an architectural design process in museums installed with toplights. *Building and Environment*, 46(1), 210-222.
- Maekawa, S., & Beltra, V. (2004). Climate controls for historic buildings. *The Getty Conservation Institute Newsletter*, 19(1), News in Conservation.
- Rakha, T., & Nassar, K. (2011). Genetic algorithms for ceiling form optimization in response to daylight levels. *Renewable Energy*, 36(9), 2348-2356.
- Shahriar, A. N. M., & Mohit, M. A. (2007). Estimating depth of daylight zone and PSALI for side lit office spaces using the CIE Standard General Sky. *Building and Environment*, 42(8), 2850-2859.
- Thomson, G. (1990). *The Museum Environment*. The museum environment (2nd ed.) Butterworth-Heinemann, London: Elsevier.
- Toledo, F. (2007). Museum passive buildings in warm, humid climate. In *Experts' Roundtable on Sustainable Climatic Management Strategies*, Tenerife, Spain, (pp. 1-26).
- Wilson, M. (2006). Lighting in museums: Lighting interventions during the European demonstration project 'Energy efficiency and sustainability in retrofitted and new museum buildings' (NNES-1999-20). *International Journal of Sustainable Energy*, 25(3-4), 153-169.



Tensile and Compressive Properties of Unidirectional *Arenga Pinnata* Fibre Reinforced Epoxy Composite

Aidah Jumahat^{1*}, Muhamad Faris Syafiq Khalid¹, Zuraidah Salleh¹ and Mohammad Jawaid²

¹Faculty of Mechanical Engineering, Universiti Teknologi MARA (UiTM), 40450 Shah Alam, Selangor, Malaysia

²Institute of Tropical Forestry and Forest Products, Universiti Putra Malaysia (UPM), 43400 Serdang, Selangor, Malaysia

ABSTRACT

This paper presents a study on the effect of *Arenga Pinnata* fibre volume fraction on the tensile and compressive properties of *Arenga Pinnata* fibre reinforced epoxy composite (APREC). The composites were produced using four different *Arenga Pinnata* fibre volume contents, which were 10vol%, 15vol%, 20vol%, and 25vol%, in unidirectional (UD) fibre alignment. Tensile and compression tests were performed on all APREC specimens in order to investigate the effect of fibre volume fraction on modulus of elasticity, strength and strain to failure. The morphological structure of fractured specimens was observed using scanning electron microscopy (SEM) in order to evaluate the fracture mechanisms involved when the specimens were subjected to tensile or compressive loading. The results indicated that the higher the amount of *Arenga Pinnata* fibres, the higher the stiffness of the composites. This is shown by the increment of tensile and compressive modulus of the specimens when the fibre volume content was increased. Tensile modulus increased up to 180% when 25vol% *Arenga Pinnata* fibre was used in APREC compared to Pure Epoxy specimen. It can also be observed that the tensile strength of the specimens increased 28% from 53.820 MPa (for Pure Epoxy) to 68.692 MPa (for Epoxy with 25vol% APREC addition). Meanwhile, compressive modulus and strength increased up to 3.24% and 9.17%, respectively. These results suggest that the addition of *Arenga Pinnata* fibres significantly improved the tensile and compressive properties of APREC.

Keywords: *Arenga Pinnata*, compressive, tensile, fibre volume fraction, unidirectional fibre alignment

ARTICLE INFO

Article history:

Received: 05 January 2017

Accepted: 17 January 2017

E-mail addresses:

aidahjumahat@salam.uitm.edu.my (Aidah Jumahat),
mfarissyafiq@yahoo.com (Muhamad Faris Syafiq Khalid),
szuraidah@salam.uitm.edu.my (Zuraidah Salleh),
jawaid@upm.edu.my (Mohammad Jawaid)

*Corresponding Author

INTRODUCTION

Natural fibres have been used in various applications since the ancient time. With

modern technology, synthetic fibres such as glass fibre, carbon fibre, and Kevlar have been developed as substitutes. Even though synthetic fibres are better in terms of their mechanical properties when compared to natural fibres, there are still some drawbacks, for example, glass fibres are expensive and harmful to human body as well as the environment. Using latest technology, the mechanical properties of natural fibres can now be improved and tailored to suit certain applications as replacement to synthetic fibres, rendering them suitable in the aerospace (Jawaid, Abdul Khalil, Hassan, Dungani, & Hadiyane, 2013; Ku, Wang, Pattarachaiyakooop, & Trada, 2011; Saba, Tahir & Jawaid, 2014), automotive (Dicker et al., 2014; Koronis, Silva, & Fontul, 2013; Sanyang, Sapuan, Jawaid, Ishak, & Sahari, 2016; Ticoalu, Aravinthan, & Cardona, 2010) and construction (Alamri, Low, & Alothman, 2012; Dicker et al., 2014; Dittenber & Gangarao, 2012; Sahari, Sapuan, Zainudin, & Maleque, 2012) sectors. Utilisation of natural fibres from plants to produce natural fibre reinforced polymer composite (NFRP) is among the most popular research topics today (Bakar, Mei Hyie, Ramlan, Hassan, & Jumahat, 2013; Manap, Jumahat, & Sapiai, 2015; Sapiai, Jumahat, & Mahmud, 2015). Natural fibres are preferred because of their attractive characteristics such as its natural availability, environment friendliness, abundance of sources and bio-degradability property (Bachtiar, Sapuan, Khalina, Zainudin, & Dahlan, 2012; Khalid & Abdullah, 2013).

Plant-based natural fibres like kenaf, hemp, sisal, jute, flax and ramie are well-known natural fibres used with either thermoplastic or thermosetting polymers in producing composite materials. The selection of natural fibre to be studied also depends on geographical availability. For example, in Europe, the focus is on flax fibre, whereas jute, kenaf, coir and sisal are more popular in Asia (Pickering, Efendy, & Le, 2016). In this present study, *Arenga Pinnata* fibre was selected to be used as reinforcement for epoxy matrix polymer. This selection is not only because of the fibre's availability in Malaysia but also due to its high durability and resistance to sea water (Ishak et al., 2013). This type of fibre has multipurpose applications such in road constructions for soil stabilisation as a substitute for geotextile fibreglass reinforcement (Ishak et al., 2013) and it is also the main component in daily items such as ropes, brushes, filters, brooms, and shelter for fish breeding (Mogea, Seibert, & Smits, 1991). *Arenga Pinnata* was found to have great potential to be used as reinforcement in polymer matrixes (Misri, Leman, Sapuan, & Ishak, 2010) like polyester and epoxy.

Researchers have been studying ways to improve the mechanical properties of natural fibre composites in order to increase their capabilities and applications (Singha & Thakur, 2008). These natural fibre reinforced polymer (NFRP) composites offer a number of advantages over synthetic fibre such as glass fibre (Faruk, Bledzki, Fink, & Sain, 2014) as mention before. The widely expanding usage of NFRP composite materials for highly loaded structures has encouraged the need for a continuous revision of mechanical testing. Tensile and compression tests are some of the various assessments performed on natural fibre reinforced polymer (Dittenber & Gangarao, 2012; Ishak et al., 2013; Jumahat, Soutis, Mahmud, & Ahmad, 2012; Sanyang et al., 2016; Uddin & Sun, 2008) to study the composite mechanical properties in structural applications such as bridges and drain covers. Difficulties that have been identified in the testing of NFRP composites include the variability of the geometrical, physical, and mechanical properties of natural fibre in the NFRP composites.

This study aims to investigate the effect of *Arenga Pinnata* fibre content on tensile and compressive properties of *Arenga Pinnata* fibre reinforced epoxy composite (APREC). Fibre content of 10vol%, 15vol%, 20vol%, and 25vol% were used to produce APREC and subjected to tensile and compressive load test. After the test, the failure surface of the specimens was observed using scanning electron microscope (SEM) to examine the failure mechanism of the composites.

MATERIALS AND METHOD

Natural fibre, *Arenga Pinnata* was used as a reinforcement for epoxy matrix in order to produce *Arenga Pinnata* fibre reinforced epoxy composite (APREC). *Arenga Pinnata* fibre was harvested from Kuala Pilah, Negeri Sembilan, Malaysia. Epoxy resin, Miracast 1517 was supplied by Miracon (M) Sdn. Bhd, Selangor, Malaysia. Generally, APREC specimens were produced with volume fraction of 10vol%, 15vol%, 20vol%, and 25vol% *Arenga Pinnata* fibre content. The composites were fabricated using hand lay-up process and then placed on cold press machine and pressed at constant pressure to flatten the composite. Unidirectional (UD) fibre alignment was chosen as the fibre orientation in producing the composite. The specimens were then subjected to tensile and compressive load until they failed, and observed under SEM to study the failure mechanism of the specimens.

For tensile test, APREC specimens were prepared using square shape mould with dimension of 250 mm length \times 25 mm width \times 3 mm thickness according to ASTM D3039 while for compression test, the dimension of the specimens was 110 mm length \times 9.8 mm width \times 4 mm thickness according to ASTM D3410. However, the procedure to fabricate the composites were similar for both tensile and compression test. Firstly, epoxy resin, hardener and *Arenga Pinnata* fibres were weighted according to mass needed for each volume percentages of the composites (10vol%, 15vol%, 20vol%, and 25vol%). The weighted *Arenga Pinnata* fibres were aligned in the prepared mould in UD alignment, then a mixture of epoxy and hardener with ratio of 100 (epoxy resin): 30 (hardener) was poured into the mould on top of the fibres. The mould was then left for 5 to 10 minutes to let epoxy resin flow in between fibres and to remove air bubbles. After that, a plastic sheet and a steel plate were placed on top of the mould before moving it into the cold press machine. The mould was set to a constant pressure of 105 kg/cm² (10,000 kPa) for 24 hours to flatten the specimen's surface and to acquire desired specimen thickness (to obtain mould volume needed). Following a curing process of 24 hours the specimens were removed from the mould, and then filed and polished to make it smooth. Figure 1 shows example of cured APREC inside mould.



Figure 1. Example of cured APREC specimen moulding

Tensile and compression tests were conducted on all prepared specimens using Instron Universal Testing Machine. The experimental setups are shown in Figure 2 and Figure 3. For tensile test, the gauge length of the specimens was set at 150 mm and the test was performed at crosshead speed of 2 mm/min, based on ASTM D3039 standard.

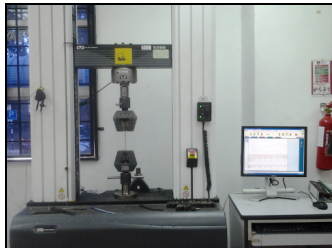


Figure 2. Tensile test setup using Instron 3382 Universal Testing Machine

One the other hand, for compression test, the test was performed according to ASTM D3410, using crosshead speed of 1 mm/min.

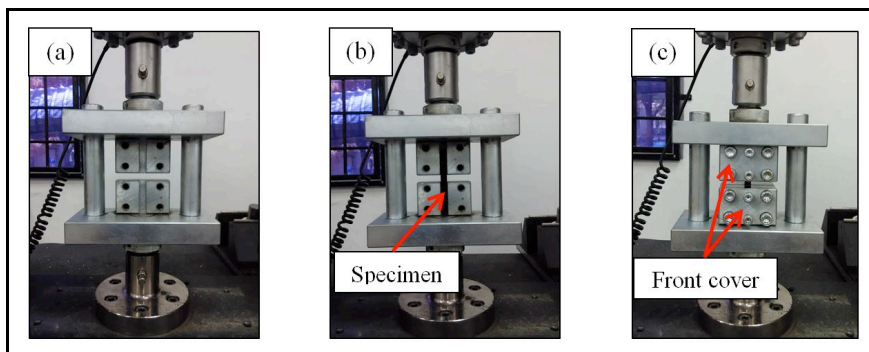


Figure 3. Compressive test jig configuration: (a) without specimen; (b) with specimen; and (c) with specimen and front cover

Bluehill 2 testing software was used to record the applied load and elongation data. These data were used to calculate the tensile and compressive properties (stress, strain, and modulus) of all specimens to investigate the effect of *Arenga Pinnata* fibre loading in APREC.

RESULTS AND DISCUSSION

Figure 4 illustrates the typical stress-strain curve of Pure Epoxy (as reference), 10vol% APREC, 15vol% APREC, 20vol% APREC, and 25vol% APREC. From the figure below, Pure Epoxy has the lowest slope gradient followed by 10vol% APREC, 15vol% APREC, 20vol% APREC, and 25vol% APREC with the highest gradient of the slope.

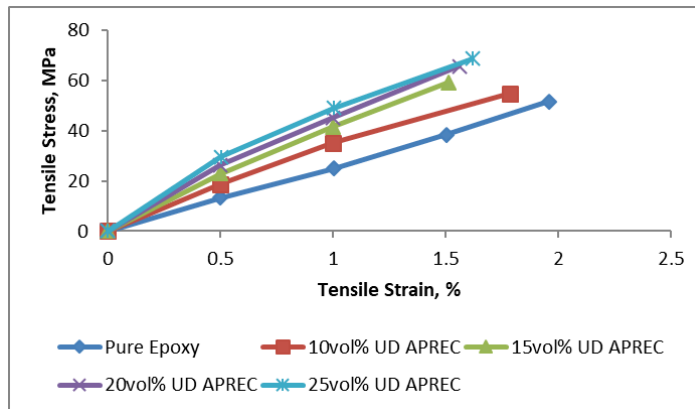


Figure 4. Typical tensile stress-train curve for Pure Epoxy, 10vol% UD APREC, 15vol% UD APREC, 20vol% UD APREC, and 25vol% UD APREC

Stress-strain curve pattern in Figure 4 shows initial linear elastic region before the stress reached around 10 MPa for APREC specimens for all volume percentage, but Pure Epoxy stress-strain curve shows almost linear line all the way until failure occurred. After the curves for APREC specimens passed the linear elastic region, they start to bend a little, indicating transformation to plastic region. Similar tensile stress-strain curve pattern had been reported by Ticoalu, Aravinthan and Cardona (2013) on untreated, 5% NaOH treatment, and 10% NaOH treatment of *Arenga Pinnata* fibres.

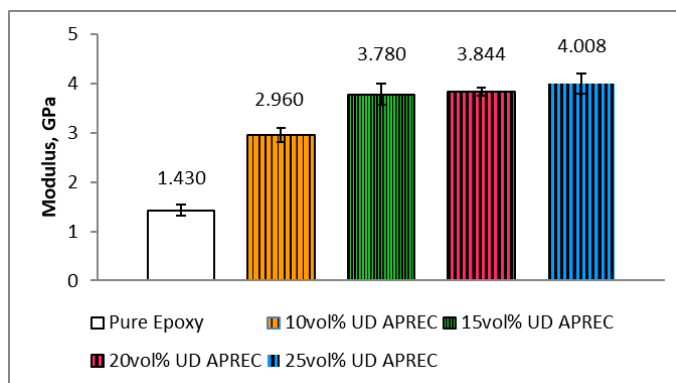


Figure 5. Tensile modulus of Pure Epoxy, 10vol% APREC, 15vol% APREC, 20vol% APREC, and 25vol% APREC

From the calculated tensile modulus shown in Figure 5, pure Epoxy acts as the reference, displayed the lowest stiffness of all specimens with 1.430 GPa. 10vol% APREC shows increment of 2.960 GPa (increased by 106.99%), 15vol% APREC with 3.780 GPa (increased by 164.34%), 20vol% APREC with 3.884 GPa (increased by 168.81%), and 25vol% APREC with 4.008 GPa (increased by 180.28%).

Tensile modulus increased with the increment of *Arenga Pinnata* fibre volume in APREC, suggested that *Arenga Pinnata* fibres had enhanced the composites' stiffness.

Table 1
Tensile strength and tensile strain of Pure Epoxy and APREC

Materials	Tensile Strength, MPa	Tensile Strain, %
Pure Epoxy	53.820 ± 0.971	1.959 ± 0.113
10vol% APREC	54.830 ± 1.533	1.787 ± 0.181
15vol% APREC	59.257 ± 0.724	1.515 ± 0.167
20vol% APREC	65.686 ± 1.368	1.562 ± 0.125
25vol% APREC	68.692 ± 1.110	1.619 ± 0.073

Tensile strength and strain of Pure Epoxy and APREC are shown in Table 1. The tensile strength result shows significant increment from Pure Epoxy which exhibited the lowest value of 53.820 MPa, followed by 10vol% APREC 54.830 MPa (1.88% increment), 15vol% APREC 59.257 MPa (10.10% increment), 20vol% APREC with 65.686 MPa (22.05% increment), and 25vol% APREC with 68.692 MPa (27.63% increment). However, tensile strain of all UD APREC specimens was slightly lower than Pure Epoxy as shown in Figure 3 where the curves of APREC specimens stopped earlier than Pure Epoxy due to premature failure caused by poor interfacial bonding between *Arenga Pinnata* fibres and epoxy matrix. This was verified by SEM images in Figure 6 showing debonding of *Arenga Pinnata* fibres from epoxy matrix and fibre pull-out.

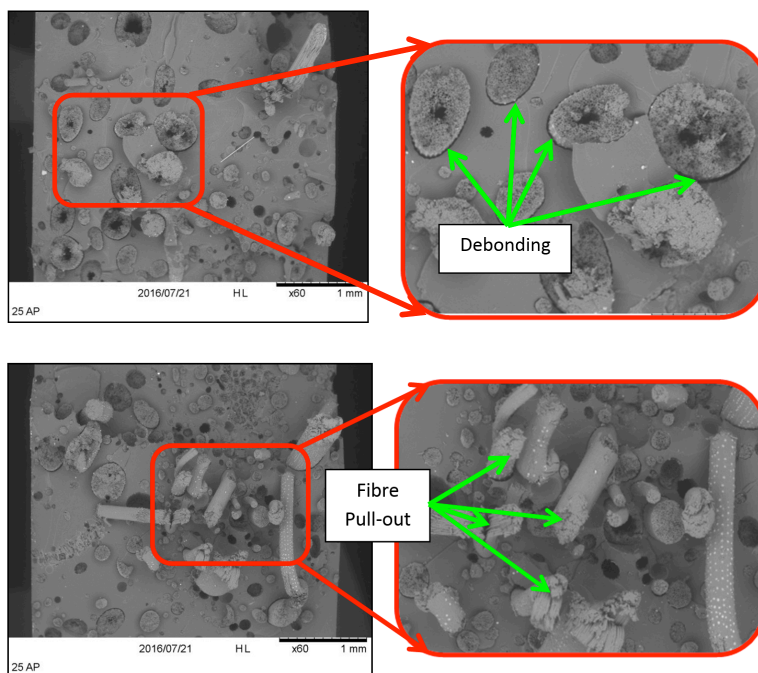


Figure 6. SEM images of UD APREC tensile failure surface

Figure 7 indicates a similar trend with tensile stress-strain curve where Pure Epoxy has the lowest gradient of the slope, followed by 10vol% APREC, 15vol% APREC, 20vol% APREC, and 25vol% APREC for the first 15% compressive strain. This implies that addition of *Arenga Pinnata* fibres increased the resistivity of the material to deform when subjected to tensile and compression. As shown in Figure 7, all specimens collapsed at around 20% compressive strain, but their compressive strength varies around 88 MPa to 100 MPa.

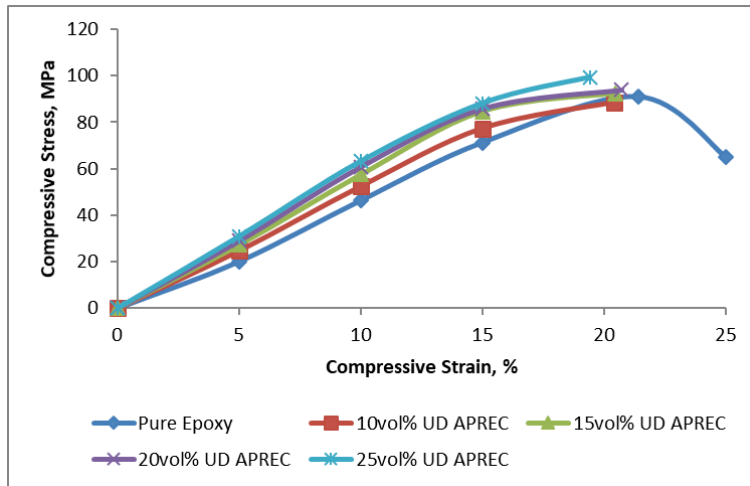


Figure 7. Typical Compressive stress-strain curve for Pure Epoxy, 10vol% APREC, 15vol% APREC, 20vol% APREC, and 25vol% APREC

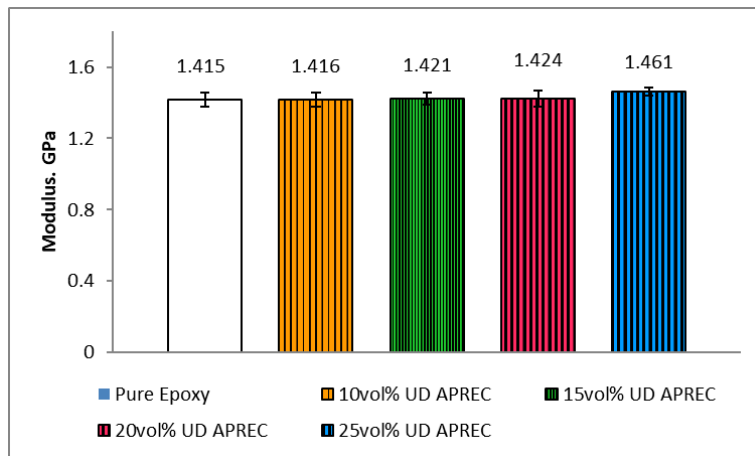


Figure 8. Compressive modulus of Pure Epoxy, 10vol% APREC, 15vol% APREC, 20vol% APREC, and 25vol% APREC

Compressive modulus of APREC specimens shows similar improvement compared to Pure Epoxy as in Figure 8 but the increments are not as much as tensile modulus. For 10vol% APREC, compressive modulus only increased by 0.06%, 15vol%, 20vol%, and 25vol% APREC had increased by 0.42%, 0.63%, and 3.24% respectively.

Table 2
Compressive strength and compressive strain of Pure Epoxy and APREC

Materials	Compressive Strength, MPa	Compressive Strain, %
Pure Epoxy	90.980 ± 5.453	21.403 ± 1.532
10vol% APREC	88.518 ± 0.188	20.409 ± 2.024
15vol% APREC	92.459 ± 3.184	20.469 ± 3.389
20vol% APREC	93.995 ± 0.642	20.730 ± 3.020
25vol% APREC	99.327 ± 2.492	19.426 ± 1.615

The addition of *Arenga Pinnata* fibres into epoxy matrix increased the compressive strength as shown in Table 2. Even though there was a slight drop in compressive strength displayed at 10vol% APREC, the compressive strength values had increased by 1.63% (15vol% APREC), 3.31% (20vol% APREC), and 9.17% (25vol% APREC) compared to Pure Epoxy. Compressive strains for all APREC specimens were just a bit lower than Pure Epoxy though the values were almost the same.

Figure 9 demonstrates the SEM image of APREC compressive failure section showing that the failure was initiated by the matrix failure. The *Arenga Pinnata* fibres surfaces were still intact after the compression test, proves that the untreated *Arenga Pinnata* fibres and epoxy matrix had poor interfacial bonding.

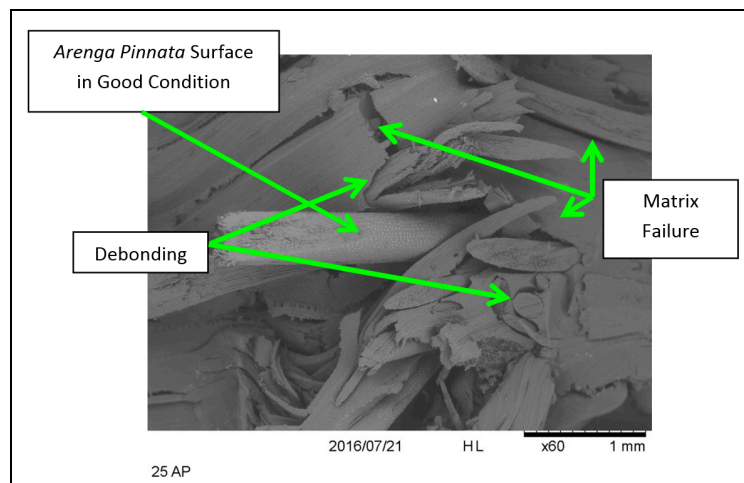


Figure 9. SEM image of UD APREC compressive failure section

CONCLUSION

Tensile and compression test were successfully carried out on 10vol %, 15vol%, 20vol%, and 25vol% APREC. Tensile modulus, tensile strength, compressive modulus and compressive strength results indicate that the addition of *Arenga Pinnata* fibre into epoxy matrix had improved the tensile and compressive properties of the epoxy. Furthermore, addition of fibre volume percentage in APREC had improved the tensile and compressive properties of the composites. Increment in modulus is the evidence that *Arenga Pinnata* plays an important role in improving the rigidity of epoxy matrix. Despite the successful improvement in mechanical properties, further enhancements are required to improve the interfacial bonding of *Arenga Pinnata* fibre and epoxy resin to improve the mechanical properties of APREC.

ACKNOWLEDGEMENTS

The authors would like to thank Institute of Research Management and Innovation (IRMI), Ministry of Education Malaysia and Institute of Graduate Studies (IPSiS) UiTM for the financial supports. This research work was performed at the Faculty of Mechanical Engineering, UiTM Malaysia under the support of GIP research grant no. 600-IRMI/MYRA 5/3/GIP (053/2017).

REFERENCES

- Alamri, H., Low, I. M., & Alothman, Z. (2012). Mechanical, thermal and microstructural characteristics of cellulose fibre reinforced epoxy/organoclay nanocomposites. *Composites Part B: Engineering*, *43*, 2762–2771.
- Bachtiar, D., Sapuan, S. M., Khalina, A., Zainudin, E. S., & Dahlan, K. Z. M. (2012). Flexural and impact properties of chemically treated sugar palm fiber reinforced high impact polystyrene composites. *Fibers and Polymers*, *13*, 894–898.
- Bakar, N. H., Mei Hyie, K., Ramlan, A. S., Hassan, M. K., & Jumahat, A. (2013). Mechanical properties of kevlar reinforcement in kenaf composites. *Applied Mechanics and Materials*, *465–466*, 847–851.
- Dicker, M. P. M., Duckworth, P. F., Baker, A. B., Francois, G., Hazzard, M. K., & Weaver, P. M. (2014). Green composites: A review of material attributes and complementary applications. *Composites Part A: Applied Science and Manufacturing*, *56*, 280–289.
- Dittenber, D. B., & Gangarao, H. V. S. (2012). Critical review of recent publications on use of natural composites in infrastructure. *Composites Part A: Applied Science and Manufacturing*, *43*, 1419–1429.
- Faruk, O., Bledzki, A. K., Fink, H.-P., & Sain, M. (2014). Progress report on natural fiber reinforced composites. *Macromolecular Materials and Engineering*, *299*, 9–26.
- Ishak, M. R., Sapuan, S. M., Leman, Z., Rahman, M. Z. A., Anwar, U. M. K., & Siregar, J. P. (2013). Sugar palm (*Arenga pinnata*): Its fibres, polymers and composites. *Carbohydrate Polymers*, *91*, 699–710.
- Jawaid, M., Abdul Khalil, H. P. S., Hassan, A., Dungani, R., & Hadiyane, A. (2013). Effect of jute fibre loading on tensile and dynamic mechanical properties of oil palm epoxy composites. *Composites Part B*, *45*, 619–624.
- Jumahat, A., Soutis, C., Mahmud, J., & Ahmad, N. (2012). Compressive properties of nanoclay/epoxy nanocomposites. *Procedia Engineering*, *41*, 1607–1613.

- Khalid, M. F. S., & Abdullah, A. H. (2013). Storage modulus capacity of untreated aged *Arenga pinnata* fibre-reinforced epoxy composite. *Applied Mechanics and Materials*, 393, 171–176.
- Koronis, G., Silva, A., & Fontul, M. (2013). Green composites: A review of adequate materials for automotive applications. *Composites Part B: Engineering*, 44, 120–127.
- Ku, H., Wang, H., Pattarachaiyakooop, N., & Trada, M. (2011). A review on the tensile properties of natural fiber reinforced polymer composites. *Composites Part B: Engineering*, 42, 856–873.
- Manap, N., Jumahat, A., & Sapiai, N. (2015). Effect of fibre treatment on longitudinal and transverse tensile properties of unidirectional kenaf composite. *Jurnal Teknologi*, 76, 87–95.
- Misri, S., Leman, Z., Sapuan, S. M., & Ishak, M. R. (2010). Mechanical properties and fabrication of small boat using woven glass/sugar palm fibres reinforced unsaturated polyester hybrid composite. *IOP Conference Series: Materials Science and Engineering*, 11, 12015.
- Mogea, J., Seibert, B., & Smits, W. (1991). Multipurpose palms: The sugar palm (*Arenga pinnata* (Wurmb) Merr.). *Agroforestry Systems*, 13, 111–129.
- Pickering, K. L., Efendy, M. G. A., & Le, T. M. (2016). A review of recent developments in natural fibre composites and their mechanical performance. *Composites Part A: Applied Science and Manufacturing*, 83, 98–112.
- Saba, N., Tahir, P., & Jawaid, M. (2014). A Review on Potentiality of Nano Filler/Natural Fiber Filled Polymer Hybrid Composites. *Polymers*, 6, 2247–2273.
- Sahari, J., Sapuan, S. M., Zainudin, E. S., & Maleque, M. a. (2012). A new approach to use *Arenga pinnata* as sustainable biopolymer: Effects of plasticizers on physical properties. *Procedia Chemistry*, 4, 254–259.
- Sanyang, M. L., Sapuan, S. M., Jawaid, M., Ishak, M. R., & Sahari, J. (2016). Recent developments in sugar palm (*Arenga pinnata*) based biocomposites and their potential industrial applications: A review. *Renewable and Sustainable Energy Reviews*, 54, 533–549.
- Sapiai, N., Jumahat, A., & Mahmud, J. (2015). Flexural and tensile properties of kenaf/glass fibres hybrid composites filled with carbon nanotubes. *Jurnal Teknologi*, 76, 115–120.
- Singha, A. S., & Thakur, V. K. (2008). Mechanical properties of natural fibre reinforced polymer composites. *October*, 31, 791–799.
- Ticoalu, A., Aravinthan, T., & Cardona, F. (2010). A review of current development in natural fiber composites for structural and infrastructure applications. *Southern Region Engineering Conference*, 1–5.
- Ticoalu, A., Aravinthan, T., & Cardona, F. (2013). A study into the characteristics of gomuti (*Arenga pinnata*) fibre for usage as natural fibre composites. *Journal of Reinforced Plastics and Composites*, 33, 179–192.
- Uddin, M. F., & Sun, C. T. (2008). Strength of unidirectional glass/epoxy composite with silica nanoparticle-enhanced matrix. *Composites Science and Technology*, 68, 1637–1643.

Hole Size Effects on the Open Hole Tensile Properties of Woven Kevlar-Glass Fibre Hybrid Composite Laminates

Norazean Shaari^{1,2} and Aidah Jumahat^{2*}

¹Department of Engineering, Faculty of Engineering and Life Sciences, Universiti Selangor (UNISEL), Jalan Timur Tambahan, 45600 Bestari Jaya, Selangor, Malaysia

²Faculty of Mechanical Engineering, Universiti Teknologi MARA (UiTM), 40450 Shah Alam, Selangor, Malaysia

ABSTRACT

The effects of hole size on open hole tensile properties of Kevlar-glass fibre hybrid composite laminates were thoroughly investigated in this work. Woven Kevlar/glass fibre epoxy composite laminates were fabricated using hand lay-up and vacuum bagging technique. Specimens of five different hole size (1 mm, 4 mm, 6 mm, 8 mm and 12 mm) were carefully prepared before the tensile test was performed according to ASTM D5766. Results indicated that hybridizing Kevlar to glass fibres improved tensile strength and failure strain of hybrid composite specimen. In addition, increasing the hole size reduced strength retention of the hybrid specimen from 96% for 1 mm hole size to 62% and 44% for 6 mm and 12 mm, respectively. Fractography analysis showed that several types of failure mechanisms were observed such as brittle failure, ductile failure, fibre breakage, delamination and fibre-matrix splitting. It is concluded that as hole size increased, failure behaviour changed from a matrix dominated failure mode to a fibre-dominated failure mode.

Keywords: Glass fibre, hole size, hybrid composites, Kevlar fibre, open hole tensile

INTRODUCTION

Over the past 40 years studies on the hole or notch strength of composite materials

have been carried out extensively due to its importance to designers. Studies have been conducted experimentally, analytically or numerically on the effect of hole and hole size towards the strength of composite laminates loaded in tension, compression or bending by several researchers (Achard, Bouvet, Castanié, & Chirol, 2014; Balaco, 2000; Callus, 2007; Chen, Tay, Baiz, & Pinho, 2013; Erçin et al., 2013; Kannan, Wu, & Cheng, 2014; Green, Wisnom, & Hallett,

ARTICLE INFO

Article history:

Received: 05 January 2017

Accepted: 17 January 2017

E-mail addresses:

norazean@unisel.edu.my (Norazean Shaari),

aidahjumahat@salam.uitm.edu.my (Aidah Jumahat)

*Corresponding Author

2007; Higgins, Mccarthy, & Mccarthy, 2008; Salleh et al., 2013; Talib, Ramadhan, Rafie, & Zahari, 2013; Wisnom & Hallett, 2009; Yudhanto, Watanabe, Iwahori, & Hoshi, 2012; Zheng, Cheng, & Yasir, 2012). This is because, it is important for a designer to consider the effect of this hole on the strength of the laminate for safety purpose and efficient design. There are many factors that created sensitivity of a laminate to a hole such as size and thickness of the laminate, geometry and size of hole, orientation and thickness of ply, quality of machining process, and constituent of materials (Chen, Tay, Baiz, & Pinho, 2013; Kannan, Wu, & Cheng, 2014; Green, Wisnom, & Hallett, 2007; Wisnom & Hallett, 2009). In addition parametric effects of drilling conditions such as feed rate, spindle speed and drill point angle are also important because drilling operation can cause damage such as delamination and matrix cracking around the hole (Nasir, Azmi, & Khalil, 2015). All of these factors often affected and deteriorated the mechanical properties and performance of the composites by changing the extent of damage growth and propagation during loading.

Open hole strength is one of the factors that should be considered in component design as it can be a limiting factor during the application. Therefore, it is important to conduct open hole tensile test in order to determine the acceptable stress levels in the component design. Erçin et al. (2013) investigated the effects of hole size loaded in tension and compression under quasi-static loading of carbon fibre reinforced polymer (CFRP) composite laminates. From the results, the authors concluded that increasing the hole size from 3 mm to 7 mm caused tensile and compressive strength reduction. Furthermore, laminate lay-ups also affected the laminate strength. Laminate with maximum fibre orientation angle between adjacent plies has low tensile strength reduction that is 6.9% as compared to laminate with minimum fibre orientation angle between adjacent plies with 10.7%. Similar research were also conducted by Kannan, Wu and Cheng (2014) on flax yarn reinforced polypropylene (PP) laminates. In the study, the role of laminate lay-up, hole size and coupling agent on the composite laminates was investigated. Three laminate lay-ups namely axial, cross ply and off-axial were prepared with 4 mm hole size. Results indicated that the cross-ply laminate showed the highest strength retention that is 98% as compared to off-axial and axial laminates with 92% and 89%, respectively. The authors also confirmed that the strength retention of flax/PP specimen decreased as the hole sizes were increased. Uniaxial flax/PP specimen showed 89% strength retention for 4 mm hole sizes and around 78% strength retention for 8 mm hole sizes. The tensile strength of all laminates lay-up was found to improve with the usage of maleic anhydride grafted polypropylene (MAPP) copolymer film as coupling agent.

Salleh et al. (2013) in their study of kenaf/glass fibre composite specimens concluded that as the hole size increases from 1mm to 16mm in both kenaf composite and kenaf/glass fibre composite specimens, a significant decrement in tensile strength and tensile stiffness was observed. Kenaf composites and kenaf/glass fibre composites lost more than 59% and 54%, respectively of their tensile strength when the hole size was larger than 8 mm. However, hybridization of glass fibre to kenaf composite has significantly increased the tensile strength of the composite specimens. A report from Callus also stated that the value of tensile and compression strength and also strain-to-failure decreased significantly when the hole size increased for small holes and gradually decreased for larger holes. Green, Wisnom and Hallett (2007) also reported the influence of open hole size, ply and laminate thickness on the

open hole tensile strength of quasi-isotropic CFRP composite laminates. The experimental investigation has confirmed that hole size and thickness are the factors that affect failure stress and mechanism. Their results showed that a maximum reduction of 64% in strength was observed when the specimen size was increased from 3.175 mm to 25.4 mm. However, for specimens with plies blocked together, the opposite trend of strength increasing with in-plane dimensions was observed. Three different failure mechanisms were observed namely brittle, pull out and delamination. Brittle happens when fibre failure occurs without extensive matrix damage while pull out occurs when there is extensive matrix damage such as delamination and matrix cracking existed.

In the present study, the effect of hole size on the open-hole tensile properties of interlaminated twill weave Kevlar-49/plain weave C-glass fibre hybrid composite laminates were investigated and evaluated. Specimens with six different hole size including unhole specimen were prepared in order to determine and compare the effect of hole size to tensile properties of pure and hybrid specimens. Further evaluation on tensile damage pattern was also performed to support tensile test results. This study is a continuation of a previous study done by Shaari, Jumahat, Abdullah and Hadderi (2015).

MATERIALS AND METHOD

In this study, composite laminates were fabricated using 2443 twill weave Kevlar-49 fibre and CWR200 plain weave C-glass fibre as the reinforcement materials while Miracast 1517 A/B epoxy resin system was used as the matrix material. An average of 2.5 mm specimen thickness of fibre reinforced polymer (FRP) composite laminates were developed and fabricated according to ASTM D5766. A mixture of epoxy resin and hardener with a ratio of 100:30 were prepared and applied to the fibres using hand lay-up followed by vacuum bagging methods. Three different composite systems were prepared namely glass fibre reinforced polymer (GFRP), Kevlar fibre reinforced polymer (KFRP) and Kevlar/glass fibre reinforced polymer (KGFRP). Hybrid specimen consists of 50% glass fibre and 50% Kevlar fibre with a stacking sequence of Kevlar fibre in the interior part while glass fibre in the exterior part (glass/Kevlar/glass). Laminate was vacuumed for one hour to remove air-trapped, bubbles and excess resin and left to cure at room temperature for 24 hours followed by post curing up to 120°C for about 12 hours at 1°C/min. Finally, specimens were cut using composite cutter before hole was drilled on the specimens using vertical drilling machine at a speed of 3000 rpm. It was very important to produce a good quality hole without any defects such as matrix cracking and edge delamination because the presence of such defects near hole region reduces the strength of a laminate.

Open hole tensile (OHT) test was performed to determine the damage tolerance of the damage composite specimens under tensile loading. A rectangular specimen with a dimension of 300 mm × 36 mm × 2.5 mm was prepared. Tabs are not required and generally not needed in hole specimen since the open hole acts as sufficient stress riser to force failure in the hole region. For hole specimen, five different hole size diameters (1 mm, 4 mm, 6 mm, 8 mm and 12 mm) were drilled on the specimen. Strain response was measured using 25 mm gauge length extensometer attached to the centre of the specimen. Testing was run using INSTRON 3382 Universal Testing Machine with crosshead speed of 2 mm/min. Tensile damage of

composite specimens was captured using Canon A2200 digital camera to investigate the failure behaviour. The fractured surfaces of tested specimens were also observed using scanning electron microscope (SEM) model Hitachi TM 3000 table top microscope manufactured by Hitachi High Technologies, Japan.

RESULTS AND DISCUSSION

Results in Figure 1 shows the tensile stress – tensile strain behaviour of unhole and 6 mm hole of GFRP, KGFRP and KFRP composite specimen. From the results, it is confirmed that hybridization of Kevlar fibre to glass fibre has improved the tensile strength and tensile strain of the composite specimens. The result also indicates tensile strength of unhole GFRP specimen is 193 MPa while tensile strength of KGFRP is 267 MPa; an increment of about 38% with hybridization of 50% Kevlar fibre. Kevlar fibre is known as a ductile type fibre (Wan, Wang, He, Huang, & Jiang, 2007); therefore it has high tensile strain or elongation at break under tensile load when compared to glass fibre which has brittle type fracture behaviour. From Figure 1(a), GFRP and KGFRP is reported to have 4.1% and 4.4% of tensile strain indicating that hybridization also improved elongation at break and failure behaviour of the specimen. Fu et al. (2001), and Haery, Zahari, Kuntjoro and Taib (2012) also concluded that hybridization has improved the tensile strength of glass fibre composites. The presence of 6 mm hole has affected tensile strength and elongation at break of all composite specimens. Hole made to the specimens reduced the tensile strength and tensile strain of all specimens from 50-62% (Shaari, Jumahat, Abdullah, & Hadderi, 2015) and 54-64%, respectively. The result of reduction in tensile strength are expected as Saleh et al. (2016) have mentioned in their study that composite laminates usually demonstrated approximately 50% reduction in strength compared to their unhole strength.

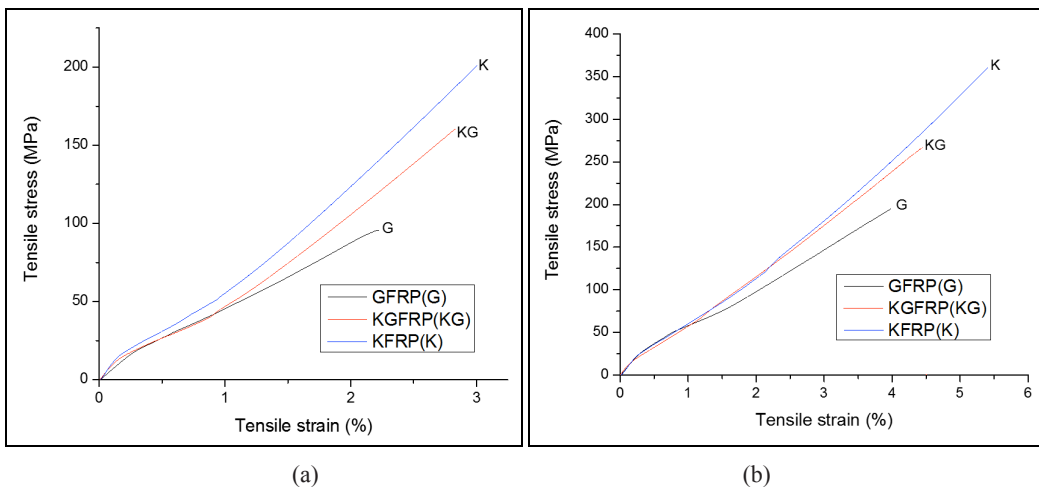


Figure 1. Tensile stress-strain of unmodified GFRP, KGFRP and KFRP of: (a) unhole specimen; and (b) 6 mm hole specimen

Ductile and brittle failure behaviour of Kevlar fibre and glass fibre are confirmed through SEM images as in Figure 2. It can be seen from both images that smooth surface in glass fibre indicates the brittle failure of glass fibre while the ductile Kevlar fibre tends to deform and has a higher strain under tensile load.

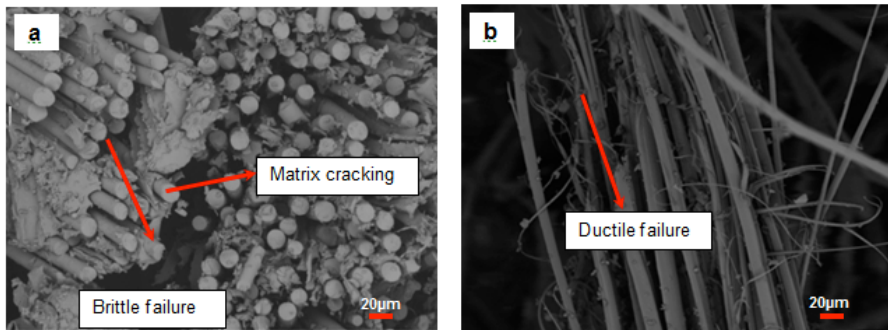


Figure 2. Tensile damage specimens of: (a) glass fibre; and (b) Kevlar fibre viewed under scanning electron microscope

Further investigation was carried out by comparing the effect of different hole size to composite laminates. The result in Figure 3 shows significant decrement in tensile strength of hybrid composite from 267 MPa to 165 MPa when the hole size increased from unhole to 6 mm and gradually decreased to 118 MPa when the size of the hole was further enlarged up to 12 mm in diameter. The hybrid composites retain about 62% of their tensile strength when the hole size was 6 mm. This is the highest strength retention obtained as compared to GFRP and KFRP specimens which have a much lower strength retention at the same hole size that is 50% and 57%, respectively. Table 1 displays the comparison of strength retention values for all specimens at all five different hole size. From the results, hybrid specimen exhibits the highest strength retention values at all five different hole sizes as compared to GFRP and KFRP specimens. At the largest hole size of 12 mm, KGFRP retains 44% of its strength while GFRP and KFRP only retain 39% of their strength. This confirmed the positive hybrid effect of the hybrid composite specimen. GFRP specimens lost 50% of its tensile strength when the hole size was 6 mm. Other research works also confirmed that larger hole size caused a decrement in tensile strength of the composites (Callus, 2007; Chen, Tay, Baiz, & Pinho, 2013; Erçin et al., 2013; Kannan, Wu, & Cheng, 2014; Green, Wisnom, & Hallett, 2007; Salleh et al., 2013). This is because, stress could be disseminated to a larger region of the specimen cross-section at small hole diameter whereas at larger hole size, the damage zone extended to greater portion of the specimen; therefore, less region remained to support the stress.

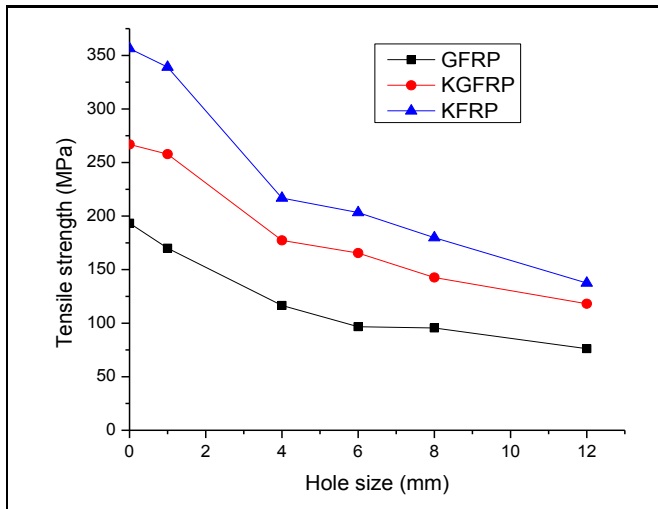


Figure 3. Tensile strength of unmodified GFRP, KGFRP and KFRP specimens with different hole size

Table 1
Open hole tensile strength and strength retention of GFRP, KGFRP and KFRP specimens

Tensile Properties/Hole Size		FRP Composite Specimen		
		GFRP	KGFRP	KFRP
Tensile strength (MPa)	Unhole	193.37±2.11	266.92±11.63	356.36±4.50
	1 mm	169.99±4.80	257.87±8.05	339.12±7.63
	4 mm	116.51±6.85	177.29±3.54	216.79±2.15
	6 mm	96.66±1.37	165.48±7.09	203.35±2.03
	8 mm	95.52±1.18	142.64±6.09	179.87±6.61
	12 mm	76.16±2.20	118.17±1.89	137.46±3.52
Strength retention (%)	1 mm	88	97	95
	4 mm	60	66	61
	6 mm	50	62	57
	8 mm	49	53	50
	12 mm	39	44	39

Macroscopic and microscopic observations of the fractured specimens were carried out to observe and analyse the tensile damage of the specimens. Specimens were viewed closely at the fractured area near the hole as in Figure 4, where it shows the tensile damage of specimens drilled with 6 mm hole. GFRP specimen (Figure 4(a)) displayed a brittle failure type in which the specimen was fractured and broken into two pieces. The specimen failure begins with fibre–matrix breakage at the open hole edge in the tensile loading direction. The damage extended into the entire fibre bundle around the hole and finally failed in brittle failure mode due to the brittle behaviour of glass fibre. The failure in KGFRP hybrid composite (Figure 4(b)) started with matrix cracking in resin-rich region followed by some fibre breakage. This is because, if hybrid composite is loaded in the fibre direction of tensile load, brittle fibre (glass fibre) will

fail before ductile fibre (Kevlar fibre) (Swolfs, Gorbatiikh, & Verpoest, 2014). Delamination area indicated with white appearance was seen around the open hole. Delamination is caused by cracked and fractured matrix which exposes the ply of glass fibres. This is the reason for the white appearance in the delamination area. This fracture behaviour can be taken as a warning sign before final failure. Meanwhile, Figure 4(c) shows ductile failure behaviour in KFRP specimen, where fibre–matrix splitting occurs at the open hole edge in the loading direction. However, due to ductile behaviour of Kevlar fibre, some of the Kevlar fibres only elongate without breaking.

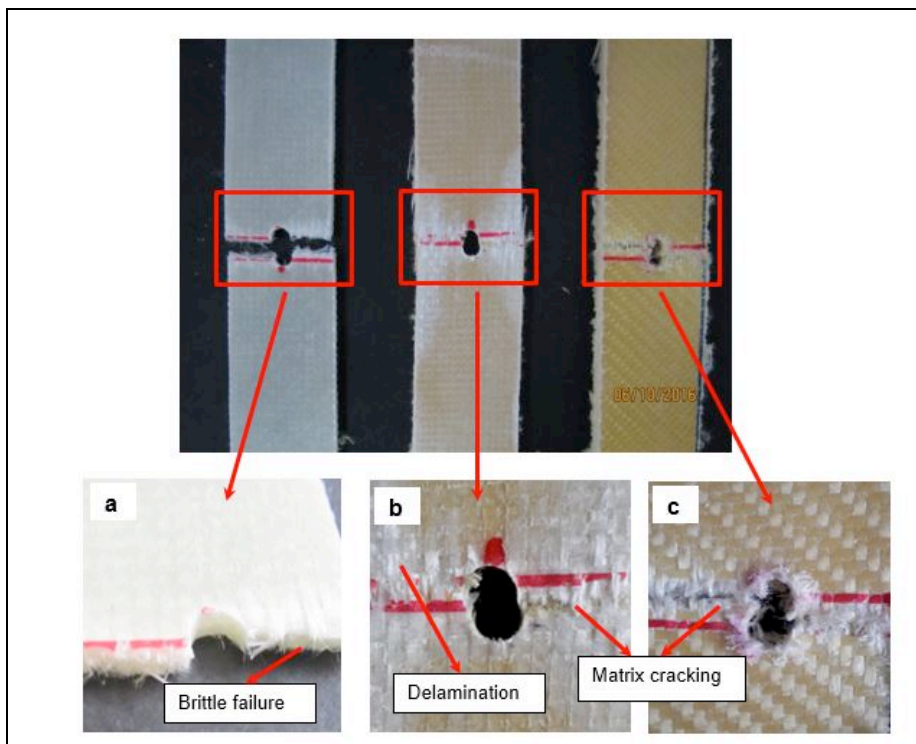


Figure 4. Tensile damage of 6 mm hole size specimens of (a) GFRP; (b) KGFRP; and (c) KFRP

Figure 5 shows tensile damage specimens of KGFRP composite laminates with various hole sizes ranging from 0 mm to 12 mm. The presence of hole acts as a stress riser in the specimen that caused the fibres near the hole edges started to fail. The higher stress near to this hole would lead the fibres to fail first. The failure mechanisms started with matrix cracking followed by delamination and fibre separation or breakage. Delamination area, which is indicated with white appearance near the open-hole region shows a reduction in area from unhole specimen to 12 mm hole size specimen. It can be concluded that for a specimen with small hole size, more loads are required to be applied before failure can occur. As the hole size increases, it acts as a stress riser, resulting in less load required for the specimen to fail. Therefore, less matrix cracking, delamination area and fibre breakage exist. The failure behaviour changed

from a matrix-dominated to a fibre-dominated failure with the increasing of hole size. Similar observations were reported by Green, Wisnom and Hallett (2007) and Lagace (1986) in their studies. This phenomenon occurred due to the interlaminar stresses around the hole boundary; which decreases in importance with the increase of hole size.

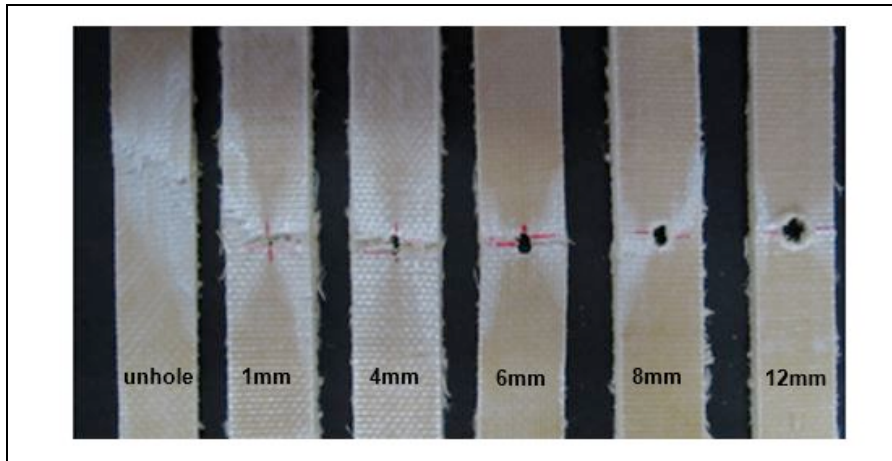


Figure 5. Tensile damage of KGFRP specimen with hole size diameter range from 0 mm to 12 mm

CONCLUSION

Open hole tensile test was successfully performed on Kevlar/glass fibre composite laminates according to ASTM D5766 with five different hole size. Experimental results concluded that strength retention decreased with the increase of hole size in all GFRP, KGFRP and KFRP specimens, in which KGFRP specimen holds the highest strength retention. Analysis of tensile damage showed that delamination was obviously seen in KGFRP specimens indicated with white appearance. As the hole size increased, the delamination area was observed to decrease. This is caused by the hole size that acted as the sufficient stress riser; therefore, the damage initiated near the hole edge.

ACKNOWLEDGEMENTS

The authors would like to thank Institute of Research Management and Innovation (IRMI), Ministry of Education Malaysia and Institute of Graduate Studies (IPSIS) UiTM for the financial support. This research work was performed at the Faculty of Mechanical Engineering, UiTM Malaysia under the support of REI research grant no. 600-IRMI/DANA5/3/REI (11/2017).

REFERENCES

Achard, V., Bouvet, C., Castanié, B., & Chirol, C. (2014). Discrete ply modelling of open hole tensile tests. *Composite Structures*, 113, 369–381.

- Balaco, A. (2000). Open-hole tensile strength of quasi-isotropic laminates. *Composites Science and Technology*, 60, 1997–2004.
- Callus, P. J. (2007). The effects of hole-size and environment on the mechanical behaviour of a Quasi-isotropic AS4 / 3501-6 laminate in tension, compression and bending. *Air Vehicles Division, Defence Science and Technology Organisation*.
- Chen, B. Y., Tay, T. E., Baiz, P. M., & Pinho, S. T. (2013). Numerical analysis of size effects on open-hole tensile composite laminates. *Composites Part A: Applied Science and Manufacturing*, 47, 52–62.
- Erçin, G. H., Camanho, P. P., Xavier, J., Catalanotti, G., Mahdi, S., & Linde, P. (2013). Size effects on the tensile and compressive failure of notched composite laminates. *Composite Structures*, 96, 736–744.
- Fu, S. Y., Lauke, B., Mäder, E., Yue, C. Y., Hu, X., & Mai, Y. W. (2001). Hybrid effects on tensile properties of hybrid short-glass-fiber-and short-carbon-fiber-reinforced polypropylene composites. *Journal of Materials Science*, 36(5), 1243–1251.
- Kannan, T. G., Wu, C. M., & Cheng, K. B. (2014). Influence of laminate lay-up, hole size and coupling agent on the open hole tensile properties of flax yarn reinforced polypropylene laminates. *Composites Part B: Engineering*, 57, 80–85.
- Green, B. G., Wisnom, M. R., & Hallett, S. R. (2007). An experimental investigation into the tensile strength scaling of notched composites. *Composites Part A: Applied Science and Manufacturing*, 38(3), 867–878.
- Haery, H. A., Zahari, R., Kuntjoro, W., & Taib, Y. M. (2012). Tensile strength of notched woven fabric hybrid glass, carbon/epoxy composite laminates. *Journal of Industrial Textiles*, 43(3), 383–395.
- Higgins, R. M. O., Mccarthy, M. A., & Mccarthy, C. T. (2008). Comparison of open hole tension characteristics of high strength glass and carbon fibre-reinforced composite materials. *Composites Science and Technology*, 68, 2770–2778.
- Nasir, A. A. A., Azmi, A. I., & Khalil, A. N. M. (2015). Parametric study on the residual tensile strength of flax natural fibre composites after drilling operation. *Procedia Manufacturing*, 2, 97–101.
- Saleh, M. N., Wang, Y., Yudhanto, A., Joesbury, A., Potluri, P., Lubineau, G., & Soutis, C. (2016). Investigating the potential of using off-axis 3d woven composites in composite joints' Applications. *Applied Composite Materials*.
- Salleh, Z., Berhan, M. N., Hyie, K. M., Taib, Y. M., Kalam, A., & Roselina, N. R. N. (2013). Open hole tensile properties of Kenaf composite and Kenaf/fibreglass hybrid composite laminates. *Procedia Engineering*, 68, 399–404.
- Shaari, N., Jumahat, A., Abdullah, S. A., & Hadderi, A. Z. (2015). Effect of hybridization on open-hole tension properties of Woven Kevlar/glass fiber hybrid composite laminates. *Jurnal Teknologi*, 76, 91–96.
- Swolfs, Y., Gorbatikh, L., & Verpoest, I. (2014). Fibre hybridisation in polymer composites: A review. *Composites Part A: Applied Science and Manufacturing*, 67, 181–200.
- Talib, A. R. A., Ramadhan, A. A., Rafie, A. S. M., & Zahari, R. (2013). Influence of cut-out hole on multi-layer Kevlar-29 / epoxy composite laminated plates. *Journal of Materials and Design*, 43, 89–98.
- Wan, Y. Z., Wang, Y. L., He, F., Huang, Y., & Jiang, H. J. (2007). Mechanical performance of hybrid bismaleimide composites reinforced with three-dimensional braided carbon and Kevlar fabrics. *Composites Part A: Applied Science and Manufacturing*, 38(2), 495–504.

- Wisnom, M. R., & Hallett, S. R. (2009). The role of delamination in strength, failure mechanism and hole size effect in open hole tensile tests on quasi-isotropic laminates. *Composites Part A: Applied Science and Manufacturing*, 40(4), 335–342.
- Yudhanto, A., Watanabe, N., Iwahori, Y., & Hoshi, H. (2012). The effects of stitch orientation on the tensile and open hole tension properties of carbon / epoxy plain weave laminates. *Materials and Design*, 35, 563–571.
- Zheng, Y., Cheng, X., & Yasir, B. (2012). Effect of stitching on plain and open-hole strength of cfrp laminates. *Chinese Journal of Aeronautics*, 25(3), 473–484.

**REFEREES FOR THE PERTANIK
JOURNAL OF SCIENCE AND TECHNOLOGY**

VOL. 25 (S) JUL. 2017
Special Edition

Advances in Science & Technology Research

The Editorial Board of the Journal of Science and Technology wishes to thank the following:

Abdullah Muhammed
(UPM, Malaysia)

Afdalina Tumian
(IIUM, Malaysia)

Ahmad Faris Mohd Adnan
(UM, Malaysia)

Ahmad Ridzwan Othman
(UiTM, Malaysia)

Arnis Asmat
(UiTM, Malaysia)

Aryani Ahmad Latiffi
(UTHM, Malaysia)

Azuddin Mamat
(UM, Malaysia)

Elvy Suhana Mohd Ramli
(UKM, Malaysia)

Hassimi Abu Hasan
(UKM, Malaysia)

Ismail Musirin
(UiTM, Malaysia)

Jamaluddin Mahmud
(UiTM, Malaysia)

Leny Suzana Suddin
(UiTM, Malaysia)

Lesley Maurice Bilung
(UNIMAS, Malaysia)

Mohamad Hasnul Bolhassan
(UNIMAS, Malaysia)

Mohammad Johari Ibahim
(UiTM, Malaysia)

Mohd Afian Omar
(SIRIM Berhad, Malaysia)

Mohd Fakhizan Romlie
(UTP, Malaysia)

Mohd Khairul Mohd Salleh
(UiTM, Malaysia)

Muhammad Ibrahim
(IIUM, Malaysia)

Musalmah Mazlan
(UiTM, Malaysia)

Nafisah Mohd Isa@Osman
(UiTM, Malaysia)

Nik Mohd Mazuan N. M. Rosdy
(UiTM, Malaysia)

Nik Rozlin Nik Mohd Masdek
(UiTM, Malaysia)

Noor Fitrah Abu Bakar
(UiTM, Malaysia)

Nor Afifah Yahaya
(UiTM, Malaysia)

Nor Farid Mohd Noor
(USM, Malaysia)

Nor Fazli Adull Manan
(UiTM, Malaysia)

Noreffendy Tamaldin
(UTeM, Malaysia)

Nurin Wahidah Mohd Zulkifli
(UM, Malaysia)

Nurul Zaizuliana Rois Anwar
(UNISZA, Malaysia)

Rahmath Abdulla
(UMS, Malaysia)

Rohah A. Majid
(UTM, Malaysia)

Rohana Hassan
(UiTM, Malaysia)

Rui Neves Madeira
(Polytechnic Institute of Setúbal, Portugal)

Sabrizan Osman
(Pejabat Kesihatan, Malaysia)

Sarina Sulaiman
(IIUM, Malaysia)

Shek Poi Ngian
(UTM, Malaysia)

Siti Amira Bte Othman
(UTHM, Malaysia)

Srazali Aripin
(IIUM, Malaysia)

Syahidah Akmal Muhammad
(USM, Malaysia)

Weitao Xu
(The University Of New South Wales, Australia)

Yoshinobu Shoji
(UiTM, Malaysia)

Zahurin Halim
(IIUM, Malaysia)

Zakiah Yusof
(UiTM, Malaysia)

Zar Chi Thent
(UiTM, Malaysia)

IIUM - International Islamic University of Malaysia
SIRIM - Scientific and Industrial Research Institute of Malaysia
UiTM - Universiti Teknologi MARA
UKM - Universiti Kebangsaan Malaysia
UM - Universiti Malaya

UNIMAS - Universiti Malaysia Sarawak
UPM - Universiti Putra Malaysia
USM - Universiti Sains Malaysia
UTeM - Universiti Teknikal Malaysia Melaka
UTHM - Universiti Tun Hussein Onn Malaysia

While every effort has been made to include a complete list of referees for the period stated above, however if any name(s) have been omitted unintentionally or spelt incorrectly, please notify the Chief Executive Editor, *Pertanika* Journals at nayan@upm.my.

Any inclusion or exclusion of name(s) on this page does not commit the *Pertanika* Editorial Office, nor the UPM Press or the University to provide any liability for whatsoever reason.

Pertanika Journals

Our goal is to bring high quality research to the widest possible audience

INSTRUCTIONS TO AUTHORS (Manuscript Preparation & Submission Guide)

Revised: June 2016

Please read the Pertanika guidelines and follow these instructions carefully. Manuscripts not adhering to the instructions will be returned for revision without review. The Chief Executive Editor reserves the right to return manuscripts that are not prepared in accordance with these guidelines.

MANUSCRIPT PREPARATION

Manuscript Types

Pertanika accepts submission of mainly **four** types of manuscripts for peer-review.

1. REGULAR ARTICLE

Regular articles are full-length original empirical investigations, consisting of introduction, materials and methods, results and discussion, conclusions. Original work must provide references and an explanation on research findings that contain new and significant findings.

Size: Generally, these are expected to be between 6 and 12 journal pages (excluding the abstract, references, tables and/or figures), a maximum of 80 references, and an abstract of 100–200 words.

2. REVIEW ARTICLE

These report critical evaluation of materials about current research that has already been published by organizing, integrating, and evaluating previously published materials. It summarizes the status of knowledge and outline future directions of research within the journal scope. Review articles should aim to provide systemic overviews, evaluations and interpretations of research in a given field. Re-analyses as meta-analysis and systemic reviews are encouraged. The manuscript title must start with "Review Article:".

Size: These articles do not have an expected page limit or maximum number of references, should include appropriate figures and/or tables, and an abstract of 100–200 words. Ideally, a review article should be of 7 to 8 printed pages.

3. SHORT COMMUNICATIONS

They are timely, peer-reviewed and brief. These are suitable for the publication of significant technical advances and may be used to:

- (a) report new developments, significant advances and novel aspects of experimental and theoretical methods and techniques which are relevant for scientific investigations within the journal scope;
- (b) report/discuss on significant matters of policy and perspective related to the science of the journal, including 'personal' commentary;
- (c) disseminate information and data on topical events of significant scientific and/or social interest within the scope of the journal.

The manuscript title must start with "*Brief Communication:*".

Size: These are usually between 2 and 4 journal pages and have a maximum of three figures and/or tables, from 8 to 20 references, and an abstract length not exceeding 100 words. Information must be in short but complete form and it is not intended to publish preliminary results or to be a reduced version of Regular or Rapid Papers.

4. OTHERS

Brief reports, case studies, comments, concept papers, Letters to the Editor, and replies on previously published articles may be considered.

PLEASE NOTE: NO EXCEPTIONS WILL BE MADE FOR PAGE LENGTH.

Language Accuracy

Pertanika **emphasizes** on the linguistic accuracy of every manuscript published. Articles must be in **English** and they must be competently written and argued in clear and concise grammatical English. Contributors are strongly advised to have the manuscript checked by a colleague with ample experience in writing English manuscripts or a competent English language editor.

Author(s) **must provide a certificate** confirming that their manuscripts have been adequately edited. A proof from a recognised editing service should be submitted together with the cover letter at the time of submitting a manuscript to Pertanika. **All editing costs must be borne by the author(s)**. This step, taken by authors before submission, will greatly facilitate reviewing, and thus publication if the content is acceptable.

Linguistically hopeless manuscripts will be rejected straightaway (e.g., when the language is so poor that one cannot be sure of what the authors really mean). This process, taken by authors before submission, will greatly facilitate reviewing, and thus publication if the content is acceptable.

MANUSCRIPT FORMAT

The paper should be submitted in one column format with at least 4cm margins and 1.5 line spacing throughout. Authors are advised to use Times New Roman 12-point font and *MS Word* format.

1. Manuscript Structure

Manuscripts in general should be organised in the following order:

Page 1: Running title

This page should **only** contain the running title of your paper. The running title is an abbreviated title used as the running head on every page of the manuscript. The running title should not exceed 60 characters, counting letters and spaces.

Page 2: Author(s) and Corresponding author information.

This page should contain the **full title** of your paper not exceeding 25 words, with name(s) of all the authors, institutions and corresponding author's name, institution and full address (Street address, telephone number (including extension), hand phone number, and e-mail address) for editorial correspondence. First and corresponding authors must be clearly indicated.

The names of the authors may be abbreviated following the international naming convention. e.g. Salleh, A.B.¹, Tan, S.G^{2*}., and Sapuan, S.M³.

Authors' addresses. Multiple authors with different addresses must indicate their respective addresses separately by superscript numbers:

George Swan¹ and Nayan Kanwal²

¹Department of Biology, Faculty of Science, Duke University, Durham, North Carolina, USA.,

²Office of the Deputy Vice Chancellor (R&I), Universiti Putra Malaysia, Serdang, Malaysia.

A **list** of number of **black and white / colour figures and tables** should also be indicated on this page. Figures submitted in color will be printed in colour. See "5. Figures & Photographs" for details.

Page 3: Abstract

This page should **repeat** the **full title** of your paper with only the **Abstract** (the abstract should be less than 250 words for a Regular Paper and up to 100 words for a Short Communication), and **Keywords**.

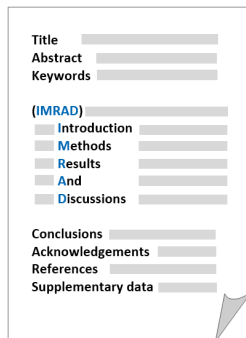
Keywords: Not more than eight keywords in alphabetical order must be provided to describe the contents of the manuscript.

Page 4: Introduction

This page should begin with the **Introduction** of your article and followed by the rest of your paper.

2. Text

Regular Papers should be prepared with the headings *Introduction, Materials and Methods, Results and Discussion, Conclusions, Acknowledgements, References, and Supplementary data* (if available) in this order.



Title _____
 Abstract _____
 Keywords _____
 (IMRAD)
 Introduction _____
 Methods _____
 Results _____
 And _____
 Discussions _____
 Conclusions _____
 Acknowledgements _____
 References _____
 Supplementary data _____

MAKE YOUR ARTICLES AS CONCISE AS POSSIBLE

Most scientific papers are prepared according to a format called IMRAD. The term represents the first letters of the words Introduction, Materials and Methods, Results, And, Discussion. It indicates a pattern or format rather than a complete list of headings or components of research papers; the missing parts of a paper are: Title, Authors, Keywords, Abstract, Conclusions, and References. Additionally, some papers include Acknowledgments and Appendices.

The Introduction explains the scope and objective of the study in the light of current knowledge on the subject; the Materials and Methods describes how the study was conducted; the Results section reports what was found in the study; and the Discussion section explains meaning and significance of the results and provides suggestions for future directions of research. The manuscript must be prepared according to the Journal's instructions to authors.

3. Equations and Formulae

These must be set up clearly and should be typed double spaced. Numbers identifying equations should be in square brackets and placed on the right margin of the text.

4. Tables

All tables should be prepared in a form consistent with recent issues of Pertanika and should be numbered consecutively with Roman numerals. Explanatory material should be given in the table legends and footnotes. Each table should be prepared on a new page, embedded in the manuscript.

When a manuscript is submitted for publication, tables must also be submitted separately as data - .doc, .rtf, Excel or PowerPoint files- because tables submitted as image data cannot be edited for publication and are usually in low-resolution.

5. Figures & Photographs

Submit an **original** figure or photograph. Line drawings must be clear, with high black and white contrast. Each figure or photograph should be prepared on a new page, embedded in the manuscript for reviewing to keep the file of the manuscript under 5 MB. These should be numbered consecutively with Roman numerals.

Figures or photographs must also be submitted separately as TIFF, JPEG, or Excel files- because figures or photographs submitted in low-resolution embedded in the manuscript cannot be accepted for publication. For electronic figures, create your figures using applications that are capable of preparing high resolution TIFF files. In general, we require **300 dpi** or higher resolution for **coloured and half-tone artwork**, and **1200 dpi or higher** for **line drawings** are required.

Failure to comply with these specifications will require new figures and delay in publication.

NOTE: Illustrations may be produced in colour at no extra cost at the discretion of the Publisher; the author could be charged Malaysian Ringgit 50 for each colour page.

6. References

References begin on their own page and are listed in alphabetical order by the first author's last name. Only references cited within the text should be included. All references should be in 12-point font and double-spaced.

NOTE: When formatting your references, please follow the **APA reference style** (6th Edition). Ensure that the references are strictly in the journal's prescribed style, failing which your article will **not be accepted for peer-review**. You may refer to the *Publication Manual of the American Psychological Association* for further details (<http://www.apastyle.org/>).

7. General Guidelines

Abbreviations: Define alphabetically, other than abbreviations that can be used without definition. Words or phrases that are abbreviated in the introduction and following text should be written out in full the first time that they appear in the text, with each abbreviated form in parenthesis. Include the common name or scientific name, or both, of animal and plant materials.

Acknowledgements: Individuals and entities that have provided essential support such as research grants and fellowships and other sources of funding should be acknowledged. Contributions that do not involve researching (clerical assistance or personal acknowledgements) should **not** appear in acknowledgements.

Authors' Affiliation: The primary affiliation for each author should be the institution where the majority of their work was done. If an author has subsequently moved to another institution, the current address may also be stated in the footer.

Co-Authors: The commonly accepted guideline for authorship is that one must have substantially contributed to the development of the paper and share accountability for the results. Researchers should decide who will be an author and what order they will be listed depending upon their order of importance to the study. Other contributions should be cited in the manuscript's Acknowledgements.

Copyright Permissions: Authors should seek necessary permissions for quotations, artwork, boxes or tables taken from other publications or from other freely available sources on the Internet before submission to Pertanika. Acknowledgement must be given to the original source in the illustration legend, in a table footnote, or at the end of the quotation.

Footnotes: Current addresses of authors if different from heading may be inserted here.

Page Numbering: Every page of the manuscript, including the title page, references, tables, etc. should be numbered.

Spelling: The journal uses American or British spelling and authors may follow the latest edition of the Oxford Advanced Learner's Dictionary for British spellings.

SUBMISSION OF MANUSCRIPTS

Owing to the volume of manuscripts we receive, we must insist that all submissions be made electronically using the **online submission system ScholarOne™**, a web-based portal by Thomson Reuters. For more information, go to our web page and [click "Online Submission"](#).

Submission Checklist

1. **MANUSCRIPT:** Ensure your MS has followed the Pertanika style particularly the first four pages as explained earlier. The article should be written in a good academic style and provide an accurate and succinct description of the contents ensuring that grammar and spelling errors have been corrected before submission. It should also not exceed the suggested length.

COVER LETTER: All submissions must be accompanied by a cover letter detailing what you are submitting. Papers are accepted for publication in the journal on the understanding that the article is **original** and the content has **not been published** either **in English** or **any other language(s)** or **submitted for publication elsewhere**. The letter should also briefly describe the research you are reporting, why it is important, and why you think the readers of the journal would be interested in it. The cover letter must also contain an acknowledgement that all authors have contributed significantly, and that all authors have approved the paper for release and are in agreement with its content.

The cover letter of the paper should contain (i) the title; (ii) the full names of the authors; (iii) the addresses of the institutions at which the work was carried out together with (iv) the full postal and email address, plus telephone numbers and emails of all the authors. The current address of any author, if different from that where the work was carried out, should be supplied in a footnote.

The above must be stated in the cover letter. Submission of your manuscript will not be accepted until a cover letter has been received.

2. **COPYRIGHT:** Authors publishing the Journal will be asked to sign a copyright form. In signing the form, it is assumed that authors have obtained permission to use any copyrighted or previously published material. All authors must read and agree to the conditions outlined in the form, and must sign the form or agree that the corresponding author can sign on their behalf. Articles cannot be published until a signed form (*original pen-to-paper signature*) has been received.

Please do **not** submit manuscripts to the editor-in-chief or to any other office directly. Any queries must be directed to the **Chief Executive Editor's** office via email to nayan@upm.my.

Visit our Journal's website for more details at <http://www.pertanika.upm.edu.my/home.php>.

HARDCOPIES OF THE JOURNALS AND OFF PRINTS

Under the Journal's open access initiative, authors can choose to download free material (via PDF link) from any of the journal issues from Pertanika's website. Under "**Browse Journals**" you will see a link, "*Current Issues*" or "*Archives*". Here you will get access to all current and back-issues from 1978 onwards.

The **corresponding author** for all articles will receive one complimentary hardcopy of the journal in which his/her articles is published. In addition, 20 off prints of the full text of their article will also be provided. Additional copies of the journals may be purchased by writing to the Chief Executive Editor.



Why should you publish in

Pertanika?

BENEFITS TO AUTHORS

PROFILE: Our journals are circulated in large numbers all over Malaysia, and beyond in Southeast Asia. Our circulation covers other overseas countries as well. We ensure that your work reaches the widest possible audience in print and online, through our wide publicity campaigns held frequently, and through our constantly developing electronic initiatives such as Web of Science Author Connect backed by Thomson Reuters.

QUALITY: Our journals' reputation for quality is unsurpassed ensuring that the originality, authority and accuracy of your work are fully recognised. Each manuscript submitted to Pertanika undergoes a rigid originality check. Our double-blind peer refereeing procedures are fair and open, and we aim to help authors develop and improve their scientific work. Pertanika is now over 38 years old; this accumulated knowledge has resulted in our journals being indexed in SCOPUS (Elsevier), Thomson (ISI) Web of Science™ Core Collection, Emerging Sources Citation Index (ESCI), Web of Knowledge [BIOSIS & CAB Abstracts], EBSCO, DOAJ, ERA, AGRICOLA, Google Scholar, ISC, TIB, Journal Guide, Citefactor, Cabell's Directories and MyCite.

AUTHOR SERVICES: We provide a rapid response service to all our authors, with dedicated support staff for each journal, and a point of contact throughout the refereeing and production processes. Our aim is to ensure that the production process is as smooth as possible, is borne out by the high number of authors who prefer to publish with us.

CODE OF ETHICS: Our Journal has adopted a Code of Ethics to ensure that its commitment to integrity is recognized and adhered to by contributors, editors and reviewers. It warns against plagiarism and self-plagiarism, and provides guidelines on authorship, copyright and submission, among others.

PRESS RELEASES: Landmark academic papers that are published in Pertanika journals are converted into press-releases as a unique strategy for increasing visibility of the journal as well as to make major findings accessible to non-specialist readers. These press releases are then featured in the university's UK and Australian based research portal, ResearchSEA, for the perusal of journalists all over the world.

LAG TIME: The elapsed time from submission to publication for the articles averages 3 to 4 months. A decision on acceptance of a manuscript is reached in 3 to 4 months (average 14 weeks).



Address your submissions to:
The Chief Executive Editor
Tel: +603 8947 1622
nayan@upm.my

Journal's Profile: www.pertanika.upm.edu.my/

Call for Papers 2017-18

now accepting submissions...

Pertanika invites you to explore frontiers from all key areas of agriculture, science and technology to social sciences and humanities.

Original research and review articles are invited from scholars, scientists, professors, post-docs, and university students who are seeking publishing opportunities for their research papers through the Journal's three titles; JTAS, JST & JSSH. Preference is given to the work on leading and innovative research approaches.

Pertanika is a fast track peer-reviewed and open-access academic journal published by Universiti Putra Malaysia. To date, Pertanika Journals have been indexed by many important databases. Authors may contribute their scientific work by publishing in UPM's hallmark SCOPUS & ISI indexed journals.

Our journals are open access - international journals. Researchers worldwide will have full access to all the articles published online and be able to download them with zero subscription fee.

Pertanika uses online article submission, review and tracking system for quality and quick review processing backed by Thomson Reuter's ScholarOne™. Journals provide rapid publication of research articles through this system.

For details on the Guide to Online Submissions, please visit http://www.pertanika.upm.edu.my/guide_online_submission.php

About the Journal

Pertanika is an international multidisciplinary peer-reviewed leading journal in Malaysia which began publication in 1978. The journal publishes in three different areas — Journal of Tropical Agricultural Science (JTAS); Journal of Science and Technology (JST); and Journal of Social Sciences and Humanities (JSSH). All journals are published in English.

JTAS is devoted to the publication of original papers that serves as a forum for practical approaches to improving quality in issues pertaining to tropical agricultural research- or related fields of study. It is published four times a year in *February, May, August* and *November*.

JST caters for science and engineering research- or related fields of study. It is published twice a year in *January* and *July*.

JSSH deals in research or theories in social sciences and humanities research. It aims to develop as a flagship journal with a focus on emerging issues pertaining to the social and behavioural sciences as well as the humanities, particularly in the Asia Pacific region. It is published four times a year in *March, June, September* and *December*.



An Award-winning
International-Malaysian Journal
— CREAM AWARD, MoHE
—Sept 2015





CFD Analysis on Indoor Temperature and Velocity: Effects of Incident Wind Angle and Outlet Position <i>Ali, N. M., Abd Razak, A., Mohamad, M. F. and Bahsan, R.</i>	227
Investigation of the Injection Moulding Plastic Flows Behaviour of PETCylindrical Containers with Multiple-Cavity Mould <i>Najiy Rizal Suriani Rizal, Muhammad Ameer Rosman, Aidah Jumahat and Noriah Yusoff</i>	239
Equivalent Dose Measurements from Digital Intra- and Extra- Oral Imaging Examinations <i>Norfariha Che Mohamed, Hapizah Nawawi, Mohd Yusmiadil Putera Mohd Yusof and Khoo Kok Siong</i>	251
Impact of Container, Temperature and Microcarriers on Inflammation and Endothelial Activation in Human Endothelial Cells <i>Muid, S., Froemming, G. R. A., Ali, A. M. and Nawawi, H.</i>	263
Low-Density Lipoprotein Concentration is an Independent Predictor for Oxidised LDL in Patients with Familial Hypercholesterolaemia <i>Nur Suhana Hamzan, Radzi Rahmat, Hapizah Mohd Nawawi and Thuhairah Hasrah Abdul Rahman</i>	275
Ceiling Geometry and Daylighting Performance of Side Lit Historical Museum Galleries UnderTropical Overcast Sky Condition <i>Sabarinah Sh Ahmad, Noraini Ahmad and Anuar Talib</i>	287
Tensile and Compressive Properties of Unidirectional <i>Arenga Pinnata</i> Fibre Reinforced Epoxy Composite <i>Aidah Jumahat, Muhamad Faris Syafiq Khalid, Zuraidah Salleh and Mohammad Jawaid</i>	299
Hole Size Effects on the Open Hole Tensile Properties of Woven Kevlar-Glass Fibre Hybrid Composite Laminates <i>Norazean Shaari and Aidah Jumahat</i>	309

Optimisation of Biomethane Production by Anaerobic Digestion of Food Waste <i>Nurul Shahida Osman, Zainon Mohd Noor, Zatilfaridah Rasdi, Iwana Izni Zainuddin and Noor Azrini Umor</i>	101
Effects of Varying Impedance Parameters for Position-based Impedance Control of A Three-fingered Robot <i>Nasir, K., Shauri, R. L. A., Salleh, N. M. and Remeli, N. H.</i>	111
Concentrated Solar Thermal Thermoelectric Power Generation under Natural and Forced Convection Cooling <i>Dee, S., Singh, B., Remeli, M. F., Tan, L. and Oberoi, A.</i>	123
Somatic Embryogenesis in Sugar Palm (<i>Arenga pinnata</i> Wurm. Merr.) from Zygotic Embryo Explants <i>Nazatul Asikin Muda and Asmah Awal</i>	133
Synchronisation of Output Voltage Waveforms in Phase Synchronous inverter with LCL Filter for Smart Grid Systems <i>Tawfikur Rahman, M. I. Ibrahimy and S. M. A. Motakabber</i>	145
Physico-chemical Properties of Residual Oil Extracted from Oil Palm Decanter Cake <i>Suhaini Raeze, Alawi Sulaiman, Azhari Samsu Baharuddin, Mohd Noriznan Mokhtar and Zainuri Busu</i>	157
Determinants of Patient's Satisfaction towards Hospital Services in a Specialist Centre <i>Siti Munira Yasin, Nazri Syamil Abdull Latip, Farnaza Ariffin, Hilwati Hashim and Mazlifah Omar</i>	169
Design of Perfect Tracking Self-Tuning Fuzzy PID Controller with Reference Model <i>Nur Sakinah Abdul Aziz, Mazidah Tajjudin and Ramli Adnan</i>	179
Synthesis and Corrosion Inhibition Studies of N-((4 and 3-chlorophenyl) carbamothioyl) Benzamide in 1M H ₂ SO ₄ <i>Norsakina Zurina Zulkifli, Karimah Kassim and Nurul Atikah Nordin</i>	189
Effect of Operating Parameters on Decolourisation of Palm Oil Mill Effluent (POME) using Electrocoagulation Process <i>Nur Syuhaidah Mohd Aris, Shariff Che Ibrahim, Borhannuddin Arifin and Yahaya Hawari</i>	197
The Impact of Vegetation on the Local Variations of Rainfall <i>Rohayu Haron Narashid, Ruslan Rainis and Zulyadini A. Rahaman</i>	207
Evaluation of Cold In-Place Recycling Mix using Polymer Modified Asphalt Emulsion <i>Mohd Izzat Asyraf Mohamad Kamal, Ahmad Kamil Arshad and Juraidah Ahmad</i>	219

Contents

Advances in Science & Technology Research

- Analysis of Agarwood Smoke Chemical Compounds using Solvent Trap, GC-FID and GC-MS 1
Nurlaila Ismail, Mastura Ibrahim, Seema Zareen, Mohd Hezri Fazalul Rahiman, Saiful Nizam Tajuddin and Mohd Nasir Taib
- Ammonia Nitrogen Adsorption using Spent Mushroom Substrate Biochar (SMSB) 9
Siti Fatimah Halim Soon Kong Yong and Chia Chay Tay
- Isolation and Adaptation of Diatoms in a New Formulated Enriched MediumS 21
Syafiq Hayati Mohd Ali, Khairul Adzfa Radzun and Norazlina Ahmad
- Low- Glycaemic Index Diet to Improve Dietary Intake among Women with Gestational Diabetes Mellitus 31
Farhanah, A. S., Barakatun Nisak, M. Y., Zalilah, M. S. and Nor Azlin, M. I.
- The Effect of Varying PID Gains on Position Transient Response of a Robotic Hand System 43
Salleh, N. M., Shauri, R. L. A., Nasir, K., Remeli, N. H. and Kamal, M. M.
- Classification of Car Paint Primers Using Pyrolysis-Gas Chromatography-Mass Spectrometry (Py-GC-MS) and Chemometric Techniques 53
Raja Zubaidah Raja Sabaradin, Norashikin Saim, Rozita Osman and Hafizan Juahir
- Experimental Study on Bearing Strength of Concrete Blocks under Concentric Compression Load 67
Mohd Raizamzamani Md Zain and Norrul Azmi Yahya
- Computational Simulation of Indoor Thermal Environment in a Tropical Educational Hall with Displacement Ventilation 77
Qi Jie Kwong, Hon Fai Chen and Azli Abd Razak
- Microstructure and Mechanical Properties of Hybrid Super ElasticNiTi Alloy with Steel Rebar for Reinforced Concrete Beam 89
Nubailah Abd. Hamid, Muhammad Akmal Ahmad Shazalli, Muhammad Hussain Ismail and Azmi Ibrahim



Pertanika Editorial Office, Journal Division
Office of the Deputy Vice Chancellor (R&I),
1st Floor, IDEA Tower II,
UPM-MTDC Technology Centre
Universiti Putra Malaysia
43400 UPM Serdang
Selangor Darul Ehsan
Malaysia

<http://www.pertanika.upm.edu.my/>
E-mail: executive_editor.pertanika@upm.my
Tel: +603 8947 1622/1620

PENERBIT
UPM
UNIVERSITI PUTRA MALAYSIA
PRESS

<http://penerbit.upm.edu.my>
E-mail : penerbit@putra.upm.edu.my
Tel : +603 8946 8855/8854
Fax : +603 8941 6172

